Multifunctional Glycan–Gold Nanoparticle Conjugates as DC–SIGN Targeted Nanomedicine against Viral Infection

Rahman Basaran

Submitted in accordance with the requirements for the degree of Doctor of Philosophy

The University of Leeds

School of Chemistry

March 2023

The candidate confirms that the work submitted is his own and that appropriate credit has been given where reference has been made to the work of others.

The right of Rahman Basaran to be identified as Author of this work has been asserted by his in accordance with the Copyright, Designs and Patents Act 1988.

© 2023 The University of Leeds and Rahman Basaran

In Loving Memory of My Grandpa, Osman Basaran

We lost him way too soon, but he shines on through….

I. Acknowledgements

Foremost, I would like to express my deepest gratitude to my primary supervisor, Professor Dejian Zhou, for his careful monitoring of my progress as well as for providing his invaluable guidance and continual support throughout my PhD. This would not have been possible without his insightful suggestions and comments. I would like to thank my second supervisor, Dr Yuan Guo, for her precious assistance and feedback greatly facilitated the way I conducted my research and interpreted my findings. As my supervisors constantly helped me on this journey with kindness, warmth, and understanding, which I have always much appreciated, I am extremely grateful to both. I would also like to thank the Turkish Ministry of National Education for giving me this opportunity and funding me as a PhD student in the UK.

I would like to sincerely thank Professor Stefan Pöhlmann and his research group (our collaborators in Germany) for their work on viral inhibition assays. I would like to thank Dr Nicole Hondow from Leeds Electron Microscopy and Spectroscopy Centre for providing the TEM images throughout this study. I would also like to acknowledge Professor Bruce Turnbull for assessing and providing feedback on my transfer and annual reports. I would like to thank the technician Dave Fogarty from the School of Chemistry for his technical help with the use of various lab equipment. I would also like to extend my thanks to Dr Terence Kee for his invaluable help and support throughout the most challenging stages of this dissertation.

Huge thanks go to all my lab-mates for being such a fantastic group of people, both in and out of the lab. I have learnt a lot together and really enjoyed working with them. It was a privilege to have shared these years. Big thanks to Yuanyuan for her warm friendship and intensive assistance with the synthesis experiments in the early stages of my PhD. Thanks to Emma for her support where required in the early times of this project. Thanks to Liz and Zeyang for our short but frequent talks we had in the lab. Many thanks to Akshath for helping with the synthesis of nanoparticles and also to whom he was a nice office mate. Our great pep talks were highly appreciated in tough times. Special thanks to Jamie for his help with protein production and making the lab work enjoyable. His infectious laugh and our funny talks will be missed. Finally, huge thanks to my lab-mate Darshita, who often brought me cakes, snacks, sweets, and so

on while I was struggling with my data for hours in my office. I am boundlessly thankful to her for always helping me out whenever I get stuck with something in my experiments and analysis or my daily life.

I would also like to thank my close friends, Taner, Yunus, Hüseyin, İnci Bahar and İbrahim, for relieving my stress by providing a way to have fun, even though they did not understand what I was doing for this thesis. Many thanks to my friends, Alican, and his wife, Melek, whom I met in Leeds and with whom I had a good time, for their funny friendships. Also, thanks to the people of Leeds Gorse Volleyball Academy, particularly the players of the team “Leeds Gators”, for providing a way of escaping from the chaotic situations of PhD life.

Of course, I cannot end my acknowledgement without thanking my wonderful family. Finishing my PhD studies without their unwavering support over the past years would have been impossible. I am forever grateful to my grandma, Hatice, my mum, Sitdıga, and my dad, Ahmet, for always being there whenever I need, believing in me and supporting me in every way. Without their constant love, I would not be in the position I am in today. The deepest thanks to my brother, Osman, and my sister, Ülkü, who are always there whenever I am in trouble, for their great help and encouragement. Big and special thanks to my lovely nieces, Ebrar Berra and Hatice Erva, with whom I always had a great time, for cheering me up when my mood was off while writing this thesis up. You both mean a lot to me. Also, many thanks to my aunt, Nevin, who is always a phone call away, for sharing my problems and always being supportive.

Finally, I turn to my wife, Pınar, without whom I would never have been able to complete this dissertation. Her endless love, moral support, and understanding were the shining light that beckoned me through my PhD. I am eternally grateful to her for spending the first years of her marriage with a man who was always experimenting in the lab. I reserve my heartfelt thanks to my son, Ahmet Arhan. Expecting the day when I would hold you in my arms was my biggest motivation which I turned to when I was struggling to get pen to paper. We are thrilled that you will be the meaning of our lives.

II. Abstract

Multivalent protein-carbohydrate interactions are of great importance in many biological processes, particularly in initiating pathogen-host cell contacts, which ultimately lead to infection. Elucidating the binding structures and patterns used within these interactions will play a key role in the design of specific and potent multivalent inhibitors against deadly viral infections such as HIV (human immunodeficiency virus), Ebola virus, and recently SARS-CoV-2 (severe acute respiratory syndrome-coronavirus-2). However, the underpinning structural mechanisms of some important multivalent protein-sugar interactions are still poorly understood, due to a lack of detailed structural information for these complex, multimeric and flexible cell membrane proteins. This work mainly focuses on elucidating the binding characteristics and structural mechanisms of two glycan binding proteins, DC-SIGN and DC-SIGNR (collectively abbreviated as DC-SIGN/R hereafter), a pair of closely related tetrameric lectins. Both DC-SIGN/R play a crucial role in facilitating virus infections by specific recognition of the high-mannose-containing glycans found on the viral surface envelopes to mediate the transmission of the virus to T cells. The key goals of this project are to understand the binding modes and mechanisms of these proteins with multivalent glycans so as to develop specific and potent multivalent inhibitors against DC-SIGN/R-mediated virus infections. Here, glycan coated-gold nanoparticle (GNP-glycans) are designed and produced as new structural and biophysical probes for DC-SIGN/R-based multivalent protein-glycan interactions. Their binding affinities with DC-SIGN/R are quantified through a new fluorescence quenching technique, taking the advantage of the GNP's excellent fluorescence quenching property. Moreover, their binding modes with DC-SIGN/R are revealed *via* dynamic light scattering and "cryo-snapshot" S/TEM imaging which measure the hydrodynamic size of binding induced protein-GNP assemblies and visualise the GNP-protein assemblies in their native dispersion state, respectively. Finally, the potencies of GNP-glycans in blocking cell surface DC-SIGN/R-mediated pseudo-Ebola virus cellular infections are also pursued and corrected to their solution binding affinity with soluble DC-SIGN/R molecules.

Chapter 2, GNPs of three different sizes (*e.g.* 5, 13 and 27 nm) were synthesised and employed as scaffolds to build up multivalent GNP-glycans to probe DC-SIGN/R-glycan multivalent binding mechanisms. A series of lipoic acid-oligo(ethylene glycol)-based glycan ligands (LA-EG_n-Man/-DiMan, where n = 2 and 4, and LA-EG_2-ManA, as positive DC-SIGN/R binding ligands) as well as LA-EG_n-OH (where n= 2 and 4, as negative controls) are successfully synthesised, purified, and characterised. A series of lipoic acid-poly(ethylene glycol)-based ligands (LA-$(PEG_{1000}\text{-}OH)_n$, where n= 1, 2, and 3, LA-PEG_{600}-OH, and LA-PEG_{750}-OMe) were also synthesised.

Chapter 3, the LA-EG_n-glycan ligands were used to coat citrate-stabilised GNPs *via* ligand exchange to prepare robust, compact, and multivalent GNP-glycans. Their binding affinities with fluorescent dye-labelled DC-SIGN/R were quantified from binding-induced quenching of the protein fluorescence. Significant results were obtained. First, increasing the GNP scaffold size enhanced the binding affinity with DC-SIGN/R. For instance, G27-DiMan bound more strongly to both DC-SIGN/R (K_ds: 0.2 nM for DC-SIGN, and 0.54 nM for DC-SIGNR) than its smaller Gx-DiMan (x=5 and 13 nm) counterparts, e.g. K_ds: 5.8 and 1.0 nM for DC-SIGN, and 14.9 and 2.7 for DC-SIGNR, respectively. This indicates that a larger GNP scaffold offers better spatial and orientation matches for surface glycans in binding to DC-SIGN/R. Second, a high glycan density strengthens GNP-glycan binding with both DC-SIGN/R. Third, the linker length also had a significant impact on GNP-glycans binding with DC-SIGN/R, particularly for smaller GNP scaffolds. Moreover, a new fluorescence quenching method has been developed to quantify the binding thermodynamics between DC-SIGN/R and GNP-glycan. DC-SIGN binding was found to be enthalpy-driven with significant entropy penalties. Whereas in DC-SIGNR, the binding enthalpic contribution was reduced, although the binding was compensated with a small favourable entropic contribution. Furthermore, GNP-glycans were found to potently block DC-SIGN/R-mediated pseudo-Ebola virus infection of host cells. For example, G27-EG_4-DiMan exhibited the remarkably low IC_{50} values of 23±1 pM and 49±2 pM against DC-SIGN- and DC-SIGNR-mediated virus infections, respectively, making it the most potent GNP-glycan based Ebola viral inhibitor ever reported.

Chapter 4, we studied the pH dependency of the DC-SIGN/R binding with GNP-glycans through fluorescence quenching and dynamic light scattering to monitor binding induced fluorescence quenching and hydrodynamic sizes of GNP-lectin complexes. Both DC-SIGN/R binding with GNP-glycans were pH-dependent: DC-SIGN binding was broadly stable (constant quenching) from pH 7.4 to 6.0, while that increased for DC-SIGNR, however, their bindings were both reduced from pH 6.0 to 4.6. Both DC-SIGN/R-GNP-glycans bindings were reversible in a pH-dependent manner.

Chapter 5, a new fluorescence quenching method was employed to study and quantify the protein corona formation on GNP-capped with various LA-PEG-ligands of varying PEG length and density. Non-target proteins, BSA (Bovine Serum Albumin) and Lys (Lysozyme), were observed to exhibit low binding affinities with such GNP-PEG conjugates with high K_d values, especially those constructed on ultra-small gold nanocluster scaffold. These proteins did not form stable protein corona layers on such PEGylated GNPs, showing that coating GNPs with LA-PEG ligands is highly effective in resisting non-specific protein interactions.

III. Table of Contents

IV. List of Schemes

V. List of Tables

VI. List of Figures

VII. List of Abbreviations

^{13}C-NMR	Carbon-13 Nuclear Magnetic Resonance
^{1}H-NMR	Proton Nuclear Magnetic Resonance
ACE2	Angiotensin-converting Enzyme 2
BSA	Bovine Serum Albumin
CBP	Carbohydrate-binding proteins
$CDCl_3$	Chloroform-d
CH_2Cl_2	Dichloromethane
$CHCl_3$	Chloroform
CLRs	C-type lectin receptors
CRD	Carbohydrate Recognition Domains
CuAAC	Cu (I)-catalysed Huisgen 1-3-dipolar [3+2] Cycloaddition
DCC	N,N'-Dicyclohexylcarbodiimide
DCs	Dendritic Cells
DC-SIGN	Dendritic-cell-Specific Intercellular Adhesion Molecule
DC-SIGNR	DC-SIGN Related Receptor
D_h	Hydrodynamic Diameter
DHLA	Dihydrolipoic Acid
DiMan	Disaccharide (Mannose-α-1,2-mannose)
DLS	Dynamic Light Scattering
DMAP	4-Dimethylaminopyridine
DMSO	Dimethyl Sulfoxide
EBOV-GP	Ebola Virus Glycoprotein
EDTA	Ethylenediaminetetraacetic Acid
EG	Ethylene Glycol
EtOAc	Ethyl Acetate
EtOH	Ethanol
FDA	Food and Drug Administration
FRET	Förster/ Fluorescence Resonance Energy Transfer
FWHM	Full width at Half Maximum
GNPs, GNRs	Gold Nanoparticles, Gold Nanorods

gp120	Glycoprotein 120
$HAuCl_4$	Chloroauric Acid
HCV	Hepatitis C
HEPES	4-(2-hydroxyethyl)-1-piperazineethanesulfonic acid
HIV	Human Immunodeficiency Virus
HR-MS	High-Resolution Mass Spectra
IC_{50}	Half Maximal Inhibitory Concentration
ICAM-2 /-3	Intercellular Adhesion Molecule-2 / -3
IPTG	Isopropyl β-D-1-thiogalactopyranoside
ITC	Isothermal Titration Calorimetry
ITPG	Isopropyl β-D-1-Thiogalactopyranoside
K_d	Apparent Binding Affinity (Dissociation Constant)
KOH	Potassium Hydroxide
kpsi	Kilo Pounds Per Square Inch
LA	Lipoic Acid
LB	Lysogeny Broth
LC-MS	Liquid Chromatography – Mass Spectrometry
LSPR	Localized Surface Plasmon Resonance
Lys	Lysozyme
Man	Mannose
ManA	Carboxylated Mannose
MBP	Mannose-binding Protein
MeOH	Methanol
MES	2-(N-morpholino) Ethane Sulfonic Acid
$MgSO_4$	Magnesium Sulphate
MLV	Murine Leukaemia Virus
MS	Mass Spectrometry
MWCO	Molecular Weight Cut Off
Na_2CO_3	Sodium Carbonate
Na_2SO_4	Sodium Sulphate
$NaBH_4$	Sodium borohydride
$NaHCO_3$	Sodium Hydrogen Carbonate

NIR	Near-infrared Region
NLRs	NOD-like Receptors
NPs	Nanoparticles
NSET	Nanometal Surface Energy Transfer
PAMPs	Pathogen-specific Carbohydrate-containing Molecular Patterns
pcDNA	Empty Plasmid
PdI	Polydispersity Index
PEG	Poly (ethylene glycol)
PMT	Photomultiplier Tube
PPh_3	Triphenylphosphine
PRRs	Pattern Recognition Receptors
QD	Quantum Dot
QE	Quenching Efficiency
R_f	Retention Factor
RLRs	Rig-I-like Receptors
rpm	Rotations Per Minute
RT	Room Temperature
SARS-CoV	Severe Acute Respiratory Syndrome-associated Coronavirus
SPAAC	Strain-promoted Azide-alkyne Cycloaddition
TBTA	Tris-(1-benzyl-4-triazolyl methyl)-amine
TCEP.HCl	Tris(2-Carboxyethyl)phosphine Hydrochloride
TEM	Transition Electron Microscopy
THF	Tetrahydrofuran
TLC	Thin Layer Chromatography
TLRs	Toll-like Receptors
TSPR	Transverse Surface Plasmon Resonance
UV-Vis	Ultraviolet – Visible
VSV-G	Vesicular Stomatitis Virus Glycoprotein
WT	Wild-type
ZW	Zwitterion

Chapter 1
Introduction

The realm of nanotechnology refers to all interdisciplinary efforts to understand the atomic and molecular world at the nanoscale, particularly in the 1-100 nm range, and to integrate them into the macroworld. The processes operate differently in the nanoworld, where the laws of science change. For instance, metallic gold, which we see as yellow in colour in the daily life, appears in different colours such as red, blue, and purple in the nanoworld, depending on its size and shape. Moreover, bulk gold is almost chemically inert, but gold in the nanoscale displays high chemical reactivity. Therefore, the distinct and tuneable physical, chemical, and biological properties of nanosized particles make them unique compared to their bulk materials. Given that the key driving force behind nanotechnological developments is to understand biological systems, harnessing the superior properties of nanoparticles can have a potential game-changer effect by bringing in new perspectives to chemical biology research. Since cell components are of the nano-size range, and notably proteins are typically around 5-10 nm in size,[1] this allows us the ability of nanotechnology to intervene and manipulate the biochemical mechanisms occurring both on cell surface and inside cells. While nanotechnology is still far from being able to control cellular mechanisms with high efficiency and precision. However, the increased knowledge gained from the intensive research on the rational design and use of nanobiotechnological tools, particularly over the last two decades, reveals that this field holds great promises. Of course, there is still much more to learn from this ground-breaking field.

This chapter first focuses on the background literature review regarding the structural, mechanical, and binding properties of two important viral receptors, DC-SIGN and DC-SIGNR (collectively abbreviated as DC-SIGN/R hereafter), and their roles in viral infection, and then the features, synthesis, characterisation, and surface functionalization of gold nanoparticles and also their ability to protein corona formation.

1.1. The Receptor Proteins DC-SIGN/R

1.1.1. The Role of Dendritic Cells in Viral Infections

The immune system is a complex organization of molecules and cells interacting with each other to recognize and eliminate invading pathogens and then form their immunological memories. Dendritic cells (DCs), the most efficient antigen-presenting cells, are central to generating immune responses and long-term protective immunity against pathogens by linking with the innate (natural) and adaptive (acquired) immune systems.[2] Immature dendritic cells are localized in peripheral mucosal tissues, which are also known as immunological sensors. When stimulated, they can induce an effective immune response to screen and remove pathogens, transmitting their information to lymphocytes. Once DCs sense and catch a pathogen, they undergo significant alterations, resulting in dendritic cell maturation, which occurs in their migration process from peripheral mucosal tissues to lymph nodes. Besides detecting pathogens and then presenting the processed antigens to T cells, DCs also express some stimulating agents to regulate effective T-cell induction.[3] Therefore, they are vital targets for manipulating the immune system and developing immunotherapeutic agents.

All cells are coated with dense carbohydrate moieties displayed on protein (glycoproteins) and lipid (glycolipids) scaffolds, forming the glycocalyx structures on the cell membranes which are involved in complicated biological processes such as intercellular interactions and cell-cell signalling.[4] Glycan profiles of pathogens are recognized by specific pattern recognition receptors (PRRs) on DCs that initiate and regulate immune pathways in response to stimuli from their environment. Different PRR classes recognize a broad range of pathogen-specific carbohydrate-containing molecular patterns (PAMPs) via carbohydrate-binding proteins (CBP) to distinguish between different types of pathogens and stimulate different programs that lead to specific immune responses, allowing DCs to perform their functions. Over 80 human CBPs have been introduced to date, which are promising targets for developing anti-infective therapies.[5, 6] Therefore, the elucidation of their binding characteristics and glycan-binding epitopes is crucial for developing potential anti-pathogenic treatment strategies. Several PRR classes are defined based on their structural properties and

their ability to induce a pathogen-adaptive immune response, including Toll-like receptors (TLRs), NOD-like receptors (NLRs), Rig-I-like receptors (RLRs), and C-type lectin receptors (CLRs).[6]

1.1.2. C-type Lectins

Lectins, known as carbohydrate-binding proteins, are ubiquitous in nature and have unique properties that contribute to the initiation of many biological processes owing to their specific and reversible interactions with carbohydrates. Different types of lectins with different multivalent binding affinities for various carbohydrates have been identified and isolated from plants, animals, and microorganisms. However, animal lectins are more complex than others despite increased knowledge about their structures and functions. C-type animal lectins are particularly notable for immunity as they can interact with a wide array of carbohydrates presented on self-antigens and pathogens.[7] They are Ca^{2+}-dependent carbohydrate-binding proteins and play essential roles in the maintenance of immune homeostasis, including cell-pathogen and cell-cell adhesion, cell signalling, and migration.[7, 8]

The hallmark of C-type lectins is that they have one or multiple carbohydrate recognition domains (CRDs), which are responsible for the Ca-dependent selective binding of various carbohydrates. The primary glycan binding sites in lectins are mediated by a Ca^{2+} ion, where glycans directly coordinates to the Ca^{2+} ion via its 3- and 4-OH groups which is the main reason for why lectins have Ca^{2+}-dependent binding.[9] An example binding interaction of a carbohydrate with a lectin CRD is shown in **Figure 1.1.1** below. Feinberg *et al.*[10] have reported that mannose oligosaccharides on pathogens bind to C-type lectin CRDs via principal calcium ion by direct interaction of vicinal hydroxyl groups on the pyranose ring of mannose. They have also noted that the particular specificity for some oligosaccharides arises due to additional contacts to the flanking sides of the CRDs.[10] Of particular interest here are the C-type lectins DC-SIGN and DC-SIGNR, whose structures and functions are described in the following section.

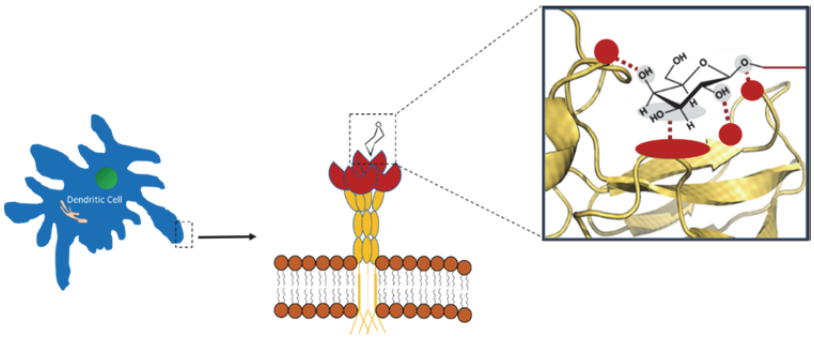

Figure 1.1.1. A schematic illustrating the binding of a sugar with the carbohydrate recognition domain of a lectin protein on a dendritic cell surface. Modified and adapted from the reference [11].

1.1.2.1. DC-SIGN

DC-SIGN (Dendritic Cell-Specific Intercellular adhesion molecule Grabbing Non-integrin), a dendritic cell lectin, is a tetrameric type-II (cytoplasmic N terminal domain) transmembrane protein involved in the initial steps of the immune response.[12] It mediates the recognition of pathogen-associated carbohydrate ligands, as well as the interactions between DCs and T cells through binding to ICAM-3 and ICAM-2 on the T cells.[13] The DC-SIGN gene is located on the human chromosome 19p13.3. It was first sequenced in the early 1990s after its ability to bind to glycoproteins, gp120, on the HIV, human immunodeficiency virus, was revealed.[14] DC-SIGN is found on the dendritic cells of the intestinal and genital mucosae, skin dermis, lymphoid organs, macrophages in the lung and placenta, and brain microvascular endothelial cells.[15, 16]

The molecular structure of DC-SIGN consists of an extracellular domain, a transmembrane domain, and an intracellular domain as shown schematically in **Figure 1.1.2**. The N-terminal tail of the protein is located in the cytoplasm and functions in recycling, internalization, and intracellular signalling processes.[16] The extracellular segment, consists of four carbohydrate recognition domains (CRDs) and a neck domain, and is responsible for glycan binding. The neck region is comprised of 7 repeats of highly conserved 23 amino-acid residues each and a half truncated repeat composed of 15 amino-acid segments at the N terminal.[17, 18] The neck region consists of a highly-structured α-helical coiled-coil that triggers the formation and stabilization of extracellular tetramer structure, which also allows for projecting the clustered CRDs away from the cell surface.[19] This domain may also act as a pH sensor, which is thought to regulate the affinity for carbohydrates.[20] DC-SIGN tetramerization entirely depends on the tandem repeats of the neck region; at least six repeats are required in order to

form stable tetramers.[18, 19] Its tetrameric structure also provides high-avidity multivalent binding structures, enabling stronger binding to pathogens with specific multivalent glycans.[14] However, DC-SIGN tetrameric structure differs from other multimeric C-type lectins such as trimeric mannose-binding protein (MBP). The diversity of oligomeric states within the same lectin family has presumably evolved them to contain different carbohydrate recognition patterns, which could also explain their distinct carbohydrate-binding specificities.[12, 21]

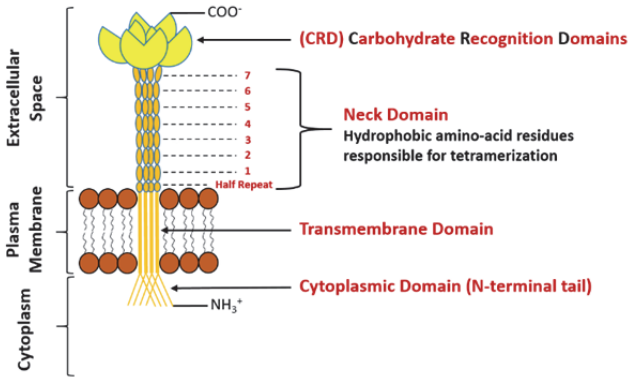

Figure 1.1.2. A schematic representation of DC-SIGN structure. Adapted and redrawn from the references [22, 23].

The CRDs are flexibly presented and projected away from the cell surface by the extended neck domain, allowing them to form the multivalent interactions with glycans presented with variable spacing on pathogens. Based on the crystal structure sizes, each CRD is ~3 nm in size.[9] A globular CRD is double-looped, consisting of 12 β-strands connected by 2 α-helices and 3 disulphide bonds.[15, 19, 24] A loop on the protein surface creates two Ca^{2+} binding sites; one provides the conformation of the carbohydrate recognition site, and the other is fundamental for the direct coordination of carbohydrate structures. The amino acid residues, including Phe313, Glu347, Asn349, Val 351, Glu354, Glu358, Ser360, Asn365, and Asp366, interact with the equatorial 3- and 4-hydroxyls of carbohydrates through the coordination of Ca ion in this site.[10] This motif is associated with the binding specificity of the mannose-containing carbohydrate structures,[19] as shown in **Figure 1.1.3** below. Mutations in this region result in the loss of glycan ligand binding properties.[21]

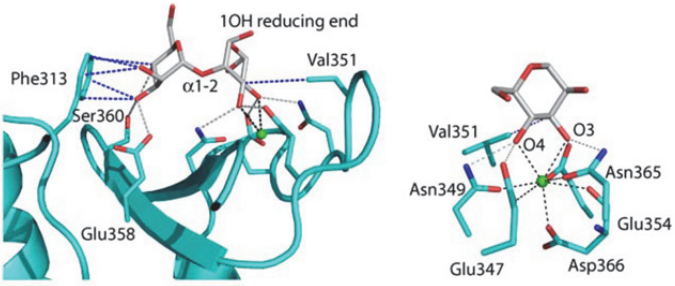

Figure 1.1.3. A schematic illustrating the structure of a DC-SIGN CRD bound to a sugar. In these ribbon diagrams, DCSIGN and the carbohydrate are given in cyan and grey, respectively. Calcium atoms are shown as green spheres. Ca^{2+} coordination bonds, hydrogen bonds, and van der Waals interactions are represented as dashed black lines, grey lines, and blue lines, respectively. The diagram on the left is indicated the side view of binding, while the right one depicts a close-up view of the mannose bound to Ca^{2+}. Taken from the reference [10].

The CRDs have a high affinity to N-linked high mannose and Lewis-type glycans. This may be due to the alternative contacts with other terminal mannose groups at a secondary binding site within the CRD, or the primary binding site might be extended to enable interactions with sub-terminal mannoses.[12] DC-SIGN CRDs also bind to sugars containing galactose, glucose, and fucose moieties in a Ca^{2+}-dependent manner as reported in a recent paper by Martinez *et al.*[25]. Although it has been suggested that DC-SIGN CRDs could easily interact with closely spaced sugars on pathogens (~5 nm between sugar binding sites), more research data are still required to support this. Furthermore, Menon *et al.*[26] have shown that DC-SIGN CRDs have a degree of conformational flexibility upon ligand binding. This not only allows all CRDs to bind to the ligand but promotes selective and improved binding for various sugar patterns.[19] The ability of DC-SIGN to interact with differently spaced glycans provided by the flexibility of its CRDs probably increases the number of sugar ligands to which it can bind with high affinity, allowing for broad spectrum pathogen recognition.[27] Moreover, the CRDs are not held in fixed positions and may have the ability of re-orientation to interact with the ligands. Though the carbohydrate affinities of individual CRDs are roughly close to each other, the tetramer structure of DC-SIGN can enhance the affinity for sugars by holding the binding sites in relatively certain positions.[16] Intrinsically, binding of flexible CRDs to a multivalent ligand would result in CRDs being fixed in a specific orientation, which would lead to an entropy penalty. This entropy cost is more than compensated by the strongly favourable enthalpy gains by forming multiple CRD-glycan interactions.[23]

1.1.2.2. DC-SIGNR

DC-SIGNR, also known as L-SIGN, is a DC-SIGN related lectin receptor and, also a type-II transmembrane protein. The gene structures of DC-SIGN and its homologous DC-SIGNR are similar, and are 73% and 80% identical at nucleic acid level[16] and amino acid sequences,[28] respectively. It is thought that these are formed by duplicating a single ancestral gene. Similar to DC-SIGN, DC-SIGN/R can also interact with gp120, which mediates HIV-1 infection in trans and cis, and also ICAM-3. In contrast to the over-expressing of DC-SIGN onto dendritic cells, DC-SIGNR is mainly found on endothelial cells in the liver, lymph nodes, and placenta.[28] However, albeit at a low level, DC-SIGN is co-localized with DC-SIGNR on lymph nodes endothelium.[12]

DC-SIGN and DC-SIGNR are very close in the overall structure. The subtle sequence differences in their gene structures apparently set some distinct functions, such as the interactions of CRDs with carbohydrates, their sugar-binding affinity and specificity, tetramer stability, and intracellular trafficking.[17] In particular, the differences in the neck regions of DC-SIGN and DC-SIGNR are thought to affect their sugar recognition and sugar-binding affinity. Crystallographic studies have shown that, differently from DC-SIGN, the DC-SIGNR neck region consists of α-helices containing short non-helical parts, and these helices assemble via electrostatic and hydrophobic interactions.[29] These differences also have a significant functional impact on their overall stabilities. For example, the neck region of DC-SIGNR is more stable against thermal denaturation than that of DC-SIGN.[17] Moreover, the differences in the neck region of DC-SIGNR might substantially impact on the interactions of its CRDs. Research by Mitchell *et al.*[12] has found that DC-SIGNR has a notably greater affinity for the carbohydrate ligands containing close-spaced two oligosaccharides than that of DC-SIGN.

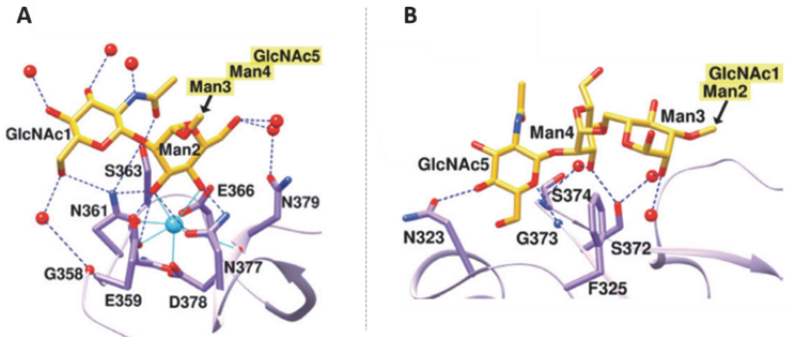

Figure 1.1.4. Interactions of the α-1-3-linked branch (A) and α-1-6-linked branch (B) of the molecule GlcNAc2-Man3 with DC-SIGNR. Only key sugars are given as ribbon diagrams and the remaining mannose residues are depicted as schematics. Ca^{2+} is shown as blue sphere, and Ca^{2+} coordination bonds and hydrogen bonds are given as blue lines and dashed lines, respectively. Reprinted from the reference [30].

DC-SIGNR is closely related to DC-SIGN in the similar CRD-glycan binding motif but is functionally different. DC-SIGNR similarly binds to mannose oligosaccharides, as shown in **Figure 1.1.4**, to that indicated for DC-SIGN. However, Guo *et al.*[31] revealed that DC-SIGNR does not bind to fucose-containing sugars such as Lewis, in glycan microarrays, which differ it from DC-SIGN.[31] This work clearly shows that DC-SIGN and DC-SIGNR have distinct ligand binding properties. The overall shape of their extracellular domains, which is not fully known, can be a crucial factor in their different ligand affinities. Based on their hydrodynamic studies, Feinberg *et al.*[23] proposed two major models for both proteins regarding the neck conformation and the arrangement of their CRDs; single tetrameric domain and Y-shaped dimers, as shown in **Figure 1.1.5** below.

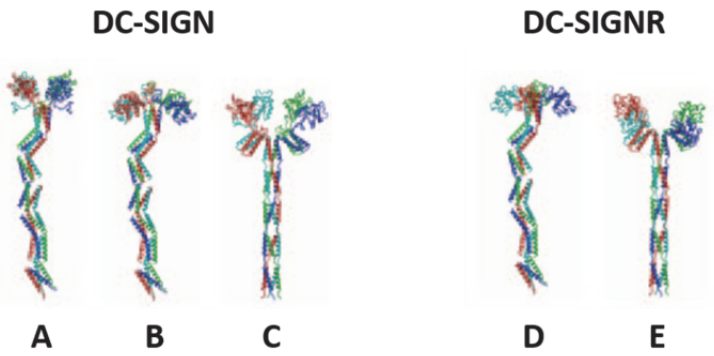

Figure 1.1.5. The predicted best-fitting models of the extracellular domains of both proteins DC-SIGN and DC-SIGNR. For DC-SIGN modelling, A and B illustrate the two single tetrameric stalk models, and C shows the Y-shaped dimer model. D and E depict the single tetrameric stalk and Y-shaped model for DC-SIGNR, respectively. Taken and adapted from the reference [23].

Furthermore, our research group has recently proposed that the orientations of CRDs in DC-SIGN/R are structurally different. As given in **Figure 1.1.6**, Guo *et al.*[32] suggested that all CRDs of DC-SIGN are uprightly faced, whereas these of DC-SIGNR are pointed in sidewardly, based on their very different binding properties with densely mono-mannose coated quantum dots (QD-Man). In this study, DC-SIGN was found to bind strongly with QD-Man, whereas DC-SIGNR showed no measurable binding. Given their CRD-Man monovalent binding motifs are identical based on their crystal structures (**Figure 1.1.4**), such differences must come from the different orientations of their CRDs. For DC-SIGN, its upwardly faced CRDs can easily bind to multiple Man onto the QD, leading to strong multivalent binding. However, sideway pointing CRDs in DC-SIGNR could not bind effectively to multiple Man on the same QD, resulting in weak binding.

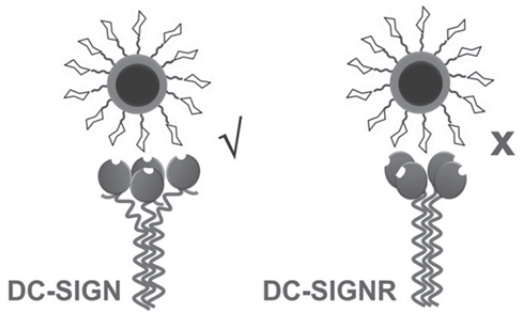

Figure 1.1.6. A schematic showing the proposed tetrameric structure for the proteins DC-SIGN/R by our research groups. Reprinted from the reference [32].

1.1.2.3. Pathobiology of DC-SIGN/R

DCs are essential for fighting against invading pathogens and regulating the immune response. DC-SIGN found on these cells can recognize and capture the viruses for further processing and presentation via binding to mannose glycans found on their envelopes, including HIV-1, HCV (Hepatitis C), Ebola virus, SARS-CoV (Severe acute respiratory syndrome-associated coronavirus), Dengue virus, and Lassa virus. Moreover, the interactions of DC-SIGN with mannose-containing oligosaccharides also enable the dendritic cell binding of some bacterial and parasitic pathogens, including yeast Candida albicans, Aspergillus fumigatus, Mycobacterium tuberculosis, Neisseria meningitidis, and Leishmania parasites. As DC-SIGN also binds to fucose-containing glycans, this receptor recognizes some pathogens through the fucose moieties on their surfaces, such as Helicobacter pylori and Schistosoma mansoni.[16, 30]

Compared to DC-SIGN, DC-SIGNR also exploits the same mannose-binding motif for many of the same viruses, including HIV-1, Ebola virus, and HCV, and therefore DC-SIGNR can also serve as a receptor for their entry and presentation. However, DC-SIGNR has different viral binding and processing properties, facilitating the interactions with endothelial cells. This distinguishes DC-SIGNR from DC-SIGN in terms of the process of some viruses in which they participate in their immunological fate. For example, Boily-Larouche *et al.*[33] highlighted that DC-SIGNR can be pivotal for HIV transmission from mother to child by crossing the placenta. Additionally, only DC-SIGNR, and not DC-SIGN, binds and transmits the West Nile Virus (WNV) with high efficiency, whereas DC-SIGN process some HIV species more efficiently than DC-SIGNR. Comprehensive analysis of the glycoproteins involved in the binding of these viruses has revealed that West Nile Virus cell surface glycoprotein E has only one glycosylation site,[34] whereas each HIV gp120 glycoprotein monomer contains 25 glycosylation sites.[35] This represents a strong evidence to exemplify their different sugar-binding properties and affinities. Even though it is still difficult to explain how DC-SIGNR binds better to West Nile Virus, this is most probably due to the differences underlying the interactions of their 4 CRDs with multiple oligosaccharides.[34] It is also noteworthy that SARS-CoV-2, a life-threatening severe pathogen that has spread rapidly throughout the world and caused the ongoing COVID-19 pandemic, can also employ these viral lectin receptors for cellular entry. ACE2, human angiotensin-converting enzyme 2, is the primary cell entry receptor for SARS-CoV-2. However, Amraei *et al.*[36] showed that SARS-CoV-2 internalization into tissues where ACE2 is absent or expressed at a low level could be driven by DC-SIGN and DC-SIGNR as the alternative receptors.

HIV is the most investigated virus regarding the internalization, processing, and presentation of pathogens through these proteins. Both DC-SIGN and DC-SIGNR initiate the pathogenesis by interacting with the N-linked high mannose glycans in the HIV envelope glycoprotein. These receptors can contribute to viral infection by either presenting viruses or facilitating viral entry into target cells. In particular, DC-SIGN can bind to HIV for up to several days with high affinity and transmit some HIV species more effectively than DC-SIGNR. Two potential mechanisms for DC-mediated HIV transmission have been proposed by Wu *et al.*[15] As highlighted below in **Figure 1.1.7**,

these are the "trans" and "cis" pathways, which have different criteria from each other. In HIV trans-infection, DC-SIGN acts as a binding receptor that facilitates the capture and transmission of HIV without infecting a dendritic cell. In other words, DC-SIGN is localized on a separate cell surface from the infected target cell and contributes to HIV transmission and spread in the host.[14] Upon binding DC-SIGN with HIV, it is mainly transmitted to outer environment accessible membrane bound vesicles, unlike most another viruses, and after their degradation, viruses can be processed and then presented to $CD4^+$ T cells to trigger an immune response. However, some viruses might escape neutralization in endo-lysosomal compartments and can be hidden in multivesicular bodies of DCs in an infectious state for days. They then infect $CD4^+$ T cells and thereby causing productive HIV infection.[16]

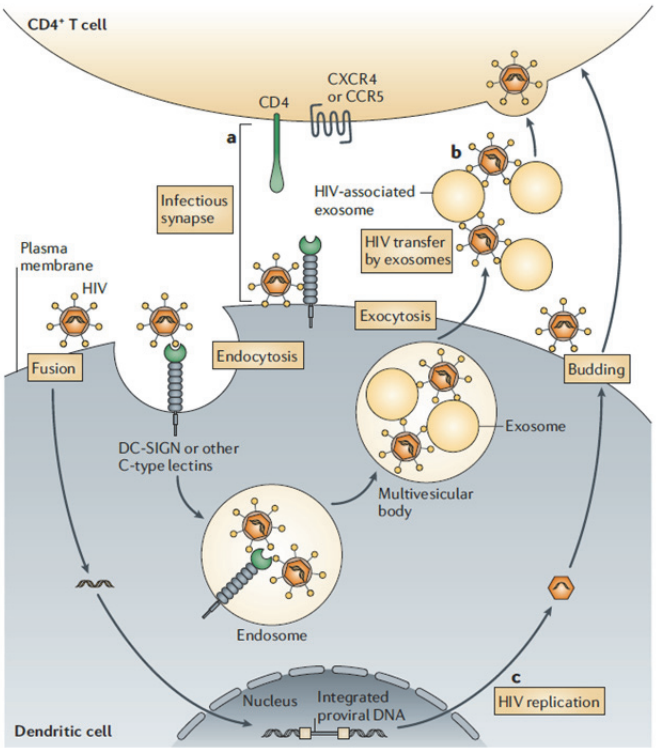

Figure 1.1.7. A schematic illustrating the mechanism of dendritic-cell mediated HIV transmission. Here, there are two different proposed pathways. The different mechanisms of trans-infection mediated by the dendritic cells are shown in pathways (a) and (b), and cis-infection is described in the pathway (c). Reprinted from the reference [15].

DC-SIGN-mediated HIV trans-infection can occur in two particular mechanisms. The first is that dendritic cells present HIV, which is captured by DC-SIGN, to T cells via "the infectious synapse". Another trans pathway is where HIV viruses infect the target cells by "exocytosis" using HIV-associated exosomes. Alternatively, another is the "cis

pathway" that HIV viruses are presented to T cells following the replication of HIV virions in infected DCs. Both pathways can function together for in long-term HIV transmission and infection,[15] but their contributions *in vivo* conditions are still under investigation.

DC-SIGN/R can also play a vital role as the cellular entry receptors for the highly lethal Ebola virus. Immature DCs capture the Ebola viruses and subsequently present them to the immune system. Alvarez *et al.*[13] have concluded that DC-SIGN, expressed in the first cellular targets for pseudo-typed Ebola virus, is involved in the early stages of infection. Though many target cells susceptible to the Ebola virus do not express DC-SIGN/R, these lectins seem to be trans receptors, which can bind the viruses and transmit them efficiently to the target cells. They have also pointed out that these proteins may facilitate to initiation of the Ebola infection in cis.[13]

Even though some models discussed above for the DC-SIGN/R-mediated infection process have been proposed, much remains to be elucidated regarding the pathophysiological aspects of these proteins. In particular, some important points about DC-SIGN/R that are still not fully known: (1) the structural details of CRDs interaction with the glycoproteins on viral envelopes; (2) how the spatial and orientational arrangements of their CRDs differentiate upon binding with carbohydrates; (3) which structural properties in CRDs form different affinity and specificity for various carbohydrates. These knowledge will significantly impact on the development of novel potential therapeutic strategies to combat infectious diseases in the future. Thus far, there is no clinically proven treatment to prevent DC-SIGN/R-mediated viral infections. However, one of the most effective strategies would be the specific targeted inhibitors against DC-SIGN/R to block the interactions of these proteins with pathogens, thereby preventing infection.

1.2. Multivalency in Protein-Ligand Interactions

All biological systems, from viruses to mammals, are built on the ability of molecules to interact with each other. Based on the fundamental thermodynamic and kinetic principles, the intra-/inter-molecular interactions govern many chemical and biological processes by establishing complex and dynamic networks. Therefore, unravelling the

complexity of molecular interactions is necessary to interpret of highly organized and information-rich biological structures.[37] Among molecular interactions, multivalent systems are one of the powerful and key principles in nature. They establish strong, selective, and reversible non-covalent interactions between m-valent ligands and n-valent receptors (where m, n > 1) by achieving high affinity, increasing strength, and kinetic stability.[38] The term valency is illustrated through the monovalent and polyvalent (trivalent) interactions shown in **Figure 1.2.1** below. Considering that the search for solutions to scientific problems begins with mimicking nature, designing of nature-inspired multivalent interactions is an essential strategy for understanding the design and engineering of diagnostic or therapeutic tools to inhibit or enhance many biological processes.

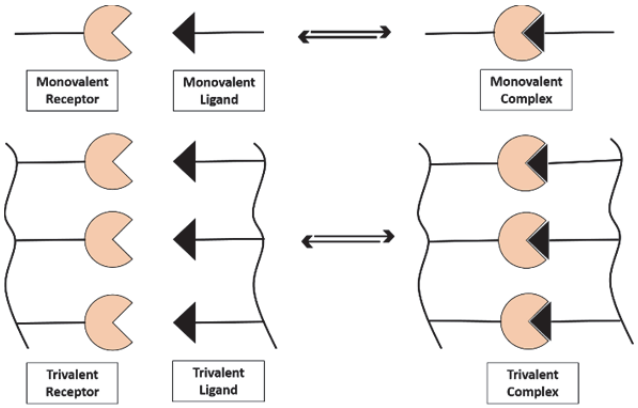

Figure 1.2.1. A schematic representation of monovalent and trivalent interactions. The valency in ligand-receptor interactions refers to the number of distinct connections of the same or similar kind. Adapted from the reference [39].

Multivalency has been dramatically exploited within biological processes such as recognition, signalling, and adhesion of pathogens like viruses and bacteria.[37] The fact that multivalent interactions result in higher affinity compared to monovalent interactions explains why nature uses it much more as a key strategy. In multivalent interactions, the increase in binding affinity and specificity can occur with the contributions of several mechanisms,[40] as shown below in **Figure 1.2.2**, including chelation, crosslinking, steric stabilization, subsite binding, and statistical rebinding. Chelation arises from the binding of multivalent ligands to multiple receptors, thus reducing the dissociation rate of the ligands and boosting the binding stability and avidity, resulting in stronger binding.[41] The binding of a multivalent ligand from the ligand clusters on a scaffold to a multivalent receptor also promotes the binding of

another ligand close to neighbouring receptors. Furthermore, if a multivalent ligand dissociates from the receptor to which it is bound, it may also rebind to neighbouring multivalent receptors. In addition, besides the primary binding sites, a multivalent ligand can also occupy the secondary binding sites of a multivalent receptor. Cross-linking, in which a multivalent ligand also occupies the binding sites of two different receptors, is another multivalent binding mode that makes these interactions superior to a monovalent counterpart. Once a ligand is released, the binding site of the receptor is rapidly re-occupied by another multivalent ligand from the presented multiples of ligands in close proximity on a scaffold. This, known as statistical rebinding, refers to the rapid exchange of locally clustered ligands, enhancing overall binding. Steric shielding in multivalent interactions is another important event that increases the binding stabilization by impeding other competitive monovalent ligands due to the physical dimensions of multivalent ligands.[40, 42] Furthermore, the binding specificity in these interactions can be improved by the spatial and orientational arrangement of these ligands based on the receptor structure and the multiple presentation of receptor-specific ligands on a scaffold,[40] as shown in **Figure 1.2.2** below.

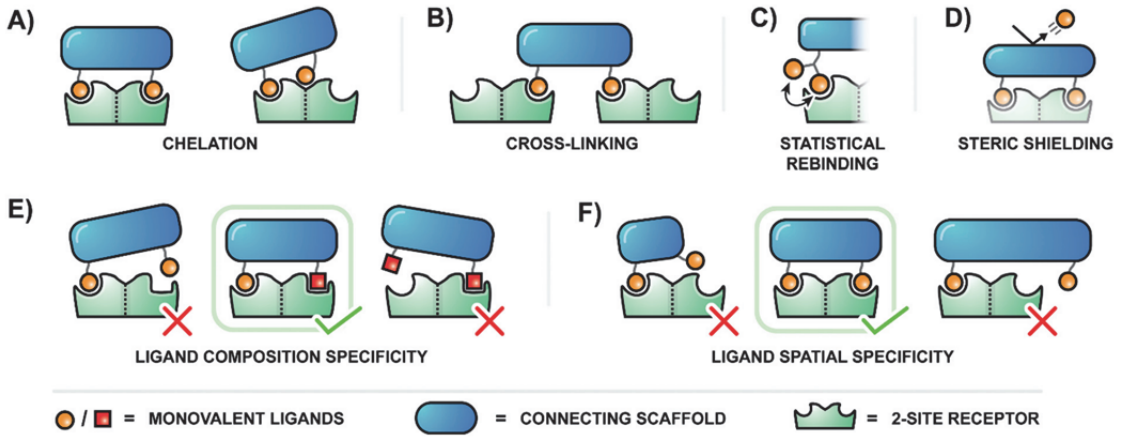

Figure 1.2.2. A schematic illustration of the various mechanisms why multivalent interactions exhibit enhanced affinity (A-D) and better specificity (E-F) compared to corresponding monovalent interactions. Reprinted from the reference [40].

The thermodynamic variables of mono/multivalent interactions also drive their binding characteristics. The fundamental thermodynamic nomenclature for multivalent interactions proposed by Mammen *et al.*[39] is highlighted in **Figure 1.2.3** below. The binding in monovalent interactions is mainly an enthalpy-driven process and thus more

predictable, whereas substantial entropic barriers may be imposed in multivalent interactions.[37] Besides the translational, rotational, and conformational entropies of the multivalent ligands, the scaffold and linker, and their structures also have entropic costs in multivalent interactions.[41, 43] The fundamental thermodynamic principle in multivalent interactions is that the binding is more enthalpy-driven than that of monovalent counterparts, and these entropic penalties are compensated by the more favourable binding enthalpy.[42] For instance, the interaction enthalpy of three ligands with a multivalent receptor is about three times greater than that for a single ligand. The entropic costs of a multivalent interaction are generally paid by the initial interactions of a multivalent ligand, which is probably about the same as the entropic cost paid for the corresponding monovalent ligand. Then, no or little entropic penalties are incorporated in all subsequent binding interactions. As three ligands are already located on the same scaffold (positive cooperativity), binding of a multivalent ligand with a multiple receptor augments the concentration of ligands at that binding site, and thereby this reduces the entropic penalties to be paid so as to bring the other ligands and the receptors together.[42, 44] However, the thermodynamic and kinetic principles of the increased affinity in multivalent interactions are still not fully understood.

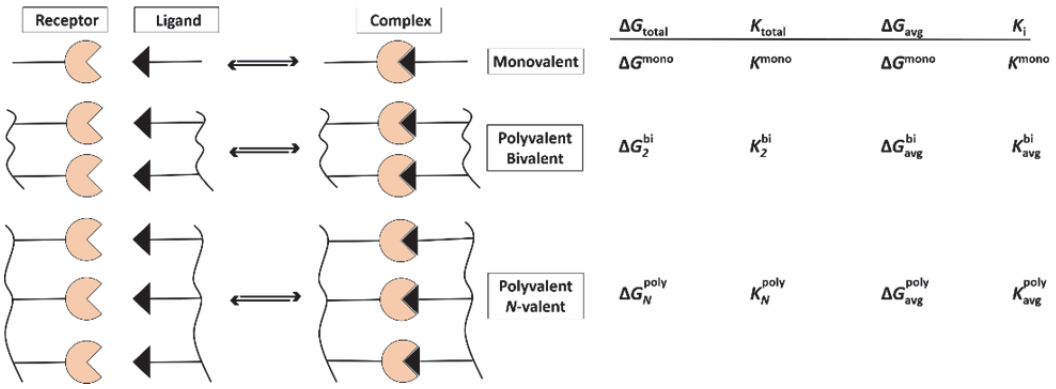

Figure 1.2.3. A schematic showing the proposed terminology for the thermodynamic relationships of the Gibbs free energy of binding (ΔG) and inhibition constants (K_i) of multivalent interactions by Mammen *et al.*[39] Redrawn from the reference [39] .

The most abundant biomolecules in nature, carbohydrates (popularly referred to as glycans), are essential components in numerous biological processes owing to their features such as storing water and energy, acting as metabolic intermediates, and signalling molecules in cell-cell or cell-environment communications, and mainly

encoding information through molecular shaping.[11, 45] Their ability to store chemical information in specific molecular recognition pathways depends on their structural, conformational, and stereochemical diversity,[11] but decoding their biological information is still one of the biggest challenges in interdisciplinary science. For example, most pathogens interact with pattern recognition receptors on target cells via carbohydrates on their cell surfaces and then penetrate through the plasma membrane of the host cells to initiate the infection process.[46, 47] As carbohydrate-based monovalent interactions are characteristically weak, with the dissociation constant (K_d) typically in the range of μM-mM,[48, 49] the low monovalent affinity to protein receptors is compensated in nature by the multiantennary sugars on cell surface glycoproteins to produce a biological impact, as shown in **Figure 1.2.4**. In other words, the multiple copies of glycans on the cell surface can enhance their binding affinity and specificity to target receptors. This phenomenon is known as the "glycocluster effect". Furthermore, the clustering of glycans enables a high avidity interaction with multivalent binding sites of target proteins, which has also been demonstrated experimentally.[50]

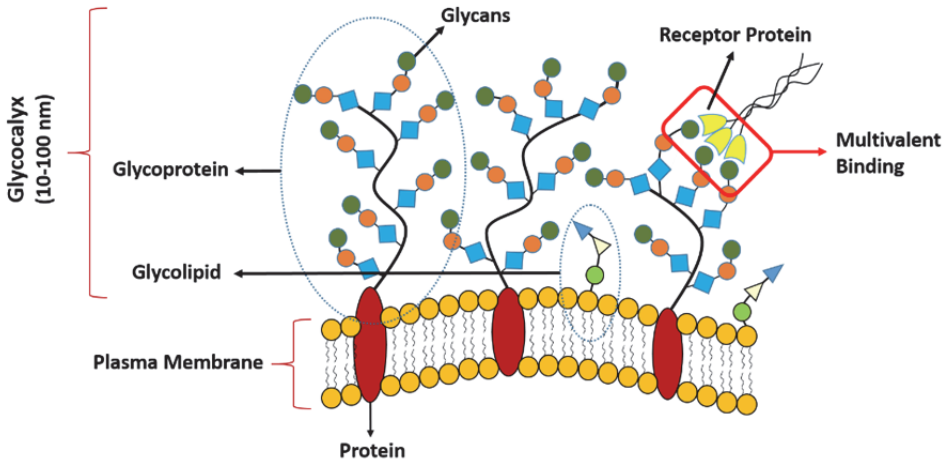

Figure 1.2.4. A schematic representation of multiple glycans presented on the cell surface (not to scale). Clustering of glycans triggers higher-order interactions with the multivalent carbohydrate binding sites of the receptor proteins with proper orientation and spacing. Adapted and redrawn from the reference [51].

Synthetic sugar-based multivalent systems designed with conceptual inspiration from nature have come to the forefront to obtain biological data about pathogens and develop potential inhibitors in about the last 20 years. The fundamental approach is here based on mimicking the cluster presentation of surface glycans on viruses or

bacteria to block the receptors that recognize them.[45, 46, 52-54] Free glycans can be directly employed in structure-activity investigations. However, some papers have indicated that glycan coating on nanoparticles may result in increased binding of up to 5 and 6 orders of magnitude compared to the free glycans.[49, 55] Within this context, in targeting specific glycan-binding proteins, nanomaterials can provide a robust scaffold for multivalent ligand presentation of sugars through chemical surface modification and conjugation thanks to their large surface/volume ratio. Gold nanoparticles, GNPs for example, offer attractive and accessible scaffolds for creating smart, multivalent, and efficient glycan-based nanoplatforms owing to their unique size and shape-dependent optical properties to be described clearly in the next section. Notably, their large surface-area-to-volume ratio gives them a particular advantage in forming multivalent structures by enabling the binding of multiple ligands and the stable three-dimensional presentation of the glycans.[56] Thus, GNPs can be rendered multifunctional after coating with multivalent sugars for selective binding to biological targets.

1.3. Gold Nanoparticles

Gold is one of the first precious metals discovered by humans, and its usage for many different purposes goes back to the fourth century BC. Despite the centuries-old history, the first scientific work on colloidal gold is based on a paper published by Michael Faraday in the mid-19th century, describing the synthesis methods and properties of colloidal gold,[57] but now a massive number of internet documents (Google ∼60 million) are available for the term “gold nanoparticles” which has been used since the early 1990s. After more than 150 years of scientific silence, gold nanoparticles, GNPs, have received tremendous interest in the past few decades due to the development of technological tools that enable us to visualize them effectively on a nanoscale level and also the increased ability to synthesise, purify, and functionalize them. Moreover, their unique features, summarized in the following section, have made them invaluable for biochemical research at the nanoscale.

1.3.1. Properties of GNPs

The modern age of GNPs has begun with the characterisation of their unique size- and shape-dependent optoelectronic properties, which are well-suited for chemical and

biological applications. These features can be briefly summarized as follows: (1) GNPs can be readily synthesised by various methods with high yields and excellent stability; however, their stability highly depends on the parameters of the solution, such as surface coating, colloid concentration, pH, ionic strength.[58] (2) They are of the easily tuneable shape and size. (3) Their surface chemistry can be simply manipulated. As their surface atoms are highly active and they have good catalytic properties, they are easily attached to other atoms. (4) They provide excellent biocompatibility using appropriate ligands for biological applications. (5) They have large surface areas that can readily be tuned through ligands containing functional groups such as thiols. These functional groups are used to anchor molecules, and GNPs can thus be rendered multifunctional with additional biomolecules such as proteins, oligonucleotides, and antibodies so that they can be made multivalent with various ligands for selective binding to biological targets. (6) They have controlled dispersity; they can easily reach the target area with a homogeneous distribution. (7) They are of low or non-cytotoxic in the short term.[59, 60] (8) They show an excellent response in the colorimetric biological analysis due to the high extinction coefficient of GNPs which are size and shape-dependent.[61, 62] (9) They can exhibit strong fluorescence for biological analysis with high quantum yields.[63] Among the properties of GNPs listed above, their strong localized surface plasmon resonance and fluorescence quenching are the most remarkable, especially for biomedical sensing and imaging purposes.

1.3.1.1. Surface Plasmon Resonance

GNPs display strong absorption and scattering properties with high efficiency upon interacting with light. The electron configuration of gold is [Xe] $4f^{14}5d^{10}6s^{1}$, and surface valance electrons in the 6s and 5d orbitals of each atom within the gold particle are highly delocalized.[64] When the GNP size is much smaller than the wavelength of light (diameter $d \ll \lambda$, where λ is the wavelength of the light),[65] the excitation of GNPs with incident light causes a resonant coherent oscillation of these surface valence electrons to one side away from the atomic core along the direction of the electric field of the light, and a net positive charge is left on the other side, thus resulting in the formation of a dipole polariton, as shown in **Figure 1.3.1.** This phenomenon is called “localized surface plasmon resonance” (LSPR, mostly abbreviated as SPR).[66] The high sensitivity

of SPR makes GNPs attractive nanomaterials for real-time monitoring and investigations of biomolecular interactions. SPR is a powerful tool that allows not only to characterise nanoparticles and determine their concentration but also to measure the specificity, binding affinity, and kinetics of biomolecular interactions.

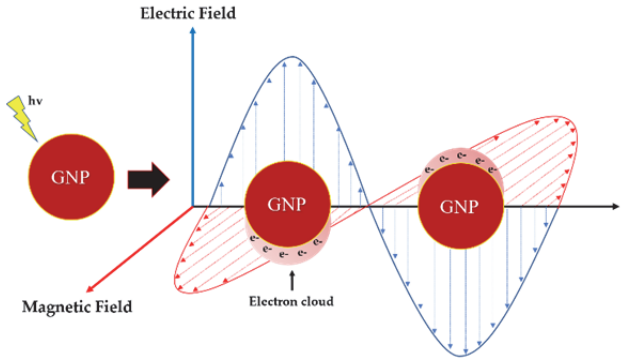

Figure 1.3.1. A schematic showing the localized surface plasmon resonance of GNPs formed by the collective oscillation of the surface conduction electrons across the GNPs in the electromagnetic field of incident light. Modified and redrawn from the reference [67].

The plasmon resonance is highly driven by the size, shape, and interparticle distance of GNPs.[68] Firstly, GNP size significantly impacts on their absorption and scattering properties. As the SPR band is observed for GNPs with a diameter of 3 nm and above, GNPs below this diameter cannot support a conduction band and behave more like molecules. Therefore, they should be called the term cluster rather than nanoparticles. Above this size, they exhibit an enhanced electromagnetic field on their surfaces. For instance, 5 nm GNPs give a strong surface plasmon resonance peak in the visible region, typically at around 520 nm.[69] The total extinction of incident light for small monodispersed GNPs (30 nm and below) is almost entirely due to the absorption of the light (their scattering properties are negligible). GNPs in this size range strongly absorb the green light and reflect the red light of the spectrum; therefore, they appear ruby red. **Figure 1.3.2** below illustrates the size-dependent colours of GNPs. As the size increases (40 nm and above), scattering begins to appear, and the larger the size, the greater the scattering.[70] The absorption and scattering equally participate in the extinction of light for GNPs with 80 nm, but for GNPs larger than this size, scattering becomes dominant in total light extinction. GNPs with a diameter of 80 nm reflect blue light and absorb red light, thus appearing blue-violet. The colour of GNPs with 100 nm and above becomes shiny because the electron cloud of their surrounds the entire

surface so that the photons of the light cannot penetrate into the electron cloud.[71] Their absorbance and scattering properties mostly provide a guidance on which GNPs size should be preferred in biomedical applications. For example, smaller GNPs are commonly preferred for photothermal therapies because the light must be absorbed with high efficiency, whereas larger GNPs are often chosen for imaging due to their higher light scattering.[71]

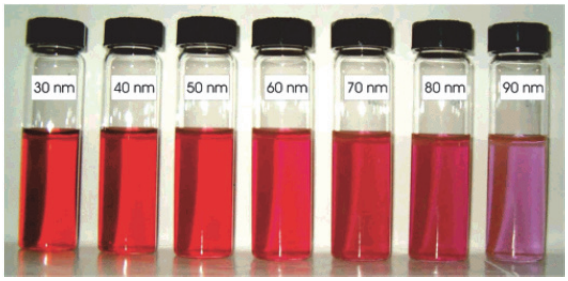

Figure 1.3.2. A schematic illustrating the size-dependent colour properties of GNPs in solutions. As GNPs increase in size (from left to right), the colour of their solutions changes gradually from red to purple.[72]

Secondly, GNP shape is another important driving factor in their optical properties. As can be seen in **Figure 1.3.3**, for example, spherical GNPs just give one strong SPR band in the visible region, whereas gold nanorods (GNRs, cylindrically shaped GNPs) exhibit two distinct absorption bands: a weak transverse plasmon band (TSPR), corresponding to electron oscillations along the width of GNRs, and an intense longitudinal plasmon band (LSPR) that corresponds to coherent electron oscillation along the length of GNRs.[73] TSPR is located in the visible region at around 520 nm, similar to that of spherical GNPs, and varies slightly with the aspect ratio of GNRs (length/width). In contrast, LSPR located at the near-infrared region (NIR) is highly sensitive to their aspect ratio of the GNRs and red-shifts to NIR with the increasing aspect ratio.[74] Near-infrared radiation can penetrate deep into biological tissues more efficiently than visible light wavelength, making GNRs with an LSPR peak in NIR crucial for medical application.[75]

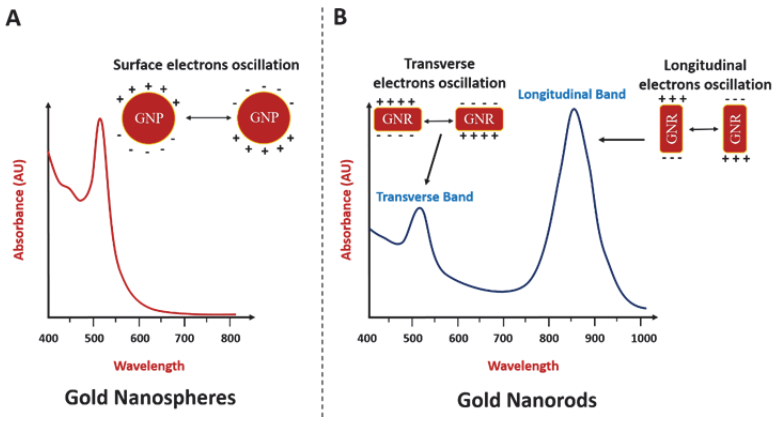

Figure 1.3.3. A schematic illustration of the optical spectra of gold nanospheres (A) and gold nanorods (B). Upon light excitation, colloidal stable gold nanospheres exhibit a single SPR peak, while gold nanorods display two SPR peaks; transverse surface plasmon band (TSPR) and longiditunal surface plasmon band (LSPR). Adapted and redrawn from the reference [76].

Finally, inter-particle distance has a significant impact on the SPR band shift because of dipole-dipole interactions. If the inter-particle distance is larger than the average particle size (dispersed state), GNPs potently absorb the green light and reflect the red light, so they seem bright red. Effectively isolated GNPs give a strong absorption band at around 520 nm. By contrast, when the inter-particle distance is less than the particle diameter (aggregated state), the colour turns bluish-purple, and SPR red-shift is observed due to inter-particle plasmon coupling. Such a colour change can even be clearly seen by the naked eye.[77] In this state, as given in **Figure 1.3.4**, GNPs show a new plasmon resonance band combined the traditional SPR of remaining isolated GNPs with another peak formed at longer wavelengths in consequence of the plasmon couplings of the particles, which causes the broadening of the new SPR band.[66, 77, 78]

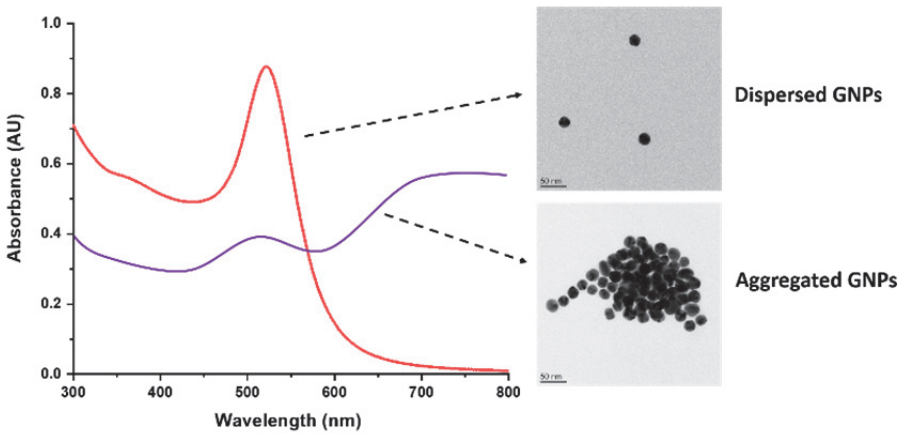

Figure 1.3.4. A schematic illustrating the UV-vis absorption spectra of dispersed and aggregated GNPs with small size. The distance between the nanoparticles can be seen from the TEM images on the right for both cases.

1.3.1.2. Fluorescence Quenching

When a molecule absorbs a certain wavelength of light in the visible or UV range of the spectrum, it gains energy and then excites from the ground state to a higher energy state, as shown by the blue arrow in the modified Jablonski diagram showing the electron states of molecules in **Figure 1.3.5**. In the excited state, firstly, the molecule rapidly loses energy without radiation through vibrations or collisions; this leads to the electrons returning to the lowest vibrational level of the excited state. They can then return to any vibrational levels of the ground states either by non-radiative relaxation or spontaneous emission. Energy is usually dissipated in the form of heat for non-radiative decay,[79] and for the latter as an emitted photon called fluorescence,[80] as shown in **Figure 1.3.5**. The initially absorbed photon has more energy than the emitted photon due to the energy lost as a result of the vibrational relaxation of the molecule, and this energy difference is called the Stokes' shift, as highlighted in **Figure 1.3.5**. The emitted light can be distinguished spectrally due to the Stokes' shift. This is referred as a rapid non-radiative decay of an excited photon from a higher vibrational level to the ground state at the same energy level, causing the fluorescence to have a lower energy and therefore a longer wavelength than the absorbed photon.[81]

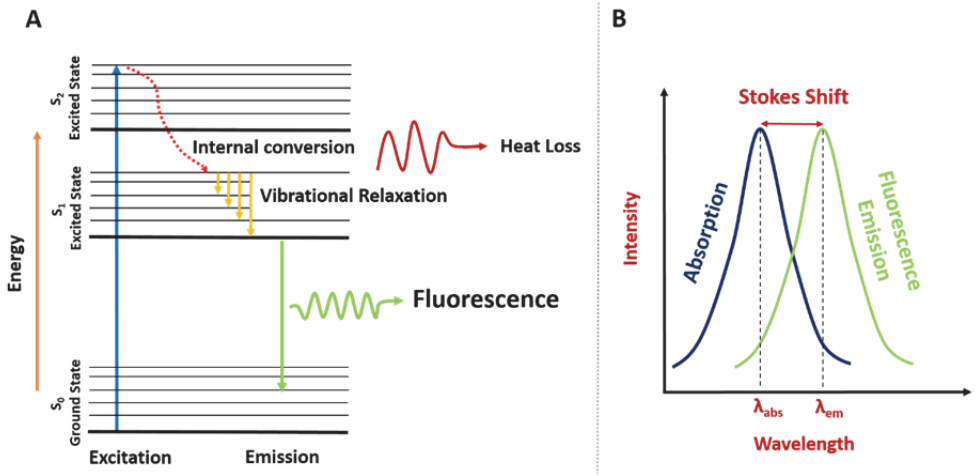

Figure 1.3.5. A schematic shows (A) the modified Jablonski diagram illustrating the principle of fluorescence, and (B) the Stokes shift describing the spectral difference between the wavelength at which the fluorescence is emitted and the wavelength at which the photon is absorbed. Adapted and redrawn from the reference [82].

Fluorescence is a molecular phenomenon to understand the nature of biological interactions due to its ease of use, reproducibility, high sensitivity, rapidity, and highly selective and real time detection;[83] therefore, fluorescence-based techniques are

widely employed research tools for biological assays and medical diagnosis. One of these important methods is the Fluorescence, or Förster, resonance energy transfer (FRET) established by the German scientist Theodor Förster. FRET is a process through which energy is transferred nonradiatively to an acceptor fluorophore from an excited donor through an intermolecular dipole-dipole interaction. In FRET, energy transfer efficiency is strongly dependent on the following parameters: (1) The distance between the donor and the acceptor. Energy transfer is inversely proportional to the 6^{th} power of the donor-to-acceptor separation distance and occurs when the distance is typically less than 10 nm,[84] making FRET extremely useful for biological applications as most biological interactions occur over this distance range; (2) The spectral overlap between the absorption spectrum of the acceptor and the emission spectrum of the donor, an example of this can be seen in **Figure 1.3.5**. The larger spectral overlap, the greater energy transfer from the excited donor to the acceptor; (3) The relative orientation in space between the donor and acceptor transition dipoles moments; (4) The quantum yield of the donor.[85] FRET efficiency, the distance, and orientation between the donor and acceptor are calculated using the following equation established according to Förster's theory.

$$E = \frac{1}{\left[1 + \left(\frac{r}{R_0}\right)^6\right]}$$

Where E is the energy transfer efficiency, r is the distance between the donor and the acceptor, R_0 is the Förster radius when the FRET efficiency is 50%.[84] R_0 typically ranges from 2 to 6 nm. The efficiency of non-radiative energy transfer is the inverse 6^{th} power of the distance between donors and acceptors.[86]

GNPs are excellent fluorescence quenchers (more than 99%)[87] due to their high molar extinction coefficients and broad energy absorption spectrum in the visible range.[88] They are several orders of magnitude more efficient than organic quenchers, making them highly useful for fluorescence-based detection systems. When a fluorophore is placed near a GNP with a strong plasmon field, the emission of a fluorophore could be tuned by the close proximity of the GNP because of the interaction between the fluorophore and the surface plasmon resonance region of the GNP. The close proximity of the fluorophore and a GNP results in fluorescence quenching.

Fluorescence quenching is commonly observed when the emission spectrum of excited fluorophore overlaps with the surface plasmon band of the GNPs.[89] In GNP-mediated fluorescence quenching, both radiative and non-radiative decay of molecules play an important role in fluorescence quenching efficiency.[65] GNPs increase the non-radiative decay of the nearby fluorescent molecules due to the energy transfer. Radiative decay of donor molecules is also reduced because of the dipole-dipole interaction between GNPs and molecules located at close proximity to their surface.[79] Fundamentally, the dipole moment on the surface of GNPs decreases the ratio of radiative to non-radiative decay rate of the fluorophore molecule, thereby leading to fluorescence quenching.[89] Non-radiative and radiative decay rates depend on various factors, including the GNP size and shape, GNP surface chemistry, the intrinsic quantum yield of the fluorophore, the distance between the fluorophore and the GNP, and also an overlap of the fluorophore emission and the GNP absorption. Regarding GNP size, fluorescence quenching is expected due to the absorption-dominant mechanism in small colloidal GNPs of diameter up to 40 nm, while fluorescence is increased because scattering is the dominant mechanism for GNPs larger than 40 nm, according to Mie's theory.[35] GNP shape is another significant factor for the quenching or enhancement of fluorescence, as it has a remarkable impact on their absorption and scattering properties.[79] In particular, more efficient fluorescence quenching can be observed for spherical GNPs. Because they do not have a net dipole moment, thus allows the donor can transfer the energy to GNPs at any position where the donor is in close proximity to GNP surface.[84]

Fluorescence quenching relies on the same principles as FRET, but it has some differences. The energy transfer from a donor fluorophore to a GNP is inversely proportional to the 4^{th} power of the distance (rather than 6^{th} power in conventional FRET), as derived from Persson and Lang,[90] thus resulting in higher energy transfer efficiency and enabling to measure much longer distances than that of FRET (<10 nm). Dulkeith *et al.*[87] found that when the distance between GNPs and dye molecules raised from 2 to 16 nm (longer distance than 10 nm), GNPs still quenched the fluorescence emission of dyes with high efficiency, and the suppression of radiative rate is most probably dominated mechanism in energy transfer instead of the non-radiative rate.

Similarly, Samanta *et al.*[91] later confirmed that the fluorescence of DNA-conjugated-QDs was quenched by GNPs even when the distance between inter-particles was up to 70 nm, showing that the distance between donors and GNPs is roughly 10 times longer than that of in traditional FRET. Another difference is that FRET does not require direct contact of the quencher with the fluorophore dye molecules and can occur through space, but in GNP-mediated fluorescence quenching, the fluorescence intensity of the fluorophore in the excited state decreases or quenches upon physical contact of GNPs, which is called "dynamic quenching".[80] This molecular contact between GNPs and fluorophores allows direct interaction of their electron clouds. In contrast, FRET is known to occur typically at distances 10-100 Å, but 30 Å and above distance between the molecules are too far for electron clouds to interact directly with each other.[92] In addition, particularly in GNP-dye studies, the acceptor is not the nanoparticle itself, but the free conduction band electrons on the GNP surface, which is also known as nanometal surface energy transfer (NSET).[93] In this dipolar interactions model, fluorescence quenching occurs through interactions of electron clouds at much more longer distances compared to FRET distance, as illustrated in **Figure 1.3.6**, since the energy transfer distance is between the donor and nanoparticle surface.[79] Therefore, the GNP-mediated fluorescence quenching method can be a highly advantageous way to quantify the binding between glycans and multivalent proteins by employing modified multivalent sugar ligands onto GNPs to augment their binding affinity and specificity.

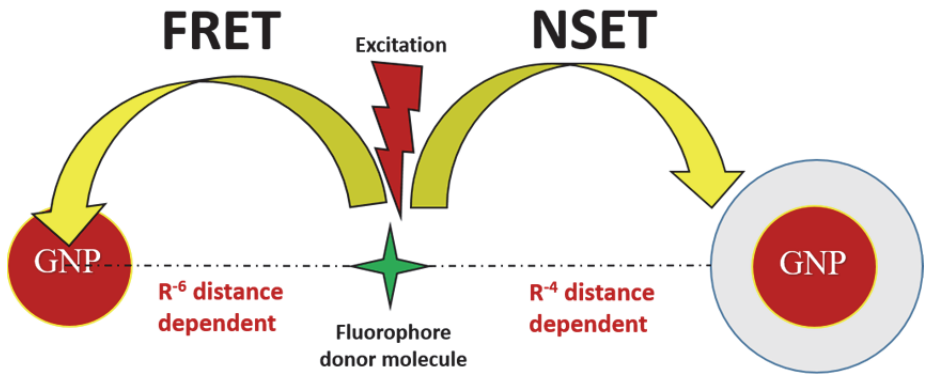

Figure 1.3.6. A schematic representation of the energy transfer from the fluorophore donor molecule to GNPs based on FRET and NSET models. In NSET, energy transfer is the inverse 4th power of the distance between the donor and GNPs. Following equations show how quenching efficiency (QE) changes with distance: $QE=1/[1+(r/R_0)^6]$ in FRET, but $QE=1/[1+(d/d_0)^4]$ in NSET). Adapted and redrawn from the reference [94].

1.3.2. GNPs Synthesis and Stabilisation

A great number of different, reliable, reproducible, and highly efficient methods have been developed and employed for GNP synthesis. They can be broadly grouped into two main categories: bottom-up (chemical), and top-down (physical) methods.[59] Among these approaches, the bottom-up techniques in which gold atoms produced by the chemical or biological reduction are assembled together to produce GNPs are the most commonly used due to their good control over GNP size, shape, distribution, and composition.[95, 96] On the other hand, in the top-down methods, GNPs are achieved by breaking down the bulk materials into nano-sized structures[97] using different physical manipulations such as UV and IR irradiation, laser ablation, and ion sputtering.[98] These approaches are, however, used less frequently due to their limited control over GNP size and shape. Notably, the surface structures of GNPs are often imperfect in these techniques, and such defects not only highly affect their surface chemistry but also may result in the loss of their desired physical properties.[99]

The first chemical synthesis of GNPs was reported by Michael Faraday in 1857,[100] wherein colloidal GNPs were synthesised using phosphorus to reduce $AuCl_4^{-4}$ ions. Then, in the early 1950s, based on Faraday's approach, Turkevich *et al.*[101] designed and introduced the most widely used method to make spherical GNPs today. The basic principle of this technique is based on the reduction of tetrachloroauric acid, $HAuCl_4$, by using a reducing agent such as citrate in an aqueous medium.[65] Naked GNPs are not colloidally stable in water or solvent; therefore, they need stabilizers to improve their dispersion.[102] Besides being a reducing agent, citrate also acts as a stabilizing agent by providing a negative surface charge to GNPs, which prevents their aggregation due to electrostatic repulsion.[103] This protocol works well for the synthesis of 10-30 nm spherical GNPs, but it has some drawbacks, particularly for the synthesis of GNPs with diameters above 30 nm. Large-size GNPs produced via this procedure become less spherical and uniform, and often have broad size distributions,[98] meaning that the batch is composed of GNPs of different sizes and shapes. The reaction yield is also relatively low, and only water can be used as a solvent in this reaction.[104, 105] Frens then modified the Turkevich method to overcome these limitations and managed to control over GNP size by varying the molar ratio of trisodium citrate to the gold

precursor.[106] The modified Turkevich-Frens method for GNP synthesis is described in **Figure 1.3.7**. Kimling *et al.*[107] showed that a low citrate concentration results in larger GNPs, and even aggregation of GNPs, but a high citrate concentration stabilizes smaller GNPs. Furthermore, the pH in the GNP synthesis reaction plays an important role in determining the GNP's size and shape. Ji *et al.*[108] confirmed that citrate also functions as a pH mediator in GNP synthesis. The controlled synthesis of GNPs with the desired size, shape, and surface stabilization makes the modified Turkevich-Frens method still highly efficient in numerous GNP-related studies.

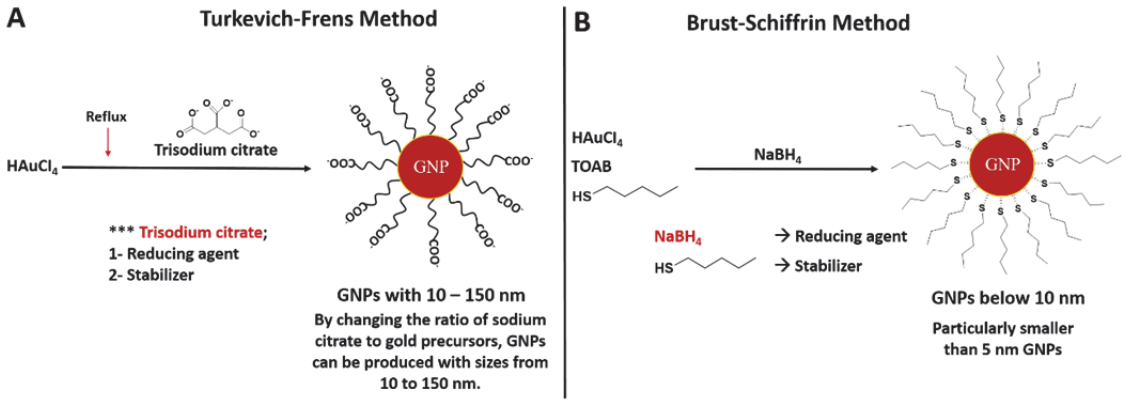

Figure 1.3.7. A schematic representing the reactions of the most employed methods ((A) Turkevich-Frens method; (B) Brust-Schiffrin strategy) for GNP synthesis. Turkevich-Frens method is one aqueous phase, whereas the Brust-Schiffrin method is biphasic synthesis.

Another well-known chemical technique for GNP synthesis is the Brust-Schiffrin method which allows the synthesis of stable GNPs with controlled sizes with low size dispersity, as shown in **Figure 1.3.7**. This method involves a two-phase synthetic strategy. Chloroauric acid is first transferred from an aqueous phase to an organic phase through the use of tetraoctylammonium bromide (TOAB), a phase transfer catalyst. Gold species are then reduced in the organic phase using sodium borohydride ($NaBH_4$), as the reducing agent, in the presence of alkanethiol, leading to the formation of thiol-protected GNPs.[109] This can be observed through a color change of the organic phase from orange to deep-brown within a few seconds. This method facilitates the synthesis of thiol-protected GNPs smaller than 5 nm with a high air and thermal stability.[110, 111] Furthermore, GNP size can be easily tuned by controlling various reaction conditions such as the thiol to gold ratio, reduction rate, and temperature.[65] The main limitation of this approach, however, is the difficulty of using the synthesised

GNPs in biological applications due to the use of water-immiscible organic solvents in the synthesis process, which makes hydrophobic GNPs indispersible in the aqueous media.[98] Besides these methods described here, there are also a wide array of alternative procedures for GNP synthesis,[112] including the biological, electrochemical, and seeding growth methods.[113]

1.4. GNPs Surface Functionalisation

GNPs are colloidally unstable without their surface stabilizers or ligands. They become stable owing to the stabilizing agents, *e.g.* citrate, that bind weakly to the surface of GNPs during synthesis to provide inter-particle electrostatic repulsion to prevent aggregation. However, for use as biomedical probes, the GNPs need to be modified with functional ligands that bind more strongly to their surface. Depending on the targeting aims, ligand molecules can provide them steric stabilization to improve the stability and compatibility with the biological environment.[114] Regarding the surface coating and functionalization, GNP-molecules assemblies are shown in **Figure 1.4.1**.

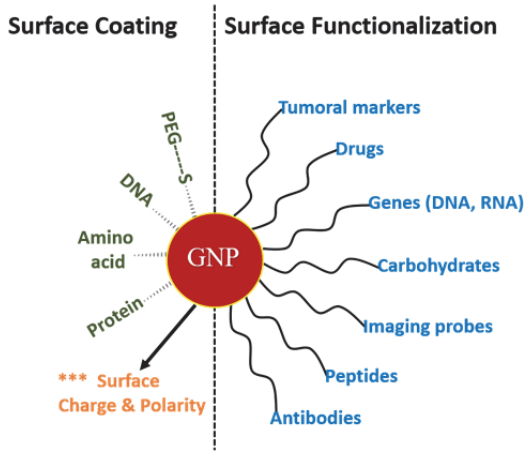

Figure 1.4.1. A schematic representation of the surface coating and functionalization of GNPs. Adapted and redrawn from the reference [115]

Liu *et al.*[116] demonstrated that PEG-coated GNPs are more stable than citrate-capped GNPs in a broad range of salt content and also provide a better specific binding to the targets. The replacement of stabilizers adsorbed onto GNPs with the modified ligands is often called as a ligand exchange reaction. The main motivation here is to control the interactions of modified GNPs with their surrounding environment by giving them new functions. Generally, three basic strategies have been employed for GNP surface

modification: (1) Adsorption of ligands onto GNP surface via hydrophobic or electrostatic interactions; (2) Covalent binding of the ligand onto their surface directly through a sulphur-containing molecule or a thiol-containing functional linker; (3) Affinity-based binding (non-covalent) through GNP surface functional groups moieties and target molecules.[68]

The physicochemical properties of GNPs mainly depend on the ligands present on their surface. In order to enable GNPs to interact with biological systems, the design of functional ligands is, therefore, a challenging task. The modified ligand structure typically consists of an anchoring molecule, a linker/spacer group, and a terminal functional group, as shown in **Figure 1.4.2**. Anchor molecules must strongly bind to the GNP surface to provide colloidal stability, even under variable conditions (pH, temperature, solvent etc.). As briefly pointed out earlier, thiol groups exhibit high affinity to the GNP surface. Au-S bonds robustly anchor the ligand molecules to the GNP surface.[102] In particular, di-thiolate groups can chelate strongly on GNP surface and keep them stable for years. Susumu *et al.*[117] reported that the dihydrolipoic acid, DHLA, based binding ligands can provide GNPs with excellent colloidal stability, even under a wide variety of biological conditions. Regarding the linker/spacer molecules, they are often used to make the GNP with desired surface properties. Their chain lengths, density, and properties have a considerable impact on the ligand efficiency as well as the overall stability, and solubility of GNP-ligand assemblies. Polyethylene glycol, PEG, is by far the most widely used linker for surface modification and stabilization of GNPs. This polymer consists of varying number of the linear repeated units ($–CH_2–CH_2–O–$) which is hydrophilic and water-soluble, depending on the molecular weight. Besides its simple structure, PEG is a biocompatible polymer due to its high chemical stability and inertness. In recent years, PEG coating has been extensively utilized as a gold platform for tuning GNP surface chemistry for different biological applications. This is because PEG is flexible, non-toxic, non-antigenic, and highly soluble in water as well as in a number of organic polar and apolar solvents,[114] and has also been approved by the FDA (Food and Drug Administration, USA) for use in humans.[118] PEG can provide GNPs with several benefits for *in vivo* purposes. These include: (i) increasing their systemic circulation and bio-distribution; (ii) providing

colloidal stability in a physiological environment with reduced degradation by metabolic enzymes; (iii) masking GNPs against the immunological system with neutral and highly hydrophilic structures; (iv) and preventing undesired interactions and aggregation with proteins and other blood components.[118, 119] Finally, the terminal functional groups can be readily designed to target selective interactions with a wide variety of cells or biomolecules.[117] Generally, biomolecules such as glycan, biotin, protein, and DNA are often used as functional end groups to promote the biological linkage of the multifunctional ligands.

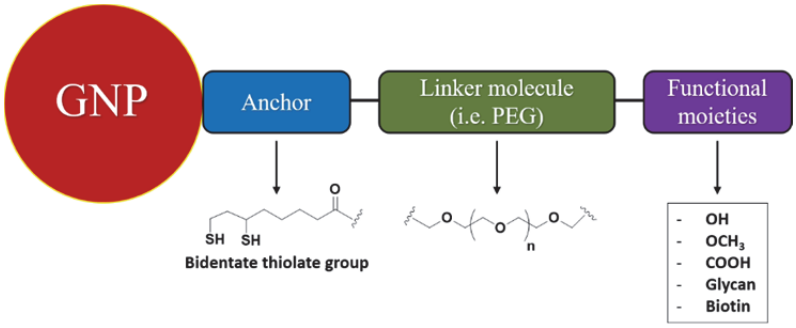

Figure 1.4.2. Modular design of multifunctional ligands. Modified and redrawn from the reference [117].

1.5. GNPs Bioconjugates

One of the major advantages of GNPs for biomedical applications is the ease of conjugation with biomolecules. Essential components of living organisms, such as glycans, DNA, proteins, and antibodies, can be readily conjugated onto the surface of GNPs of different sizes and shapes. Binding biomolecules to GNP surfaces can provide some valuable attributes not found in their structures. In order to establish clinically desirable functions, features such as high cellular uptake, intracellular activity, and controlled release of functional biomolecules can be achieved in this way.[120] An early example of this strategy was the production of oligonucleotide-GNP conjugates by Mirkin *et al.*[121] and Alivisatos *et al.*[122] via thiol-gold bond formation. The functionalization of GNPs with DNA provides a great platform that is crucial for biological diagnostic and imaging, because polyvalent DNA-GNPs exhibit high-affinity binding to complementary nucleic acids, resulting in high intracellular binding of the target molecules, thus increasing the efficiency of gene regulation.[60] The enhanced stability of DNA-GNP conjugates also makes nucleic acids highly stable and resistant to enzymatic degradation, which has been an obstacle to biological research. This

important feature makes DNA-GNP conjugates extremely promising candidates for specific molecular recognition in cell-based studies.[123] Furthermore, the most striking property of DNA-GNP conjugates is their ability to penetrate a broad array of different cell types, making them a useful universal cellular delivery platform as reported by Rosi *et al.*[124]

GNPs are also a perfect platform for protein conjugation because their easily modifiable surface areas allow for high protein loading. The selective binding and cellular uptake of proteins grafted onto GNPs into the tumor can contribute to targeted drug delivery. For instance, multivalent GNPs loaded with Herceptin, an immune system-related protein antibody against the Herceptin-2 receptor, over-expressed in breast and ovarian tumor cells, have taken into the tumor due to the avidity between the receptor and antibody. GNPs coated with cancer-related protein specific antibodies have been used to image tumor cells and antibody-GNP conjugates have been shown to bind cancer cells with six times higher affinity than non-cancerous cells.[120] Moreover, antibody-labelled GNPs have long been employed in immunohistochemical studies. As shown in **Figure 1.5.1**, modification of GNPs surface with antibodies can be generally achieved in three interactions: (i) the ionic interaction between negatively charged GNPs and antibodies; (ii) the hydrophobic interaction between GNPs surface and the antibody; and (iii) the Au-S covalent binding between GNP surface gold atoms and antibody cysteine. These techniques can also be used together to effectively design labelling agents in bio-imaging and bio-detection studies.[125] For instance, Chen *et al.*[126] have adsorbed antibodies onto GNPs via combining ionic and hydrophobic attractions and used them as electrochemical immunosensors. Herein, it is worth noting that GNP-glycan bioconjugates will be thoroughly discussed in the later chapters.

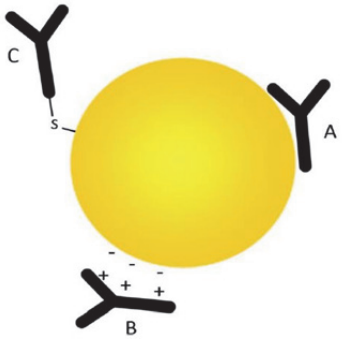

Figure 1.5.1. A scheme illustrating the interactions between GNPs surface and antibody. (A) Hydrophobic interaction, (B) ionic interaction, and (C) covalent bond. Reprinted from the reference [125].

1.6. Click Chemistry

Proper surface chemistry is essential for nanoparticles to work effectively in the biological environment. Although several different methods have been used for surface engineering of nanoparticles, allowing for effective binding of small molecules, polymers, and complex ligands (carbohydrates, DNA, proteins), most of these still suffer from some limitations. The click chemistry first introduced by Sharpless *et al.* in 2001 provided a universal contribution to the surface chemistry of nanoparticles.[127] The term "click chemistry" describes a group of reactions that are modular, selective, high yielding, broad in scope, simple to perform, and physiologically stable.

Click chemistry is a highly efficient method to produce a large variety of bioconjugates with different nanoparticles, such as GNP, carbon nanotubes, silica. This reaction can be done in two ways. Firstly, the Cu (I) catalysed Huisgen 1-3-dipolar [3+2] cycloaddition (CuAAC) between an azide and a terminal alkyne is one of the most widely used methods for obtaining GNP-bioconjugates. The reaction scheme is highlighted in **Scheme 1.6.1** below. Unlike conventional thermal Huisgen 1,3- dipolar azide-alkyne cycloaddition, which typically requires very long reaction times and about 100 °C, the copper catalysis dramatically reduces the activation energy barrier, allowing for reactions to perform at RT in both aqueous and organic solvents. This Cu-catalysed click reactions have a wide tolerance for solvent, temperature (avoiding high temperatures) and pH.[128-130]

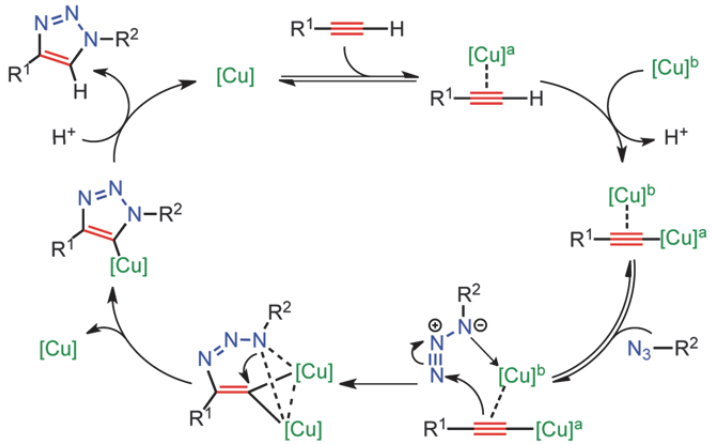

Scheme 1.6.1. A mechanistic reaction scheme for copper-catalysed click chemistry.[131]

Ligand exchange is a widely employed strategy for the surface functionalization of GNPs. However, in some cases, for example, the azido-functionalized GNPs may lose their unique properties due to aggregation and the reduced-chemical stability in the solution.[132] This can be overcome by click reaction using suitable ligands, which can improve not only their stability but also bioavailability. Fleming *et al.*[133] presented the first example of click chemistry with azido-functionalized GNPs. However, some deficiencies such as low yield and the lack of reactivity due to aggregation of copper ions, remained. Boisselier *et al.*[134] incorporated PEG chains into the GNP surface ligands in the copper sulphate-ascorbic acid catalytic system, they confirmed that alkyne functionalized PEG containing ligands bind to GNP surface with a high yield. Nevertheless, a few papers shows CuAAC reaction conditions caused NPs to be aggregated, but the exact reasons for their aggregation are not yet fully known. On the other hand, a large amount of research has reported its successful use for the surface functionalization of GNPs.[132] In addition, copper can cause various structural damage to the biomolecules through oxidative stress. Some chelating ligands such as TBTA (tris-(benzyl-triazolyl methyl)-amine) are, therefore, used to stabilize copper and avoid its possible biological damage, by preventing the formation of undesired by-products.[135]

Another approach is the copper-free click chemistry reaction, known as strain-promoted azide-alkyne cycloaddition (SPAAC), containing a 1, 3-dipolar cycloaddition. This reaction is free of a cytotoxic copper catalyst and occurs at a lower activation barrier,[136] making it suitable to produce GNP-conjugates for *in vivo* applications. The

release of the high ring strain within the cyclooctynes drives this reaction. As a result, cyclooctynes react selectively with azides to form triazoles, as shown in **Scheme 1.6.2** below, at standard room temperature and pressure without the need for metal catalysis. He *et al.*[137] and Wang *et al.*[138] have given examples of the successful use of SPAAC to synthesise mannose- and peptide-coated GNPs, respectively.

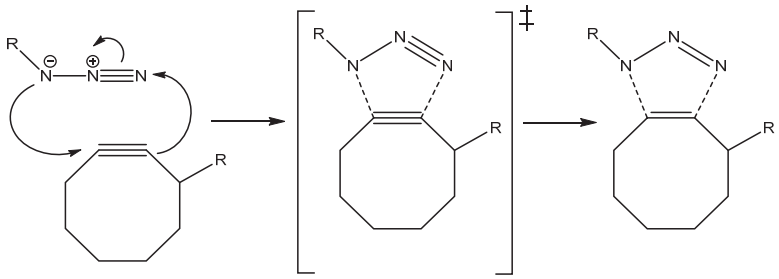

Scheme 1.6.2. A reaction scheme showing the copper-free strain promoted azide-alkyne cycloaddition. The reaction occurs due to the interaction between an azide and the strained alkyne, in absence of any metal catalysts including copper.

1.7. GNPs Toxicity

GNPs have tremendous potential for use as a promising platform in a wide range of biomedical applications. Since every substance in nature has a toxic effect at certain concentrations, their toxicity and biocompatibility must be comprehensively determined before use in therapy, diagnosis, and imaging.[69] Their toxicity research done so far roughly analyzed under three main headings. The first is the effect of GNP size on potential toxicity. GNPs, particularly those smaller than 100 nm, have a similar size to many cellular components, notably proteins and cell membranes, so they can easily cross natural barriers and interact with biological materials.[139] Cornor *et al.*[140] reported that 4, 12, and 18 nm GNPs coated with different capping molecules such as glucose, biotin, and citrate were not toxic in human leukaemia cell lines. A similar result was found by Shukla *et al.*[141] that 3.5 nm GNPs do not have a detrimental impact on immune system cell lines. Villers *et al.*[142] also showed that 10 nm citrate-coated GNPs were not toxic to dendritic cells. However, some research have reported some toxic effects for GNPs with 2 nm and below. For example, Pan *et al.*[139] investigated the toxicity of GNPs with diameters ranging from 0.8 to 15 nm in different cell cultures. They found that 1.4 nm GNPs induced mitochondrial cell damage, necrosis, and oxidative stress in the studied cell lines. However, regardless of the cell type tested, 15

nm GNPs were non-toxic even at molar concentrations 100 times higher than that of 1.4 nm GNPs. Furthermore, Goodman *et al.*[143] showed that cationic 2 nm GNPs are toxic at certain doses, but 2 nm GNP with negative charge surfaces are not toxic for the same cell lines at the same concentration. This is possible because cationic nanoparticles may interact with the negatively charged cell membranes strongly and harm the membrane structure.[144]

Another important parameter that impacts the possible toxic effects is shape. GNP geometry is notably crucial for their interactions with cell membranes and also cellular uptake. Schaeublin *et al.*[145] investigated the effects of GNPs and GNRs on ROS production, cell viability, and protein levels in human keratinocyte cell lines. They revealed that GNPs did not have any harmful impacts monitored by GNRs. Their size- and shape-dependent toxic effect in *in vivo* studies can be reduced or even eliminated by modifying their surface with appropriate ligands. Since GNPs make their first contact with biomolecules and cells via their surface, the toxic effect is closely related to their surface charge and the chemical structure of the surface ligands.[146] For example, Goodman *et al.*[143] showed that amine-modified GNPs were mildly toxic, but those modified with carboxylic acid were relatively non-toxic. Therefore, PEG coating dramatically contributes to the reduction of observed toxicity. O'Neal *et al.*[147] observed that animals treated with PEG-coated gold nanoshells remained healthy, depending on their size and dose, even more than 3 months after injections, and found that they did not adversely affect on their health *in vivo*.[148] In addition to those briefly explained above, as summarized in **Figure 1.7.1**, a variety of other reasons, including their aggregation-induced accumulation, the route of their administration, and the specific characteristics of the applied tissues, can play a role in their possible toxicity.[149] Overall, a great number of studies have confirmed that GNPs have little or no toxicity, so they have been generally accepted as a safe and biocompatible material for *in vivo* studies, depending on their size and concentration. GNPs still remain a step ahead of other metal nanoparticles for biological applications. [150] However, given that *in vivo* conditions are significantly different from *in vitro* conditions, their toxicity research should be systematically performed under certain conditions and for each particular case.

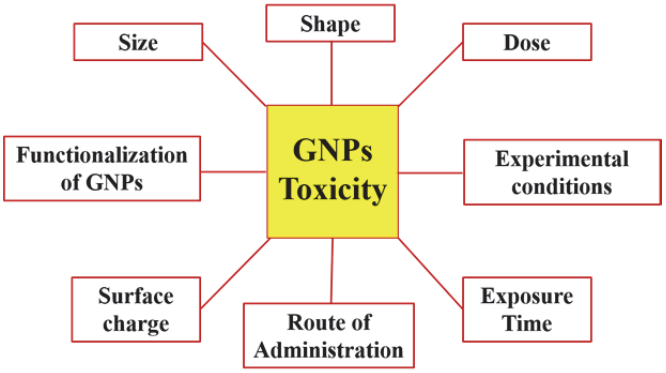

Figure 1.7.1. A summary of the factors affecting the toxicity of GNPs. Adapted from the reference [151] .

1.8. The Colloidal & Stealth Ability of GNPs: Protein Corona Formation

The fact that relatively little is known about the interaction of synthetic GNP-conjugates with biological media still poses a severe obstacle to design their efficacy, particularly under *in vivo* conditions. When GNPs are exposed to various physiological fluids, mainly blood, after their systemic injections, some biomolecules in that environment, especially proteins, can adsorb onto the GNP surface, which causes a new layer called "protein corona". As shown in **Figure 1.8.1**, the protein corona is split into two shells surrounding the NPs: a hard corona (inner shell) and a soft corona (outer shell). Whereas the hard corona contains strongly bound or adsorbed proteins that bind irreversibly on the GNPs surface, the soft corona is created by proteins that are weakly and reversibly attached to GNPs and can change over time. This dynamic layer can alter their physical and chemical properties, such as size, charge, surface composition, and functionality, thereby giving them a new biological identity.[152] Protein corona formation can regulate a number of biological responses of GNP-conjugates, including their circulation time, cellular uptake, bioavailability, and toxicity, consequently, the GNP conjugates may not be able to maintain their designed targeting properties such as bioactivity, specificity, selectivity, and orientation.

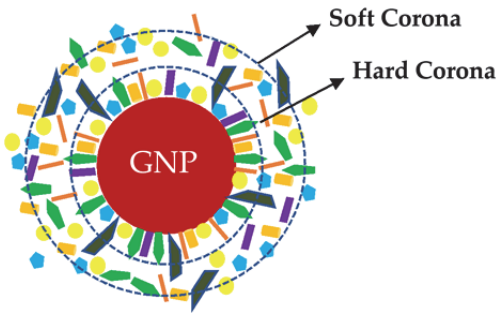

Figure 1.8.1. A schematic illustration of a protein corona proposed by Wolfram *et al.*[152] (Adapted and redrawn from the reference [153])

Protein corona formation mainly depends on the physicochemical properties of the GNPs (i.e. size, shape, charge, and surface functional groups), their surrounding conditions (such as medium viscosity, temperature, and pH), the duration of nanoparticle exposure, and the type and concentration of proteins in the exposure medium.[153] In this regard, the ligands on the GNPs surface are also highly important for determining the protein corona formation. As a universal coating, PEG is commonly used to prevent undesired interactions with proteins without loss of colloidal stability, due to its highly flexible, hydrophilic chain that can be adjusted to a wide array of conformations. Both the size and density of PEG (5 kDa) coating on GNPs affect the binding/adsorption of proteins and their macrophage uptake. If the PEG density is less than 0.16 PEG molecules per nm^2, their macrophage uptake depends on the adsorbed proteins. In contrast, adsorbed protein-independent uptake is observed if the density is higher than 0.64 PEG molecules per nm^2.[58, 154] However, no matter what density and molecular weight, coating with PEG alone cannot completely inhibit protein adsorption, and a certain number of proteins will always adsorb onto the GNPs surface. Garcia-Alvarez *et al.*[155] highlighted that after systemic injections, PEG-coated GNPs were not entirely inert and could interact with several blood proteins in rodents. Although PEGylation is a promising approach to reduce protein adsorption, it cannot offer complete protection of GNPs against the reticuloendothelial system. Compared to citrate-GNPs, GNPs coated with lactose and PEG have been shown to display a similar ability to reduce interactions with non-target proteins, but lactose coating exhibited more inhibition of macrophage phagocytosis than PEG coating.[156]

Protein corona formation is a complex and dynamic process, even unique for every nanoparticle. Proteins that are present in excess initially bind to the nanoparticle

surface, and these proteins are then replaced by higher affinity proteins. This phenomenon, known as the "Vroman effect", is another aspect to drive GNP's behaviour in the body.[153] In addition, the type of proteins in the layers is also critical in modulating the immune response towards GNPs. Two types of proteins are basically adsorbed onto the nanoparticle surface. Firstly, GNPs should be protected against opsonins such as IgG, fibrinogen, and complement factors because these proteins enhance their recognition by macrophages and subsequently increase their clearance from the body.[157] On the contrary, dysopsonins, including human serum albumin, and apolipoproteins can prolong the circulation time of GNPs by avoiding detection and removal by the immune system. Indeed, they offer a potential way to create a "stealth effect" for GNPs through the masking and protective effect of such molecules adsorbed onto GNPs against the reticuloendothelial system, enabling them to be more biocompatible with the human body.[158] However, when GNPs reach the target site with masking proteins, they may not be able to interact with their biological targets because of the surface ligands are still occupied by these masking proteins. The binding/adsorbing mechanisms of proteins onto GNPs are still not fully understood, but the elucidation of binding/adsorbing patterns is of great importance in designing effective GNP-conjugates for *in vivo* applications.

1.9. Research Gaps

A deeper understanding of the functions of glycans is indispensable to decoding the language of life. However, as glycan studies have been overshadowed by protein and nucleic acid research, carbohydrate-mediated biological interactions have received relatively little attention until the early 1980s due to funding issues. Along with the growing knowledge that glycans are directly or indirectly involved in the overwhelming majority of biological processes in living organisms, scientific interest has increased significantly in this field over the past few decades. In particular, the fact that carbohydrates are the basic way to interfere with viral infections has made them great attractive targets in inhibitor design. Also, the ability to perform glycoengineering on the GNPs surface has opened a new portal since the early 2000s. Because GNPs have excellent optical properties, particularly strong surface plasmon absorption and superb

fluorescence quenching, highly sensitive fluorescence-based readout systems can be developed to further investigate their interactions with virus surface lectins, and vice versa. Such new knowledge can be guide the production of effective viral inhibitors. Owing to the increasing knowledge about GNPs, they can now be synthesised with high colloidal stability and desired dimensions using efficient and straightforward methods. Their surface can then be easily modified by employing glycan-containing ligands via ligand exchange. As already mentioned in the earlier section, the specific topology and spatial orientation of binding domains on the viral receptors, DC-SIGN and DC-SIGNR, is still a significant knowledge gap in the literature. Besides, despite there are some useful reports about their monovalent interactions, the lack of a clear understanding about the nature of their multivalent interactions still poses a major challenge to designing and developing potent multivalent inhibitors against these lectins mediated viral infections. Therefore, GNPs coated with specific, functional glycan ligands could be promising probes for not only elucidating the structural properties and multivalent interactions of these receptor proteins, but also for potently blocking viral infections.

1.10. Aims of This Project

The key objective of this project is to synthesise and characterise a set of GNP-glycan conjugates with different sizes, glycan density and linker flexibility (length) to probe their binding characteristics with the tetrameric lectin viral receptors, DC-SIGN/R. These will provide detailed information about the structural and biochemical mechanisms of the multivalent lectin-glycan interactions for these viral receptor lectins which are exploited viruses, such as HIV and Ebola, to facilitate infection. A perfect spatial- and -orientation match between the GNPs surface glycans and lectin glycan-binding sites will result in high-affinity multivalent binding, allowing us to derive the binding site information and design specific multivalent glycans to potently block DC-SIGN/R mediated viral infections. While the binding biophysical data (*e.g.* binding affinities, kinetics, and thermodynamics) are mainly quantified by traditional methods, such as surface plasmon resonance (SPR) and isothermal titration calorimetry (ITC). However, these methods cannot reveal the key structural information, such as the

spatial distance, orientation of glycan binding domains and the binding modes of multimeric proteins. Such information is essential for designing spatially matched therapeutics against specific multimeric lectins.

In this project, we aim to develop a new, rapid, and highly sensitive fluorescence quenching-based readout to elucidate the structural and biochemical mechanisms of DC-SIGN/R based multivalent protein-glycan interactions. Besides the effect of some key parameters, including GNPs size, terminal functional groups, PEG density, and chain length on the binding of GNP-glycans DC-SIGN/R, and their ability to prevent protein corona formation *in vitro* will be investigated and analyzed using the GNP-fluorescence quenching method. We will also correlate these in vitro binding data with their DC-SIGN/R targeting specifically and selectively on cell surfaces. To the best of our knowledge, this research presents the first study of protein corona formation via GNP's fluorescence quenching. By tuning GNP size, and surface glycan type, density, flexibility, as well as inter-glycan distance, we hope to derive the optimal GNP-glycan structure which cannot only offer high binding affinity but also excellent specificity against specific target lectins by forming simultaneous multivalent binding.

Specifically, this project contains the following tasks:

1) GNPs of different sizes will be synthesised and fully characterised for their size, shape and uniformity using a range of characterisation techniques. The GNPs will be employed as a scaffold to build up multivalent GNP-sugar conjugates.
2) A series of lipoic acid (LA) oligoethylene glycol (EG_n) based multifunctional glycan ligands (*e.g.*, LA-EG_n-Man/-DiMan/-ManA and –OH, where n=2 or 4) will be synthesised, purified, and characterised, and then they will be used to coat citrate stabilized GNPs via ligand exchange to prepare robust and compact GNP-glycans. Here we specifically chose mannose monosaccharide (Man) and dimannose disaccharide (DiMan) because they are easier to synthesise. In addition, previous studies have shown that a polyvalent display of DiMan on a small gold nanoparticle scaffold gave stronger binding affinities to DC-SIGN than other (oligo)mannosides.[159]
3) Their binding affinity with dye-labelled DC-SIGN/R will be quantified via fluorescence quenching to derive their apparent binding dissociation constant

(K_d). The structure and binding models of DC-SIGN/R to GNP-glycans will then be verified by TEM and DLS techniques. Their binding specificity will also be tried to elucidate by competitive experiments using free glycans.

4) The inhibition potency of such multivalent GNP-glycan conjugates will then be explored against pseudo-Ebola infection of DC-SIGN/R expressing cells. We expect that the results will not only yield important structural information for these viral receptors but also lead to potent multivalent GNP-glycan inhibitors that can potently block viral entry to target cells, thereby preventing deadly viral infections.

1.11. References

1. O. V. Salata, *Journal of Nanobiotechnology*, 2004, **2**, 3.
2. E. Martin-Gayo and X. G. Yu, *Frontiers in Immunology*, 2019, **10**.
3. Y. van Kooyk and T. B. Geijtenbeek, *Nat Rev Immunol*, 2003, **3**, 697-709.
4. M. Anderluh, 2012.
5. B. Ernst and J. L. Magnani, *Nature Reviews Drug Discovery*, 2009, **8**, 661-677.
6. M. Bermejo-Jambrina, J. Eder, L. C. Helgers, N. Hertoghs, B. M. Nijmeijer, M. Stunnenberg and T. B. H. Geijtenbeek, *Frontiers in Immunology*, 2018, **9**.
7. G. Yilmaz and C. R. Becer, *Polymer Chemistry*, 2015, **6**, 5503-5514.
8. K. Drickamer and M. E. Taylor, *Curr Opin Struct Biol*, 2015, **34**, 26-34.
9. H. Feinberg, D. A. Mitchell, K. Drickamer and W. I. Weis, *Science*, 2001, **294**, 2163-2166.
10. H. Feinberg, R. Castelli, K. Drickamer, P. H. Seeberger and W. I. Weis, *J Biol Chem*, 2007, **282**, 4202-4209.
11. S. Cecioni, A. Imberty and S. Vidal, *Chem Rev*, 2015, **115**, 525-561.
12. D. A. Mitchell, A. J. Fadden and K. Drickamer, *J Biol Chem*, 2001, **276**, 28939-28945.
13. C. P. Alvarez, F. Lasala, J. Carrillo, O. Muñiz, A. L. Corbí and R. Delgado, *J Virol*, 2002, **76**, 6841-6844.
14. E. J. Soilleux, *Clin Sci (Lond)*, 2003, **104**, 437-446.
15. L. Wu and V. N. KewalRamani, *Nat Rev Immunol*, 2006, **6**, 859-868.
16. F. Zhang, S. Ren and Y. Zuo, *Int Rev Immunol*, 2014, **33**, 54-66.
17. Q. D. Yu, A. P. Oldring, A. S. Powlesland, C. K. Tso, C. Yang, K. Drickamer and M. E. Taylor, *J Mol Biol*, 2009, **387**, 1075-1080.
18. P. Valverde, J. D. Martínez, F. J. Cañada, A. Ardá and J. Jiménez-Barbero, *Chembiochem*, 2020, **21**, 2999-3025.
19. M. Anderluh, G. Jug, U. Svajger and N. Obermajer, *Curr Med Chem*, 2012, **19**, 992-1007.

20. G. Tabarani, M. Thépaut, D. Stroebel, C. Ebel, C. Vivès, P. Vachette, D. Durand and F. Fieschi, *J Biol Chem*, 2009, **284**, 21229-21240.
21. Y. van Kooyk and T. B. H. Geijtenbeek, *Nature Reviews Immunology*, 2003, **3**, 697-709.
22. U. Svajger, M. Anderluh, M. Jeras and N. Obermajer, *Cell Signal*, 2010, **22**, 1397-1405.
23. H. Feinberg, Y. Guo, D. A. Mitchell, K. Drickamer and W. I. Weis, *J Biol Chem*, 2005, **280**, 1327-1335.
24. N. Rahimi, *Biology (Basel)*, 2020, **10**.
25. J. D. Martínez, P. Valverde, S. Delgado, C. Romanò, B. Linclau, N. C. Reichardt, S. Oscarson, A. Ardá, J. Jiménez-Barbero and F. J. Cañada, *Molecules*, 2019, **24**.
26. S. Menon, K. Rosenberg, S. A. Graham, E. M. Ward, M. E. Taylor, K. Drickamer and D. E. Leckband, *Proc Natl Acad Sci U S A*, 2009, **106**, 11524-11529.
27. T. Johannssen and B. Lepenies, *Trends Biotechnol*, 2017, **35**, 334-346.
28. Y. Guo, W. Bruce Turnbull and D. Zhou, *Methods Enzymol*, 2018, **598**, 71-100.
29. H. Feinberg, C. K. Tso, M. E. Taylor, K. Drickamer and W. I. Weis, *J Mol Biol*, 2009, **394**, 613-620.
30. J. A. Robinson and K. Moehle, *Pure and Applied Chemistry*, 2014, **86**, 1483-1538.
31. Y. Guo, H. Feinberg, E. Conroy, D. A. Mitchell, R. Alvarez, O. Blixt, M. E. Taylor, W. I. Weis and K. Drickamer, *Nature Structural & Molecular Biology*, 2004, **11**, 591-598.
32. Y. Guo, C. Sakonsinsiri, I. Nehlmeier, M. A. Fascione, H. Zhang, W. Wang, S. Pöhlmann, W. B. Turnbull and D. Zhou, *Angew Chem Int Ed Engl*, 2016, **55**, 4738-4742.
33. G. Boily-Larouche, A. L. Iscache, L. S. Zijenah, J. H. Humphrey, A. J. Mouland, B. J. Ward and M. Roger, *PLoS One*, 2009, **4**, e7211.
34. C. W. Davis, H. Y. Nguyen, S. L. Hanna, M. D. Sánchez, R. W. Doms and T. C. Pierson, *J Virol*, 2006, **80**, 1290-1301.
35. A. B. Ward and I. A. Wilson, *Immunol Rev*, 2017, **275**, 21-32.
36. R. Amraei, W. Yin, M. A. Napoleon, E. L. Suder, J. Berrigan, Q. Zhao, J. Olejnik, K. B. Chandler, C. Xia, J. Feldman, B. M. Hauser, T. M. Caradonna, A. G. Schmidt, S. Gummuluru, E. Muhlberger, V. Chitalia, C. E. Costello and N. Rahimi, *bioRxiv*, 2021, DOI: 10.1101/2020.06.22.165803.
37. J. Huskens, L. J. Prins, R. Haag and B. J. Ravoo, *Multivalency: concepts, research and applications*, John Wiley & Sons, 2018.
38. C. Fasting, C. A. Schalley, M. Weber, O. Seitz, S. Hecht, B. Koksch, J. Dernedde, C. Graf, E. W. Knapp and R. Haag, *Angew Chem Int Ed Engl*, 2012, **51**, 10472-10498.
39. M. Mammen, S. K. Choi and G. M. Whitesides, *Angew Chem Int Ed Engl*, 1998, **37**, 2754-2794.
40. S. B. Yeldell and O. Seitz, *Chemical Society Reviews*, 2020, **49**, 6848-6865.
41. C. Chittasupho, *Ther Deliv*, 2012, **3**, 1171-1187.
42. A. K. Bakshi, T. Haider, R. Tiwari and V. Soni, *Drug Delivery and Translational Research*, 2022, DOI: 10.1007/s13346-021-01103-4.
43. R. S. Kane, *Langmuir*, 2010, **26**, 8636-8640.

44. V. M. Krishnamurthy, L. A. Estroff and G. M. Whitesides, in *Fragment-based Approaches in Drug Discovery*, 2006, DOI: https://doi.org/10.1002/3527608761.ch2, pp. 11-53.
45. A. Bernardi, J. Jiménez-Barbero, A. Casnati, C. De Castro, T. Darbre, F. Fieschi, J. Finne, H. Funken, K.-E. Jaeger, M. Lahmann, T. K. Lindhorst, M. Marradi, P. Messner, A. Molinaro, P. V. Murphy, C. Nativi, S. Oscarson, S. Penadés, F. Peri, R. J. Pieters, O. Renaudet, J.-L. Reymond, B. Richichi, J. Rojo, F. Sansone, C. Schäffer, W. B. Turnbull, T. Velasco-Torrijos, S. Vidal, S. Vincent, T. Wennekes, H. Zuilhof and A. Imberty, *Chemical Society Reviews*, 2013, **42**, 4709-4727.
46. M. Marradi, I. García and S. Penadés, *Prog Mol Biol Transl Sci*, 2011, **104**, 141-173.
47. M. Bermejo-Jambrina, J. Eder, L. C. Helgers, N. Hertoghs, B. M. Nijmeijer, M. Stunnenberg and T. B. H. Geijtenbeek, *Front Immunol*, 2018, **9**, 590.
48. S. Bhatia, L. C. Camacho and R. Haag, *J Am Chem Soc*, 2016, **138**, 8654-8666.
49. X. Chen, O. Ramström and M. Yan, *Nano Res*, 2014, **7**, 1381-1403.
50. I. S. MacPherson, J. S. Temme, S. Habeshian, K. Felczak, K. Pankiewicz, L. Hedstrom and I. J. Krauss, *Angew Chem Int Ed Engl*, 2011, **50**, 11238-11242.
51. M. L. Huang and K. Godula, *Glycobiology*, 2016, **26**, 797-803.
52. W. Lu and R. J. Pieters, *Expert Opin Drug Discov*, 2019, **14**, 387-395.
53. B. Arnáiz, O. Martínez-Ávila, J. M. Falcon-Perez and S. Penadés, *Bioconjug Chem*, 2012, **23**, 814-825.
54. P. Bojarová and V. Křen, *Biomaterials Science*, 2016, **4**, 1142-1160.
55. Y. Y. Chien, M. D. Jan, A. K. Adak, H. C. Tzeng, Y. P. Lin, Y. J. Chen, K. T. Wang, C. T. Chen, C. C. Chen and C. C. Lin, *Chembiochem*, 2008, **9**, 1100-1109.
56. N. C. Reichardt, M. Martín-Lomas and S. Penadés, *Chemical Society Reviews*, 2013, **42**, 4358-4376.
57. D. A. Giljohann, D. S. Seferos, W. L. Daniel, M. D. Massich, P. C. Patel and C. A. Mirkin, *Angew Chem Int Ed Engl*, 2010, **49**, 3280-3294.
58. I. Papp, C. Sieben, K. Ludwig, M. Roskamp, C. Böttcher, S. Schlecht, A. Herrmann and R. Haag, *Small*, 2010, **6**, 2900-2906.
59. A. K. Khan, R. Rashid, G. Murtaza and A. Zahra, *Tropical Journal of Pharmaceutical Research*, 2014, **13**, 1169-1177.
60. H. Daraee, A. Eatemadi, E. Abbasi, S. Fekri Aval, M. Kouhi and A. Akbarzadeh, *Artif Cells Nanomed Biotechnol*, 2016, **44**, 410-422.
61. S. Watanabe, K. Yoshida, K. Shinkawa, D. Kumagawa and H. Seguchi, *Colloids and Surfaces B: Biointerfaces*, 2010, **81**, 570-577.
62. X. Liu, M. Atwater, J. Wang and Q. Huo, *Colloids Surf B Biointerfaces*, 2007, **58**, 3-7.
63. Z. Miao, Z. Gao, R. Chen, X. Yu, Z. Su and G. Wei, *Curr Med Chem*, 2018, **25**, 1920-1944.
64. V. Amendola, M. Meneghetti, M. Stener, Y. Guo, S. Chen, P. Crespo, M. A. García, A. Hernando, P. Pengo and L. Pasquato, in *Comprehensive Analytical Chemistry*, eds. M. Valcárcel and Á. I. López-Lorente, Elsevier, 2014, vol. 66, pp. 81-152.

65. K. Saha, S. S. Agasti, C. Kim, X. Li and V. M. Rotello, *Chemical Reviews*, 2012, **112**, 2739-2779.
66. S. K. Ghosh and T. Pal, *Chem Rev*, 2007, **107**, 4797-4862.
67. V. Amendola, R. Pilot, M. Frasconi, O. M. Maragò and M. A. Iatì, *J Phys Condens Matter*, 2017, **29**, 203002.
68. M. Cordeiro, F. Ferreira Carlos, P. Pedrosa, A. Lopez and P. V. Baptista, *Diagnostics (Basel)*, 2016, **6**.
69. E. Boisselier and D. Astruc, *Chem Soc Rev*, 2009, **38**, 1759-1782.
70. P. K. Jain, K. S. Lee, I. H. El-Sayed and M. A. El-Sayed, *The Journal of Physical Chemistry B*, 2006, **110**, 7238-7248.
71. X. Huang and M. A. El-Sayed, *Journal of Advanced Research*, 2010, **1**, 13-28.
72. P. N. Njoki, I. I. S. Lim, D. Mott, H.-Y. Park, B. Khan, S. Mishra, R. Sujakumar, J. Luo and C.-J. Zhong, *The Journal of Physical Chemistry C*, 2007, **111**, 14664-14669.
73. J. Cao, T. Sun and K. T. V. Grattan, *Sensors and Actuators B: Chemical*, 2014, **195**, 332-351.
74. X. Huang, P. K. Jain, I. H. El-Sayed and M. A. El-Sayed, *Nanomedicine (Lond)*, 2007, **2**, 681-693.
75. S. Zhao, Y. Luo, Z. Chang, C. Liu, T. Li, L. Gan, Y. Huang and Q. Sun, *Nanoscale Research Letters*, 2021, **16**, 170.
76. S. O. Pereira, A. Barros-Timmons and T. Trindade, *Polymers*, 2018, **10**, 189.
77. C. Lee, P. Wang, M. A. Gaston, A. A. Weiss and P. Zhang, in *Biosensors and Biodetection: Methods and Protocols Volume 1: Optical-Based Detectors*, eds. A. Rasooly and B. Prickril, Springer New York, New York, NY, 2017, DOI: 10.1007/978-1-4939-6848-0_7, pp. 109-116.
78. Y.-C. Yeh, B. Creran and V. M. Rotello, *Nanoscale*, 2012, **4**, 1871-1880.
79. M. Swierczewska, S. Lee and X. Chen, *Physical Chemistry Chemical Physics*, 2011, **13**, 9929-9941.
80. B. Valeur and M. N. Berberan-Santos, *Molecular fluorescence: principles and applications*, John Wiley & Sons, 2012.
81. in *Principles of Fluorescence Spectroscopy*, ed. J. R. Lakowicz, Springer US, Boston, MA, 2006, DOI: 10.1007/978-0-387-46312-4_1, pp. 1-26.
82. A. B. Chinen, C. M. Guan, J. R. Ferrer, S. N. Barnaby, T. J. Merkel and C. A. Mirkin, *Chemical Reviews*, 2015, **115**, 10530-10574.
83. S. Sargazi, I. Fatima, M. Hassan Kiani, V. Mohammadzadeh, R. Arshad, M. Bilal, A. Rahdar, A. M. Díez-Pascual and R. Behzadmehr, *International Journal of Biological Macromolecules*, 2022, **206**, 115-147.
84. J. Shi, F. Tian, J. Lyu and M. Yang, *Journal of Materials Chemistry B*, 2015, **3**, 6989-7005.
85. S. Das, M. Dutta and D. Das, *Analytical Methods*, 2013, **5**, 6262-6285.
86. P. R. Selvin, *Nature Structural Biology*, 2000, **7**, 730-734.
87. E. Dulkeith, M. Ringler, T. A. Klar, J. Feldmann, A. Muñoz Javier and W. J. Parak, *Nano Letters*, 2005, **5**, 585-589.

88. N.-T. Chen, S.-H. Cheng, C.-P. Liu, J. S. Souris, C.-T. Chen, C.-Y. Mou and L.-W. Lo, *International Journal of Molecular Sciences*, 2012, **13**, 16598-16623.
89. K. A. Kang, J. Wang, J. B. Jasinski and S. Achilefu, *Journal of Nanobiotechnology*, 2011, **9**, 16.
90. B. N. J. Persson and N. D. Lang, *Physical Review B*, 1982, **26**, 5409-5415.
91. A. Samanta, Y. Zhou, S. Zou, H. Yan and Y. Liu, *Nano Letters*, 2014, **14**, 5052-5057.
92. in *Principles of Fluorescence Spectroscopy*, ed. J. R. Lakowicz, Springer US, Boston, MA, 2006, DOI: 10.1007/978-0-387-46312-4_9, pp. 331-351.
93. D. Ghosh and N. Chattopadhyay, *Journal of Luminescence*, 2015, **160**, 223-232.
94. C. Chen and N. Hildebrandt, *TrAC Trends in Analytical Chemistry*, 2020, **123**, 115748.
95. K. Liu, Z. He, J. F. Curtin, H. J. Byrne and F. Tian, *Scientific Reports*, 2019, **9**, 7421.
96. J. Zhou, J. Ralston, R. Sedev and D. A. Beattie, *J Colloid Interface Sci*, 2009, **331**, 251-262.
97. K. X. Lee, K. Shameli, Y. P. Yew, S. Y. Teow, H. Jahangirian, R. Rafiee-Moghaddam and T. J. Webster, *Int J Nanomedicine*, 2020, **15**, 275-300.
98. S. J. Amina and B. Guo, *Int J Nanomedicine*, 2020, **15**, 9823-9857.
99. K. N. Thakkar, S. S. Mhatre and R. Y. Parikh, *Nanomedicine*, 2010, **6**, 257-262.
100. M. Faraday, *Philosophical Transactions of the Royal Society of London*, 1857, **147**, 145-181.
101. J. Turkevich, P. C. Stevenson and J. Hillier, *Discussions of the Faraday Society*, 1951, **11**, 55-75.
102. E. Oh, K. Susumu, A. J. Mäkinen, J. R. Deschamps, A. L. Huston and I. L. Medintz, *The Journal of Physical Chemistry C*, 2013, **117**, 18947-18956.
103. H. Tyagi, A. Kushwaha, A. Kumar and M. Aslam, *Nanoscale Research Letters*, 2016, **11**, 362.
104. J. Dong, P. L. Carpinone, G. Pyrgiotakis, P. Demokritou and B. M. Moudgil, *Kona*, 2020, **37**, 224-232.
105. K. Zabetakis, W. E. Ghann, S. Kumar and M.-C. Daniel, *Gold Bulletin*, 2012, **45**, 203-211.
106. G. Frens, *Nature Physical Science*, 1973, **241**, 20-22.
107. J. Kimling, M. Maier, B. Okenve, V. Kotaidis, H. Ballot and A. Plech, *J Phys Chem B*, 2006, **110**, 15700-15707.
108. X. Ji, X. Song, J. Li, Y. Bai, W. Yang and X. Peng, *Journal of the American Chemical Society*, 2007, **129**, 13939-13948.
109. M. Brust, M. Walker, D. Bethell, D. J. Schiffrin and R. Whyman, *Journal of the Chemical Society, Chemical Communications*, 1994, DOI: 10.1039/C39940000801, 801-802.
110. M. Brust, J. Fink, D. Bethell, D. J. Schiffrin and C. Kiely, *Journal of the Chemical Society, Chemical Communications*, 1995, DOI: 10.1039/C39950001655, 1655-1656.
111. P. Zhao, N. Li and D. Astruc, *Coordination Chemistry Reviews*, 2013, **257**, 638-665.
112. R. Herizchi, E. Abbasi, M. Milani and A. Akbarzadeh, *Artif Cells Nanomed Biotechnol*, 2016, **44**, 596-602.
113. C. Ziegler and A. Eychmüller, *The Journal of Physical Chemistry C*, 2011, **115**, 4502-4506.
114. R. A. Sperling and W. J. Parak, *Philos Trans A Math Phys Eng Sci*, 2010, **368**, 1333-1383.
115. S. Her, D. A. Jaffray and C. Allen, *Advanced Drug Delivery Reviews*, 2017, **109**, 84-101.

116. Y. Liu, M. K. Shipton, J. Ryan, E. D. Kaufman, S. Franzen and D. L. Feldheim, *Anal Chem*, 2007, **79**, 2221-2229.

117. K. Susumu, H. T. Uyeda, I. L. Medintz, T. Pons, J. B. Delehanty and H. Mattoussi, *Journal of the American Chemical Society*, 2007, **129**, 13987-13996.

118. L. J. Cruz, P. J. Tacken, R. Fokkink and C. G. Figdor, *Biomaterials*, 2011, **32**, 6791-6803.

119. F. Danhier, E. Ansorena, J. M. Silva, R. Coco, A. Le Breton and V. Préat, *Journal of controlled release*, 2012, **161**, 505-522.

120. R. Mout, D. F. Moyano, S. Rana and V. M. Rotello, *Chemical Society Reviews*, 2012, **41**, 2539-2544.

121. C. A. Mirkin, R. L. Letsinger, R. C. Mucic and J. J. Storhoff, *Nature*, 1996, **382**, 607-609.

122. A. P. Alivisatos, K. P. Johnsson, X. Peng, T. E. Wilson, C. J. Loweth, M. P. Bruchez and P. G. Schultz, *Nature*, 1996, **382**, 609-611.

123. D. A. Giljohann, D. S. Seferos, P. C. Patel, J. E. Millstone, N. L. Rosi and C. A. Mirkin, *Nano Lett*, 2007, **7**, 3818-3821.

124. N. L. Rosi, D. A. Giljohann, C. S. Thaxton, A. K. Lytton-Jean, M. S. Han and C. A. Mirkin, *Science*, 2006, **312**, 1027-1030.

125. M. H. Jazayeri, H. Amani, A. A. Pourfatollah, H. Pazoki-Toroudi and B. Sedighimoghaddam, *Sensing and Bio-Sensing Research*, 2016, **9**, 17-22.

126. Z. P. Chen, Z. F. Peng, P. Zhang, X. F. Jin, J. H. Jiang, X. B. Zhang, G. L. Shen and R. Q. Yu, *Talanta*, 2007, **72**, 1800-1804.

127. N. Li and W. H. Binder, *Journal of Materials Chemistry*, 2011, **21**, 16717-16734.

128. C. R. Becer, R. Hoogenboom and U. S. Schubert, *Angew Chem Int Ed Engl*, 2009, **48**, 4900-4908.

129. E. Lallana, A. Sousa-Herves, F. Fernandez-Trillo, R. Riguera and E. Fernandez-Megia, *Pharm Res*, 2012, **29**, 1-34.

130. S. I. Presolski, V. P. Hong and M. G. Finn, *Curr Protoc Chem Biol*, 2011, **3**, 153-162.

131. B. T. Worrell, J. A. Malik and V. V. Fokin, *Science*, 2013, **340**, 457-460.

132. V. Poonthiyil, T. K. Lindhorst, V. B. Golovko and A. J. Fairbanks, *Beilstein J Org Chem*, 2018, **14**, 11-24.

133. D. A. Fleming, C. J. Thode and M. E. Williams, *Chemistry of Materials*, 2006, **18**, 2327-2334.

134. E. Boisselier, L. Salmon, J. Ruiz and D. Astruc, *Chemical Communications*, 2008, DOI: 10.1039/B812249K, 5788-5790.

135. T. R. Chan, R. Hilgraf, K. B. Sharpless and V. V. Fokin, *Org Lett*, 2004, **6**, 2853-2855.

136. J. Dommerholt, F. Rutjes and F. L. van Delft, *Top Curr Chem (Cham)*, 2016, **374**, 16.

137. X.-P. He, X.-L. Hu, H.-Y. Jin, J. Gan, H. Zhu, J. Li, Y.-T. Long and H. Tian, *Analytical Chemistry*, 2015, **87**, 9078-9083.

138. X. Wang, P. Gobbo, M. Suchy, M. S. Workentin and R. H. E. Hudson, *RSC Advances*, 2014, **4**, 43087-43091.

139. Y. Pan, S. Neuss, A. Leifert, M. Fischler, F. Wen, U. Simon, G. Schmid, W. Brandau and W. Jahnen-Dechent, *Small*, 2007, **3**, 1941-1949.

140. E. E. Connor, J. Mwamuka, A. Gole, C. J. Murphy and M. D. Wyatt, *Small*, 2005, **1**, 325-327.

141. R. Shukla, V. Bansal, M. Chaudhary, A. Basu, R. R. Bhonde and M. Sastry, *Langmuir*, 2005, **21**, 10644-10654.

142. C. Villiers, H. Freitas, R. Couderc, M. B. Villiers and P. Marche, *J Nanopart Res*, 2010, **12**, 55-60.

143. C. M. Goodman, C. D. McCusker, T. Yilmaz and V. M. Rotello, *Bioconjugate Chemistry*, 2004, **15**, 897-900.

144. M. Turner, V. B. Golovko, O. P. Vaughan, P. Abdulkin, A. Berenguer-Murcia, M. S. Tikhov, B. F. Johnson and R. M. Lambert, *Nature*, 2008, **454**, 981-983.

145. N. M. Schaeublin, L. K. Braydich-Stolle, E. I. Maurer, K. Park, R. I. MacCuspie, A. R. M. N. Afrooz, R. A. Vaia, N. B. Saleh and S. M. Hussain, *Langmuir*, 2012, **28**, 3248-3258.

146. Y.-P. Jia, B.-Y. Ma, X.-W. Wei and Z.-Y. Qian, *Chinese Chemical Letters*, 2017, **28**, 691-702.

147. D. P. O'Neal, L. R. Hirsch, N. J. Halas, J. D. Payne and J. L. West, *Cancer Lett*, 2004, **209**, 171-176.

148. S. Lal, S. E. Clare and N. J. Halas, *Accounts of Chemical Research*, 2008, **41**, 1842-1851.

149. E. Caballero-Díaz and M. Valcárcel, in *Comprehensive Analytical Chemistry*, eds. M. Valcárcel and Á. I. López-Lorente, Elsevier, 2014, vol. 66, pp. 207-254.

150. M. S. Kang, S. Y. Lee, K. S. Kim and D. W. Han, *Pharmaceutics*, 2020, **12**.

151. J. Milan, K. Niemczyk and M. Kus-Liśkiewicz, *Materials*, 2022, **15**, 3355.

152. J. Wolfram, Y. Yang, J. Shen, A. Moten, C. Chen, H. Shen, M. Ferrari and Y. Zhao, *Colloids Surf B Biointerfaces*, 2014, **124**, 17-24.

153. V. H. Nguyen and B. J. Lee, *Int J Nanomedicine*, 2017, **12**, 3137-3151.

154. C. D. Walkey, J. B. Olsen, H. Guo, A. Emili and W. C. W. Chan, *Journal of the American Chemical Society*, 2012, **134**, 2139-2147.

155. R. García-Álvarez, M. Hadjidemetriou, A. Sánchez-Iglesias, L. M. Liz-Marzán and K. Kostarelos, *Nanoscale*, 2018, **10**, 1256-1264.

156. I. García, A. Sánchez-Iglesias, M. Henriksen-Lacey, M. Grzelczak, S. Penadés and L. M. Liz-Marzán, *Journal of the American Chemical Society*, 2015, **137**, 3686-3692.

157. A. M. Alkilany, L. Zhu, H. Weller, A. Mews, W. J. Parak, M. Barz and N. Feliu, *Adv Drug Deliv Rev*, 2019, **143**, 22-36.

158. Y. K. Lee, E. J. Choi, T. J. Webster, S. H. Kim and D. Khang, *Int J Nanomedicine*, 2015, **10**, 97-113.

159. O. Martínez-Ávila, K. Hijazi, M. Marradi, C. Clavel, C. Campion, C. Kelly and S. Penadés, *Chemistry – A European Journal*, 2009, **15**, 9874-9888.

Chapter 2
Materials, Methods, and Experimental Procedures

This chapter provides a detailed description of the following five main headings: (1) synthesis, purification, and characterisation of a range of LA-PEG based multifunctional ligands, (2) synthesis of spherical gold nanoparticles of different sizes, (3) preparation of GNP-glycan conjugates, (4) production and purification of both labelled and wild-type proteins DC-SIGN/R, and (5) labelling the proteins BSA and Lysozyme with dye compounds. Viral inhibition studies of the synthesised GNP-glycans were carried out by our collaborator, Professor Stefan Pöhlmann's group, at the German Primate Centre in Germany. The author of this thesis analysed the data and reported his own conclusions in **Chapter 3.8** regarding the findings.

In this project, a series of alkyl-terminated PEG-based thiol functionalised linkers ligands were synthesised, and functional groups were then attached via click chemistry. All synthesised ligands were fully characterised using a range of analytical and spectroscopic techniques, including thin layer chromatography (TLC), high-resolution mass spectra (HR-MS), liquid chromatography–mass spectrometry (LC-MS), and nuclear magnetic resonance spectroscopy (NMR). Afterward, these ligands were easily capped on the surface of citrate-stabilized GNPs by cap-exchange reactions, owing to the strong chelative binding of the lipoic acid, LA, group in the ligands onto the GNP surface. The successful cap-exchange of GNPs with the ligands was verified using a number of methods, such as salt stability tests, UV-vis spectroscopy, and dynamic light scattering (DLS), as explained in more detail in the next chapter.

2.1. Characterisation Techniques of the Synthesised Products

The physical and chemical properties of GNPs are incredibly critical for their interactions with biological systems. Their intrinsic key parameters, including size, shape, and morphology, and the chemical composition of surface coating and density, are of great importance in determining their biocompatibility or possible toxicity.[1] Therefore, it is necessary to characterise them before their biological applications. A range of validated techniques are utilized; among which three are extensively

employed, *i.e.* ultraviolet-visible spectroscopy, dynamic light scattering, and transmission electron microscopy.

2.1.1. Ultraviolet-Visible Spectroscopy

Ultraviolet-visible (UV-vis) spectroscopy is a simple and fast spectral technique to quantify the light absorbed and emitted by a sample. The measured value is a quantity given as extinction, described as the sum of absorbed and scattered light. In this method, as shown in **Figure 2.1.1**, a sample is positioned between a photodetector and a light source, and the light intensity is then measured before and after the sample. UV-vis measurements are correlated at each point to measure the wavelength-dependent spectrum of the sample and plotted as extinction with the obtained data.[2]

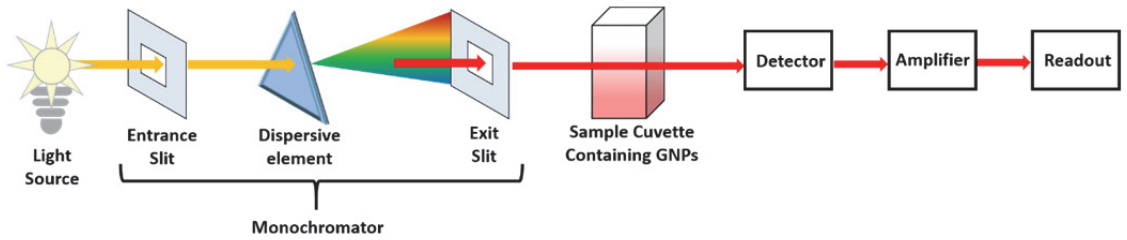

Figure 2.1.1. The basic principle of UV-vis spectrophotometer.

As pointed out before, GNPs exhibit a strong SPR peak in the visible region (typically at around 520 nm), which can be measured by UV-vis spectroscopy. The SPR peak is highly sensitive to their size, shape, dispersion (aggregation state), and also concentration;[3, 4] this makes UV-vis an excellent tool for their characterisation. The SPR peak absorbance increases with the increasing GNP diameter.[5] The bandwidth of the LSPR absorbance peak can also be associated with the dispersity of GNPs in an aqueous solution.[6] Concerning their geometry, SPR peak(s) gives some insight into their shape; for example, spherical GNPs give only one strong SPR band, whereas gold nanorods (GNRs) display two distinct absorption bands, LSPR and TSPR, due to their anisotropic shape, as explained in earlier parts.[7] Also, the surface functionalization of GNPs can be easily monitored using UV-vis. The binding of ligands to the GNP surface usually results in a red-shift of the SPR peak by a few nm, allowing for easy observation of whether the GNPs surface is functionalized or not. Similarly, the aggregation of GNPs leads to a significant red-shift in the spectrum,[8] accompanied with a widening of

the SPR peak and decreasing in peak intensity. In addition, GNPs concentration in a batch can be calculated by the Lambert-Beer Law using the UV absorbance and extinction coefficients of GNPs via the equation below.

$$A = \varepsilon \, . \, l \, . \, c$$

Where A is the UV absorbance, ε is the molar extinction coefficient GNPs, l is the path length, and c is the concentration of GNP-conjugates.

2.1.2. Dynamic Light Scattering (DLS)

Dynamic light scattering, DLS, is a well-established technique for determining the hydrodynamic diameter of particles with high resolution across a broad size range, from sub-nanometre (~0.1 nm)[9] to ~10 μm[10] in a solution. This method is based on the scattering of incident light as a result of hitting the particles in a solution. The spatial dynamics of the light scattering and the fluctuations of its optical properties are then recorded. The light scattering ability is proportional to the sixth power of the NP core radius. Depending on size, NPs generally display two types of light scattering; Rayleigh scattering and Mie scattering. When the wavelength of the incident light is much bigger than the NP size (particle diameter d ≪ λ light's wavelength), NPs display Rayleigh scattering; in the opposite case, they exhibit Mie scattering. In the solution, larger nanoparticles diffuse more slowly than smaller ones.[11] The light scattered from the particles fluctuates over time due to the Brownian motion of particles, which refers to their spontaneous random move through a solution. Backscattered light is detected at 173° because this angle avoids reflections from the sample cuvette and also provides much higher sensitivity due to the much larger scattered volume at this detection angle.[12] A basic schematic of a typical DLS instrumentation is shown in **Figure 2.1.2**. DLS measurements detect the scattered light from the particle over time, which then correlate them mathematically with the particle size. The hydrodynamic diameter of the particles is then calculated using the Stokes-Einstein equation below.[13]

$$D_h = \frac{K_b T}{3\pi\eta D_t}$$

Where D_h is the hydrodynamic radius of the particle in solution, K_b is Boltzmann's constant, T is the thermodynamic temperature, η is the solvent viscosity, and D_t is the translational diffusion coefficient.

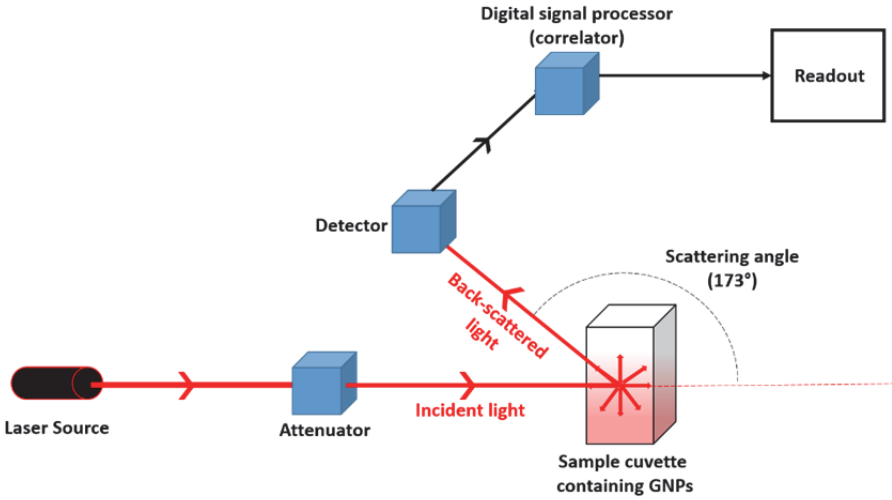

Figure 2.1.2. A schematic diagram showing the principles of DLS measurement.

Scattered light from GNPs provides some helpful information about their physical (GNP size, shape, and distribution)[14] and chemical (GNP surface chemistry) properties by comparing their D_hs before and after functionalization.[11] GNPs offer extraordinarily light scattering; DLS, therefore, it is also a powerful tool for determining the kinetic information and biomolecular binding interactions between GNPs and biomolecules.[15, 16] In addition, it also has a high sensitivity to monitoring the formation and process of GNPs aggregation.[11] In DLS measurement, the particles are solvated and then fluctuate over time in the solution, the light scattered from their surface cannot verify their actual size. As GNPs suspended in water are surrounded by an aqueous layer, their hydrodynamic diameters are expected to be a few nanometers larger than their actual size,[8] as demonstrated in **Figure 2.1.3**. Hence DLS measurement can provide an average colloidal size of GNPs.

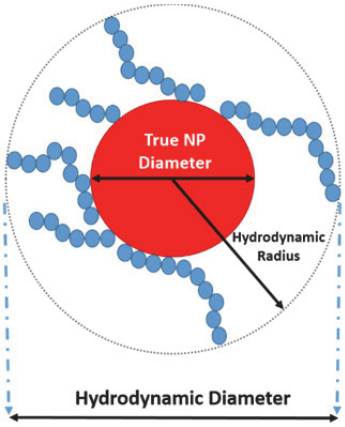

Figure 2.1.3. A schematic representing the hydrodynamic and actual size of GNPs.

2.1.3. Transmission Electron Microscopy

Transmission electron microscopy, TEM, is a highly sophisticated instrument to investigate the structural and chemical properties of nanomaterials at the atomic scale.[17] TEM has the ability to display electrons at a higher resolution than the light microscope, owing to the smaller "de Broglie" wavelength of electrons in which electrons exhibit wave-like behaviour. The use of electrons as a source provides a strong interaction with the nanoparticles. This produces a variety of signals (*e.g.* Rayleigh / Mie scattered electrons, photons, etc.) that can be used to obtain data about the structure and physical properties of nanomaterials (*e.g.* optical, magnetic, and electrical properties) and are recorded through multiple lenses. With high count rates and a large detector area, TEM has a high sensitivity for elemental analysis, even in subnanometer dimensions.[18] TEM usually produces two-dimensional images that require more interpretation in order to reconstruct the 3D structure, but it can provide excellent resolution, down to the atomic level. By applying the latest technological developments and robust algorithms in TEM optics (*e.g.* monochromators, aberration correlators, and detectors), the three-dimensional structure images of nanomaterials have been obtained with high reliability.[19]

TEM usually analyses the GNPs samples in the dry state under a high vacuum, allowing us to identify their exact structural morphology and size easily.[11] TEM images of GNPs with different sizes are given in **Figure 2.1.4**. However, in their distribution and colloidal stability, TEM is not as informative as DLS because drying sample can lead to GNP aggregation and assembly.[20] In addition, GNP surface modifications are not easily detected by standard TEM imaging; this requires special equipment such as cryo-TEM.[21] The reason here is that the organic shell has much lower electron absorption than gold, therefore negative stain should be used to make the organic coating more visible.

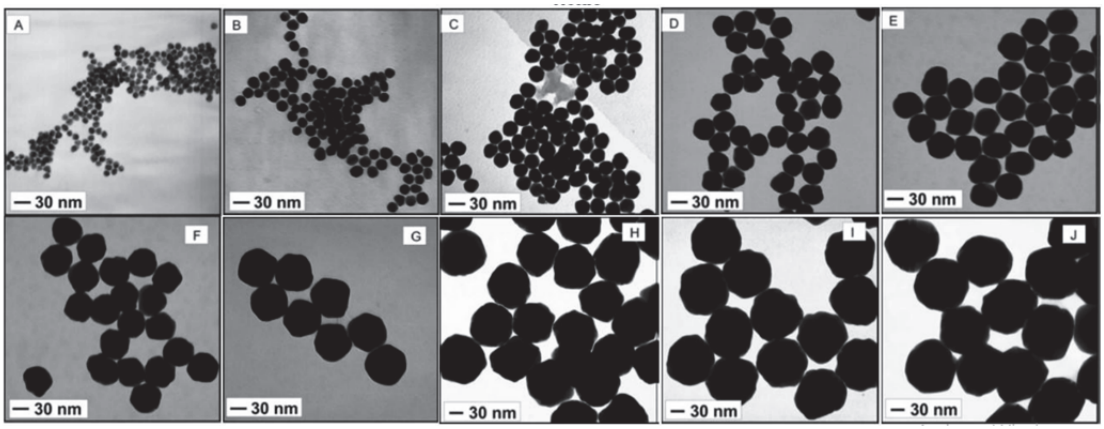

Figure 2.1.4. TEM micrographs of GNPs with different sizes. Top row shows the size of GNPs from 10 nm (A) to 50 nm (E), and bottom row represents their sizes from 60 nm (F) to 100 nm (J) (from left to right).[22]

2.2. Materials and Instruments

2.2.1. Materials and Reagents

All the chemicals and reagents which were used for the synthesis of multifunctional ligands were purchased from Sigma Aldrich, Fisher, or Alfa Aesar unless otherwise noted, except PEG_{750} (where the number indicates the average molecular weight of PEG), which was purchased from Fluka. Only 5 nm citrate-stabilized GNPs were purchased from Sigma-Aldrich (Product Code - 741949). All reagents used for the protein production and labelling were purchased from Sigma-Aldrich or Fisher, except the dye which was purchased from Atto-Tec, GmbH. The mannose monosaccharide and disaccharide were synthesised by Dr. Yuanyuan Liu, a previous academic visitor of the Zhou group, and Dr. Darshita Budhadev, a postdoc within the group. Carboxylated mannan was produced by Dr. Gavin Miller's group from Keele University, UK. The ligand N_3-PEG_{750}-OMe were synthesised by a previous PhD student, Weili Wang, from the Zhou group. LA-Zwitterion ligand and LA-(PEG_{1000}-OH)$_2$ was produced by Dr. Yuanyuan Liu. The linker ligands LA-(EG_n-C≡CH)$_m$ (where n=2 and 4; m=1, 2, and 3) were synthesised by Dr. Darshita Budhadev within the group. Dry solvents were obtained from an Innovative Technologies Solvent Drying System. Ultra-pure water (resistance >18.2 MΩ.cm), which was used for all experiments and making solutions & buffers, was obtained from Milli-Q Ultrapure Water Purification System.

2.2.2. Instruments and Methods

All moisture-sensitive reactions were performed in oven-dried glassware under a nitrogen atmosphere. Evaporations were carried out at reduced pressure using a Bruker rotary evaporator and a Virtis Benchtop K freeze dryer. Column chromatography was performed using silica gel 60 A, and the progress of the reactions was monitored by thin layer chromatography, TLC, analysis on aluminium sheets pre-coated with silica (Merck Silica Kieselgel 60 F_{254}), then for identifying the compounds present in the reaction mixture, TLC-plates were stained with iodine, orcinol, or *p*-anisaldehyde stains, commercially available. The polar lipoic acid-sugar derivatives were purified by size exclusion chromatography via Biogel P2 column using 20 mM ammonium formate as an eluent to yield the desired pure product.

All ^{1}H and ^{13}C NMR spectra were recorded on a Bruker AV4 NEO-500 (500 MHz for ^{1}H, 125 MHz for ^{13}C) and a Bruker AV3HD-400 (400 MHz for ^{1}H, 100 MHz for ^{13}C) spectrometer in appropriate undeuterated solvents. All chemical shifts (δs) are denoted in parts per million (ppm) calibrated using residual undeuterated solvents as internal references ($CDCl_3$: δ ^{1}H = 7.26 ppm, δ ^{13}C = 77.16 ppm; CD_3OD: δ ^{1}H = 3.31 ppm, δ ^{13}C = 49.15 ppm; D_2O: δ ^{1}H = 4.80 ppm). The coupling constants (*J*) are in parentheses and expressed in Hertz, Hz, and the peak patterns are indicated with the following abbreviations: s = singlet, d = doublet, t = triplet, q = quartet, m = multiplet, br = broad, dd = doublet of doublets, dt = doublet of triplets, td = triplet of doublets, dq= doublet of quartets, qt = quartet of triplets, ddd = doublet of doublet of doublets, dtd = doublet of triplet of doublets. High-resolution mass spectra (HR-MS) were obtained on a Bruker Daltonics MicroTOF mass spectrometer, and deconvoluted mass values (*m/z*) are reported in Daltons, and protein labelling efficiency was also calculated from the ratio of the integral of the labelled protein HR-MS peak to the sum of that of the labelled and unlabelled protein peaks. The mass spectrometry data were also collected using a Bruker HCT Ultra coupled to Ultimate 3000 HPLC (Thermo Scientific). Methanol was used as a solvent to ionise the products; this provides a high-precision detection of ionized samples by classifying the resulting ions by vacuum with respect to mass-charge ratios (*m/z*).

UV-vis absorption spectra were recorded on either a Cary 60 UV-vis spectrophotometer (Agilent Technologies) over 200-800 nm using 1 mL quartz cuvette with an optical path length of 1 cm or on a Nanodrop 2000 spectrophotometer (Thermo Scientific) over the range of 200-800 nm using one drop of the solution with an optical path length of 1 mm. All measurements were done in pure water unless otherwise stated in experimental procedure. A Zetasizer NanoZS DLS system (Malvern) was used to perform all DLS measurements using a sample volume of 400 µL in 1 cm disposable polystyrene cuvettes. This is equipped with a 633 nm (red) laser and a detector configured to collect backscattered light at 173°. Each sample was measured in pure water at RT with a fixed ten consecutive runs and each run lasts 120 seconds, unless otherwise stated in experimental procedure. Each size distribution was analysed in triplicate to calculate an average of hydrodynamic diameter (D_h) in volume population and standard deviation. The distribution histograms were fitted by standard Gaussian function with fitting parameters shown in all graph to determine the mean D_h size, full-width at half-maximum (FWHM), and polydispersity index (PdI). PdI is basically an indication of the particle size distribution within a sample such that its value > 0.5 shows the polydisperse distribution.[23] It is calculated by squaring the FWHM/mean diameter based on the Gaussian distribution. Fluorescence quenching measurements were performed on a Cary Eclipse Fluorescence Spectrophotometer and a Horiba FluroMax 4 spectrometer, using a using a 0.70 mL quartz cuvette. Centrifugations were performed using a Thermo Scientific Heraeus Fresco 21 and a Beckman Coulter Avanti JXN-30 centrifuge, depending on the speed and volume, at RT unless otherwise noted. Purification or concentration by centrifugation was carried out using Merck Millipore 10 kDa and 30 kDa molecular weight cut-off (MWCO) Amicon Ultra centrifugal filters for protein and GNPs, respectively.

2.3. Experimental Procedures: Ligand Synthesis

2.3.1. Synthesis of OH-PEG$_{1000/600}$-N$_3$

The synthesis of OH-PEG$_{1000/600}$-N$_3$ (where the numbers 1000 and 600 refer to an average molecular weight of PEG) was based on the published protocol by Susumu *et al.*[24] and Zhang *et al.*[25] The ligands were obtained in two-step synthesis including the

substitution reaction of one hydroxyl group with a dimethyl sulfone, and subsequent substitution with an azide. The synthesis routes can be found in **Scheme 2.3.1** below.

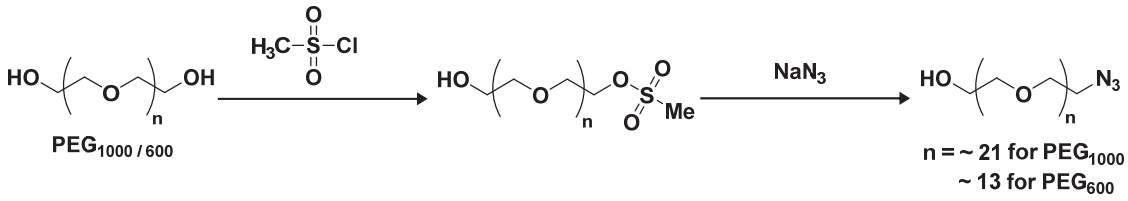

Scheme 2.3.1. A reaction scheme showing the synthesis of (A) HO-PEG_{1000}-N_3 and (B) HO-PEG_{600}-N_3.

2.3.1.1. Synthesis of Methanesulfonyl-PEG_{1000}-OH

Poly(ethylene glycol), PEG, with an average molecular weight of 1000 (30 g, 30 mmol), tetrahydrofuran, THF, (50 mL), and methanesulfonyl chloride (3.44 g, 2.32 mL, 30 mmol) were placed in a 250 mL two-necked round-bottomed flask and magnetically stirred in an ice bath under N_2 atmosphere. After cooling to below 5 °C with an ice bath, triethylamine (3.64 g, 5 mL, 36 mmol) was added dropwise into the mixture through the addition funnel over 30 mins while stirring. Afterward, the solution was left to warm up gradually to RT and stirred overnight. The product was checked by TCL using $CHCl_3$: MeOH (10:1 (vol/vol)) as an eluting solvent. Once the reaction was completed, the mixture was diluted with ultrapure water (66 mL), and $NaHCO_3$ (4.13 g) was then added to the solution; the resulting mixture was transferred to a separator funnel and extracted with $CHCl_3$ (60 mL x 3). The organic layer was collected, and the solvent was evaporated to dryness on a rotary evaporator under reduced pressure, yielding **compound 1**, as a white waxy solid (29.69 g, 27.8 mmol, 93 % yield).

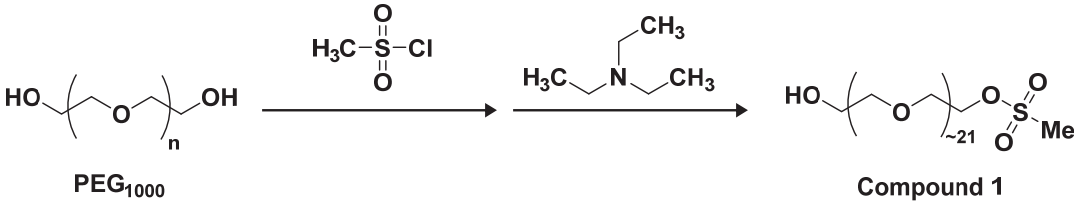

Scheme 2.3.2. A reaction scheme showing the synthesis of HO-PEG_{1000}-OSO_2CH_3.

TLC: ($CHCl_3$/MeOH 10:1) R_f 0.62; **^{1}H-NMR (400 MHz, $CDCl_3$):** δ (ppm) 4.40 – 4.35 (m, 2H), 3.78 – 3.75 (m, 2H), 3.73 – 3.70 (m, 2H), 3.65 (d, 10H, *J*=3.0 Hz), 3.64 (d, 63H, *J*=1.5 Hz), 3.63 (s, 5H), 3.61 – 3.59 (m, 2H), 3.48 (s, 3H), 3.08 (s, 3H); **^{13}C-NMR (100 MHz, $CDCl_3$):** δ (ppm) 77.3, 77.0, 76.7, 72.6, 70.5, 70.3, 69.3, 69.0, 61.7, 37.7; **HR-MS:** The corresponding MS spectrum displayed a series of species with m/z ratios separated by multiple number of 44 (the molecular weight of EG unit): 862.47, 906.49, 950.52, 994.54, 1038.57, 1082.60, and 1126.70. The corresponding expected $[M+NH_4]^+$ peaks with PEG repeat number of 16, 17, 18, 19, 20, 21, and 22 were 862.50, 906.53, 950.56, 994.59, 1038.62, 1082.65, and 1126.68, respectively. (n = ∼21).

2.3.1.2. Synthesis of HO-PEG$_{1000}$-N$_3$

The crude product methanesulfonyl-PEG$_{1000}$-OH, **compound 1**, (10 g, 9.4 mmol), sodium azide (2.0 g), THF (50 mL), H_2O (30 mL), and $NaHCO_3$ (12.5 g) were added to a 500-mL round-bottomed flask under stirring in an ice bath. After the biphasic reaction mixture was heated under N_2 to distill off the THF, then it was refluxed overnight. The next day the mixture was cooled down to RT, transferred to a separator funnel and then extracted with $CHCl_3$ (100 mL x 5). The combined organic layers were dried over Mg_2SO_4 (20 g, ~30 mins) with constant stirring, and filtered off. The resulting product was concentrated and purified by silica gel column chromatography using $CHCl_3$:MeOH (10:1 (vol/vol)) as an eluting solvent. The fractions containing of the desired pure product (confirmed by TLC) were combined, and evaporated to dryness to afford the desired product, **compound 2**, as a slightly yellowish oil (8.4 g, 8.3 mmol, ~89 % yield).

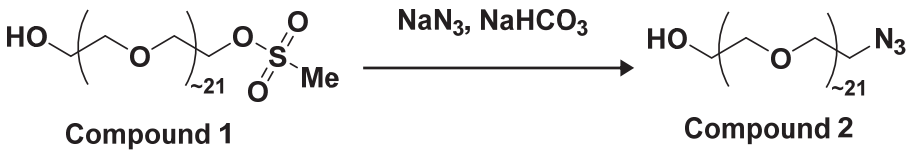

Scheme 2.3.3. A reaction scheme showing the synthesis of HO-PEG$_{1000}$-N$_3$.

TLC: ($CHCl_3$/MeOH 10:1) R_f 0.53; **^{1}H-NMR (400 MHz, $CDCl_3$):** δ (ppm) 4.22 – 4.17 (m, 1H), 3.72 – 3.68 (m, 2H), 3.67 – 3.58 (m, 82H), 3.37 (dd, 2H, *J*=5.6, 4.6 Hz); **^{13}C-NMR (100 MHz, $CDCl_3$):** δ (ppm) 77.3, 77.0, 76.7, 72.5, 70.7, 70.5, 70.3, 70.0, 68.1, 61.7; **HR-MS:** The corresponding MS spectrum displayed a series of species with m/z ratios separated by multiple number of 44 (the molecular weight of EG unit): 449.28, 471.29, 493.31, 515.32, 537.34, 559.35, and 581.37. The corresponding expected $[M+Na+K]^{2+}$ peaks with PEG repeat number of 17, 18, 19, 20, 21, 22, and 23 were 449.27, 471.29, 493.30, 515.31, 537.32, 559.34, and 581.35, respectively. (n = ~21)

A- ^{1}H-NMR of HO-PEG$_{1000}$-N$_3$

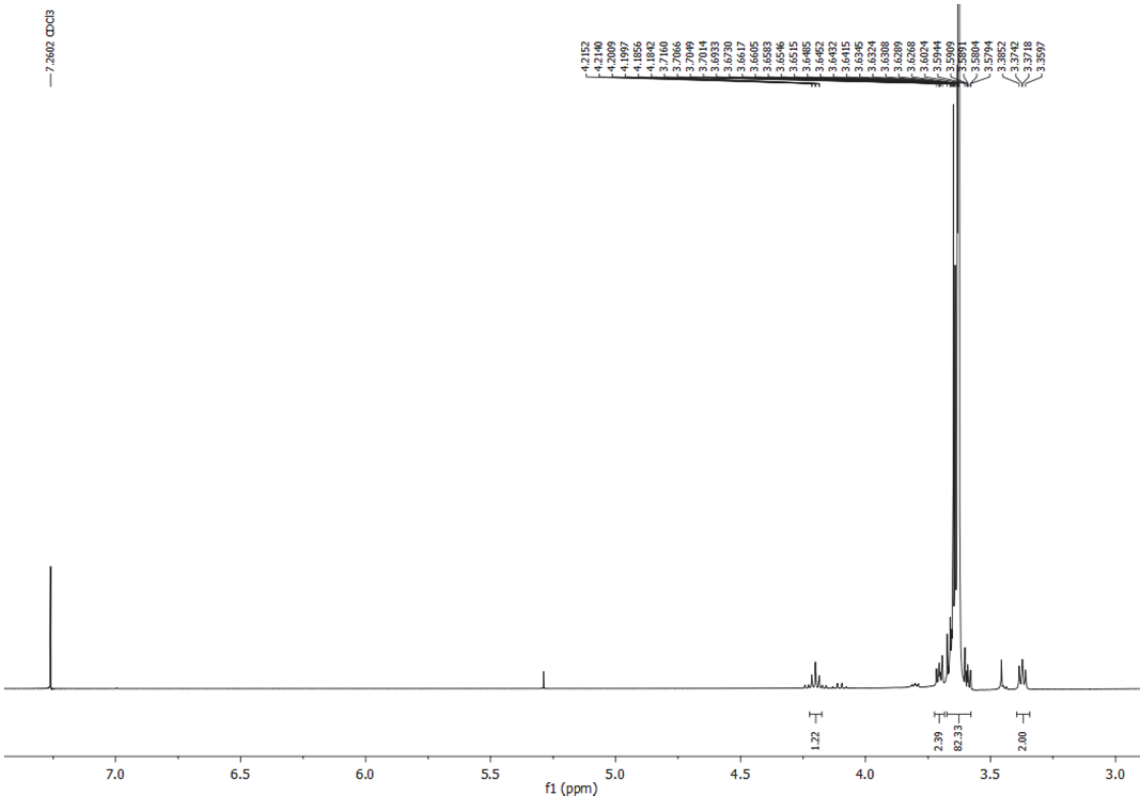

B- ^{13}C-NMR of HO-PEG$_{1000}$-N$_3$

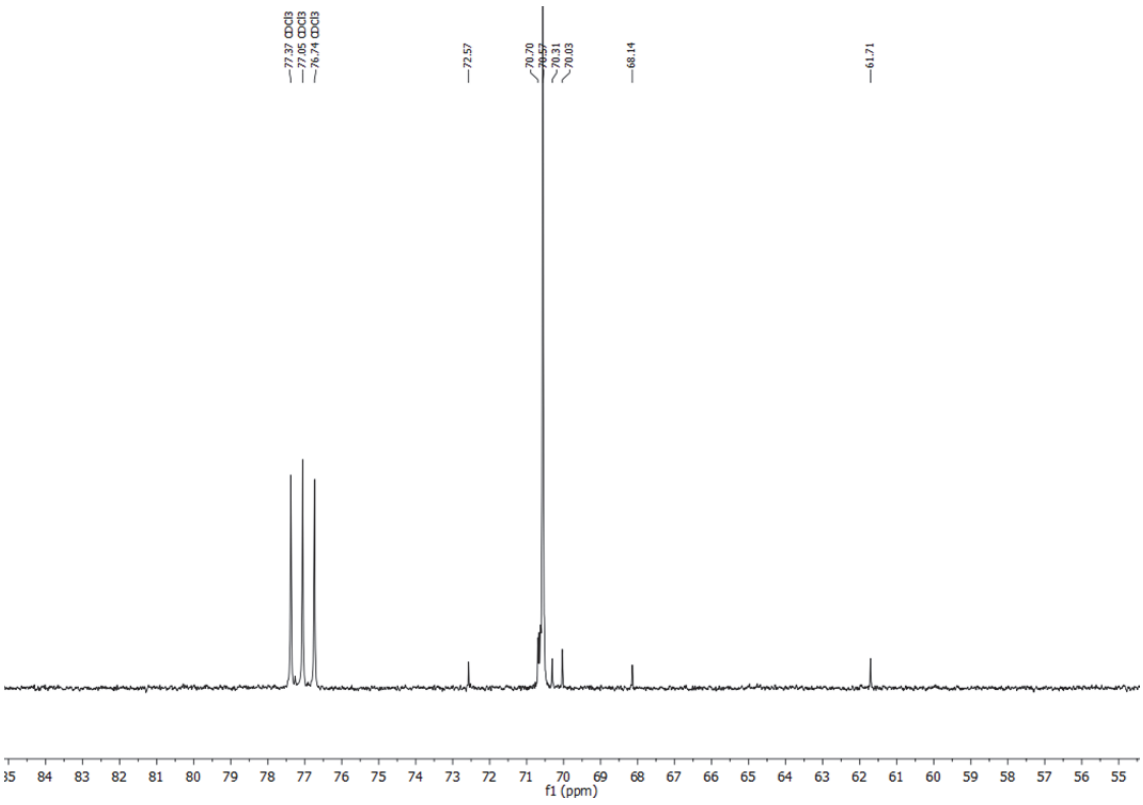

C- HR-MS of HO-PEG$_{1000}$-N$_3$

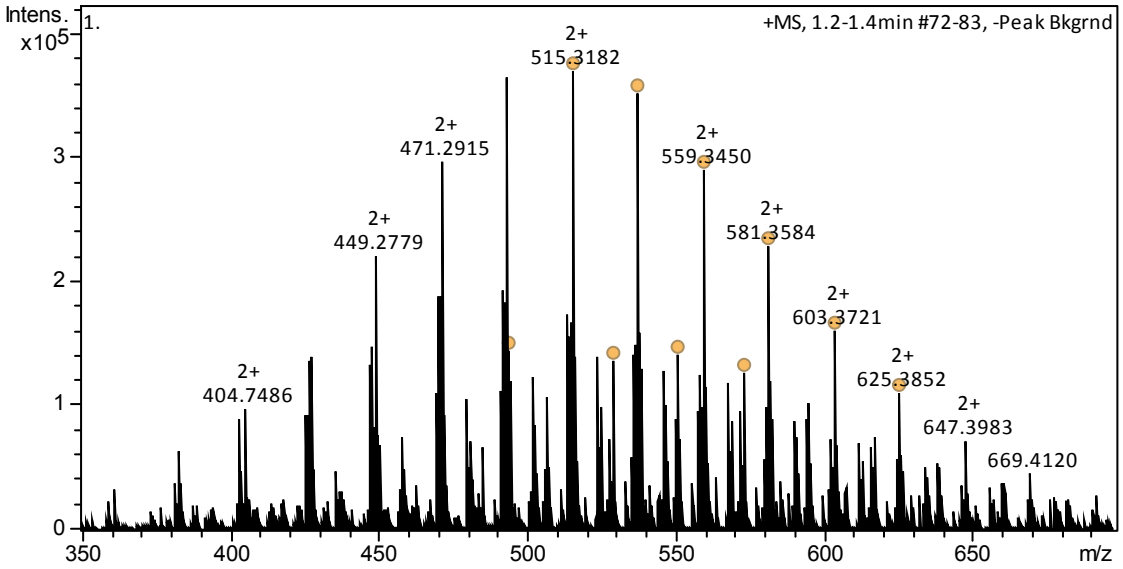

Figure 2.3.1. Spectral characterisation for final product of synthesis **HO-PEG$_{1000}$-N$_3$ (2)** showing **(A)** ^{1}H-NMR spectrum **(B)** ^{13}C-NMR spectrum and **(C)** HR-MS mass peaks of the pure sample.

2.3.1.3. Synthesis of Methanesulfonyl-PEG$_{600}$-OH

Poly(ethylene glycol), PEG, with an average molecular weight of 600 (30 g, 50 mmol), tetrahydrofuran (50 mL) and methanesulfonyl chloride (5.74 g, 3.87 mL, 50 mmol) were placed in a 250 ml two-necked round-bottomed flask and magnetically stirred in an ice bath under N_2 atmosphere. After cooling to below 5 °C with an ice bath, triethylamine (7.69 mL, 55 mmol) was added dropwise into the mixture through the addition funnel over 30 mins while stirring. After that, the solution was left to warm up gradually to RT and stirred overnight. The reaction was checked by TCL using $CHCl_3$:MeOH (10:1 (vol/vol)) as elution solvent. After the reaction was completed, the mixture was diluted with ultrapure water (20 mL) and $NaHCO_3$ (12.5 g) was then added to the solution, the resulting mixture was transferred to a separator funnel and extracted with $CHCl_3$ (60 mL x 3). The organic layer was collected and combined, and the solvent was evaporated to dryness on a rotary evaporator under reduced pressure, yielding **compound 3** as a white waxy solid (27.4 g, 38.4 mmol, ~77 % yield).

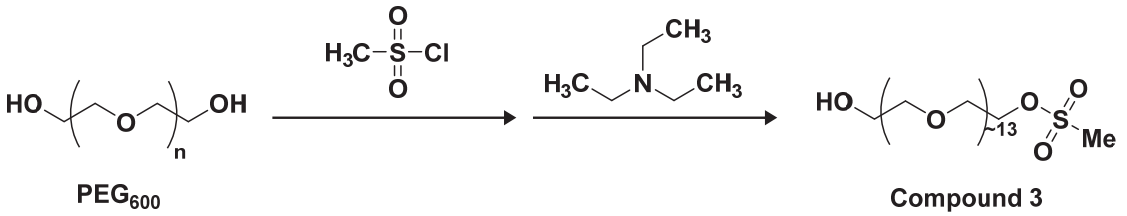

Scheme 2.3.4. A reaction scheme showing the synthesis of HO-PEG_{600}-OSO_2CH_3.

TLC: ($CHCl_3$/MeOH 10:1) R_f 0.44; **^{1}H-NMR (400 MHz, $CDCl_3$):** δ (ppm) 4.33 – 4.29 (m, 2H), 3.72 – 3.69 (m, 2H), 3.66 – 3.63 (m, 3H), 3.63 – 3.59 (m, 10H), 3.59 (s, 6H), 3.58 (s, 6H), 3.58 (m, 24H), 3.57 (s, 4H), 3.55 – 3.52 (m, 4H), 3.02 (s, 3H); **^{13}C-NMR (100 MHz, $CDCl_3$):** δ (ppm) 77.4, 77.1, 76.8, 72.5, 70.5, 70.2, 69.3, 68.9, 61.6, 37.6; **HR-MS:** The corresponding MS spectrum displayed a series of species with m/z ratios separated by multiple number of 44 (the molecular weight of EG unit): 642.33, 686.36, 730.39, 774.41, 818.44, and 862.47. The corresponding expected $[M+NH_4]^+$ peaks with PEG repeat number of 11, 12, 13, 14, 15, and 16 were 642.35, 686.38, 730.41, 774.44, 818.47, and 862.50, respectively. (n = ∼13)

2.3.1.4. Synthesis of HO-PEG_{600}-N_3

The crude product methanesulfonyl-PEG_{600}-OH, **compound 3**, (10 g, 14 mmol), sodium azide (2.5 g), THF (20 mL), and H_2O (20 mL) were added to a 500-mL round-bottomed flask under stirring in an ice bath. After the biphasic reaction mixture was heated under N_2 to distill off the THF, then it was refluxed overnight. The next day the mixture was cooled down to RT, transferred to a separator funnel and then extracted with $CHCl_3$ (100 mL x 5). The combined organic layers were dried over Mg_2SO_4 (20 g, ∼30 mins) with constant stirring, and filtered off. The resulting product was concentrated and purified by silica gel column chromatography using $CHCl_3$:MeOH (10:1 (vol/vol)) as an eluting solvent. The fractions containing of the desired pure product (confirmed by TLC) were combined, and evaporated to dryness to afford the desired product, **compound 4**, as a slightly yellowish oil (8.0 g, 12.1 mmol, ∼87 % yield).

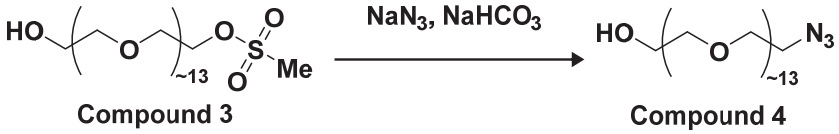

Scheme 2.3.5. A reaction scheme showing the synthesis of HO-PEG_{600}-N_3.

TLC: ($CHCl_3$/MeOH 10:1) R_f 0.58; **^{1}H-NMR (400 MHz, $CDCl_3$):** δ (ppm) 3.67 (q, 3H, *J*=4.4 Hz), 3.65 – 3.63 (m, 3H), 3.62 (s, 6H), 3.61 (s, 7H), 3.61 – 3.60 (m, 33H), 3.57 – 3.55 (m, 3H), 3.35 (dd, 2H, *J*=5.6, 4.6 Hz); **^{13}C-NMR (100 MHz, $CDCl_3$):** δ (ppm) 77.4, 77.1, 76.7, 72.5, 70.6, 70.6, 70.5, 70.3, 70.0, 61.6; **HR-MS:** The corresponding MS spectrum displayed a series of species with m/z ratios separated by multiple number of 44 (the molecular weight of EG unit): 545.34, 589.36, 633.39, 677.41, 721.44, 765.47, and 809.49. The corresponding expected $[M+NH_4]^+$ peaks with PEG repeat number of 11, 12, 13, 14, 15, and 16 were 545.35, 589.38, 633.41, 677.44, 721.47, 765.50, and 809.52, respectively. (n = ∼13)

A- ^{1}H-NMR of HO-PEG$_{600}$-N$_3$

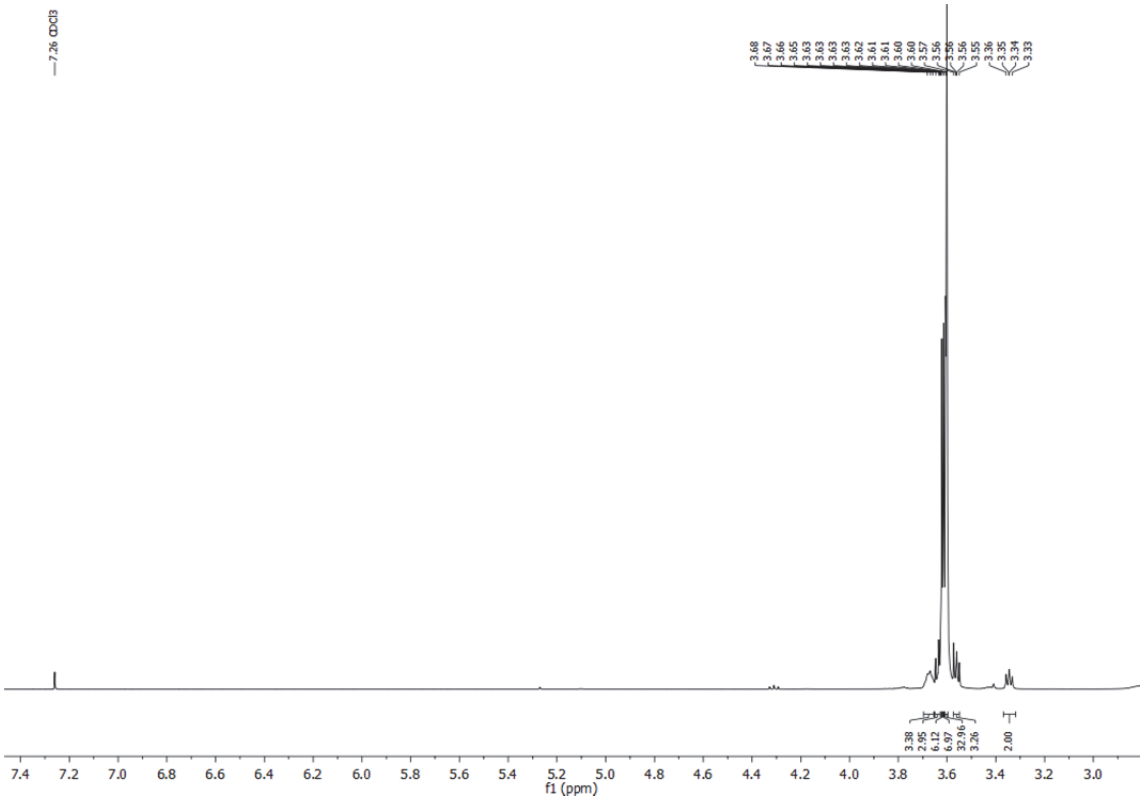

B- ^{13}C-NMR of HO-PEG$_{600}$-N$_3$

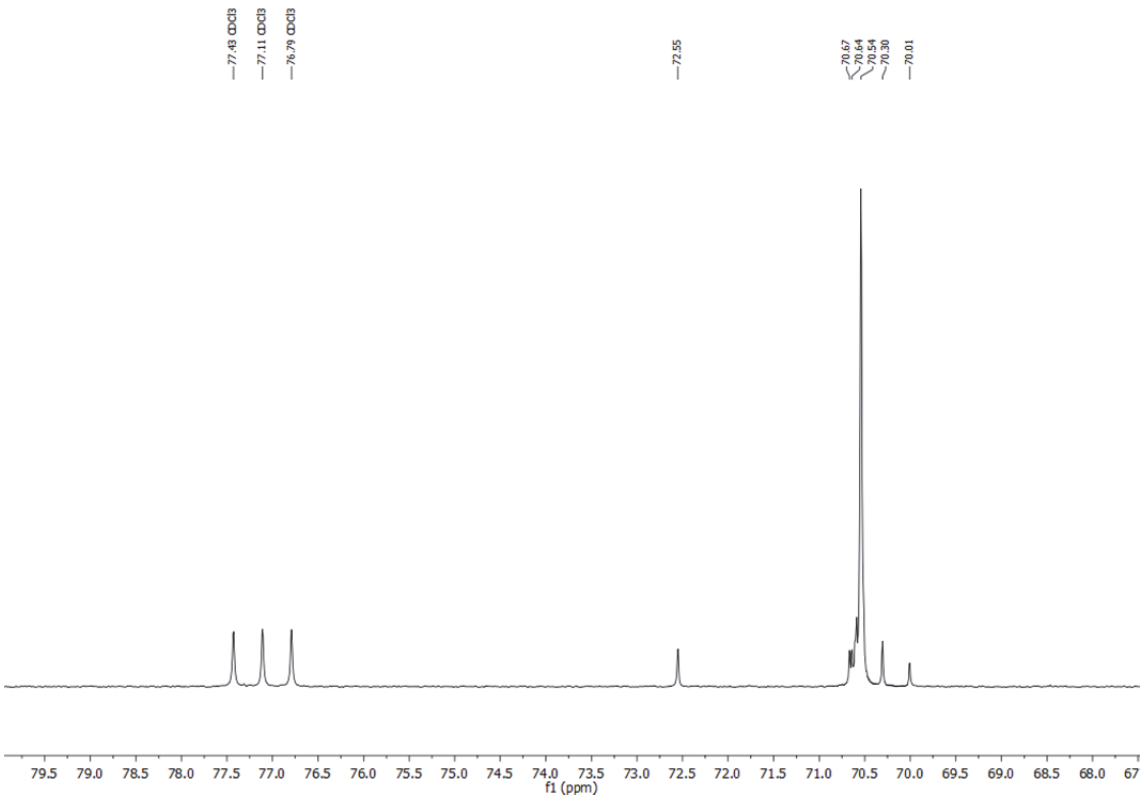

C- HR-MS of HO-PEG$_{600}$-N$_3$

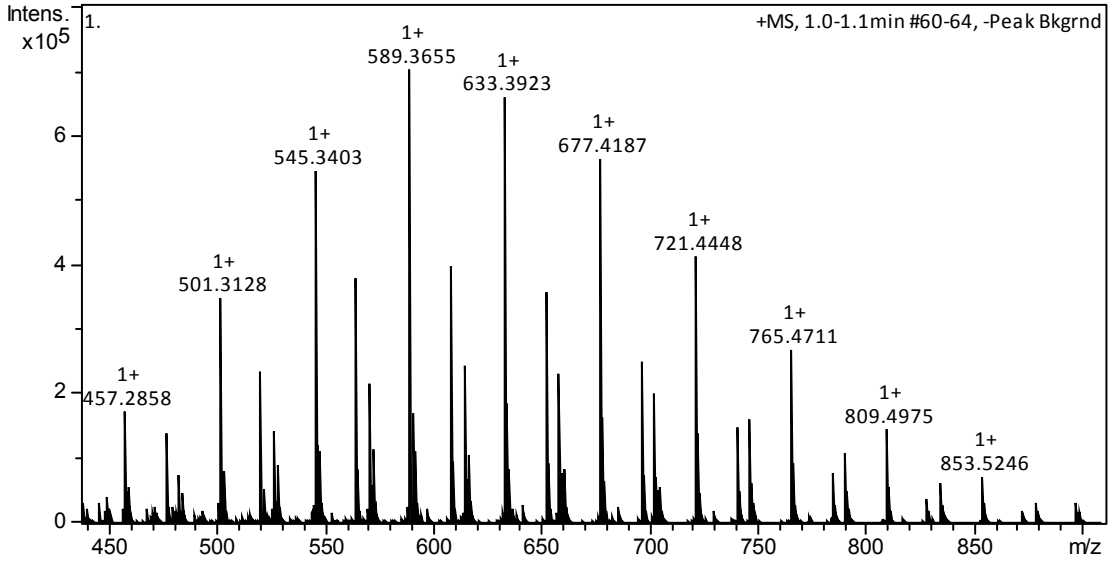

Figure 2.3.2. Spectral characterisation for final product of synthesis **HO-PEG$_{600}$-N$_3$ (4)** showing **(A)** ^{1}H-NMR spectrum **(B)** ^{13}C-NMR spectrum and **(C)** HR-MS mass peaks of the pure sample.

2.3.2. LA-PEG$_{750}$-OMe

The synthesis of LA-PEG$_{750}$-OMe from N$_3$-PEG$_{750}$-OMe is based on the protocols published by Mei *et al.*[26] and Zhang *et al.*[25]. The synthesis included the reduction of an azide to amine and then coupling to α-lipoic acid (LA) using a DCC/DMAP assisted coupling reaction. **Scheme 2.3.6** below shows the reactions to produce LA-PEG$_{750}$-OMe.

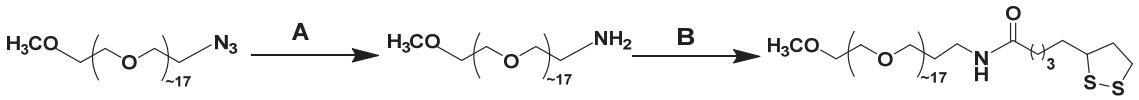

Scheme 2.3.6. A scheme showing the reactions for the synthesis of LA-PEG$_{750}$-OMe. (A) EtOAc, HCl, and PPh$_3$. (B) TA, DCC, DMAP, CH_2Cl_2.

2.3.2.1. Synthesis of NH$_2$-PEG$_{750}$-OCH$_3$

N$_3$-EG$_{17}$-OCH$_3$ (8.0 g, 10 mmol), Ethyl acetate, EtOAc, (150 mL) and 1 M HCl (25 mL, 25 mmol) were added into a 500 ml two-necked flask with an additional funnel. Triphenylphosphine, PPh$_3$, (2.8 g, 10 mmol) in EtOAc (100 mL) was added slowly under N_2 protection and cooled at 0 °C. Temperature was maintained at below 5 °C throughout the addition. After that, reaction mixture was warmed to RT and stirred overnight. The next day, the reaction mixture was transferred into a separatory funnel to separate the biphasic mixture. The aqueous layer was washed with EtOAc (100 mL x

2) to remove any unreacted PPh_3 and its oxide by-product. This layer was then basified in an ice bath using KOH (13.5 g) to pH > 10. The aqueous solution was then extracted with $CHCl_3$ (60 mL x 5). The combined organic layer was dried using $MgSO_4$ and the solid was filtered off. The solvent was then removed in vacuo, yielding the desired product, **compound 5**, as a light-yellow oil (6.19 g, 7.5 mmol, 75 % yield).

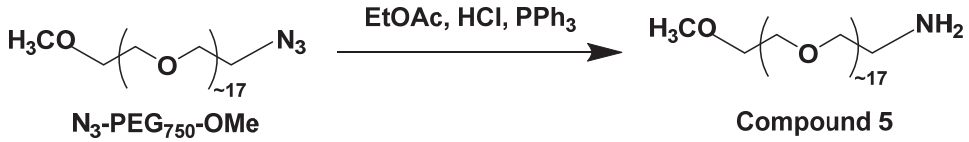

N_3-PEG_{750}-OMe Compound 5

Scheme 2.3.7. A reaction scheme showing the synthesis of NH_2-PEG_{750}-OCH_3.

TLC: ($CHCl_3$/MeOH 10:1) R_f 0.35; **^{1}H-NMR (400 MHz, $CDCl_3$):** δ (ppm) 3.65-3.60 (m, 68 H), 3.56-3.52 (t, 2H), 3.38 (s, 3H), 3.10 (t, 2H), 1.61 (br, s, 2H); **^{13}C-NMR (100 MHz, $CDCl_3$):** δ (ppm) 77.4, 77.2, 77.0, 76.7, 71.9, 70.5, 30.9; **HR-MS:** The corresponding MS spectrum displayed a series of species with m/z ratios separated by multiple number of 44 (the molecular weight of EG unit): 691.29, 735.46, 780.10, 822.86, 867.32, and 911.18. The corresponding expected $[M+H]^+$ peaks with PEG repeat number of 14, 15, 16, 17, 18, and 19 were 692.44, 736.45, 780.49, 823.48, 868.54, and 912.54, respectively. (n = ∼17)

2.3.2.2. Synthesis of LA-EG_{750}-OCH_3

NH_2-PEG_{750}-OMe (6.2 g, 7.5 mmol), **compound 5**, DCC (1.55 g, 7.5 mmol) and LA, lipoic acid, (1.55 g, 7.5 mmol) were added to a round bottom flask dissolved in CH_2Cl_2 (80 mL) and cooled to 0 °C under N_2 protection. DMAP (0.18 g, 1.5 mmol) was then added slowly over 30 mins in a solution of CH_2Cl_2 (30 mL). The mixture was stirred at 0 °C for 1 hour, and was then allowed to warm to RT and left stirring for a further 48 h. The reaction mixture was then filtered off, and the solid residue was rinsed with CH_2Cl_2. The solvent was dried in vacuo and the residue was then saturated with $NaHCO_3$. The aqueous layer was extracted with ether (100 mL x 2) and then transferred to a new separatory funnel. This aqueous layer was extracted with CH_2Cl_2 (100 mL x 2). The combined organic layer was dried over $MgSO_4$, and then evaporated to dryness on the rotary evaporator, yielding the desired product, **compound 6**, as a yellowish oily solid (4.65 g, 4.6 mmol, 61.3 % yield).

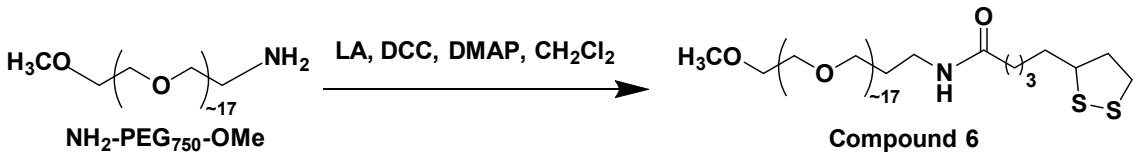

Scheme 2.3.8. A reaction scheme showing the synthesis of LA-PEG_{750}-OCH_3.

TLC: ($CHCl_3$/MeOH 10:1) R_f ~0.6; **^{1}H-NMR (400 MHz, $CDCl_3$):** δ (ppm) 6.24 (s, 1H), 3.82 (d, *J* = 4.8 Hz, 1H), 3.65 (d, *J* = 5.5 Hz, 138H), 3.54 (dd, *J* = 6.1, 3.3 Hz, 8H), 3.45 (p, *J* = 5.0 Hz, 3H), 3.37 (s, 8H), 3.22 – 3.07 (m, 2H), 2.46 (dq, *J* = 10.5, 5.3, 4.2 Hz, 1H), 2.33 (dt, *J* = 14.9, 7.3 Hz, 1H), 2.19 (t, *J* = 7.5 Hz, 2H), 1.90 (dq, *J* = 13.7, 7.0 Hz, 2H), 1.73 – 1.61 (m, 7H), 1.45 (ddd, *J* = 13.3, 8.3, 4.9 Hz, 3H), 1.31 – 1.19 (m, 3H), 1.17 – 1.01 (m, 1H); **^{13}C-NMR (100 MHz, $CDCl_3$):** δ (ppm) 77.3, 77.0, 76.8, 71.7, 70.3, 69.9, 69.8, 69.7, 58.7, 56.2, 50.5, 40.0, 39.0, 38.2, 36.0, 34.4, 28.7, 25.2, 17.9; **HR-MS:** The corresponding MS spectrum displayed a series of species with m/z ratios separated by multiple number of 44 (the molecular weight of EG unit): 396.71, 418.72, 440.74, 462.75, 484.76, 506.78, 528.79, 550.80, 572.83, and 594.84. The corresponding expected $[M+H]^{2+}$ peaks with PEG repeat number of 8, 9, 10, 11, 12, 13, 14, 15, 16, and 17 were 396.71, 418.72, 440.74, 462.75, 484.76, 506.78, 528.79, 550.80, 572.83, 594.84, respectively. (n = ~17)

A- ^{1}H-NMR of LA-EG_{750}-OCH_3

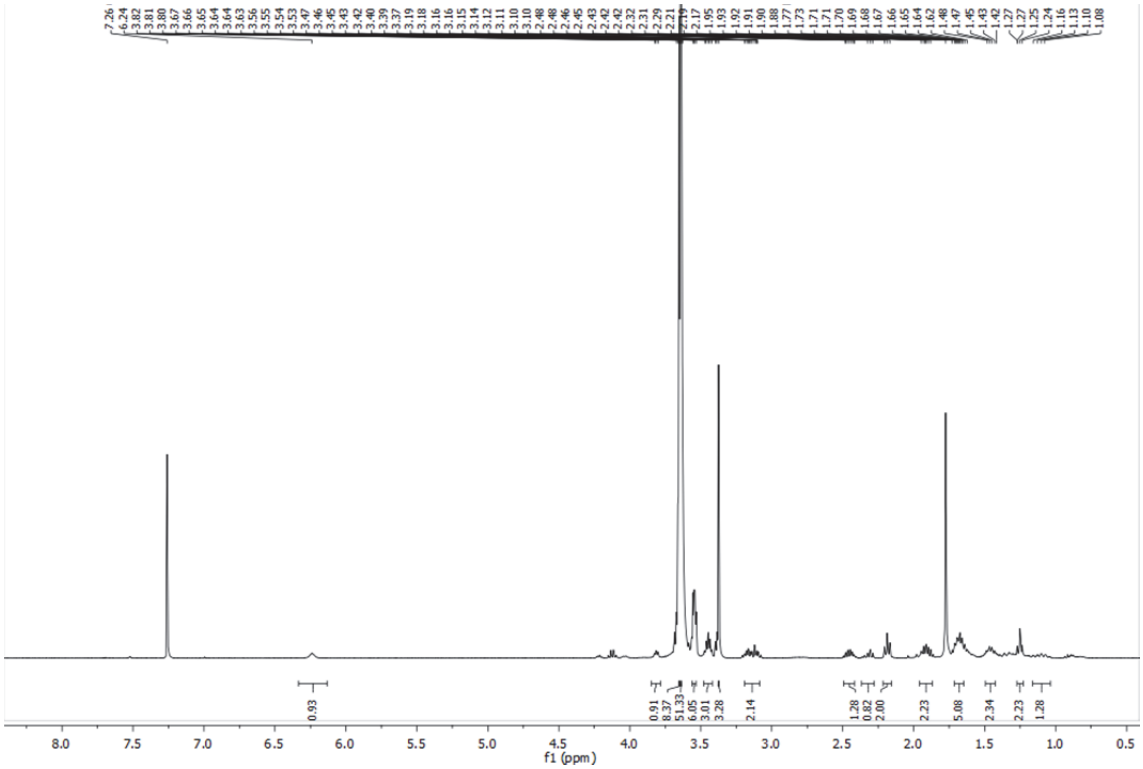

B- ^{13}C-NMR of LA-EG$_{750}$-OCH$_3$

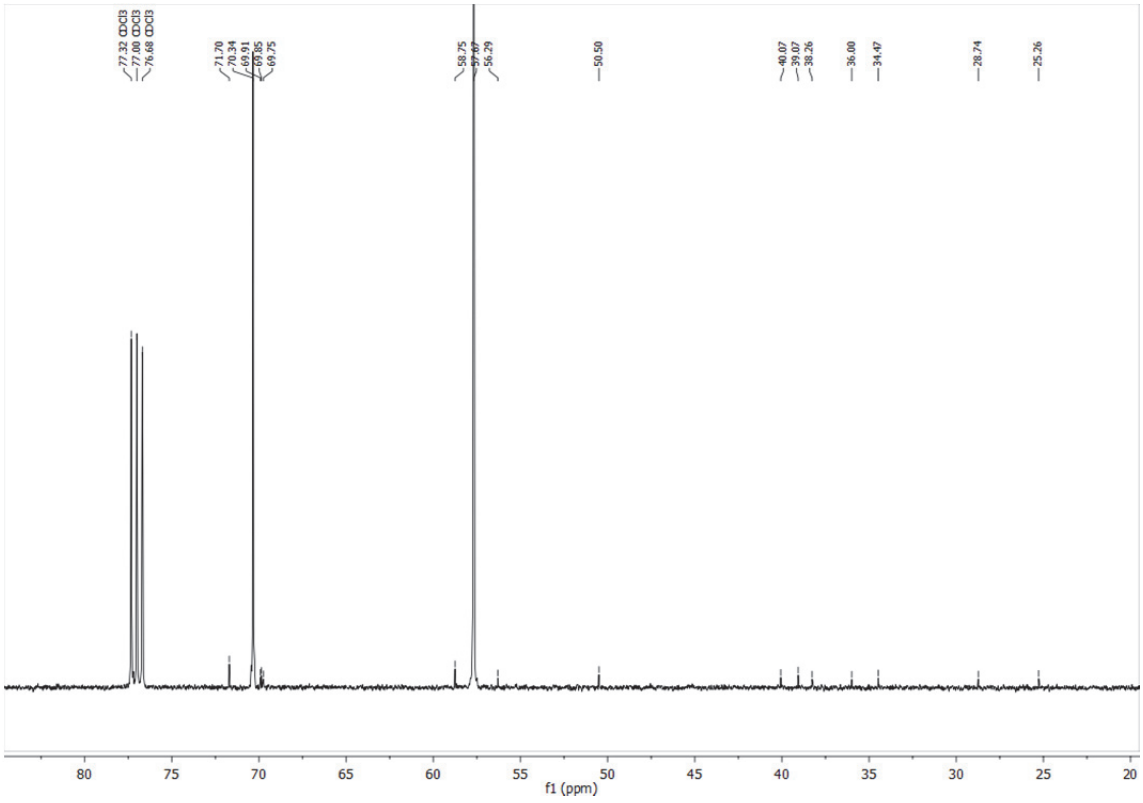

C- HR-MS of LA-EG$_{750}$-OCH$_3$

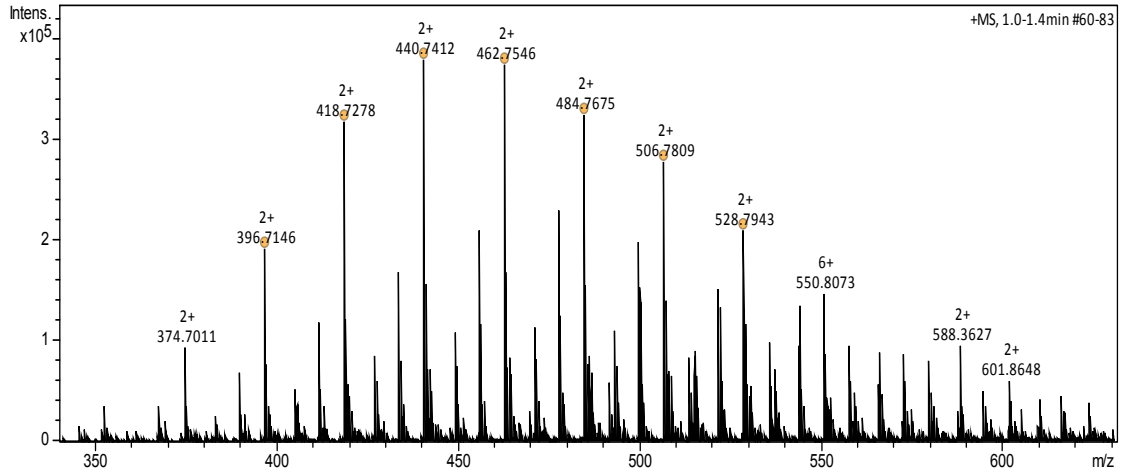

Figure 2.3.3. Spectral characterisation for final product of synthesis **LA-PEG$_{750}$-OMe (6)** showing **(A)** ^{1}H-NMR spectrum **(B)** ^{13}C-NMR spectrum and **(C)** HR-MS mass peaks of the pure sample.

2.4. Click Chemistry Experimental

The synthesis of LA-PEG/EG-based based multifunctional ligands was successfully achieved via copper-catalysed click chemistry reaction by following the protocol established by Ribeiro-Viana *et al.*[27] The click reactions proceed readily at RT and give

the products in relatively high yield. The reactions were done in 1:1 THF:H_2O (vol/vol) solution by mixing the alkyl terminated LA-based ligands (1 mol equiv.), and azido-modified PEG/sugar ligands (1.1 mol equiv.), $CuSO_4.5H_2O$ (0.1 mol equiv.), TBTA (0.19 mol equiv.), and sodium ascorbate (0.4 mol equiv.), respectively, and easily completed overnight at RT. Sodium ascorbate was used as a reducing agent to catalyse the reduction of Cu(II) to Cu(I) ions. TBTA (tris-(1-benzyl-4-triazolyl methyl)-amine) was added to stabilize the oxidation state of the copper ions and accelerate the cyclic reaction in click chemistry.

2.4.1. Synthesis of LA-PEG$_{1000}$-OH Ligand

To produce LA-PEG$_{1000}$-OH Ligand, OH-PEG$_{1000}$-N_3, **compound 2**, (225 mg, 0.22 mmol), LA-EG-C≡CH (66.3 mg, 0.2 mmol), $CuSO_4.5H_2O$ (5.5 mg, 0.02 mmol), TBTA (16 mg, 0.03 mmol), and sodium ascorbate (16 mg, 0.08 mmol) were dissolved in 2 mL of THF/H_2O (1:1 (vol/vol)). The reaction mixture was wrapped with aluminium foil and stirred overnight at RT in darkness. The next day, after evaporation of the solvent, the resulting LA-PEG$_{1000}$-OH ligand, **compound 7**, was purified by silica gel column chromatography using at a ratio of 5:1 (vol/vol) $CHCl_3$: MeOH. (33.5 mg, 0.024 mmol, 12% yield).

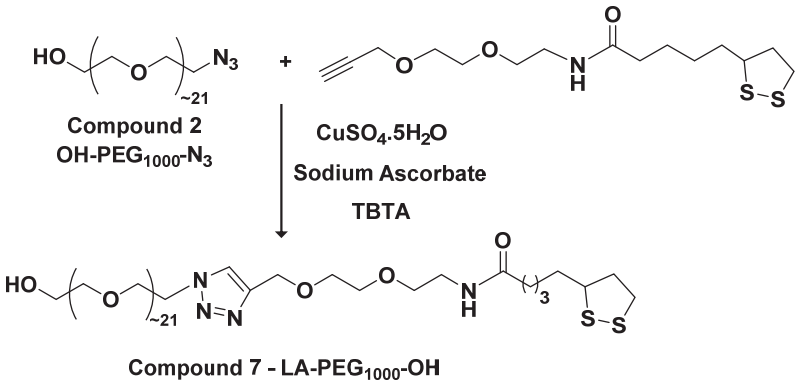

Scheme 2.4.1. A reaction scheme showing the synthesis of LA-PEG$_{1000}$-OH.

TLC: ($CHCl_3$/MeOH 10:1) R_f ~0.4; **^{1}H-NMR (500 MHz, D_2O):** δ (ppm) 3.89 (t, 2H, *J*=5.0 Hz), 3.63 (s, 6H), 3.61 (bs, 81H), 3.55 (s, 5H), 3.43 – 3.40 (m, 5H), 3.29 (d, 3H, *J*=5.5 Hz), 2.55 – 2.43 (m, 1H), 2.42 – 2.29 (m, 1H), 2.22 – 2.13 (m, 4H), 1.93 – 1.88 (m, 2H), 1.77 – 1.69 (m, 2H), 1.53 (dt, 4H, *J*=14.6, 7.3 Hz), 1.40 – 1.31 (m, 2H; **^{13}C-NMR (125 MHz, D_2O):** δ (ppm) 71.7, 69.5, 69.5, 69.4, 69.2, 60.3, 50.1, 44.5, 39.1, 36.1, 35.8, 32.6, 28.1, 22.8; **HR-MS:** The corresponding MS spectrum displayed a series of species with m/z ratios separated by multiple number of 44 (the molecular weight of EG unit): 460.29, 482.28, 504.29, 526.30, 548.32, 570.33, 592.34, 614.36, 636.37, 658.38, 680.40, and 702.41. The corresponding expected $[M+Na+K]^{2+}$ peaks with PEG repeat number of 8, 9, 10, 11, 12, 13, 14, 15, 16, and 17 were 460.24, 482.27, 504.27, 526.28, 548.30, 570.31, 592.33, 614.34, 636.36, 658.37, 680.39, 702.40, respectively. (n = ~21)

A- ^{1}H-NMR of LA-PEG$_{1000}$-OH

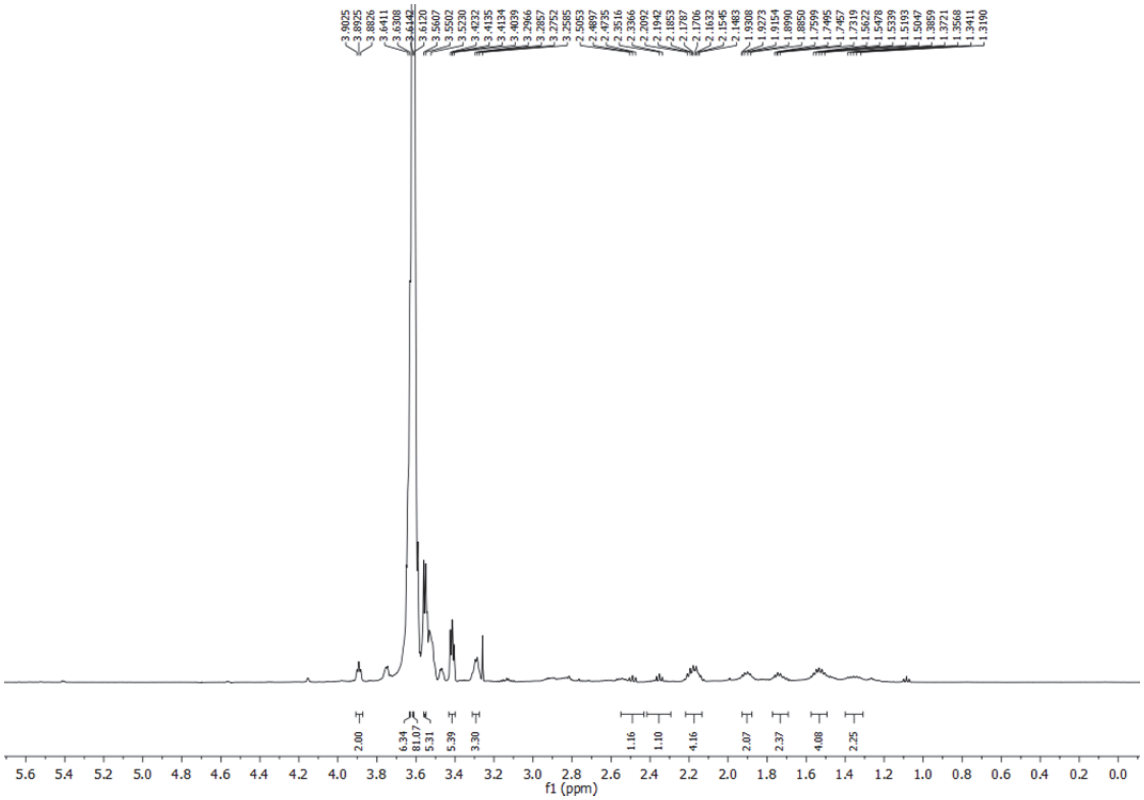

B- ^{13}C-NMR of LA-PEG$_{1000}$-OH

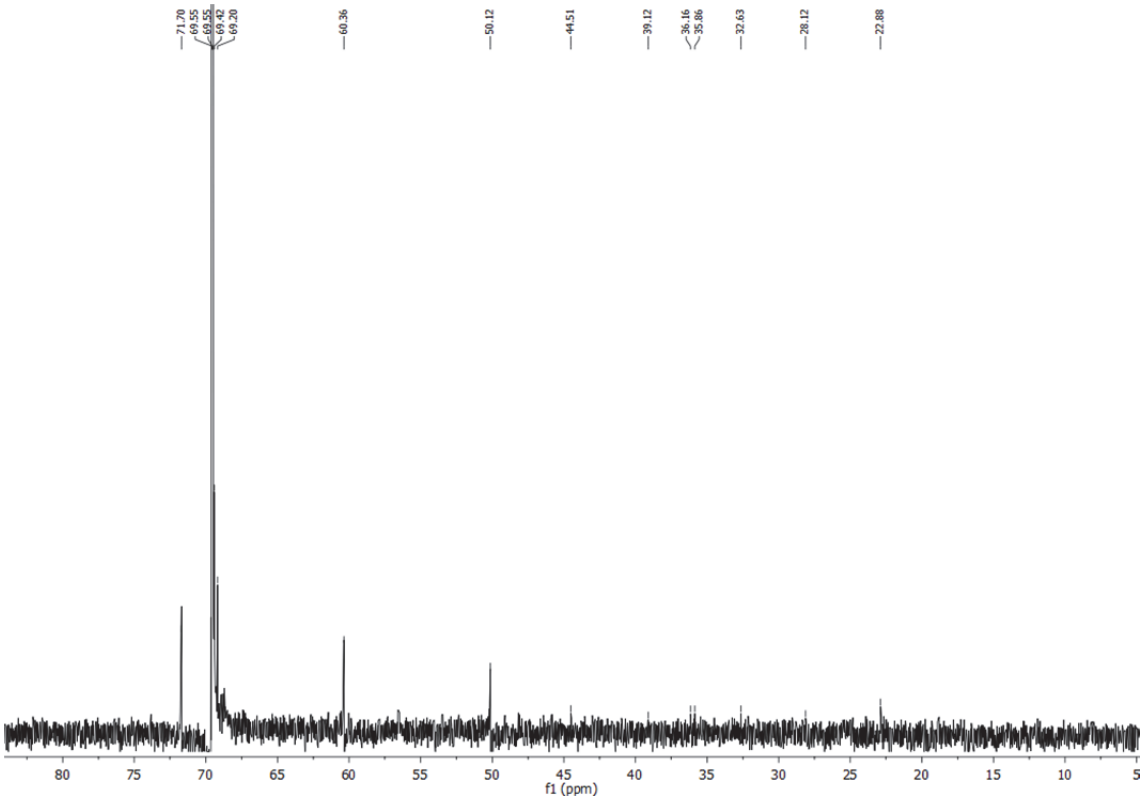

C- HR-MS of LA-PEG$_{1000}$-OH

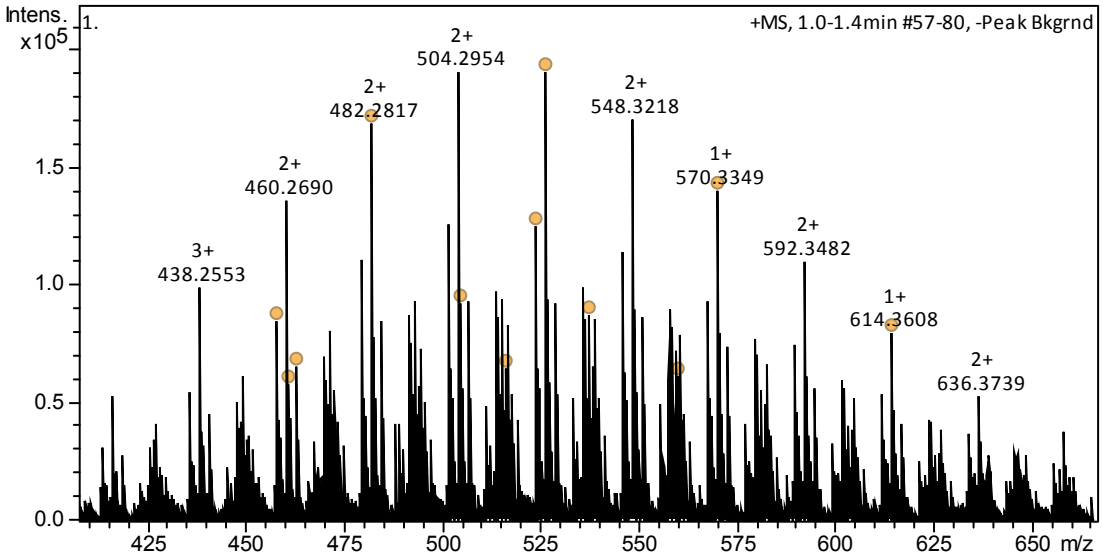

Figure 2.4.1. Spectral characterisation for final product of synthesis **LA-PEG$_{1000}$-OH (7)** showing **(A)** ^{1}H-NMR spectrum **(B)** ^{13}C-NMR spectrum and **(C)** HR-MS mass peaks of the pure sample.

2.4.2. Synthesis of LA-(PEG$_{1000}$-OH)$_3$ Ligand

OH-PEG$_{1000}$-N$_3$, **compound 2**, (657 mg, 0.6 mmol), LA-(EG-C≡CH)$_3$ (84 mg, 0.2 mmol), $CuSO_4$. $5H_2O$ (5.5 mg, 0.02 mmol), TBTA (16 mg, 0.03 mmol), and sodium ascorbate (16 mg, 0.08 mmol) were dissolved in 2 mL of THF/H_2O (1:1 (vol/vol)). The reaction mixture was wrapped with aluminium foil and stirred overnight at RT in darkness. The next day, after evaporation of the solvent, the resulting LA-(PEG$_{1000}$-OH)$_3$ ligand, **compound 8**, was purified by silica gel column chromatography using at a ratio of 5:1 $CHCl_3$:MeOH (225 mg, 0.064 mmol, 10% yield).

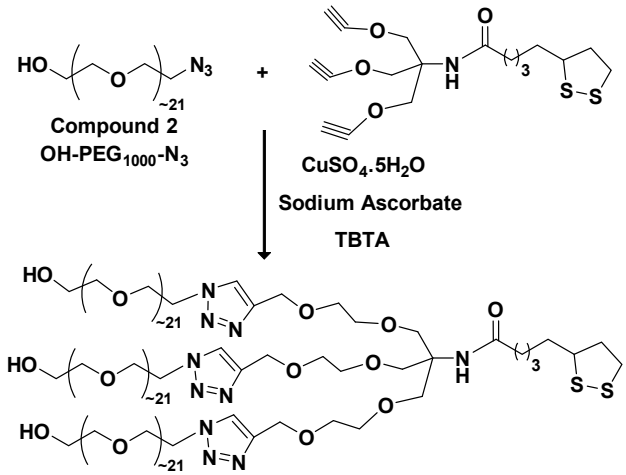

Scheme 2.4.2. A reaction scheme showing the synthesis of LA-(PEG_{1000}-OH)$_3$.

TLC: ($CHCl_3$/MeOH 10:1) R_f ~0.3; **^{1}H-NMR (500 MHz, D_2O):** δ (ppm) 3.87 (d, 6H, J=4.8 Hz), 3.65 – 3.63 (m, 31H), 3.61 (bs, 232H), 3.56 – 3.54 (m, 34H), 2.52 – 2.46 (m, 2H), 2.41 – 2.29 (m, 2H), 2.24 – 2.15 (m, 2H), 2.15 – 2.04 (m, 3H), 1.91 – 1.87 (m, 1H), 1.77 – 1.72 (m, 2H), 1.52 – 1.42 (m, 4H), 1.30 – 1.22 (m, 2H); **^{13}C-NMR (125 MHz, D_2O):** δ (ppm) 71.7, 69.6, 69.5, 69.4, 68.7, 60.3, 50.5, 42.2, 40.3, 32.6, 29.5, 25.4; **HR-MS:** The corresponding MS spectrum displayed a series of species with m/z ratios separated by multiple number of 44 (the molecular weight of EG unit): 491.76, 557.83, and 623.87. The corresponding expected $[M+NH_4]^{2+}$ peaks with 2, 3, and 4 were 491.77, 557.81, and 623.86, respectively.

A-^{1}H-NMR of LA-(PEG_{1000}-OH)$_3$

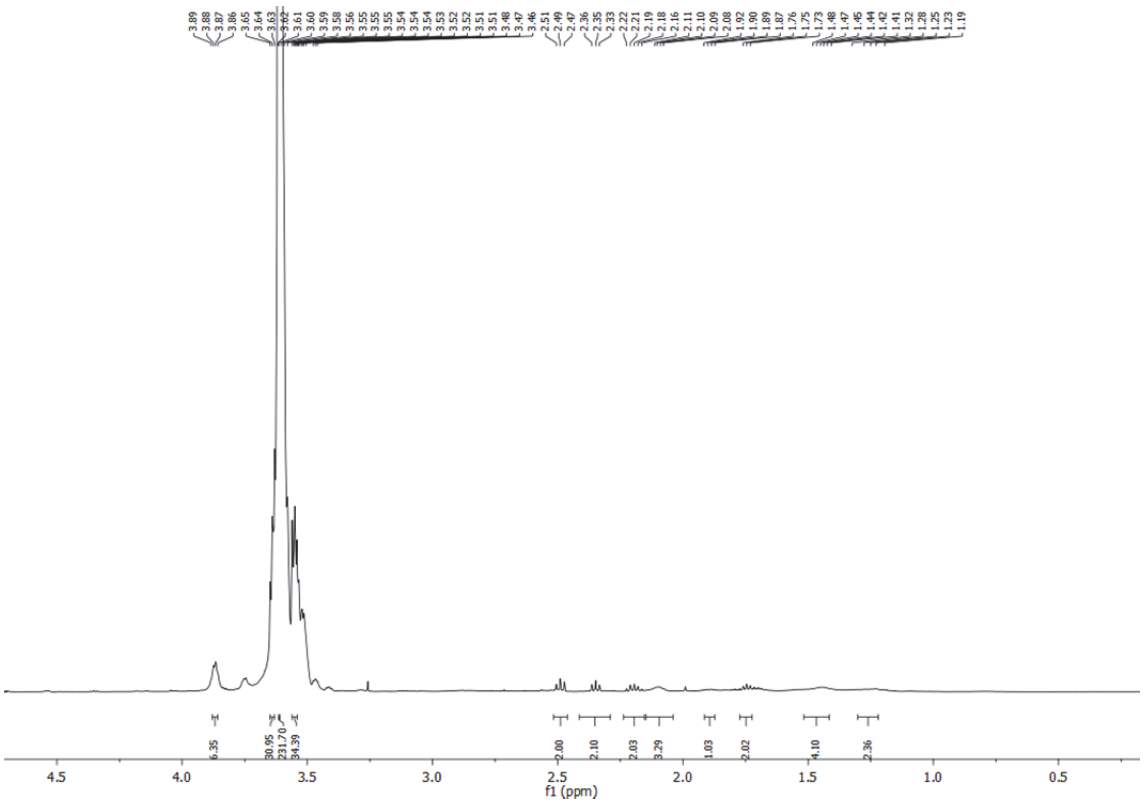

B-^{13}C-NMR of LA-(PEG$_{1000}$-OH)$_3$

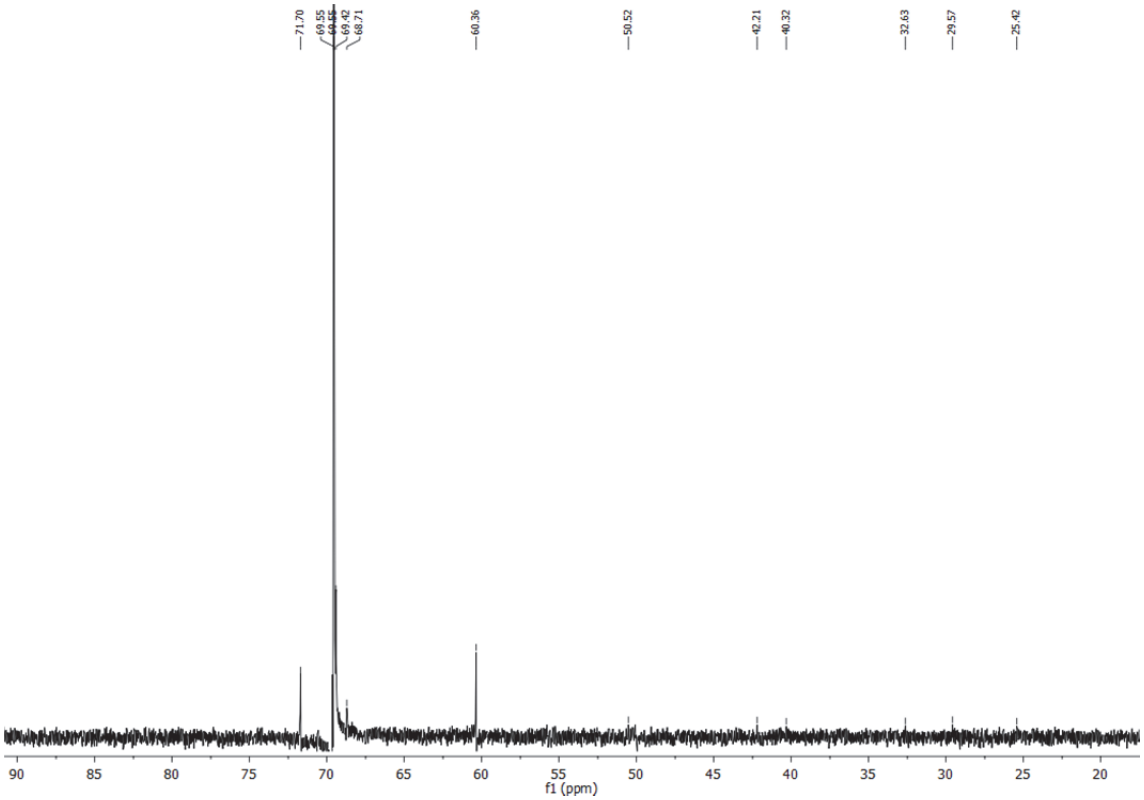

C- HR-MS of LA-(PEG$_{1000}$-OH)$_3$

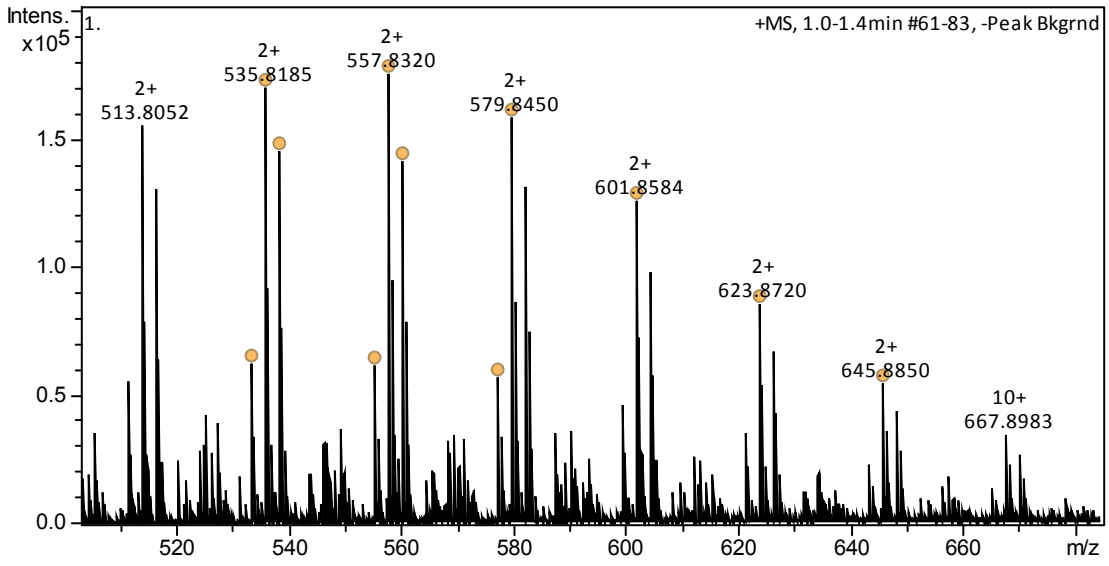

Figure 2.4.2. Spectral characterisation for final product of synthesis **LA-(PEG$_{1000}$-OH)$_3$ (8)** showing **(A)** ^{1}H-NMR spectrum **(B)** ^{13}C-NMR spectrum and **(C)** HR-MS mass peaks present within the pure sample.

2.4.3. Synthesis of LA-EG_2-ManA

LA-EG_2-C≡CH (15 mg, 0.045 mmol), 1-Azido-3,6-dioxaoct-8-yl-a-D-mannuronic acid, N_3-EG_2-ManA, (17 mg, 0.048 mmol), $CuSO_4.5H_2O$ (0.4 mg, 0.0016 mmol), TBTA (1.5 mg, 0.0028 mmol), and sodium ascorbate (1.2 mg, 0.006 mmol) were dissolved in 2 mL of THF/H_2O (1:1 (vol/vol)). The resulting solution stirred overnight at RT in darkness. Next day, the consumption of all starting compounds was confirmed by TLC. The solvent was then evaporated and the crude product was purified by size exclusion chromatography using Biogel P2 column using ammonium formate as an eluent to obtain the pure product, **compound 9**, (23.7 mg, 0.034 mmol, 72% yield).

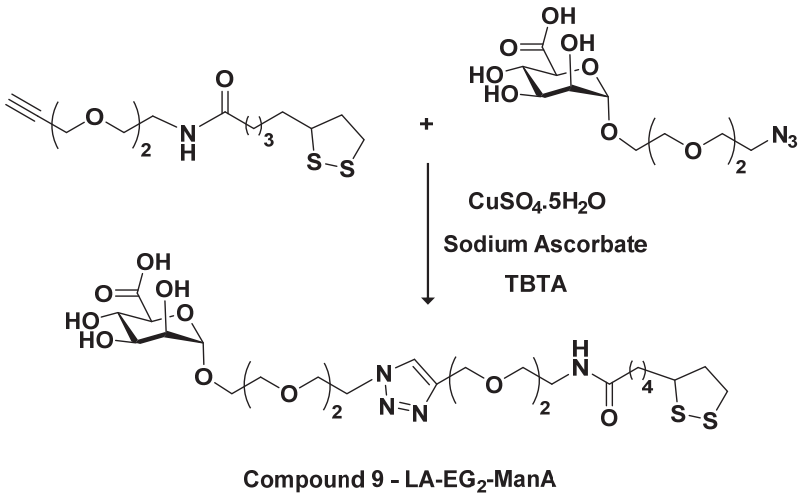

Scheme 2.4.3. A reaction scheme showing the synthesis of LA-EG_2-ManA.

TLC: ($CHCl_3$/MeOH 1:1) R_f 0.62; **^{1}H NMR (500 MHz, D_2O)** δ (ppm): 8.44 (s, 1H), 8.10 (s, 1H), 4.90 (d, 1H), 4.70 (s, 2H), 4.65 (t, 2H), 3.99 (t, 2H), 3.85 (m, 5H), 3.69 (m, 12H), 3.61 (t, 2H), 3.37 (t, 2H), 3.20 (m, 2H), 2.47 (m, 1H), 2.24 (t, 2H), 1.96 (m, 1H), 1.72 (m, 1H), 1.60 (m, 3H), 1.38 (m, 2H); **^{13}C NMR (125 MHz, D_2O)** δ (ppm): 176.9 (C=O), 170.9, 143.8 (C=CH), 125.4 (C=CH), 99.9, 72.8, 70.3, 69.8, 69.6, 69.4, 69.4, 69.4, 68.9, 68.8, 68.7, 66.6, 63.0, 56.4, 50.1, 50.0, 40.2, 38.8, 38.0, 35.4, 33.6, 27.7, 24.9; **LC-MS:** calculated *m/z* for $C_{27}H_{46}N_4O_{12}S_2$ $(M+H)^+$ 683.26; found 683.22.

A-^{1}H-NMR of LA-EG$_2$-ManA

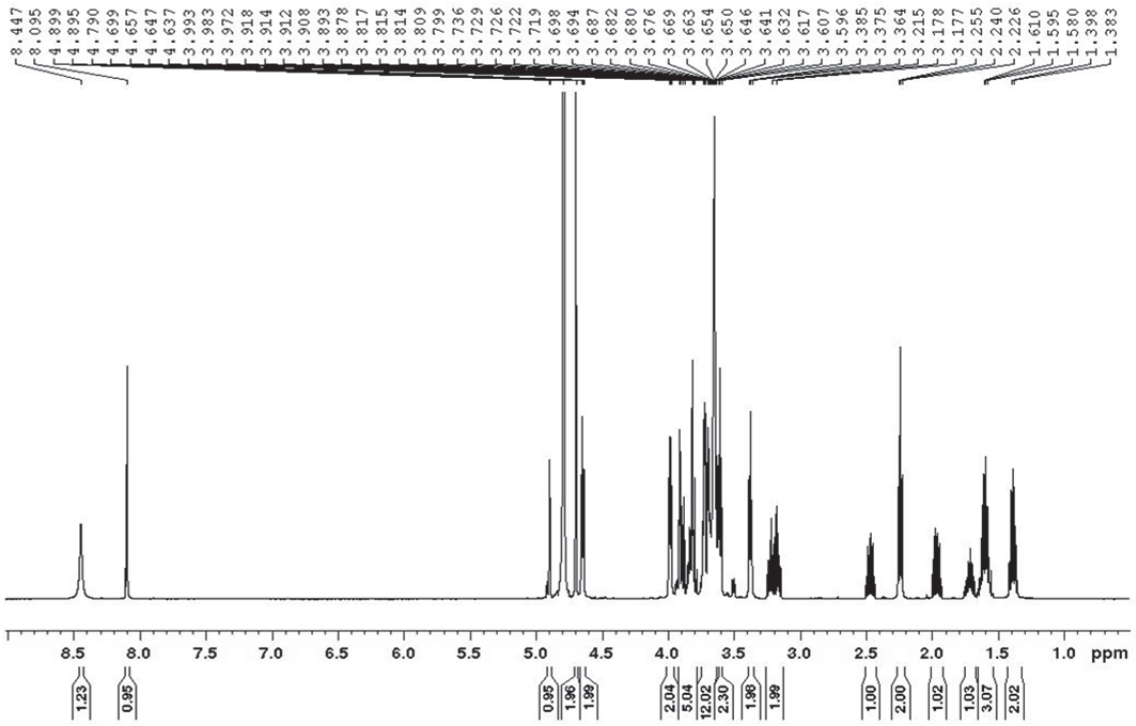

B-^{13}C-NMR of LA-EG$_2$-ManA

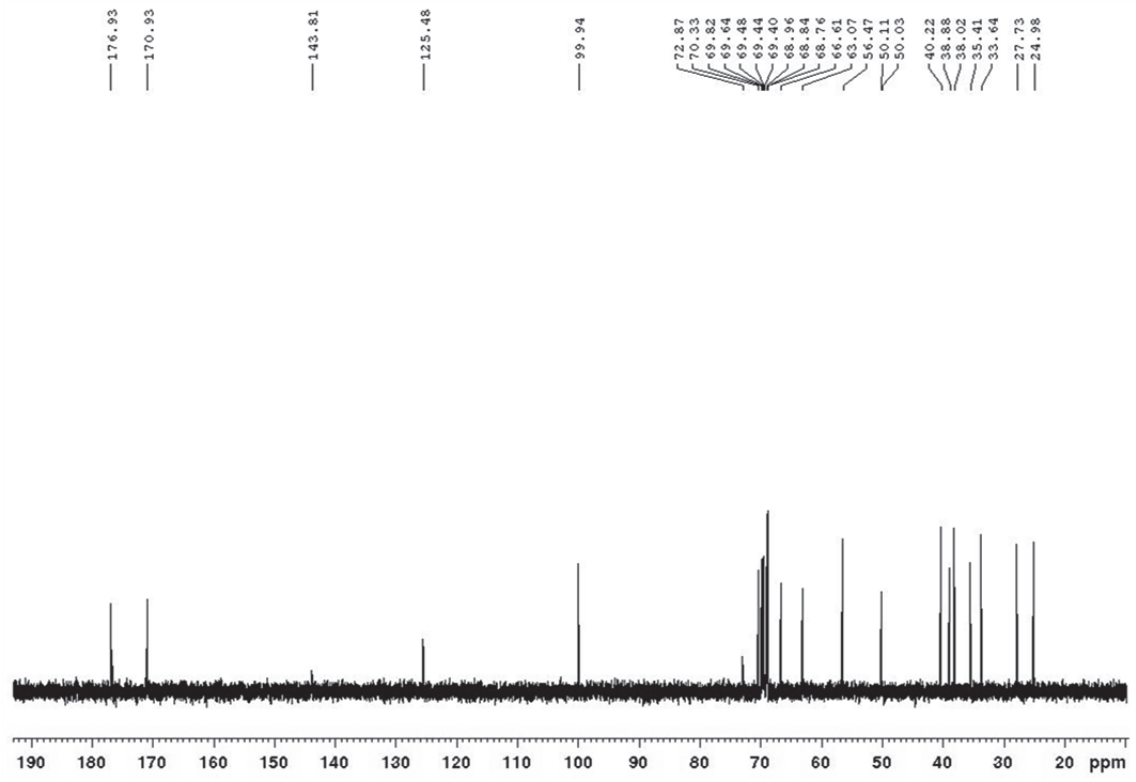

C- LC-MS of LA-EG_2-ManA

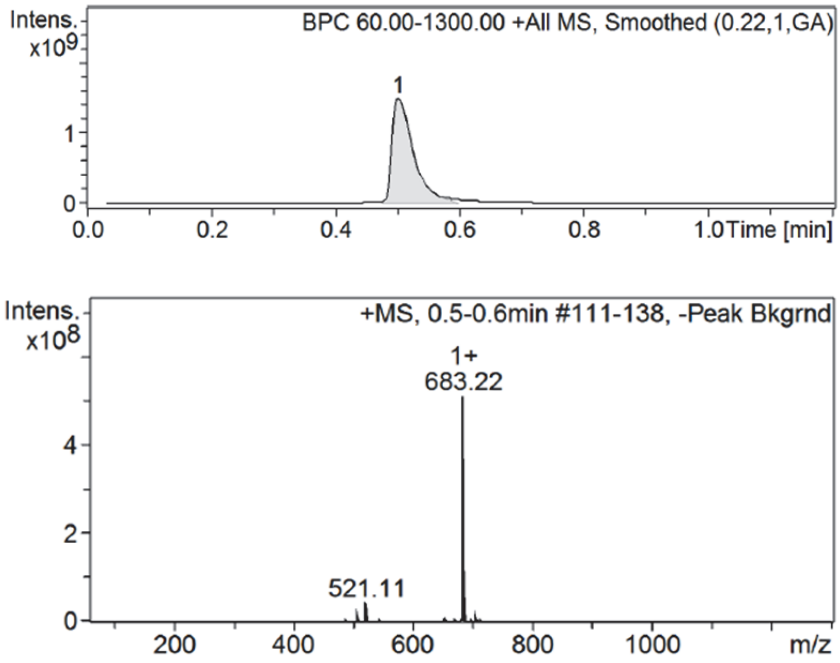

Figure 2.4.3. Spectral characterisation for final product of synthesis **LA-EG_2-ManA (9)** showing **(A)** ^{1}H-NMR spectrum **(B)** ^{13}C-NMR spectrum and **(C)** LC-MS analysis (chromatogram and molecular ion peaks).

2.4.4. Synthesis of LA-EG_2-Man

LA-EG_2-C≡CH (37.2 mg, 0.112 mmol), 1-Azido-3,6-dioxaoct-8-yl-α-D-mannopyraside, N_3-EG_2-Man (41.4 mg, 0.123 mmol), $CuSO_4.5H_2O$ (1.0 mg, 0.0043 mmol), TBTA (3.74 mg, 0.007 mmol), and sodium ascorbate (3.0 mg, 0.0151 mmol) were dissolved in 2 mL of THF/H_2O ((1:1) (vol/vol)). The resulting solution was stirred overnight at RT in darkness. Next day, the consumption of all starting compounds was confirmed by TLC. The solvent was then evaporated and the desired ligand was purified by size exclusion chromatography using Biogel P2 column using ammonium formate as an eluent to obtain the pure product, **compound 10**, (53.8 mg, 0.08 mmol, 65 % yield).

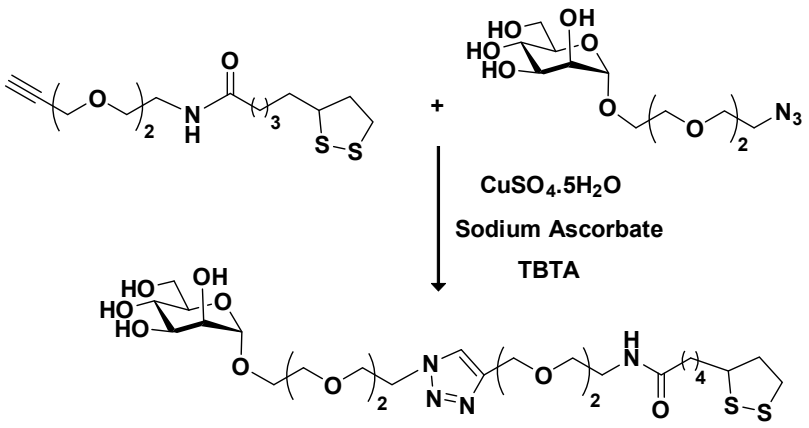

Compound 10 - LA-EG$_2$-Man

Scheme 2.4.4. A reaction scheme showing the synthesis of LA-EG$_2$-Man.

TLC: ($CHCl_3$/MeOH 3:1) R_f 0.52; **^{1}H NMR (500 MHz, CD_3OD)** δ (ppm): 8.04 (s, 1H, triazole-H), 4.8 (d, 1H, *J* 1.6 Hz, Man H-1), 4.65 (s, 2H), 4.6 (t, 2H, *J* 5 Hz), 3.9 (t, 2H, *J* 5.1 Hz), 3.86-3.81 (m, 3H), 3.8 (dd, 1H, *J* 1.7 Hz, 3.4 Hz, Man H-2), 3.72 (d, 1H, *J* 5.5 Hz), 3.69-3.67 (m, 3H), 3.66 (s, 2H), 3.65-3.63 (m, 2H), 3.62-3.61 (m, 4H), 3.60-3.57 (m, 2H), 3.53 (t, 2H, *J* 5.5 Hz), 3.39-3.34 (m, 3H), 3.20-3.15 (m, 1H), 3.12-3.07 (m, 1H), 2.49-2.42 (m, 1H), 2.20 (t, 2H, *J* 7.4 Hz), 1.92-1.85 (m, 1H), 1.73-1.59 (m, 4H), 1.50-1.40 (m, 2H); **^{13}C NMR (125 MHz, CD_3OD)** δ (ppm): 176.1 (C=O), 145.7 (C=CH), 126.0 (C=CH), 101.7 (Man C-1), 74.6, 72.6, 72.1 (Man C-2), 71.6, 71.5, 71.4, 71.3, 70.8, 70.6, 70.4, 68.6, 67.7, 65.0, 63.0 (Man C-6), 57.6, 51.5, 41.3, 40.3, 39.3, 36.8, 35.7, 29.8, 26.7; **LC-MS:** calculated *m/z* for $C_{27}H_{48}N_4O_{11}S_2$ $(M+H)^+$ 669.28; found 669.59.

A-^{1}H-NMR of LA-EG$_2$-Man

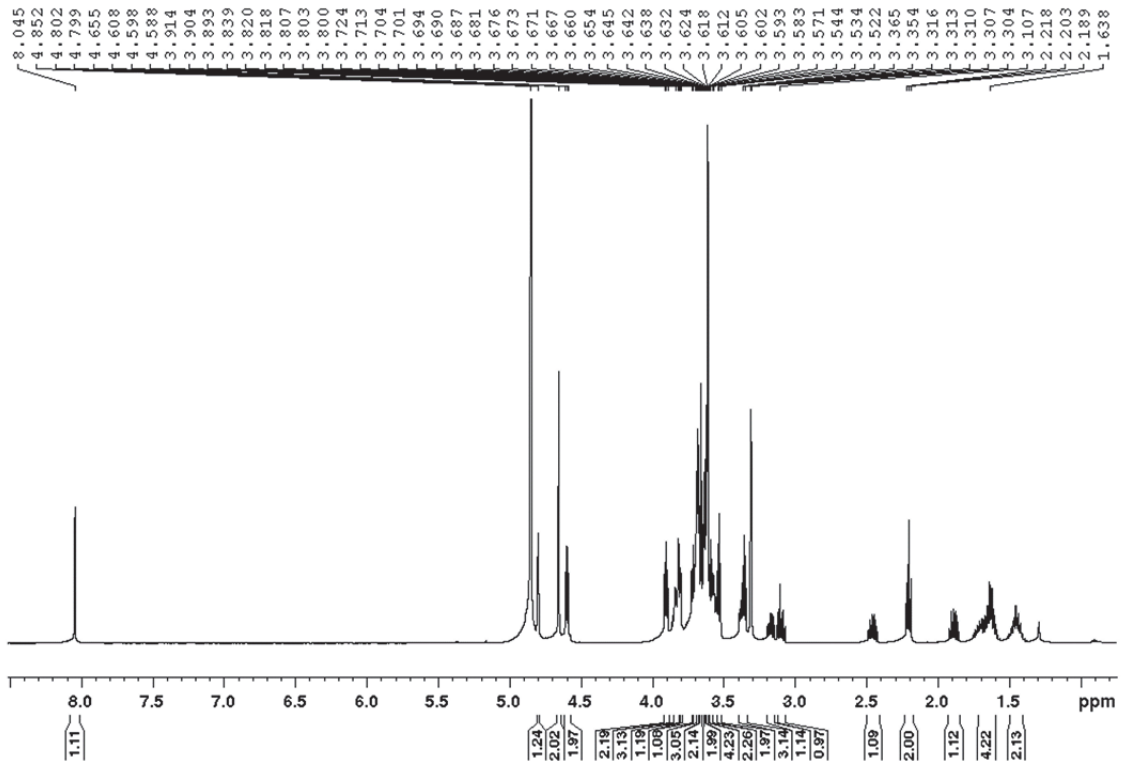

B-^{13}C-NMR of LA-EG$_2$-Man

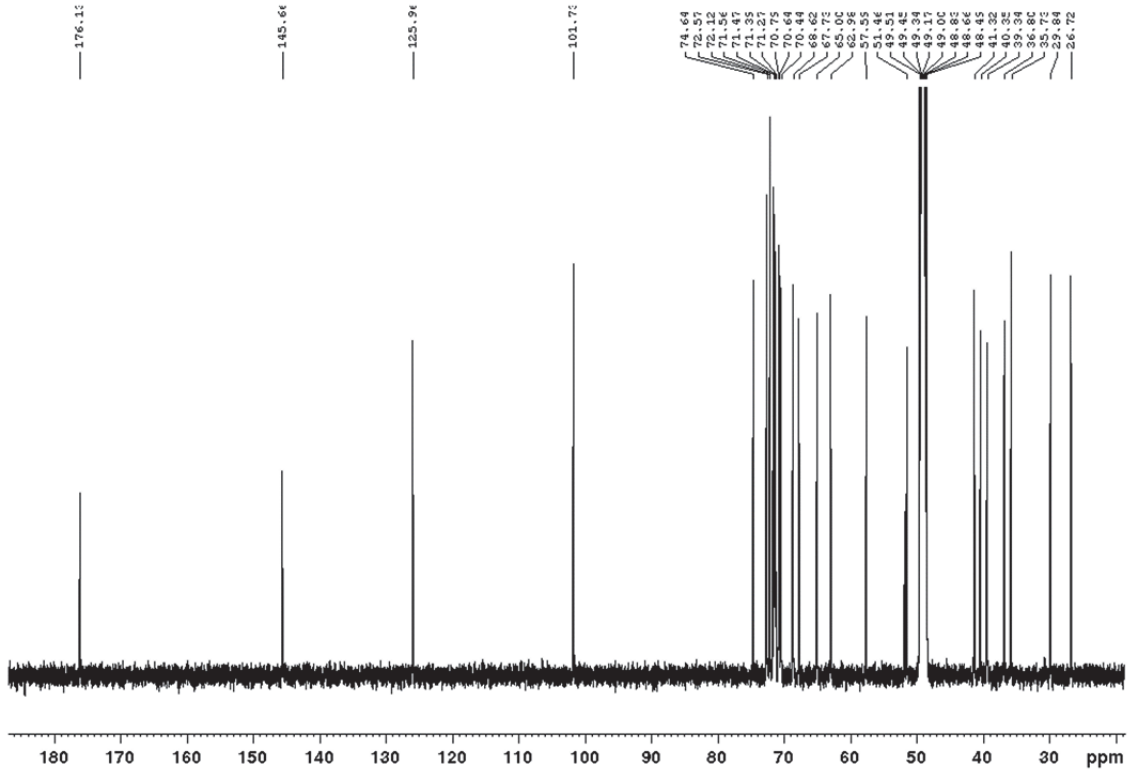

C- LC-MS of LA-EG$_2$-Man

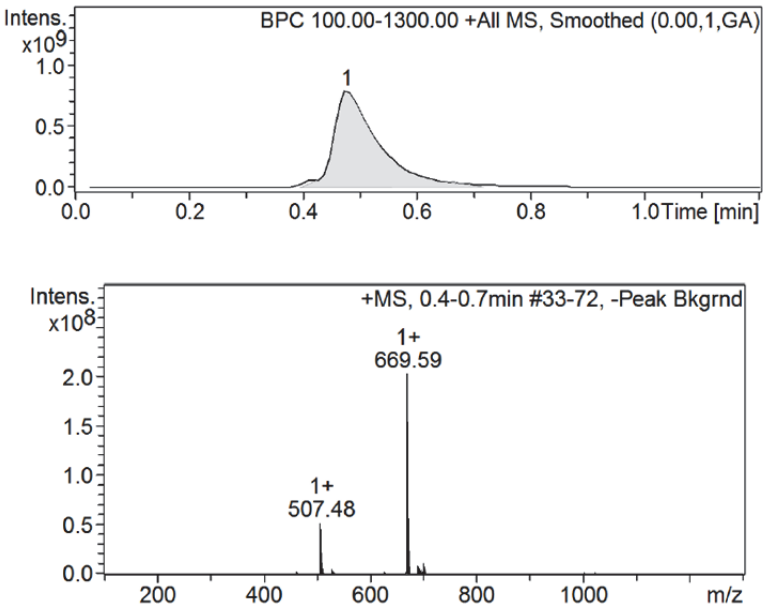

Figure 2.4.4. Spectral characterisation for final product of synthesis **LA-EG$_2$-Man (10)** showing **(A)** ^{1}H-NMR spectrum **(B)** ^{13}C-NMR spectrum and **(C)** LC-MS analysis (chromatogram and molecular ion peaks).

2.4.5. Synthesis of LA-EG_2-DiMan

LA-EG_2-C≡CH (30 mg, 0.090 mmol), 1-Azido-3,6-dioxaoct-8-yl-α-D-mannopyranosyl-(1→2)-α-D-mannopyraside, N_3-EG_2-DiMan (50 mg, 0.1 mmol), $CuSO_4.5H_2O$ (0.8 mg, 0.0032 mmol), TBTA (3 mg, 0.0056 mmol), and sodium ascorbate (2.4 mg, 0.0121 mmol) were dissolved in 2 mL of THF/H_2O ((1:1) (vol/vol)). The resulting solution was stirred overnight at RT in darkness. Next day, the consumption of all starting compounds was confirmed by TLC. The solvent was then evaporated and the desired ligand was purified by size exclusion chromatography using Biogel P2 column using ammonium formate as an eluent to obtain the pure product, **compound 11**, (65.7 mg, 0.079 mmol, 79 % yield).

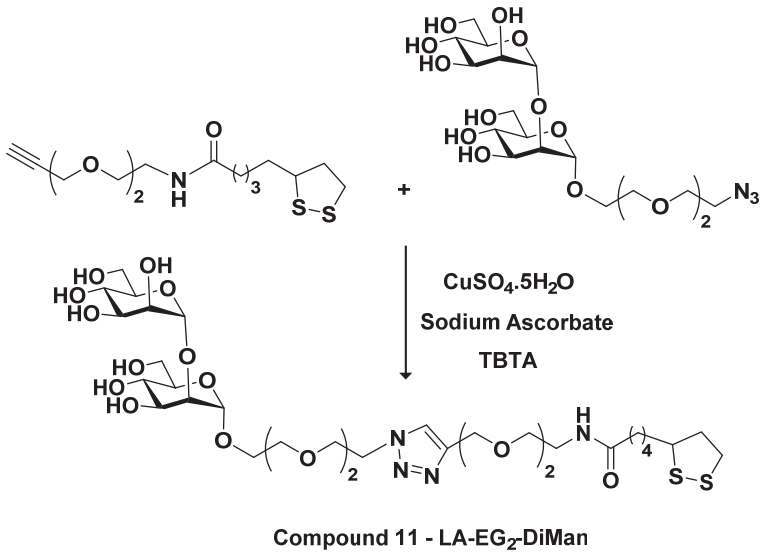

Compound 11 - LA-EG_2-DiMan

Scheme 2.4.5. A reaction scheme showing the synthesis of LA-EG_2-DiMan.

TLC: ($CHCl_3$/MeOH 3:1) R_f 0.63; **^{1}H NMR (500 MHz, CD_3OD)** δ (ppm): 8.05 (s, 1H, triazole-H), 5.11 (d, *J* 1.7 Hz, 1H), 4.96 (d, *J* 1.8 Hz, 1H), 4.66 (s, 2H), 4.60 (t, 2H, *J* 5.1 Hz), 3.97 (dd, 1H, *J* 3.3, 1.8 Hz), 3.91 (dd, 2H, *J* 5.5, 4.7 Hz), 3.88 – 3.78 (m, 6H), 3.72 – 3.65 (m, 8H), 3.62 (dt, 6H, *J* 5.0, 1.3 Hz), 3.58 (dt, 3H, *J* 11.2, 1.6 Hz), 3.53 (t, 2H, *J* 5.5 Hz), 3.43 – 3.32 (m, 3H), 3.17 (ddd, 1H, *J* 10.9, 7.1, 5.4 Hz), 3.10 (dt, 1H, *J* 11.0, 6.9 Hz, 1H), 2.46 (dtd, 1H, *J* 12.1, 6.7, 5.4 Hz), 2.20 (t, 2H, *J* 7.4 Hz), 1.89 (dq, 1H, *J* 12.7, 6.9 Hz), 1.77 – 1.57 (m, 4H), 1.45 (qt, 2H, *J* 9.4, 5.9 Hz); **^{13}C NMR (125 MHz, CD_3OD)** δ (ppm): 176.1 (C=O), 145.7 (C=CH), 126.0 (C=CH), 104.2 (Man C-1), 100.1 (Man C-1'), 80.6, 75.1, 74.7, 72.4, 72.1, 71.9, 71.6, 71.5, 71.4, 71.3, 70.8, 70.6, 70.5, 69.0, 68.8, 67.9, 65.0, 63.2, 63.1, 57.6, 51.5, 41.3, 40.4, 39.3, 36.8, 35.7, 29.8, 26.7; **LC-MS:** calculated *m/z* for $C_{33}H_{58}N_4O_{16}S_2$ $(M+H)^+$ 831.33; found 831.73.

A-^{1}H-NMR of LA-EG$_2$-DiMan

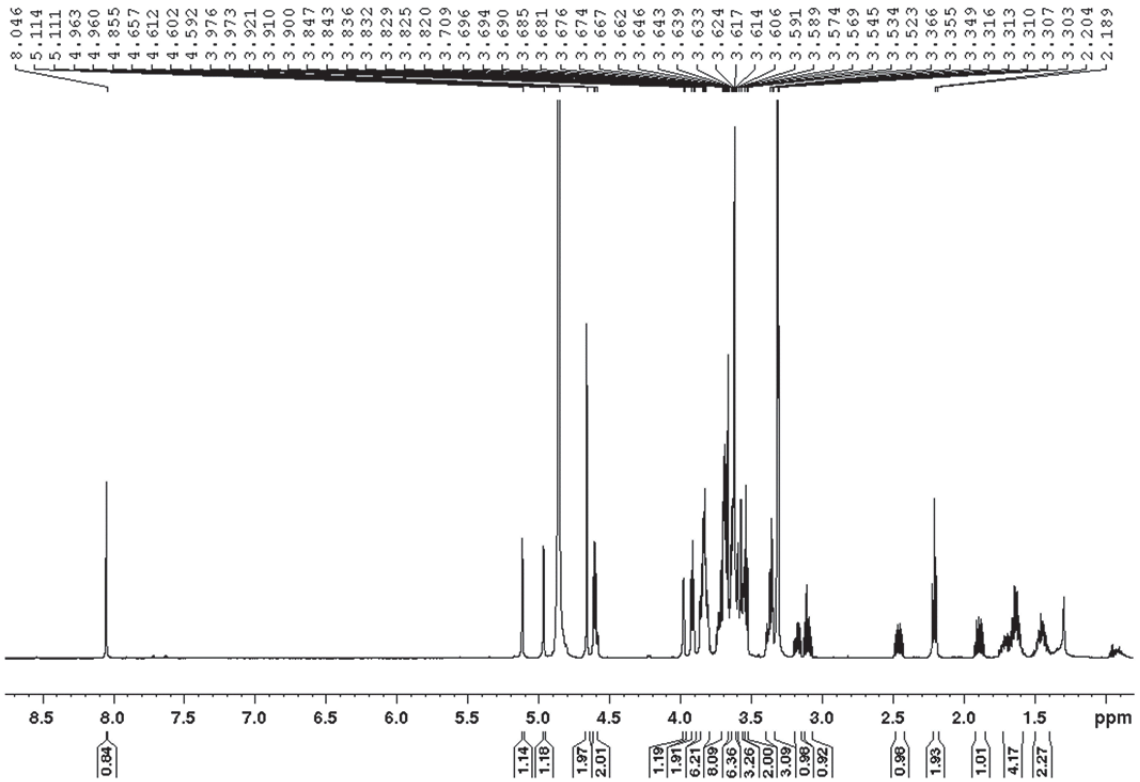

B-^{13}C-NMR of LA-EG$_2$-DiMan

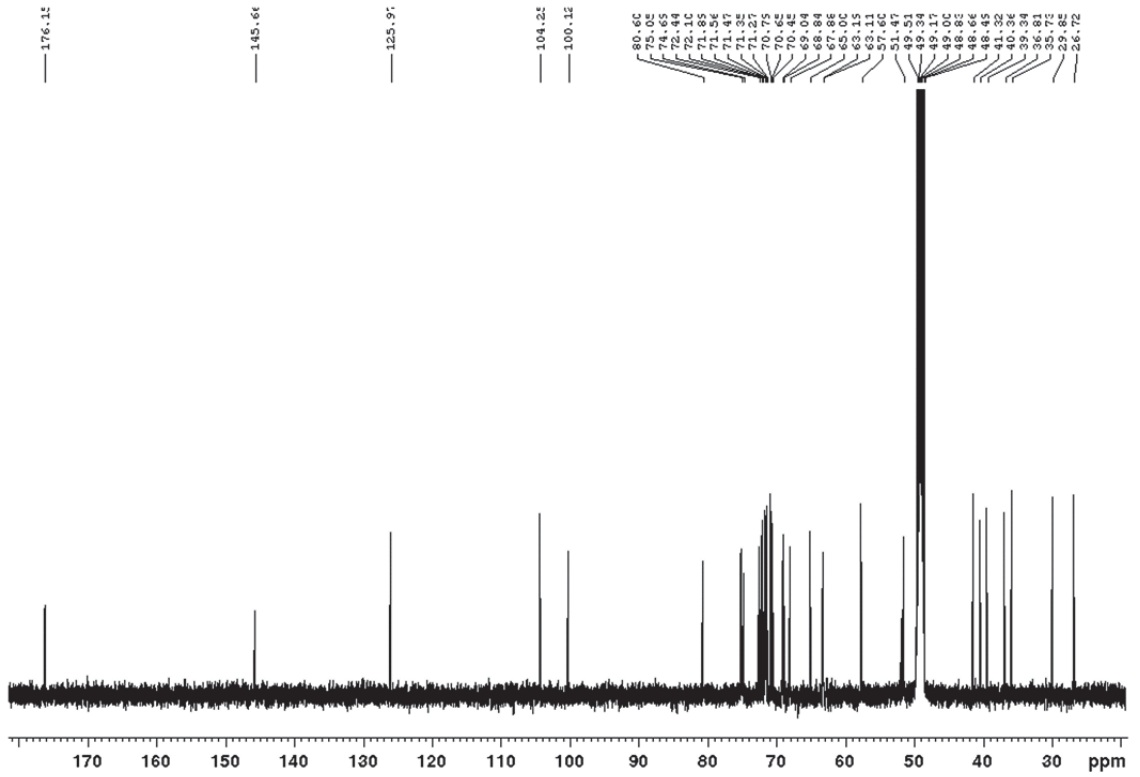

C- LC-MS of LA-EG$_2$-DiMan

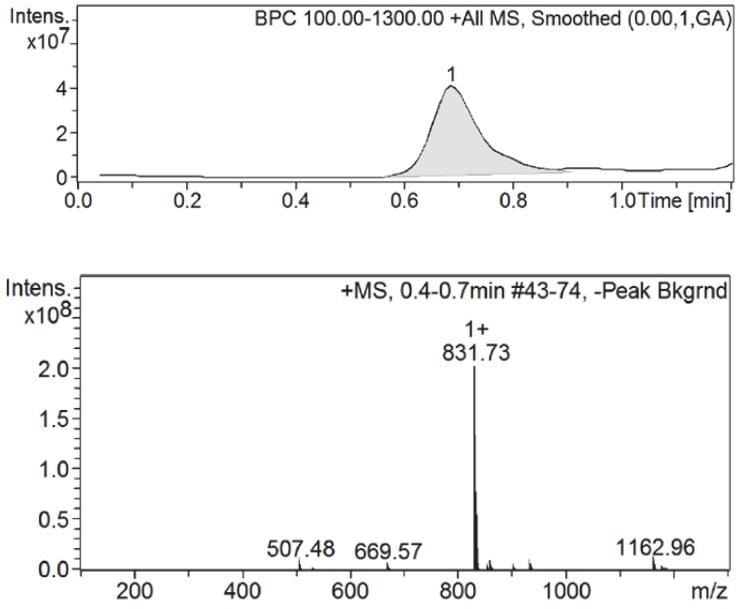

Figure 2.4.5. Spectral characterisation for final product of synthesis **LA-EG$_2$-DiMan (11)** showing **(A)** ^{1}H-NMR spectrum **(B)** ^{13}C-NMR spectrum and **(C)** LC-MS analysis (chromatogram and molecular ion peaks).

2.4.6. Synthesis of LA-EG$_2$-OH

LA-EG$_2$-C≡CH (40 mg, 0.120 mmol), 2-[2-(2-Azidoethoxy)ethoxy]ethanol, N$_3$-EG$_2$-OH (23.1 mg, 0.132 mmol), $CuSO_4.5H_2O$ (1.07 mg, 0.0043 mmol), TBTA (4.01 mg, 0.0075 mmol), and sodium ascorbate (3.21 mg, 0.0162 mmol) were dissolved in 2 mL of THF/H_2O ((1:1) (vol/vol)). The resulting solution was stirred overnight at RT in darkness. Next day, the consumption of all starting compounds was confirmed by TLC. The solvent was then evaporated and the desired ligand was purified by size exclusion chromatography using Biogel P2 column using ammonium formate as an eluent to obtain the pure product, **compound 12**, (44.1 mg, 0.087 mmol, 66 % yield).

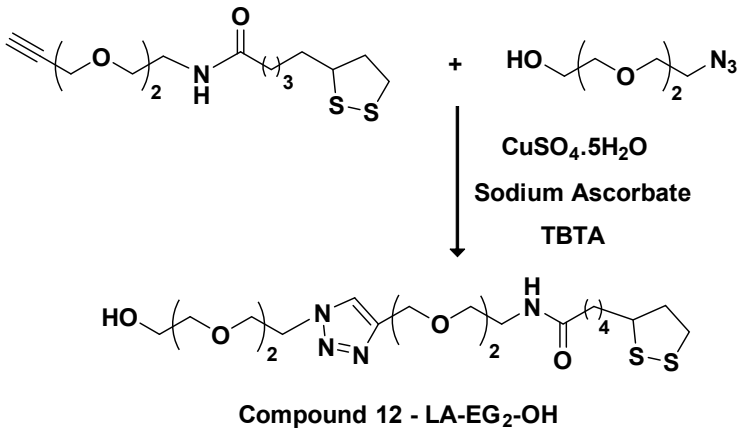

Compound 12 - LA-EG$_2$-OH

Scheme 2.4.6. A reaction scheme showing the synthesis of LA-EG$_2$-OH.

TLC: ($CHCl_3$/MeOH 10:1) R_f 0.55; **^{1}H NMR (500 MHz, D_2O)** δ (ppm): 8.01 (s, 1H), 4.62 (s, 2H), 4.57 (t, 2H, *J*=5.0 Hz), 3.91 (t, 2H, *J*=5.1 Hz), 3.66 – 3.63 (m, 2H), 3.63 – 3.56 (m, 7H), 3.56 – 3.51 (m, 4H), 3.48 – 3.46 (m, 2H), 3.30 (t, 2H, *J*=5.3 Hz), 3.27 (s, 1H), 3.18 – 3.06 (m, 2H), 2.39 (dq, 1H, *J*=12.3, 6.1 Hz), 2.16 (t, 2H, *J*=7.2 Hz), 1.89 (dq, 1H, *J*=13.6, 6.8 Hz), 1.64 (dtd, 1H, *J*=13.6, 7.9, 5.5 Hz), 1.57 – 1.47 (m, 3H), 1.31 (p, 2H, *J*=7.4 Hz); **^{13}C NMR (125 MHz, D_2O)** δ (ppm): 176.9 (C=O), 143.8 (C=CH), 125.4 (C=CH), 71.6, 69.6, 69.4, 69.3, 68.9, 68.8, 68.7, 63.0, 60.3, 56.4, 49.9, 40.2, 38.8, 38.0, 35.4, 33.6, 27.7, 24.9; **LC-MS:** calculated *m/z* for $C_{21}H_{38}N_4O_6S_2$ $(M+H)^+$ 507.22, found 507.45.

A- ^{1}H-NMR of LA-EG$_2$-OH

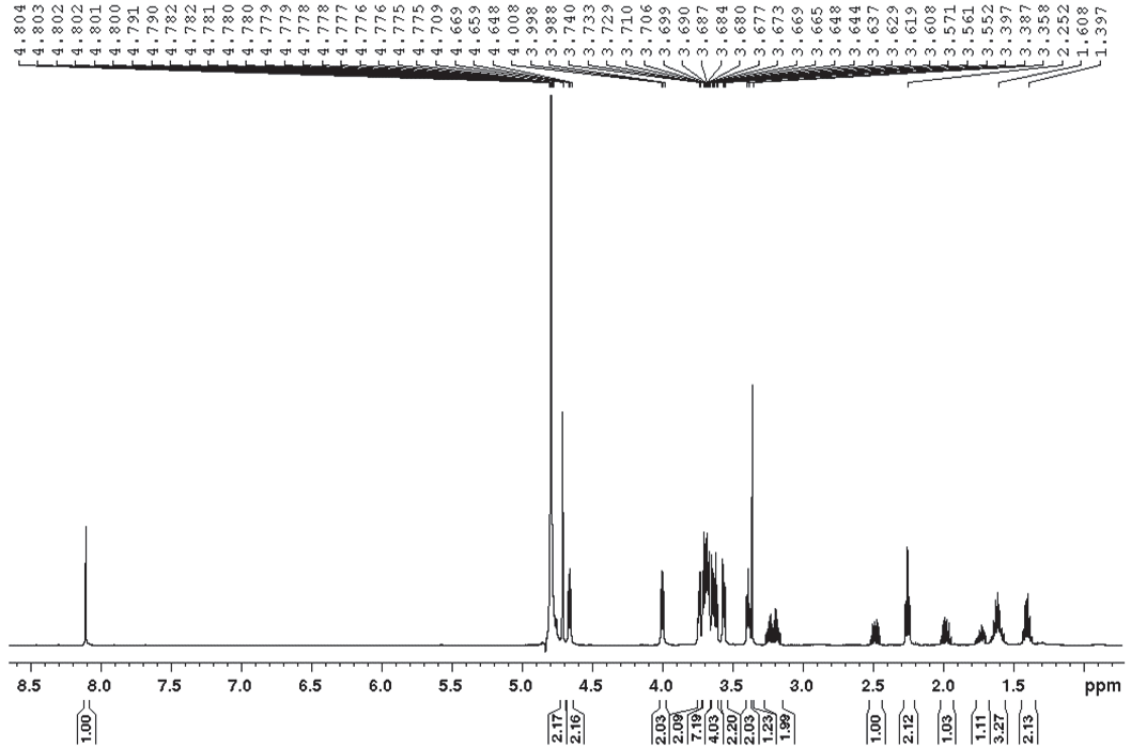

B- ^{13}C-NMR of LA-EG$_2$-OH

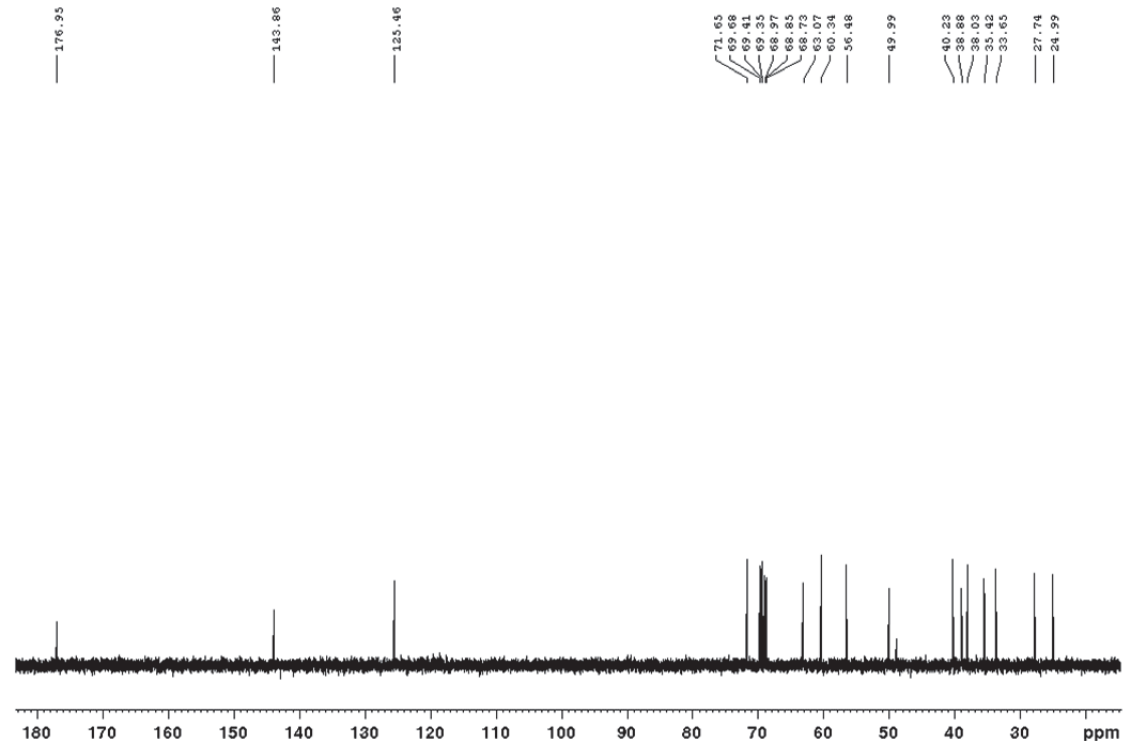

C- LC-MS of LA-EG_2-OH

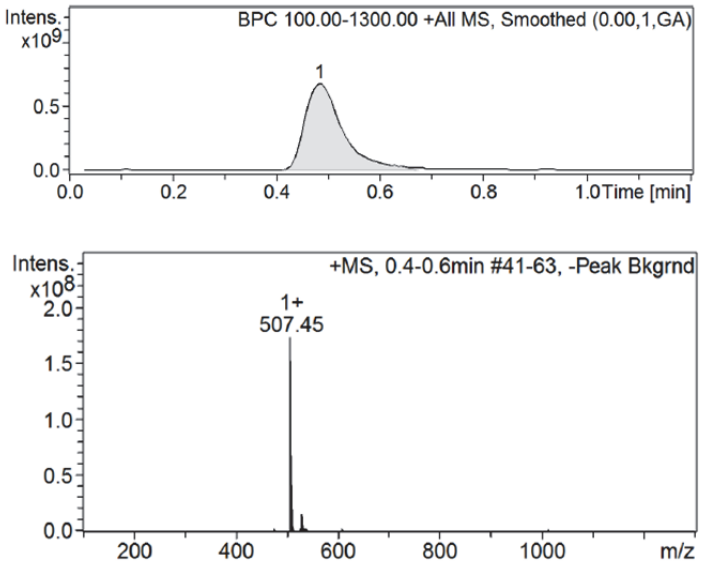

Figure 2.4.6. Spectral characterisation for final product of synthesis **LA-EG_2-OH (12)** showing **(A)** ^{1}H-NMR spectrum **(B)** ^{13}C-NMR spectrum and **(C)** LC-MS analysis (chromatogram and molecular ion peaks).

2.4.7. Synthesis of LA-EG_4-Man

LA-EG_4-C≡CH (55 mg, 0.131 mmol), 1-Azido-3,6-dioxaoct-8-yl-α-D-mannopyraside, N_3-EG_2-Man (49 mg, 0.145 mmol), $CuSO_4.5H_2O$ (1.17 mg, 0.0047 mmol), TBTA (4.38 mg, 0.0082 mmol), and sodium ascorbate (3.5 mg, 0.0176 mmol) were dissolved in 2 mL of THF/H_2O ((1:1) (vol/vol)). The resulting solution was stirred overnight at RT in darkness. Next day, the consumption of all starting compounds was confirmed by TLC. The solvent was then evaporated and the desired ligand was purified by size exclusion chromatography using Biogel P2 column using ammonium formate as an eluent to obtain the pure product, **compound 13**, (67 mg, 0.088 mmol, 61 % yield).

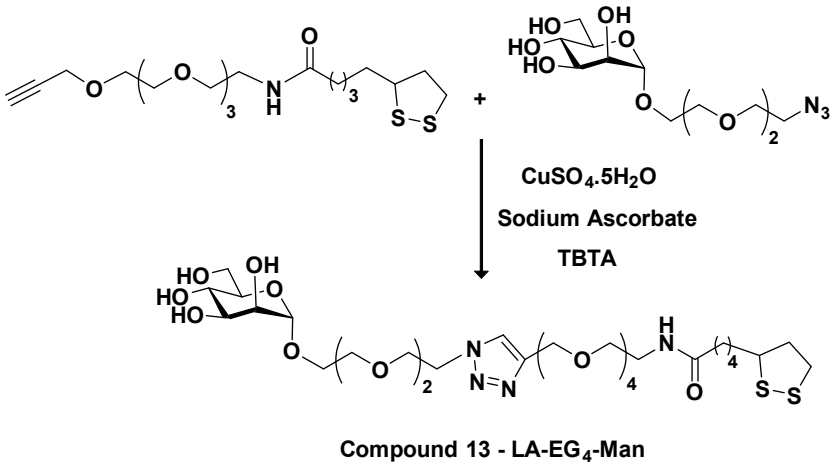

Compound 13 - LA-EG_4-Man

Scheme 2.4.7. A reaction scheme showing the synthesis of LA-EG_4-Man.

TLC: ($CHCl_3$/MeOH 3:1) R_f 0.52; **^{1}H NMR (400 MHz, CD_3OD)** δ (ppm): 8.03 (s, 1H), 4.79 (d, 1H, *J*=1.7 Hz), 4.64 (s, 2H), 4.59 (t, 2H, *J*=5.1 Hz), 3.92 – 3.88 (m, 2H), 3.85 – 3.78 (m, 3H), 3.73 – 3.58 (m, 23H), 3.53 (t, 2H, *J*=5.4 Hz), 3.34 (d, 4H, *J*=3.1 Hz), 3.21 – 3.05 (m, 2H), 2.45 (dtd, 1H, *J*=12.1, 6.6, 5.3 Hz), 2.20 (t, 2H, *J*=7.4 Hz), 1.88 (dq, 1H, *J*=12.6, 6.9 Hz), 1.77 – 1.57 (m, 4H), 1.53 – 1.36 (m, 2H); **^{13}C NMR (100 MHz, CD_3OD)** δ (ppm): 176.08, 145.74, 125.83, 101.69, 74.59, 72.53, 72.08, 71.54, 71.45, 71.42, 71.35, 71.23, 70.71, 70.68, 70.42, 68.58, 67.72, 64.99, 62.90, 57.59, 51.43, 49.85, 49.64, 49.43, 49.21, 49.00, 48.79, 48.57, 48.36, 41.32, 40.32, 39.35, 36.80, 35.73, 29.85, 26.70; **LC-MS:** calculated *m/z* for $C_{31}H_{56}N_4O_{13}S_2$ $(M+H)^+$ 757.33, found 757.63.

A- ^{1}H-NMR of LA-EG_4-Man

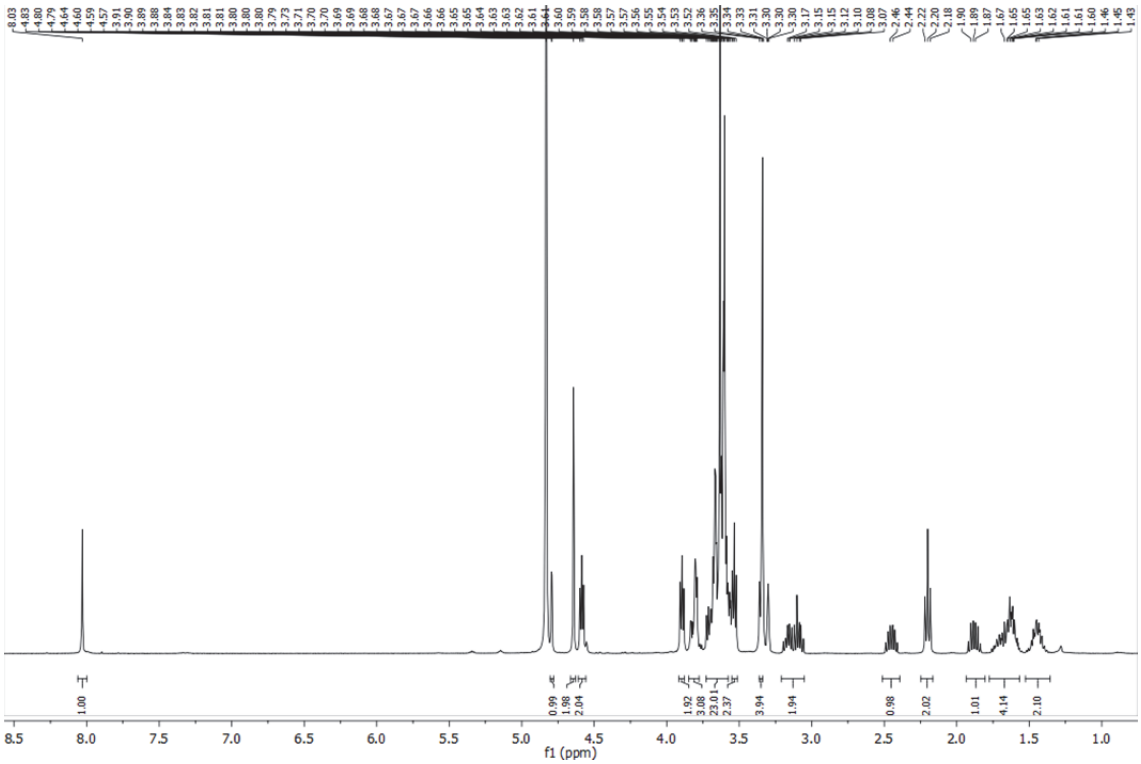

B- ^{13}C-NMR of LA-EG$_4$-Man

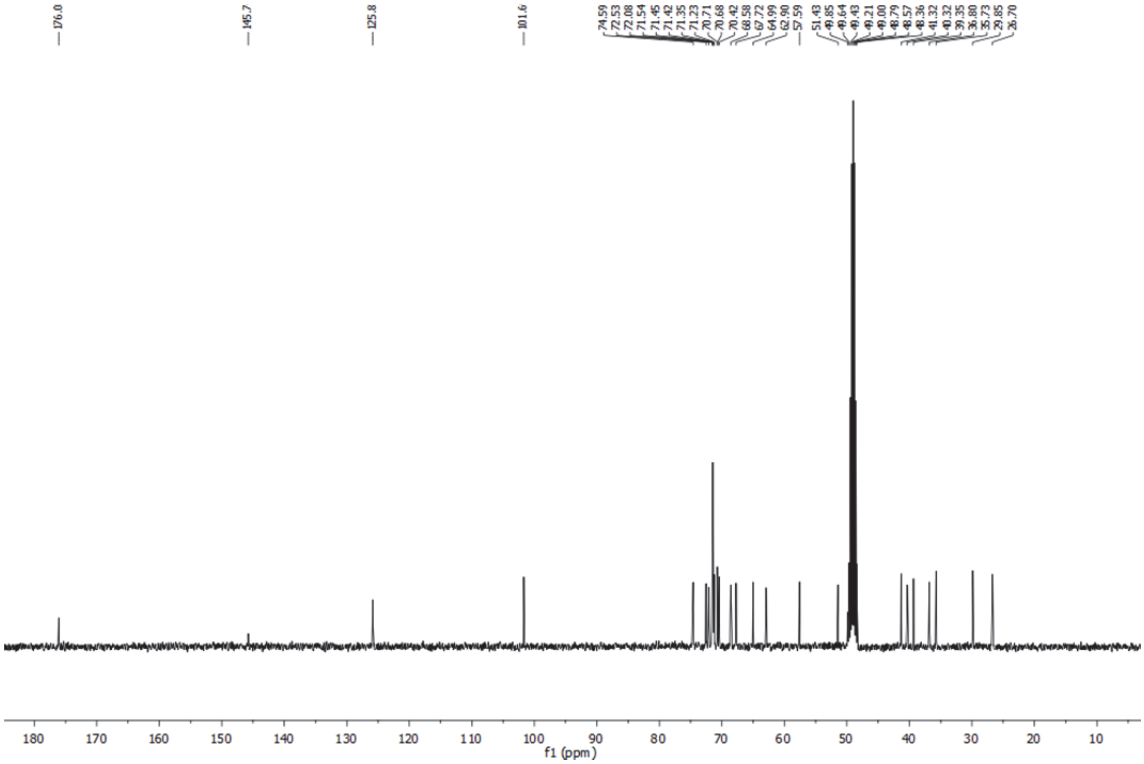

C- LC-MS of LA-EG$_4$-Man

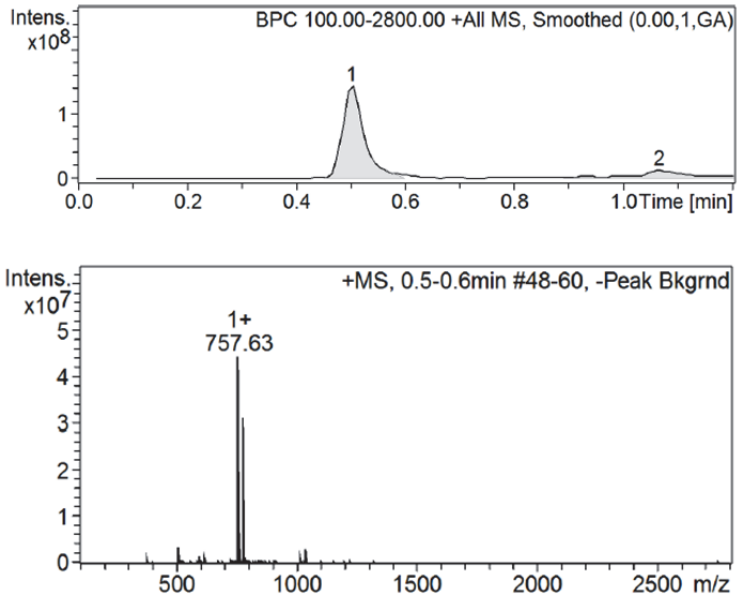

Figure 2.4.7. Spectral characterisation for final product of synthesis **LA-EG$_4$-Man (13)** showing **(A)** ^{1}H-NMR spectrum **(B)** ^{13}C-NMR spectrum and **(C)** LC-MS analysis (chromatogram and molecular ion peaks).

2.4.8. Synthesis of LA-EG_4-DiMan

LA-EG_4-C≡CH (50 mg, 0.120 mmol), 1-Azido-3,6-dioxaoct-8-yl-α-D-mannopyranosyl-(1→2)-α-D-mannopyraside, N_3-EG_2-DiMan (66 mg, 0.132 mmol), $CuSO_4.5H_2O$ (1.07 mg, 0.0043 mmol), TBTA (4.01 mg, 0.0075 mmol), and sodium ascorbate (3.21 mg, 0.0162 mmol) were dissolved in 2 mL of THF/H_2O ((1:1) (vol/vol)). The resulting solution was stirred overnight at RT in darkness. Next day, the consumption of all starting compounds was confirmed by TLC. The solvent was then evaporated and the desired ligand was purified by size exclusion chromatography using Biogel P2 column using ammonium formate as an eluent to obtain the pure product, **compound 14**, (93.4 mg, 0.101 mmol, 77 % yield).

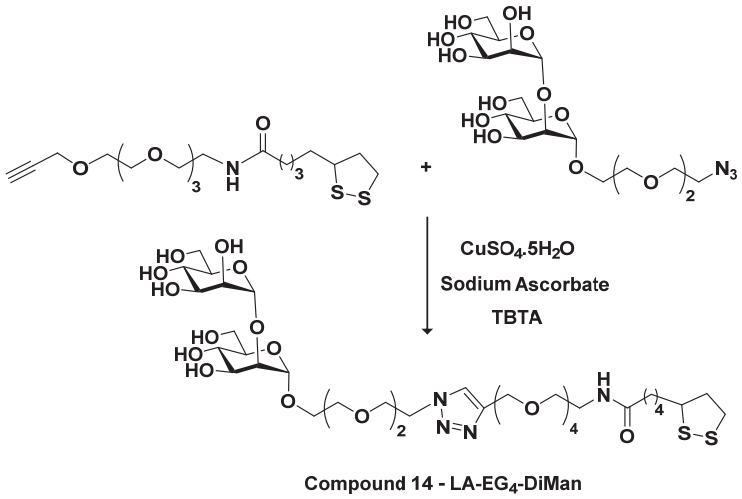

Scheme 2.4.8. A reaction scheme showing the synthesis of LA-EG_4-DiMan.

TLC: ($CHCl_3$/MeOH 3:1) R_f 0.57; **^{1}H NMR (400 MHz, D_2O)** δ (ppm): 8.10 (s, 1H), 5.12 (s, 1H), 5.03 (s, 1H), 4.73 – 4.60 (m, 3H), 4.08 (s, 1H), 3.99 (dd, 3H, *J*=10.2, 5.1 Hz), 3.94 – 3.82 (m, 5H), 3.69 (dh, 31H, *J*=12.8, 7.1, 6.7 Hz), 3.45 – 3.30 (m, 2H), 3.30 – 2.33 (m, 2H), 2.26 (t, 2H, *J*=7.3 Hz), 1.99 (dt, 1H, *J*=12.9, 6.9 Hz), 1.78 – 1.54 (m, 4H), 1.42 (q, 1H, *J*=7.6 Hz); **^{13}C NMR (100 MHz, D_2O)** δ (ppm): 176.7, 144.1, 125.5, 102.2, 98.3, 78.6, 73.2, 72.7, 70.2, 70.1, 69.9, 69.6, 69.6, 69.5, 69.5, 69.4, 69.2, 68.9, 68.8, 68.7, 66.9, 66.8, 66.5, 66.5, 63.2, 63.1, 61.4, 61.1, 60.8, 59.3, 56.5, 50.1, 50.0, 46.6, 40.2, 38.9, 38.1; **LC-MS:** calculated *m/z* for $C_{37}H_{66}N_4O_{18}S_2$ $(M+H)^+$ 919.38, found 919.78.

A- ^{1}H-NMR of LA-EG$_4$-DiMan

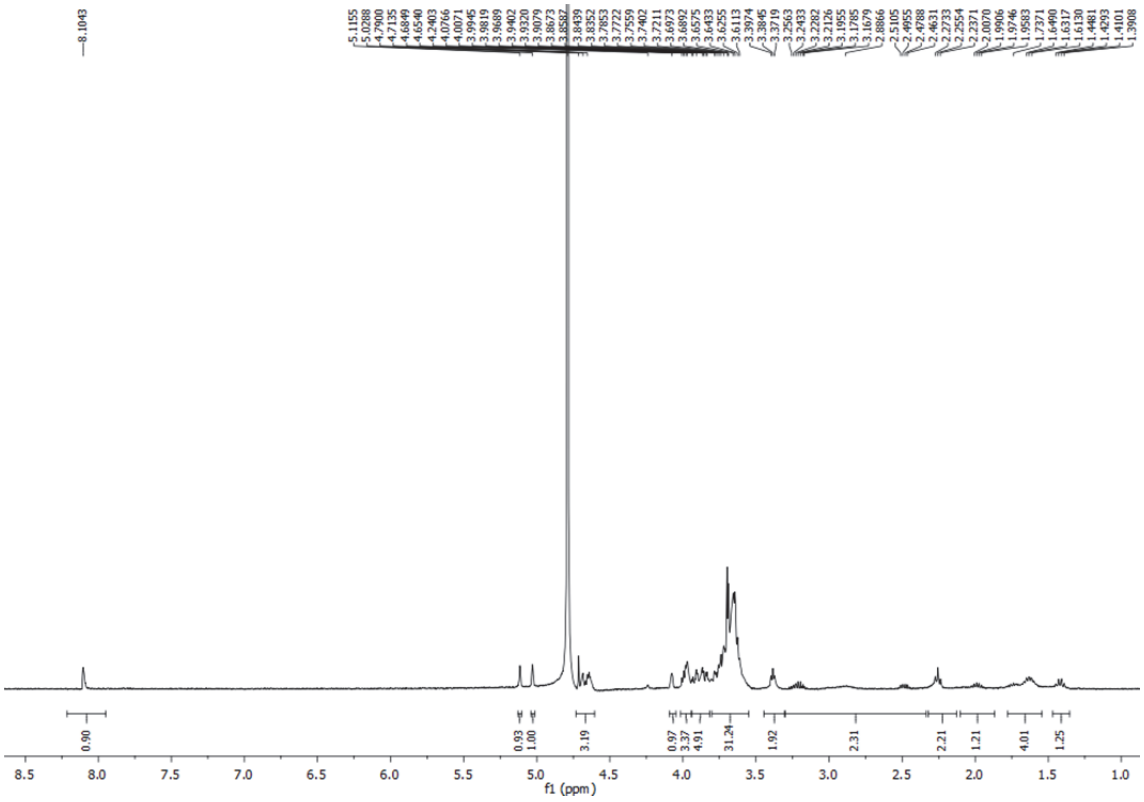

B- ^{13}C-NMR of LA-EG$_4$-DiMan

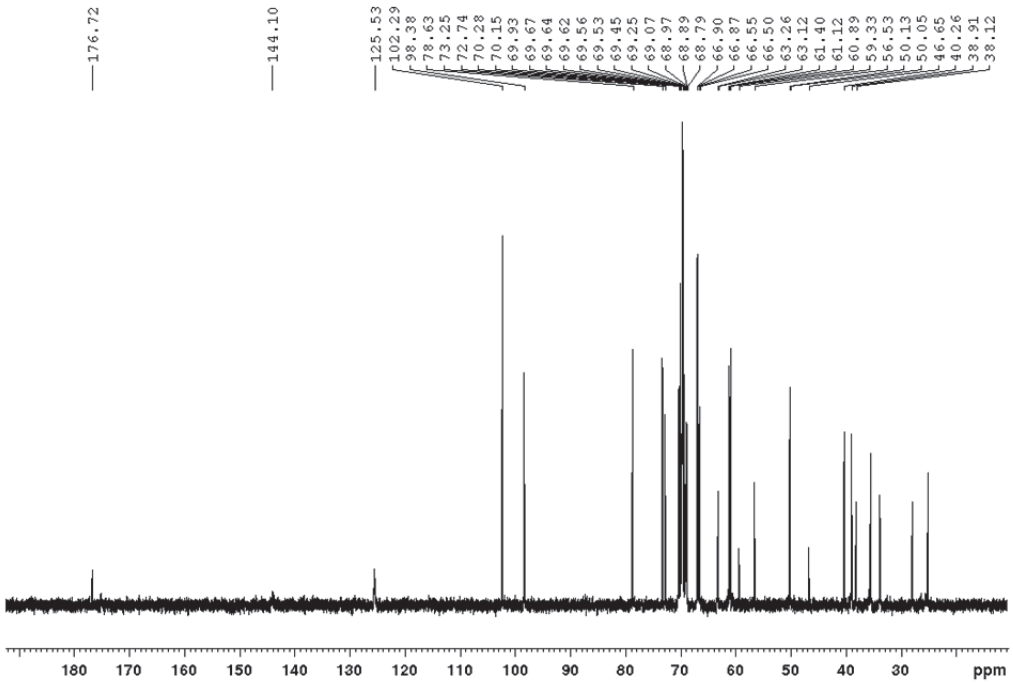

C- LC-MS of LA-EG$_4$-DiMan

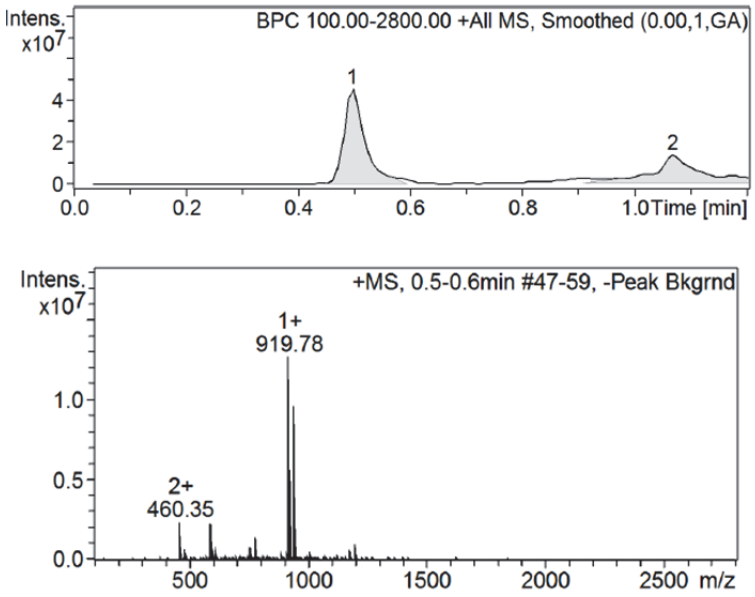

Figure 2.4.8. Spectral characterisation for final product of synthesis **LA-EG$_4$-DiMan (14)** showing **(A)** ^{1}H-NMR spectrum **(B)** ^{13}C-NMR spectrum and **(C)** LC-MS analysis (chromatogram and molecular ion peaks).

2.4.9. Synthesis of LA-EG$_4$-OH

LA-EG$_4$-C≡CH (50 mg, 0.120 mmol), 2-[2-(2-Azidoethoxy)ethoxy]ethanol, N_3-EG$_2$-OH (23.1 mg, 0.132 mmol), $CuSO_4.5H_2O$ (1.07 mg, 0.0043 mmol), TBTA (4.01 mg, 0.0075 mmol), and sodium ascorbate (3.21 mg, 0.0162 mmol) were dissolved in 2 mL of THF/H_2O ((1:1) (vol/vol)). The resulting solution was stirred overnight at RT in darkness. Next day, the consumption of all starting compounds was confirmed by TLC. The solvent was then evaporated and the desired ligand was purified by size exclusion chromatography using Biogel P2 column using ammonium formate as an eluent to obtain the pure product, **compound 15**, (58.8 mg, 0.098 mmol, 75 % yield).

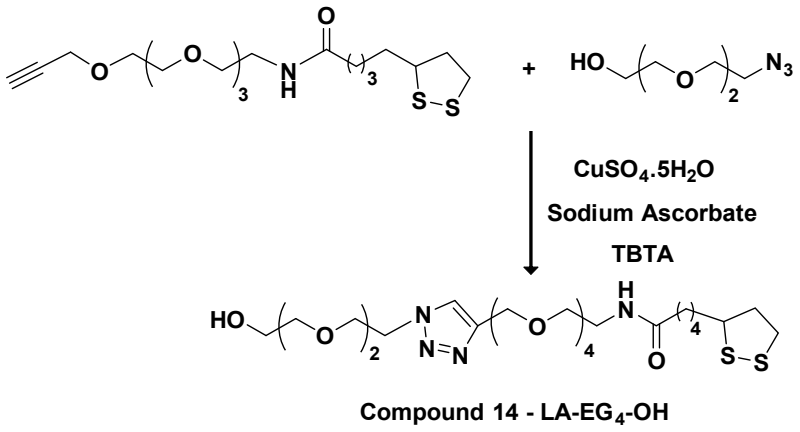

Compound 14 - LA-EG$_4$-OH

Scheme 2.4.9. A reaction scheme showing the synthesis of LA-EG$_4$-OH.

TLC: ($CHCl_3$/MeOH 10:1) R_f 0.45; **^{1}H NMR (500 MHz, D_2O)** δ (ppm): 8.01 (s, 1H), 3.93 – 3.87 (m, 2H), 3.66 – 3.59 (m, 17H), 3.58 – 3.56 (m, 4H), 3.55 – 3.51 (m, 5H), 3.48 – 3.45 (m, 2H), 3.29 (t, 2H, *J*=5.2 Hz), 3.15 – 3.07 (m, 1H), 2.39 (dq, 1H, *J*=12.4, 6.1 Hz), 2.16 (t, 2H, *J*=7.3 Hz), 1.88 (dq, 1H, *J*=13.8, 6.9 Hz), 1.70 – 1.60 (m, 1H), 1.53 (ddd, 3H, *J*=14.9, 7.6, 5.3 Hz), 1.31 (p, 2H, *J*=7.6 Hz); **^{13}C NMR (125 MHz, D_2O)** δ (ppm): 183.1, 142.9, 125.4, 71.6, 69.6, 69.4, 68.9, 68.7, 65.9, 61.5, 60.3, 56.4, 49.9, 48.4, 43.9, 43.7, 43.2, 41.7, 38.0, 36.3, 33.6, 33.4, 24.9, 17.3; **LC-MS:** calculated *m/z* for $C_{25}H_{46}N_4O_8S_2$ $(M+H)^+$ 595.28, found 595.57.

A- ^{13}H-NMR of LA-EG$_4$-OH

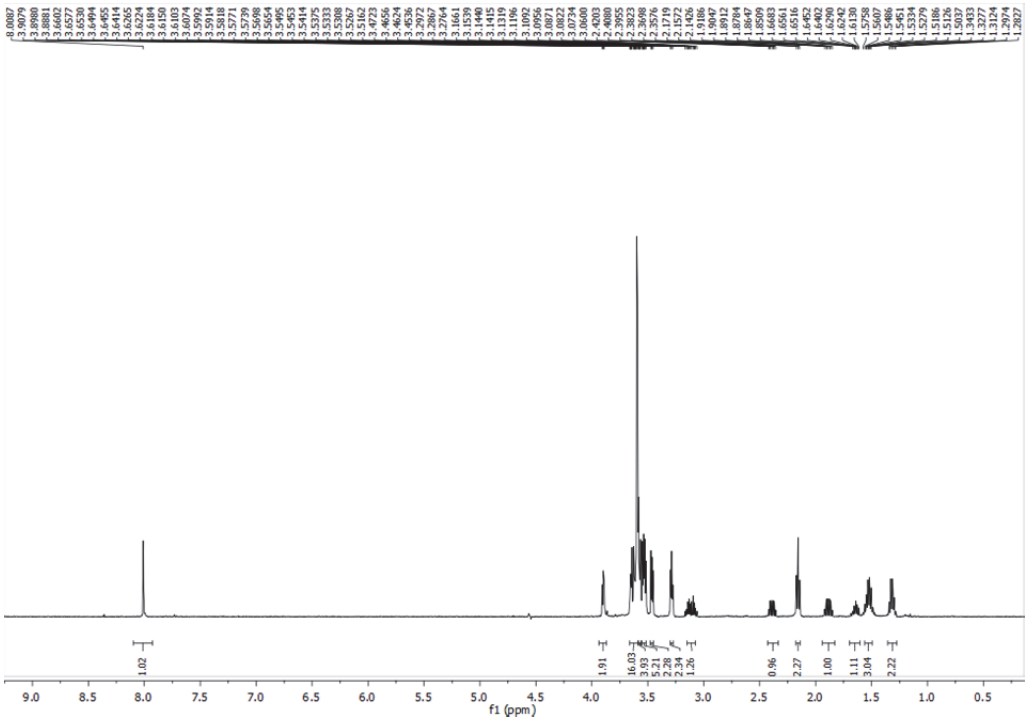

B- ^{13}C-NMR of LA-EG$_4$-OH

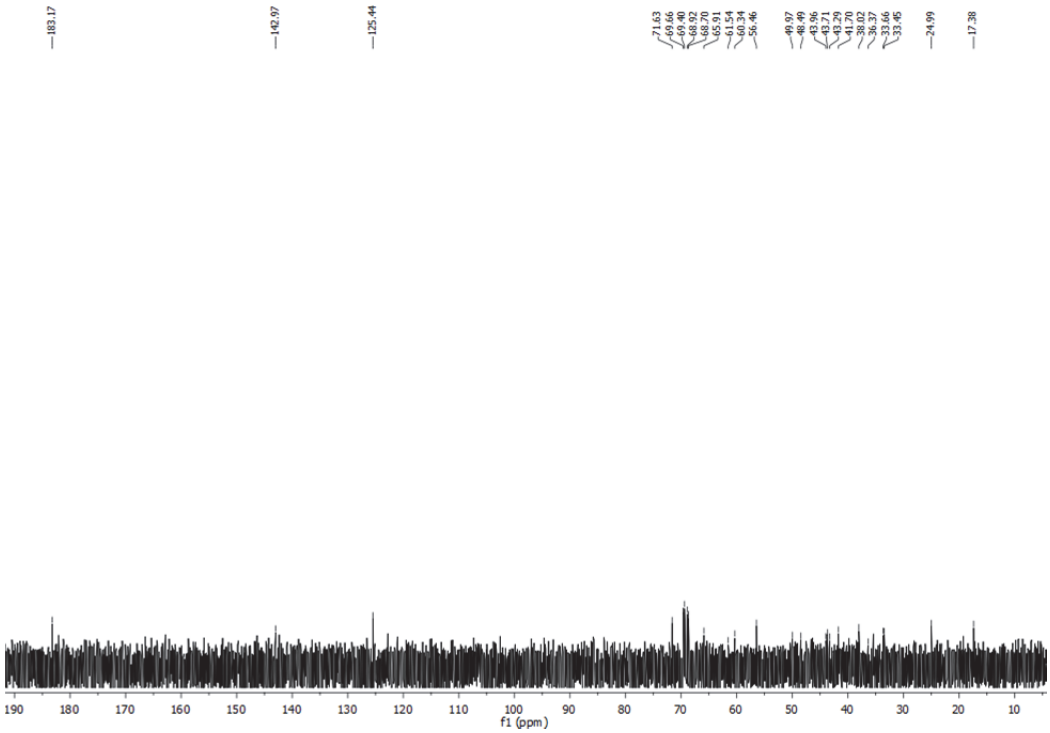

C- LC-MS of LA-EG$_4$-OH

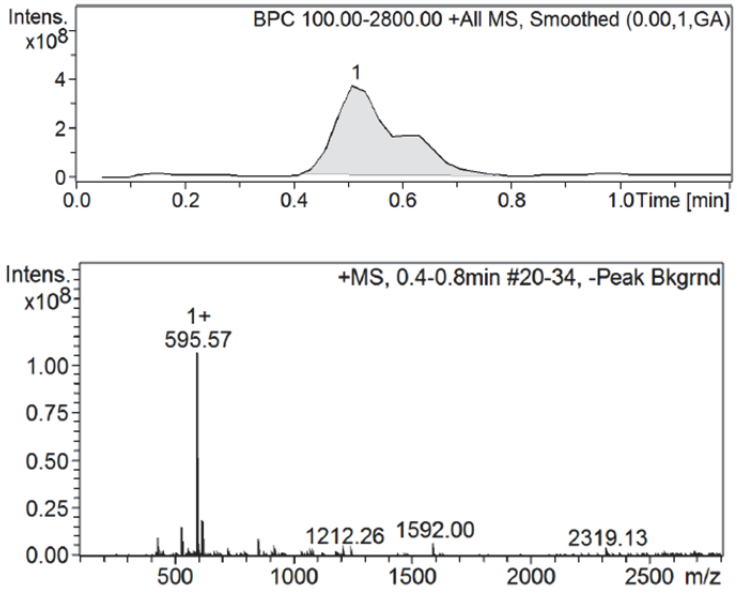

Figure 2.4.9. Spectral characterisation for final product of synthesis **LA-EG$_4$-OH (15)** showing **(A)** ^{1}H-NMR spectrum **(B)** ^{13}C-NMR spectrum and **(C)** LC-MS analysis (chromatogram and molecular ion peaks).

2.5. Gold Nanoparticle Synthesis

Firstly, the cleanliness of all glassware and stirrer bars used in the GNP synthesis is critical to producing high-quality GNPs and preventing aggregation. Therefore, aqua regia, a mixture of hydrochloric acid and nitric acid solution, was used to clean the glassware and remove trace amounts of organic compounds from the equipment. This solution was prepared by mixing concentrated hydrochloric acid and nitric acid with a volume ratio of 3:1. All glassware and stirrer bars were immersed in aqua regia and soaked for 24 hrs. The next day they were rinsed thoroughly with ultrapure water at least ten times. The used aqua regia solution was neutralized with sodium bicarbonate and then disposed of with copious amounts of water via the drain. As it is extremely corrosive, oxidizer, and explosive, and also dissolving organic compounds in aqua regia releases toxic gases, all procedure was, therefore, conducted in a fume hood with the sash down. When handling it, lab safety glasses, visor, lab coat, and nitrile gloves were worn.

2.5.1. Synthesis of 1.3 nm GNCs (Gold Nanoclusters)

The synthesis of 1.3 nm GNCs in the presence of LA-PEG_{750}-OMe ligand was performed based on the method reported by Aldeek *et al.*[28] GNCs synthesis was carried out in aqueous solution using three starting materials (using a 1:1:10 molar ratio of $HAuCl_4$:LA-PEG_{750}-OCH_3: NaOH) under stirring in an ice batch and the reduction was started by the addition of $NaBH_4$. In this reaction, di-thiol based LA-PEG_{750}-OCH_3 ligand was used to enhance the colloidal stability of GNCs, and NaOH was required to control the reduction process as the pH provides the reduction slower which is useful to make clusters and reduces the hydrolytic rate of $NaBH_4$. In the synthesis, the ligand LA-PEG_{750}-OCH_3 (100 mM, 250 µL) was first dissolved in 50 mL pure water containing 5 mM NaOH (125 µL from 2 M stock solution) and the mixture was stirred at RT for 5 mins. $HAuCl_4.3H_2O$ (25 mM, 1 mL) (ratio of Au: Ligand = 1:1) was then added to the reaction, followed by further stirring of the mixture at RT for 10 mins. $NaBH_4$ (50 mM, 4 mL) was directly added and the reaction was then stirred overnight in an ice-batch. The next day, the reaction mixture was transferred to a 10 K MWCO centrifugal filter and centrifuged three times at 4 000 rpm for 20 mins to remove free LA-PEG_{750}-OCH_3 ligands from the mixture. Then, purified LA-PEG_{750}-OCH_3-capped GNCs were stored at 4 °C until further use. The resulting GNCs were then characterised by DLS, UV-vis, and TEM imaging to identify their structural and physical properties as shown in **Figure 2.5.1.**

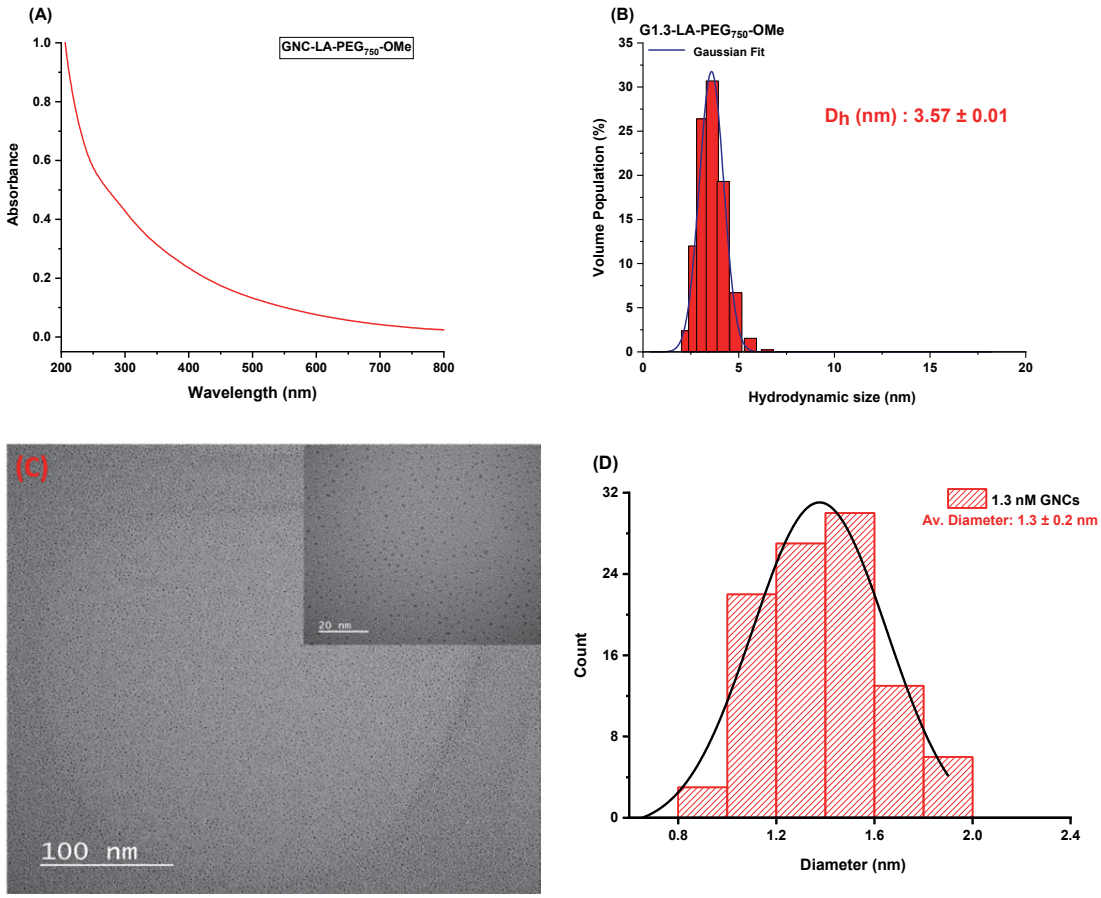

Figure 2.5.1. GNC-LA-PEG_{750}-OCH_3 characterisation results. (A) UV-vis spectra of GNC-LA-PEG_{750}-OCH_3, (B) D_h distribution of GNC-LA-PEG_{750}-OCH_3. It was fitted by Gaussian function and the data were shown in volume population, (C) Typical TEM images of GNC-LA-PEG_{750}-OCH_3 dispersed in pure water. Its higher magnification image is shown in the inset of the image, (D) TEM histogram of GNC-LA-PEG_{750}-OCH_3. The black curve shows the Gaussian fit of the histogram.

Their UV-vis spectra did not exhibit a SPR peak at 590 nm, indicating that clusters had smaller size than 2 nm and their fluorescence quenching mechanisms can be different from bigger GNPs. A D_h size distribution peaking for GNC-LA-PEG_{750}-OCH_3 was observed at 3.57 ± 0.01 nm with a PdI of 0.16, which confirmed that they were highly uniform and the size of GNCs was less than 2 nm when considering the length of LA-PEG_{750}-OCH_3 ligand. Finally, the core size and morphology of GNCs were verified by TEM images and they had also an average size of *ca.* 1.3 ± 0.2 nm.

2.5.1.1. Molecular Weight Calculation of GNCs

The molecular weight of GNCs cannot be calculated according to the Beer-Lambert formula since their UV-vis spectra do not display an absorption peak. Therefore, TEM images and statistics were used to calculate the estimated molar concentration of GNCs and make them into a solution that is known their weight concentrations. The

average diameter size of prepared GNCs calculated from 100 particles was 1.38 nm with a standard deviation of ± 0.27 nm. As can be seen from the TEM images, it is clear that GNCs are pretty much spherical in shape. Since the estimated size of a cluster is a sphere with the diameter of 1.38 nm, its volume and surface area were calculated using equations below:

$$V = \frac{4}{3}\pi \left({}^{D}/_{2}\right)^{3} = 1.38\, nm^{3}$$

$$Surface\ Area = \pi D^{2} = \pi\,(1.38)^{2} = 5.98\, nm^{2}$$

Gold crystallizes in a face-centered cubic structure. As the number of gold atoms per unit cell is 4 and the unit cell length for gold is 0.408 nm,[29] the total number of gold atoms is:

$$Number\ of\ gold\ atoms = \frac{4 \times Diameter}{(a)^{3}} = \frac{4 \times 1.38}{(0.408)^{3}} = 81.3$$

As each thiol occupies 0.214 nm^2 surface area,[30] the number of LA-PEG$_{750}$-OCH$_3$ ligand on each GNC figures out as:

$$Number\ of\ ligand\ on\ AuNC\ surface = \frac{Surface\ area}{(0.214\, nm \times 2)} = \frac{5.98\, nm^{2}}{0.428\, nm^{2}} = 14$$

Since the molecular weight of LA-PEG$_{750}$-OMe is 938 gmol^{-1} and the molar mass of gold is 197 gmol^{-1}, average GNCs molecular weight was calculated using equation below.

$$MW\ of\ GNCs = 81.3 \times 197 + 14 \times 938 = 29\,100\, gmol^{-1}$$

2.5.2. Synthesis of 13 nm GNPs

The protocols applied for the synthesis of 13 and 27 nm GNPs were taken and adapted from the published method of Ji et al.[31]

Freshly prepared aqueous solution of gold (III) chloride trihydrate (1 mM, 400 mL) was placed in a 500 mL three-necked round-bottomed flask and the solution was then heated to reflux in a 130 °C oil bath under stirring. When the solution began to reflux, trisodium citrate solution (38 mM, 40 mL) was then quickly added. The solution colour turned from yellow to wine red in ~1 min, indicating the formation of GNPs. The

reaction was further refluxed under magnetic stirring for another 1 h to ensure the reaction was complete. The resulting solution was removed from the oil bath and was allowed to cool down to RT naturally under stirring. The resulting 13 nm GNP stock was then transferred to a clean glass container and stored at RT till use. The resulting 13 nm GNPs were then characterised by DLS, UV-vis, and TEM imaging as shown in **Figure 2.5.2**.

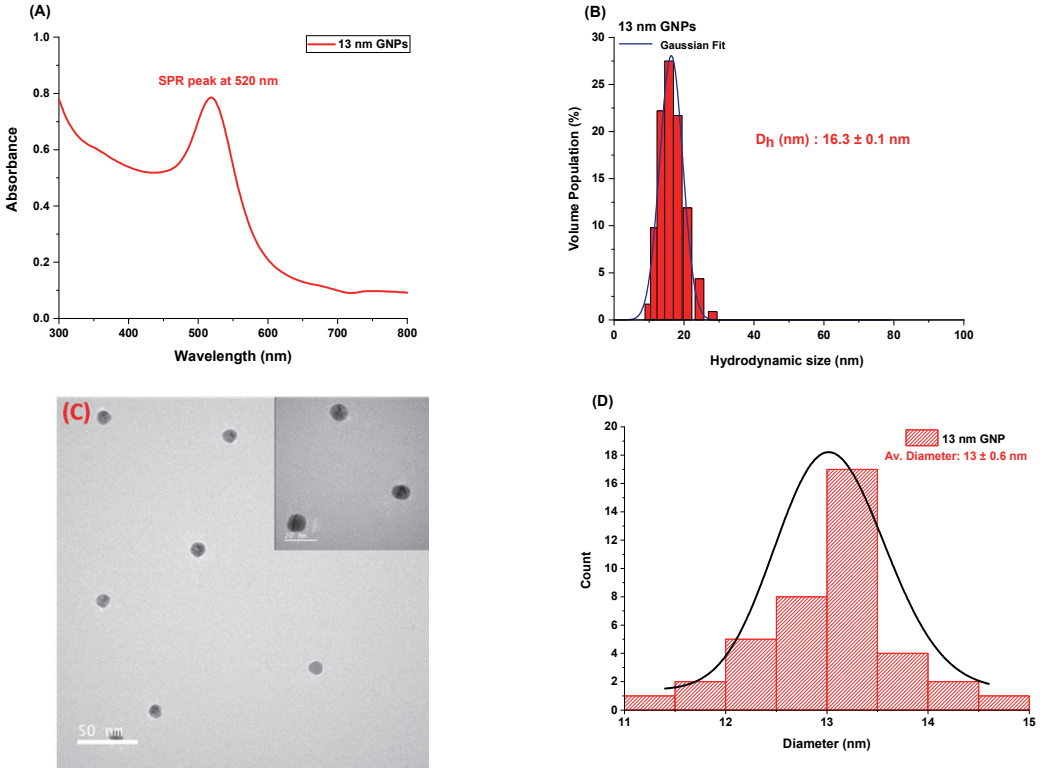

Figure 2.5.2. Characterisation results of G13. (A) UV-vis absorbance spectrum of G13 at 520 nm, (B) D_h size distribution of ~16 nm of G13. It was fitted by Gaussian function and the data were shown in volume population, (C) Typical TEM images of G13. Its higher magnification image is shown in the inset of the image, (D) TEM histogram of G13, and the black curve shows the Gaussian fit of the histogram.

Their UV-vis characterisation exhibited a single and strong plasmonic absorption at 520 nm as expected, showing the formation of non-aggregated GNPs. The obtained D_h value at 16.3 ± 0.1 nm with a PdI of 0.22 for 13 nm GNPs verified that they were uniform and aggregation-free GNPs. Their core size and morphology were determined by TEM imaging, and their average sizes were calculated from TEM images using ImageJ Analysis Software. They were of spherical shape and had an average size of 13 ± 0.6 nm, with a large monodispersity.

2.5.3. Synthesis of 27 nm GNPs

Freshly prepared aqueous solution of gold (III) chloride trihydrate (0.25 mM, 400 mL) was placed in a 500 mL two-necked round-bottomed flask and NaOH (1 mM, 50 mL) was then added directly into the solution. The mixture was stirred for 30 mins and then heated to reflux in a 130 °C oil bath under magnetic stirring. After the solution was started to reflux, trisodium citrate solution (166 mM, 6 mL) was then quickly added. The solution colour changed from yellow to light red in 15 mins. After adding trisodium citrate, the reaction was refluxed for another 1 h to complete the synthesis. The resulting solution was then taken out of the oil bath, and kept stirring for 1 hr till it was cooled down to RT. This produced 27 nm GNP stock which was then transferred to a clean glass container and stored at RT till use.

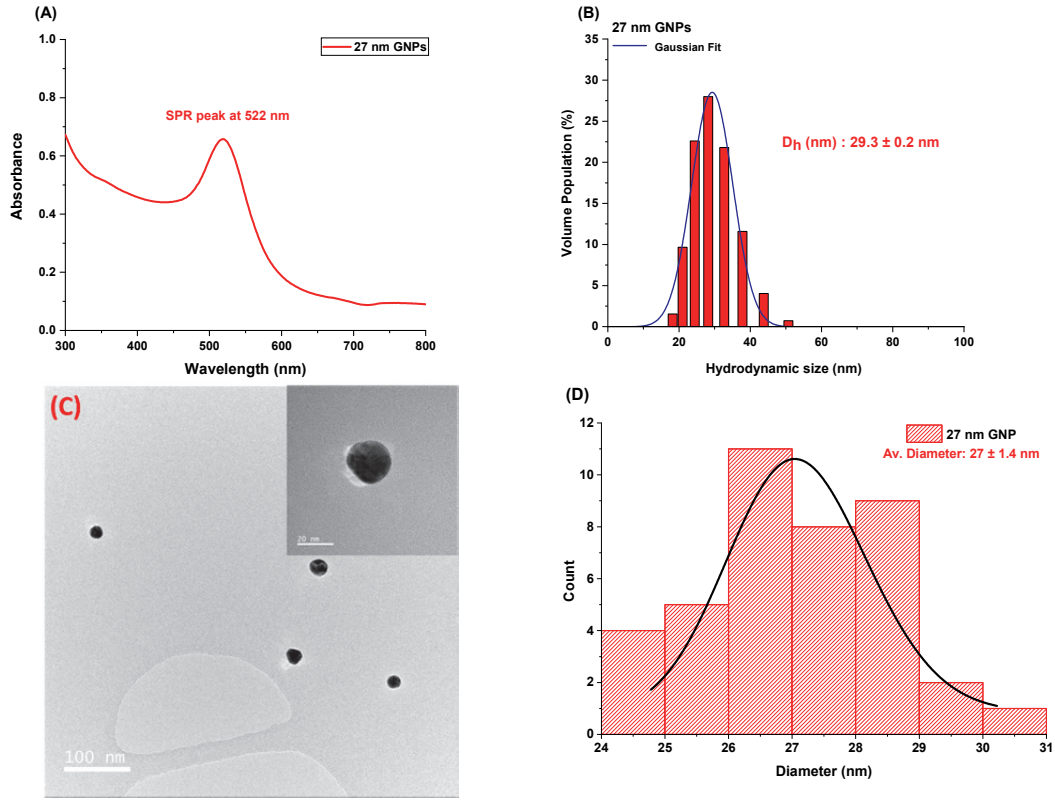

Figure 2.5.3. Characterisation results of G27. (A) UV-vis absorbance spectrum of G27 at 522 nm, (B) D_h size distribution of ~29 nm of G27. It was fitted by Gaussian function and the data were shown in volume population, (C) Typical TEM images of G27. Its higher magnification image is shown in the inset of the image, (D) TEM histogram of G27, the black curve shows the Gaussian fit of the histogram.

The resulting 27 nm GNPs were then characterised by DLS, UV-vis, and TEM imaging as shown in **Figure 2.5.3**. Their UV-vis characterisation showed a single absorption peak at 522 nm. With increasing GNP core size, their absorption peak red-shifts to a longer wavelength as expected. They also displayed only a single distribution with a D_h of 29.3

± 0.2 nm with a PdI of 0.21, confirming that they were uniform and aggregation-free GNPs. Their TEM images demonstrate the presence of spherical dark-coloured dots of GNPs in a mono-dispersion state with an average diameter of 27 ± 1.4 nm.

2.6. Preparation of GNP-conjugates

Prior to cap exchange reactions with LA-PEG based ligands, the disulphide bond in LA anchoring group was reduced to dihydrolipoic acid using Tris(2-carboxyethyl)phosphine hydrochloride, TCEP.HCl, to facilitate their binding to GNP surface. Therefore, TCEP.HCl was added to the LA-PEG based ligands at a ligand: TCEP molar ratio of 1:1.2 in H_2O and then the ligand-TCEP mixture was kept at RT for 30 mins to obtain the reduced DHLA-PEG ligands. An increase of molecular weight by the addition of two protons was verified by LC-MS. This reduction step was done only for LA-PEG based ligands, and not for LA-EG_n-glycan ligands with shorter EG chains because we had found latter that these LA-based ligand could directly self-assemble onto GNP surface efficiently without reduction.

The conjugations of the DH/LA-based functional ligands onto GNPs were successfully performed via ligand exchange reactions, as shown in **Scheme 2.6.1**. Regarding the cap-exchange for 5 nm GNPs, commercial available 5 nm GNPs (6 mL, 91 nM) suspended in citrate solution were concentrated to 250 µL using a 30 K MWCO spin column and washed with H_2O (3 x 250 µL) to remove any impurities. They were then directly combined with the ligands at a molar ratio of GNP: Ligand = 1: 1 000. The mixture was left stirring at RT in darkness overnight. Following ligand exchange, the resulting mixture was transferred to a 30 K MWCO centrifugal filter and centrifuged at 4 000 rpm for 20 mins, and residues washed with H_2O (3 x 250 µL) to remove any unbound free ligands. The filtrate and washing through liquids were collected and combined to determine the unbound free ligands using phenol-sulphuric acid method to determine the glycan valency.

For conjugation of 13 and 27 nm GNPs, their suspensions in citrate solutions were directly combined with the required LA-ligands at a GNP:ligand molar ratio of 1:3 000 for 13 nm GNP and 1:10 000 for 27 nm GNPs, and the resulting solutions were stirred at RT in darkness overnight. After the ligand exchange reactions, the resulting mixtures

were divided 500 µL portions into eppendorf tubes, and centrifuged at 17 000 x g for 30 mins for 13 nm GNP-conjugates or 6 000 x g for 15 mins for 27 nm GNP-conjugates to remove any unbound free ligands. After removal of supernatant, the GNP residues were washed with pure water (3 x 500 µL) followed by centrifugation three times to remove any unbound free ligands. Particularly for 27 nm GNPs, the eppendorf tubes were pre-washed with 0.025% Tween-20 before being used for GNP-conjugate purification to prevent the GNPs from sticking to the eppendorf walls.

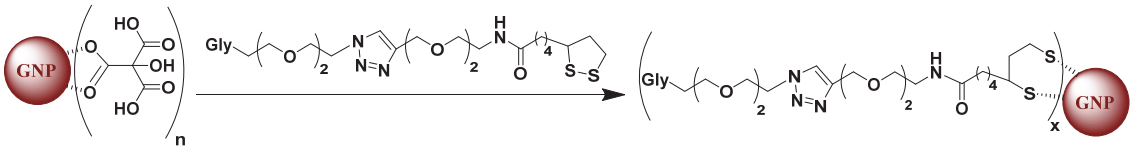

Scheme 2.6.1. A schematic representation of the ligand exchange reaction between GNPs and the multifunctional glycan ligands.

Their concentrations were calculated using the Beer-Lambert equation below from their absorbance spectra at ~520 nm.

$$A = \varepsilon . l . c$$

Where A is the absorbance, ε is the molar extinction coefficient for gold nanoparticles, *l* is the path length, and c is the concentration of GNP-conjugates. The extinction coefficients of GNPs were calculated using the data of Figure B showing the plots of extinction coefficient against the GNP size in diameter. The molar extinction coefficients of 5, 13, and 27 nm GNPs were used the calculation of their concentrations were 1.10 x 10^7 $M^{-1}cm^{-1}$, 2.32 x 10^8 $M^{-1}cm^{-1}$, and 2.39 x 10^9 $M^{-1}cm^{-1}$, respectively.

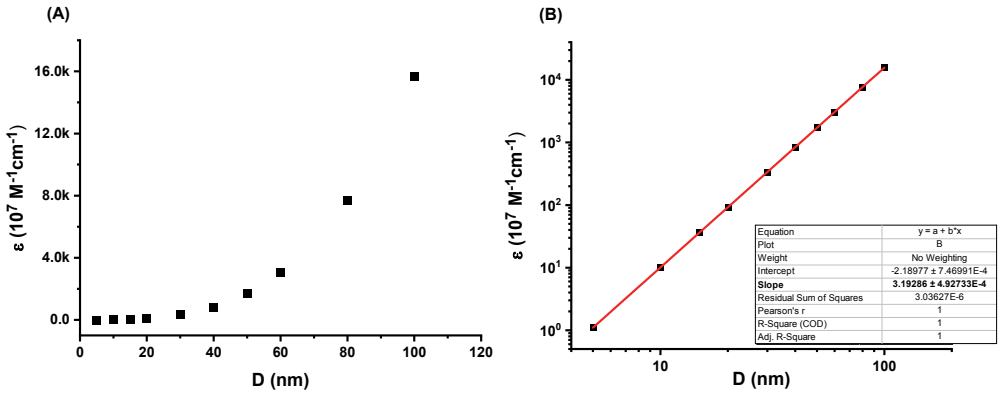

Figure 2.6.1. Plots of the GNP absorption coefficients (Ɛ) versus the GNP diameters with different sizes. The extinction coefficients of GNPs were obtained from the Sigma-Aldrich website.[32] (A) A linear-linear plot. (B) A $\log_{10}$-$\log_{10}$ plot reveals a good linear relationship (R^2 = 1) with a slope of 3.19, indicating that Ɛ increases linearly with the cubic diameter of GNPs ($D^{3.19}$). The extinction coefficients of GNPs scale linearly with roughly to their volumes.

2.6.1. Characterisation of GNP-conjugates

All GNP-conjugates were highly stable and did not exhibit any change in physical appearance or precipitation after more than one year of storage at 4 ˚C. After performing ligand exchange reactions, the characterisation of the synthesised GNP-conjugates was done with the salt-stability test, DLS and UV-vis. Since GNPs have strong binding affinities to thiol-containing ligands, citrate ligands on GNPs can be readily displaced by these ligands that give functionality to GNPs because of the weak adsorption of citrate ligands. After the ligand exchange reaction, the stability of GNP-conjugates can be easily and quickly checked by the addition of excess salt to the solutions. In the presence of high salt concentrations, the surface charge of GNPs without surface modification becomes neutral, which leads to aggregation by decreasing in the inter-particle distance. As a result of salt-induced aggregation, particles tend to sediment to the bottom and then the solution colour changes from red to purple-violet. This phenomenon is not seen for stable GNPs with the effective surface functionalisation.

2.6.1.1. Characterisation of G5 coated with PEG-based ligands

After ligand exchange reactions, their colloidal stabilities were checked in a buffer containing up to 250 mM salt and G5-conjugates did not form aggregations, indicating the successful surface coating of GNPs. Upon conjugation with multifunctional ligands, D_hs of 5 nm GNPs become slightly larger as expected, which could be considered as an evidence of successful functionalisation. Hydrodynamic size histograms of G5 coated with PEGylated ligands and EG_2-DiMan diluted with LA-ZW ligands are given in **Figure 2.6.2**. A summary of the resulting hydrodynamic sizes for G5-conjugates after ligand exchange reactions are given in **Table 2.6.1** below. The obtained D_h values matched well with the G5 core size and the extended length of multifunctional ligands and the corresponding UV-vis data, as shown in **Figure 2.6.3**, also showed no sign of a red-shift, suggesting the formation of robust, uniform and aggregation-free G5-conjugates.

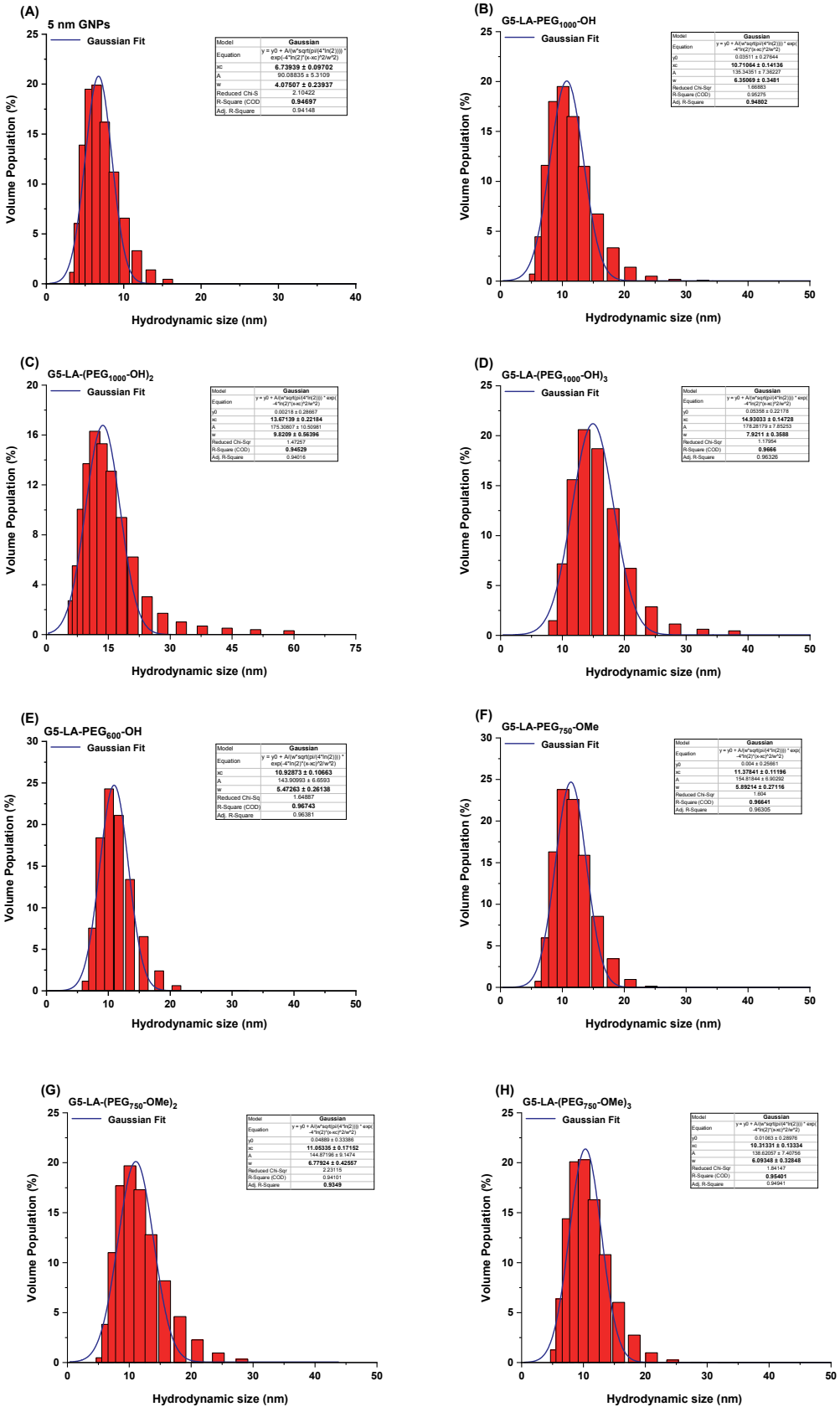

Figure 2.6.2. Hydrodynamic size histograms for (A) 5 nm GNPs; (B) G5-LA-PEG_{1000}-OH; (C) G5-LA-$(PEG_{1000}\text{-OH})_2$; (D) G5-LA-$(PEG_{1000}\text{-OH})_3$; (E) G5-LA-PEG_{600}-OH; (F) G5-LA-PEG_{750}-OMe; (G) G5-LA-$(PEG_{750}\text{-OMe})_2$; (H) G5-LA-$(PEG_{750}\text{-OMe})_3$. They were fitted by Gaussian function with fitting parameters shown in each graph. Data were shown in volume population.

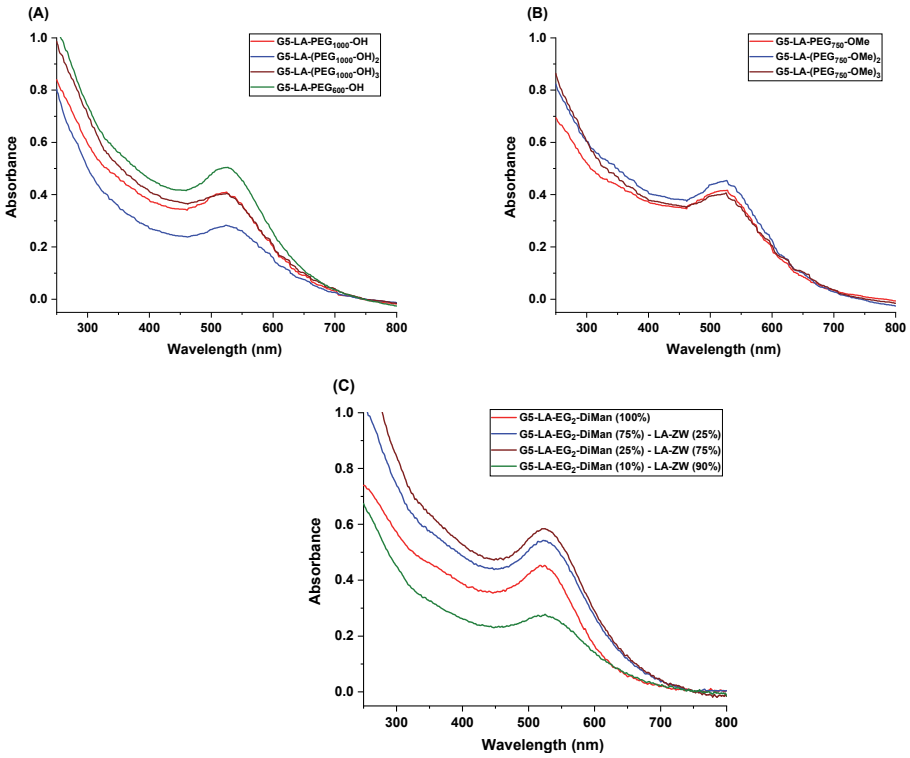

Figure 2.6.3. UV-vis spectra for (A) G5-LA-PEG_{1000}-OH, G5-LA-$(PEG_{1000}\text{-OH})_2$, G5-LA-$(PEG_{1000}\text{-OH})_3$, G5-LA-PEG_{600}-OH; (B) G5-LA-PEG_{750}-OMe, G5-LA-$(PEG_{750}\text{-OMe})_2$, G5-LA-$(PEG_{750}\text{-OMe})_3$; (C) G5-LA-EG_2-DiMan (100%), G5-LA-EG_2-DiMan (75%) - LA-ZW (25%), G5-LA-EG_2-DiMan (25%) - LA-ZW (75%), G5-LA-EG_2-DiMan (10%) - LA-ZW (90%).

Table 2.6.1. Summary of the D_hs of the 5 nm GNPs before and after ligand exchange as measured by DLS.

G5-PEG/EG_2-DiMan conjugates	Gaussian Fitting Parameters			
	Hydrodynamic size (D_h /nm)	FWHM (nm)	PdI	R^2
5 nm GNPs	6.7 ± 0.1	4.1 ± 0.2	0.37	0.946
G5-LA-PEG_{1000}-OH	10.7 ± 0.1	6.3 ± 0.3	0.34	0.952
G5-LA-$(PEG_{1000}\text{-OH})_2$	13.6 ± 0.2	9.8 ± 0.5	0.51	0.945
G5-LA-$(PEG_{1000}\text{-OH})_3$	14.9 ± 0.1	7.9 ± 0.3	0.28	0.966
G5-LA-PEG_{600}-OH	10.9 ± 0.1	5.4 ± 0.2	0.24	0.967
G5-LA-PEG_{750}-OMe	11.3 ± 0.1	5.8 ± 0.2	0.26	0.966
G5-LA-$(PEG_{750}\text{-OMe})_2$	11.1 ± 0.1	6.7 ± 0.4	0.36	0.941
G5-LA-$(PEG_{750}\text{-OMe})_3$	10.3 ± 0.1	6.1 ± 0.3	0.35	0.954
G5-LA-EG_2-DiMan (100%)	11.5 ± 0.2	8.1 ± 0.5	0.47	0.941
G5-LA-EG_2-DiMan (75%) – LA-ZW (25%)	10.4 ± 0.2	6.8 ± 0.5	0.42	0.922
G5-LA-EG_2-DiMan (25%) – LA-ZW (75%)	10.1 ± 0.1	6.1 ± 0.4	0.36	0.923
G5-LA-EG_2-DiMan (10%) – LA-ZW (90%)	17.5 ± 0.2	10.5 ± 0.6	0.36	0.941

2.6.1.2. Characterisation of G5-glycans

The colloidal stabilities of G5-glycans were checked by the addition of salt in the range from 12.5 mM to 250 mM, and no aggregation was observed in their stock solutions, confirming that their ligand exchange reactions were completed and the surfaces of 5 nm GNPs were effectively functionalised. Also, their hydrodynamic size distributions given in **Figure 2.6.4** showed that G5-glycans displayed a single D_h species of ~11 nm with a narrow distribution. When considered the D_h of 5 nm GNPs without surface capping ligands is around ~7 nm, their D_h values agree with the GNP core size as well as the length of LA-$EG_{2/4}$-glycans and LA-$EG_{2/4}$-OH ligands, suggesting that the formation of stable, robust, and uniform G5-glycan conjugates. As shown in **Figure 2.6.4**, their UV-vis spectra were recorded over a range of 300-900 nm and no significant red-shifts or broadening of the SPR peaks were observed, confirming the successful conjugations and that there was no aggregation in G5-glycan stock solution.

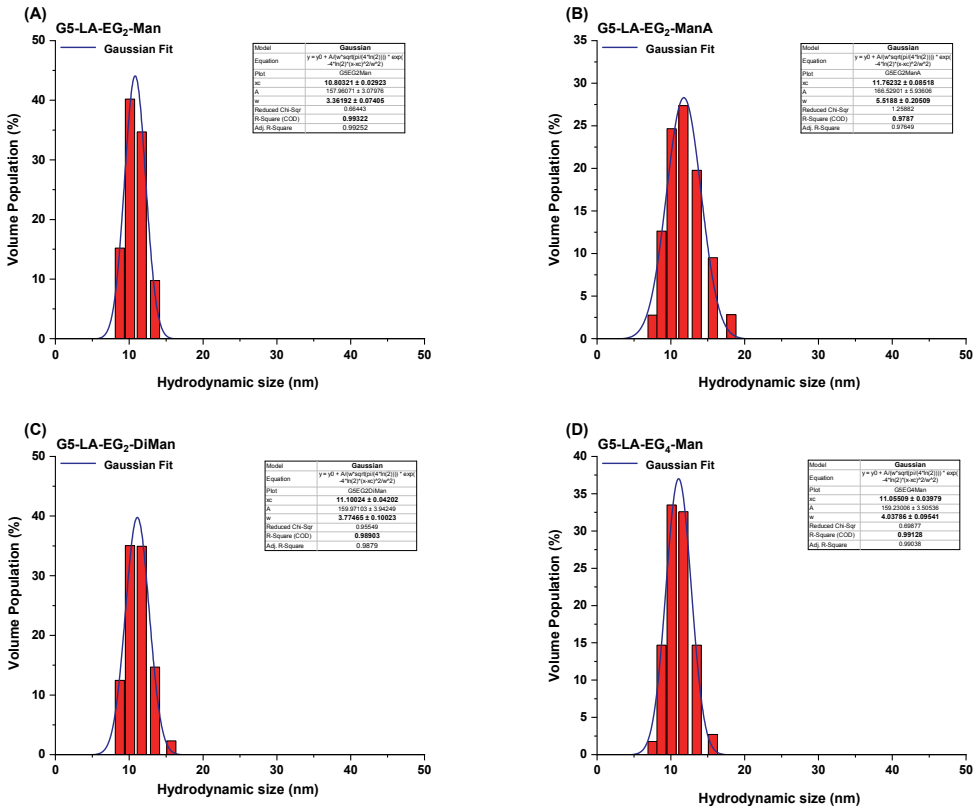

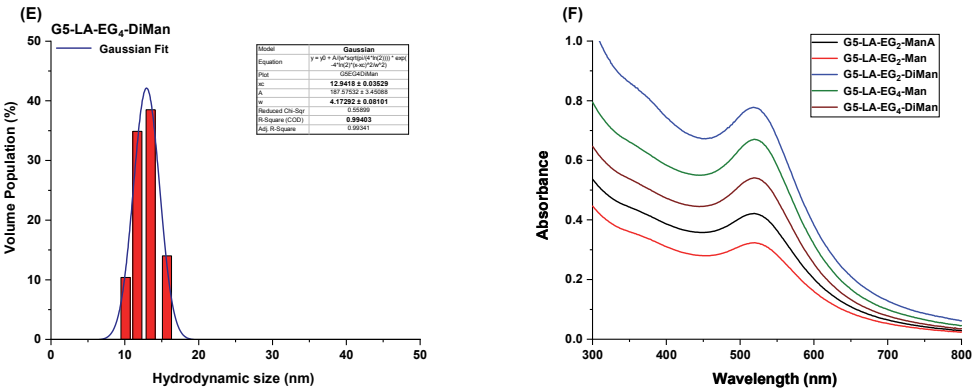

Figure 2.6.4. Hydrodynamic size histograms for (A) G5-LA-EG_2-Man; (B) G5-LA-EG_2-ManA; (C) G5-LA-EG_2-DiMan; (D) G5-LA-EG_4-Man; (E) G5-LA-EG_4-DiMan. They were fitted by Gaussian function with fitting parameters shown in each graph. Data were shown in volume population. The graph (F) shows all their UV-vis spectra.

Table 2.6.2. Summary of the D_hs of the G5-glycans after ligand exchange as measured by DLS.

G5-glycan conjugates	Gaussian Fitting Parameters			
	Hydrodynamic size (D_h /nm)	FWHM (nm)	PdI	R^2
G5-LA-EG_2-Man	10.8 ± 0.1	3.3 ± 0.1	0.09	0.993
G5-LA-EG_2-ManA	11.7 ± 0.1	5.5 ± 0.1	0.22	0.978
G5-LA-EG_2-DiMan	11.1 ± 0.1	3.7 ± 0.1	0.11	0.989
G5-LA-EG_4-Man	11.0 ± 0.1	4.0 ± 0.1	0.13	0.991
G5-LA-EG_4-DiMan	12.9 ± 0.1	4.1 ± 0.1	0.10	0.994

2.6.1.3. Characterisation of G13-glycans

The colloidal stabilities of all G13-glycan conjugates were monitored in a buffer containing up to 250 mM salt and they also did not form precipitations, indicating that the successful surface functionalisation of 13 nm GNPs. Their hydrodynamic size histograms were shown in **Figure 2.6.5** and **Figure 2.6.6**, and a summary of hydrodynamic sizes for G13-glycan conjugates are given in **Table 2.6.3**. G13 particles with a D_h of 16 nm exhibited a single D_h distribution of ~20 nm after replacing of citrate ligands with glycan ligands on G13 surface. After GNPs have undergone ligand exchange, a small D_h change for GNPs is expected. The observed D_h changes in 13 nm GNPs, along with their colloidal stability in water, indicate that the ligand exchange has been carried out successfully. Also, their UV-vis data given in **Figure 2.6.7** below showed no sign of a significant red-shift, confirming that produced G13-glycans are stable and uniform.

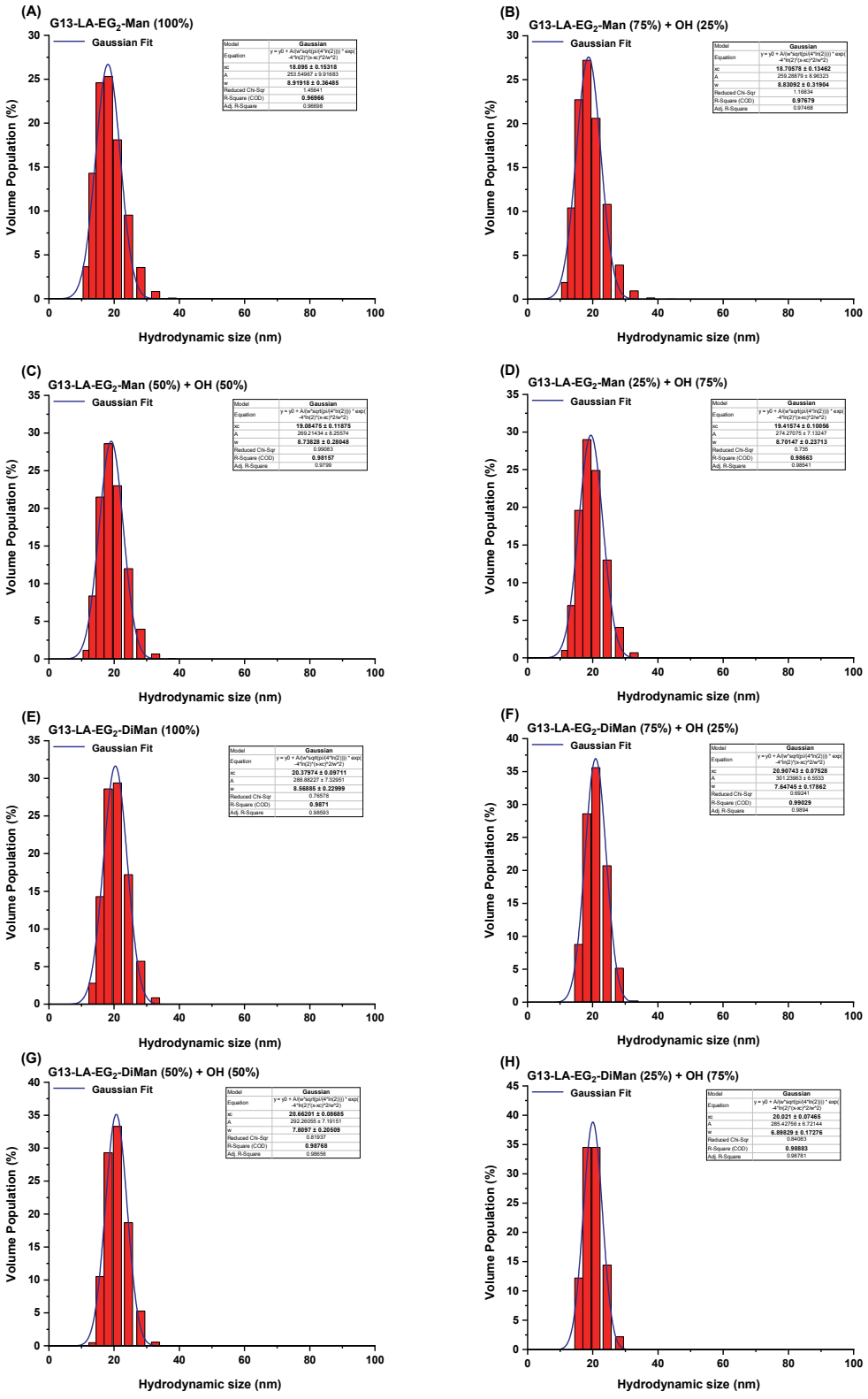

Figure 2.6.5. Hydrodynamic size histograms for (A) G13-LA-EG_2-Man (100%); (B) G13-LA-EG_2-Man (75%); (C) G13-LA-EG_2-Man (50%); (D) G13-LA-EG_2-Man (25%); (E) G13-LA-EG_2-DiMan (100%); (F) G13-LA-EG_2-DiMan (75%); (G) G13-LA-EG_2-DiMan (50%); (H) G13-LA-EG_2-DiMan (25%). They were fitted by Gaussian function with fitting parameters shown in each graph. Data were shown in volume population.

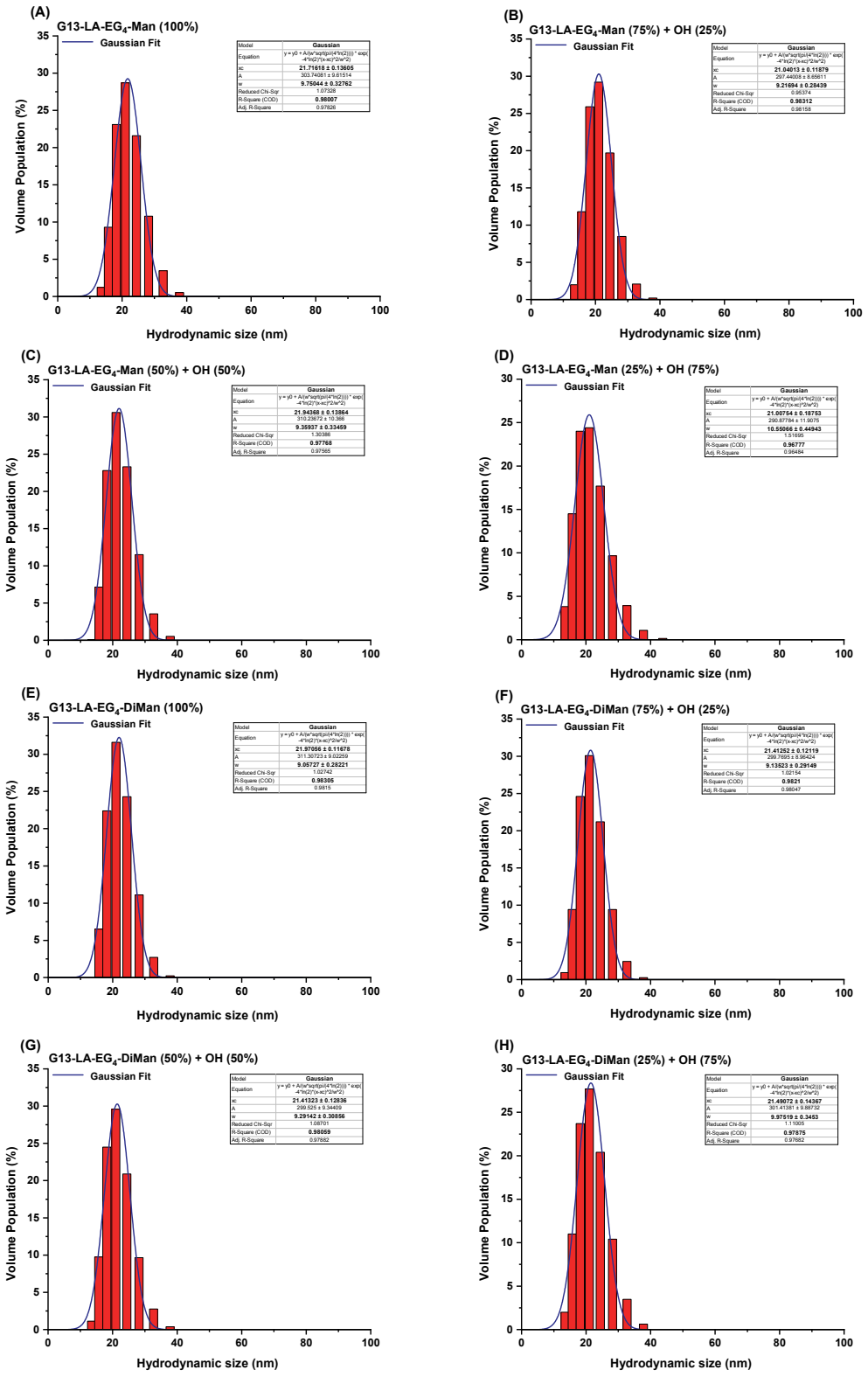

Figure 2.6.6. Hydrodynamic size histograms for (A) G13-LA-EG_4-Man (100%); (B) G13-LA-EG_4-Man (75%); (C) G13-LA-EG_4-Man (50%); (D) G13-LA-EG_4-Man (25%); (E) G13-LA-EG_4-DiMan (100%); (F) G13-LA-EG_4-DiMan (75%); (G) G13-LA-EG_4-DiMan (50%); (H) G13-LA-EG_4-DiMan (25%). They were fitted by Gaussian function with fitting parameters shown in each graph. Data were shown in volume population.

Table 2.6.3. Summary of the D_hs of the G13-glycans after ligand exchange as measured by DLS.

G13-glycan conjugates	Gaussian Fitting Parameters			
	Hydrodynamic size (D_h /nm)	FWHM (nm)	PdI	R^2
G13-LA-EG$_2$-Man (100%)	18.1 ± 0.1	8.9 ± 0.3	0.24	0.969
G13-LA-EG$_2$-Man (75%) + LA-EG$_2$-OH (25%)	18.7 ± 0.1	8.8 ± 0.3	0.22	0.976
G13-LA-EG$_2$-Man (50%) + LA-EG$_2$-OH (50%)	19.0 ± 0.1	8.7 ± 0.2	0.20	0.981
G13-LA-EG$_2$-Man (25%) + LA-EG$_2$-OH (75%)	19.4 ± 0.1	8.7 ± 0.2	0.20	0.986
G13-LA-EG$_2$-DiMan (100%)	20.3 ± 0.1	8.5 ± 0.2	0.17	0.987
G13-LA-EG$_2$-DiMan (75%) + LA-EG$_4$-OH (25%)	20.9 ± 0.1	7.6 ± 0.1	0.13	0.990
G13-LA-EG$_2$-DiMan (50%) + LA-EG$_4$-OH (50%)	20.6 ± 0.1	7.8 ± 0.2	0.14	0.987
G13-LA-EG$_2$-DiMan (25%) + LA-EG$_4$-OH (75%)	20.0 ± 0.1	6.8 ± 0.1	0.11	0.988
G13-LA-EG$_4$-Man (100%)	21.7 ± 0.1	9.7 ± 0.3	0.19	0.980
G13-LA-EG$_4$-Man (75%) + LA-EG$_4$-OH (25%)	21.0 ± 0.1	9.2 ± 0.2	0.19	0.983
G13-LA-EG$_4$-Man (50%) + LA-EG$_4$-OH (50%)	21.9 ± 0.1	9.3 ± 0.3	0.18	0.977
G13-LA-EG$_4$-Man (25%) + LA-EG$_4$-OH (75%)	21.0 ± 0.1	10.5 ± 0.4	0.25	0.967
G13-LA-EG$_4$-DiMan (100%)	21.9 ± 0.1	9.0 ± 0.2	0.16	0.983
G13-LA-EG$_4$-DiMan (75%) + LA-EG$_4$-OH (25%)	21.4 ± 0.1	9.1 ± 0.3	0.18	0.982
G13-LA-EG$_4$-DiMan (50%) + LA-EG$_4$-OH (50%)	21.4 ± 0.1	9.3 ± 0.3	0.18	0.980
G13-LA-EG$_4$-DiMan (25%) + LA-EG$_4$-OH (75%)	21.4 ± 0.1	9.9 ± 0.3	0.21	0.978

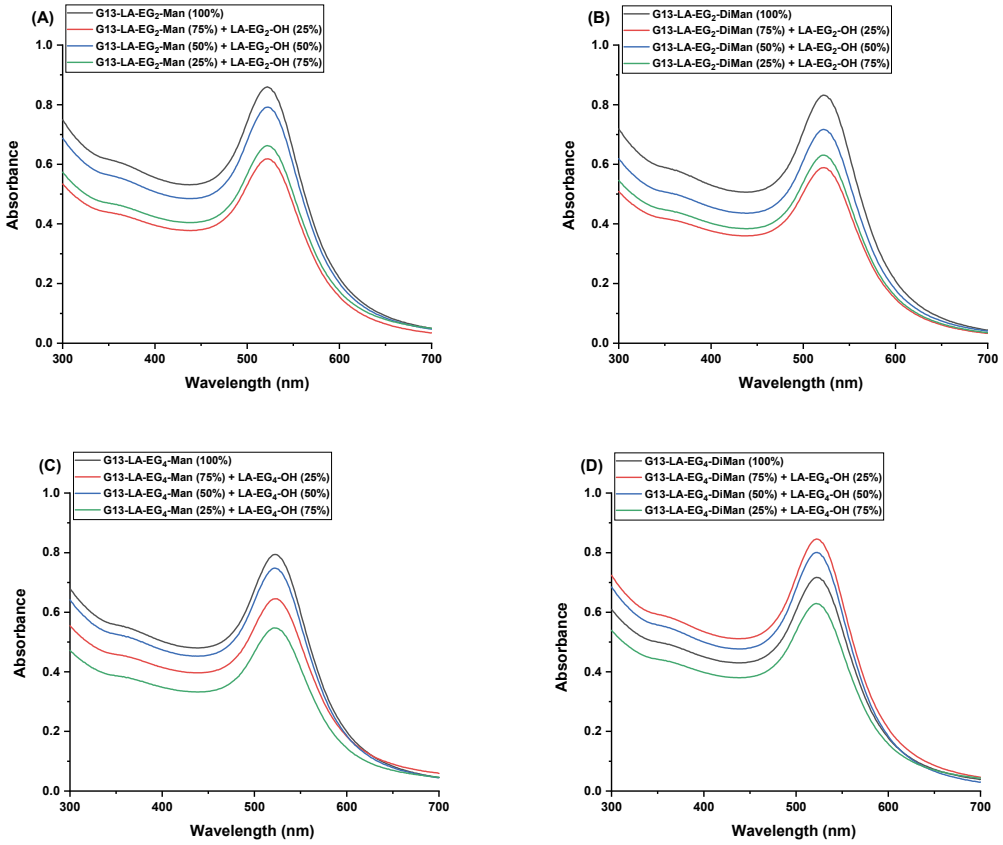

Figure 2.6.7. UV-vis spectra of (A) G13-EG_2-Man conjugates; (B) G13-EG_2-DiMan conjugates; (C) G13-EG_4-Man conjugates; (D) G13-EG_4-DiMan conjugates.

2.6.1.4. Characterisation of G27-glycans

The stability of G27-glycan conjugates were checked by using excess salt in the range up to 250 mM and their stock solutions did not showed any aggregation and color change, suggesting that the surfaces of G27 were covered successfully with the corresponding ligands. Also, hydrodynamic size histograms are shown in **Figure 2.6.8** and **Figure 2.6.9**, and a summary of hydrodynamic sizes for G27-glycan conjugates are given in **Table 2.6.4**. G27 particles with a D_h of ~29 nm exhibited a single D_h distribution of ~32 nm after replacing of citrate ligands with glycan ligands on G27 surface. The obtained D_h values for G27-glycan conjugates were consistent with the G27 core size and the length of glycan ligands. Furthermore, UV-vis data of G27-glycan conjugates given in **Figure 2.6.10** overlaid well with the spectra of non-functionalised G27 with no significant red-shift and broadening of the SPR peaks, confirming successful ligand exchange.

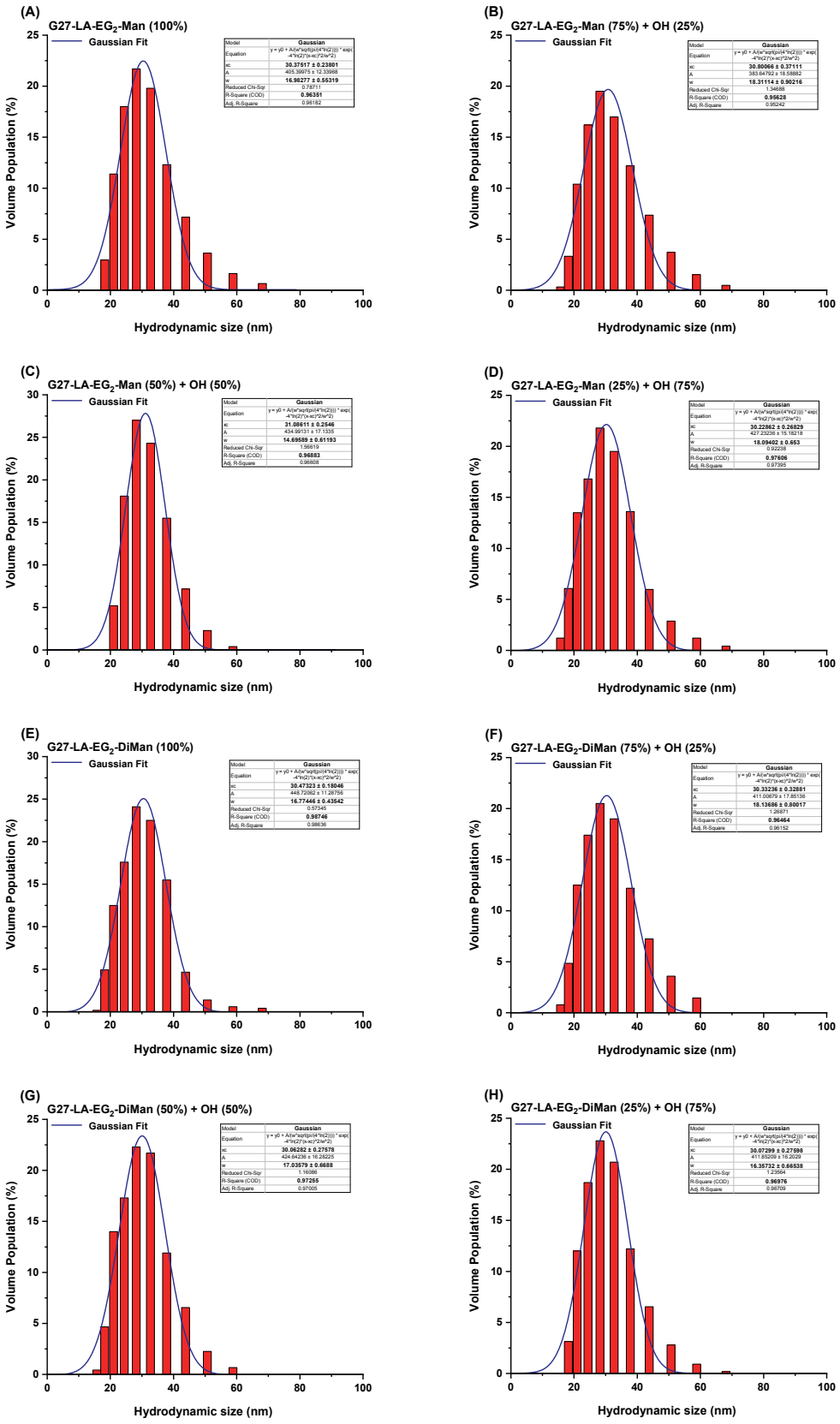

Figure 2.6.8. Hydrodynamic size histograms for (A) G27-LA-EG_2-Man (100%); (B) G27-LA-EG_2-Man (75%); (C) G27-LA-EG_2-Man (50%); (D) G27-LA-EG_2-Man (25%); (E) G27-LA-EG_2-DiMan (100%); (F) G27-LA-EG_2-DiMan (75%); (G) G27-LA-EG_2-DiMan (50%); (H) G27-LA-EG_2-DiMan (25%). They were fitted by Gaussian function with fitting parameters shown in each graph. Data were shown in volume population.

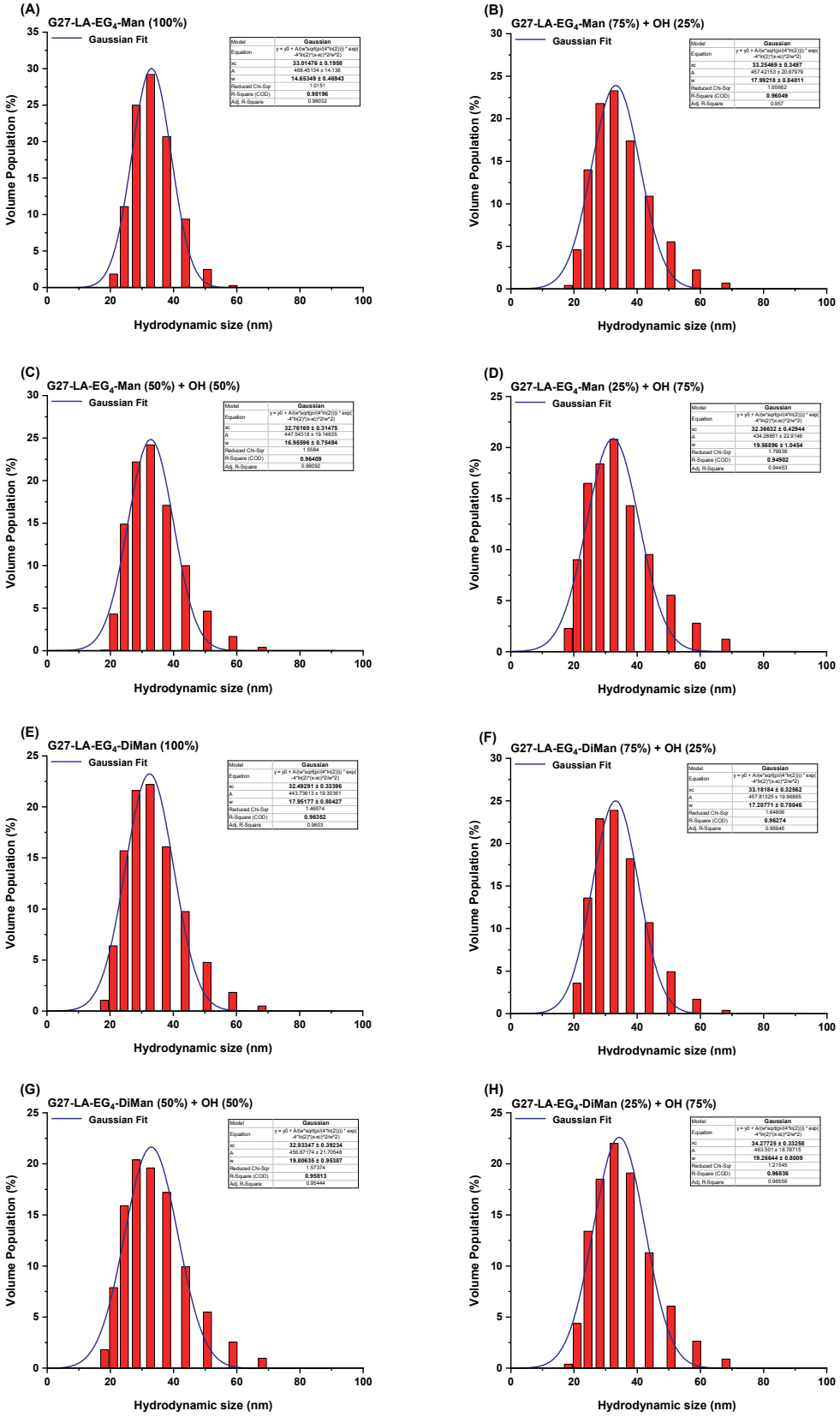

Figure 2.6.9. Hydrodynamic size histograms for (A) G27-LA-EG_2-Man; (B) G27-LA-EG_2-ManA; (C) G27-LA-EG_2-DiMan; (D) G27-LA-EG_4-Man; (E) G27-LA-EG_4-DiMan; (A) G27-LA-EG_2-Man; (B) G27-LA-EG_2-ManA; (C) G27-LA-EG_2-DiMan;. They were fitted by Gaussian function with fitting parameters shown in each graph. Data were shown in volume population.

Table 2.6.4. Summary of the D_hs of the G27-glycans after ligand exchange as measured by DLS.

G27-glycan conjugates	Gaussian Fitting Parameters			
	Hydrodynamic size (D_h /nm)	FWHM (nm)	PdI	R^2
G27-LA-EG$_2$-Man (100%)	30.3 ± 0.2	16.9 ± 0.5	0.31	0.963
G27-LA-EG$_2$-Man (75%) + LA-EG$_2$-OH (25%)	30.8 ± 0.3	18.3 ± 0.9	0.35	0.956
G27-LA-EG$_2$-Man (50%) + LA-EG$_2$-OH (50%)	31.0 ± 0.2	14.7 ± 0.6	0.22	0.968
G27-LA-EG$_2$-Man (25%) + LA-EG$_2$-OH (75%)	30.2 ± 0.2	18.0 ± 0.6	0.35	0.976
G27-LA-EG$_2$-DiMan (100%)	30.4 ± 0.1	16.7 ± 0.4	0.30	0.987
G27-LA-EG$_2$-DiMan (75%) + LA-EG$_4$-OH (25%)	30.3 ± 0.3	18.1 ± 0.8	0.35	0.964
G27-LA-EG$_2$-DiMan (50%) + LA-EG$_4$-OH (50%)	30.0 ± 0.2	17.0 ± 0.6	0.32	0.972
G27-LA-EG$_2$-DiMan (25%) + LA-EG$_4$-OH (75%)	30.0 ± 0.2	16.3 ± 0.6	0.29	0.969
G27-LA-EG$_4$-Man (100%)	33.0 ± 0.2	14.6 ± 0.4	0.19	0.981
G27-LA-EG$_4$-Man (75%) + LA-EG$_4$-OH (25%)	33.2 ± 0.3	17.9 ± 0.8	0.29	0.960
G27-LA-EG$_4$-Man (50%) + LA-EG$_4$-OH (50%)	32.7 ± 0.3	16.9 ± 0.7	0.26	0.964
G27-LA-EG$_4$-Man (25%) + LA-EG$_4$-OH (75%)	32.3 ± 0.4	19.5 ± 1.0	0.36	0.949
G27-LA-EG$_4$-DiMan (100%)	32.5 ± 0.3	17.9 ± 0.8	0.30	0.963
G27-LA-EG$_4$-DiMan (75%) + LA-EG$_4$-OH (25%)	33.1 ± 0.3	17.2 ± 0.7	0.27	0.962
G27-LA-EG$_4$-DiMan (50%) + LA-EG$_4$-OH (50%)	32.9 ± 0.4	19.8 ± 1.0	0.36	0.958
G27-LA-EG$_4$-DiMan (25%) + LA-EG$_4$-OH (75%)	34.2 ± 0.3	19.2 ± 0.8	0.31	0.968

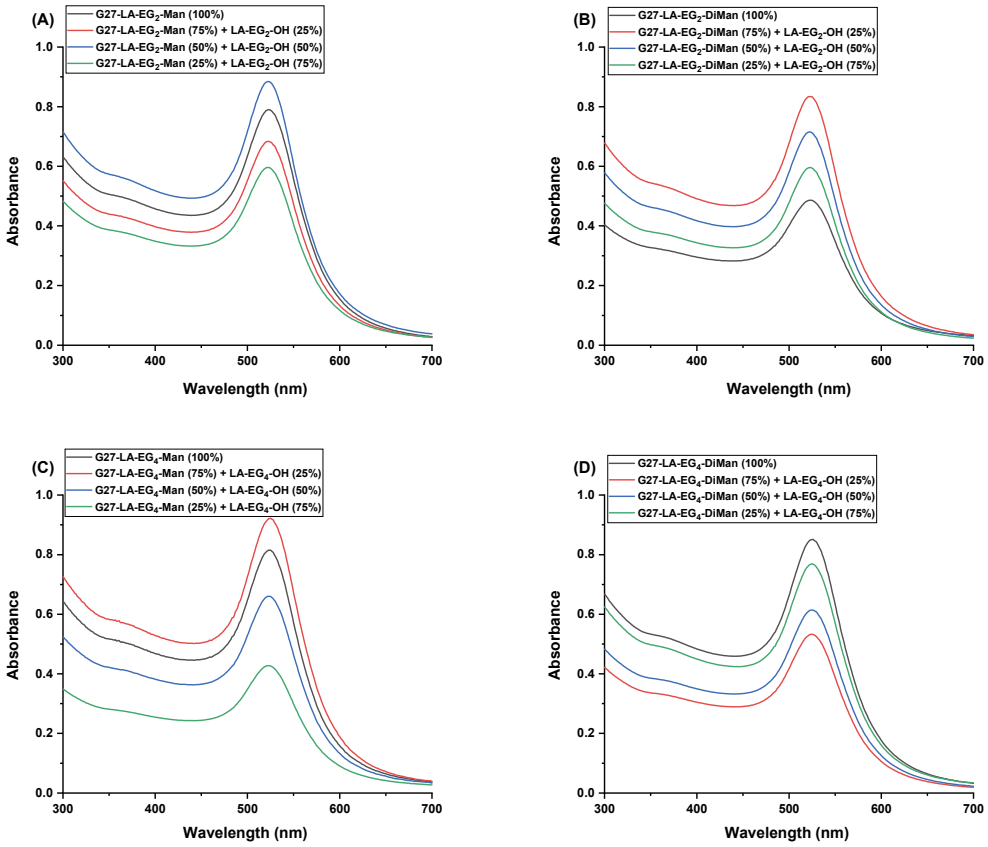

Figure 2.6.10. UV-vis spectra of (A) G27-EG_2-Man conjugates; (B) G27-EG_2-DiMan conjugates; (C) G27-EG_4-Man conjugates; (D) G27-EG_4-DiMan conjugates.

2.7. GNP Surface Glycan Density

The dilution of the surface glycan concentration using LA-$EG_{2/4}$-OH ligands was carried out to further investigate how GNP surface glycan density affect DC-SIGN/R binding. Here, the surface of G13 and G27 coated with LA-$EG_{2/4}$-Man/-DiMan ligands was diluted using LA-$EG_{2/4}$-OH ligands to a surface glycan density of 75%, 50% and 25%. This dilution was performed by the addition of LA-$EG_{2/4}$-OH ligands in the above mentioned percentages as well as LA-$EG_{2/4}$-glycan ligands in ligand exchange reactions. Surface-diluted GNP-glycan conjugates were characterised by salt stability test, DLS, and UV-vis spectra, as shown earlier sections.

After purification by centrifugation, the supernatants were also kept and the amount of ligand in the supernatant will be determined by phenol-sulphuric acid method described by Guo *et al.*[33] so as to confirm the amount of glycan ligands loaded onto GNPs. The calibration curves plotted between the absorbance versus the amount of ligand for LA-Man and LA-DiMan, as given in **Figure 2.7.1**[34] produced by Dr Darshita

Budhadev who is a postdoc within the group, were used to determine the carbohydrate ligand loaded on the GNPs. Unconjugated LA-glycan ligands in supernatants (including washing liquids) were combined, freeze-dried, and then re-dissolved in 1.40 mL pure water. 25 µL of each solution was diluted with water to a final volume of 125 µL. This solution was then mixed with 125 µL of 5% phenol and 625 µL of H_2SO_4, and then allowed to incubate at RT for 30 mins. The absorbance of the solution was recorded at 490 nm and the dilution factors were then corrected to calculate the total amount of unconjugated glycan ligand. The measurements were done in duplicate for each sample and the average number of LA-glycan ligands conjugated to each GNP were given in **Table 2.7.1.**

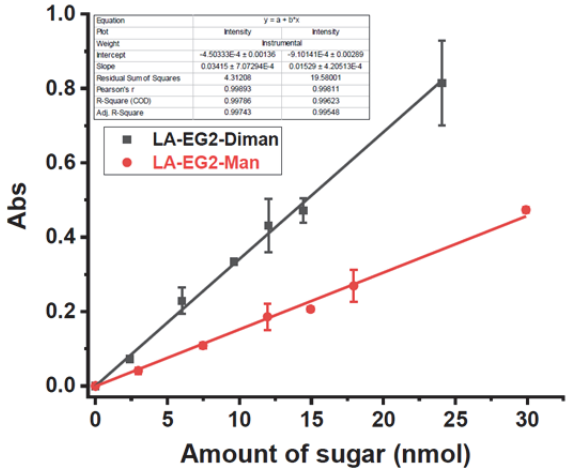

Figure 2.7.1. The calibration curves showing the absorbance *vs.* the ligand amount relationship for LA-Man and LA-DiMan.[34]

Table 2.7.1. Summary of the average number of LA-glycan ligands conjugated to each GNP

GNP-glycan conjugates	Sugar Conjugated per GNP	GNP-glycan conjugates	Sugar Conjugated per GNP
G5-LA-EG_2-Man	560 ± 42	**G13-LA-EG_2-Man (100%)**	1950 ± 127
G5-LA-EG_2-ManA	530 ± 48	**G13-LA-EG_2-Man (75%)**	1560 ± 105
G5-LA-EG_2-DiMan	670 ± 63	**G13-LA-EG_2-Man (50%)**	940 ± 86
G5-LA-EG_4-Man	600 ± 44	**G13-LA-EG_2-Man (25%)**	440 ± 37
G5-LA-EG_4-DiMan	730 ± 52	**G13-LA-EG_2-ManA (100%)**	1800 ± 148
G13-LA-EG_2-DiMan (100%)	2120 ± 178	**G13-LA-EG_4-Man (100%)**	2040 ± 167
G13-LA-EG_2-DiMan (75%)	1620 ± 138	**G13-LA-EG_4-Man (75%)**	1530 ± 114
G13-LA-EG_2-DiMan (50%)	1020 ± 94	**G13-LA-EG_4-Man (50%)**	930 ± 76
G13-LA-EG_2-DiMan (25%)	500 ± 45	**G13-LA-EG_4-Man (25%)**	430 ± 41
G13-LA-EG_4-DiMan (100%)	2200 ± 172	**G27-LA-EG_2-Man (100%)**	5800 ± 432
G13-LA-EG_4-DiMan (75%)	1640 ± 137	**G27-LA-EG_2-Man (75%)**	4550 ± 356
G13-LA-EG_4-DiMan (50%)	1040 ± 88	**G27-LA-EG_2-Man (50%)**	2810 ± 174
G13-LA-EG_4-DiMan (25%)	520 ± 47	**G27-LA-EG_2-Man (25%)**	1560 ± 118
G27-LA-EG_2-DiMan (100%)	5940 ± 484	**G27-LA-EG_4-Man (100%)**	6110 ± 415
G27-LA-EG_2-DiMan (75%)	4570 ± 366	**G27-LA-EG_4-Man (75%)**	4740 ± 308
G27-LA-EG_2-DiMan (50%)	2840 ± 223	**G27-LA-EG_4-Man (50%)**	2940 ± 226
G27-LA-EG_2-DiMan (25%)	1530 ± 116	**G27-LA-EG_4-Man (25%)**	1520 ± 104
G27-LA-EG_4-DiMan (100%)	6290 ± 440		
G27-LA-EG_4-DiMan (75%)	4870 ± 332		
G27-LA-EG_4-DiMan (50%)	3150 ± 247		
G27-LA-EG_4-DiMan (25%)	1540 ± 122		

2.7.1. Calculation of the average inter-glycan distance on the GNP

The average inter-glycan distance (d) of G13/G27-EG_4-DiMan were calculated by using the D_h values and corresponding glycan valencies, based on the method reported by Hill *et al.*[35] For a GNP with a radius of r (r equals half of the hydrodynamic radius: 1/2 D_h of GNP-glycan) and covered with N ligand, the estimation footprint of each ligand (k) onto the GNP surface was calculated by using the following equation).

$$k = \frac{4\pi r^2}{N}$$

Where r is hydrodynamic radius of the GNP-DiMan measured by DLS, where r = 21.9/2 = 10.95 nm for G13-DiMan and 32.4/2 = 16.2 nm for G27-DiMan. The average deflection angle of each ligand on the GNP surface (θ, in degrees) was calculated via the equation below.

$$\theta = \frac{2 \times 180\, x \sqrt{\frac{k}{\pi}}}{r\pi}$$

The estimated θ for G13-DiMan and G27-DiMan (N = 2200 and 6290) were 4.88^{o} and 2.89^{o}, respectively. By using these data, the inter-glycan distance on the GNP surface (X) was then calculated via the following equation and the results were given in **Table 2.7.2** below.

$$X = 2\, r\, \sin\left(\frac{\theta}{2}\right)$$

The average interglycan distances were estimated as ~0.93 and ~0.80 for G13-DiMan and G27-DiMan, respectively. These values matches well within the most of inter-glycan sequon spaces (*e.g.* 0.7–1.3 nm) found on the HIV surface glycoprotein gp120.[36] The good consistency for inter-glycan distances between GNP-glycans and HIV gp120 suggested that G13- and G27-DiMan mimics viral glycoproteins well to probe interactions between DC-SIGN/R and viruses.

Table 2.7.2. Summary of the chemical & physical parameters of the G13/27-EG_4-DiMan conjugates.

GNP-glycan	Glycan valency	D_h (nm)	Glycan footprint on GNP surface (nm^2)	Inter-glycan spacing (d) in nm
G13-EG_4-DiMan	2200 ± 172	21.9 nm	0.684	0.93 nm
G27-EG_4-DiMan	6290 ± 440	32.4 nm	0.524	0.80 nm

2.8. Protein Production and Labelling

In this project, the extracellular segments of DC-SIGN/R were used to investigate their multivalent binding interactions with GNP-conjugates by fluorescence quenching. Therefore, labelling of CRDs with dye molecules at close to the binding site without affecting their glycan binding properties was necessary. Feinberg *et al.*[37] showed that in the CRD crystal structure, the residues Q274 in DC-SIGN and R287 in DC-SIGNR on the protein surface were not involved in carbohydrate binding and thus mutations on such residues should not have an impact on their glycan binding properties. These residues were therefore considered as suitable for site-specific dye labelling. In this regard, a cysteine residue was introduced by mutagenesis using DNA recombinant techniques in the corresponding wild-type sequences via synthetic DNA fragments to replace these residues, as indicated by stars below in **Figure 2.8.1**. The integrity and successful mutation of the cloned fragments were also confirmed by DNA sequencing. These constructed extracellular segments, DC-SIGN Q274C and DC-SIGNR R287C, were then expressed in E. coli, and the bacterial glycerol stocks were prepared for their further use. As described previously,[38] mutagenesis and stock preparation were performed by my supervisor Dr. Yuan Guo. This mutation allows for site-specific labelling of CRDs and the mutant proteins have been shown to fully preserve the glycan binding properties and tetrameric structure of wild-type proteins.[39, 40] Cysteine residues are involved in disulphide bonds, which make contribution to the stabilization of protein tertiary structure. Disulphide bonds are cleaved through the use of β-mercaptoethanol during protein purification and then free thiols are released. As maleimide dyes are highly thiol-reactive compounds at physiological pH (6.5-7.5), free thiol groups can easily react with dye molecules,[41] thus allowing for site-specific dye-labelling of CRDs.

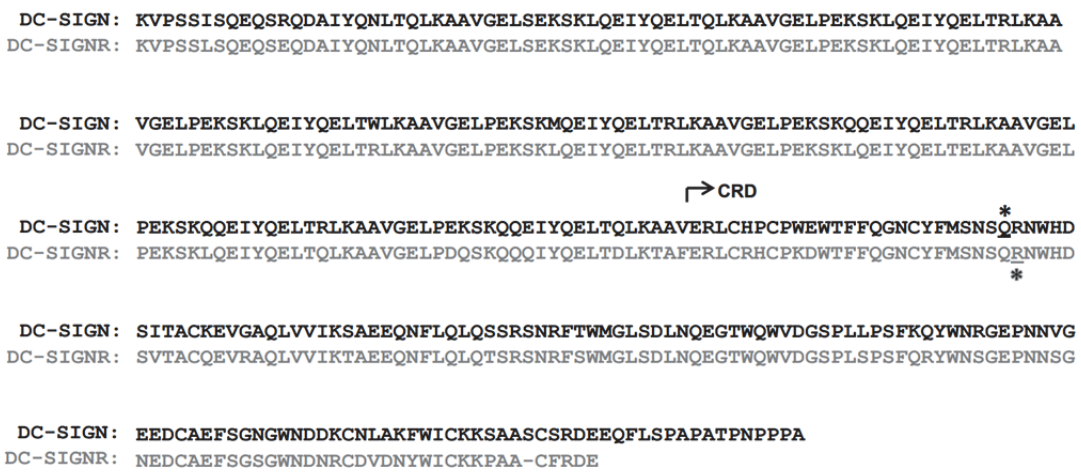

Figure 2.8.1. A schematic showing the sequences of DC-SIGN/R extracellular segments. Cysteine amino acids were introduced for site-specific labelling, indicated by asterisks (*).[38]

2.8.1. Protocol for Protein Purification

Day-1

1 L of sterile Lysogeny Broth (LB) for each four larger flasks and 100 mL of LB for two smaller flasks were prepared, and two smaller ones were then inoculated by adding a solution of Ampicillin to the sterile LB medium. A bacterial culture was prepared by adding a flake of bacterial glycerol stock and was then incubated overnight, no longer than 16 hrs, at 37 ˚C with shaking 200 rpm.

Day-2

A solution of Ampicillin (200 mg) was prepared in ultra-pure water (4 mL) and then 1 mL of this solution added to each larger flasks. Around 30 mL of the overnight culture was added to each of the flasks. The cultures were then incubated at 37 ˚C with shaking at 200 rpm until the optical density reached 0.7 (nearly taking 3 hours) at 550 nm (Water was used as a blank). Once the optical value reached 0.7, 100 mg/L of ITPG, Isopropyl β-D-1-thiogalactopyranoside, was added to induce the bacterial protein production, the flasks were then placed in the incubator for 150 mins, at 37 ˚C with shaking 200 rpm. The cells were then harvested by centrifugation at 5 000 rpm for 10 mins at 4 ˚C. The supernatant was discarded, and the cells were suspended into a 400 mL volume using 10 mM Tris buffer (pH 7.8) and were then centrifuged again at 8 000 rpm for 10 mins at 4 ˚C. After the supernatant was discarded, the pelleted cells were then frozen at -80 ˚C.

Day-3

The frozen pellets were re-suspended in cold 10 mM Tris pH 7.8 buffer (100 mL) and sonicated with a large probe (8 times × 2 mins bursts, 50% cycle and 60% power). The solution was allowed to cool down on the ice during each sonicating step to prevent protein denaturation. After the solution was passed through a cell disruptor with 23 kpsi, kilo pounds per square inch, at 4 ˚C, it was centrifuged at 10 000 rpm for 15 mins at 4 ˚C. The supernatant was discarded, and the pellet was re-suspended in 6 M Guanidine.HCl (100 mL), 100 mM Tris buffer (pH 7.0) and β-mercaptoethanol (20 µL) by sonication (3 times x 2 mins. bursts, 50% cycle and 60% power). The solution was then incubated on ice for 1 hour. The resulting mixture was centrifuged at 23 000 rpm for 30 mins at 4 ˚C. The supernatant was then slowly poured to 250 mL loading buffer (1.25 M NaCl, 25 mM Tris pH 7.8, and 25 mM $CaCl_2$) with gentle stirring. The protein was then dialysed against 4 L of loading buffer overnight.

Day-4

As the equilibrium between the solution and the buffer was established, the dialysis buffer was changed three times a day to restart the dialysis.

Day-5

The dialysed material was collected and centrifuged again at 20 000 rpm for 30 mins at 4 ˚C and the supernatant was then pooled. 2.5 mL Man-sepharose affinity column was prepared and this column was equilibrated with 30 mL loading buffer. The protein was then loaded onto the column. After the column was washed with 25 mL of loading buffer, the protein was eluted from the column with elution buffer (1.25 M NaCl, 25 mM Tris buffer pH 7.8, and 2.5 mM EDTA) and 10 elution fractions of approximately 1.5 mL were collected. Proteins were then purified by size exclusion chromatography (30×1 cm Superdex 200 column, Amersham, Bioscience) eluted with 10 mM Tris pH 7.8, 100 mM NaCl, 2.5 mM EDTA at a flow rate of 0.3 mL/min.

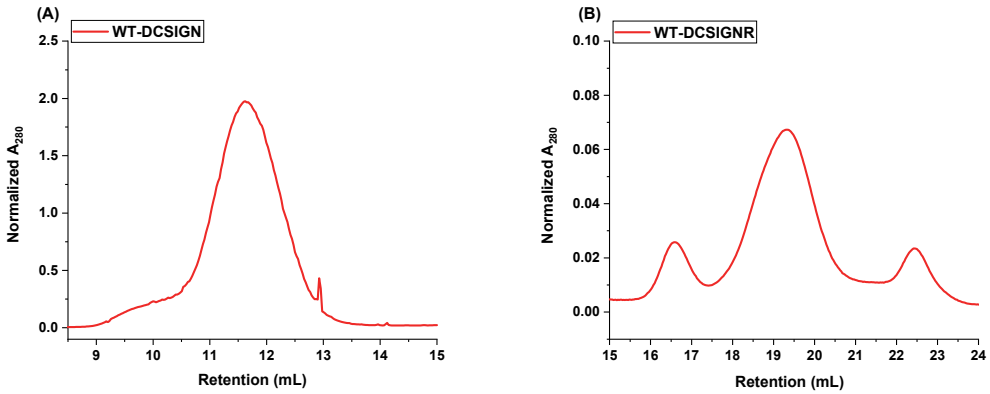

Figure 2.8.2. Size exclusion chromatography graphs of (A) DC-SIGN and (B) DC-SIGNR. The dominant peaks eluted out at ~11.5 mL for DC-SIGN and ~19.5 mL for DC-SIGNR correspond to the desired tetrameric proteins.

Their concentrations were measured by their absorption at 280 nm (A_{280}) via UV-vis spectroscopy, where the extinction coefficient at 280 nm for the monomers of DC-SIGN is 70400 M^{-1} cm^{-1} and for DC-SIGNR is 60890 M^{-1} cm^{-1}. Purified proteins were then confirmed by HR-MS, as given in **Figure 2.8.3.** The calculated molecular weights of DC-SIGN and DC-SIGNR based on amino acid sequences are 39197.22 and 37478.99, and found 39201.61, and 37470.40, respectively.

A- DC-SIGN (DC020)

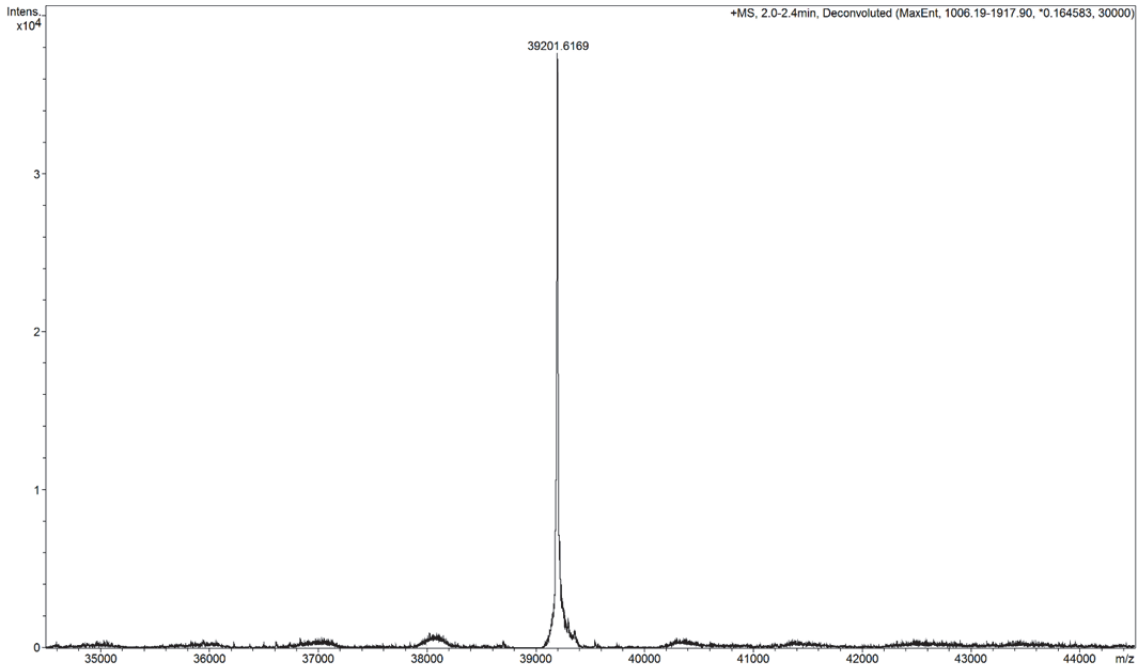

B- DC-SIGNR (DSR034)

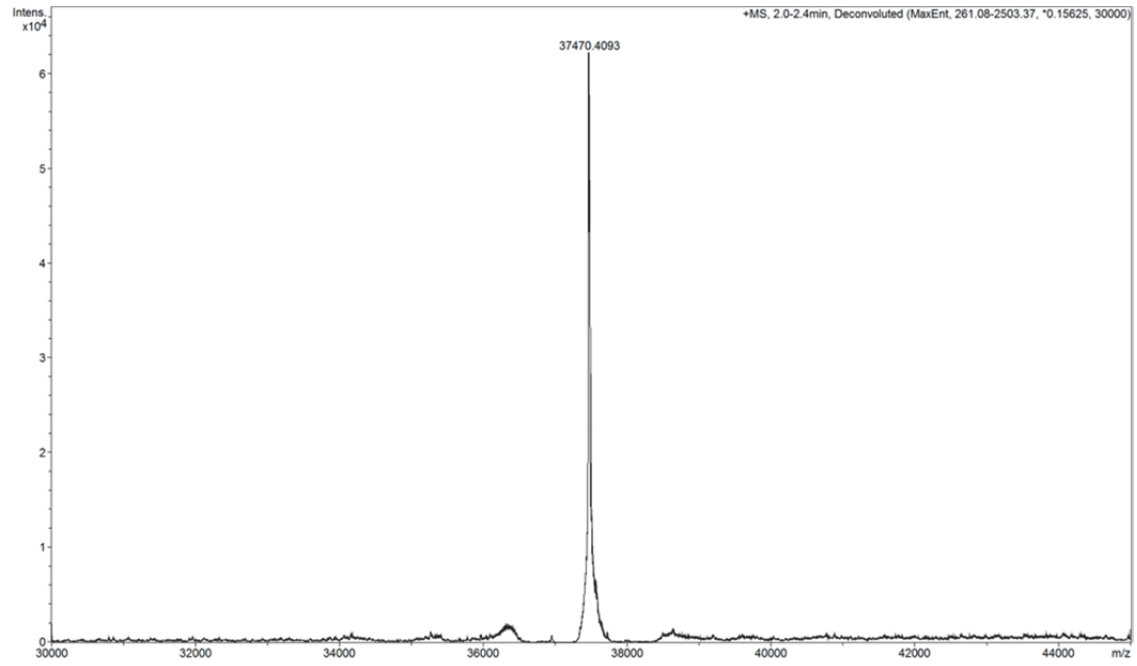

Figure 2.8.3. HR-MS spectra of (A) wild-type DC-SIGN (DC020) and (B) DC-SIGNR (DSR034).

2.8.2. Protein Labelling Protocol

Day-1

Mannose-sepharose column used in the protein purification was washed with five column volumes Ca^{2+}-containing buffer (25 mL, 20 mM HEPES pH 7.4, 150 mM NaCl, 25 mM $CaCl_2$) to remove any unbound or weakly bound proteins. This was enabled the buffer exchange and Tris in the previously used buffers was removed from the column, preventing it from interfering with the thiol-maleimide reaction. The bound proteins were then eluted with eluting buffer (20 mM HEPES pH 7.4, 150 mM NaCl, 2.5 mM EDTA) and 10 elution fractions of 1.5 mL were then collected (10 × 1.5 mL). In order to effective protein labelling, the buffer pH was maintained at 7.4 to facilitate thiol-maleimide reaction. The protein absorbance at 280 nm was measured using a nanodrop instrument to analyse the elution profile. The protein was mainly eluted at E2, E3 and E4, and then $CaCl_2$ (500 mM pH 7.3 in H_2O) was added to each fraction to obtain the final concentration of 25 mM. The selected fractions (E2, E3, and E4) were combined and concentrated using 10 kDa MWCO spin column because of the high protein concentration required for efficient protein labelling. DC-SIGN/R protein was labelled with the molar ratio of protein:dye 1:2 using maleimide-ATTO-594 or ATTO-

643 dyes. Dyes were dissolved in DMSO, dimethyl sulfoxide, at a concentration of 100 µg/10 µL. Afterwards, the required amount of dye was added to the protein solution and mixed. The mixture was wrapped with aluminium foil and allowed to mix at RT for 2 hours and kept at 4 ˚C in the fridge overnight.

Day-2

A mannose-sepharose affinity column was prepared based on the amount of protein to be used and washed with binding buffer (20 mM HEPES pH 7.8, 100 mM NaCl, 10 mM $CaCl_2$). The mixture containing the labelled protein and excess dye was loaded onto the column, and then it was washed with binding buffer to remove excess dye (labelled proteins were bound to the column). After no blue colour (free dye) was observed in the solution, the EDTA-containing elution buffer (20 mM HEPES pH 7.8, 100 mM NaCl, 2.5 mM EDTA) was added to elute the labelled proteins (DC-SIGN/R-glycan binding being Ca^{2+} dependent) and the fractions of labelled proteins were collected. The labelled protein appeared as a blue band and collected as one fraction. $CaCl_2$ (500 mM, pH 7.3 in H_2O) was then added to yield a final concentration of 10 mM. The concentration of labelled proteins was calculated according to the Beer-Lambert law using the following equation.

$$\mathrm{Protein_{conc.}} = \frac{\mathrm{A_{280}} - \left(\mathrm{A_{dye}} \cdot \mathrm{CF_{280}}\right)}{\varepsilon_{280} \cdot l}$$

Where A_{280} is the UV absorbance of protein at 280 nm, A_{dye} is the maximum dye absorbances at 609 nm for Atto-594 dye or 643 nm for Atto-643 dye, CF_{280} is the correction factor at 280 nm, used to correct the dye absorbance contribution at 280 nm, 0.51 for Atto-594 and 0.04 for Atto-643 dye, ε_{280} is the extinction coefficient at 280 nm, for DC-SIGN Q274C is 70 400 $M^{-1}cm^{-1}$ and for DC-SIGNR R274C is 60 890 $M^{-1}cm^{-1}$, and l is the path length of the light in cm.

Maleimide dyes show high affinity and selectivity towards free thiol groups which are mostly present in cysteine residues of proteins. As outlined in **Scheme 2.8.1** below, maleimide labelling is a process in which the lone pair on the free sulfhydryl groups of the introduced free cysteine residue in these proteins attacks the double bond of maleimide dyes. The labelling efficiency of the proteins were verified by HR-MS (**Figure**

2.8.4), calculated by dividing the labelled peak area of the protein by the total (labelled and unlabelled) peak area. An increase of molecular weight of ~882 Da was observed for both labelled proteins, corresponding to the Atto-643 dye molecular weight. The average dye labelling efficiency (per protein monomer) was ~82% and ~90% per monomer for DC-SIGN and DC-SIGNR, respectively.

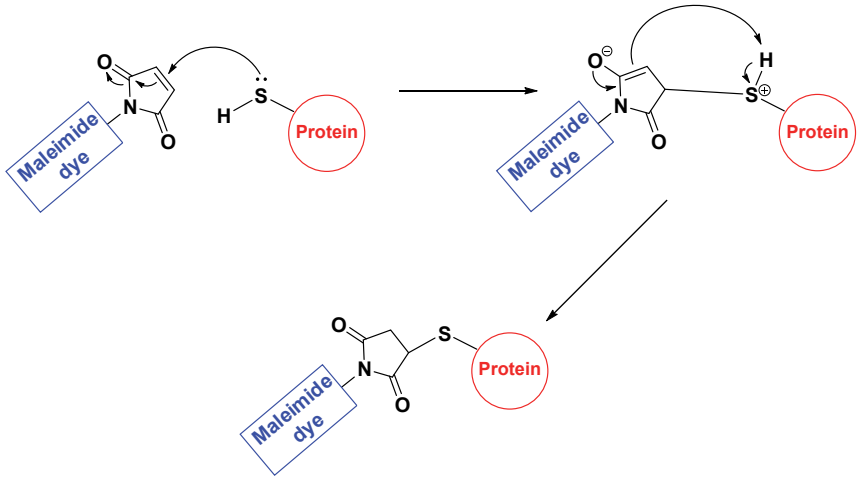

Scheme 2.8.1. A schematic showing the nucleophilic addition reaction mechanism used for labelling a protein with a maleimide dye.

A- DC-SIGN-Atto-643 (DC020 Q274C-Atto 643)

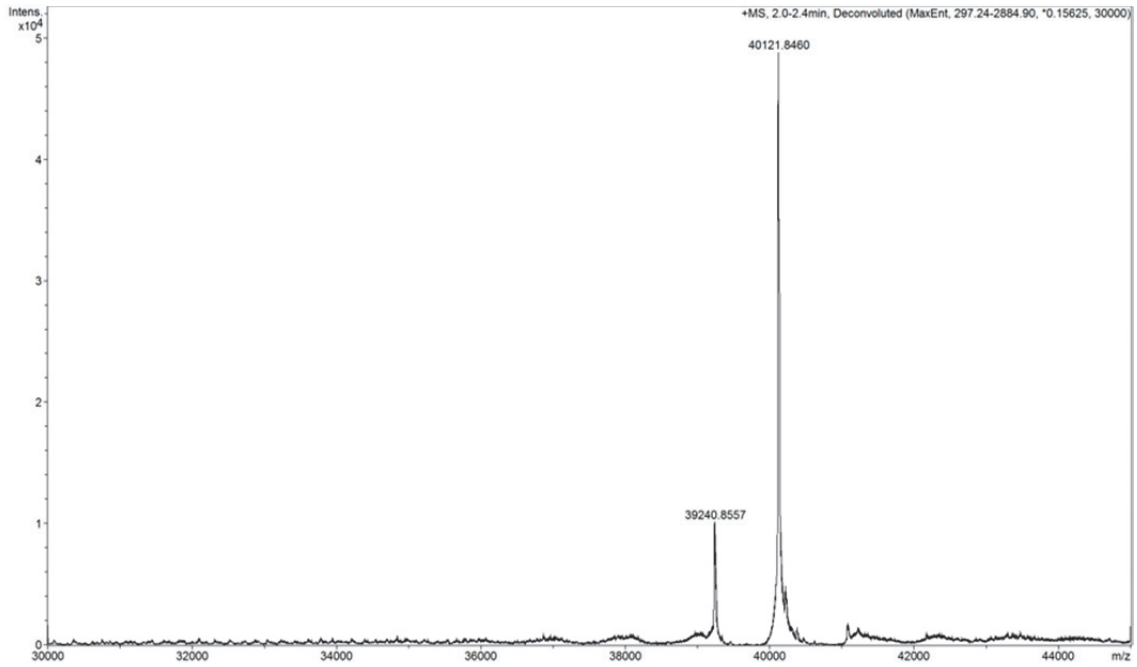

B- DC-SIGNR-Atto643 (DSR034 R287C-Atto 643)

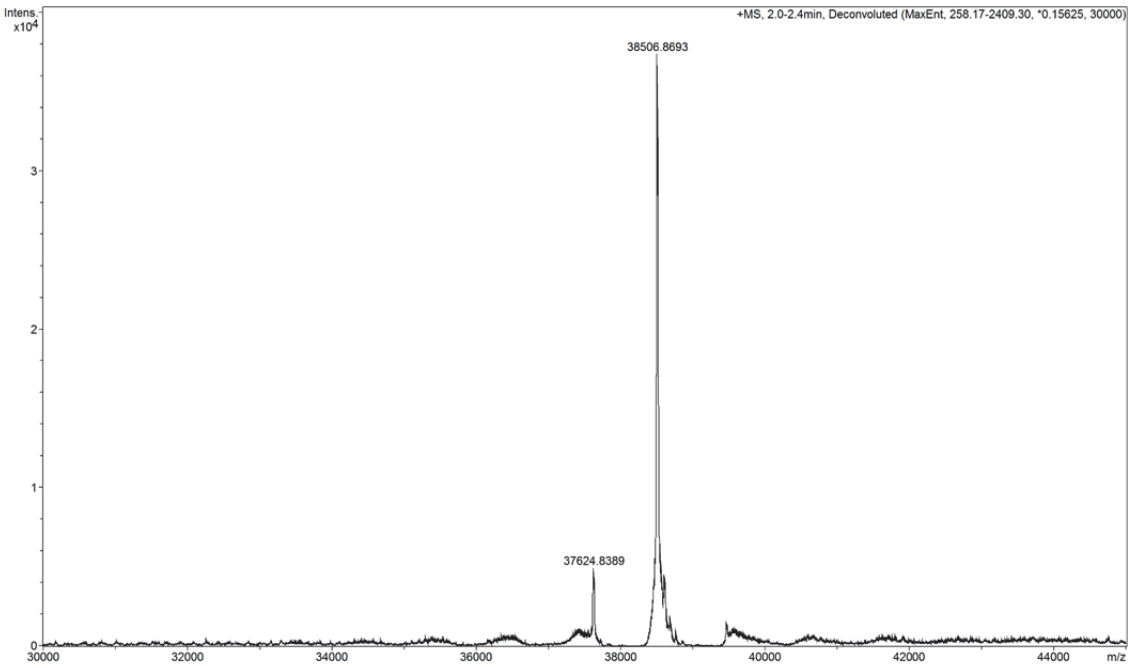

Figure 2.8.4. HR-MS spectra of (A) DC-SIGN-Atto 643 (DC020 Q274C-Atto 643) and (B) DC-SIGNR-Atto 643 (DSR034 R287C-Atto 643).

2.8.3. Labelling BSA and Lysozyme with NHS-Atto-594 Dye

The protein BSA (5 mg) and Lysozyme (3 mg) was separately dissolved in $NaHCO_3$ (500 µL, 50 mM, and pH: 8.3). A six and three molar equivalent of Atto-594 maleimide dye in DMSO were then added to the protein BSA and Lysozyme solutions, respectively. The reactions were then incubated in dark at RT for 2 hrs under gentle stirring. Afterward, 10 mL of gel filtration column filled with Sephadex G25 was prepared and the solutions were then loaded onto the columns. Dye-labelled BSA and Lysozyme were then separated from the free dye with PBS elution buffer (10 mM $NaHPO_4$, 2 mM KH_2PO_4, 100 mM NaCl, pH 7.4). The concentration of the labelled proteins was calculated depends on the Beer-Lambert law using the following equations.

$$\text{Protein}_{\text{conc.}} = \frac{\text{A}_{280} - (\text{A}_{609} \cdot \text{CF}_{280})}{(\text{Ɛ}_{280} \cdot l)}$$

Where the extinction coefficients at 280 nm, $Ɛ_{280}$, of BSA and Lysozyme are 44 000 $M^{-1}cm^{-1}$ and 36 000 $M^{-1}cm^{-1}$, respectively, A_{609} is the maximum dye absorbances at 609 nm, l is the path length, and CF_{280} is the correction factor at 280 nm, used to correct the dye absorbance contribution at 280 nm, 0.51 for Atto-594 dye.

2.9. Fluorescence Spectroscopy

Fluorescence data for Atto-594 dye labelled proteins were recorded on a Cary Eclipse Fluorescence Spectrophotometer using a fixed excitation wavelength (λ_{ex}) of 595 nm, while for Atto-643 dye labelled proteins fluorescence data were recorded on a Horiba FluoroMax-4 Spectrofluorometer using a fixed excitation wavelength (λ_{ex}) of 643 nm. Emission spectra over 605-750 nm for Atto-594 and 643-800 for Atto-643 were collected with excitation and emission slit widths of 5 nm and a slow scan speed. A photomultiplier (PMT) was selected 700 V for low concentration or 600 V for high concentration of the protein to compensate the fluorescence signal. The protein: GNP ratios are reported within the relevant parts of the next chapters where required. After mixing dye-labelled proteins with GNPs, they were incubated at RT for 20 mins before their fluorescence spectra were recorded. All measurements were carried out in the binding buffer (20 mM HEPES, pH 7.8, 100 mM NaCl, 10 mM $CaCl_2$) containing 1 mg/mL BSA to reduce any non-specific binding of GNP-conjugates.

The obtained fluorescence spectra were then integrated between 643-800 nm for Atto-643 dye labelled proteins and 605-750 nm for Atto-594 dye labelled proteins, and these integrated values for Atto 594 dye labelled proteins were used to calculate the fluorescence quenching efficiency (QE%) of GNPs, as shown in the equation below. The calculations for QE% of GNPs (for Atto-643 dye labelled proteins) were described in **Chapter 3.3.3**.

$$QE\ (\%) = \frac{(P - NP)}{P}\ x\ 100$$

Where P is the spectral area for protein, and NP is the spectral integral for GNP+protein. Fluorescence quenching percentage are directly proportional to the amount of protein bound to GNPs, in order to calculate apparent binding constant, K_d, the binding curves were then fitted by Hill Equation below.

$$y = \frac{R_{max} \cdot x^n}{(k^n + x^n)}$$

Where R_{max} is the maximum fluorescence quenching percentage, x is the protein concentration, k is the apparent binding affinity, K_d, that gives 50% of R_{max}, n is the Hill coefficient. Fluorescence of dye labelled molecules can be completely quenched upon

binding on the GNP surface. Thus, R_{max} is set to 1, showing the maximum fluorescence quenching percentage (100%).

2.10. References

1. X. Hu, Y. Zhang, T. Ding, J. Liu and H. Zhao, *Front Bioeng Biotechnol*, 2020, **8**, 990.
2. UV/Vis/IR Spectroscopy Analysis of NPs, NanoComposix (Nanocomposix.com), (accessed September 2022, 2022).
3. S. Mourdikoudis, R. M. Pallares and N. T. K. Thanh, *Nanoscale*, 2018, **10**, 12871-12934.
4. V. Amendola and M. Meneghetti, *The Journal of Physical Chemistry C*, 2009, **113**, 4277-4285.
5. W. Haiss, N. T. K. Thanh, J. Aveyard and D. G. Fernig, *Analytical Chemistry*, 2007, **79**, 4215-4221.
6. H. Hinterwirth, S. K. Wiedmer, M. Moilanen, A. Lehner, G. Allmaier, T. Waitz, W. Lindner and M. Lämmerhofer, *J Sep Sci*, 2013, **36**, 2952-2961.
7. E. Boisselier and D. Astruc, *Chem Soc Rev*, 2009, **38**, 1759-1782.
8. I. Ielo, G. Rando, F. Giacobello, S. Sfameni, A. Castellano, M. Galletta, D. Drommi, G. Rosace and M. R. Plutino, *Molecules*, 2021, **26**, 5823.
9. M. Kaszuba, D. McKnight, M. T. Connah, F. K. McNeil-Watson and U. Nobbmann, *Journal of Nanoparticle Research*, 2008, **10**, 823-829.
10. C. M. Maguire, M. Rösslein, P. Wick and A. Prina-Mello, *Sci Technol Adv Mater*, 2018, **19**, 732-745.
11. S. Bhattacharjee, *J Control Release*, 2016, **235**, 337-351.
12. Better Size Instrument, Nanoparticle Size and Zeta Potential Analyzer https://www.bettersizeinstruments.com/, (accessed September 2022).
13. C. M. Hoo, N. Starostin, P. West and M. L. Mecartney, *Journal of Nanoparticle Research*, 2008, **10**, 89-96.
14. M. Zimbone, L. Calcagno, G. Messina, P. Baeri and G. Compagnini, *Materials Letters*, 2011, **65**, 2906-2909.
15. J. D. Driskell, C. A. Jones, S. M. Tompkins and R. A. Tripp, *Analyst*, 2011, **136**, 3083-3090.
16. H. Jans and Q. Huo, *Chemical Society Reviews*, 2012, **41**, 2849-2866.
17. D. J. Smith, in *Nanocharacterisation (2)*, The Royal Society of Chemistry, 2015, DOI: 10.1039/9781782621867-00001, pp. 1-29.
18. M. A, PhD thesis, 2016.
19. K. Quester, M. Avalos-Borja and E. Castro-Longoria, *Micron*, 2013, **54-55**, 1-27.
20. D. Sýkora, V. Kašička, I. Mikšík, P. Řezanka, K. Záruba, P. Matějka and V. Král, *Journal of Separation Science*, 2010, **33**, 372-387.
21. P. Goldberg-Oppenheimer and O. Regev, *Small*, 2007, **3**, 1894-1899.
22. P. N. Njoki, I. I. S. Lim, D. Mott, H.-Y. Park, B. Khan, S. Mishra, R. Sujakumar, J. Luo and C.-J. Zhong, *The Journal of Physical Chemistry C*, 2007, **111**, 14664-14669.

23. E. Alehosseini, H. Shahiri Tabarestani, M. S. Kharazmi and S. M. Jafari, *Foods*, 2022, **11**.
24. K. Susumu, H. T. Uyeda, I. L. Medintz, T. Pons, J. B. Delehanty and H. Mattoussi, *Journal of the American Chemical Society*, 2007, **129**, 13987-13996.
25. H. Zhang, G. Feng, Y. Guo and D. Zhou, *Nanoscale*, 2013, **5**, 10307-10315.
26. B. C. Mei, K. Susumu, I. L. Medintz and H. Mattoussi, *Nat Protoc*, 2009, **4**, 412-423.
27. R. Ribeiro-Viana, M. Sánchez-Navarro, J. Luczkowiak, J. R. Koeppe, R. Delgado, J. Rojo and B. G. Davis, *Nature Communications*, 2012, **3**, 1303.
28. F. Aldeek, M. A. H. Muhammed, G. Palui, N. Zhan and H. Mattoussi, *ACS Nano*, 2013, **7**, 2509-2521.
29. A. Rahman, A. Rahman, W. Ghann, H. Kang and J. Uddin, *Int J Biosen Bioelectron*, 2018, **4**, 159-164.
30. H. Zhao, S. Sen, T. Udayabhaskararao, M. Sawczyk, K. Kučanda, D. Manna, P. K. Kundu, J. W. Lee, P. Král and R. Klajn, *Nat Nanotechnol*, 2016, **11**, 82-88.
31. X. Ji, X. Song, J. Li, Y. Bai, W. Yang and X. Peng, *Journal of the American Chemical Society*, 2007, **129**, 13939-13948.
32. Sigma-Aldrich - Gold Nanoparticles: Properties and Applications https://www.sigmaaldrich.com/TR/en/technical-documents/technical-article/materials-science-and-engineering/biosensors-and-imaging/gold-nanoparticles, (accessed 20.01.2023, 2023).
33. Y. Guo, W. Bruce Turnbull and D. Zhou, *Methods Enzymol*, 2018, **598**, 71-100.
34. D. Budhadev, E. Poole, I. Nehlmeier, Y. Liu, J. Hooper, E. Kalverda, U. S. Akshath, N. Hondow, W. B. Turnbull, S. Pöhlmann, Y. Guo and D. Zhou, *Journal of the American Chemical Society*, 2020, **142**, 18022-18034.
35. H. D. Hill, J. E. Millstone, M. J. Banholzer and C. A. Mirkin, *ACS Nano*, 2009, **3**, 418-424.
36. G. B. Stewart-Jones, C. Soto, T. Lemmin, G. Y. Chuang, A. Druz, R. Kong, P. V. Thomas, K. Wagh, T. Zhou, A. J. Behrens, T. Bylund, C. W. Choi, J. R. Davison, I. S. Georgiev, M. G. Joyce, Y. D. Kwon, M. Pancera, J. Taft, Y. Yang, B. Zhang, S. S. Shivatare, V. S. Shivatare, C. C. Lee, C. Y. Wu, C. A. Bewley, D. R. Burton, W. C. Koff, M. Connors, M. Crispin, U. Baxa, B. T. Korber, C. H. Wong, J. R. Mascola and P. D. Kwong, *Cell*, 2016, **165**, 813-826.
37. H. Feinberg, D. A. Mitchell, K. Drickamer and W. I. Weis, *Science*, 2001, **294**, 2163-2166.
38. Y. Guo, C. Sakonsinsiri, I. Nehlmeier, M. A. Fascione, H. Zhang, W. Wang, S. Pöhlmann, W. B. Turnbull and D. Zhou, *Angew Chem Weinheim Bergstr Ger*, 2016, **128**, 4816-4820.
39. Y. Guo, I. Nehlmeier, E. Poole, C. Sakonsinsiri, N. Hondow, A. Brown, Q. Li, S. Li, J. Whitworth, Z. Li, A. Yu, R. Brydson, W. B. Turnbull, S. Pöhlmann and D. Zhou, *J Am Chem Soc*, 2017, **139**, 11833-11844.
40. Y. Guo, C. Sakonsinsiri, I. Nehlmeier, M. A. Fascione, H. Zhang, W. Wang, S. Pöhlmann, W. B. Turnbull and D. Zhou, *Angew Chem Int Ed Engl*, 2016, **55**, 4738-4742.
41. J. S. Nanda and J. R. Lorsch, *Methods Enzymol*, 2014, **536**, 79-86.

Chapter 3
GNP-glycans binding with DC-SIGN/R: affinity, thermodynamics and virus inhibition

3.1. Introduction

Multivalent carbohydrate-protein interactions are widespread and critical in modulating many essential biological functions, including pathogen-host cell recognition and infection, cell-cell communication as well as regulation of immune responses. As most monovalent carbohydrate-protein interactions are intrinsically too weak to produce a biologically functional impact,[1] most lectins (carbohydrate-binding proteins) form multimeric structures and form multivalent interactions with multiple carbohydrates to increase binding affinity and specificity. The infection processes of many viruses, including HIV, Ebola, West Nile,[2] and more recently, SARS-CoV-2,[3] are initiated or facilitated (in case of SARS-CoV-2) by binding of their surface glycan structures to host cell multimeric C-type lectins or vice versa. Therefore, multivalent glycoconjugates that can potently inhibit or block these protein-carbohydrate interactions can be used as effective inhibitors to prevent viral infections. The main challenge here is to make their binding specific for the target lectins only without affecting other related lectins by forming spatially matched multivalent interactions. Despite significant progress over the past two decades, more research are still needed because the orientation and spatial arrangement of multiple carbohydrate-binding sites in some important multimeric lectins remain to be not fully understood.

Herein, DC-SIGN and DC-SIGNR (abbreviated collectively as DC-SIGN/R), a pair of closely related tetrameric lectins are employed as model multimeric lectins to study their multivalent glycan binding properties. DC-SIGN/R are highly attractive targets here because they mediate the initiation of many important viral infections by binding to their surface specific glycans. However, despite intensive efforts, their overall tetrameric structures remain to be determined. The lack of detailed knowledge about the spatial and orientational arrangement of their carbohydrate binding sites has posed a major obstacle for the design of potent and specific multivalent inhibitors

against such lectin mediated viral infections. To probe the structural mechanisms underlying their multivalent glycan binding affinity and specificity, our research group has developed a novel glycan-nanoparticle based multimodal readout (combining QD-FRET affinity measurement, hydrodynamic size and S/TEM analysis of lectin-glycan-nanoparticle assemblies), which has successfully dissected the distinct glycan-nanoparticle binding mode between DC-SIGN (tetravalent binding with one glycan nanoparticle) and DC-SIGNR (crosslinking with different glycan-nanoparticles). Based on these, they have proposed that their different glycan-nanoparticle binding properties are due to the different orientation of their four carbohydrate-recognition domains (CRDs); those in DC-SIGN CRDs are uprightly faced, while those in DC-SIGNR are pointed in sidewardly.[4]

The development of potent glycoconjugates to block viral attachment and infection of host cells has a unique advantage over other therapeutic approaches because they can prevent the viral mutation and acquire resistance.[5] Free glycans can be directly employed for this purpose, however they are most likely to be very ineffective because of their weak monovalent binding character with target lectins. However, glycan coated nanoparticles can bind multivalently with target multimeric lectins, resulting in greatly increased binding of up to 5-6 orders of magnitude stronger than the corresponding free glycans.[6] In this regard, nanomaterials can act as robust scaffolds for displaying multivalent sugar ligands for targeting lectins potently and specifically. In particular, gold nanoparticles, GNPs, are excellent scaffolds for constructing smart, multivalent, and efficient glycan-based nanoplatforms owing to their unique properties described clearly in **Chapter 1.3.1**. Notably, their large surface-area-to-volume ratio gives them a particular advantage in forming multivalent structures by enabling the formation of stable three-dimensional glycan presentations. Furthermore, glycan-functionalised GNPs (GNP-glycans) have excellent colloidal stability and show no sign of aggregation in biologically relevant environments, changes in GNP-glycan aggregation triggered by lectin binding can be easily detected by UV-vis absorption and/or particle hydrodynamic sizes. Until recently, most of the lectin-glycan binding interactions have been probed by conventional biophysical methods such as surface plasmon resonance (SPR) and isothermal titration calorimetry (ITC).[7] However, despite

good capacity in providing quantitative binding affinity and thermodynamic data, these methods cannot provide any structural information of lectins, such as binding site orientation, binding mode, and distances between binding sites, which are necessary to design and develop specific multivalent glycan inhibitors. In this project, by exploiting the strong fluorescence quenching properties of GNPs, the multivalent binding between GNP-glycans and model lectin DC-SIGN/R have been investigated via a novel fluorescence quenching technique (as shown schematically in **Figure 3.1.1**) in combination with hydrodynamic size and electron microscopy analysis to not only provide quantitative binding affinity but also reveal the binding mechanisms. The fundamental aim here is to develop a generic new method suitable for quantifying multivalent binding affinities and thermodynamic parameters between lectins and various sized GNP-glycans by utilizing GNP's super fluorescence quenching properties. Within this context, a variety of lipoic acid–oligo(ethylene glycol) based multifunctional glycan (LA-EG_n-glycan) ligands are first designed and synthesised. Moreover, lipoic acid–oligo(ethylene glycol) based control ligands of the same length but lacking of the terminal glycan groups are also designed and produced as negative controls for non-specific interactions with lectins. GNPs of different sizes are then coated with these functional ligands via self-assembly, thereby forming GNP-glycan conjugates to investigate their interactions with DC-SIGN/R. Interestingly, the dimannose ligand coated 5 nm GNPs exhibit a similar size and glycan densities to that of the trimeric gp160, the HIV surface heavily glycosylated glycoproteins, which bind to DC-SIGN to mediate viral trans-infection, therefore studies on GNP-glycan-DC-SIGN interactions can potentially help explain HIV-DC-SIGN interaction mechanisms. Binding interactions of GNP-glycans with DC-SIGN/R are then investigated by fluorescence quenching and their binding equilibrium dissociation constants, K_ds, are determined by fitting the resulting fluorescence quenching efficiency-concentration relationships with the Hill's equation. By comparing the K_ds obtained between DC-SIGN/R and various GNP-glycans, the effects of GNP size, EG chain linker length, terminal functional group, and sugar type and density on their multivalent interactions with DC-SIGN/R are obtained. Moreover, the binding specificity of GNP-glycans to DC-SIGN/R is also checked by mannose competition studies and using GNP-LA-EG_n-OH (denoted as GNP-OH hereafter) controls lacking the terminal glycans. The ability of GNP-glycans to inhibit

DC-SIGN/R-driven virus infection of host cells are also studied and compared with their respective lectin binding K_d values. Furthermore, the correlation between the binding mode of GNP-glycans with DC-SIGN/R and their binding thermodynamics is also investigated.

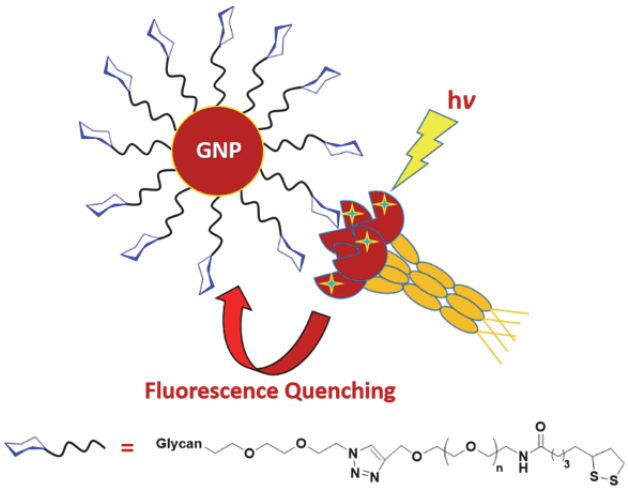

Figure 3.1.1. A schematic diagram to illustrate the principle of probing multivalent binding interactions between GNP-glycans and DC-SIGN/R via fluorescence quenching method.

3.2. Multivalent GNP-conjugate Design

In order to establish a specific and selective binding to the target tetrameric DC-SIGN/R, ligands containing multiple binding sites were first designed and constructed. The ligand design was based on the following principles: ligands must be able to bind strongly and specifically to both the GNPs scaffolds and also the CRDs in DC-SIGN/R; and they must be stable and highly suitable for their use in biological processes. Therefore, our multifunctional ligands are designed to contain three unique functional domains: A dihydrolipoic acid (DHLA) group to provide strong chelative binding onto the GNP surface; a flexible oligo(ethylene glycol) (EG) linker domain to promote biological stability, water solubility, and also preventing non-specific adsorption; and the terminal functional group to allow for specific binding with target lectins. Multivalent GNP-glycan conjugates was produced in three main steps: 1) synthesis of multivalent ligand, 2) synthesis of various sized GNPs, and 3) GNP cap-exchange using the glycan ligands, as described in details in **Chapter 2.6**. **Figure 3.2.1** below shows schematically the modular design of GNP-ligand conjugates. Their characterisations are also given in **Chapter 2.6.1**.

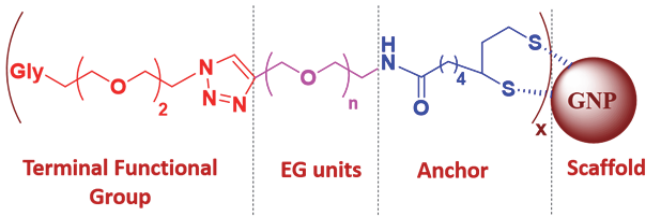

Figure 3.2.1. A schematic representation of a GNP capped with a multifunctional ligand containing an anchor, hydrophilic EG linker, and terminal functional group.

3.3. Fluorescence Quenching for GNP-conjugates with DC-SIGN/R Binding

3.3.1. Fluorescence Quenching for G5-LA-PEGs with Atto-594 labelled DC-SIGN Binding

Previous studies from our group have shown that 5 nm GNPs (abbreviated as G5 hereafter) coated with mannose-based glycan ligands (α-Man and Man-α-1,2-Man) exhibit high binding affinity with DC-SIGN.[2, 8] In order to demonstrate the binding affinity and specificity of G5-glycans with DC-SIGN, 5 nm GNPs coated with several dihydrolipoic acid-poly (ethylene glycol)-based control ligands (without terminal glycan) were produced and characterised, and then their interactions with Atto-594 dye labelled DC-SIGN were measured by fluorescence quenching. Our initial hypothesis here was that since these control ligands do not contain any terminal carbohydrates, there should be no specific binding between these control GNPs and DC-SIGN; thus fluorophores labelled on DC-SIGN should not participate in energy transfer with GNPs, and hence no or negligible fluorescence quenching should be observed. To determine the apparent equilibrium binding dissociation constant (K_d) of the multivalent interactions between PEGylated GNPs and DC-SIGN, fluorescence spectra of DC-SIGN alone and PEGylated GNPs+DC-SIGN were recorded over a range of different concentrations at a fixed molar ratio of 1:5 for GNP: DC-SIGN. This ratio was chosen to compensate for the low fluorescence signals (hence large errors in quenching efficiency measurement) at low protein concentrations, and was kept constant throughout the all concentration range studied. All measurements were carried out in the binding buffer (20 mM HEPES, pH 7.8, 100 mM NaCl, 10 mM $CaCl_2$) containing 1 mg/mL BSA to reduce any nonspecific binding of GNP-conjugates. The fluorescence spectra for only DC-SIGN and GNP-PEGs+DC-SIGN samples are shown in **Figure 3.3.1** below.

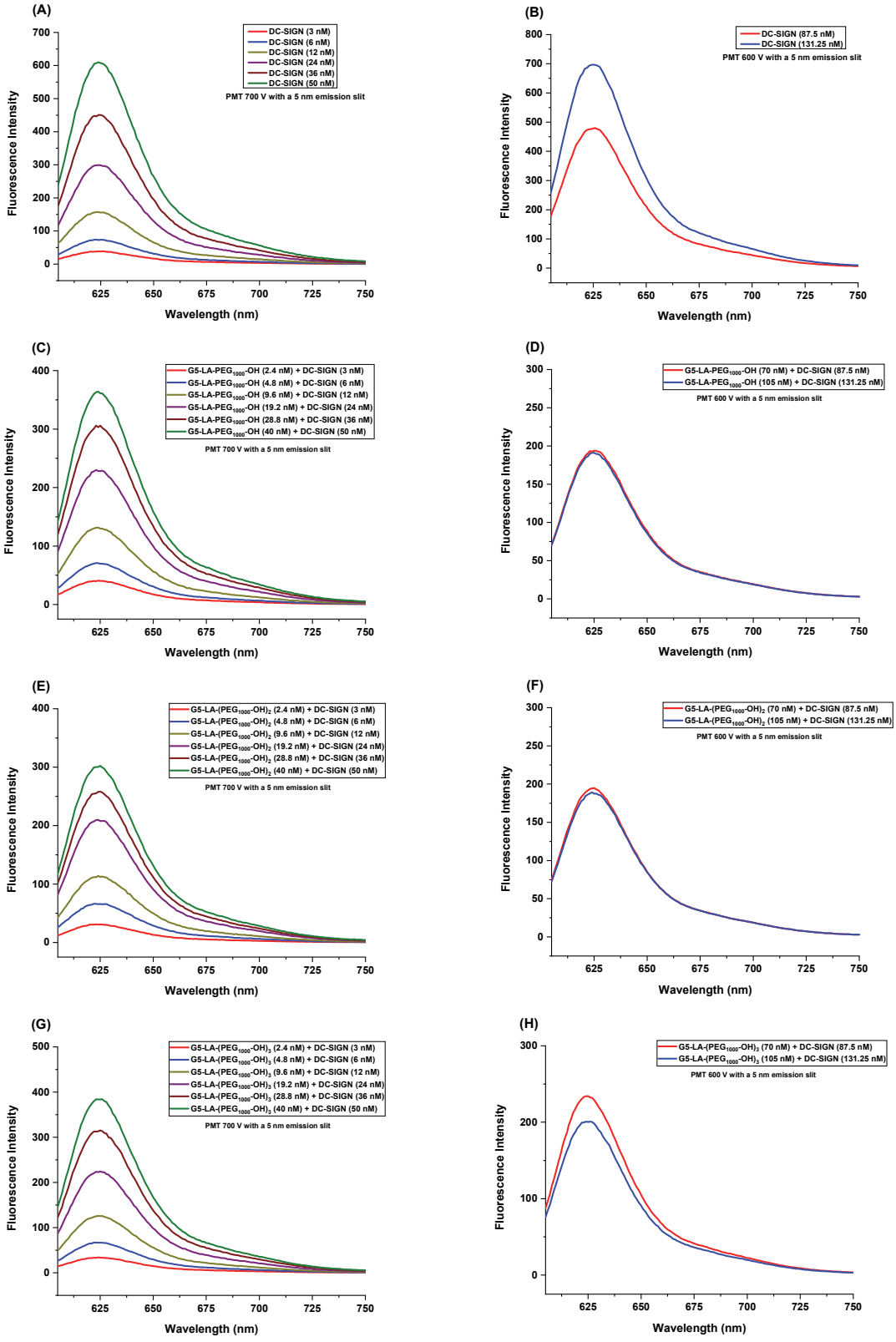

Figure 3.3.1. Fluorescence spectra of the labelled DC-SIGN (A) at low concentrations and (B) high concentrations; Fluorescence spectra of labelled DC-SIGN with GNPs capped with different DHLA-PEG-based ligands; (C) G5-LA-PEG_{1000}-OH+DC-SIGN using a PMT=700 V; (D) G5-LA-PEG_{1000}-OH+DC-SIGN using a PMT=600 V; (E) G5-LA-$(PEG_{1000}\text{-}OH)_2$+DC-SIGN using a PMT=700 V; (F) G5-LA-$(PEG_{1000}\text{-}OH)_2$+DC-SIGN using a PMT=600 V; (G) G5-LA-$(PEG_{1000}\text{-}OH)_3$+DC-SIGN using a PMT=700 V; (H) G5-LA-$(PEG_{1000}\text{-}OH)_3$+DC-SIGN using a PMT=600 V. Each sample was done in duplicate and their average fluorescence spectra was constructed.

Based on the obtained fluorescence spectra, their fluorescence quenching efficiency was determined. The quenching efficiency provides a measure of the fluorescence of the dye fluorophore measured in the presence and absence of fluorescence quenching material. The percentage quenching was calculated from the integral value of the fluorescence intensity of the dye-labelled proteins with and without the presence of the GNP-conjugates. The fluorescence quenching efficiency versus protein concentration plots were then fitted by the Hill's function to derive the apparent binding dissociation constant (K_d) for each GNP sample that gave the 50 % quenching. The resulting binding curves are given in **Figure 3.3.2**, and their apparent K_ds and Hill fitting parameters are listed in **Table 3.3.1**.

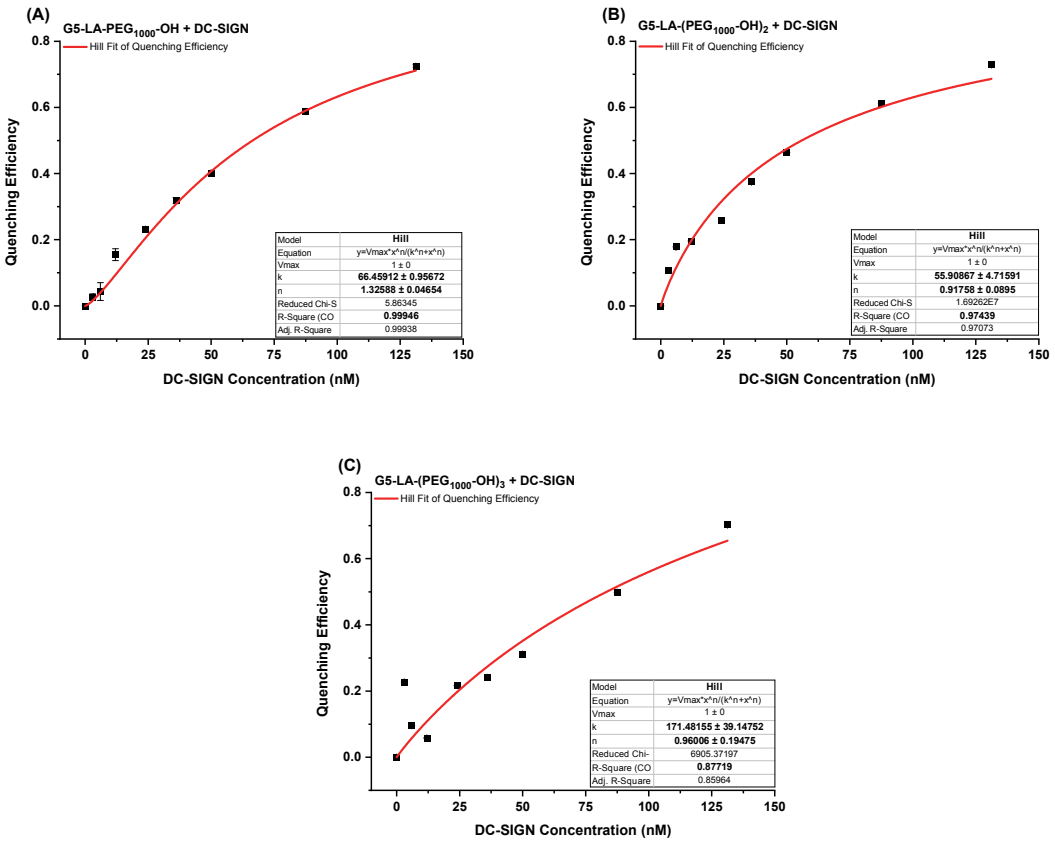

Figure 3.3.2. Percentage fluorescence quenching efficiency curves. (A) G5-LA-PEG_{1000}-OH+DC-SIGN; (B) G5-LA-$(PEG_{1000}\text{-}OH)_2$+DC-SIGN; (C) G5-LA-$(PEG_{1000}\text{-}OH)_3$+DC-SIGN. Data were fitted by Hill's equation.

Table 3.3.1. Summary of Hill's equation fitting parameters for G5-LA-$(PEG_{1000}\text{-}OH)_m$+DC-SIGN binding curves to derive the apparent K_ds.

G5-conjugates + DC-SIGN	Hill's Equation Fitting Parameters		
	K_d / nM	n	R^2
G5-PEG_{1000}-OH – DC-SIGN	66.4 ± 1	1.3 ± 0.04	0.999
G5-$(PEG_{1000}\text{-}OH)_2$ – DC-SIGN	55.9 ± 5	0.9 ± 0.08	0.974
G5-$(PEG_{1000}\text{-}OH)_3$ – DC-SIGN	171.4 ± 39	0.9 ± 0.19	0.877

Mixing GNPs covered with inert PEG ligands (GNP-LA-$(PEG_{1000}\text{-}OH)_m$) where m=1, and 2) with Atto-594 dye-labelled DC-SIGN both produced unexpected quenching results with apparent K_d of ~60 nM. We have initially anticipated that coating GNPs with a dense layer of PEG ligands may make them highly effective in resisting the non-specific adsorption of DC-SIGN on the GNP surface, and act as an excellent negative control for specific DC-SIGN-glycan binding interaction. However, to our surprise, upon mixing of GNPs with DC-SIGN, the DHLA-branched PEG ligands on the GNP surface considerably quenched DC-SIGN fluorescence. This observation has suggested that GNP-OH and DC-SIGN were within close proximity, where quenching may occur either statically through binding or dynamically via collision within the binding buffer. As DC-SIGN binds specifically to mannose glycans with high affinity, the binding interactions of PEGylated control GNPs with DC-SIGN were not expected, indicating that the long linker length (PEG ~21 units) on the GNP surface may not form a dense enough PEG coating. We then reasoned that higher PEG density onto GNPs might reduce or prevent non-specific DC-SIGN binding (hence fluorescence quenching). Therefore, PEG_{600}, which is shorter than PEG_{1000} used above, was used to create a denser PEG coating by shortening the length of the PEG graft (PEG ~13 units) and quenching studies were repeated with GNPs coated with LA-PEG_{600}-OH ligands. **Figure 3.3.3** below shows the fluorescence spectra of G5-PEG_{600}-OH+DC-SIGN and its resulting binding curve.

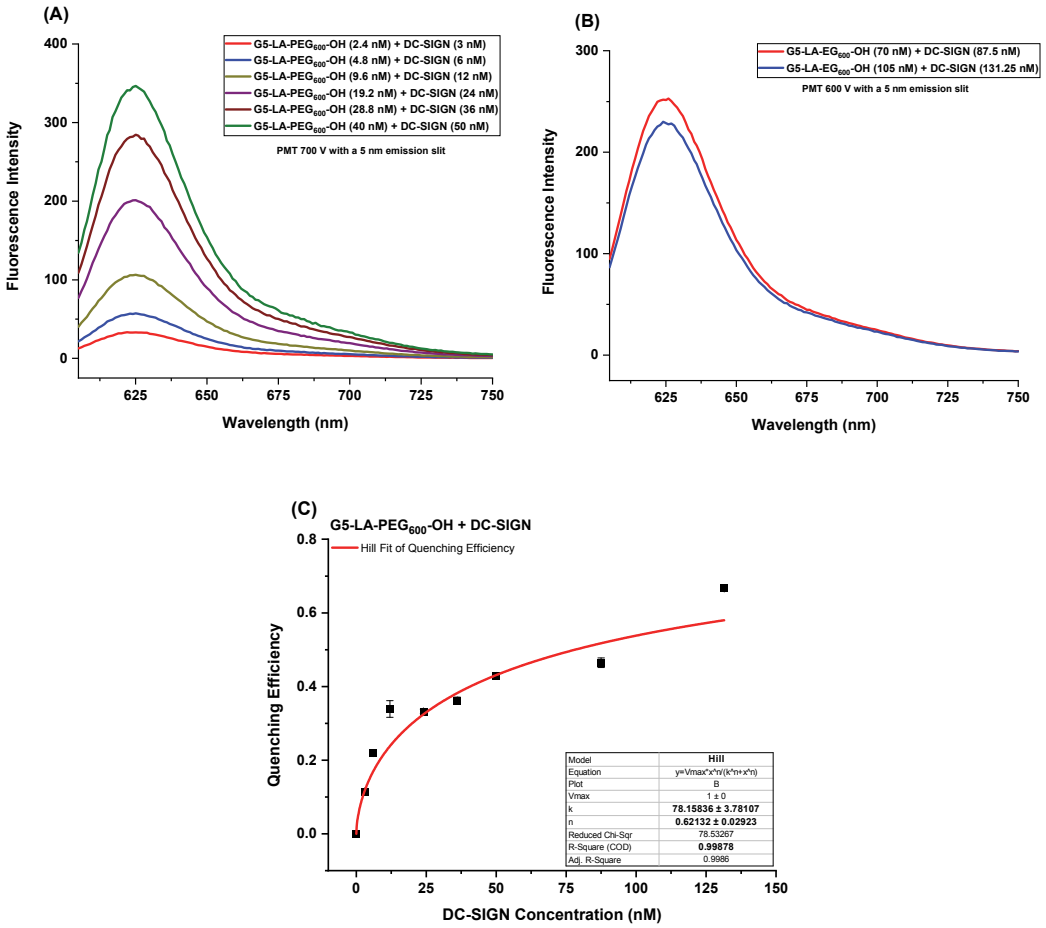

Figure 3.3.3. Fluorescence spectra of (A) G5-LA-PEG_{600}-OH+labelled DC-SIGN using a PMT=700 V and (B) G5-LA-PEG_{600}-OH+labelled DC-SIGN using a PMT=600 V. Each sample was done in duplicate and their average fluorescence spectra was constructed. (C) Percentage fluorescence quenching efficiency curve of G5-LA-PEG_{600}-OH+labelled DC-SIGN. Data fitted by Hill's equation.

Similarly, GNPs coated with LA-PEG_{600}-OH ligands also showed considerable fluorescence quenching with apparent K_d of ~78 nM. This result shows that coating G5 with a shorter PEG ligand cannot completely eliminate the quenching of the DC-SIGN fluorescence, suggesting that DC-SIGN may have some kind of interaction with these PEGylated GNPs, due to possible interaction between the GNP surface OH groups and DC-SIGN mediated by Ca^{2+} ions. Consequently, the multivalent ligands with different PEG density (PEG_{750}) and different functional group (OMe) were produced for further investigations and the interactions between GNPs coated with these ligands and different, non-target proteins BSA and Lysozyme were investigated in detail in **Chapter 5**.

3.3.1.1. Effect of 5 nm GNP Surface Sugar Ligands diluted with DHLA-ZW on Fluorescence Quenching

To probe how GNP surface glycan density impacts DC-SIGN binding, dilution of GNP surface glycan density was carried out using inert DHLA-Zwitterion (DHLA-ZW) ligands, as shown in **Figure 3.3.4**. This was done successfully by mixing a certain amount of the spacer ligand DHLA-ZW in cap exchange reactions of GNPs with glycan ligands. The LA-ZW ligands were first reduced to DHLA-ZW by using dithiothreitol (DTT) in the presence of tetramethyl ammonium hydroxide and then underwent cap exchange reactions.[9] As DHLA-glycans and DHLA-ZW ligands chelate to the GNP surface via the same DHLA units, they should display similar binding affinities with the GNP surface and therefore are not expected to phase separate after coating. Therefore, the GNP surface glycan density can be readily controlled by the DHLA-ZW and DHLA-glycan ligand ratios. Dilution of GNP surface glycan density would increase the distance between the sugar ligands on the GNPs and allow us to investigate how it impacts their binding affinity with DC-SIGN. Based on the previous quantum dot-FRET studies of our research group, we have expected to see a decreased fluorescence quenching upon dilution of GNP surface glycan density. Here, three different GNP surface sugar densities were prepared with DHLA-ZW spacer ligands; GNPs with 75%, 25%, and 10% glycan densities, and their quenching results were compared with those of GNPs coated with 100% LA-EG_2-DiMan ligands. The fluorescence spectra of G5-EG_2-DiMan-ZW+DC-SIGN and their resulting binding curves were given in **Figure 3.3.5**, and Figure **3.3.6** below, respectively, and **Table 3.3.2** shows the relevant fitting parameters.

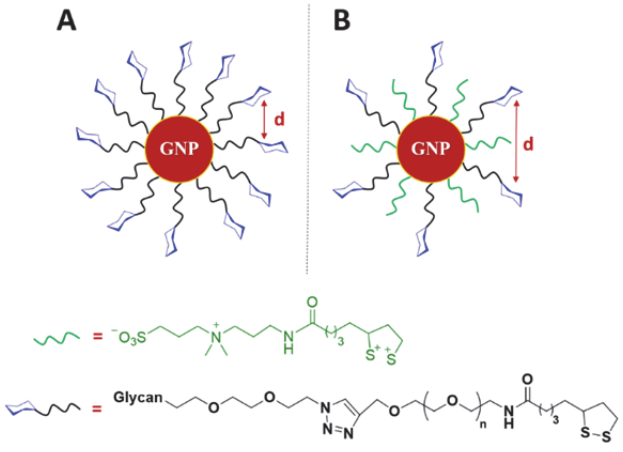

Figure 3.3.4. A schematic representation of modulating inter-glycan distance (d), (A) before and (B) after diluting the GNP surface glycan valency with LA-ZW ligands.

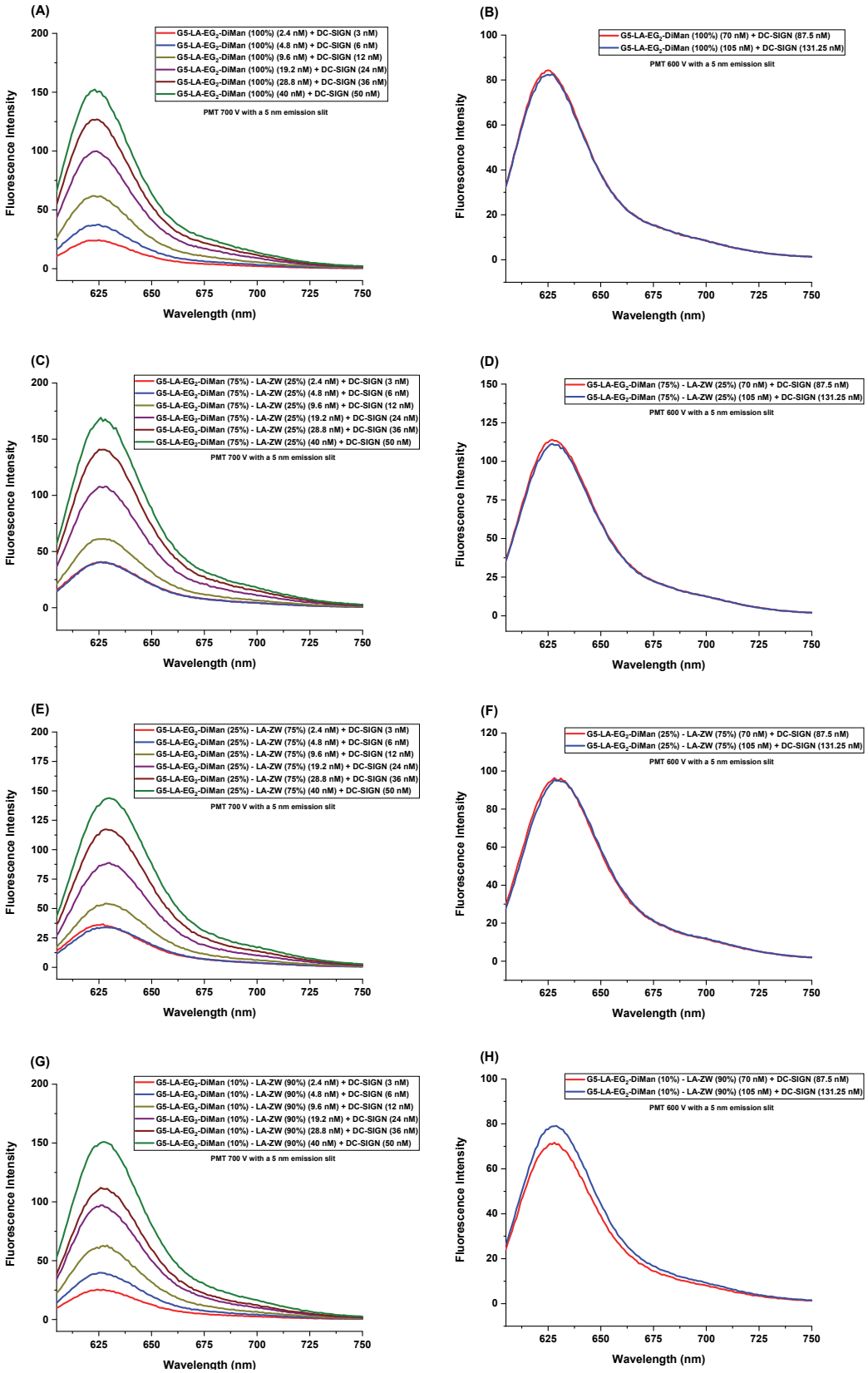

Figure 3.3.5. Fluorescence spectra of (A) G5-EG_2-DiMan (100%)+DC-SIGN using a PMT=700 V; (B) G5-EG_2-DiMan (100%)+DC-SIGN using a PMT=600 V; (C) G5-LA-EG_2-DiMan (75%)–LA-ZW (25%)+ DC-SIGN using a PMT=700 V; (D) G5-LA-EG_2-DiMan (75%)–LA-ZW (25%)+ DC-SIGN using a PMT=600 V; (E) G5-LA-EG_2-DiMan (25%)–LA-ZW (75%)+DC-SIGN using a PMT=700 V; (F) G5-LA-EG_2-DiMan (25%)–LA-ZW (75%)+DC-SIGN using a PMT=600 V; (G) G5-LA-EG_2-DiMan (10%)–LA-ZW (90%)+DC-SIGN using a PMT=700 V; (H) G5-LA-EG_2-DiMan (10%)–LA-ZW (90%)+DC-SIGN using a PMT=600 V. Each sample was done in duplicate and their average fluorescence spectra was constructed.

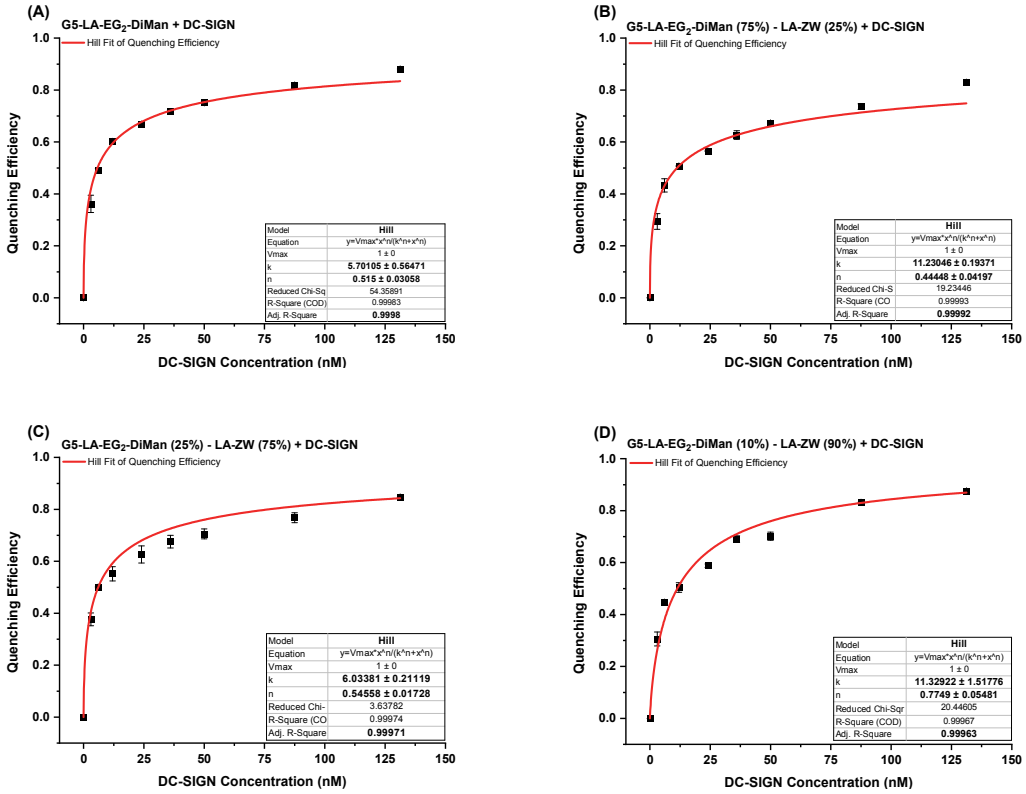

Figure 3.3.6. Percentage fluorescence quenching efficiency curves versus protein concentration. (A) G5-LA-EG_2-DiMan (100%)+DC-SIGN; (B) G5-LA-EG_2-DiMan (75%)-LA-ZW (25%)+DC-SIGN; (C) G5-LA-EG_2-DiMan (25%)-LA-ZW (75%)+DC-SIGN; (D) G5-LA-EG_2-DiMan (10%)-LA-ZW (90%)+DC-SIGN. Data were fitted by Hill's equation.

Table 3.3.2. Summary of Hill's equation fitting parameters for G5-LA-EG_2-DiMan/-LA-ZW conjugates+DC-SIGN binding curves to derive the apparent K_ds.

G5 sample + DC-SIGN	Hill's Equation Fitting Parameters		
	K_d / nM	n	R^2
G5-EG_2-DiMan (100%) + DC-SIGN	5.7 ± 0.5	0.52 ± 0.03	0.999
G5-EG_2-DiMan (75%) – LA-ZW (25%) + DC-SIGN	11.2 ± 0.2	0.44 ± 0.04	0.999
G5-EG_2-DiMan (25%) – LA-ZW (75%) + DC-SIGN	6.1 ± 0.2	0.55 ± 0.01	0.999
G5-EG_2-DiMan (10%) – LA-ZW (90%) + DC-SIGN	11.3 ± 1.5	0.77 ± 0.05	0.999

G5-LA-EG_2-DiMan (100%) gave strong binding with DC-SIGN as verified from an apparent K_d of 5.7 nM; however, dilution of the GNP surface glycan density using DHLA-ZW ligands did not significantly alter the apparent binding K_ds with DC-SIGN compared to that of G5 covered with 100% glycan ligands, unlike those observed in previous QD-FRET studies.[2] The quenching data obtained from control PEG ligands and GNP surface glycan dilutions were unexpected. Given the universal fluorescence quenching behaviour of GNPs, the possible reason could be the inner filter effect,[10] i.e.

absorption of the excitation wavelength (λ_{ex}: 590 nm) by G5. Therefore, smaller GNPs (*e.g.* < 2 nm) which do not absorb at 590 nm were produced, and their DC-SIGN/R binding interactions were probed to verify this hypothesis.

3.3.2. Fluorescence Quenching of G1.3 with Atto-594 Labelled DC-SIGN/R Binding

Since we hypothesized that the reason behind the unexpected quenching results might be the absorption of GNPs larger than 2 nm at the excitation wavelength (λ_{ex}: 590 nm), we wanted to confirm this by producing GNPs smaller than 2 nm coated with control DHLA-PEG ligands (without terminal glycans). Metallic gold nanoparticles of less than 2 nm in diameter do not exhibit a defined plasmon absorption band and act like molecules, so they are called gold clusters (abbreviated as GNCs hereafter) instead of nanoparticles.[11] 1.3 nm GNC-LA-PEG_{750}-OMe were synthesised and characterised in accordance with this purpose, as described in Chapter 2, and their binding interactions with DC-SIGN/R were then quantified by fluorescence quenching as above. The fluorescence spectra and their fluorescence quenching efficiency curves for 1.3 nm GNC-LA-PEG_{750}-OMe+DC-SIGN/R samples are shown in **Figure 3.3.7** below.

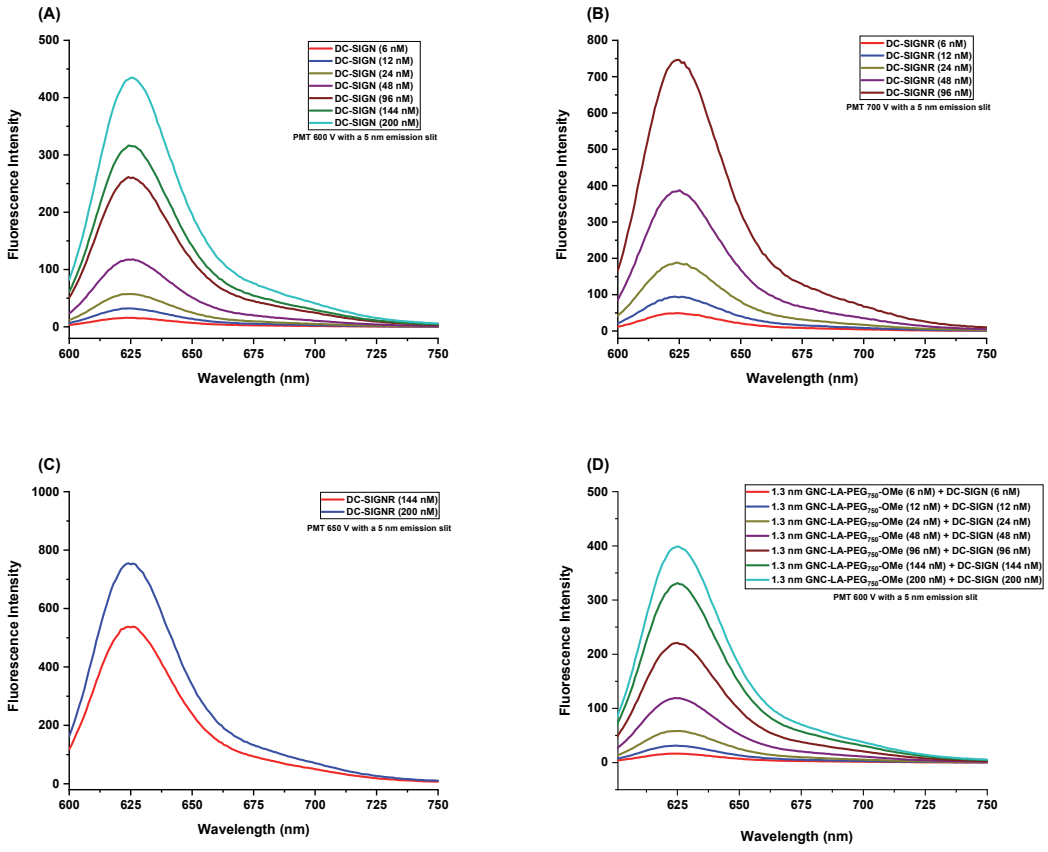

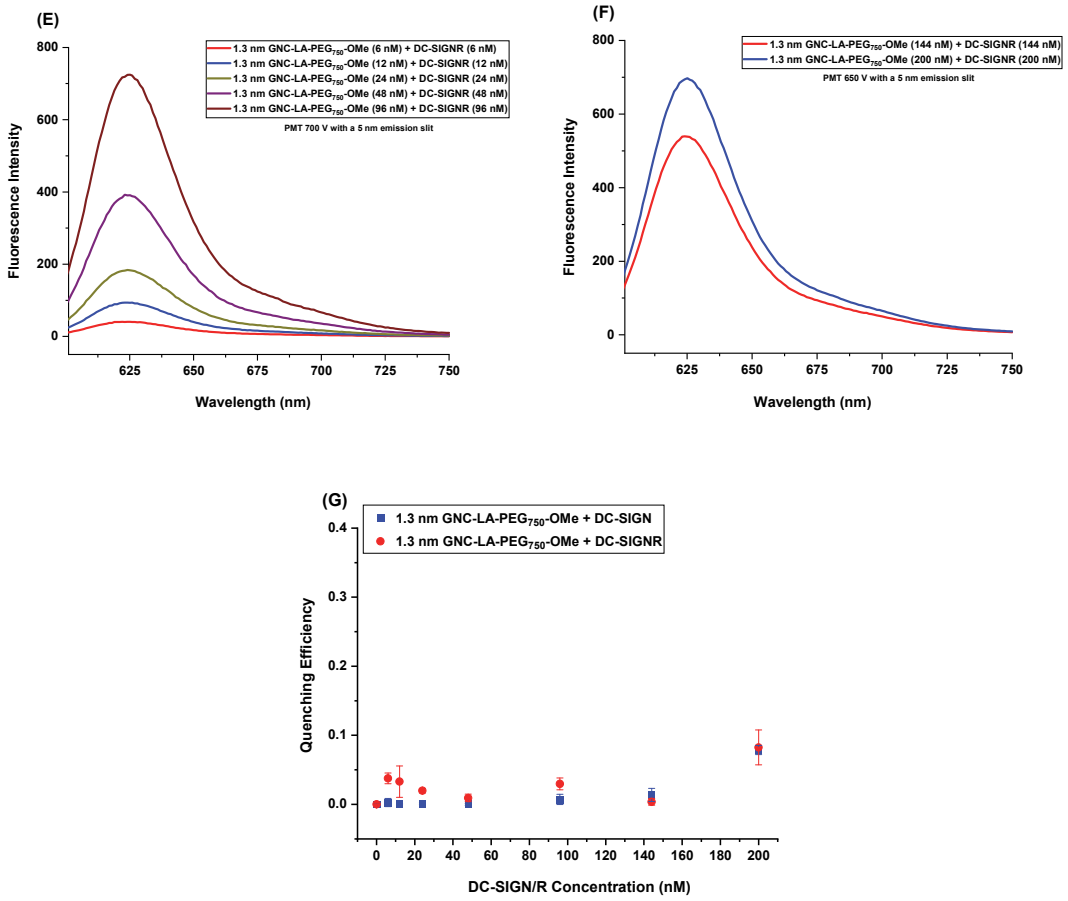

Figure 3.3.7. Fluorescence spectra of (A) DC-SIGN using a PMT=600 V; (B) DC-SIGNR (low concentration) using a PMT=700 V; (C) DC-SIGNR (high concentration) using a PMT=650 V; (D) 1.3 nm GNC-LA-PEG_{750}-OMe + DC-SIGN using a PMT=600 V; (E) 1.3 nm GNC-LA-PEG_{750}-OMe + DC-SIGNR using a PMT=700 V; (F) GNC-LA-PEG_{750}-OMe + DC-SIGNR using a PMT=650 V. Each sample was done in duplicate and their average fluorescence spectra was constructed. (G) The fluorescence quenching efficiency versus the proteins DC-SIGN/R concentration for 1.3 nm GNC-LA-PEG_{750}-OMe. The dots could not be fitted since the fitting programme did not get them to converge correctly in the concentration range studied.

When considering the quenching efficiency results, as expected, 1.3 nm GNCs coated with inert LA-PEG_{750}-OMe did not exhibit significant binding with DC-SIGN/R, where the quenching thus verifying our hypothesis. This confirms that the control ligand coated GNCs did not interact specifically with DC-SIGN/R, and the previous observed fluorescence quenching with DHLA-PEG ligand capped G5s were due to an intrinsic property of G5 (most likely its inner filter effect). The fluorescence quenching data shown in **Figure 3.3.7** remained very close to 0 throughout the concentration range studied.

3.3.3. Fluorescence Quenching for GNP-glycans with Atto-643 labelled DC-SIGN/R

G5s display considerable absorption at 590 nm, the excitation wavelength used in fluorescence measurement of Atto-594 dye-labelled DC-SIGN/R, which can cause

fluorescence quenching via its inner filter effect. To reduce this effect, DC-SIGN/R were labelled with the Atto-643 dye, whose fluorescence can be efficiently excited at 630 nm, to minimise GNP's inner filter effect and to provide more accurate quantification of quenching efficiency. The dye Atto-643, similar to Atto-594, is also highly suitable for fluorescence measurements since it shows an incredibly high fluorescence quantum yield after conjugation to biomolecules. The primary characteristics of the dye Atto-643 include strong absorption, high thermal- and photo-stability, and also high hydrophilicity; thus, it exhibits excellent water solubility and significantly less tendency for unspecific binding. Its absorption and fluorescence spectra are not affected by pH over the range of 2 to 11, making it a highly stable fluorophore under most biological conditions.[12] As Atto-643 can be effectively excited by the longer wavelength than Atto-594 (i.e. ~630 vs 590 nm) where GNPs has much lower absorption, this will significantly reduce the contribution of universal quenching induced by GNP's inner filter effect, and thus enabling us to produce more reliable quenching data.

Here, we probed how GNP scaffold size, ligand linker length, and GNP surface glycan valency affect their binding with DC-SIGN/R via fluorescence quenching. The GNP scaffold size may have a significant impact on the inhibitory properties of GNP-glycans in preventing viral infections. A good multivalent ligand presentation can be created by tuning the dimensions of the GNP scaffold, providing a better spatial topology with target multimeric proteins, thus increasing their binding affinity and selectivity. As most virus surface trimeric glycoprotein spikes are ~12-13 nm in size, for example HIV surface gp120 spikes,[13] a 13 nm GNP (G13) was also produced to mimic virus spikes in addition to the G5 used above. Furthermore, 27 nm GNPs were also synthesised to investigate how GNP size impacts DC-SIGN/R binding. Moreover, the linker length must be well-tuned to reduce non-specific interactions and ensure high stability of GNP-glycan conjugates. A longer EG linker may provide better binding to the targets by increasing glycan flexibility and glycan presentation, but this may also result in more disordered terminal glycans to decrease binding affinity. On the other hand, shortening the EG length may lead to more rigid glycan presentations which may prevent the efficient binding of GNP-glycans with target lectins. The linker length is

therefore another key factor in the design of GNP-glycans for potent, specific lectin targeting. Here, to find out how linker length affects GNP-glycan binding with target lectins the EG linker length was varied from 2 to 4. Finally, the tuning of the sugar density on the GNP surface is also studied. Whilst a low carbohydrate density on GNPs could lead to decreased binding affinity and specificity, a high glycan density does not always result in an enhanced binding affinity either.[14] Therefore, there could be an optimal glycan density on the GNP surface for binding to the target protein receptors. For this purpose, a GNP surface glycan densities of 75%, 50%, and 25% were prepared by diluting the LA-EG_n-glycan ligands using control ligands (LA-EG_n-OH, where n=2 and 4) of the same length to determine how the glycan valency on the GNP surface controls their binding affinity with DC-SIGN/R. In the following section, the binding interactions of 5, 13, and 27 nm GNPs capped with LA-$EG_{2/4}$-Man and -DiMan ligands of varying glycan densities with DC-SIGN/R (labelled with Atto-643) were investigated by fluorescence quenching method.

In order to quantify the apparent binding affinity, K_d, of GNP-glycans with DC-SIGN/R, fluorescence spectra were recorded over a range of increasing protein concentrations at a fixed GNP-glycan concentration. The reason behind this is that as GNP size increases, its molar extinction coefficient increases linearly with the cubic of the GNP diameter,[15] resulting in greatly increased absorption (hence inner filter effect) which can interfere binding quantification by fluorescence quenching for the bigger GNPs. To overcome this problem, fixed concentrations of 10, 4, and 0.5 nM for the 5, 13, and 27 nm GNPs were used in fluorescence quenching experiments, respectively. Fluorescence data were recorded using a fixed excitation wavelength (λ_{ex}) of 630 nm and emission spectra over 643-800 nm for Atto-643 under fixed excitation and emission slit widths of 5 nm and a slow scan speed. Fluorescence intensity was measured with the following protein:GNP molar ratio: 1, 2, 4, 8, and 16 for G5-glycans; 1, 2, 4, 8, 16, and 32 for G13-glycans; and 4, 8, 16, 32, and 64 for G27-glycans to find out the fluorescence intensity-concentration relationships for both DC-SIGN/R with and without the GNP-glycans. As shown in **Figure 3.3.8**, fluorescence spectra were then integrated between 643 nm and 800 nm and were used to calculate the resulting

fluorescence quenching efficiency (QE) as shown in the equation given in **Figure 3.3.8** below. The QE here represents the percentage of proteins bound to GNP-glycans.

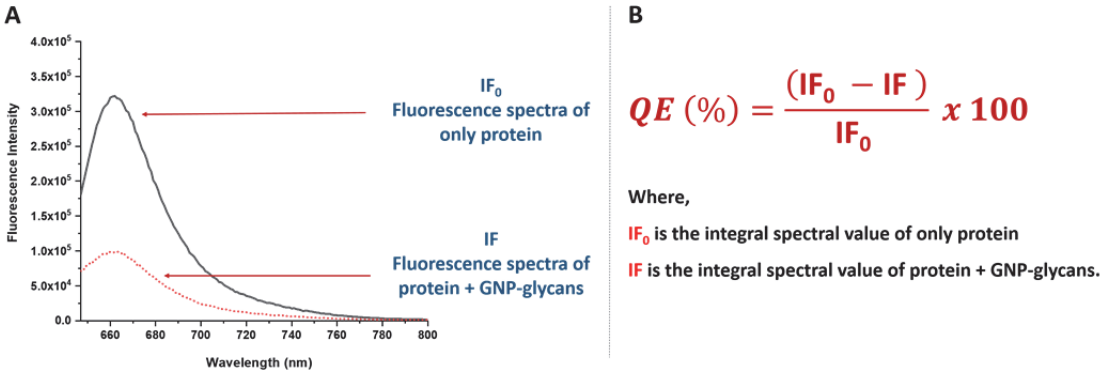

Figure 3.3.8. (A) Fluorescence spectra of dye-labelled proteins recorded with and without GNP-glycan. (B) The equation for calculating the percentage quenching efficiency.

QE x protein concentrations were then plotted against protein concentrations, and then the slopes of the plots were determined for each GNP-glycan binding with DC-SIGN/R. As GNPs are efficient fluorescence quenchers where bound proteins are expected to be quenched, the slope values therefore represent the percentage of the bound proteins on GNPs. Eventually, the binding affinities (K_ds) were calculated by using the following equation, where C is the GNP-glycan concentration.

$$K_d = \frac{[\, C\ x\ (1 - slope)^2\ ]}{slope}$$

3.3.3.1. Binding Interactions of G5-glycans with Atto-643 labelled DC-SIGN/R

The binding interactions of G5-EG_2-Man/-DiMan/-ManA and G5-EG_4-Man/-DiMan conjugates with DC-SIGN/R were investigated via fluorescence quenching following the procedure described above. Fluorescence spectra were recorded at a fixed G5-glycan concentration of 10 nM with increasing protein concentrations (Protein: GNP molar ratios of 1, 2, 4, 8, and 16). The measurements were performed in a binding buffer containing 1 mg/mL BSA to reduce non-specific absorption on GNP and protein surfaces. In addition, interactions of GNPs coated with terminal glycan-free negative control ligands (-OH ligands) with DC-SIGN/R were also determined in order to eliminate the GNP inner filter effect and thereby determine specific binding. The fluorescence spectra for G5-EG_4-DiMan + DC-SIGN/R samples are shown in **Figure**

3.3.9, and the rest of those for other G5-glycan+DC-SIGN/R samples are given in **Appendix A.2**.

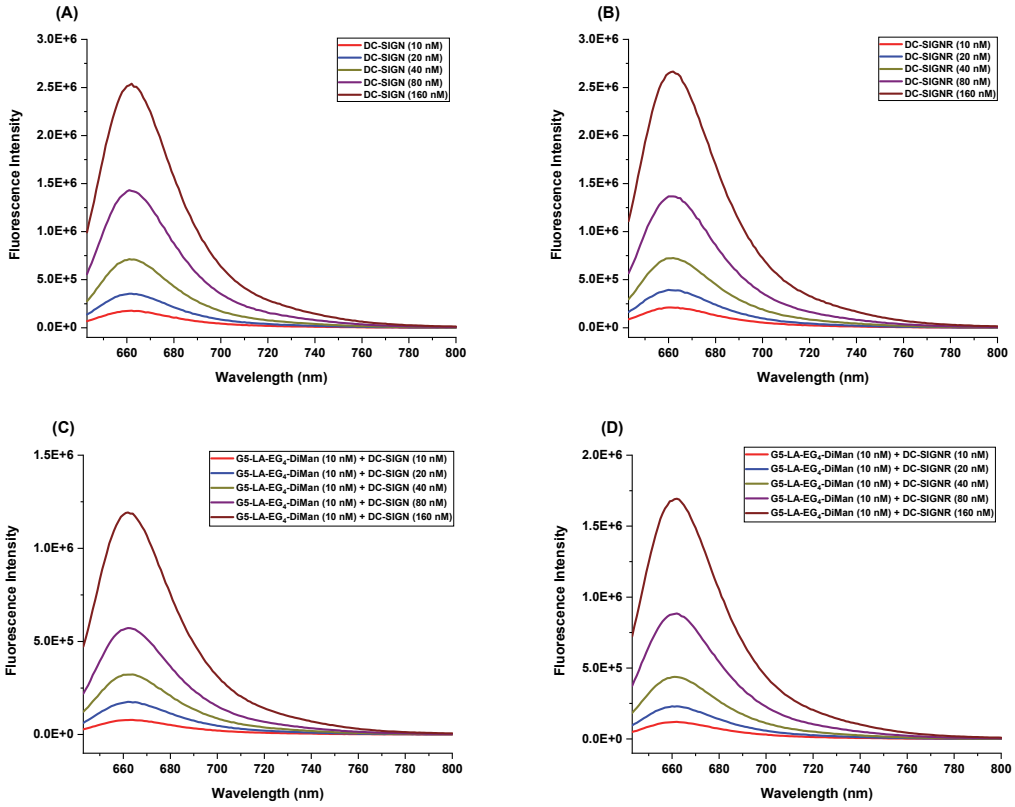

Figure 3.3.9. The fluorescence spectra of (A) DC-SIGN; (B) DC-SIGN/R; (C) G5-EG_4-DiMan+DC-SIGN; (D) G5-EG_4-DiMan+DC-SIGNR. Each concentration was done in duplicate and their average fluorescence spectra was constructed.

After calculating the integral values of the fluorescence spectra, their QE% was quantified, and QE x protein concentrations versus protein concentration plots were constructed to determine slope values, as given in **Figure 3.3.10**. As the fluorescence intensity is directly proportional to the protein concentration in the sample, QE values observed at increasing protein: GNP molar ratios are only accurate at linear range as shown in the plots in **Figure 3.3.10** below; any deviation from the linearity indicates the change of binding. The linearity is also an indicator of the consistency of measurements over the entire range, and the closer value of R^2 is to 1 shows the better the fit of the line to the data. The apparent binding K_ds were calculated after subtracting the correction factor of 5 nm GNP inner filter effect obtained using G5-OH conjugate from the normal slopes. The calculated apparent binding K_d for each G5-glycans with DC-SIGN/R with the fitting parameters can be seen in **Table 3.3.3** below.

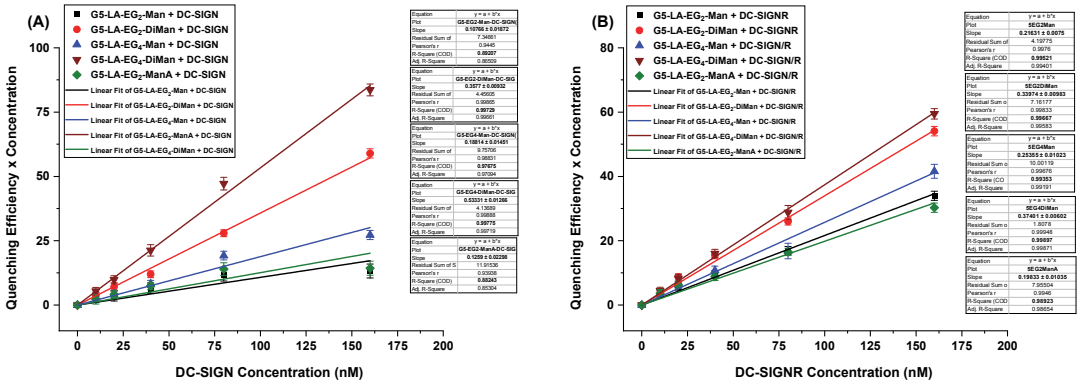

Figure 3.3.10. The QE x protein concentration versus protein concentration plots of (A) G5-glycans+DC-SIGN and (B) G5-glycans+DC-SIGNR.

Table 3.3.3. The linear fitting parameters of QE x protein concentration versus protein concentration plots for G5-glycans+DC-SIGN/R after subtracting the correction factor for minimising 5 nm GNP inner filter effects.

G5-glycan + Protein	Fitting Parameters		
	Slope	R^2	K_d / nM
G5-EG_2-Man – DC-SIGN	0.047 ± 0.018	0.892	193.2 nM
G5-EG_2-DiMan – DC-SIGN	0.297 ± 0.010	0.997	16.6 nM
G5-EG_2-ManA – DC-SIGN	0.066 ± 0.023	0.882	132.1 nM
G5-EG_4-Man – DC-SIGN	0.128 ± 0.014	0.976	59.4 nM
G5-EG_4-DiMan – DC-SIGN	0.473 ± 0.012	0.997	5.8 nM
G5-EG_2-Man – DC-SIGNR	0.156 ± 0.007	0.995	45.6 nM
G5-EG_2-DiMan – DC-SIGNR	0.279 ± 0.011	0.996	18.6 nM
G5-EG_2-ManA – DC-SIGNR	0.138 ± 0.010	0.990	53.8 nM
G5-EG_4-Man – DC-SIGNR	0.193 ± 0.010	0.993	33.7 nM
G5-EG_4-DiMan – DC-SIGNR	0.314 ± 0.006	0.998	14.9 nM

Based on the apparent binding K_ds shown in **Table 3.3.3**, three notable conclusions can be drawn for G5-glycans with DC-SIGN/R binding: (1) Changing the sugars on the 5 nm GNP surface from monosaccharide mannose or carboxylated mannose to disaccharide mannose resulted in significantly increased binding affinity for both lectins. This result agrees well with those reported in literature.[16] This may be due to more DiMan sugars can bind to secondary binding sites of CRDs in DC-SIGN/R along with their primary binding sites, (2) G5-EG_4-DiMan displayed stronger binding with DC-SIGN than with DC-SIGNR (K_d of 5.8 *vs.* ~15 nM), which is similar with the previous results with QDs and GNPs of our group. 3) Increasing the linker chain length from 2 to 4 EG units resulted

increased binding affinity for both DC-SIGN and DC-SIGNR. This shows that a glycan ligand with a slightly longer linker on the 5 nm GNP scaffold favours the spatial and orientational match with CRDs in DC-SIGN/R, possibly by providing the terminal glycans with better flexibility.

3.3.3.2. Binding Interactions of G13-glycans with Atto-643 labelled DC-SIGN/R

The binding interactions of G13-EG_2-Man/-DiMan/-ManA and G13-EG_4-Man/-DiMan conjugates with DC-SIGN/R were investigated via fluorescence quenching following the same procedure. Fluorescence spectra were first recorded at a fixed G13-glycan concentration of 4 nM with increasing protein concentrations (Protein: GNP molar ratios of 1, 2, 4, 8, 16, and 32). The measurements were performed in a binding buffer containing 1 mg/mL BSA to reduce non-specific absorption on GNP and protein surfaces. In addition, interactions of GNPs coated with terminal glycan-free negative control ligands (-OH ligands) with DC-SIGN/R were also determined in order to eliminate the GNP inner filter effect and thereby determine specific binding. GNP-glycans diluted to 75%, 50% and 25% of surface glycan density were also tested to probe the effects of surface sugar valency for 13 nm GNPs on DC-SIGN/R binding. The fluorescence spectra for DC-SIGN/R and G13-EG_4-DiMan + DC-SIGN/R samples are shown in **Figure 3.3.11**, **Figure 3.3.12**, and **Figure 3.3.13**, respectively, and the rest of those for other G13-glycan+DC-SIGN/R samples are given in **Appendix A.3**.

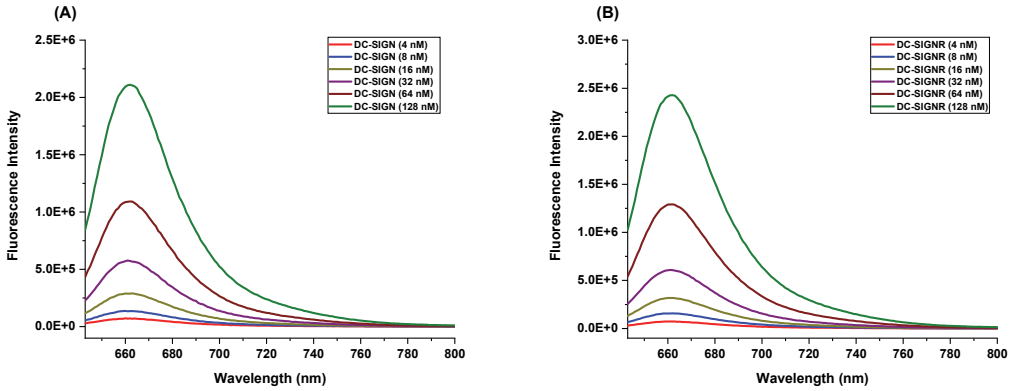

Figure 3.3.11. Fluorescence spectra of the labelled DC-SIGN (A) and DC-SIGNR (B) at the corresponding concentrations.

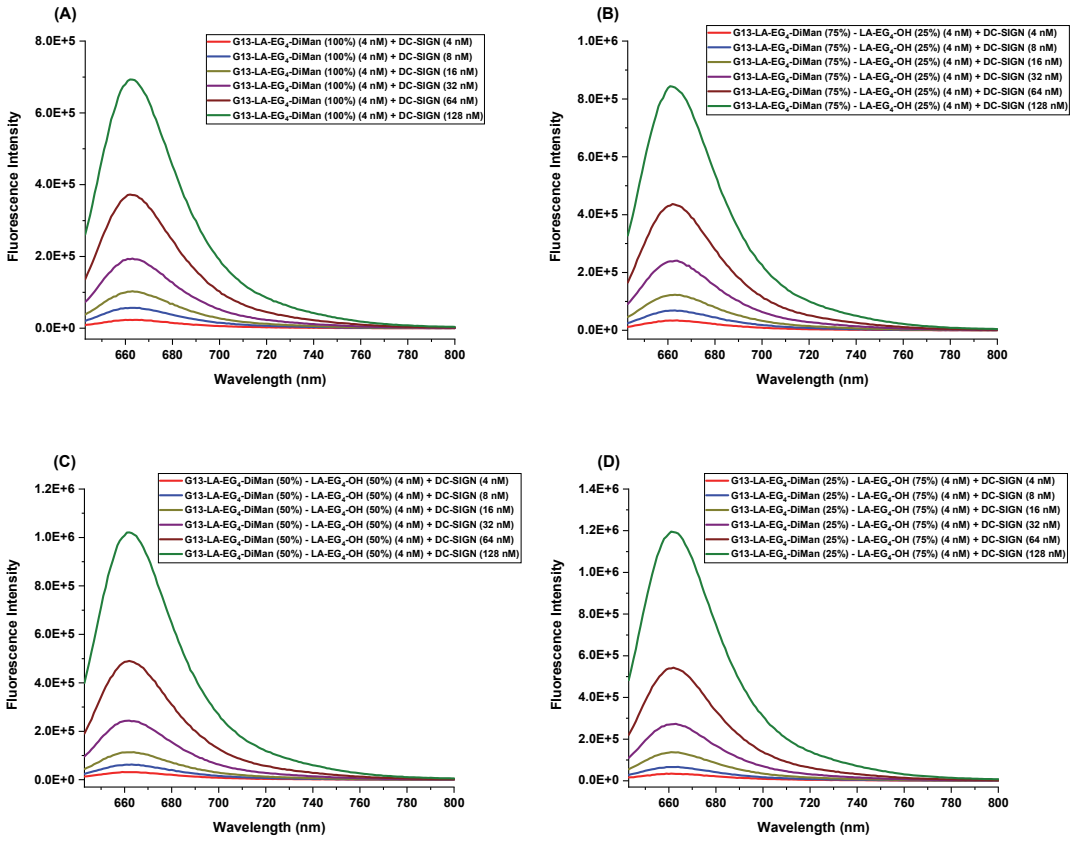

Figure 3.3.12. The fluorescence spectra of (A) G13-EG_4-DiMan (100%)+DC-SIGN; (B) G13-EG_4-DiMan(75%)-LA-EG_4-OH(25%)+DC-SIGN; (C) G13-EG_4-DiMan(50%)-LA-EG_4-OH(50%)+DC-SIGN; (D) G13-EG_4-DiMan(25%)-LA-EG_4-OH(75%)+DC-SIGN. Each concentration was done in duplicate and their average fluorescence spectra was constructed.

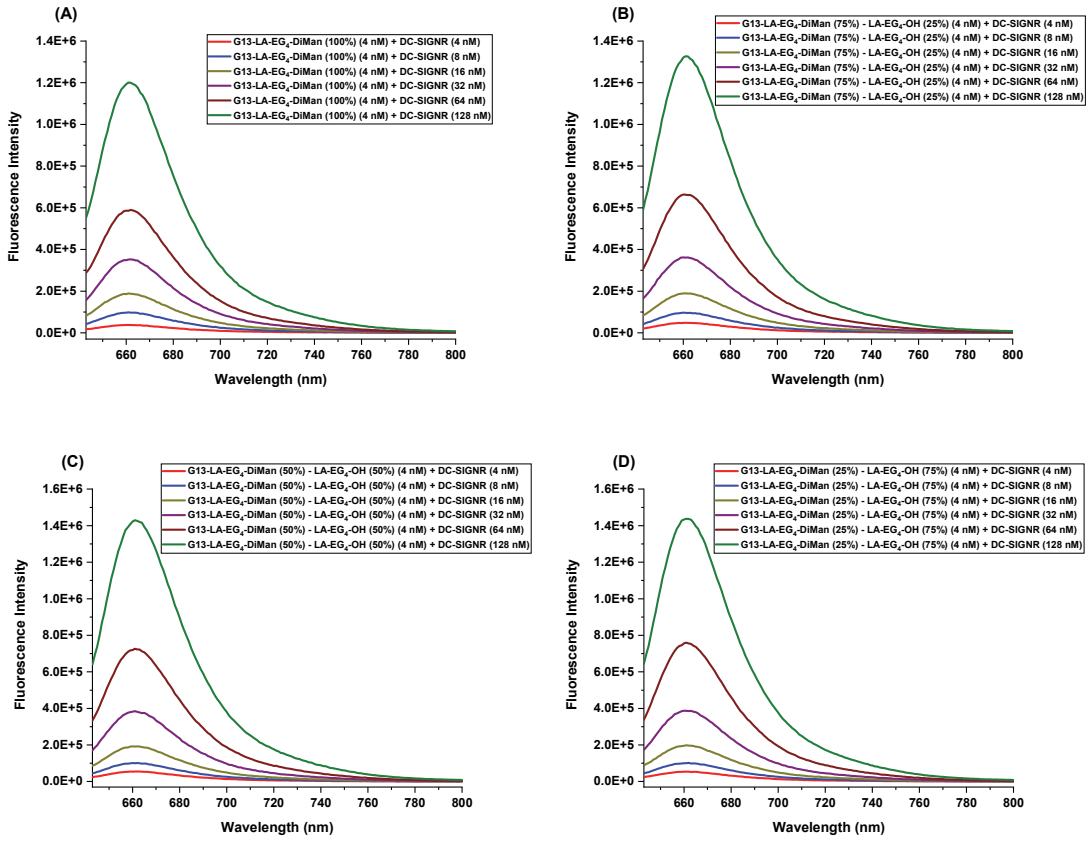

Figure 3.3.13. The fluorescence spectra of (A) G13-EG_4-DiMan (100%)+DC-SIGNR; (B) G13-EG_4-DiMan(75%)-LA-EG_4-OH(25%)+DC-SIGNR; (C) G13-EG_4-DiMan(50%)-LA-EG_4-OH(50%)+DC-SIGNR; (D) G13-EG_4-DiMan(25%)-LA-EG_4-OH(75%)+DC-SIGNR. Each concentration was done in duplicate and their average fluorescence spectra was constructed.

QE was then calculated from the obtained fluorescence spectra, and the linear plots of QE x protein concentrations versus protein concentration were established to determine slope values. As can be seen in **Figure 3.3.14**, the slope decreases with the reduction of the GNP surface glycan density, suggesting that the binding affinity to DC-SIGN/R decreases with the reducing sugar valency on GNPs. The calculated apparent binding K_d for each G13-glycans with DC-SIGN/R and the fitting parameters were given in **Table 3.3.4** and **Table 3.3.5** below, respectively.

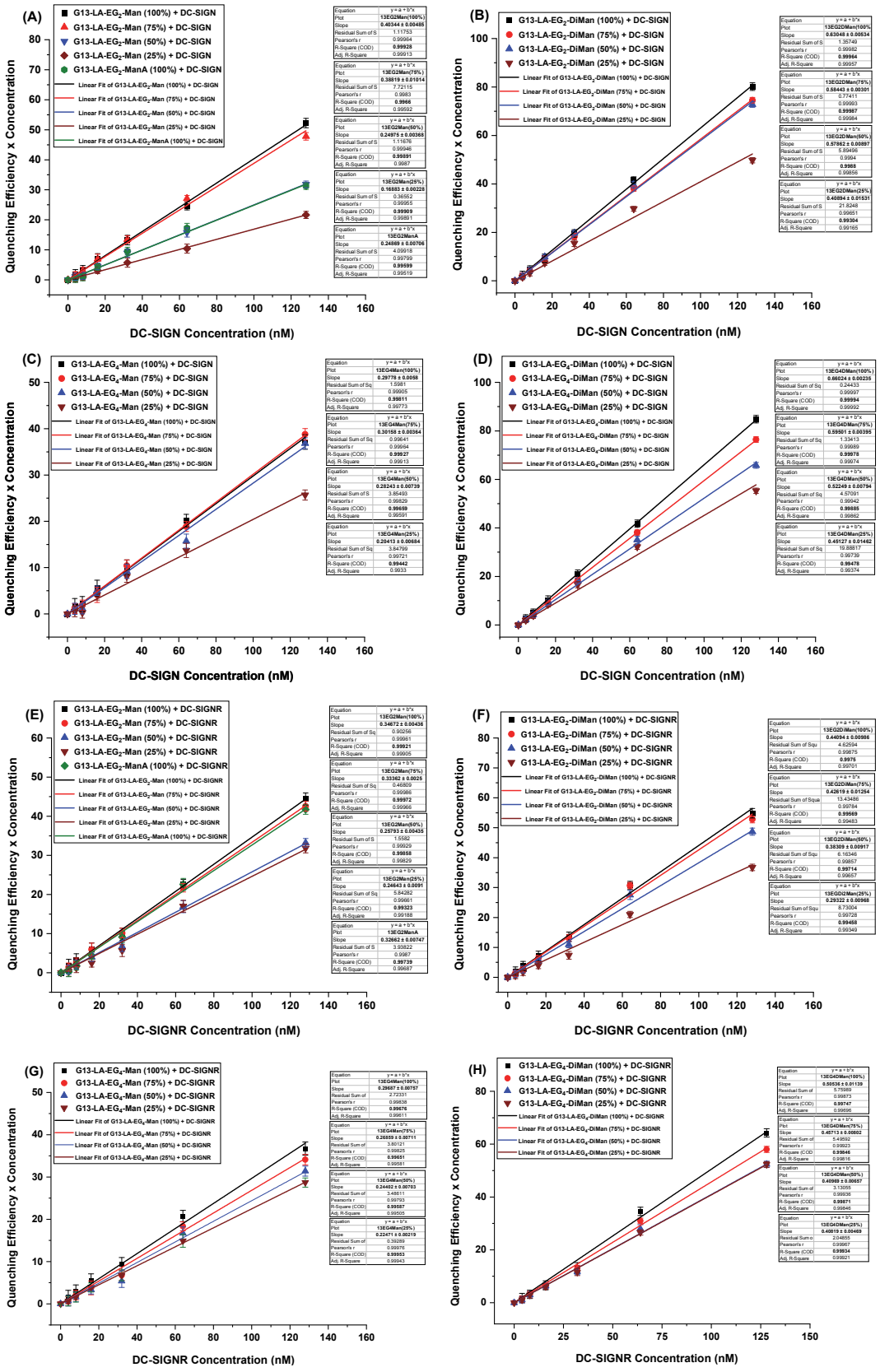

Figure 3.3.14. The QE x protein concentration versus protein concentration plots of (A) G13-EG_2-Man conjugates+DC-SIGN; (B) G13-EG_2-DiMan conjugates+DC-SIGN; (C) G13-EG_4-Man conjugates+DC-SIGN; (D) G13-EG_4-DiMan conjugates+DC-SIGN; (E) G13-EG_2-Man conjugates+DC-SIGNR; (F) G13-EG_2-DiMan conjugates+DC-SIGNR; (G) G13-EG_4-Man conjugates+DC-SIGNR; (H) G13-EG_4-DiMan conjugates+DC-SIGNR.

Table 3.3.4. The linear fitting parameters of QE x protein concentration versus protein concentration plots for G13-glycans+DC-SIGN after subtracting the correction factor for minimising 13 nm GNP inner filter effects.

G13-glycan + DC-SIGN	Fitting Parameters		
	Slope	R^2	K_d / nM
G13-EG_2-Man (100%) – DC-SIGN	0.343 ± 0.004	0.999	5.0 nM
G13-EG_2-Man (75%) – DC-SIGN	0.358 ± 0.003	0.999	4.6 nM
G13-EG_2-Man (50%) – DC-SIGN	0.192± 0.006	0.998	13.6 nM
G13-EG_2-Man (25%) – DC-SIGN	0.108 ± 0.002	0.998	29.4 nM
G13-EG_2-DiMan (100%) – DC-SIGN	0.570 ± 0.005	0.999	1.3 nM
G13-EG_2-DiMan (75%) – DC-SIGN	0.524 ± 0.003	0.999	1.7 nM
G13-EG_2-DiMan (50%) – DC-SIGN	0.518 ± 0.010	0.998	1.8 nM
G13-EG_2-DiMan (25%) – DC-SIGN	0.348 ± 0.015	0.993	4.8 nM
G13-EG_4-Man (100%) – DC-SIGN	0.237 ± 0.005	0.998	9.8 nM
G13-EG_4-Man (75%) – DC-SIGN	0.241 ± 0.003	0.999	9.6 nM
G13-EG_4-Man (50%) – DC-SIGN	0.222 ± 0.007	0.996	11.1 nM
G13-EG_4-Man (25%) – DC-SIGN	0.140 ± 0.006	0.994	21.2 nM
G13-EG_4-DiMan (100%) – DC-SIGN	0.603 ± 0.003	0.999	1.0 nM
G13-EG_4-DiMan (75%) – DC-SIGN	0.535 ± 0.004	0.999	1.6 nM
G13-EG_4-DiMan (50%) – DC-SIGN	0.462 ± 0.008	0.998	2.5 nM
G13-EG_4-DiMan (25%) – DC-SIGN	0.391 ± 0.014	0.994	3.8 nM
G13-EG_2-ManA (100%) – DC-SIGN	0.188 ± 0.007	0.995	14.1 nM

Table 3.3.5. The linear fitting parameters of QE x protein concentration versus protein concentration plots for G13-glycans+DC-SIGNR after subtracting the correction factor for minimising 13 nm GNP inner filter effects.

G13-glycan + DC-SIGNR	Fitting Parameters		
	Slope	R^2	K_d / nM
G13-EG_2-Man (100%) – DC-SIGNR	0.286 ± 0.004	0.999	7.1 nM
G13-EG_2-Man (75%) – DC-SIGNR	0.273 ± 0.002	0.999	7.7 nM
G13-EG_2-Man (50%) – DC-SIGNR	0.197 ± 0.004	0.998	13.1 nM
G13-EG_2-Man (25%) – DC-SIGNR	0.186 ± 0.001	0.994	14.2 nM
G13-EG_2-DiMan (100%) – DC-SIGNR	0.381 ± 0.001	0.998	4.0 nM
G13-EG_2-DiMan (75%) – DC-SIGNR	0.353 ± 0.001	0.997	4.7 nM
G13-EG_2-DiMan (50%) – DC-SIGNR	0.323 ± 0.001	0.997	5.6 nM
G13-EG_2-DiMan (25%) – DC-SIGNR	0.233 ± 0.001	0.995	10.1 nM
G13-EG_4-Man (100%) – DC-SIGNR	0.236 ± 0.007	0.996	9.9 nM
G13-EG_4-Man (75%) – DC-SIGNR	0.208 ± 0.007	0.996	12.1 nM
G13-EG_4-Man (50%) – DC-SIGNR	0.184 ± 0.007	0.996	14.4 nM
G13-EG_4-Man (25%) – DC-SIGNR	0.164 ± 0.002	0.999	17.1 nM
G13-EG_4-DiMan (100%) – DC-SIGNR	0.445 ± 0.001	0.997	2.7 nM
G13-EG_4-DiMan (75%) – DC-SIGNR	0.397 ± 0.008	0.998	3.6 nM
G13-EG_4-DiMan (50%) – DC-SIGNR	0.349 ± 0.006	0.998	4.8 nM
G13-EG_4-DiMan (25%) – DC-SIGNR	0.348 ± 0.004	0.999	4.9 nM
G13-EG_2-ManA (100%) – DC-SIGNR	0.241 ± 0.007	0.998	9.6 nM

The obtained apparent binding K_ds (**Table 3.3.4** and **3.3.5**) provide four general conclusions about DC-SIGN/R binding of G13-glycans: (1) As the surface glycan density of G13-glycans increases, their binding K_ds to DC-SIGN/R decreases (binding affinity increases), as expected, (2) G13-EG_4-DiMan (100%) showed stronger binding with both proteins (with K_ds of 1.0 and 2.7 nM for DC-SIGN and DC-SIGNR, respectively) than G13 coated with Man and ManA, suggesting that G13-EG_4-DiMan (100%) may be able to bind to secondary binding sites of CRDs in DC-SIGN/R, similar to that observed with G5-EG_4-DiMan, (3) G13-DiMan (100%) exhibited stronger binding with DC-SIGN than DC-SIGNR, which also agreed well with the results observed for G5-DiMan, (4) The EG linker length in G13-glycans also has a significant impact on their DC-SIGN/R binding properties. Increasing the linker length from 2 to 4 EG units in G13-glycans resulted in stronger binding affinity for both proteins. This may indicate that 4 EG units can set off the better spatial topology and orientational match for G13-DiMan's terminal glycans for interacting with both proteins.

3.3.3.3. Binding Interactions of G27-glycans with Atto-643 labelled DC-SIGN/R

The binding interactions of G27-$EG_{2/4}$-Man/-DiMan conjugates with DC-SIGN/R were investigated via fluorescence quenching following the same procedure. Fluorescence spectra were first recorded at a fixed G13-glycan concentration of 4 nM with increasing protein concentrations (Protein: GNP molar ratios of 2, 4, 8, 16, 32 and 64). The measurements were performed again in a binding buffer containing 1 mg/mL BSA to reduce non-specific absorption on GNP and protein surfaces. In addition, interactions of GNPs coated with terminal glycan-free negative control ligands (-OH ligands) with DC-SIGN/R were also determined in order to eliminate the GNP inner filter effect and thereby determine specific binding. GNP-glycans diluted to 75%, 50% and 25% of surface glycan density were also tested to probe the effects of surface sugar valency for 27 nm GNPs on DC-SIGN/R binding. The fluorescence spectra for DC-SIGN/R and G27-EG_4-DiMan + DC-SIGN/R samples are shown in **Figure 3.3.15**, **Figure 3.3.16**, and **Figure 3.3.17**, respectively, and the rest of those for other G13-glycan+DC-SIGN/R samples are given in **Appendix A.4**.

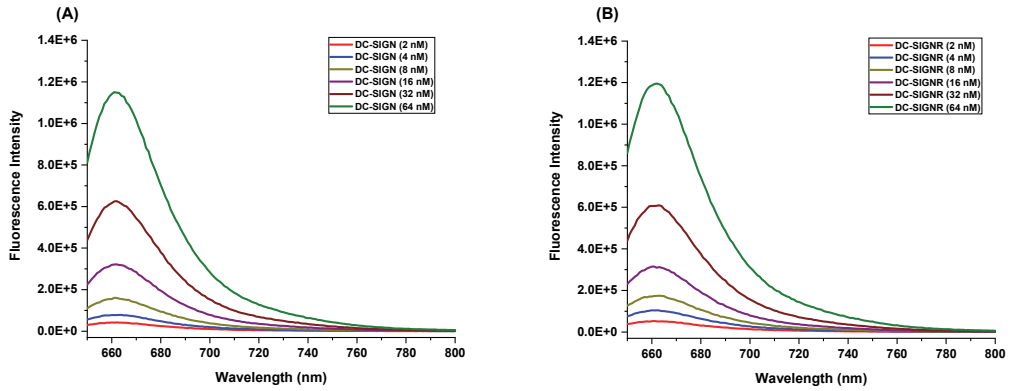

Figure 3.3.15. Fluorescence spectra of the labelled DC-SIGN (A) and DC-SIGNR (B) at the corresponding concentrations.

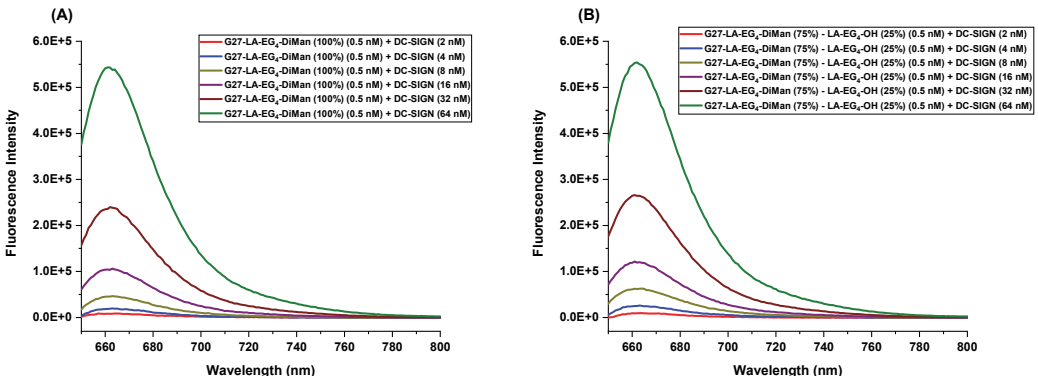

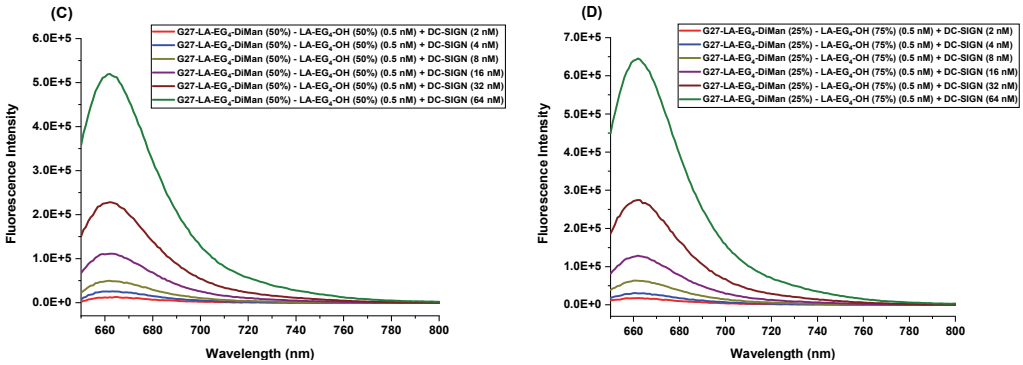

Figure 3.3.16. The fluorescence spectra of (A) G27-EG_4-DiMan (100%) + DC-SIGN; (B) G27-EG_4-DiMan(75%)-LA-EG_4-OH(25%) + DC-SIGN; (C) G27-EG_4-DiMan(50%)-LA-EG_4-OH(50%) + DC-SIGN; (D) G27-EG_4-DiMan(25%)-LA-EG_4-OH(75%) + DC-SIGN. Each concentration was done in duplicate and their average fluorescence spectra was constructed.

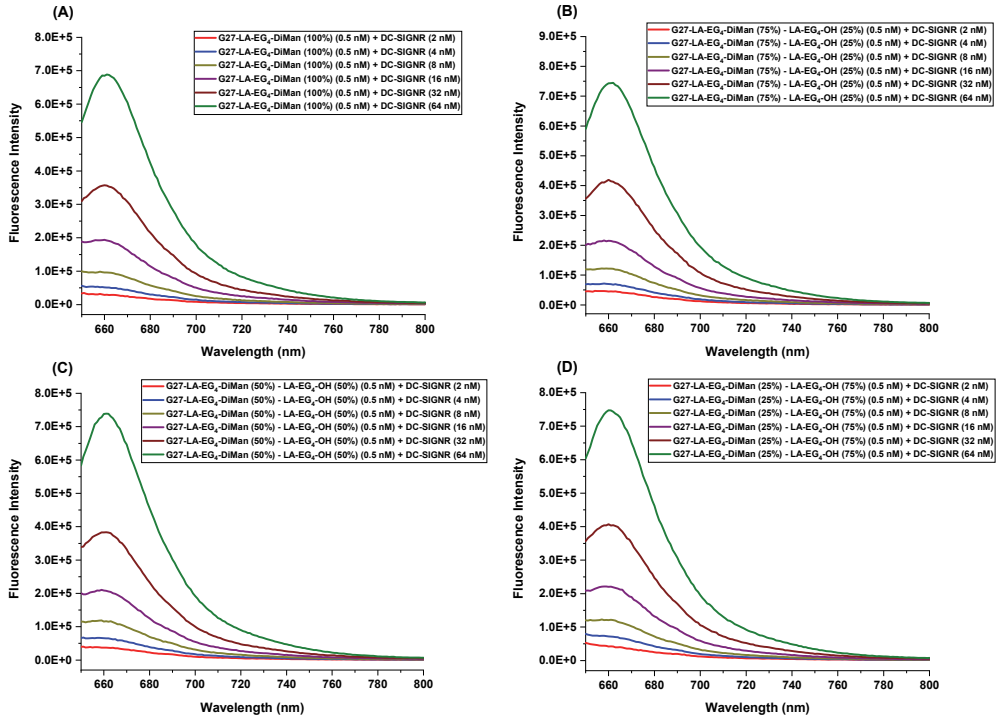

Figure 3.3.17. The fluorescence spectra of (A) G27-EG_4-DiMan (100%) + DC-SIGNR; (B) G27-EG_4-DiMan(75%)-LA-EG_4-OH(25%) + DC-SIGNR; (C) G27-EG_4-DiMan(50%)-LA-EG_4-OH(50%) + DC-SIGNR; (D) G27-EG_4-DiMan(25%)-LA-EG_4-OH(75%) + DC-SIGNR. Each concentration was done in duplicate and their average fluorescence spectra was constructed.

After determining the integral values of the fluorescence spectra, as in G5- and G13-glycans, QE was calculated, and then QE x protein concentration versus protein concentration plots were constructed. As given in **Figure 3.3.18** below, the slope values for G27-glycans show the same trend as G13-glycans; the lower the sugar density on the surface of 27 nm GNPs the lower the slope values, showing that high sugar density on GNPs increases DC-SIGN/R binding. The calculated apparent binding K_d for each G27-glycans with DC-SIGN/R and the fitting parameters can be seen in **Table 3.3.6** and **Table 3.3.7** below, respectively.

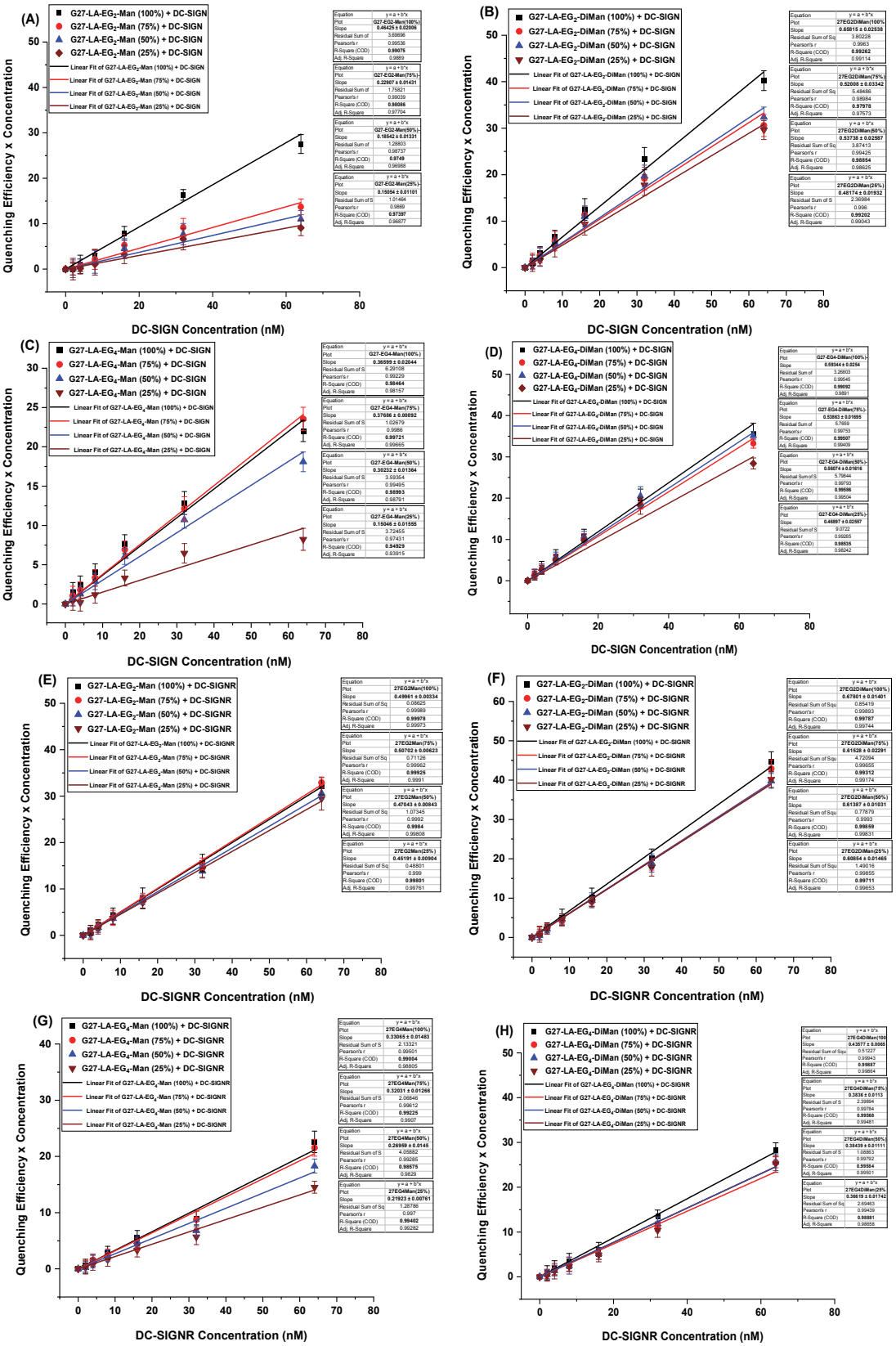

Figure 3.3.18. The QE x protein concentration versus protein concentration plots of (A) G27-EG_2-Man conjugates+DC-SIGN; (B) G27-EG_2-DiMan conjugates+DC-SIGN; (C) G27-EG_4-Man conjugates+DC-SIGN; (D) G27-EG_4-DiMan conjugates+DC-SIGN; (E) G27-EG_2-Man conjugates + DC-SIGNR; (F) G27-EG_2-DiMan conjugates + DC-SIGNR; (G) G27-EG_4-Man conjugates + DC-SIGNR; (H) G27-EG_4-DiMan conjugates + DC-SIGNR.

Table 3.3.6. The linear fitting parameters of QE x protein concentration versus protein concentration plots for G27-glycans+DC-SIGN after subtracting the correction factor for minimising 27 nm GNP inner filter effects.

G27-glycan + DC-SIGN	Fitting Parameters		
	Slope	R^2	K_d / nM
G27-EG_2-Man (100%) – DC-SIGN	0.384 ± 0.002	0.990	0.5 nM
G27-EG_2-Man (75%) – DC-SIGN	0.150 ± 0.014	0.980	2.4 nM
G27-EG_2-Man (50%) – DC-SIGN	0.105 ± 0.013	0.975	3.8 nM
G27-EG_2-Man (25%) – DC-SIGN	0.070 ± 0.011	0.974	6.2 nM
G27-EG_2-DiMan (100%) – DC-SIGN	0.573 ± 0.025	0.993	0.2 nM
G27-EG_2-DiMan (75%) – DC-SIGN	0.435 ± 0.033	0.980	0.36 nM
G27-EG_2-DiMan (50%) – DC-SIGN	0.450 ± 0.025	0.988	0.33 nM
G27-EG_2-DiMan (25%) – DC-SIGN	0.395 ± 0.002	0.992	0.46 nM
G27-EG_4-Man (100%) – DC-SIGN	0.280 ± 0.020	0.985	0.93 nM
G27-EG_4-Man (75%) – DC-SIGN	0.291 ± 0.008	0.997	0.9 nM
G27-EG_4-Man (50%) – DC-SIGN	0.215 ± 0.013	0.990	1.4 nM
G27-EG_4-Man (25%) – DC-SIGN	0.080 ± 0.015	0.950	5.4 nM
G27-EG_4-DiMan (100%) – DC-SIGN	0.523 ± 0.025	0.990	0.2 nM
G27-EG_4-DiMan (75%) – DC-SIGN	0.468 ± 0.017	0.995	0.3 nM
G27-EG_4-DiMan (50%) – DC-SIGN	0.490 ± 0.016	0.995	0.26 nM
G27-EG_4-DiMan (25%) – DC-SIGN	0.400 ± 0.025	0.985	0.45 nM

Table 3.3.7. The linear fitting parameters of QE x protein concentration versus protein concentration plots for G27-glycans+DC-SIGN after subtracting the correction factor for minimising 27 nm GNP inner filter effects.

G27-glycan + DC-SIGNR	Fitting Parameters		
	Slope	R^2	K_d / nM
G27-EG_2-Man (100%) – DC-SIGNR	0.414 ± 0.003	0.999	0.42 nM
G27-EG_2-Man (75%) – DC-SIGNR	0.422 ± 0.006	0.999	0.41 nM
G27-EG_2-Man (50%) – DC-SIGNR	0.390 ± 0.008	0.998	0.5 nM
G27-EG_2-Man (25%) – DC-SIGNR	0.366 ± 0.010	0.998	0.55 nM
G27-EG_2-DiMan (100%) – DC-SIGNR	0.593 ± 0.010	0.997	0.15 nM
G27-EG_2-DiMan (75%) – DC-SIGNR	0.530 ± 0.023	0.993	0.21 nM
G27-EG_2-DiMan (50%) – DC-SIGNR	0.528 ± 0.001	0.998	0.22 nM
G27-EG_2-DiMan (25%) – DC-SIGNR	0.523 ± 0.001	0.997	0.22 nM
G27-EG_4-Man (100%) – DC-SIGNR	0.250 ± 0.014	0.999	1.1 nM
G27-EG_4-Man (75%) – DC-SIGNR	0.240 ± 0.012	0.992	1.2 nM
G27-EG_4-Man (50%) – DC-SIGNR	0.189 ± 0.014	0.985	1.7 nM
G27-EG_4-Man (25%) – DC-SIGNR	0.139 ± 0.007	0.994	2.7 nM
G27-EG_4-DiMan (100%) – DC-SIGNR	0.367 ± 0.006	0.998	0.54 nM
G27-EG_4-DiMan (75%) – DC-SIGNR	0.313 ± 0.011	0.995	0.75 nM
G27-EG_4-DiMan (50%) – DC-SIGNR	0.314 ± 0.011	0.995	0.75 nM
G27-EG_4-DiMan (25%) – DC-SIGNR	0.296 ± 0.017	0.988	0.83 nM

The K_d data for G27-glycans binding with DC-SIGN/R (**Table 3.3.6** and **3.3.7**) give three notable findings: (1) Of the more than 50 different types of GNP-glycans studied in this thesis, G27-EG_4-DiMan (100%) exhibited the strongest binding to DC-SIGN with a K_d of as low as 0.2 nM. This suggests that 27 nm GNP scaffolds covered with 100% of LA-EG_4-DiMan based multifunctional ligand provides a better geometrical and orientational match for binding to DC-SIGN than those for 5 and 13 nm GNP scaffolds. (2) Similarly to those observed for G5- and G13-DiMan, G27-DiMan displayed more robust binding to both proteins with low K_d values than the corresponding G27-Man conjugates, as expected. (3) Increasing the linker length from 2 to 4 EG units does not make a major difference in the binding affinities of G27-glycans with both proteins, suggesting that the sugar ligands on G27 appears to have suitable spatial topology (possibly due to reduced surface curvature) for strong binding with both lectins.

3.4. Mannose Competition Studies

In order to verify whether the fluorescence quenching observed was due to the specific binding between GNP-glycans and DC-SIGN/R, mannose competition studies were performed by adding increasing concentrations of free mannose, which could compete with GNP-glycans in binding to DC-SIGN/R. Also, GNPs coated with LA-EG_n-OH ligands lacking the terminal glycans were used to quantify the non-specific quenching obtained from the inner filter effects of GNPs. Because the absorption of the excitation and emission light by GNPs would decrease the fluorescence intensity of the proteins in the absence of any specific binding, this would yield over-estimation of the actual quenching efficiency induced by binding. Adding free mannose to compete with GNP-glycans for DC-SIGN/R binding would result in reduced fluorescence quenching, and thus recovery of the protein fluorescence. The experiments were done using fixed concentrations of the GNP-glycans and labelled DC-SIGN/R (protein: GNP ratios for G5-, G13-, and G27-DiMan were 5, 10, and 60, respectively) with increasing concentrations of mannose. **Figure 3.4.1** below shows the fluorescence spectra of GNP_n-EG_4-DiMan (n= 5, 13, and 27) and DC-SIGN/R mixture in the presence of varying free mannose concentration. As a control, the fluorescence spectra of the control Gx-EG_4-OH (x= 5, 13, and 27) and DC-SIGN/R mixture in the presence of different mannose competitor was also recorded and shown in **Appendix A.5**.

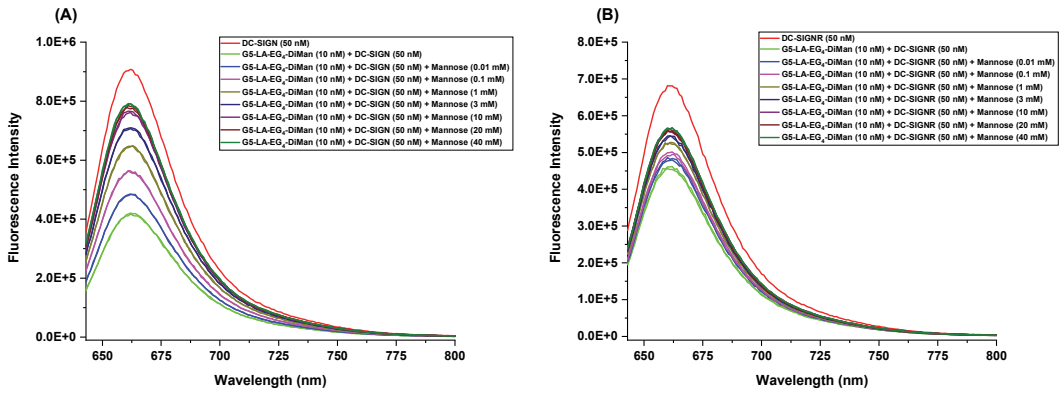

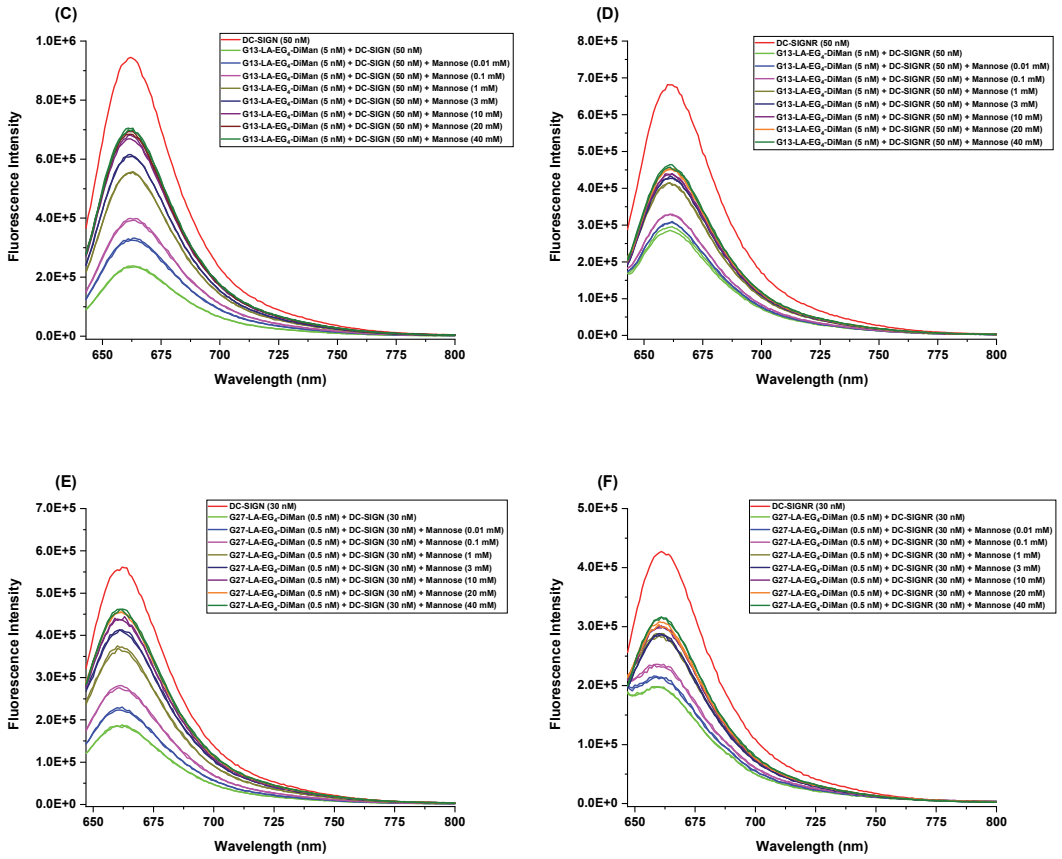

Figure 3.4.1. The fluorescence spectra of GNP-glycan + DC-SIGN/R upon the addition of an increasing concentration of free mannose. (A) G5-EG_4-DiMan + DC-SIGN; (B) G5-EG_4-DiMan + DC-SIGNR; (C) G13-EG_4-DiMan + DC-SIGN; (D) G13-EG_4-DiMan + DC-SIGNR; (E) G27-EG_4-DiMan + DC-SIGN; (F) G27-EG_4-DiMan + DC-SIGNR. Each sample was done in duplicate.

An increase in the fluorescence intensity for both proteins was observed with the increasing mannose concentrations. This confirmed that free mannose effectively competed with GNP-DiMan in binding DC-SIGN/R, and the observed fluorescence quenching for GNP-DiMan and DC-SIGN/R samples are truly due to the specific lectin-glycan interactions. In order to obtain the true quenching data arising from specific binding, the results observed for the GNP-glycans were subtracted by those obtained from the GNP-EG_4-OH controls to correct the contribution from GNP's inner filter effect. The fluorescence recovery was then quantified by the fluorescence intensity ratio of GNP-glycan + DC-SIGN/R with mannose (defined as I) to that without mannose (defined as I_0). The fluorescence recovery ratio (I/I_0-1) versus mannose concentrations plots were then fitted by the Hill equation to derive the maximal fluorescence recovery ratio (Vmax), mannose concentration giving 50% of Vmax (K), and competition coefficient (n) values. **Figure 3.4.2** shows the resulting fluorescence recovery plots as a

function of mannose concentration for each GNP-DiMan with DC-SIGN/R. **Table 3.4.1** below summarizes the fitting parameters of mannose competition assays obtained from the **Figure 3.4.2.**

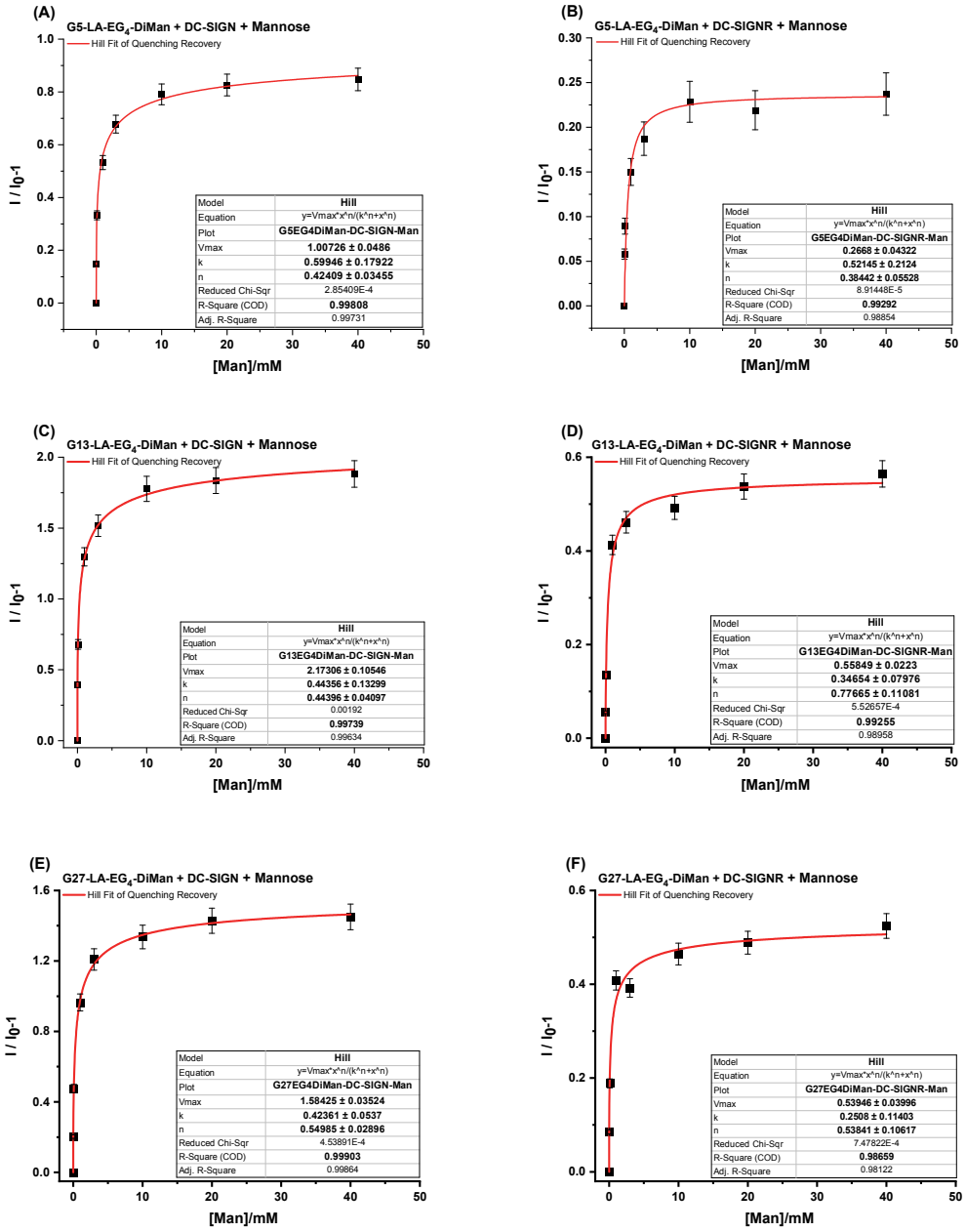

Figure 3.4.2. The plots of the fluorescence recovery ratio (I/I_0-1) versus concentration free mannose for competing against GNP-DiMan binding with DC-SIGN/R. (A) G5-EG_4-DiMan + DC-SIGN; (B) G5-EG_4-DiMan + DC-SIGNR; (C) G13-EG_4-DiMan + DC-SIGN; (D) G13-EG_4-DiMan + DC-SIGNR; (E) G27-EG_4-DiMan + DC-SIGN; (F) G27-EG_4-DiMan + DC-SIGNR. The data were fitted by Hill's equation.

Table 3.4.1. Summary of the fitting parameters for the fluorescence recovery ratio versus free mannose concentration plots.

GNP-glycan + Protein	Hill Fitting Parameters			
	V_{max}	K (mM)	n	R^2
G5-EG_4-DiMan – DC-SIGN	1.01 ± 0.05	0.60 ± 0.18	0.42 ± 0.03	0.998
G5-EG_4-DiMan – DC-SIGNR	0.25 ± 0.04	0.52 ± 0.21	0.38 ± 0.05	0.993
G13-EG_4-DiMan – DC-SIGN	2.17 ± 0.11	0.44 ± 0.13	0.44 ± 0.04	0.997
G13-EG_4-DiMan – DC-SIGNR	0.56 ± 0.02	0.35 ± 0.08	0.78 ± 0.11	0.992
G27-EG_4-DiMan – DC-SIGN	1.58 ± 0.04	0.42 ± 0.05	0.55 ± 0.03	0.999
G27-EG_4-DiMan – DC-SIGNR	0.54 ± 0.04	0.25 ± 0.11	0.54 ± 0.11	0.986

The maximal fluorescence recovery ratios (V_{max}) observed for DC-SIGN are 3-4 fold higher than those of DC-SIGNR for each GNP-DiMan with different sizes, consistent with that DC-SIGN binding gives stronger fluorescence quenching and hence stronger mannose competition-mediated fluorescence recovery. The K values represent the mannose concentration that give 50% of the maximal fluorescence recovery, which are generally higher for DC-SIGN than for DC-SIGNR. This result is also consistent with the higher binding affinity of DC-SIGN over DC-SIGNR in binding with GNP-DiMan observed in the earlier section.

3.5. Binding Mode Investigation of GNP-glycans with DC-SIGN/R

GNP-protein assemblies were probed by measuring their hydrodynamic sizes via dynamic light scattering (DLS) to verify the binding modes of GNP-glycan conjugates with both DC-SIGN and DC-SIGNR. Here, the binding interactions of G13/27-EG_4-DiMan conjugates, which exhibited the most robust binding with DC-SIGN/R in fluorescence quenching studies, were investigated. Firstly, the hydrodynamic sizes (D_hs) of GNP-glycans with wild-type (WT) DC-SIGN/R at various protein: GNP ratios (2, 4, 8, 16, 32, 64, and 128 for 13 nm G13-DiMan and 10, 20, 40, 80, 160, and 320 for G27-DiMan) were monitored to estimate the saturation ratio of the proteins that can pack onto each GNP-glycan surface. GNP-protein interactions were tested in binding buffer (20 mM HEPES, 100 mM NaCl, 10 mM $CaCl_2$, pH 7.8 containing 1 mg/mL BSA) by mixing a fixed concentration of 5 nM for G13-DiMan and 1 nM for G27-DiMan with increasing concentrations of wild-type proteins. The resulting D_h size distribution histograms for

WT-DC-SIGN/R and G13/27-DiMan are given in **Figure 3.5.1**, and all other D_h size histograms for binding interactions of G13/27-DiMan conjugates with native DC-SIGN/R are given in **Appendix A.6**. The D_hs for GNP-protein assemblies at different protein: GNP ratios are summarized in **Figure 3.5.2**.

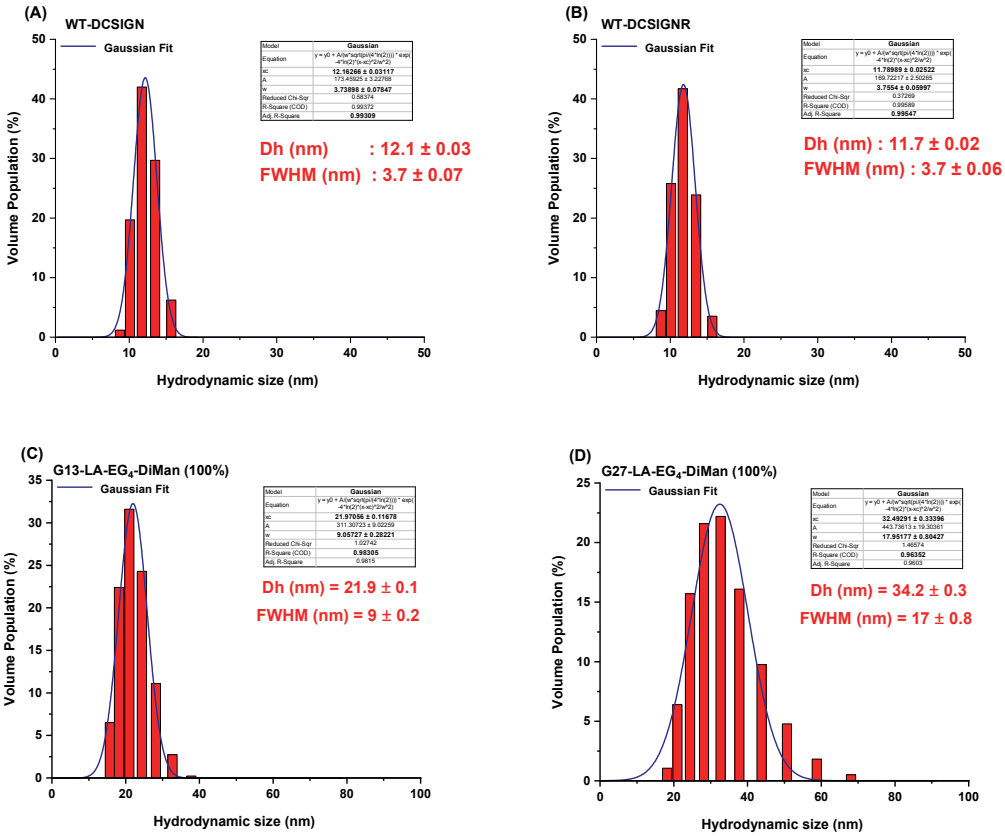

Figure 3.5.1. Hydrodynamic size distribution histograms for (A) wild-type DC-SIGN; (B) wild-type DC-SIGNR; (C) G13-EG_4-DiMan; and (D) G27-EG_4-DiMan. They were fitted by Gaussian function with fitting parameters and data were shown in volume population.

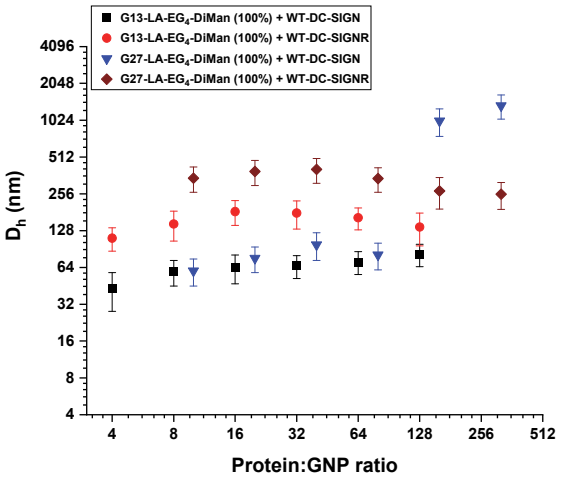

Figure 3.5.2. Summary of the D_h sizes for DC-SIGN/R binding with G13/27-EG_4-DiMan under different protein:GNP ratios. D_h values here are displayed as Mean *D*h ± ½ FWHM. Data were constructed in a $\log_2$-$\log_2$ plot to better show the difference in binding behaviours. Mean D_h= ($xc_1.A_1\%$) + ($xc_2.A_2\%$); FWHM = ($w_1.A_1\%$) + ($w_2.A_2\%$).

Both WT-DCSIGN/R displayed a single D_h species of ~12 nm with a narrow distribution (full width at half-maximum, FWHM= ~3.7 nm). In general, the D_h sizes gradually increased after mixing GNP-DiMan with increasing amounts of proteins, before reaching saturation where roughly constant, D_hs were observed. However, the trend for D_h size evolution *vs.* protein: GNP ratio (PGR) for DC-SIGN was different from DC-SIGNR, the latter consistently yielded larger D_hs than the former (except for G27-DiMan at very high PGR of 160:1 and 320:1). The saturated D_h values for DC-SIGN bound G13-EG_4-DiMan and G27-EG_4-DiMan appeared as ~55 and ~75 nm, respectively, which roughly match those expected for GNP-DiMan bound with a single layer of DC-SIGN molecules. Considering that each CRD and the neck length of tetramer DC-SIGN is ~3 nm and ~25 nm, respectively,[16] and also the D_hs of GNP-glycans, the observed D_hs are consistent with binding. In contrast, the saturated D_hs of the DC-SIGNR bound counterparts (*e.g.* ~200 and ~500 nm) would be too big to be isolated single particles, a strong indication of nanoparticle aggregation of clustering induced by DC-SIGNR-G13/G27-DiMan crosslinking each other, similar to that observed with G5-DiMan previously. Based on the PGR that gave the saturated D_h values, the PGRs of ~32 and ~80 were estimated to be able to completely saturate the binding of G13- and G27-DiMan, respectively.

To verify this, time-dependent DLS studies were performed for G13/27-DiMan with wild-type DC-SIGN/R to monitor their D_h evolution of the resulting GNP-DiMan-lectin complexes over time. The summarized time-dependent D_h data are shown in Figure **3.5.3**, and the detailed time-dependent D_h size distributions are given in **Appendix A.7**.

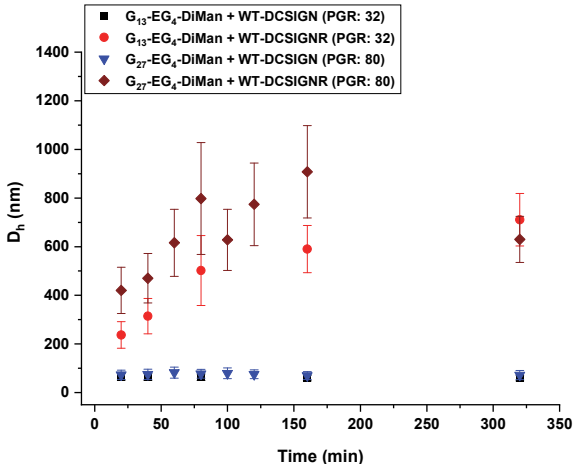

Figure 3.5.3. The summary of the time-dependent D_hs for DC-SIGN/R binding with G13/27-EG_4-DiMan. D_h values here are displayed as Mean *D*h ± ½ FWHM. Data were constructed in a $\log_2$-$\log_2$ plot to better show the difference in binding behaviours. Mean D_h= ($xc_1.A_1$%) + ($xc_2.A_2$%); FWHM = ($w_1.A_1$%) + ($w_2.A_2$%).

The binding of WT-DC-SIGN with G13- and G27-DiMan gave only a single species with a D_h of ~63 nm and ~77 nm, respectively. Moreover, such species formed very rapidly and showed no change of D_h over time. These results suggest that all four binding sites in DC-SIGN CRDs have bound simultaneously to one GNP-DiMan. This would form a single layer protein surrounding the GNP surface and prevent GNPs from approaching to each other, resulting in isolated single GNP-protein assemblies. In contrast, the binding of DC-SIGNR with G13-27-DiMan gave much higher initial D_h values (>200 and > 400 nm for G13-/G27-DiMan, respectively at 20 mins), which also showed significant time dependent increase (i.e. to >600 and 900 nm at 160 min), and finally reached ~700 nm at 320 min. Such D_h sizes were too large to be an individual GNP-protein assemblies. This result clearly indicates that DC-SIGNR and G13/G27-DiMan crosslink each other to form large scale GNP-DC-SIGNR assemblies, which eventually precipitate out of the solution after 5 hours of mixing. In contrast, DC-SIGN-GNP-DiMan assemblies were found to be highly stable and showed no signs of precipitation. Their differences were directly visualised from the optical photos taken with DLS samples at 5 hours post sample preparation shown in **Figure 3.5.4**. Overall, these results revealed that the binding modes of G13/27-DiMan with DC-SIGN and DC-SIGNR are clearly different: all four CRDs in DC-SIGN bind simultaneously (tetravalent binding) to a single GNP-DiMan to form isolated single particles, while DC-SIGNR and GNP-DiMan inter-crosslink each other and form large assemblies. Moreover, their different binding

modes were also verified by TEM imaging of cryo-prepared samples to capture the native dispersion states of GNP-glycans in binding buffer.

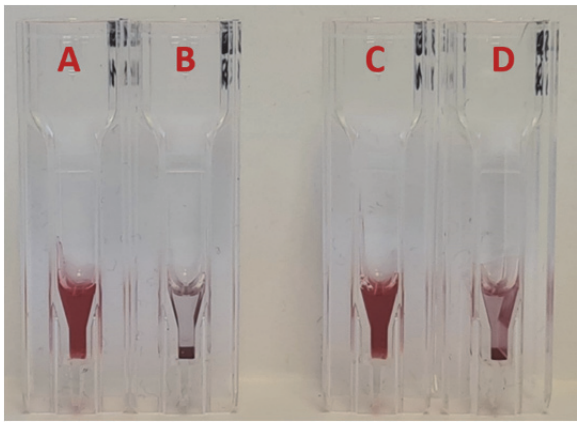

Figure 3.5.4. Photos taken with the DLS samples at 5 hours after mixing GNP-DiMan and proteins. (A) G27-EG_4-DiMan + WT-DC-SIGN (PGR: 80); (B) G27-EG_4-DiMan + WT-DC-SIGNR (PGR: 80); (C) G13-EG_4-DiMan + WT-DC-SIGN (PGR: 32); (D) G13-EG_4-DiMan + WT-DC-SIGNR (PGR: 32).

3.6. Transmission Electron Microscopy for Binding Modes Determination of GNP-DiMan-DC-SIGN/R Assemblies

The exact binding modes of DC-SIGN/R to GNP-glycan were verified by "cryo-snapshot" TEM imaging. This technique has been shown to allow for capturing the native dispersion state of GNP-protein assemblies in solution without drying induced artefacts often observed in conventional TEM imaging. The samples were first vitrified by rapid plunge-freezing into liquid ethane followed by drying under vacuum before being loaded on the grids for cryo-TEM imaging.[8] Here, considering the fluorescence quenching and DLS data, we aimed to determine the binding modes of both proteins with G27-EG_4-DiMan, which gave the strongest binding affinity with DC-SIGN/R. Since the DLS data above showed that saturate binding on G27-EG_4-DiMan was reached at a PGR of 80, both samples were prepared at this PGR. Based on time-dependent DLS data, G27-DiMan was mixed with DC-SIGN/R in binding buffer for 40 mins before being plunge-frozen followed by TEM imaging. Typical cryo-TEM images for the G27-DiMan-DC-SIGN/R assemblies given in **Figure 3.6.1** below were recorded at the same magnification, allowing for easy comparison of the G27-DiMan dispersion state for both samples.

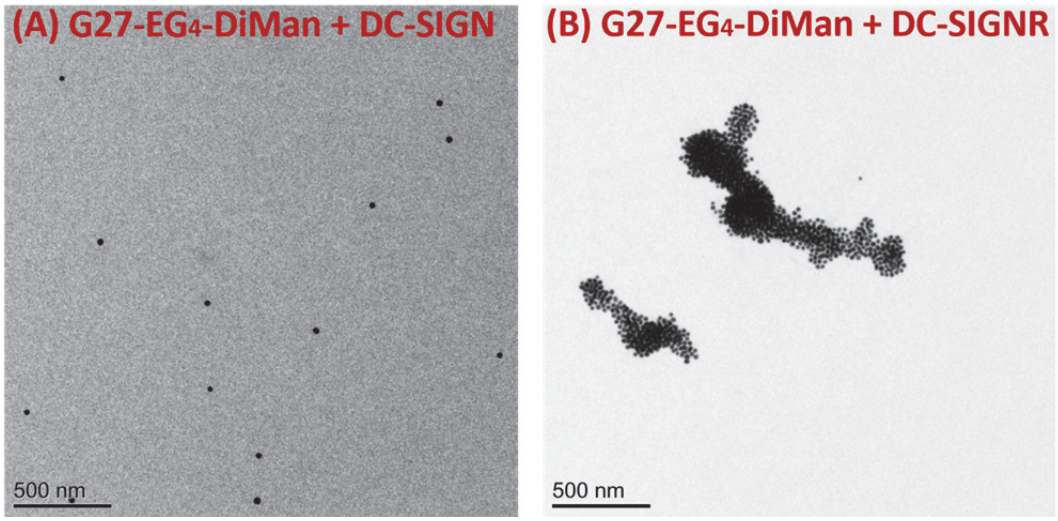

Figure 3.6.1. Cryo-TEM images of G27-EG_4-DiMan after 40 mins incubation with wild-type DC-SIGN (A) and DC-SIGNR (B) at a protein: GNP molar ratio of 80 in binding buffer. Scan bar 500 nm.

The TEM images clearly showed that binding of wild-type DC-SIGN with G27-EG_4-DiMan gave completely dispersed and isolated single particles, whereas binding of wild-type DC-SIGNR produced large-clustered GNP assemblies. These results fully agreed with the DLS observations in which the D_h sizes of G27-DiMan-DC-SIGN and G27-DiMan-DC-SIGNR assemblies were observed at around ~75 nm, and ~420 nm, respectively, 40 minutes after mixing GNPs with proteins. In summary, the combined TEM and DLS results indicate that DC-SIGN and DC-SIGNR have distinct binding modes for G27-DiMan; DC-SIGN binds simultaneously with all 4 binding sites to one GNP-DiMan and forms isolated particles, while DC-SIGNR cross-links with different GNP-DiMans to form extended assemblies. These results are in complete agreement with the previous reports of DC-SIGN/R's different binding modes with G5-DiMan and/or (4 nm) QD-DiMan from our research group.[2, 8] Overall, these results suggest that increasing the GNP scaffold size from 5 nm to 27 nm does not alter the binding mode of DC-SIGN/R with glycan-nanoparticles, although, this can significantly increase their binding affinity. Therefore, the surface curvature of glycan-nanoparticle is important in determining the binding affinity and specificity of multivalent lectin-glycan interactions.

3.7. GNP-glycan Binding Thermodynamics with DC-SIGN/R

The binding thermodynamics of GNP-glycan with DC-SIGN/R were quantified by measuring their temperature-dependent binding affinity through fluorescence quenching. Binding experiments were repeated at three different temperatures (25 ^{o}C, 30 ^{o}C, and 35 ^{o}C) for different-sized GNP-glycan with a high binding affinity (low K_d) with DC-SIGN/R and their controls. Temperature was controlled by dry bath for samples and the cuvette temperature was maintained by using a water pump system. The relevant fluorescence spectra and the QE x protein concentration versus protein concentration plots were given in **Appendix A.8**. The corresponding quenching efficiencies for each GNP-glycan-protein pair were determined using same method as above. Their apparent binding K_ds at the three different temperatures were calculated using the fitting slopes as described in the earlier section and listed in **Table 3.7.1**.

Table 3.7.1. Summary of the apparent binding K_d values of GNP-glycans with DC-SIGN/R at varying temperatures.

GNP-glycans		DC-SIGN		DC-SIGNR	
	T / ^{o}C	K_d / nM	R^2	K_d / nM	R^2
G5-EG$_4$-DiMan	25	5.4 ± 0.2	0.999	15.8 ± 0.8	0.997
	30	8.5 ± 0.1	0.999	17.6 ± 1.2	0.997
	35	26.3 ± 1.8	0.994	22 ± 1.6	0.998
G13-EG$_4$-DiMan	25	1.4 ± 0.03	0.999	2 ± 0.07	0.999
	30	1.8 ± 0.06	0.999	2.8 ± 0.03	0.999
	35	4.1 ± 0.2	0.998	3.5 ± 0.1	0.999
G27-EG$_4$-DiMan	25	0.11 ± 0.01	0.999	0.27 ± 0.02	0.998
	30	0.20 ± 0.01	0.998	0.30 ± 0.01	0.999
	35	0.45 ± 0.06	0.990	0.35 ± 0.02	0.998

The calculated K_d values at different temperatures were then combined with Van't Hoff analysis to obtain binding thermodynamic data. Van't Hoff plots were established to derive the binding enthalpy and entropy changes by integrating two Gibbs free energy equations (Eq. 1 and 2) below and using ln(K_d) versus the inverse of temperature (1/T) linear fits. **Figure 3.7.1** below shows the Van't Hoff plots of GNP-glycans for DC-SIGN/R binding at different temperatures.

Under the standard state conditions;

$$\Delta G = -RTln(K_a) = RTln(K_d) \quad \text{(Eq. 1)}$$

$$\Delta G = \Delta H - T\Delta S \quad \text{(Eq. 2)}$$

$$lnK_d = \frac{\Delta H}{R}\frac{1}{T} - \frac{\Delta S}{R}$$

Where ΔG is the changes in binding Gibbs free energy, K_a is the equilibrium association constant, K_d is the equilibrium dissociation constant and its relationship with K_a being $K_a = 1/K_d$, T is the absolute temperature in degrees Kelvin and R is the ideal gas constant.

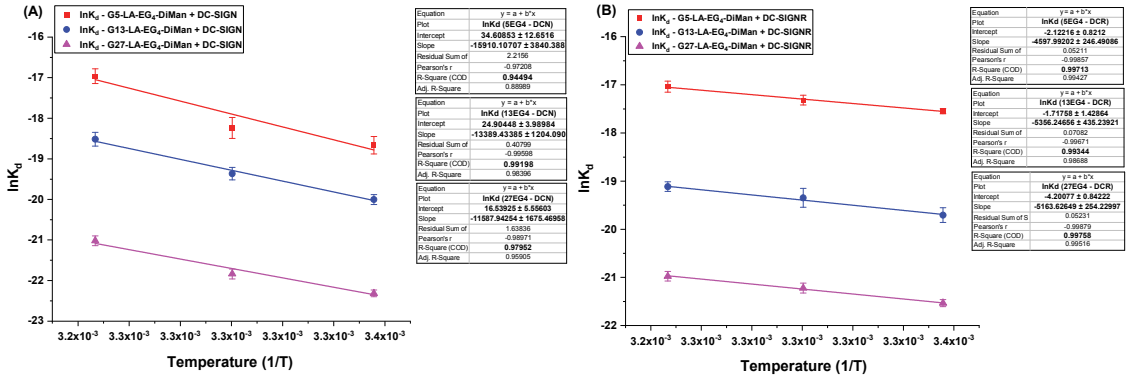

Figure 3.7.1. Van't Hoff plots of the ln(K_d) − 1/T relationships for GNP-DiMan binding with (A) DC-SIGN and (B) DC-SIGNR. All data is here given after subtracting the correction factors for GNP inner filter effects by the normal slopes.

The linear fits of ln(K_d) against the reciprocal temperature were used to extract the binding enthalpy and entropy changes. The slope and intercept of fitted Van't Hoff plots are correspond to the standard binding enthalpy change divided by the gas constant (ΔH/R) and the negative of standard entropy change divided by the gas constant, -ΔS/R, respectively. The binding thermodynamic parameters for GNP-DiMan binding with DC-SIGN/R were obtained and shown in **Figure 3.7.2**, and summarised in **Table 3.7.2** below.

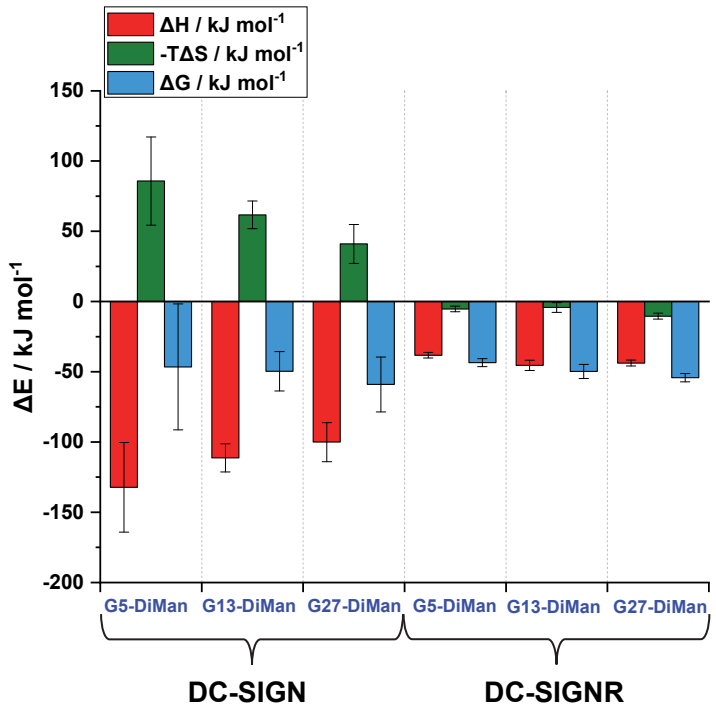

Figure 3.7.2. Comparison of the standard enthalpy (red), entropy (green), and Gibbs free energy (blue) changes of GNP-DiMan binding with DC-SIGN/R.

Table 3.7.2. Summary of the binding thermodynamic parameters for GNP-DiMan binding with DC-SIGN/R. Standard deviation values here obtained from the fitting errors of Van't Hoff plots.

	Binding Thermodynamic Parameters			
	ΔH/kJ mol^{-1}	**ΔS/J mol^{-1} K^{-1}**	**-TΔS/J mol^{-1}**	**ΔG/kJ mol^{-1}**
G5-EG$_4$-DiMan – DC-SIGN	-132 ± 32	-288 ± 105	86 ± 31	-47 ± 44
G13-EG$_4$-DiMan – DC-SIGN	-111 ± 10	-207 ± 33	62 ± 9	-50 ± 14
G27-EG$_4$-DiMan – DC-SIGN	-100 ± 14	-138 ± 46	41 ± 14	-59 ± 19
G5-EG$_4$-DiMan – DC-SIGNR	-38.2 ± 2.0	17.6 ± 6.0	-5.2 ± 2.0	-43.5 ± 3.0
G13-EG$_4$-DiMan – DC-SIGNR	-45.5 ± 4.0	14.3 ± 11.0	-4.2 ± 4.0	-49.7 ± 5.0
G27-EG$_4$-DiMan – DC-SIGNR	-43.8 ± 2.0	34.9 ± 7.0	-10.4 ± 2.0	-54.2 ± 3.0

Based on the thermodynamic data for Gx-DiMan (x= 5, 13, and 27 nm) binding with DC-SIGN (**Table 3.7.2**), two notable conclusions can be drawn: (1) Binding interactions of all three different sized GNP-DiMan with DC-SIGN are enthalpy-driven with negative binding enthalpy change, as expected. The ΔH for DC-SIGN binding with 5, 13, and 27 nm GNP-DiMan were found to be similar (after accounting for the experimental errors) and at -132 ± 32 kJ mol^{-1}, -111 ± 10 kJ mol^{-1} and -100 ± 14 kJ mol^{-1}, respectively. These values are about 4 times that of the ΔH value of the monovalent DC-SIGN CRD-DiMan binding previously measured with ITC (-25.8 kJ mol^{-1}),[17] suggesting that all four CRDs in

DC-SIGN have participated in glycan binding. The good agreement of ΔH values obtained here with those measured in ITC confirms that our fluorescence quenching technique can act as a reliable new approach to probe DC-SIGN binding thermodynamics. (2) The multivalent binding entropy penalties (ΔS values) for GNP-DiMan with DC-SIGN were found to be reduced with the increasing GNP scaffold size. The total entropy cost of the multivalent receptor-ligand interaction reflects the contributions of the changes in translational, rotational, and conformational entropies of receptors and ligands on association and also the changes in the entropy of their surrounding media[18] (*e.g.* binding buffer or water). Therefore, the most likely reason behind the reduced entropic penalty for bigger GNPs could be the presence of more free (not bound to CRDs) and flexible DiMan ligands on the surface of larger GNP scaffold, which has largely retained their conformational and rotational degrees of freedom. Taken together, DC-SIGN binding thermodynamic data were in good agreement with TEM and DLS results and revealed that GNP-DiMan conjugates bind simultaneously to four CRDs of DC-SIGN.

In contrast, the binding thermodynamics of GNP-DiMan with DC-SIGNR differs from those with DC-SIGN, and two conclusions can be drawn. (1) The highly favourable ΔH values obtained in DC-SIGN binding were significantly reduced for DC-SIGNR binding of all GNP-DiMan. The standard binding ΔH values of all GNP-DiMan with DC-SIGNR were similar, but they were ~half those obtained with DC-SIGN. This result may indicate that each DC-SIGNR may bind with GNP-DiMan using only two of its four CRDs. This is consistent with the observation in the DLS measurements that DC-SIGNR cross-links with different GNP-DiMans presumably first with 2 CRDs to form partially bound GNP-DC-SIGNR units which subsequently crosslink to form large assemblies. The later step happens over a relatively long period and may not be captured in the measurement here. (2) The entropic penalty observed for G27-DiMan with DC-SIGNR, as in DC-SIGN binding, may be due to the fact that the large number of free and flexible DiMan sugars on their surface maintain their translational and rotational degrees of freedom as well as unbound free flexible CRDs of DC-SIGNR. Overall, the results indicate that DC-SIGN binding is enthalpy-driven process with larger entropic penalties, whereas the favourable enthalpy terms in DC-SIGNR binding are reduced, but are compensated by

small favourable binding entropic contributions, leading to similar overall binding ΔG values for both protein receptors.

3.8. Inhibiting DC-SIGN/R-Mediated Ebola Virus Host Cell Entry.

Note: These experiments were performed by our collaborator, Professor Stefan Pöhlmann's group at the German Primate Centre, Germany. The author of this thesis analysed these data and reported his own conclusions regarding the findings.

Given the strong apparent binding K_ds of GNP-glycans and DC-SIGN/R, we anticipated these GNP-glycans to be excellent inhibitors against DC-SIGN/R-mediated viral infections, *e.g.* HIV and Ebola virus. Therefore, the GNP-DiMans were tested for their ability to inhibit DC-SIGN/R mediated entry of the Ebola virus in a model cellular infection assay.[8] In this model, a murine leukaemia virus vector (MLV) carrying the Ebola virus surface glycoprotein (EBOV-GP) and encoding the luciferase gene, and also human embryonic kidney cells 293T trans-infected to express DC-SIGN and DC-SIGNR in their cell membranes were used. Viruses can efficiently bind cell surface DC-SIGN/R receptors via EBOV-GP to entre cells, leading to production of the luciferase gene inside the infected cells, thereby express luciferase. The enzyme luciferase catalyses a light-producing reaction in the presence of oxygen using luciferin as substrate. Its ability to produce bioluminescence has made this enzyme a widely used tool for monitoring biological processes.[19] Luciferase activity expressed in cells can be readily measured in cell lysate. Following the treatment of DC-SIGN/R expressing cells with GNP-DiMan, the glycan-nanoparticles will bind to these lectin viral receptors, preventing them from being able to bind to virus particles. This will reduce virus cellular entry and hence luciferase production. A basic illustration of the model used to determine the inhibition potency of GNP-DiMan is schematised in **Figure 3.8.1** below.

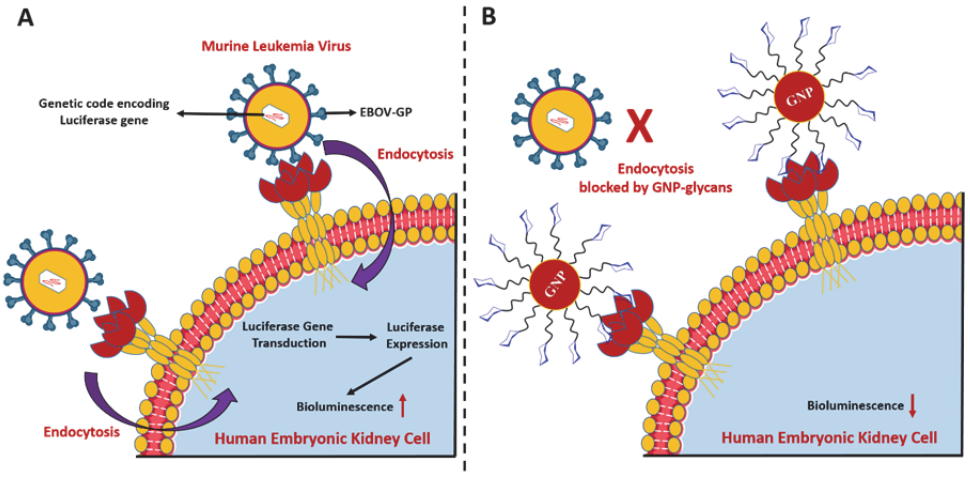

Figure 3.8.1. A schematic illustration of (A) the luciferase gene transduction via murine leukaemia virus (MLV) bearing the Ebola glycoprotein (EBOV-GP) into cells and (B) the inhibition of MLV virus binding upon occupying of DC-SIGN by GNP-DiMan, thus blocking the transduction of luciferase gene.

Viruses bearing on vesicular stomatitis virus glycoprotein (VSV-G) that does not employ DC-SIGN/R for cell entry and also cells transfected with an empty plasmid DNA lacking the luciferase gene were used as negative controls to verify whether the inhibition is specific or not, as published previously by our research group.[8] After pre-treatment with GNP-DiMan, cells were washed twice and then incubated with MLV carrying EBOV-GP and control viruses bearing VSV-G for 72 hours. After incubation, luciferase activities in cell lysate were measured to monitor the gene transduction and expression. Since the binding affinity (K_d) of mannose-coated GNPs with both proteins were found to be weaker than their dimannose counterparts, only the three strong binding Gx-DiMan (x=5, 13, and 27 nm) were tested. Also, the potency of Gx-ManA (x=5 and 13 nm) in inhibiting DC-SIGN-mediated Ebola virus infection were also investigated, as there were no previously reports about the inhibition properties of this sugar type. Finally, the GNP-OH controls lacking terminal glycan were also tested in order to verify the observed inhibition effects of GNP-DiMan were due to specific lectin-glycan interactions. The raw luciferase activities of 293T cells pre-treated with GNP-DiMan were shown in **Figure 3.8.2** below, while those for the controls were given in **Appendix A.9**.

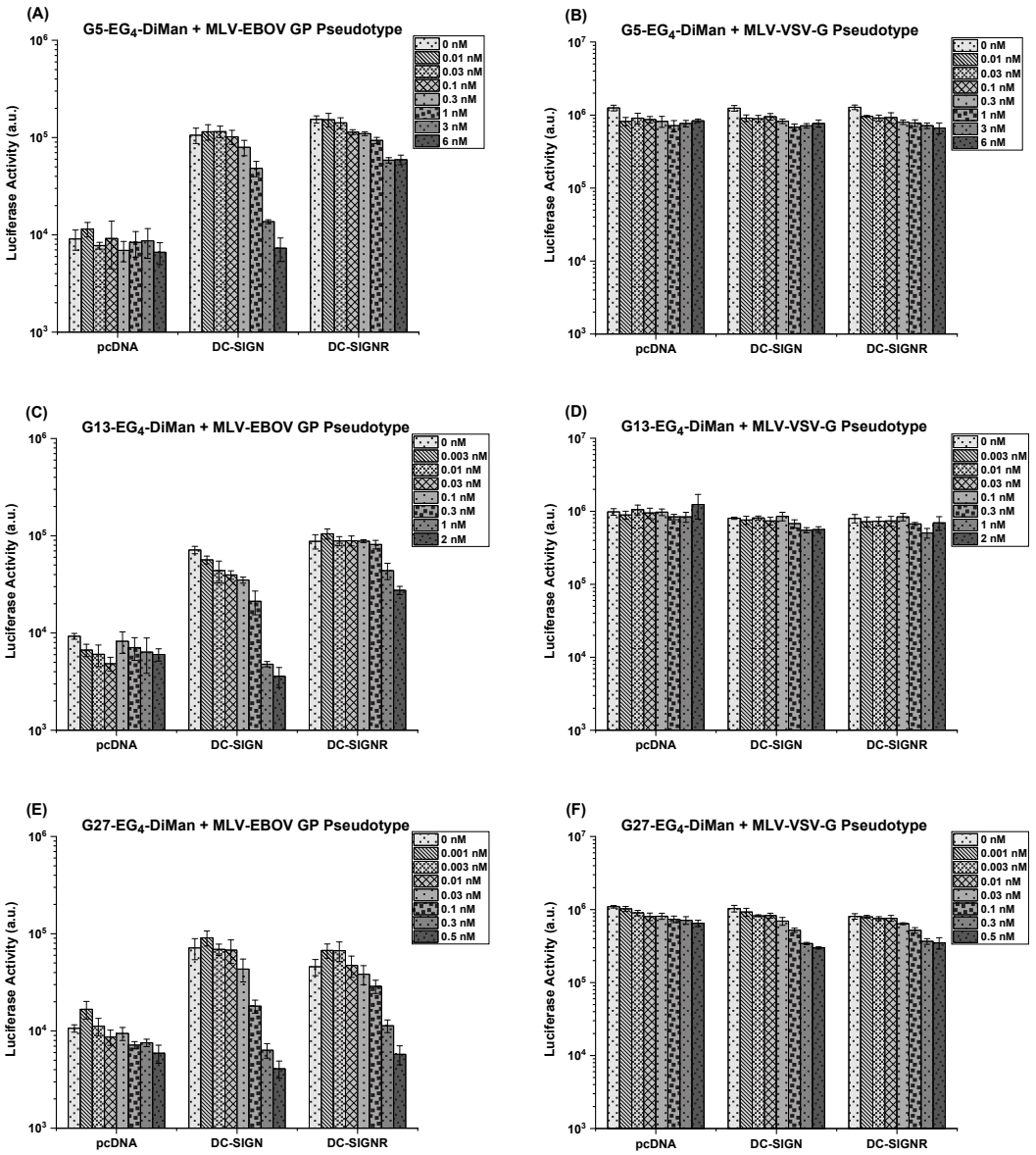

Figure 3.8.2. The cellular luciferase activities of 293T cells pre-treated with varied concentrations of G5-DiMan (A, B), G13-DiMan (C, D), and G27-DiMan (E, F) and then trans-infected MLV vector carrying the EBOV-GP (A, C, E) or the control VSV-G (B, D, F). The data are presented as mean±standard deviation three separate experiments.

Figure 3.8.2 show that luciferase activities of EBOV-driven infections are significantly reduced in the presence of GNP-glycan, while these driven by VSV-G are almost unaffected. This result indicates that the observed inhibition is due to the specific and strong binding of GNP-DiMan to cell surface DC-SIGN/R receptors. The IC_{50} values, the GNP-DiMan concentration that yields 50% inhibition, were derived from fitting downward-sloping dose-response curves obtained using normalized dose-dependent inhibition data using the equation below.

$$NA = \frac{IC_{50}}{IC_{50} + C}$$

Where NA, IC_{50}, and C were the normalized luciferase activity, GNP-DiMan concentration that inhibit 50% of luciferase activity, and GNP concentration, respectively. **Figure 3.8.3** below show the normalised inhibition activity plots of GNP-DiMan as potential inhibitors.

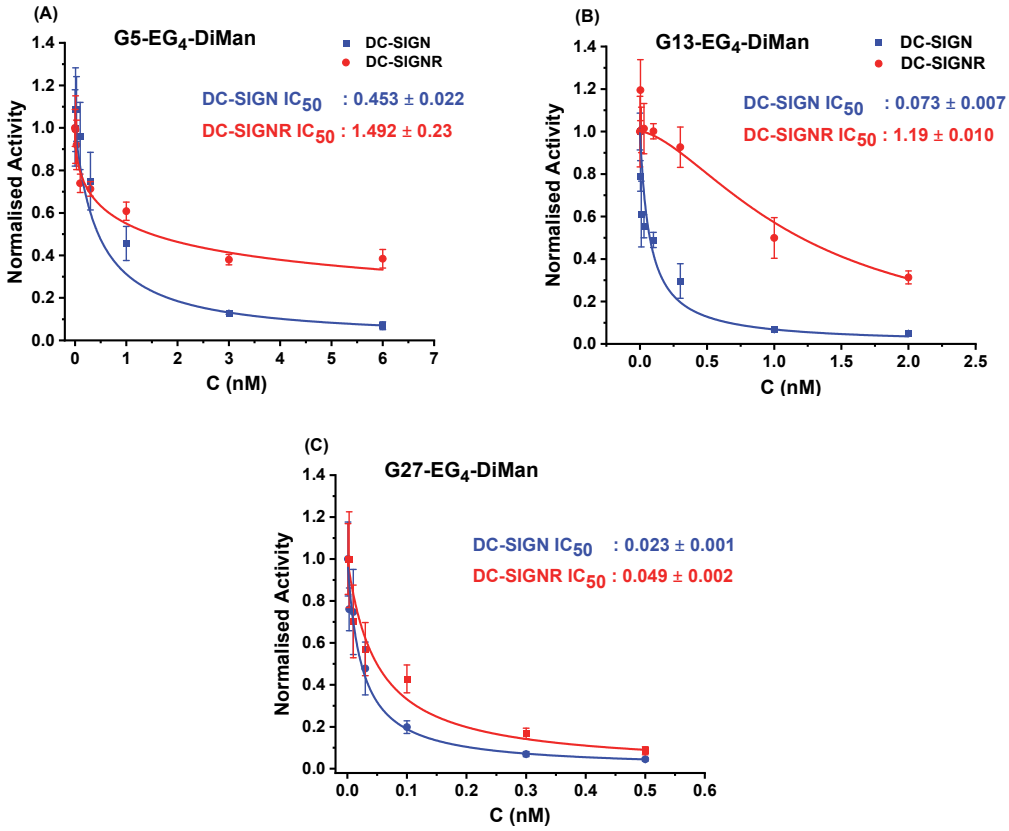

Figure 3.8.3. Normalised inhibition activity plots of the 293T cells expressing DC-SIGN/R after treatment with GNP-DiMan as potential inhibitors. After subtracting their pcDNA control, the luciferase activities were normalized by corresponding values in the absence of GNP-DiMan. Data were fitted by the competitive binding model: $NA=IC_{50}/IC_{50}+C_{GNP}$, where NA is the normalized luciferase activity, IC_{50} is the concentration that gives 50% inhibition, and C_{GNP} is GNP-DiMan concentration.

IC_{50} values of Gx-DiMan (x= 5, 13, and 27 nm) in blocking DC-SIGN-mediated entry of EBOV-MLV were calculated as 0.45 ± 0.002, 0.073 ± 0.007, and 0.023 ± 0.001 nM, respectively. The observed IC_{50} values are in the picomolar level, confirming that these GNP-glycan are potent inhibitors. Notably, G27-DiMan, having an IC_{50} of 23±1 pM, is considerably more potent than even the most potent glycoconjugate inhibitors against DC-SIGN mediated Ebola virus infection reported in the literature.[8] To the best of our knowledge, this represents the most potent glycoconjugate inhibitor against DC-SIGN

mediated Ebola cellular infection reported so far. **Table 3.8.1** below compares the potency (IC_{50} values) of similar materials in inhibiting DC-SIGN-mediated virus infections. Particularly, compared to QD-DiMan (IC_{50}: 0.70 ± 0.2 nM)[2] and G5-DiMan (0.095 ± 0.017 nM)[8] which are among the strongest Ebola inhibitors previously reported in our research group, G27-DiMan's inhibition potency is ∼30-fold and ∼4-fold stronger inhibition potency, respectively. It is also noteworthy that, besides a stronger inhibition potency than QD-DiMan, G27-DiMan is also much less cytotoxic than cadmium-based QDs, making it more suitable as potential applications under *in vivo* conditions. The calculated IC_{50} values against DC-SIGNR-mediated virus transduction were 1.5 ± 0.023, 1.2 ± 0.01, and 0.049 ± 0.002 nM for 5, 13, and 27 nm GNP-EG_4-DiMan, respectively, indicating that for all three GNP scaffold size, GNP-DiMan is less effective in blocking DC-SIGNR-mediated viral transduction than that of DC-SIGN-dependent. However, the IC_{50} value of 49 pM for G27-DiMan is quite remarkable because previously reported IC_{50} values for DC-SIGNR-mediated transduction were all in nanomolar range. Interestingly, G27-DiMan's ∼2.2-fold higher potency in inhibiting DC-SIGN-mediated gene transduction over that of DC-SIGNR-dependent agrees well with their binding K_d differences measured by fluorescence quenching (i.e. 0.2 *vs*. 0.54 nM). Moreover, ManA-coated GNPs tested for the first time exhibited much higher IC_{50} values (weaker affinity) compared to DiMan-coated GNPs, showing the lower inhibition potency of GNP-ManA conjugates. In comparison to GNP-DC-SIGN/R binding affinity measured by fluorescence quenching and inhibition studies data, the K_d and IC_{50} values do not match directly, possibly due to the different binding environments used in these studies (*e.g.* solution vs. cell membranes). However, as shown in **Table 3.8.2**, there is a clear positive correlation between K_d and IC_{50} values, that is, the stronger the binders the better the inhibitors. The positive K_d–IC_{50} correlation suggests that our fluorescence quenching-based K_d measurements could potentially acts as a rational and rapid method for the estimation of the viral inhibition potential of GNP-glycans.

Table 3.8.1. A summary of the IC_{50} values of mannose-DC-SIGN binding to compare to the literature.

Glycoconjugates (Glycan Scaffold)	IC_{50} for DC-SIGN	Reference
Glycodendrimers	300 nM	Lasala *et al.*[20]
Virus-like glycodendri-nanoparticles	0.91 nM	Ribeiro-Viana *et al.*[21]
Globular Multivalent Glycofullenes	0.67 nM	Muñoz *et al.*[22]
Pseudosaccharide Functionalized Dendrimers	31.5 nM	Luczkowiak *et al.*[23]
QD-DiMan (our research group)	0.70 nM	Guo *et al.*[2]
5 nm GNP-DiMan (our research group)	0.095 nM	Budhadev *et al.*[8]
27 nm GNP-DiMan	**0.023 nM**	**(This work)**

Table 3.8.2. Comparison of the apparent K_d and the IC_{50} values of Gx-EG_4-DiMan (where x = 5, 13, and 27 nm) with DC-SIGN/R.

GNP-glycans	DC-SIGN		DC-SIGNR	
	Apparent K_d (nM)	IC_{50} (nM)	Apparent K_d (nM)	IC_{50} (nM)
G5-EG_4-DiMan	5.8 nM	0.453 ± 0.022	14.9 nM	1.492 ± 0.23
G13-EG_4-DiMan	1.0 nM	0.073 ± 0.007	2.7 nM	1.19 ± 0.010
G27-EG_4-DiMan	0.2 nM	0.023 ± 0.001	0.54 nM	0.049 ± 0.002

3.9. Conclusion

In conclusion, we have designed and successfully produced a range of new and robust polyvalent GNP-glycans probes in which different size GNPs were used as scaffolds for dissecting the nature of multivalent lectin-glycan interactions. We have quantified the multivalent interactions of GNP-glycan with the model tetrameric lectins DC-SIGN/R via a new fluorescence quenching method by taking advantage of the extraordinary fluorescence quenching properties of GNPs. The apparent binding affinities, K_ds, for GNP-glycans-DC-SIGN/R binding revealed three significant results. (1) The binding affinity of GNP-glycan with DC-SIGN/R increases with the increasing GNP scaffold size, where K_ds for Gx-DiMan (x=5, 13, and 27 nm) were found as 5.8, 1.0, and 0.2 nM for DC-SIGN, and 14.9, 2.7, and 0.54 nM for DC-SIGNR, respectively. These data suggest that the larger GNP size provides the glycan ligands with more favourable positional and spatial conformation for multivalent interactions with DC-SIGN/R. (2) Increasing surface glycan density on GNPs is beneficial for improving the binding affinity with DC-SIGN/R. In addition, changing the ligand terminal sugars on the GNP surface from monomannose to dimannose resulted in a significant increase in their binding affinity

with DC-SIGN/R. This may be due to the binding of disaccharide mannose sugars to the secondary binding sites as well as the primary binding site of DC-SIGN/R CRDs.[16] (3) Ligand linker length also plays a highly important role in multivalent lectin-glycan binding, the effect is particularly pronounced for GNP-glycan build upon smaller GNPs, and the effect is reduced with the increasing GNP scaffold size. However, in terms of linker length, only 2 and 4 EG units were tested in this study, and thus varying EG lengths to greater extend will be needed in order to draw more conclusive results. Furthermore, DLS studies were performed to elucidate the binding modes of DC-SIGN/R to GNP-glycan, and the obtained D_h sizes of the GNP-glycan-DC-SIGN/R assemblies show that all 4 CRDs in DC-SIGN bind simultaneously to only one GNP-glycan conjugate; while DC-SIGNR cross-links with different GNP-glycans. These observations were also confirmed by the cryo-TEM imaging of the resulting GNP-glycan-DC-SIGN/R assemblies. The different binding mode is due to the different CRD orientations of DC-SIGN and DC-SIGNR, which is fully consistent with the model of DC-SIGN/R CRDs previously proposed by our group.[4]

In addition to providing quantitative binding affinity and binding modes data, we have also developed a new finely-tuned fluorescence quenching-based method to probe DC-SIGN/R binding thermodynamic with GNP-glycans. We found that DC-SIGN binding is enthalpy-driven, with a large, favourable ΔH and a negative entropy contribution to the overall binding free energy changes, but in DC-SIGNR binding, the contribution of ΔH is decreased significantly which is compensated with a small favourable binding entropic term. Also, viral inhibition data revealed that GNP-glycans are highly potent inhibitors against DC-SIGN/R-mediated Ebola viral entry. Particularly, G27-EG_4-DiMan potently block DC-SIGN and DC-SIGNR mediated EBOV-GP driven viral infections of host cells with IC_{50} values to 23±1 pM and 49±2 pM, making it the most potent GNP-glycan inhibitor ever reported against DC-SIGN/R mediated pseudo-Ebola viral infection. Overall, the fluorescence quenching-based affinity measurement can serve as a sensitive, reliable, and rapid method for estimating glyconanoparticle inhibition potency against EBOV-GP-mediated viral infections. Moreover, this strategy can be extended to develop new glycoconjugates based therapeutics against many diseases, such as virus infections, allergies, and cancer.

3.10. References

1. S. Bhatia, L. C. Camacho and R. Haag, *J Am Chem Soc*, 2016, **138**, 8654-8666.
2. Y. Guo, I. Nehlmeier, E. Poole, C. Sakonsinsiri, N. Hondow, A. Brown, Q. Li, S. Li, J. Whitworth, Z. Li, A. Yu, R. Brydson, W. B. Turnbull, S. Pöhlmann and D. Zhou, *J Am Chem Soc*, 2017, **139**, 11833-11844.
3. R. Amraei, W. Yin, M. A. Napoleon, E. L. Suder, J. Berrigan, Q. Zhao, J. Olejnik, K. B. Chandler, C. Xia, J. Feldman, B. M. Hauser, T. M. Caradonna, A. G. Schmidt, S. Gummuluru, E. Muhlberger, V. Chitalia, C. E. Costello and N. Rahimi, *bioRxiv*, 2021, DOI: 10.1101/2020.06.22.165803.
4. Y. Guo, C. Sakonsinsiri, I. Nehlmeier, M. A. Fascione, H. Zhang, W. Wang, S. Pöhlmann, W. B. Turnbull and D. Zhou, *Angew Chem Int Ed Engl*, 2016, **55**, 4738-4742.
5. Y. Watanabe, J. D. Allen, D. Wrapp, J. S. McLellan and M. Crispin, *Science*, 2020, **369**, 330-333.
6. X. Chen, O. Ramström and M. Yan, *Nano Res*, 2014, **7**, 1381-1403.
7. A. Bernardi, J. Jiménez-Barbero, A. Casnati, C. De Castro, T. Darbre, F. Fieschi, J. Finne, H. Funken, K.-E. Jaeger, M. Lahmann, T. K. Lindhorst, M. Marradi, P. Messner, A. Molinaro, P. V. Murphy, C. Nativi, S. Oscarson, S. Penadés, F. Peri, R. J. Pieters, O. Renaudet, J.-L. Reymond, B. Richichi, J. Rojo, F. Sansone, C. Schäffer, W. B. Turnbull, T. Velasco-Torrijos, S. Vidal, S. Vincent, T. Wennekes, H. Zuilhof and A. Imberty, *Chemical Society Reviews*, 2013, **42**, 4709-4727.
8. D. Budhadev, E. Poole, I. Nehlmeier, Y. Liu, J. Hooper, E. Kalverda, U. S. Akshath, N. Hondow, W. B. Turnbull, S. Pöhlmann, Y. Guo and D. Zhou, *Journal of the American Chemical Society*, 2020, **142**, 18022-18034.
9. Y. Guo, W. Bruce Turnbull and D. Zhou, *Methods Enzymol*, 2018, **598**, 71-100.
10. M. Ouellette, F. Masse, M. Lefebvre-Demers, Q. Maestracci, P. Grenier, R. Millar, N. Bertrand, M. Prieto and É. Boisselier, *Sci Rep*, 2018, **8**, 14357.
11. E. Boisselier and D. Astruc, *Chem Soc Rev*, 2009, **38**, 1759-1782.
12. Atto-643 Product Information, https://www.atto-tec.com/fileadmin/user_upload/Katalog_Flyer_Support/ATTO_643.pdf, (accessed 16/01/2023).
13. J. H. Lee, G. Ozorowski and A. B. Ward, *Science*, 2016, **351**, 1043-1048.
14. A. G. Barrientos, J. M. d. l. Fuente, M. Jiménez, D. Solís, F. J. Cañada, M. Martín-Lomas and S. Penadés, *Carbohydrate Research*, 2009, **344**, 1474-1478.
15. X. Liu, M. Atwater, J. Wang and Q. Huo, *Colloids Surf B Biointerfaces*, 2007, **58**, 3-7.
16. H. Feinberg, D. A. Mitchell, K. Drickamer and W. I. Weis, *Science*, 2001, **294**, 2163-2166.
17. A. Holla and A. Skerra, *Protein Eng Des Sel*, 2011, **24**, 659-669.
18. J. D. Chodera and D. L. Mobley, *Annu Rev Biophys*, 2013, **42**, 121-142.
19. S. M. Marques and J. C. Esteves da Silva, *IUBMB Life*, 2009, **61**, 6-17.
20. F. Lasala, E. Arce, J. R. Otero, J. Rojo and R. Delgado, *Antimicrob Agents Chemother*, 2003, **47**, 3970-3972.

21. R. Ribeiro-Viana, M. Sánchez-Navarro, J. Luczkowiak, J. R. Koeppe, R. Delgado, J. Rojo and B. G. Davis, *Nature Communications*, 2012, **3**, 1303.

22. A. Muñoz, D. Sigwalt, B. M. Illescas, J. Luczkowiak, L. Rodríguez-Pérez, I. Nierengarten, M. Holler, J. S. Remy, K. Buffet, S. P. Vincent, J. Rojo, R. Delgado, J. F. Nierengarten and N. Martín, *Nat Chem*, 2016, **8**, 50-57.

23. J. Luczkowiak, S. Sattin, I. Sutkevičiūtė, J. J. Reina, M. Sánchez-Navarro, M. Thépaut, L. Martínez-Prats, A. Daghetti, F. Fieschi, R. Delgado, A. Bernardi and J. Rojo, *Bioconjugate Chemistry*, 2011, **22**, 1354-1365.

Chapter 4
pH-dependent binding between GNP-glycans and DC-SIGN/R

4.1. Introduction

pH is a vital parameter for each biological process to guide the activities and functions of all biomolecules and cells, it also plays an important role in viral infections. Once viruses enter the body, they attach to host cells by binding of their surface glycoproteins to the cell surface protein receptors, like DC-SIGN/R. Following their cellular uptake, the infection process begin by making copies of itself in the body. It has been suggested that the cellular interactions of many viruses, including HIV,[1] Ebola,[2] and SARS-CoV-2[3] that use DC-SIGN/R-mediated infections may be pH-dependent. After viral surface glycoproteins binding to DC-SIGN, their cellular internalization occurs. The lectin-virus complexes are then passed through the endosomal/lysosomal compartments, where they are exposed to gradually reduced pH in these cellular compartments which is crucial for the infectivity of viruses.[4] The low pH of endosomes generally leads to the dissociation of these lectin-ligand assemblies, but the underlying molecular mechanism is still not fully understood. Studies show that the ligands are released from DC-SIGN-ligands complexes at a pH of ~6, which is comparable to the early endosomal pH levels. In case of no dissociation in endosomes, they may alternatively be trafficked to lysosomes for degradation.[5, 6] After releasing the ligands, DC-SIGN can returns to the cell surface, indicating that DC-SIGN might function as a recycling receptor. Guo *et al*.[6] showed that neoglycoprotein ligand bound to DC-SIGN were successfully internalized and degraded, and the ligand processing rate was approximately 10-fold higher than DC-SIGN's cellular expression level over a 2-hour period, indicating that each DC-SIGN might have been recycled 10 times over 2 hours. This significantly higher ligand process rate confirms that DC-SIGN is a recycling endocytic receptor. In contrast, no neoglycoprotein internalisation was detected in cells expressing DC-SIGNR and no sign of degradation were observed either. Moreover, even at pH less than 5, DC-SIGNR did not show a decrease in the capacity of ligand binding compared to that at neutral pH. This indicates that DC-SIGNR does not release

ligands at low pH or mediate endocytosis of such neoglycoproteins, suggesting that it may function only as an adhesion protein for this ligand. Although the DC-SIGN and DC-SIGNR are two closely related proteins, their ligand binding and processing are very different, which may help explain why these proteins have different viral trans-infection properties. However, in another study, Gramberg *et al.*[2] found that cells expressing DC-SIGN/R at neutral pH bind efficiently to EBOV-GP, and after treatment at pH 6 or lower, EBOV-GP was released from both DC-SIGN/R. Although they have also highlighted that DC-SIGNR-EBOV-GP complexes are more resistant to low pH mediated release of ligands than DC-SIGN does.

Endocytic activity usually occurs following the appropriate internalization signals in the cytoplasmic tail of lectin proteins.[7] The release of ligands bound to lectins at endosomal compartments is then induced by pH changes. The changes in endosomal pH may affect the tetramer oligomerization of DC-SIGN/R, which can lead to altered ligand binding-release activities. The acidic endosomal pH is also an important determinant for recycling of endocytic receptors.[5] After internalization, Tabarani *et al.*[1] reported that the gradual decrease in pH could cause the structural changes in CRDs and hence triggered the ligand dissociation. They reported that DC-SIGN-ligand complexes formed at pH 7.4 could resist mild acidification at pH 6.4 (early endosomes), but released the ligands at pH 5.9 (late endosomes) because of the loss of tetrameric stability of CRDs. Likewise, Synder *et al.*[8] showed that HIV-1 virus showed high affinity for DC-SIGN at neutral pH, but lost this affinity in acidic environment (pH ~5). In addition, similar pH-dependent fusion of Dengue virus to dendritic cells was also observed.[9] It was concluded that all these might be due to the disruption of the DC-SIGN receptor structure at low pH. In particular, the secondary structures of CRDs are also deteriorated at low pH with the disappearance of the tetrameric form of the neck region, resulting in loss of their binding capacity.

The dynamics of the pH-dependent ligand binding/release processes of DC-SIGN/R are still not fully understood. Herein, we probed whether the binding of Gx-EG_4-DiMan (x=13 and 27 nm) conjugates with DC-SIGN/R is pH-dependent or not in solution. Their binding interactions were investigated over a pH range of 4.6 to 7.4 via fluorescence quenching and DLS. Furthermore, whether the binding was reversible for both DC-

SIGN/R was tested by monitoring the D_h sizes after pH was switched at regular intervals. Elucidating the effects of pH on GNP-DC-SIGN binding is of great importance, allowing us to gain further insights into the biological functions of these important lectin viral receptors.

4.2. pH-dependency Fluorescence Quenching Studies

In order to determine whether the DC-SIGN/R binding with Gx-EG_4-DiMan is pH dependent, fluorescence quenching experiments were performed at various pH levels. Fluorescence spectra were recorded using a fixed molar ratio of protein: GNP-glycan of 10 and 60 for G13 and G27, respectively, at eight pH points over the range from 4.6 to 7.4. All measurements were carried out in a MES (2-(N-morpholino) ethane sulfonic acid) buffer instead of the HEPES buffer. HEPES is a highly effective buffer at physiological pH (pH range of 6.8-8.2, p*K*a = 7.3), but MES has a lower p*K*a of 6.1, which is better suited for buffering at a lower pH range from 5.2 to 7.1.[10] The MES buffers containing 100 mM NaCl, 25 mM MES, and 10 mM $CaCl_2$ were adjusted to the desired pH values using concentrated NaOH. BSA was not added to the MES buffer as it may affect the results due to its pH dependency.[11] In addition, a pH-dependence study of the Atto-643 dye only was also performed to find out whether the dye fluorescence is pH dependent. The fluorescence spectra for DC-SIGN/R and Atto-643 dye, and also Gx-EG_4-DiMan (x=13 and 27 nm) + DC-SIGN/R samples at different pH values are shown in **Figure 4.2.1**, and **Figure 4.2.2**, respectively.

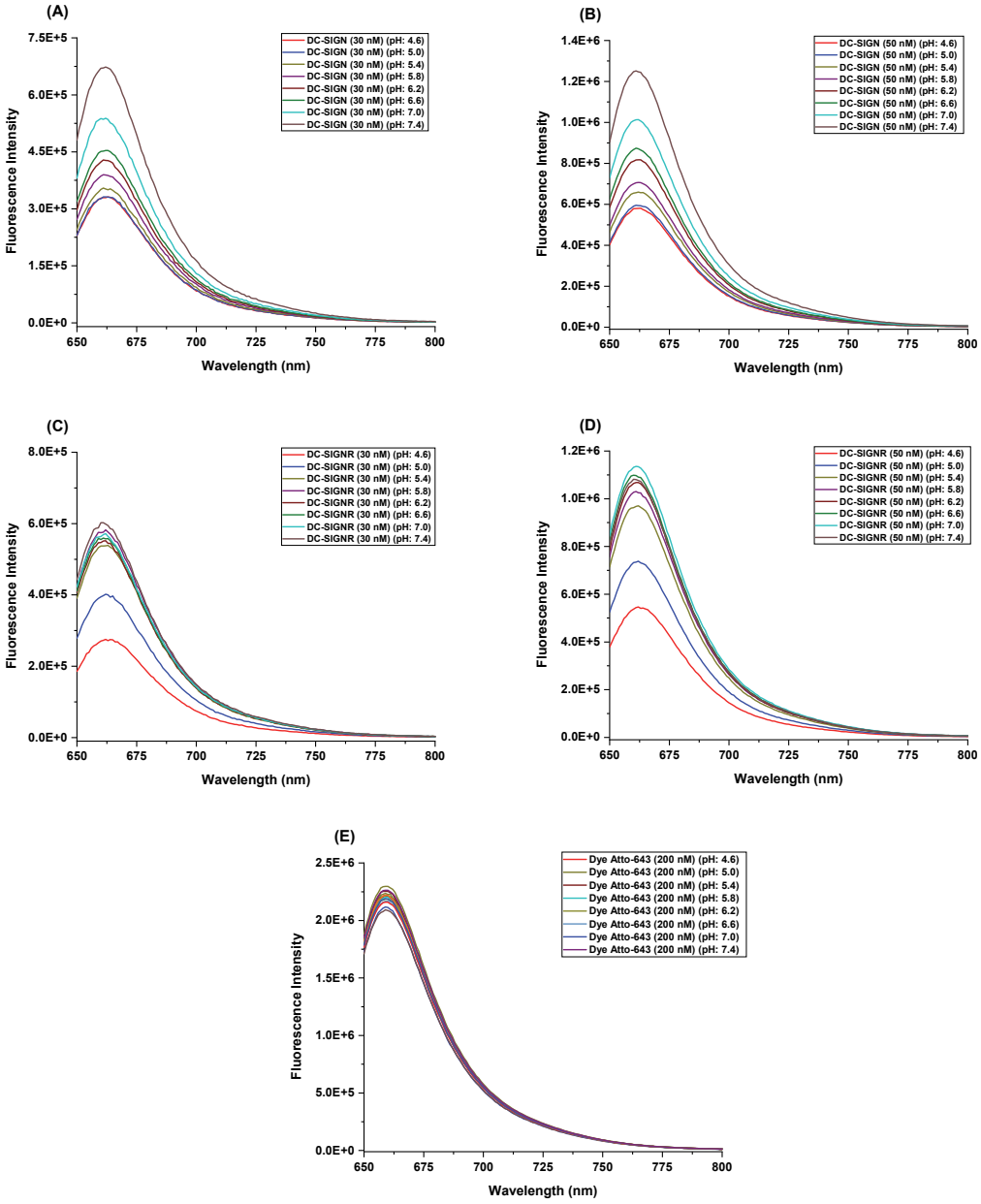

Figure 4.2.1. The fluorescence spectra for (A) DC-SIGN at 30 nM, (B) DC-SIGN at 50 nM, (C) DC-SIGNR at 30 nM, (D) DC-SIGNR at 50 nM, and (E) Atto-643 dye at different pH points over the range from 4.6 to 7.4.

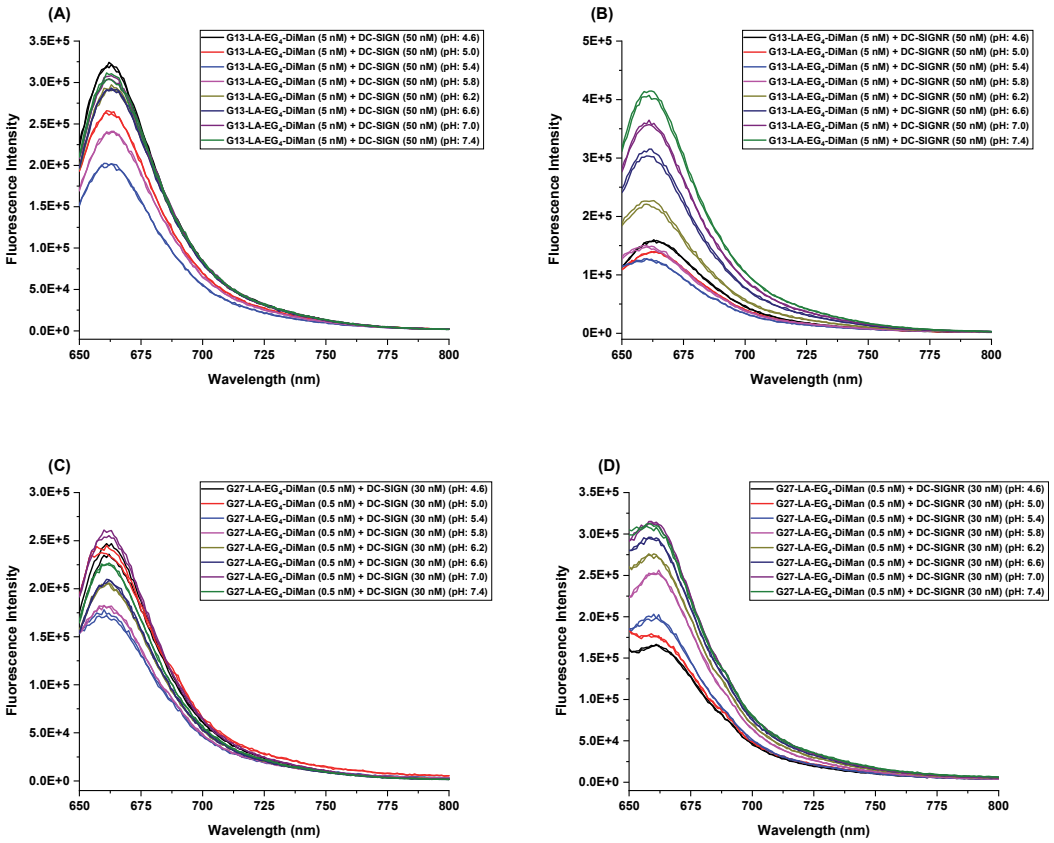

Figure 4.2.2. The fluorescence spectra for (A) G13-EG_4-DiMan + DC-SIGN, (B) G13-EG_4-DiMan + DC-SIGNR, (C) G27-EG_4-DiMan + DC-SIGN, (D) G27-EG_4-DiMan + DC-SIGNR at different pH points over the range from 4.6 to 7.4.

The free Atto-643 dye displayed similar fluorescence intensities at different pH values, as shown in **Figure 4.2.1.** This supports that its fluorescence is not affected over the pH range of 2 to 11.[12] Therefore, any pH-dependent fluorescence responses observed in pure DC-SIGN/R, and GNP-DiMan-DC-SIGN/R complexes must be caused by conformational changes of DC-SIGN/R, and the resulting changes in binding interactions, and not from the dye itself. Similarly, after calculating the integral values of the fluorescence spectra, their QE% was quantified, and QE% versus pH plots were constructed as given in **Figure 4.2.3** below.

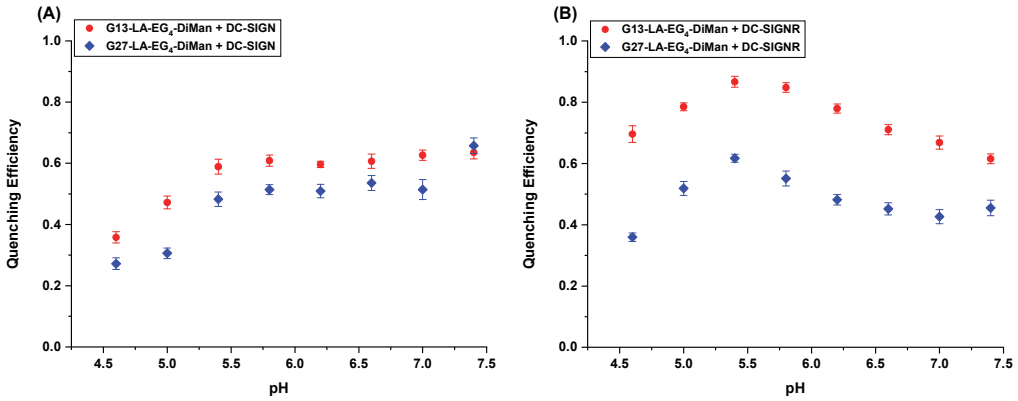

Figure 4.2.3. The fluorescence quenching efficiency versus pH points for (A) G13/27-EG_4-DiMan+DC-SIGN and (B) G13/27-EG_4-DiMan+DC-SIGNR. The quenching efficiency data could not be fitted with the non-linear fitting programmes in the pH range studied as they did not get the data to converge correctly.

The effects of pH on the binding interactions of Gx-DiMan (x=13 and 27 nm) with DC-SIGN/R revealed that the quenching efficiency was augmented for both proteins and GNP-glycans as pH was increased up to 5.4, then the quenching efficiency was almost plateaued out for DC-SIGN from pH 5.4 to 7.4, but it was slightly decreased for DC-SIGNR. This indicates that both DC-SIGN/R may exhibit some degrees of conformational differences depending on the pH changes, especially in range of pH 4.6-5.4. DC-SIGNR appears to be more stable in slightly acidic media, which is consistent to the report that DC-SIGNR does not release ligands at earlier endosomal pHs.[6] DC-SIGN, on the other hand, seems to be more compact at physiological pH. To verify these assumptions, D_h size changes of GNP-DiMans with DC-SIGN/R were monitored via DLS to determine the pH-dependent conformational changes in DC-SIGN/R.

4.3. pH-dependent DLS studies

pH dependency of binding between GNP-glycans and both WT-DC-SIGN/R was also investigated via DLS by monitoring binding induced D_h size changes. Similarly, all measurements were done using a fixed molar ratio of protein: GNP-glycan (10 and 60 for G13 and G27, respectively) in MES buffer at eight pH points over the range from 4.6 to 7.4. The resulting D_h size distribution histograms for WT-DC-SIGN/R and Gx-DiMan (x=13 and 27 nm) are given in **Figure 4.3.1**, **Figure 4.3.2**, **Figure 4.3.3**, and **Figure 4.3.4** respectively. The D_hs for GNP-protein assemblies at different pHs are also summarized in **Figure 4.3.5.**

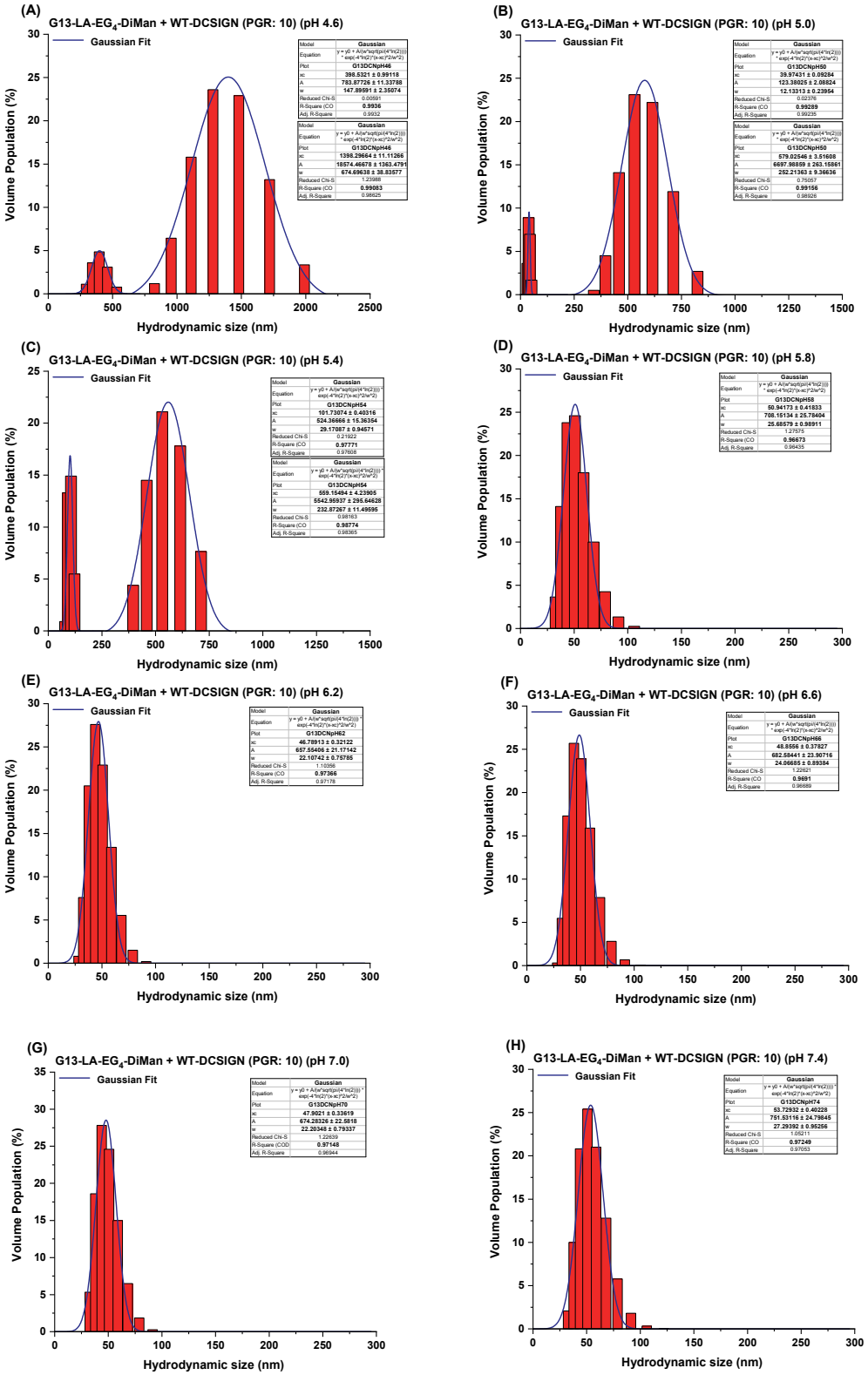

Figure 4.3.1. The DLS histograms of G13-EG_4-DiMan+DC-SIGN at (A) pH 4.6, (B) pH 5.0, (C) pH 5.4, (D) pH 5.8, (E) pH 6.2, (F) pH 6.6, (G) pH 7.0, (H) pH 7.4.

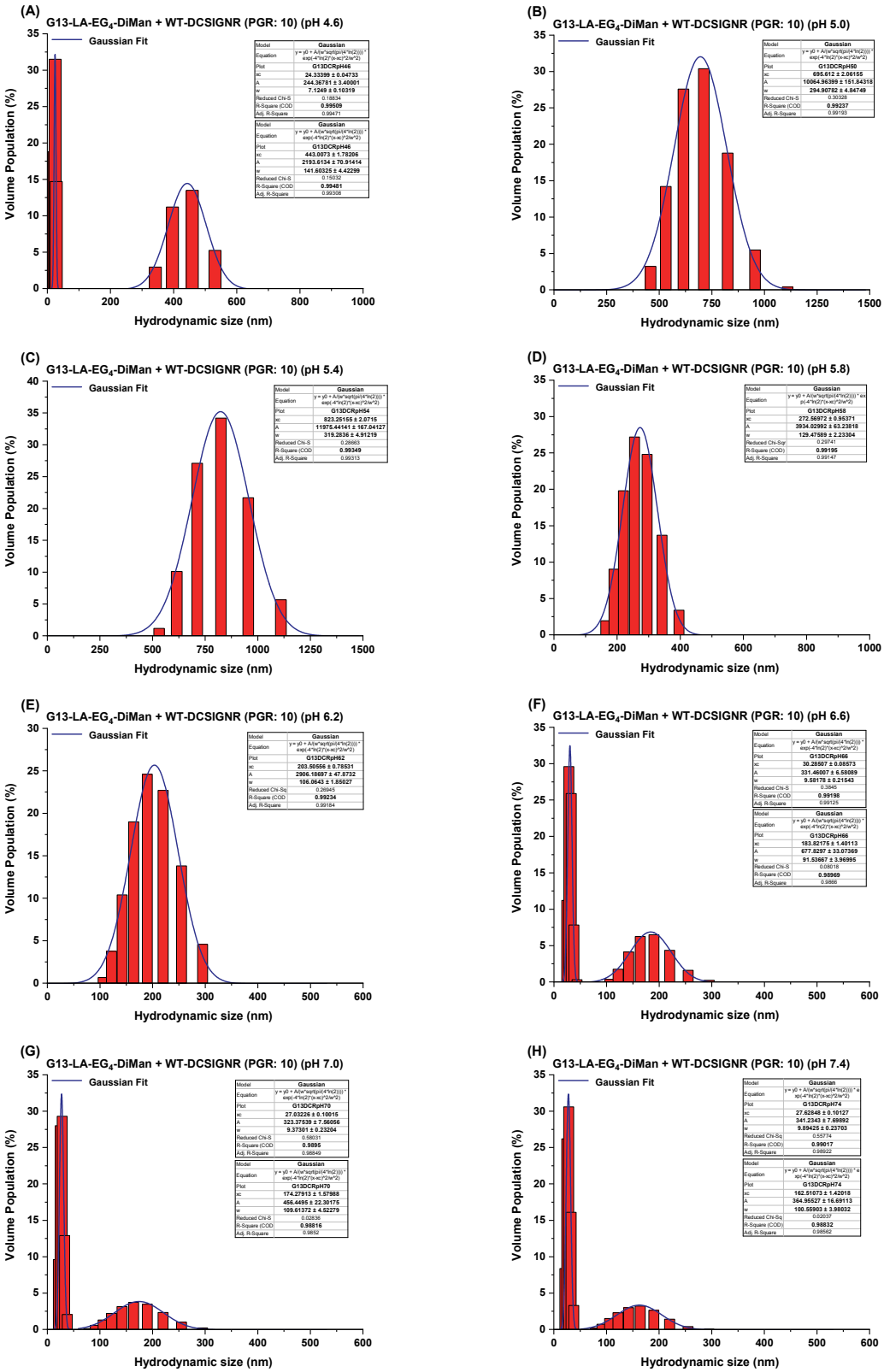

Figure 4.3.2. The DLS histograms of G13-EG_4-DiMan+DC-SIGNR at (A) pH 4.6, (B) pH 5.0, (C) pH 5.4, (D) pH 5.8, (E) pH 6.2, (F) pH 6.6, (G) pH 7.0, (H) pH 7.4.

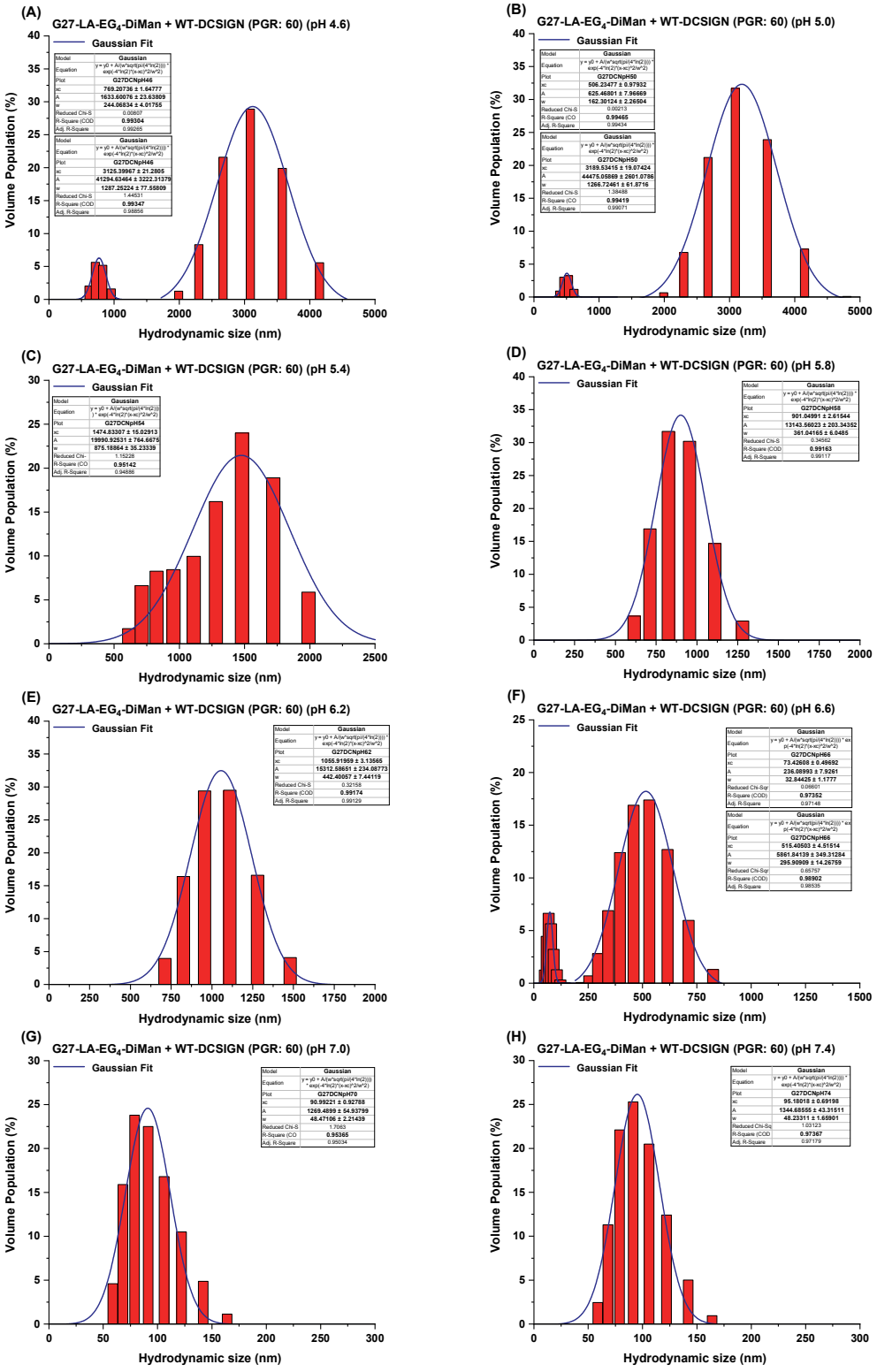

Figure 4.3.3. The DLS histograms of G27-EG_4-DiMan+DC-SIGN at (A) pH 4.6, (B) pH 5.0, (C) pH 5.4, (D) pH 5.8, (E) pH 6.2, (F) pH 6.6, (G) pH 7.0, (H) pH 7.4.

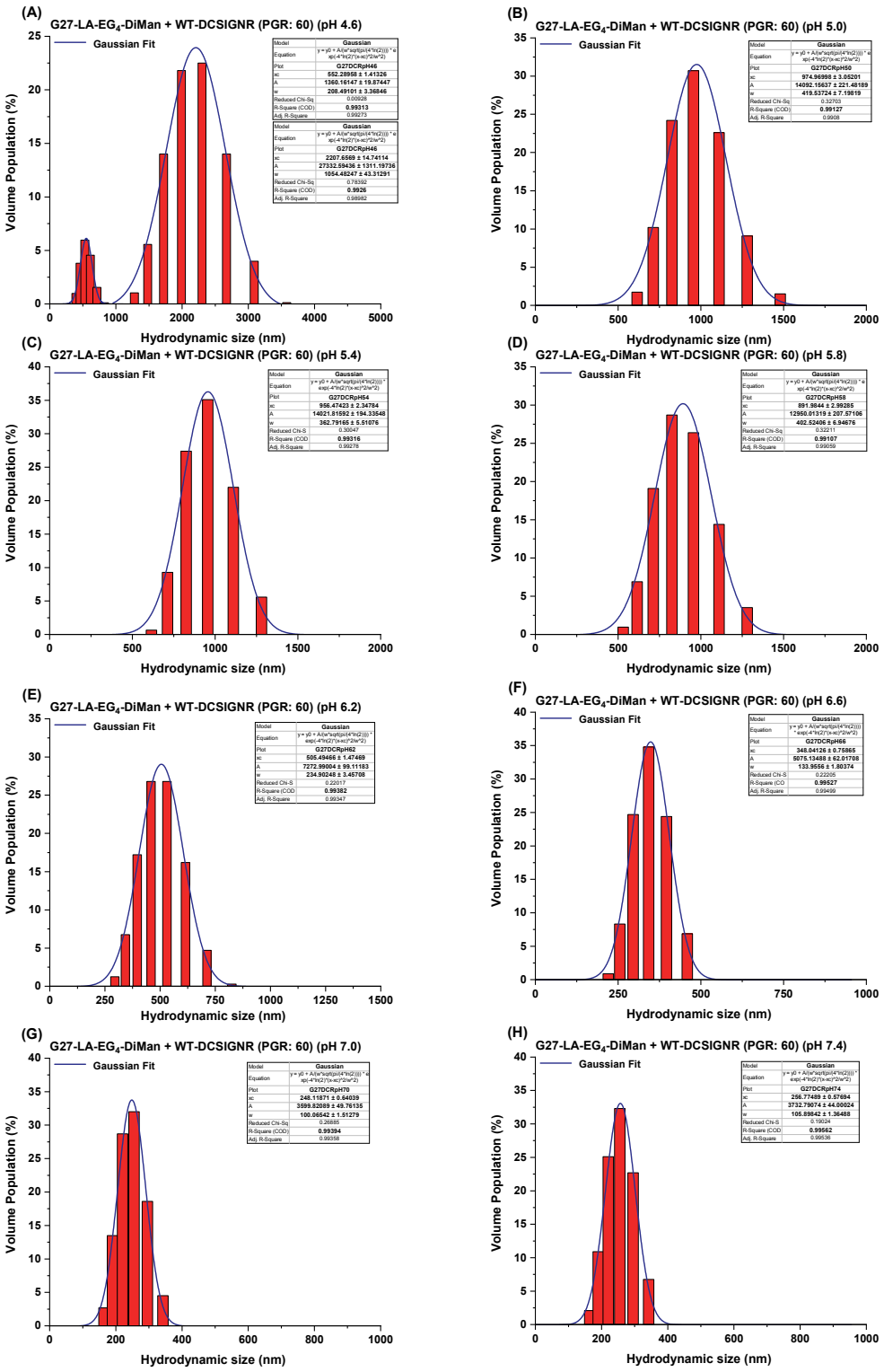

Figure 4.3.4. The DLS histograms of G27-EG$_4$-DiMan+DC-SIGNR at (A) pH 4.6, (B) pH 5.0, (C) pH 5.4, (D) pH 5.8, (E) pH 6.2, (F) pH 6.6, (G) pH 7.0, (H) pH 7.4.

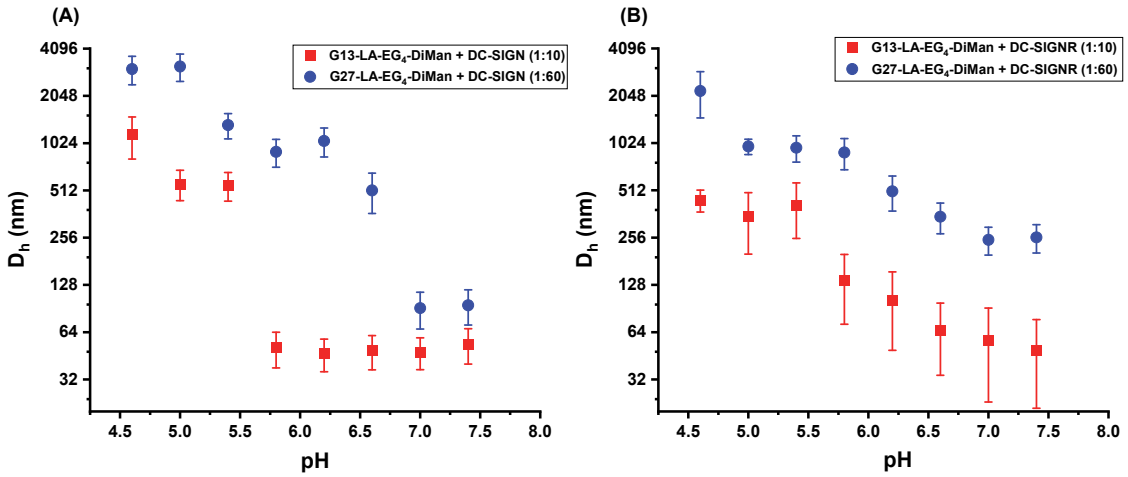

Figure 4.3.5. Summary of the D_h sizes for DC-SIGN/R binding with G13/27-EG_4-DiMan under different pH conditions. D_h values here are displayed as Mean Dh ± ½ FWHM. Mean D_h= ($xc_1.A_1$%) + ($xc_2.A_2$%); FWHM = ($w_1.A_1$%) + ($w_2.A_2$%).

Upon mixing both proteins with GNP-DiMans at different pHs, it was observed that D_h sizes of the resulting GNP-DiMan-lectin complexes decreased with the increasing buffer pH, which can be associated with the conformational changes in proteins as well as their binding behaviours with GNP-DiMan. The large D_hs observed at low pHs indicated that DC-SIGN/R and/or their complexes with GNP-DiMan were extensively aggregated, and not forming rational assemblies by specific lectin-glycan binding between them. Given the much smaller D_hs of the proteins and GNP-glycans on their own, the large D_hs monitored at low pHs could not match that expected for individual GNP-protein assemblies via specific lectin-glycan interactions. Indeed, the much higher D_hs at low pHs were also consistent to the lower fluorescence quenching efficiency (indicating reduced binding) observed for both proteins at low pHs. This showed that there was a positive correlation between the pH-dependent fluorescence quenching efficiency and D_h sizes. Both DLS and fluorescence quenching results suggest that low pH media are likely caused somehow conformational change in proteins which may lead to protein aggregation, leading to reduced binding to GNP-glycans. This result may help explain why glycan ligands are released from DC-SIGN/R-ligand complexes in intracellular compartments, mainly in endosomes and lysosomes that have lower pH levels relative to the cell cytosol.

4.4. pH Switching Studies

In order to check whether the binding is reversible for both DC-SIGN/R, D_hs of GNP-glycans+DC-SIGN/R were monitored by switching the MES buffer pH between pH 7.4 and 5.0 by adding NaOH or HCl. All measurements were carried out using a fixed molar ratio of protein: GNP-glycan (10 and 60 for G13 and G27, respectively) in MES buffer as above. After calibrations on how much HCl and NaOH were needed to change the buffer pH to the desired value, pH-dependent D_h sizes were measured by cycling the MES buffer pH between 7.4 and 5.0 upon alternate addition of 1 M NaOH and 1 M HCl. Four pH switching cycles were carried out to find out how reversible these bindings were. The kinetics of the pH switching was followed by making D_h measurements every 5 mins till D_h sizes stabilized. All D_h size distribution histograms resulting from pH switching for WT-DC-SIGN/R and Gx-DiMan (x=13 and 27 nm) are given in **Appendix A.10**. The monitored D_hs for GNP-protein assemblies upon pH changing between 7.4 and 5.0 are also summarised in **Figure 4.4.1.**

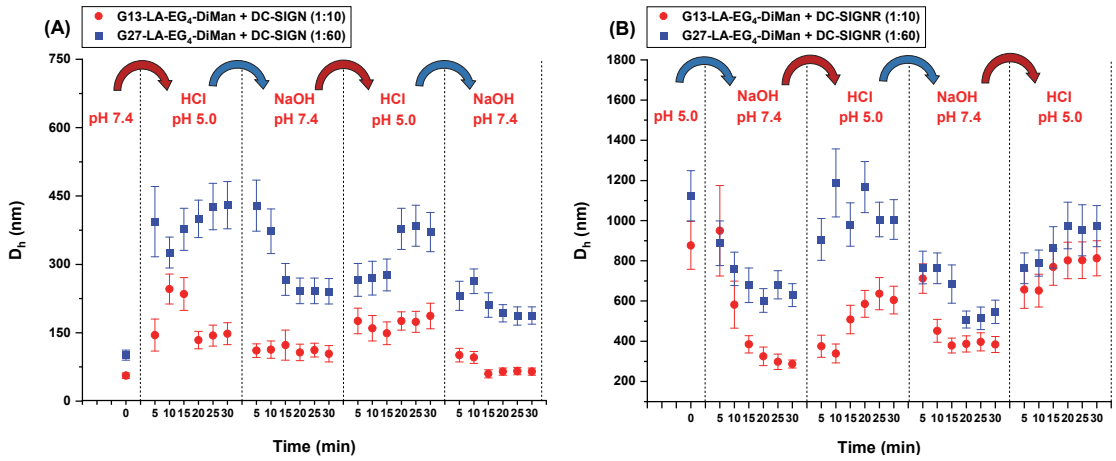

Figure 4.4.1. Summary of the D_h sizes for DC-SIGN/R binding with G13/27-EG_4-DiMan versus time upon pH switching between 7.4 and 5.0. D_h values here are displayed as Mean *D*h ± ½ FWHM. Mean D_h= ($xc_1.A_1$%) + ($xc_2.A_2$%); FWHM = ($w_1.A_1$%) + ($w_2.A_2$%).

D_hs of G13/27-DiMan + DC-SIGN/R samples became stable around 30 mins after pH values were switched. In fact, the D_hs of Gx-DiMan + DC-SIGN samples matched those expected for single Gx-DiMan coated with a single layer of DC-SIGN molecules, consistent DC-SIGN's simultaneous binding mode with Gx-DiMan as revealed in the previous chapter. The D_h sizes of both DC-SIGN/R + Gx-DiMan (x=13 and 27 nm) samples were smaller sizes at pH 7.4 than their pH 5.0 counterpart indicating that DC-

SIGN/R-GNP-DiMan complexes were more extensively aggregated at pH 5. However, when the D_h sizes stabilized 30 mins after pH was switched to 5.0, a significant increase in D_h sizes was observed, suggesting that the formation of large scale GNP-DC-SIGN assemblies. The reduced DC-SIGN/R binding at a slightly acidic environment may be associated with pH-induced loss of tetramer function in DC-SIGN/R. However, D_h sizes was brought back almost to the physiological level, indicating that both DC-SIGN/R binding to GNP-DiMan were reversible in a pH-dependent manner. It should be noted that, while switching pH from 5.0 to 7.4 generally produced smaller assemblies (smaller D_hs), the final stabilised D_hs for DC-SIGN-Gx-DiMan complex were still larger than those prepared at pH 7.4 (this is especially true for G27-DiMan), indicating that only partial restoration of the original Gx-DiMan-DC-SIGN binding were achieved with the 30 min.

4.5. Conclusion

In conclusion, we here probed the pH dependent binding/dissociation process for both DC-SIGN/R with GNP-DiMan via fluorescence quenching and DLS studies. We also sought to reveal whether the binding of both proteins to GNP-DiMan were pH-dependent reversible or not. The pH-dependent fluorescence quenching results showed that DC-SIGN displayed strong binding to Gx-DiMan at physiological pH and the binding was roughly stable from pH 7.4 to 6.0, but as significantly reduced at lower pH. This can explain the strong binding of DC-SIGN with target glycan ligands at extracellular physiological pH and the subsequent dissociation of ligands from DC-SIGN-ligand complexes in the acidic intracellular compartments. In contrast, DC-SIGNR binding to GNP-DiMan exhibited similar low fluorescence quenching efficiency at low pH (*e.g.* 4.6) and physiological pH (*e.g.* 7.4) levels, its fluorescence quenching efficiency was increased and maximised at endosomal pH levels (~6.0). This result suggested that the ligands were not readily released from the internalized DC-SIGNR-ligand assemblies in endosomal compartments. The DLS results indicated that the formation of the expected DC-SIGN/R-GNP-DiMan assemblies both gradually decreased at lower pHs, but increased at higher pHs, suggesting that there was a correlation between pH-dependent fluorescence quenching and DLS studies. pH switching studies also revealed

that both DC-SIGN/R binding with GNP-DiMan were partially reversible in a pH dependent manner. Overall, DC-SIGN binding with ligands was decreased at slightly acidic pH and then its increased rebinding (reversible) when pH was switched to 7.4, supporting that DC-SIGN is a recycling endocytic receptor.[6] The reduced ligand binding with decreasing pH might have occurred due to conformational change or the loss/decrease of tetramer function in DC-SIGN. The acidification of environmental pH might be caused the protonation of the CRD domains to which DC-SIGN binds ligands, resulting in changes in structure and thus decreased function. In addition, the strong DC-SIGNR binding with ligands in a slightly acidic medium (e.g. pH 6.0) indicated that the ligand dissociation from DC-SIGNR-ligand complexes was more difficult in intracellular endosomal pH, making DC-SIGNR more difficult to return to the cell surface to act as a ligand recycling receptor. This result is consistent to earlier findings that DC-SIGNR mainly acts only as an adhesion protein, not a recycling endocytic receptor.

4.6. References

1. G. Tabarani, M. Thépaut, D. Stroebel, C. Ebel, C. Vivès, P. Vachette, D. Durand and F. Fieschi, *J Biol Chem*, 2009, **284**, 21229-21240.
2. T. Gramberg, E. Soilleux, T. Fisch, P. F. Lalor, H. Hofmann, S. Wheeldon, A. Cotterill, A. Wegele, T. Winkler, D. H. Adams and S. Pöhlmann, *Virology*, 2008, **373**, 189-201.
3. Z. Y. Yang, Y. Huang, L. Ganesh, K. Leung, W. P. Kong, O. Schwartz, K. Subbarao and G. J. Nabel, *J Virol*, 2004, **78**, 5642-5650.
4. F. Baribaud, R. W. Doms and S. Pöhlmann, *Expert Opin Ther Targets*, 2002, **6**, 423-431.
5. S. Wragg and K. Drickamer, *Journal of Biological Chemistry*, 1999, **274**, 35400-35406.
6. Y. Guo, H. Feinberg, E. Conroy, D. A. Mitchell, R. Alvarez, O. Blixt, M. E. Taylor, W. I. Weis and K. Drickamer, *Nature Structural & Molecular Biology*, 2004, **11**, 591-598.
7. A. S. Powlesland, E. M. Ward, S. K. Sadhu, Y. Guo, M. E. Taylor and K. Drickamer, *J Biol Chem*, 2006, **281**, 20440-20449.
8. G. A. Snyder, J. Ford, P. Torabi-Parizi, J. A. Arthos, P. Schuck, M. Colonna and P. D. Sun, *J Virol*, 2005, **79**, 4589-4598.
9. T. Zhou, Y. Chen, L. Hao and Y. Zhang, *Cell Mol Immunol*, 2006, **3**, 279-283.
10. Good's buffers (biological buffers) - Uptima, https://www.interchim.fr/ft/0/062000.pdf, (accessed 10.01.2023).
11. B. Fehér, J. Lyngsø, B. Bartók, J. Mihály, Z. Varga, R. Mészáros, J. S. Pedersen, A. Bóta and I. Varga, *Journal of Molecular Liquids*, 2020, **309**, 113065.

12. Atto-643 Product Information, https://www.atto-tec.com/fileadmin/user_upload/Katalog_Flyer_Support/ATTO_643.pdf, (accessed 16/01/2023).

Chapter 5
Probing protein corona formation on GNPs via fluorescence quenching

5.1. Introduction

GNPs are among the most widely used nanomaterials in biomedical research because of their outstanding optical, photothermal, and electromagnetic properties. The ability to integrate them into biological systems requires an in-depth molecular-level understanding of their interactions in a physiological environment. Upon introduction into a complex biological milieu (*e.g.* plasma, saliva, and other protein-containing biological fluids), as the surface of GNPs has high free energy, GNPs are rapidly covered by biomolecules, mainly proteins, forming a protein-dense coating called protein corona.[1] When GNPs are exposed to dynamic biological media, their surface is first coated by high abundance proteins within seconds, creating a transition corona. Tenzer *et al.*[2] found that almost 300 proteins were adsorbed on the nanoparticle surface in less than 30 seconds after the nanoparticles contacted human blood plasma. Subsequently, the proteins with low affinity to the GNPs were progressively and selectively replaced by proteins with high affinities over time, known as Vroman's effect, thus forming a hard corona layer. Based on the proposed model of protein corona formation by Wolfram *et al.*,[3] the soft corona represents a more loosely associated and rapidly exchanging proteins on GNPs over short time scales. Since the hard corona contains tightly adsorbed proteins on GNPs for longer periods, this layer of proteins defines a new identity for GNPs, as shown in **Figure 5.1.1**. As the protein corona surrounding the GNPs is what is ultimately "seen" by cells,[4] this layer is of utmost importance in determining their critical physiological response for further biological processes, including their cellular uptake, biodistribution, circulation lifetime, toxicity, and therapeutic effects.

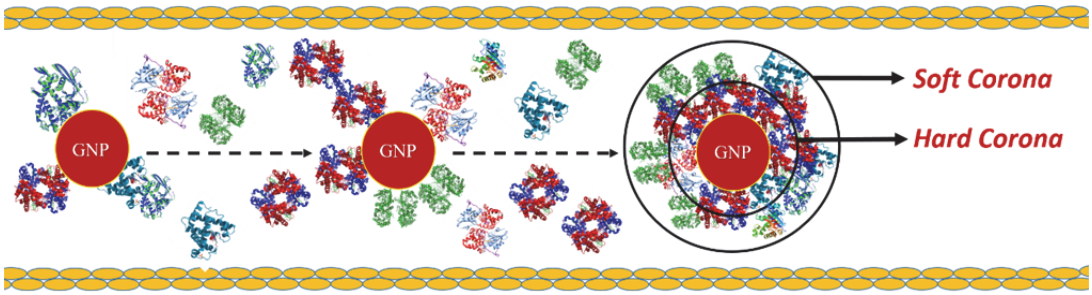

Figure 5.1.1. A schematic representation of understanding the protein corona formation on GNPs. Different proteins are shown as different ribbon diagrams. The gradual protein corona formation on a GNP surface flowing through a biological fluid is illustrated.

Coating the GNPs with a protein corona layer lowers the surface energy of GNPs, thereby promoting their dispersion in the body.[1] Furthermore, the protein corona layer can mask GNPs from recognition by the cells of the reticuloendothelial system, which eliminates them. Paradoxically, this coverage can also result in losing the targeting properties of GNPs.[5] GNPs are usually grafted with a hydrophilic stealth polymer such as polyethylene glycol (PEG) to avoid this dilemma. Thiolated PEG is datively bound to the GNP surface due to the strong binding affinity of sulphur to gold atoms. GNP surface modification with PEG molecules gives them some distinct advantages over bare (or citrate-stabilised) GNPs: (1) PEG moieties can block or reduce the non-specific binding of proteins to the GNP surface, allowing them to reach the relevant site and interact specifically with the targets.[6] (2) Its hydrophilic nature improves the colloidal stability and bioavailability of GNPs in complex biological media.[7] (3) PEG can prevent the recognition of GNPs by macrophages, thereby improving their circulation lifetime by hindering their non-specific uptake.[8] (4) Since PEG is not biodegradable, it accelerates the blood clearance of GNPs at their repeated doses, thus preventing GNP accumulation.[9] Although some reports have highlighted that PEG covered-GNPs are not entirely inert,[9, 10] thus are unable to completely prevent protein corona formation. Moreover, they may also be recognised by immune system cells at increasing concentrations. Nevertheless, PEG grafting remains the best universal coating strategy for GNP surface to reduce non-specific interactions.

Thus far, only a few tens of the more than 3700 proteins found in human blood plasma have been identified to form an ultimate protein corona.[11] The results obtained from many studies show that a basic protein corona layer is composed of nearly 2-6 proteins adsorbed with high abundance and many more specific proteins adsorbed with low

abundance.[12, 13] Albumin is the most abundant protein in the blood, accounting for ~60% of the total proteins, and albumin is known to be one of the major components of the protein corona on the GNP surface after introduction to human blood.[2] Notably, albuminization is a crucial process by which albumin binds densely and tightly to the GNP surface caused by its high affinity for gold surfaces (K_d for GNP surface: $\sim 10^{-6}$ M)[14], creating an albumin-rich protein corona layer on the GNP surface.[4] In addition to the main components of the protein corona, despite their relatively low concentration in plasma, some specific proteins are also found in the corona structure. This is because the mechanisms of protein corona are not at thermodynamic equilibrium,[1] so its composition and organization are exchanging over time, particularly for proteins with lower abundance and affinity.[15] Moreover, upon binding the surface of larger GNPs, the structure, stability and activity/function of both high (e.g. albumin) and low abundance (e.g. lysozyme) proteins can alter. However, proteins on the smaller GNPs have been shown to retain their native-like function and structure for a longer period.[11]

There are two different strategies for understanding the dynamic structure of protein corona formation. The models of the bottom-up approach provide to extract the binding affinity, kinetics, and equilibrium values of protein adsorption quantitatively by mixing only one type of nanoparticle with one type of protein. Conversely, top-down strategies are based on the exposure of GNPs to protein mixtures and then the quantification of proteins adsorbed onto the GNP surface by immunoblotting or mass spectrometry analyses.[7] However, as the exchange processes of the protein corona are quite difficult to model in top-down techniques, they are insufficient to determine which proteins are present on GNPs at specific times.[2] Considering their sensitivity and reproducibility, they are less preferred in studies of protein corona formation. Although the bottom-up methods designed in combination with some techniques such as proteomics, centrifugation, and LC-MS are more commonly used for analysing the protein corona formation, they also have many limitations, such as aggregation, washing steps, and misinterpreting the results.[11] Therefore, there are still barriers to overcome regarding mechanistic insight into the protein corona structure and its formation steps.

Herein, we have designed and developed a new fluorescence quenching method for probing the protein corona formation on GNPs. This novel method is a kind of bottom-up approach that produces the binding affinity data for one type of protein with one type of nanoparticle at a time. The interactions between GNPs coated with several dihydrolipoic acid (DHLA)-PEG-based multifunctional ligands and Atto-594 dye-labelled bovine serum albumin (BSA) and Lysozyme (Lys) proteins were quantified via binding induced protein fluorescence quenching, by exploiting the superb fluorescence quenching properties of GNPs. Based on the derived apparent binding K_d values, the ability to form protein corona of BSA and Lys on GNPs was compared.

5.2. Design and Synthesis of Multivalent GNP-conjugates

In this chapter, the protein corona formation on 1.3 nm GNCs and 5 nm GNPs coated DHLA-PEG -based multivalent ligands containing terminal hydroxy- and methoxy-groups with the proteins BSA and Lys were studied. Their synthesis and characterisation are given in **Chapter 2.2**. GNP-glycan conjugates were not tested here because glycan terminal groups may interact specifically with the biomolecules in human blood, misleading interpretation of protein corona formation on the GNP surface.

5.3. Binding Interactions of G1.3-LA-PEG$_{750}$-OMe with BSA and Lys

The binding interactions (or lack of it) between 1.3 nm GNC-LA-PEG$_{750}$-OMe and BSA/Lys were measured via fluorescence quenching to derive their apparent binding K_d values. Fluorescence spectra of BSA and Lys with and without GNCs were recorded over a range of different concentration at a fixed molar ratio of 1:1 for GNC:BSA. This ratio was kept consant throughout all the concentration ranges studied. The binding buffer containing $CaCl_2$ was not used in protein corona studies to prevent $Ca_3(PO_4)_2$ precipitations that would affect the binding. Instead, all measurements were performed in the PBS buffer (Phosphate-buffered saline, 10 mM $NaHPO_4$, 2 mM KH_2PO_4, 100 mM NaCl, pH 7.4). Different PMT (Photomultiplier tube) voltages were set for the proteins BSA and Lys during the measurements to avoid the signal saturation of the fluorimeter at higher protein concentrations as the Atto-594 dye-labelling

efficiency of each protein was different. The all fluorescence spectra and also the fluorescence quenching efficiency versus the proteins BSA/Lys concentration for 1.3 nm GNC-LA-PEG$_{750}$-OMe were given in **Figure 5.3.1** below.

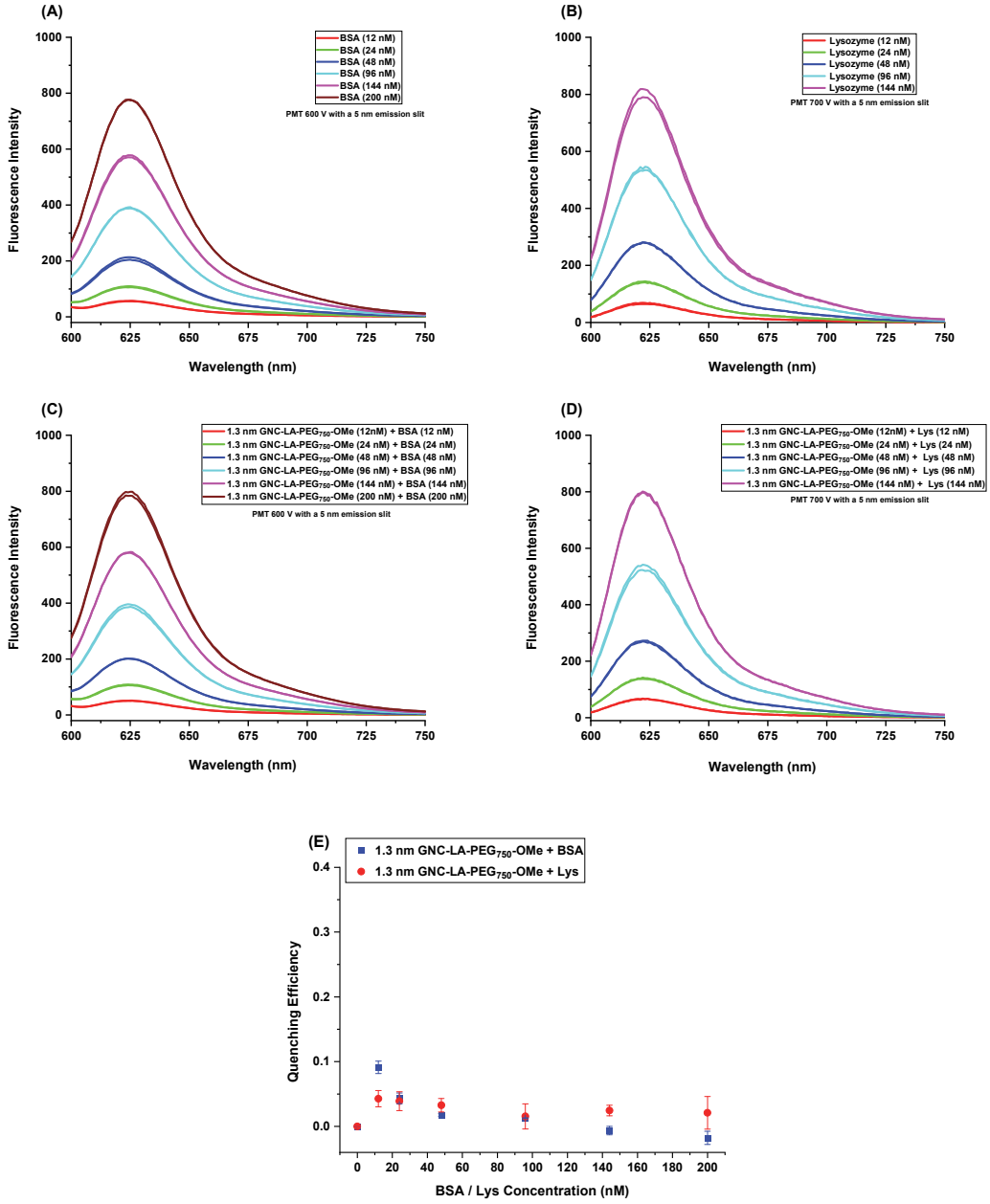

Figure 5.3.1. Fluorescence spectra of (A) BSA using a PMT=600 V; (B) Lysozyme using a PMT=700 V; (C) 1.3 nm GNC-LA-PEG$_{750}$-OMe + BSA using a PMT=600 V; (D) 1.3 nm GNC-LA-PEG$_{750}$-OMe + Lys using a PMT=700 V; (E) The fluorescence quenching efficiency versus the proteins DC-SIGN/R concentration for 1.3 nm GNC-LA-PEG$_{750}$-OMe. The data could not be fitted since the fitting programme did not get them to converge correctly in the range of concentrations studied. Each sample was done in duplicate.

After calculating the integral values of the fluorescence spectra, the quenching efficiency of 1.3 nm GNC was calculated, as shown in **Chapter 2.9**. Then, in order to derive the binding K_d values, the fluorescence efficiency versus protein concentration

relationship was tried to be fitted with the Hill function. However, the data could not be fitted to give satisfactory results because the quenching data remained constantly low throughout the concentration range studied, indicating minimal binding. The results suggested that both BSA and Lys did not show significant adsorption on the PEGylated GNC surface, thus they could not form a substantial protein corona on the GNC surface.

5.4. Binding Interactions of G5-PEGs with BSA and Lys

5.4.1. Binding Interactions of G5-PEGs with BSA

The binding interactions of G5-$(PEG_{1000}\text{-}OH)_n$ (n=1 and 3) and G5-$(PEG_{750}\text{-}OMe)_n$ (n=1, 2, and 3) with Atto-594 labelled BSA were investigated through fluorescence quenching to determine the effects of multifunctional ligands with branched and different terminal functional groups (-OH and -OMe) on protein corona formation. The samples were made in the PBS buffer (10 mM $NaHPO_4$, 2 mM KH_2PO_4, 100 mM NaCl, pH 7.4) and their fluorescence spectra were measured over a range of concentrations at a fixed molar ratio of 1:5 for GNP:BSA. The reason for using a fixed molar ratio of 1:5 for GNP:BSA was due to the low fluorescence signal at low protein concentrations would lead to large errors in calculating the fluorescence quenching efficiency. The fluorescence spectra for only BSA, G5-$(PEG_{1000}\text{-}OH)_n$ (n=1 and 3)+BSA, and G5-$(PEG_{750}\text{-}OMe)_n$ (n=1, 2 and 3)+BSA samples are given in **Figure 5.4.1**, **Figure 5.4.2**, and **Figure 5.4.3**, respectively.

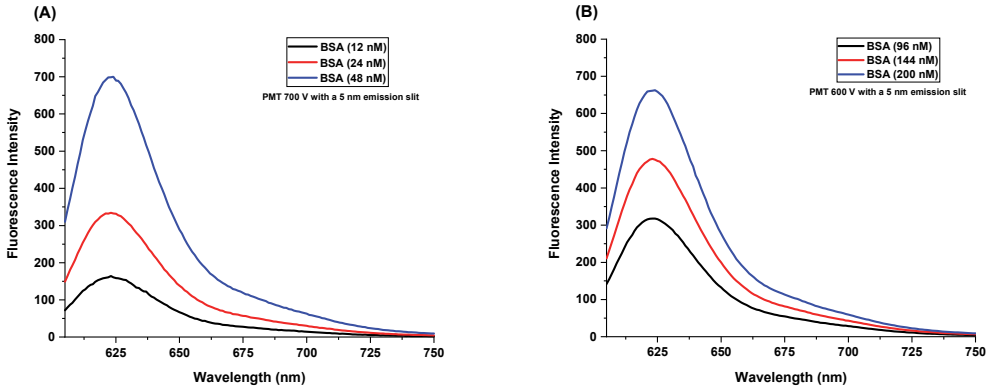

Figure 5.4.1. Fluorescence spectra of the dye-labelled BSA at low (A) and high (B) concentrations.

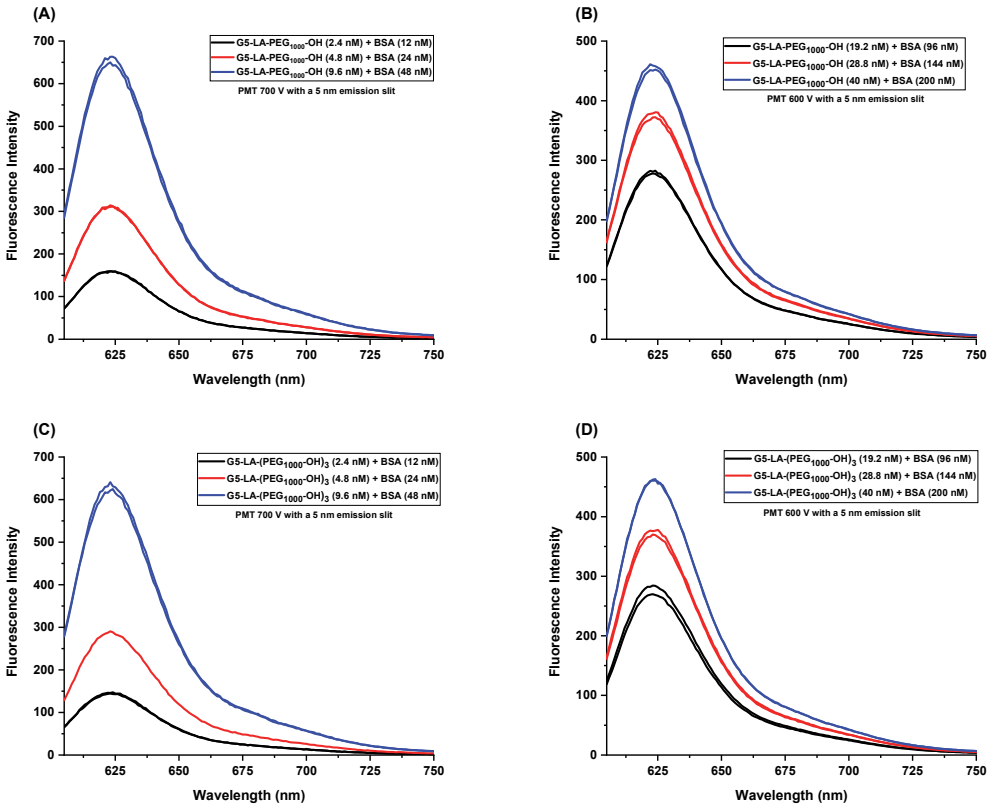

Figure 5.4.2. The fluorescence spectra of labelled BSA with GNPs capped with hydroxyl-terminated PEG-based ligands. (A) G5-PEG_{1000}-OH+BSA at low concentrations using a PMT 700 V; (B) G5-PEG_{1000}-OH+BSA at high concentrations using a PMT 600 V; (C) G5-$(PEG_{1000}\text{-}OH)_3$+BSA at low concentrations using a PMT 700 V; (D) G5-$(PEG_{1000}\text{-}OH)_3$+BSA at high concentrations using a PMT 600 V. Each concentration was done in duplicate.

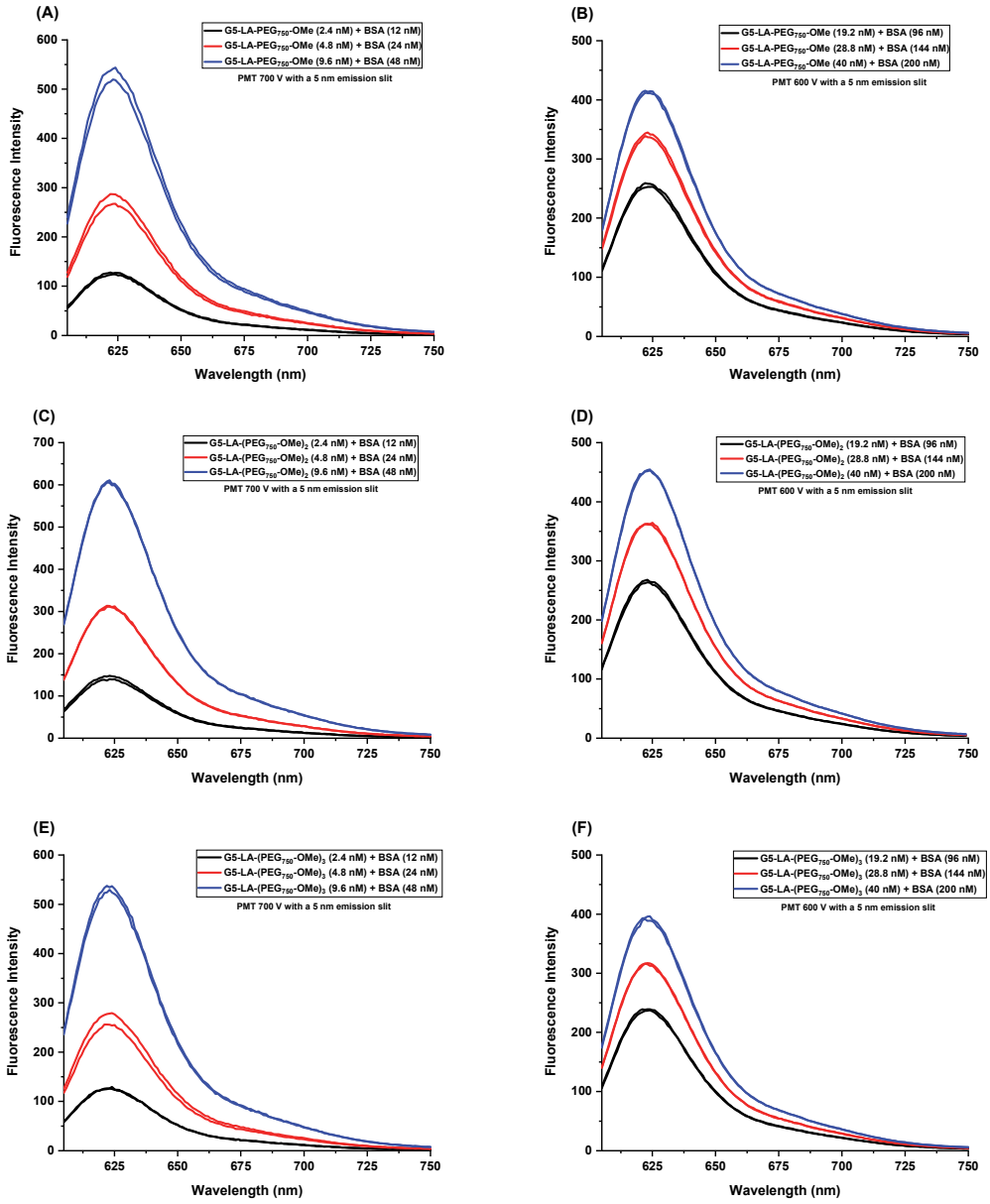

Figure 5.4.3. The fluorescence spectra of labelled BSA with GNPs capped with methoxy-terminated PEG-based ligands. (A) G5-EG_{17}-OMe+BSA at low concentrations using a PMT 700 V; (B) G5-PEG_{750}-OMe+BSA at high concentrations using a PMT 600 V; (C) G5-$(PEG_{750}\text{-OMe})_2$+BSA at low concentrations using a PMT 700 V; (D) G5-$(PEG_{750}\text{-OMe})_2$+BSA at high concentrations using a PMT 600 V; (E) G5-$(PEG_{750}\text{-OMe})_3$+BSA at low concentrations using a PMT 700 V; (F) G5-$(PEG_{750}\text{-OMe})_3$+BSA at high concentrations using a PMT 600 V. Each concentration was done in duplicate.

The fluorescence quenching was calculated from the integral values of the fluorescence intensity of the dye-labelled BSA with and without the G5-PEGs. The fluorescence quenching efficiency versus protein concentration plots were then fitted by the Hill's function to derive the apparent binding affinity K_d for each G5-PEG sample. The resulting binding curves are given in **Figure 5.4.4** and their apparent K_ds and Hill fitting parameters can be listed in **Table 5.4.1** below.

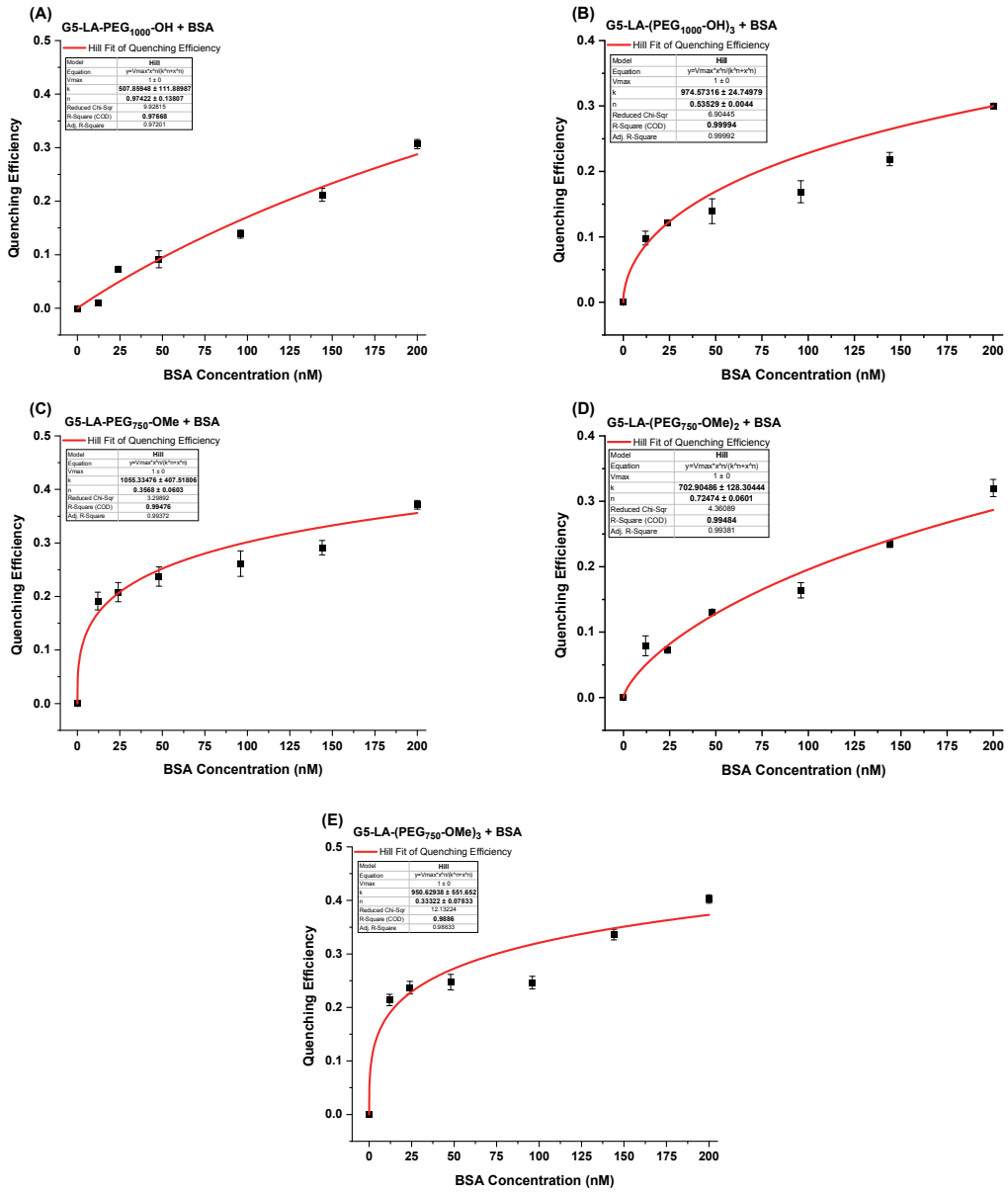

Figure 5.4.4. Percentage fluorescence quenching efficiency curves. (A) G5-LA-PEG_{1000}-OH+BSA; (B) G5-LA-$(PEG_{1000}\text{-OH})_3$+BSA; (C) G5-LA-PEG_{750}-OMe+BSA; (D) G5-LA-$(PEG_{750}\text{-OMe})_2$+BSA; (E) G5-LA-$(PEG_{750}\text{-OMe})_3$+BSA. Data were fitted by Hill's equation.

Table 5.4.1. Summary of Hill's equation fitting parameters for G5-PEGs+BSA binding curves.

G5-PEGs + BSA	Hill's Equation Fitting Parameters		
	K_d / nM	n	R^2
G5-PEG_{1000}-OH – BSA	507 ± 111	0.97 ± 0.13	0.976
G5-$(PEG_{1000}\text{-OH})_3$ – BSA	974 ± 24	0.53 ± 0.01	0.999
G5-PEG_{750}-OMe – BSA	1055 ± 407	0.35 ± 0.06	0.994
G5-$(PEG_{750}\text{-OMe})_2$ – BSA	702 ± 128	0.72 ± 0.06	0.994
G5-$(PEG_{750}\text{-OMe})_3$ – BSA	950 ± 551	0.33 ± 0.07	0.988

Based on the apparent binding K_ds shown in **Table 5.4.1**, BSA appeared to be weakly adsorbed onto the surface of G5-PEGs, leading to considerable quenching, especially at high concentrations. This result is different from that observed with 1.3 nm GNCs. The LA ligands with different PEG branches and terminal functional groups (hydroxyl- and methoxy- moieties) did not exhibit a significant difference in their apparent binding affinity with BSA. Moreover, the ligands containing PEG_{1000} and PEG_{750} were not able to completely prevent the non-specific interactions with BSA. This result broadly agrees with that reported by Garcia-Alvarez *et al.*[10], indicating that a certain amount of plasma protein will always adsorb on the GNP surfaces, regardless of the density and molecular weight of the PEG coating. Also, all calculated Hill coefficients (*n* values) for BSA adsorption were less than 1, indicating that G5-PEGs-BSA interactions display negative cooperative binding, *i.e.* the binding of one BSA molecule on the G5-PEG surface reduces the binding affinity of further BSA molecules on the same G5-PEG surface. In addition, in comparison to that observed with the 1.3 nm GNCs, the amount of BSA adsorbed onto the 5 nm GNP surface was increased, suggesting that BSA has increased tendency to form corona on the surface of similar or large sized GNPs in proportion to its own size.

5.4.2. Binding Interactions of G5-PEGs with Lysozyme

The binding interactions of G5-$(PEG_{1000}\text{-}OH)_n$ (n=1 and 3) and G5-$(PEG_{750}\text{-}OMe)_n$ (n=1, 2, and 3) with the protein lysozyme were investigated using the same procedures as those used BSA as above. While lysozyme is less abundant in plasma than BSA, and it is still useful to examine its protein corona formation on GNPs in order to reach a general conclusion. All fluorescence measurements were done in the PBS buffer under a fixed molar ratio of 1:5 for GNP: Lys as above. The fluorescence spectra for only Lys and G5-$(PEG_{1000}\text{-}OH)_n$ (n=1 and 3)+Lys and also G5-$(PEG_{750}\text{-}OMe)_n$ (n=1, 2, and 3)+Lys samples are given in **Figure 5.4.5** and **Figure 5.4.6**, respectively.

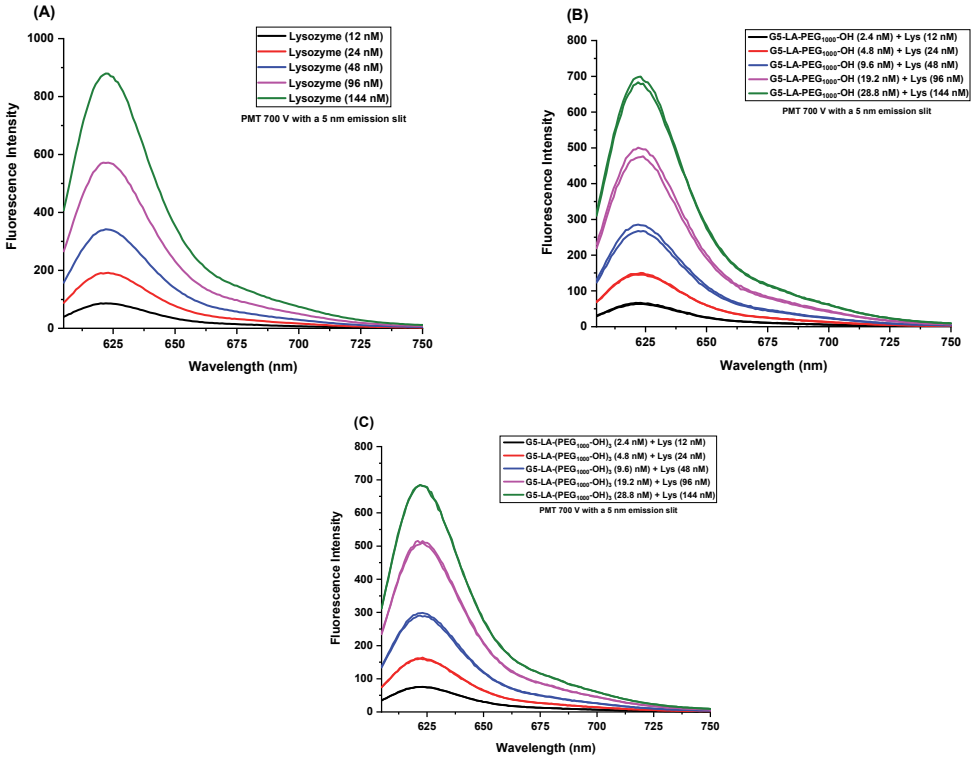

Figure 5.4.5. Fluorescence spectra of the only dye-labelled Lys and the labelled Lys with G5 capped with hydroxyl-terminated PEG-based ligands. (A) The only dye-labelled Lys at different concentrations using a PMT 700 V; (B) G5-PEG_{1000}-OH+Lys using a PMT 700 V; (C) G5-$(PEG_{1000}\text{-OH})_3$+Lys using a PMT 700 V. Each concentration was done in duplicate.

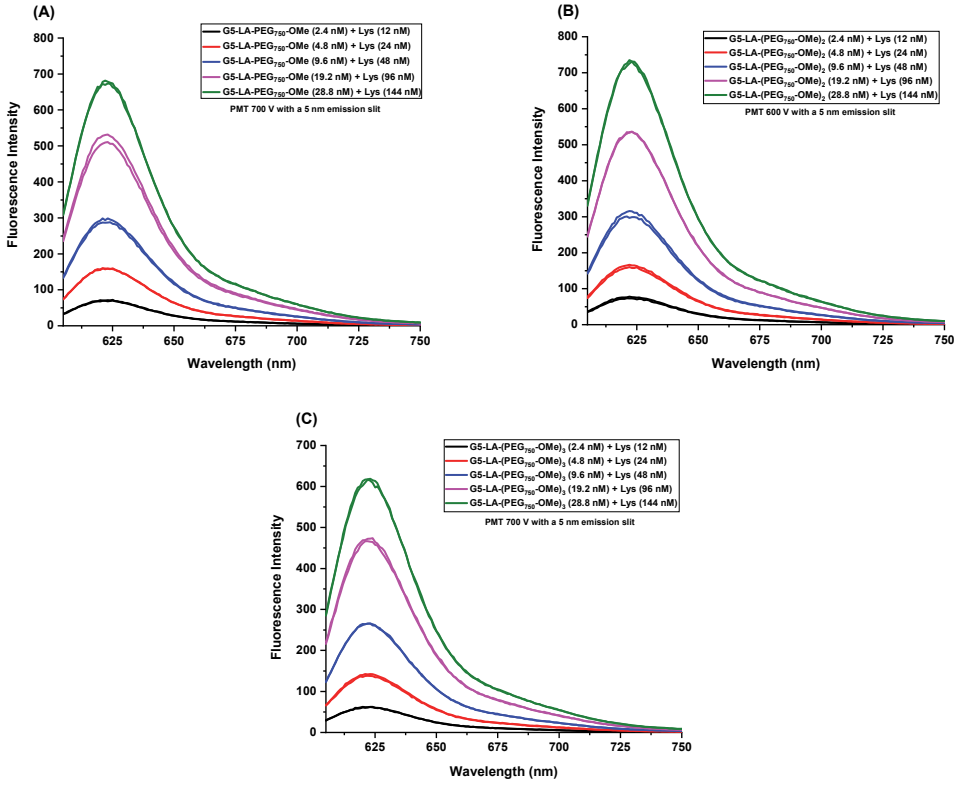

Figure 5.4.6. The fluorescence spectra of the labelled Lys with G5 capped with methoxy-terminated PEG-based ligands. (A) G5-PEG_{750}-OMe+Lys using a PMT 700 V; (B) G5-$(PEG_{750}\text{-OMe})_2$+Lys using a PMT 700 V; (C) G5-$(PEG_{750}\text{-OMe})_3$+Lys using a PMT 700 V. Each concentration was done in duplicate.

After determining the integrated fluorescence intensities of the dye-labelled Lys with and without the G5-PEGs, the respective QEs at varying concentrations were obtained. The QE *vs.* protein concentration plots were then fitted by Hill's function to obtain their apparent binding K_d values for each G5-PEG sample. The resulting binding curves are given in **Figure 5.4.7** and their apparent K_ds and Hill fitting parameters are listed in **Table 5.4.2** below.

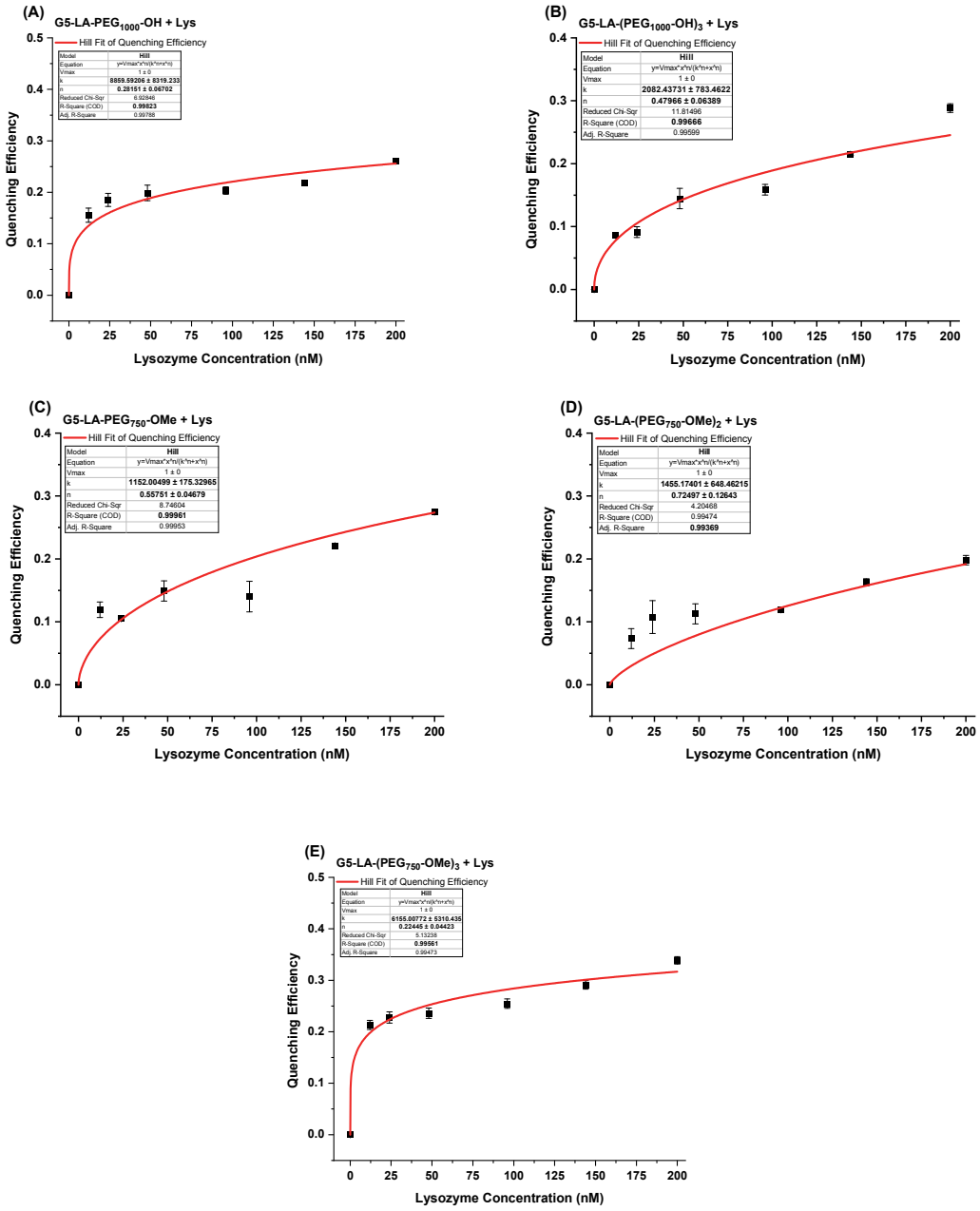

Figure 5.4.7. Plots of fluorescence quenching efficiency *vs.* lysosome concentration fitted by the Hill's equation. (A) G5-LA-PEG_{1000}-OH+Lys; (B) G5-LA-$(PEG_{1000}\text{-OH})_3$+Lys; (C) G5-LA-PEG_{750}-OMe+Lys; (D) G5-LA-$(PEG_{750}\text{-OMe})_2$+Lys; (E) G5-LA-$(PEG_{750}\text{-OMe})_3$+Lys.

Table 5.4.2. Summary of Hill's equation fitting parameters for G5-PEGs+Lys binding curves.

G5-PEGs + Lys	Hill's Equation Fitting Parameters		
	K_d / nM	n	R^2
G5-PEG$_{1000}$-OH – Lys	8859 ± 8319	0.28 ± 0.06	0.998
G5-(PEG$_{1000}$-OH)$_3$ – Lys	2082 ± 783	0.47 ± 0.06	0.996
G5-PEG$_{750}$-OMe – Lys	1152 ± 175	0.55 ± 0.04	0.999
G5-(PEG$_{750}$-OMe)$_2$ – Lys	1455 ± 648	0.72 ± 0.12	0.994
G5-(PEG$_{750}$-OMe)$_3$ – Lys	6155 ± 5310	0.22 ± 0.04	0.995

Comparing the apparent K_d values revealed that Lys had weaker binding affinity to the G5-PEG surface than that of BSA. The binding affinity of Lys appeared to be increased with the increasing of the PEG branches on each LA-PEG-ligands, although care should be taken because of the rather large fitting errors for the some of these data, e.g. G5-PEG$_{1000}$-OH and G5-(PEG$_{750}$-OMe)$_3$. As a result, these different binding K_d values actually do not have significant statistical differences. Therefore, these studies need to be further repeated to reduce error bars in order to reach firm conclusions about how PEG branching affect their Lys binding.

These results showed that the various PEG coatings on the G5 surface could not entirely prevent non-specific adsorptions of Lys, similar to that observed for BSA, irrespective of the PEG density and molecular weights. Moreover, similar to those of BSA, all binding Hill coefficients (*n* values) were also less than 1 (indicative of negative binding cooperativity), suggesting that binding of one Lys on the G5-PEG surface decreased the binding affinity of successive Lys molecules. This is desirable, ensuring that no dense protein corona will form on G5-PEG surface to mask the targeting properties of GNPs. Overall, the binding results of Lys with different sized GNP-PEGs were very similar to those of BSA, which also displayed increased binding affinity with larger sized GNPs.

5.5. Conclusion

In summary, we have developed a new sensitive fluoresce quenching method for measuring the binding affinity of proteins with PEGylated GNPs to probe the protein corona formation. Once GNPs enter the body fluids, their surfaces are covered by

biomolecules, particularly proteins, and hence can prevent their interactions with targets.[11] To address this problem, we sought to elucidate the effects of GNP core sizes and ligand parameters such as surface ligand PEG length, density and terminal functional group on protein corona formation. Based on the knowledge that a dense PEG coating on GNPs could resist non-specific interactions of proteins, we coated GNPs with single and branched PEG ligands of different molecular weights (PEG_{750} and PEG_{1000}) and investigated how these affect protein adsorption. Moreover, we have prepared PEGylated GNPs of different core sizes (*e.g.* 1.3 and 5 nm) and measured their protein binding affinities. Finally, we also probed how the different PEG terminal functional groups on the GNP (-OH and -OMe) affect their binding of proteins. Using model serum proteins of high (*e.g.* BSA) and low (*e.g.* Lys) abundance, we studied their ability of protein corona formation on the GNPs to establish a correlation between protein abundance and affinity.

Four conclusions can be drawn from this study. (1) The PEG coating on the GNP surface could not completely prevent the non-specific adsorption of serum proteins, BSA and Lys, similar to those reported in the literature. Although this result was obtained from two relatively short PEG lengths of average MWs of 750 and 1000 Da (PEG_{750} and PEG_{1000}), the use of longer PEGs (e.g. PEG_{2000}, PEG_{5000}, PEG_{10000}) will be needed to confirm whether this conclusion remains true. Cui *et al.*[16] found that BSA could adsorb on the surface of GNPs coated with PEG_{2000}, but it did not bind to the PEG_{5000} coated GNP surfaces. (2) The binding affinity of proteins was augmented with the increasing GNP scaffold size. Indeed, as GNP size decreases, its surface-to-volume ratio increases due to its surface area shrinks more slowly than the volume.[17] Thus the smaller GNPs, with higher surface-to-volume ratios, may be able to bind more proteins than their larger counterparts at the same gold amounts. However, some proteins may simply too big to fit the surface of very small GNPs, and thus will not be able to form a protein corona. For instance, the size of BSA is ~4 x 4 x 14 nm^3,[3, 18] it may not be able to bind efficiently to 1.3 nm GNC with a D_h of 3.5 nm, however, it could bind with good affinity to G5-PEGs with a D_h of ~10 nm, which is comparable or even bigger than BSA. In addition, compared with the 1.3 nm GNCs, the lower surface curvature for G5 could provide less conformational freedom for PEG linkers, which would thermodynamically

reduce the entopic penalties, thus enhancing the binding of proteins; (3) No obvious effect of the different terminal functional groups on the protein corona formation of BSA and Lys was observed. However, as the number of branching of methoxy-terminated ligands increased, a reducing binding affinity for Lys was observed, suggesting that proteins may not easily find suitable spaces to pack on the GNP surfaces. Also, compared to the previous results reported by Cui *et al.*[16], we anticipated that increasing GNP surface PEG chain density (e.g. using branched PEG-ligands) could reduce protein corona formation. They found that the binding affinity K_d of BSA to citrated stabilized GNPs was ~300 nM. The K_d values increased by 2-3 fold (affinity decreased 2-3 fold) for our branched PEG ligand-coated GNPs. Therefore, coating GNPs with appropriate branched PEG ligands should be a good strategy to block protein corona formation. (4) BSA exhibited higher binding affinity for PEGylated GNPs than Lys. This agreed fully with the results previously reported,[14, 16] that high abundance serum proteins in human blood dominated the contents of protein corona. Overall, this study provided a new fluorescence quenching method to investigate protein corona formation on PEGylated GNPs. It should be noted that it is difficult to directly compare our data with those reported in literature.

5.6. References

1. M. P. Monopoli, C. Åberg, A. Salvati and K. A. Dawson, *Nature Nanotechnology*, 2012, **7**, 779-786.
2. S. Tenzer, D. Docter, J. Kuharev, A. Musyanovych, V. Fetz, R. Hecht, F. Schlenk, D. Fischer, K. Kiouptsi, C. Reinhardt, K. Landfester, H. Schild, M. Maskos, S. K. Knauer and R. H. Stauber, *Nature Nanotechnology*, 2013, **8**, 772-781.
3. J. Wolfram, Y. Yang, J. Shen, A. Moten, C. Chen, H. Shen, M. Ferrari and Y. Zhao, *Colloids Surf B Biointerfaces*, 2014, **124**, 17-24.
4. J. Piella, N. G. Bastús and V. Puntes, *Bioconjug Chem*, 2017, **28**, 88-97.
5. P. C. Ke, S. Lin, W. J. Parak, T. P. Davis and F. Caruso, *ACS Nano*, 2017, **11**, 11773-11776.
6. B. Pelaz, P. del Pino, P. Maffre, R. Hartmann, M. Gallego, S. Rivera-Fernández, J. M. de la Fuente, G. U. Nienhaus and W. J. Parak, *ACS Nano*, 2015, **9**, 6996-7008.
7. B. D. Johnston, W. G. Kreyling, C. Pfeiffer, M. Schäffler, H. Sarioglu, S. Ristig, S. Hirn, N. Haberl, S. Thalhammer, S. M. Hauck, M. Semmler-Behnke, M. Epple, J. Hühn, P. Del Pino and W. J. Parak, *Advanced Functional Materials*, 2017, **27**, 1701956.

8. C. D. Walkey, J. B. Olsen, H. Guo, A. Emili and W. C. W. Chan, *Journal of the American Chemical Society*, 2012, **134**, 2139-2147.
9. S. Schöttler, G. Becker, S. Winzen, T. Steinbach, K. Mohr, K. Landfester, V. Mailänder and F. R. Wurm, *Nat Nanotechnol*, 2016, **11**, 372-377.
10. R. García-Álvarez, M. Hadjidemetriou, A. Sánchez-Iglesias, L. M. Liz-Marzán and K. Kostarelos, *Nanoscale*, 2018, **10**, 1256-1264.
11. P. Aggarwal, J. B. Hall, C. B. McLeland, M. A. Dobrovolskaia and S. E. McNeil, *Advanced Drug Delivery Reviews*, 2009, **61**, 428-437.
12. C. D. Walkey and W. C. Chan, *Chem Soc Rev*, 2012, **41**, 2780-2799.
13. M. Rahman, S. Laurent, N. Tawil, L. H. Yahia and M. Mahmoudi, in *Protein-Nanoparticle Interactions: The Bio-Nano Interface*, eds. M. Rahman, S. Laurent, N. Tawil, L. H. Yahia and M. Mahmoudi, Springer Berlin Heidelberg, Berlin, Heidelberg, 2013, DOI: 10.1007/978-3-642-37555-2_2, pp. 21-44.
14. S. H. D. P. Lacerda, J. J. Park, C. Meuse, D. Pristinski, M. L. Becker, A. Karim and J. F. Douglas, *ACS Nano*, 2010, **4**, 365-379.
15. Y. K. Lee, E. J. Choi, T. J. Webster, S. H. Kim and D. Khang, *Int J Nanomedicine*, 2015, **10**, 97-113.
16. M. Cui, R. Liu, Z. Deng, G. Ge, Y. Liu and L. Xie, *Nano Research*, 2014, **7**, 345-352.
17. M. E. Aubin-Tam and K. Hamad-Schifferli, *Biomed Mater*, 2008, **3**, 034001.
18. J. Mariam, S. Sivakami and P. M. Dongre, *Drug Delivery*, 2016, **23**, 2668-2676.

Chapter 6
Overall summary and future work directions

6.1. General Conclusions

The overall aim of this thesis is to reveal the biophysical mechanisms of multivalent lectin-glycan interactions using densely glycosylated gold nanoparticles (GNP-glycans) as multifunctional probes. Here, the binding interactions of GNP-glycans with DC-SIGN and DC-SIGNR, a pair of closely related tetrameric viral lectin receptors, have been investigated by a novel multimodal readout strategy comprising fluorescence quenching based affinity quantitation, hydrodynamic size analysis (DLS), and transmission electron microscopy (TEM) analysis of binding induced lectin-GNP assemblies. Initial works using 5 nm GNP (G5)-coated with LA-PEG-OH control ligands gave unexpected strong bindings with K_d values of ~60 nM for Atto-594 labelled DC-SIGN. Repeating the experiments using the same ligand capped 1.3 nm GNCs and Atto-643 labelled DC-SIGN revealed that the reason behind this unexpected fluorescence quenching was due to the inner filter effect of G5, *via* its strong absorption at the excitation wavelength. Therefore, all latter binding studies were performed with DC-SIGN/R labelled with Atto-643, a redder emitting dye that effectively minimised GNP's inner filter effect. The binding studies between GNP-glycan and Atto-643 labelled DC-SIGN/R revealed three significant findings. (1) The GNP scaffold size strongly affects GNP-glycans' affinity with DC-SIGN/R. Apparent binding K_ds for Gx-DiMan (n = 5, 13, and 27 nm) were found as 5.8, 1.0, and 0.2 nM for DC-SIGN, and 14.9, 2.7, and 0.54 nM for DC-SIGNR, respectively. Therefore, increasing the GNP scaffold size can provide a better spatial and geometric fit for the binding interactions between GNP surface glycan ligands and DC-SIGN/R. (2) A polyvalent display of dimannose glycans on the GNP surface produced stronger affinity enhancement in binding to DC-SIGN/R over the monomannose counterparts. This is likely due to that monomannose binds only to the primary binding sites on DC-SIGN/R CRDs, whereas dimannose may be able to bind to both the primary and secondary binding sites.[1] (3) Increasing GNP surface glycan density is generally beneficial for enhancing GNP-glycan's binding affinity with DC-

SIGN/R. (4) Ligand EG_n linker length has a strong effect in the GNP-glycan binding with DC-SIGN/R, particularly for the smaller sized GNP scaffold. However, only EG units of 2 and 4 have been studied here, and a wider range of EG lengths will be needed in order to obtain more conclusive data. (5) The binding modes between DC-SIGN/R and GNP-glycans have been studied by DLS, revealing that all four CRDs in DC-SIGN simultaneously bind to one GNP-glycan, while those in DC-SIGN/R crosslink different GNP-glycans, which has been verified by cryo-TEM imaging. Overall, these findings are in full agreement with those observed previously in our group with glycan-quantum dots, and are consistent with the different CRD orientations in DC-SIGN/R proposed by our research group.[2] CRDs in DC-SIGN face the same direction, but those in DC-SIGNR are positioned sideways as a pair of dimers.

In chapter 3, DC-SIGN/R binding thermodynamics with GNP-glycans were also probed by the fluorescence quenching method. We found that DC-SIGN-GNP-glycan binding is entirely an enthalpy-driven process and incurs large entropic penalties. In contrast, the strong favourable binding enthalpic contribution is significantly reduced in DC-SIGNR over DC-SIGN, although its binding is compensated with a small favourable binding entropy change. The viral inhibition studies revealed that the produced GNP-glycans are highly potent inhibitors against DC-SIGN/R mediated Ebola viral cell entry. In particular, we have revealed that G27-EG_4-DiMan is the most potent GNP-glycan inhibitor ever reported against DC-SIGN/R- mediated EBOV-GP-driven viral infections of host cells, with impressively low IC_{50} values of 23±1 pM and 49±2 pM, respectively. There is a strong positive correlation between IC_{50} and K_d values, indicating that our novel fluorescence quenching-based affinity measurement technique can serve as a rapid, reliable, and sensitive method to predict the inhibition potency of glyconanoparticles against lectin-mediated viral infection at the cellular level.

Chapter 4 reported the pH-dependency studies of DC-SIGN/R binding with GNP-glycan via fluorescence quenching and DLS. DC-SIGN was found to bind strongly with glycan ligands at over the pH range of 6.0 to 7.4, however, its binding affinity was significantly decreased as pH was reduced to 6.0 and below. This observation completely agrees with what expected for DC-SIGN based upon its biological function of endocytic recycle receptor. Following DC-SIGN-mediated cellular internalization of ligands into

endosomes at physiological pH, the gradual acidification of intracellular endosomes will lead to dissociation of ligands from the DC-SIGN-ligand complex, allowing DC-SIGN to cycle back onto cell surfaces for further ligand binding and internalisation.[3] In contrast, DC-SIGNR displayed increased binding affinity with ligands as pH was reduced from 7.4 to 6.0, its reached the maximum at pH 6.0, then further reducing pH led to weakened affinity. This result is consistent to DC-SIGNR being not an endocytic recycling receptor. In addition, both DC-SIGN/R binding with GNP-DiMan were found to be reversible in a pH-dependent manner.

Chapter 5 presented the studies of protein corona formation on PEGylated GNP surfaces. Considering the vital role of protein corona formation for GNPs in therapeutic usage, this was investigated by fluorescence quenching method for the first time. The binding affinity of two model proteins, BSA and Lys, which are of high and low abundances in human blood plasma, respectively, to PEGylated GNP surfaces was quantified. Some significant results are obtained as follows: (1) PEG coatings on the GNP surface cannot completely prevent the adsorption of BSA and Lys, which are fully consistent with the results reported by Garcia-Alvarez *et al.*[4] (2) The binding affinity of proteins are enhanced with the increasing GNP scaffold size. (3) The different terminal functional groups of GNP surface PEG ligands do not have significant impact on their binding with BSA and Lys. (4) The fact that the high abundant BSA has a higher binding affinity than that low abundance Lys for PEGylated GNP surfaces indicates the former should be the major component of protein corona formed on the GNP surface.

6.2. Future Works

6.2.1. Chapter 3 – Future Work

I would first suggest that further work should extend the GNP scaffold size ranges used to construct GNP-glycans, particularly with GNPs of 30 nm and above, to probe how further increasing GNP scaffold size affects their binding with DC-SIGN/R. This would extend my current observations on the positive correlation between the GNP scaffold size and their DC-SIGN/R binding affinity over a wider size range, to find out whether it will level off at a certain threshold size. Moreover, only spherical GNPs of three different sizes (5, 13 and 27 nm) were used in this thesis. It will be interesting to use

other shaped particles, e.g. gold nanorods and nanotriangles, to construct GNP-glycans to study how scaffold shape affect their binding interactions with DC-SIGN/R. Changing the scaffold shape with lower surface curvatures may provide a better geometric fit for glycan ligands in binding to the CRDs in DC-SIGN/R over the spherical ones. In addition, to obtain a clearer conclusion on how EG linker length between the GNP anchoring (LA) and terminal glycan moieties affects their binding affinity with DC-SIGN/R, future work also need to be investigate over a wider range of different EG linker lengths. Besides the EG linker units of 2 and 4 studied here, I specifically suggest to extend the EG_n linker length to 8, 12, and 16, and compare their DC-SIGN/R binding affinities to establish a correlation between the linker length, GNP scaffold size and their lectin binding affinity. A longer EG linker length may provide greater conformational flexibility for the terminal glycans, potentially offering a better spatial and orientational match for the CRDs in DC-SIGN/R to enhance binding affinity. However, too long an EG_n linker may also reduce the ordering of the terminal glycans and cause some being buried within the long and flexible EG chains, leading to reduced affinity. Therefore, there could be an optimal EG_n length for each specific sized GNPs. Also, a novel fluorescence quenching method has been introduced to examine the DC-SIGN/R binding thermodynamics in this thesis. To more clearly demonstrate its viability and sensitivity, I strongly recommend to repeat the thermodynamic experiments using the isothermal titration calorimetry method (ITC), which is the most widely used technique for binding thermodynamic studies,[5] and then compare the results with those obtained in fluorescence quenching to verify its credibility. I have introduced G27-EG_4-DiMan as the most potent glycan-nanoparticle inhibitor against DC-SIGN/R mediated pseudo-Ebola viral infection in this thesis. The affinity data to be obtained from the above suggested experiments will further help to create more specific multivalent glycan inhibitors.

6.2.2. Chapter 4 – Future Work

I have shown that both DC-SIGN/R binding with GNP-glycans were pH-dependent, and their binding were reversible in a pH-dependent manner. To fully understand the pH dependency of DC-SIGN/R binding, future work is needed to perform cryo-TEM imaging by performing rapid plunge-freezing of GNP-glycan-protein samples at each

investigated pH points, followed by vacuum drying and S/TEM imaging. This would allow direct capturing the native dispersion state of GNP-protein assemblies at different pH values, free of drying induced artefacts often observed in conventional TEM imaging. It will also be helpful to evaluate the effect of pH on the tetrameric oligomerization stability of both DC-SIGN/R by size exclusion chromatography at different pH values, ranging from 4.6 to 7.4 followed by native PAGE analysis. This may help elucidate the relationship between their poorly understood pH-dependent ligand binding/dissociation mechanisms and their tetrameric structure. Further studies are needed to measure the luciferase activities for determination of the pH-dependent inhibition abilities of GNP-glycans against pseudo-Ebola infection over a range of pHs in cell lines expressing DC-SIGN/R, which may vary depending on the ligand binding/release property of these proteins. This could be important to bring the research closer to *in vivo* conditions to figure out how the dynamics of ligand binding/internalization of DC-SIGN/R found on the cell surface are affected at different pH values. Fully understanding the effect of pH on both DC-SIGN/R functions will helpful in solving current struggles in achieving efficient targeting of nanomedicines against viral infections *in vivo*.

6.2.3. Chapter 5 – Future Work

In this chapter, the ability of the protein corona formation of BSA and Lys proteins on GNPs coated with glycan-free PEGylated ligands has been investigated for the first time through the fluorescence quenching method. Further research will extend this study with GNPs containing glycan ligands. Moreover, only 1.3 and 5 nm GNPs have been employed in this thesis, the protein corona experiments are needed for the 13 and 27 nm GNPs, particularly given that G27-DiMan is the most potent GNP-based inhibitor for DC-SIGNR-mediated viral infection ever reported. Furthermore, besides the proteins BSA and Lys, the binding interactions of other proteins, such as globulins, lipoproteins, and fibrinogens, which are present in considerable amounts in human blood plasma, with GNP coated with various ligands share be probed using the same method. All results can then be compared to create a rational relationship between the abundance of proteins in plasma and the relative abundance found on the protein corona layer on GNPs. As pH conditions can be an essential factor in the binding

interactions of proteins with GNPs, as highlighted in Chapter 4, the binding affinities of proteins to the GNP surface at different pHs would be beneficial for evaluating the protein corona formation.

6.3. References

1. H. Feinberg, D. A. Mitchell, K. Drickamer and W. I. Weis, *Science*, 2001, **294**, 2163-2166.
2. Y. Guo, C. Sakonsinsiri, I. Nehlmeier, M. A. Fascione, H. Zhang, W. Wang, S. Pöhlmann, W. B. Turnbull and D. Zhou, *Angew Chem Int Ed Engl*, 2016, **55**, 4738-4742.
3. Y. Guo, H. Feinberg, E. Conroy, D. A. Mitchell, R. Alvarez, O. Blixt, M. E. Taylor, W. I. Weis and K. Drickamer, *Nature Structural & Molecular Biology*, 2004, **11**, 591-598.
4. R. García-Álvarez, M. Hadjidemetriou, A. Sánchez-Iglesias, L. M. Liz-Marzán and K. Kostarelos, *Nanoscale*, 2018, **10**, 1256-1264.
5. D. Prozeller, S. Morsbach and K. Landfester, *Nanoscale*, 2019, **11**, 19265-19273.

Appendix

A.1. Hydrodynamic Size Histograms for G5-LA-EG$_2$-DiMan and G5-LA-EG$_2$-DiMan-diluted with DHLA-ZW Ligands

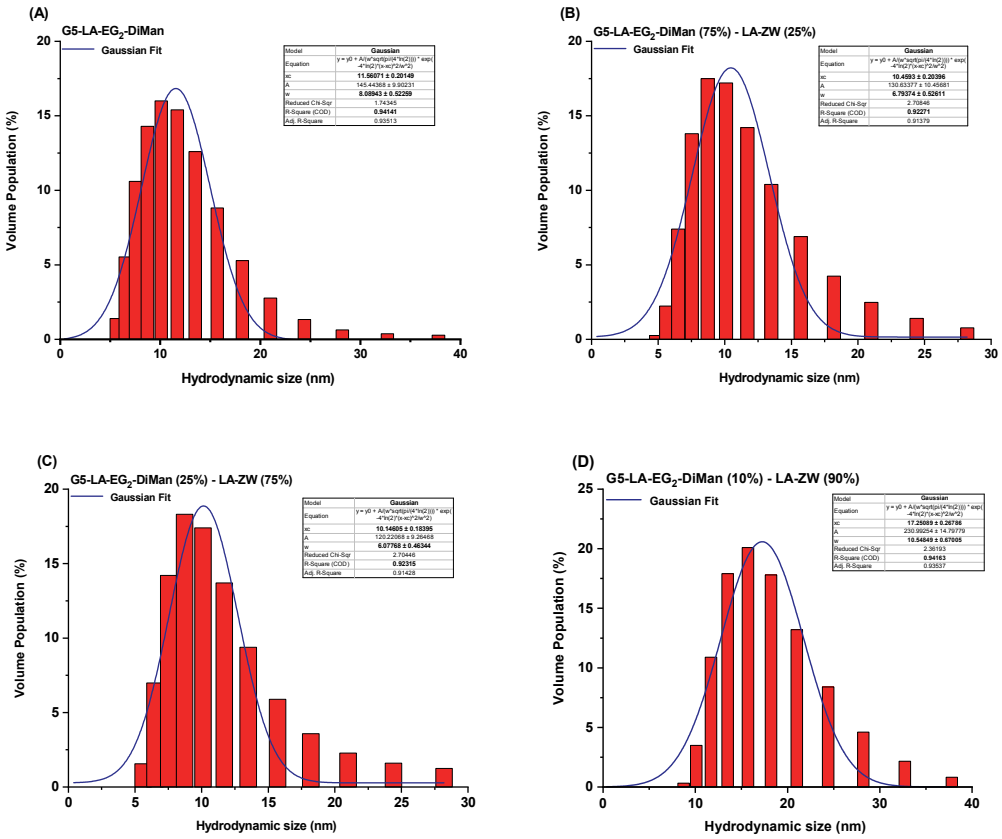

Figure A.1.1. Hydrodynamic size histograms for (A) G5-LA-EG$_2$-DiMan (100%); (B) G5-LA-EG$_2$-DiMan (75%) - LA-ZW (25%); (C) G5-LA-EG$_2$-DiMan (25%) - LA-ZW (75%); (D) G5-LA-EG$_2$-DiMan (10%) - LA-ZW (90%). They were fitted by Gaussian function with fitting parameters shown in each graph. Data were shown in volume population.

A.2. Fluorescence Spectra for G5-Glycans with DC-SIGN/R

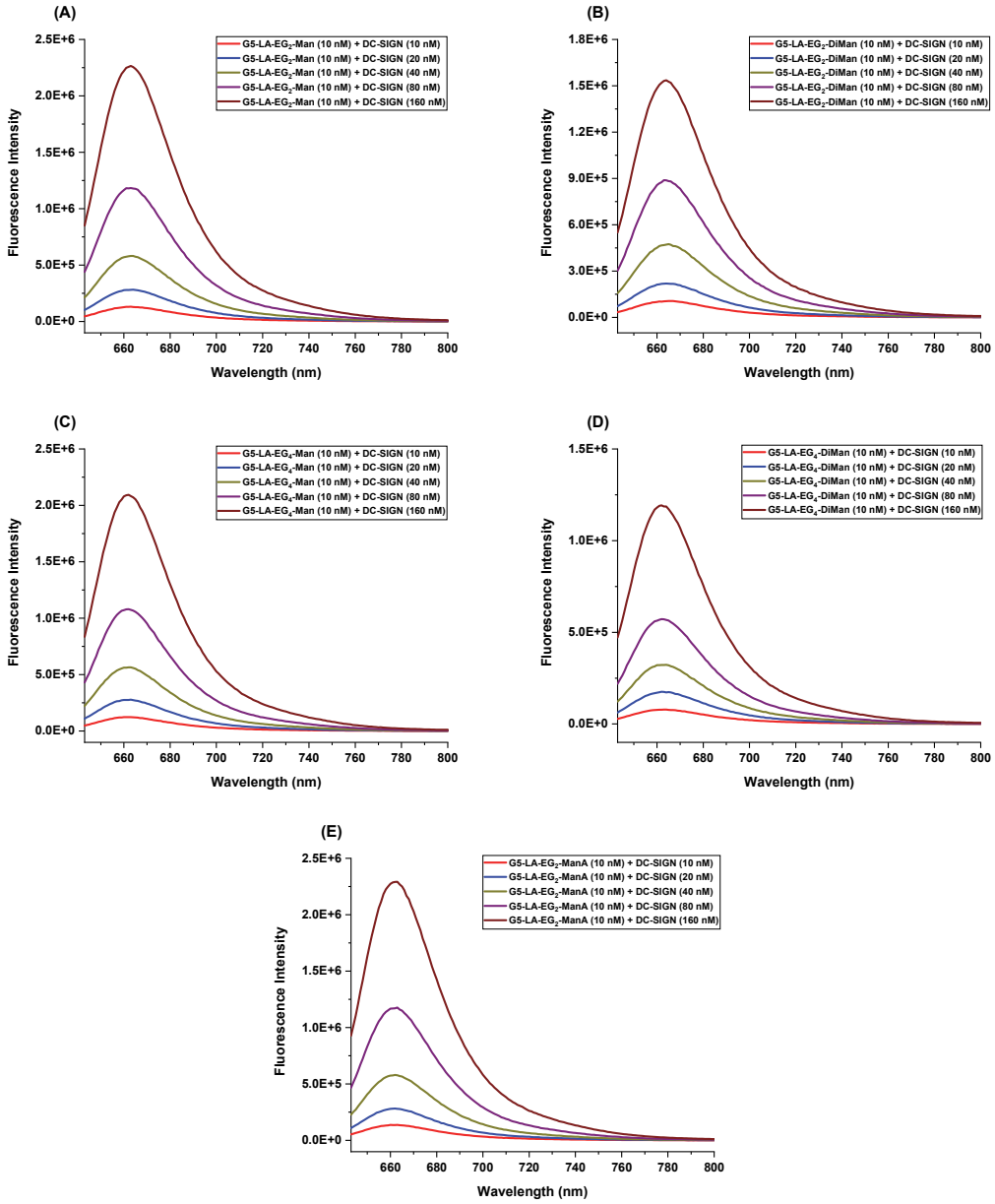

Figure A.2.1. The fluorescence spectra of (A) G5-EG_2-Man+DC-SIGN; (B) G5-EG_2-DiMan+DC-SIGN; (C) G5-EG_4-Man+DC-SIGN; (D) G5-EG_4-DiMan+DC-SIGN; (E) G5-EG_2-ManA+DC-SIGN. Each concentration was done in duplicate and their average fluorescence spectra was constructed.

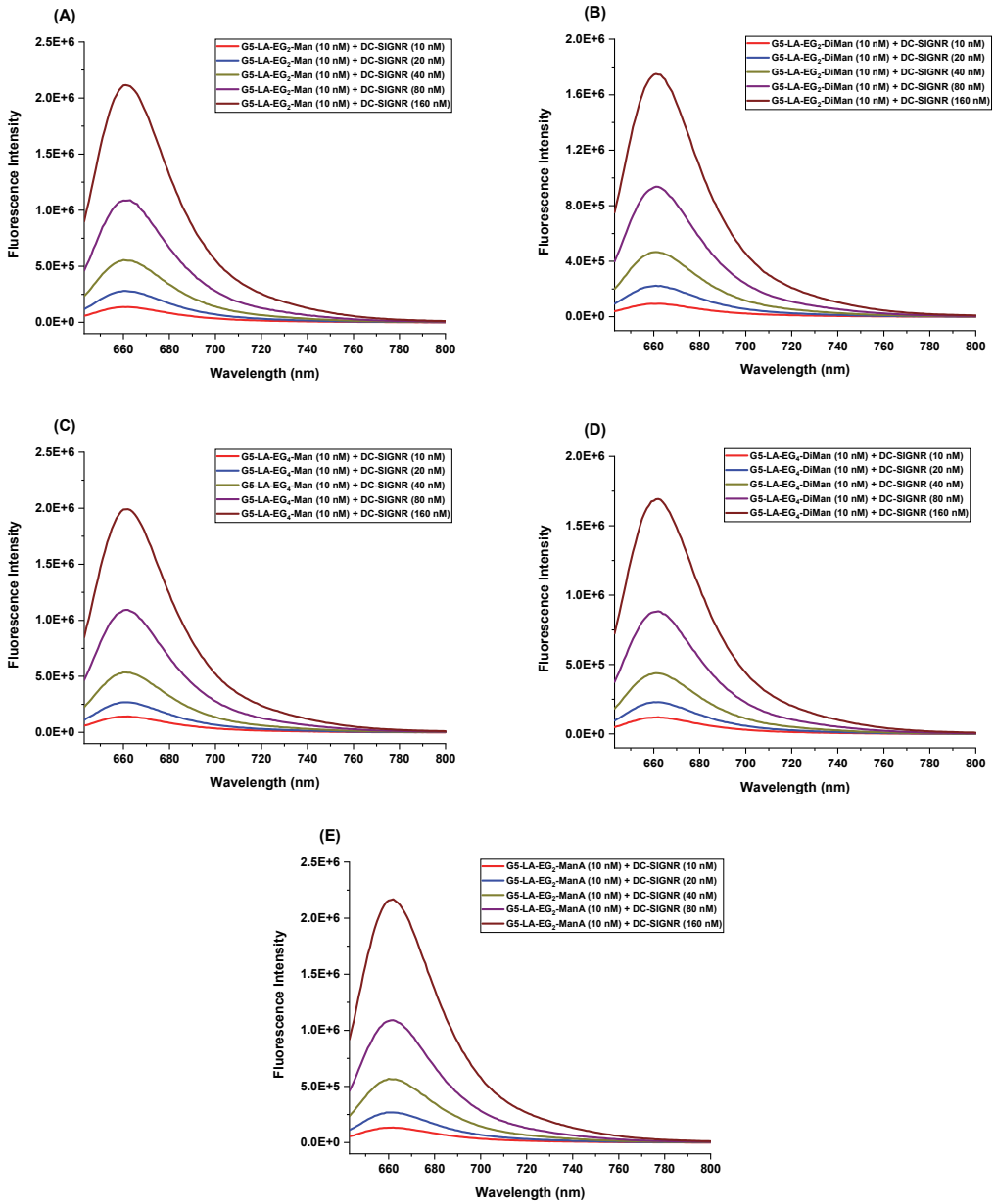

Figure A.2.2. The fluorescence spectra of (A) G5-EG_2-Man+DC-SIGNR; (B) G5-EG_2-DiMan+DC-SIGNR; (C) G5-EG_4-Man+DC-SIGNR; (D) G5-EG_4-DiMan+DC-SIGNR; (E) G5-EG_2-ManA+DC-SIGNR. Each concentration was done in duplicate and their average fluorescence spectra was constructed.

A.3. Fluorescence Spectra for G13-Glycans with DC-SIGN/R

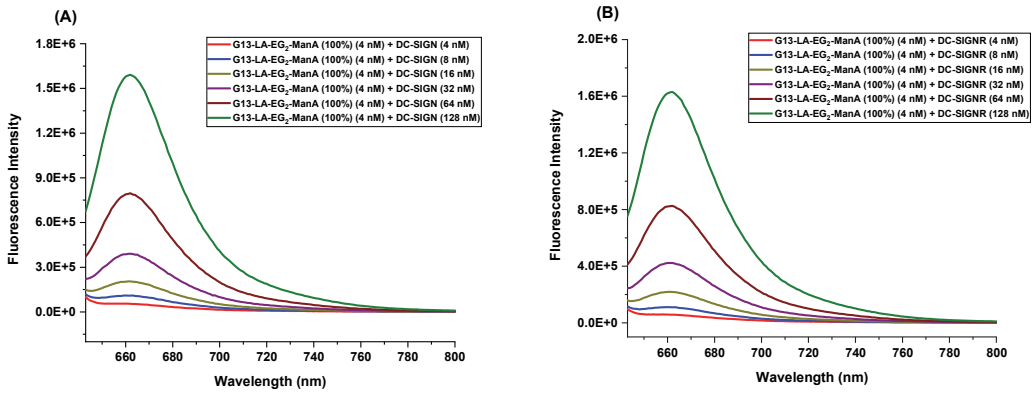

Figure A.3.1. The fluorescence spectra of (A) G13-EG_2-ManA (100%)+DC-SIGN; (B) G13-EG_2-ManA(100%)+DC-SIGNR. Each concentration was done in duplicate and their average fluorescence spectra was constructed.

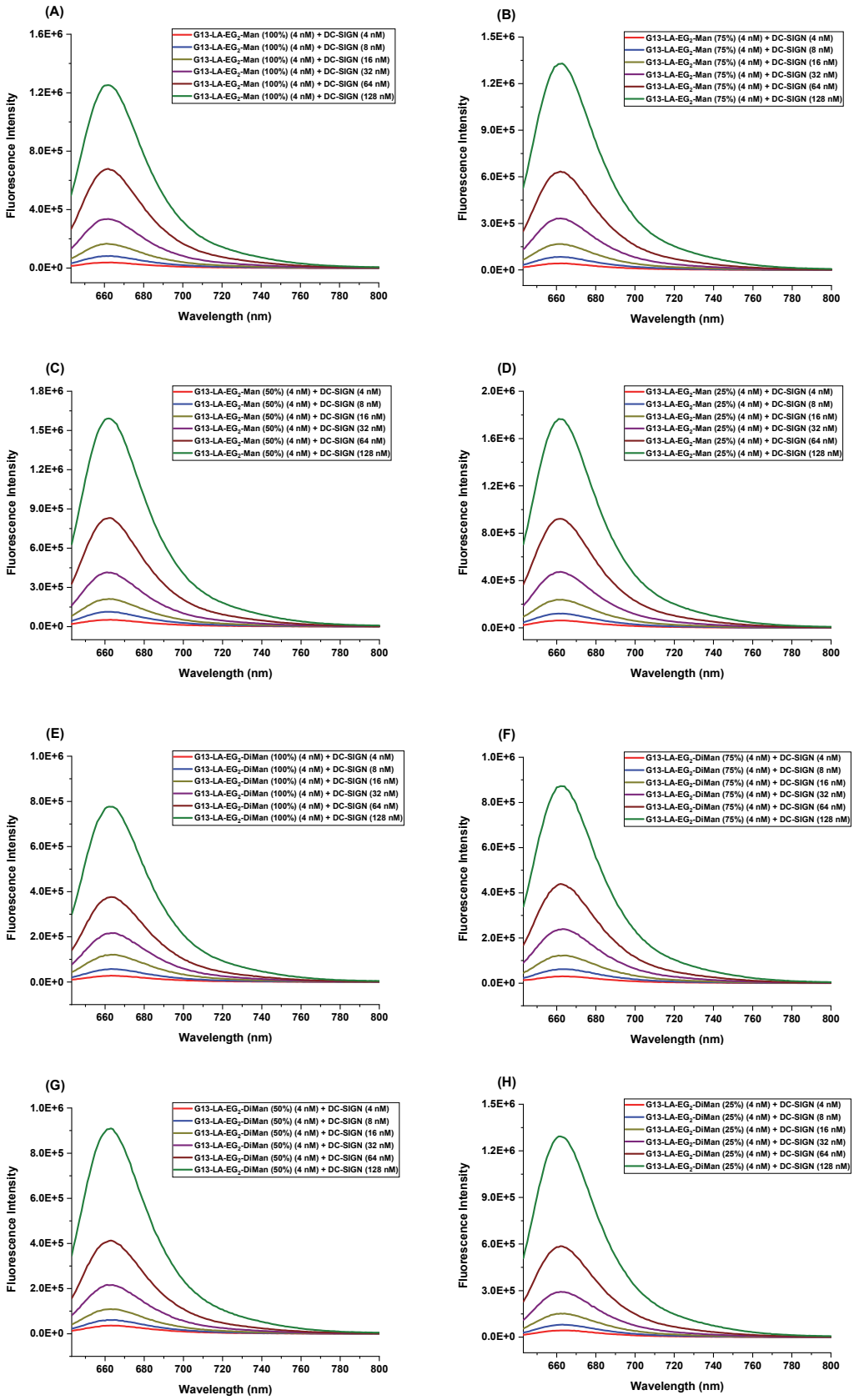

Figure A.3.2. The fluorescence spectra of (A) G13-EG_2-Man (100%)+DC-SIGN; (B) G13-EG_2-Man(75%)+DC-SIGN; (C) G13-EG_2-Man(50%)+DC-SIGN; (D) G13-EG_2-Man(25%)+DC-SIGN; (E) G13-EG_2-DiMan (100%)+DC-SIGN; (B) G13-EG_2-DiMan(75%)+DC-SIGN; (C) G13-EG_2-DiMan(50%)+DC-SIGN; (D) G13-EG_2-DiMan(25%)+DC-SIGN. Each concentration was done in duplicate and their average fluorescence spectra was constructed.

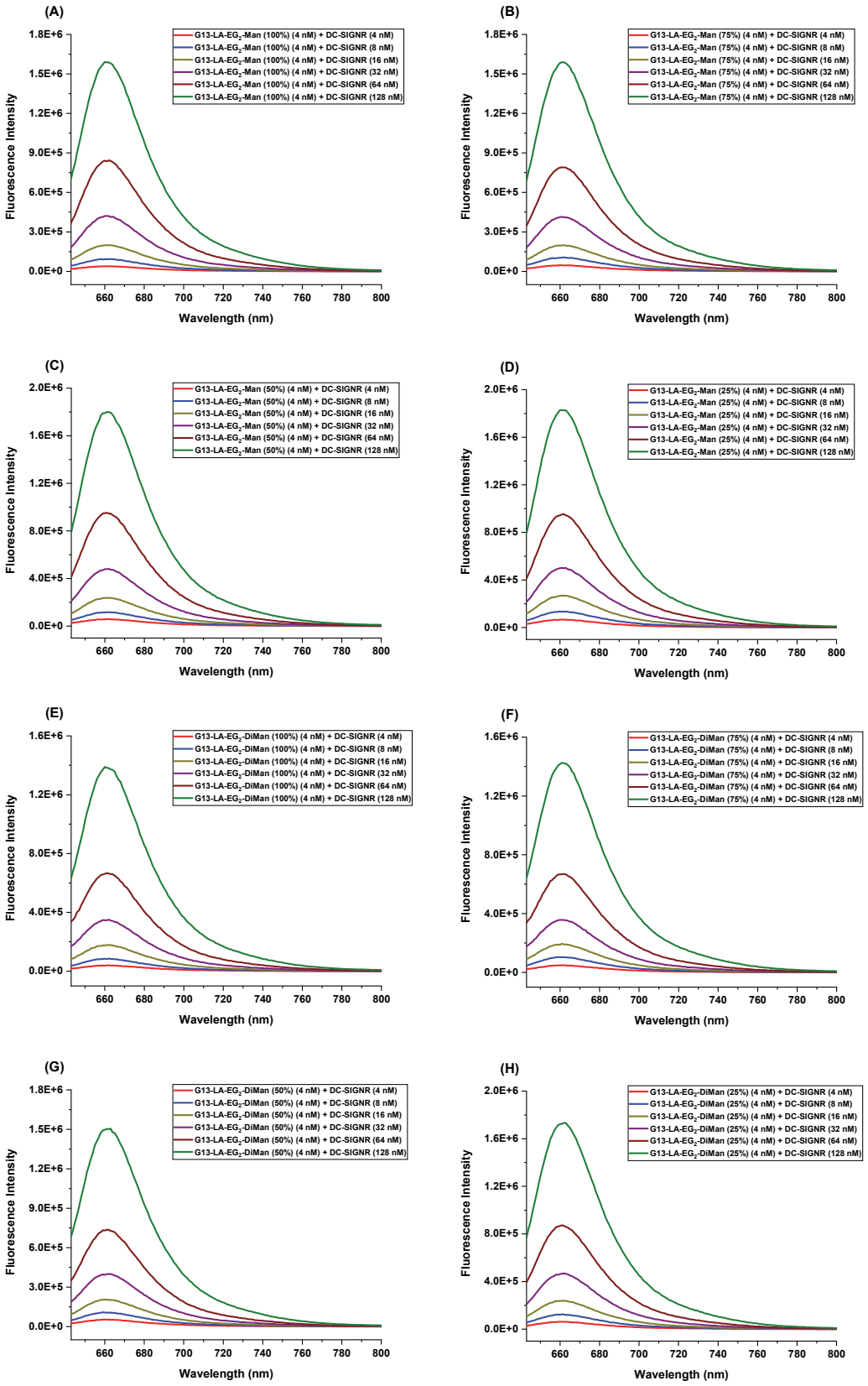

Figure A.3.3. The fluorescence spectra of (A) G13-EG_2-Man (100%)+DC-SIGNR; (B) G13-EG_2-Man(75%)+DC-SIGNR; (C) G13-EG_2-Man(50%)+DC-SIGNR; (D) G13-EG_2-Man(25%)+DC-SIGNR; (E) G13-EG_2-DiMan (100%)+DC-SIGNR; (B) G13-EG_2-DiMan(75%)+DC-SIGNR; (C) G13-EG_2-DiMan(50%)+DC-SIGNR; (D) G13-EG_2-DiMan(25%)+DC-SIGNR. Each concentration was done in duplicate and their average fluorescence spectra was constructed.

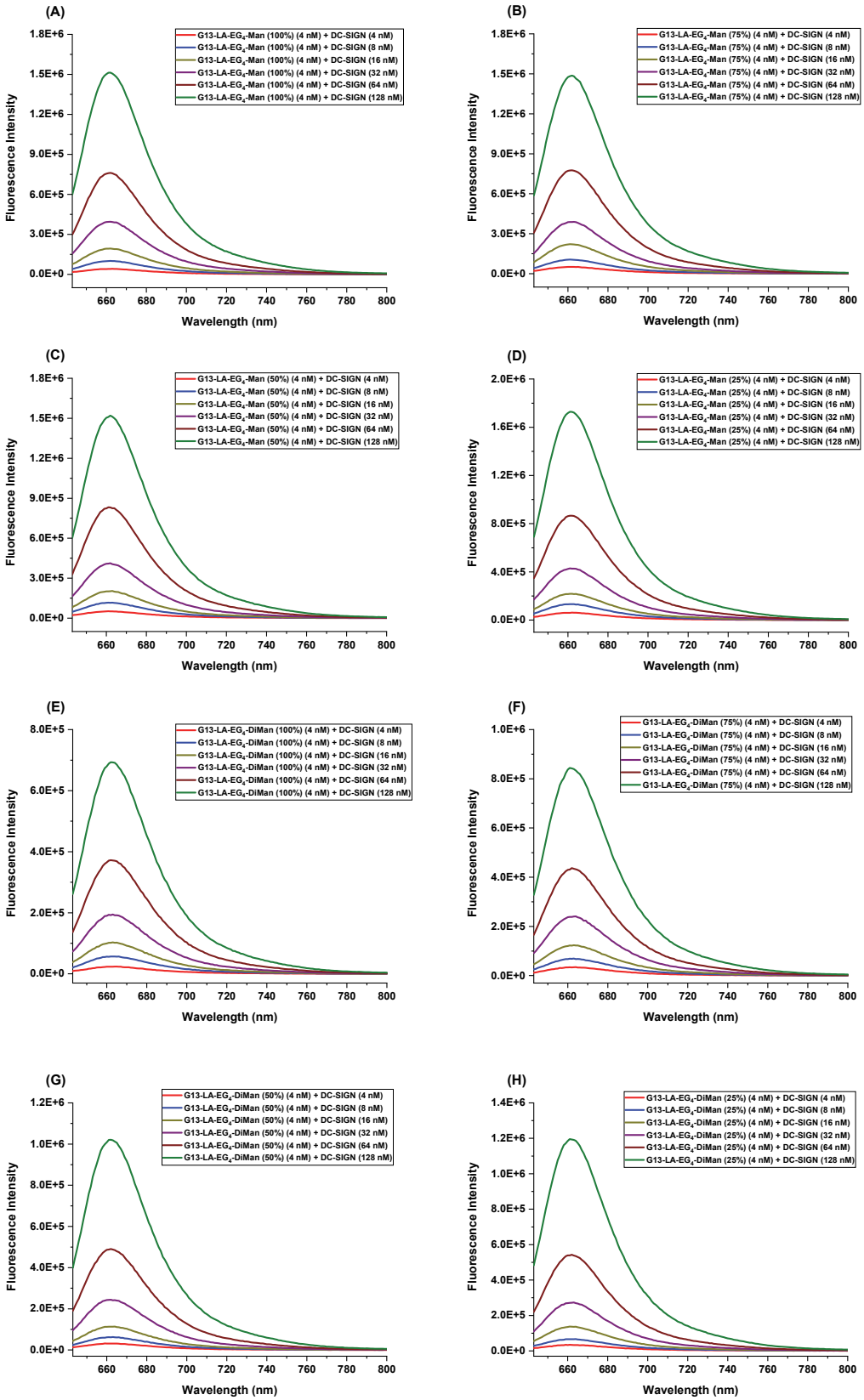

Figure A.3.4. The fluorescence spectra of (A) G13-EG_4-Man (100%)+DC-SIGN; (B) G13-EG_4-Man(75%)+DC-SIGN; (C) G13-EG_4-Man(50%)+DC-SIGN; (D) G13-EG_4-Man(25%)+DC-SIGN; (E) G13-EG_4-DiMan (100%)+DC-SIGN; (B) G13-EG_4-DiMan(75%)+DC-SIGN; (C) G13-EG_4-DiMan(50%)+DC-SIGN; (D) G13-EG_4-DiMan(25%)+ DC-SIGN. Each concentration was done in duplicate and their average fluorescence spectra was constructed.

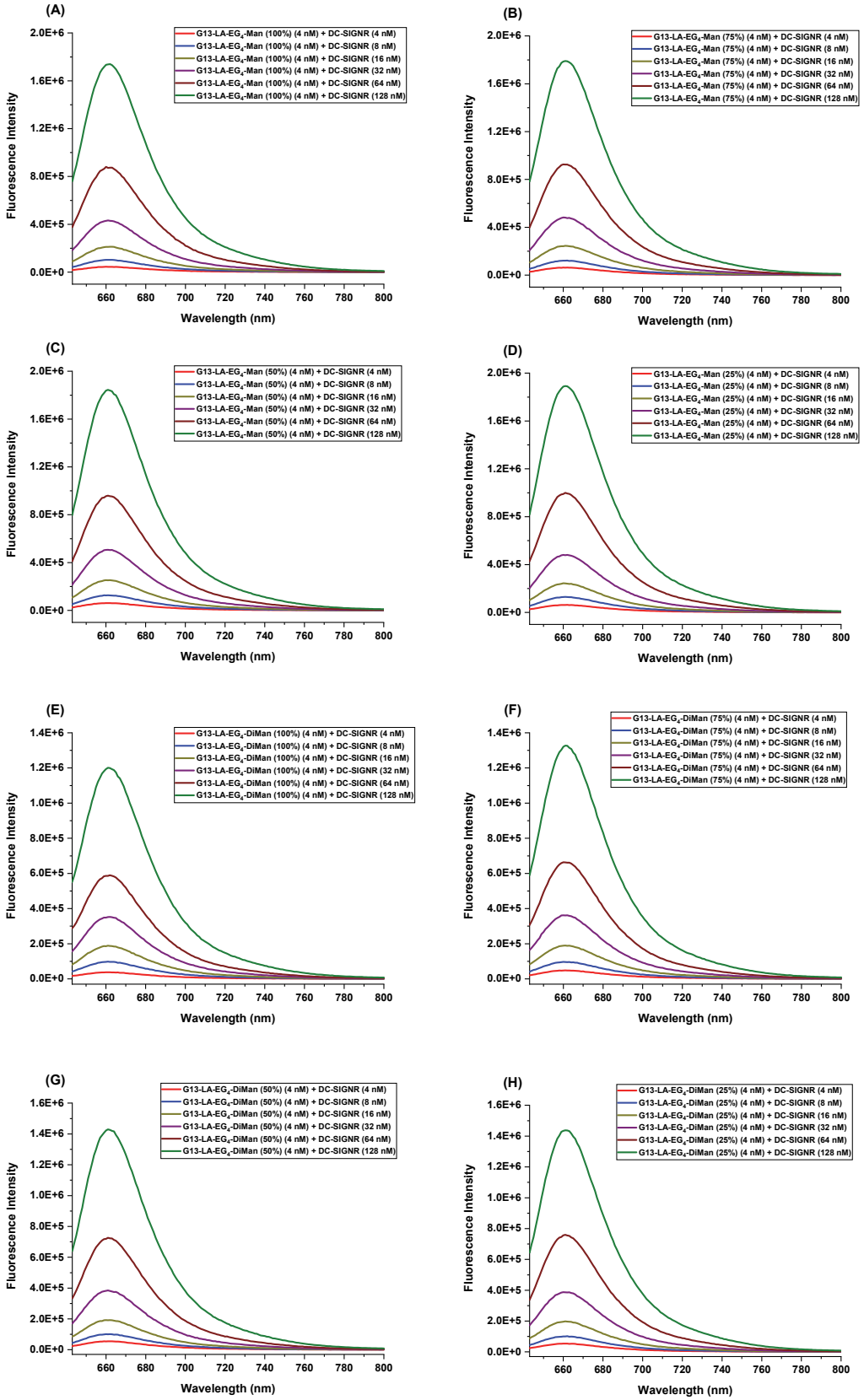

Figure A.3.5. The fluorescence spectra of (A) G13-EG_4-Man (100%)+DC-SIGNR; (B) G13-EG_4-DiMan(75%)+DC-SIGNR; (C) G13-EG_4-Man(50%)+DC-SIGNR; (D) G13-EG_4-Man(25%)+DC-SIGNR; (E) G13-EG_4-DiMan (100%)+DC-SIGNR; (B) G13-EG_4-DiMan(75%)+DC-SIGNR; (C) G13-EG_4-DiMan(50%)+DC-SIGN; (D) G13-EG_4-DiMan(25%)+DC-SIGN. Each concentration was done in duplicate and their average fluorescence spectra was constructed.

A.4. Fluorescence Spectra for G27-glycans with DC-SIGN/R

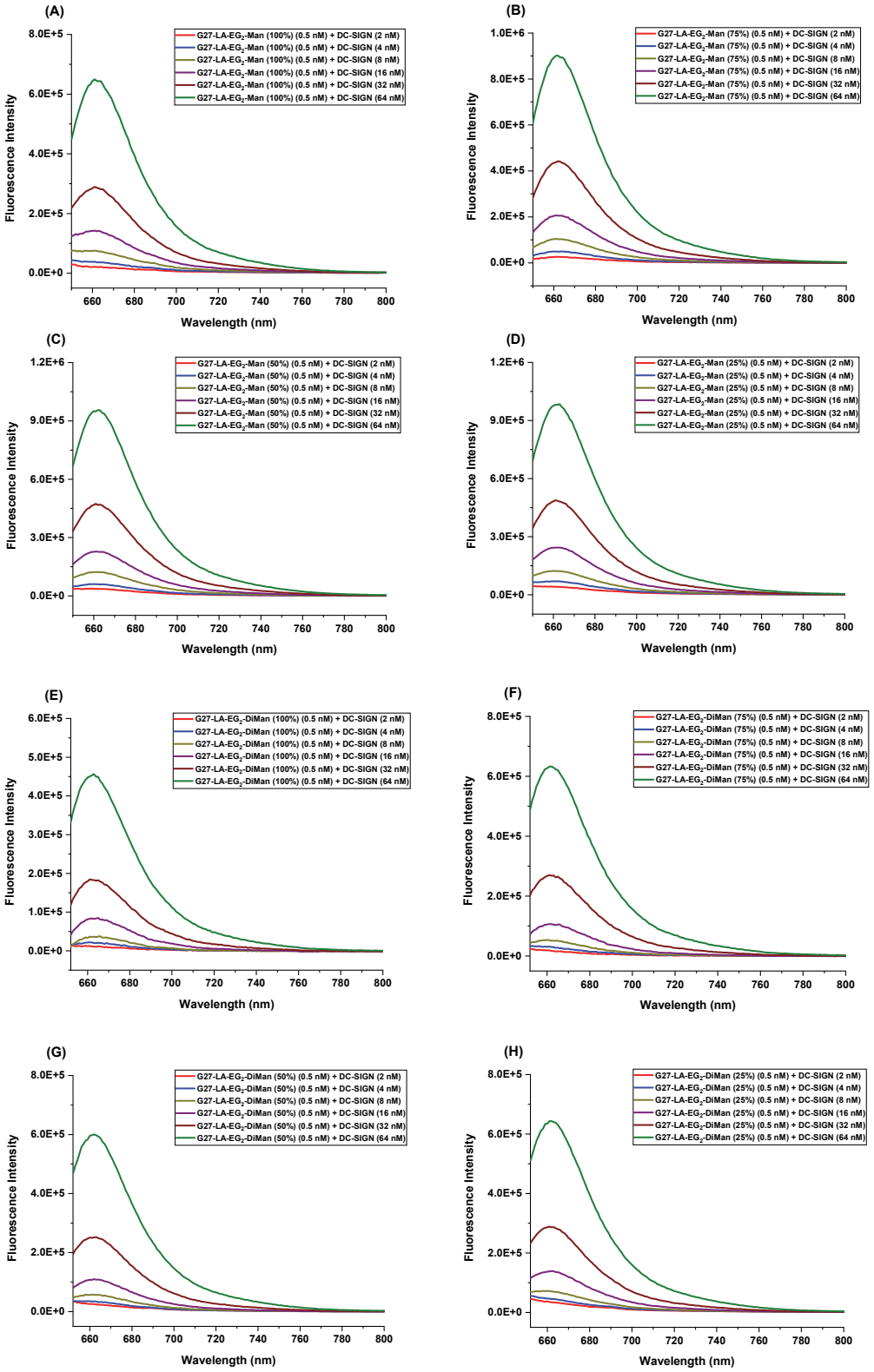

Figure A.4.1. The fluorescence spectra of (A) G27-EG_2-Man (100%)+DC-SIGN; (B) G27-EG_2-Man(75%)+DC-SIGN; (C) G27-EG_2-Man(50%)+DC-SIGN; (D) G27-EG_2-Man(25%)+DC-SIGN; (E) G27-EG_2-DiMan (100%)+DC-SIGN; (B) G27-EG_2-DiMan(75%)+DC-SIGN; (C) G27-EG_2-DiMan(50%)+DC-SIGN; (D) G27-EG_2-DiMan(25%)+ DC-SIGN. Each concentration was done in duplicate and their average fluorescence spectra was constructed.

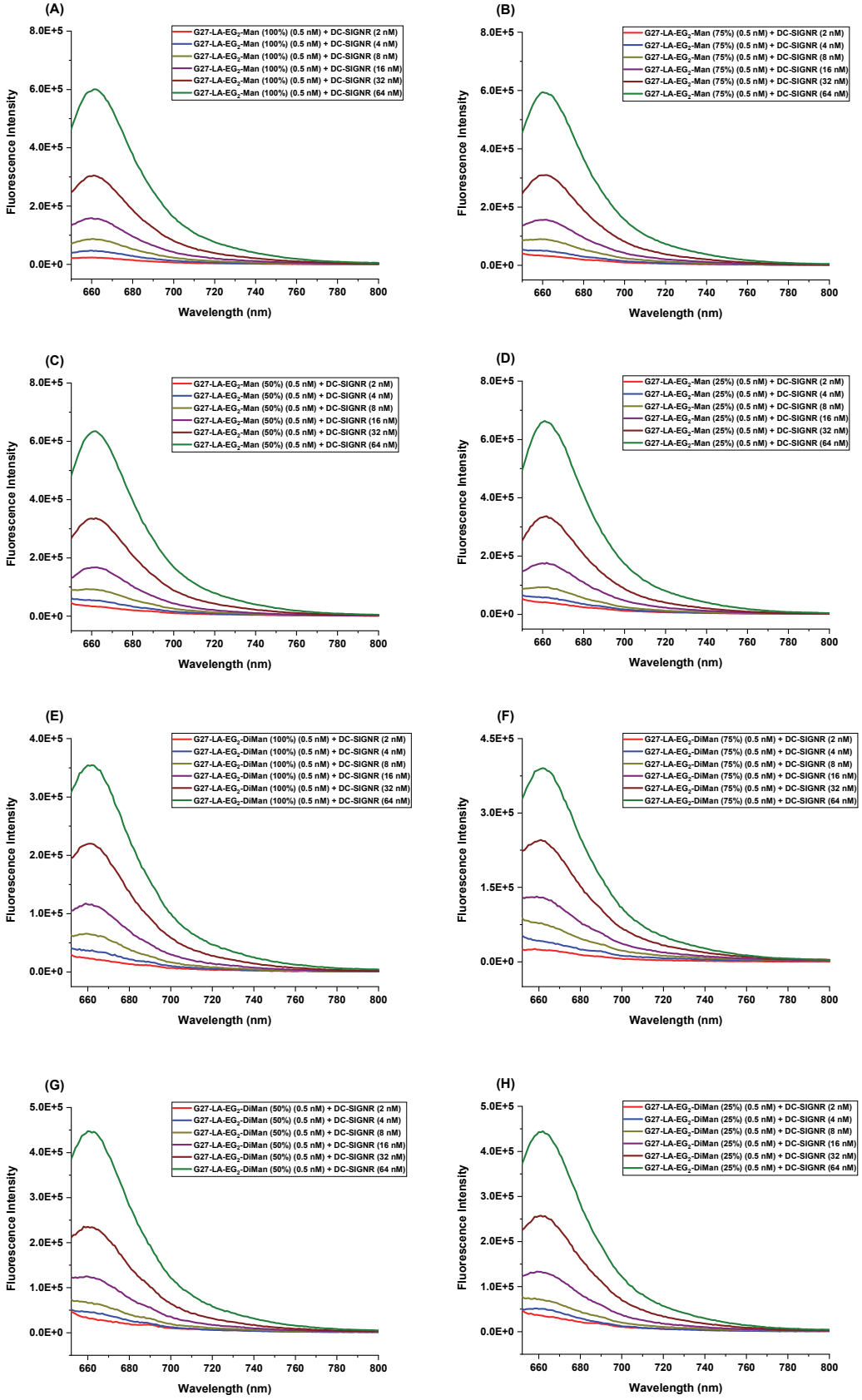

Figure A.4.2. The fluorescence spectra of (A) G27-EG_2-Man (100%)+DC-SIGNR; (B) G27-EG_2-Man(75%)+DC-SIGNR; (C) G27-EG_2-Man(50%)+DC-SIGNR; (D) G27-EG_2-Man(25%)+DC-SIGNR; (E) G27-EG_2-DiMan (100%)+DC-SIGNR; (B) G27-EG_2-DiMan(75%)+DC-SIGNR; (C) G27-EG_2-DiMan(50%)+DC-SIGNR; (D) G27-EG_2-DiMan(25%)+DC-SIGNR. Each concentration was done in duplicate and their average fluorescence spectra was constructed.

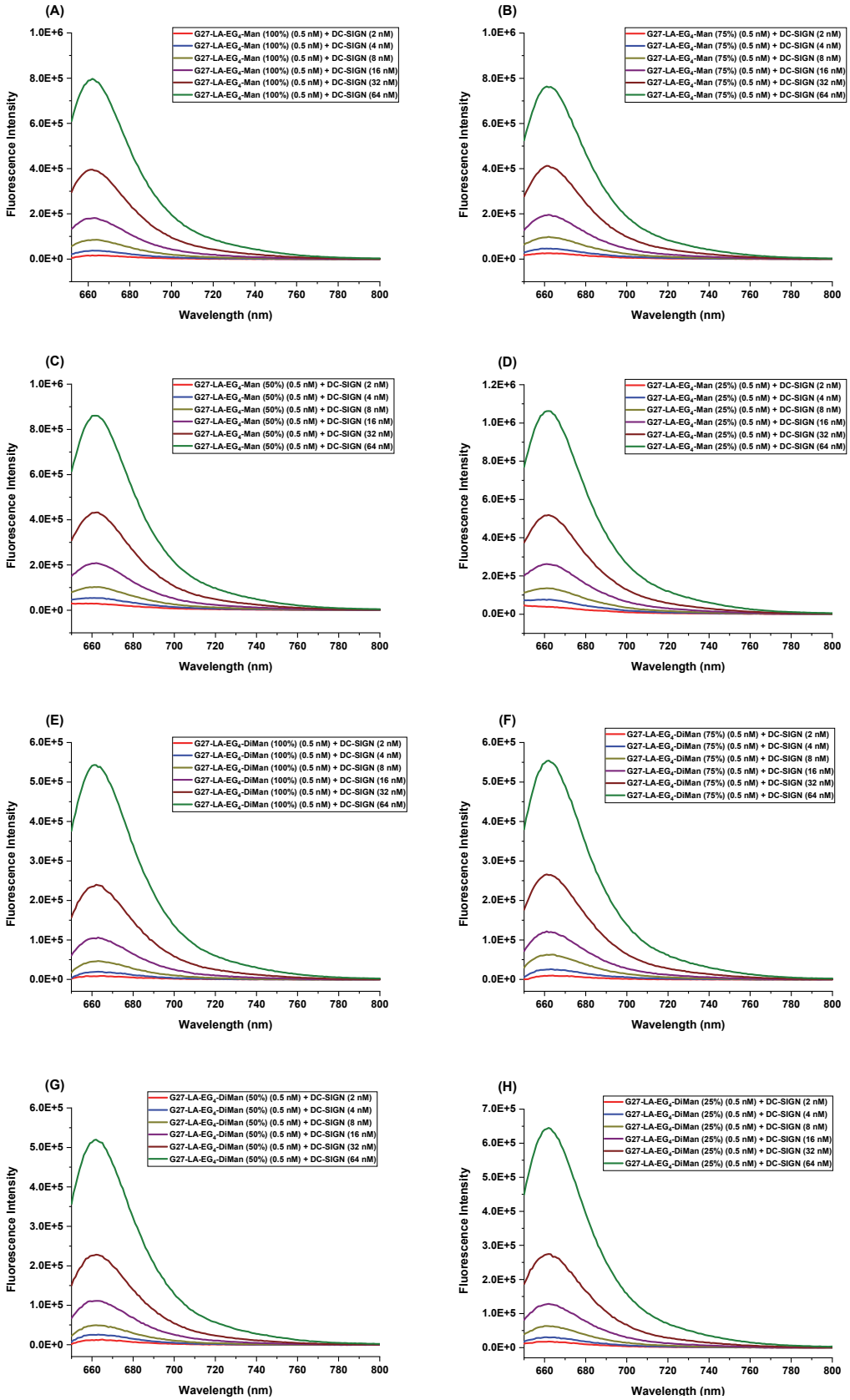

Figure A.4.3. The fluorescence spectra of (A) G27-EG_4-Man (100%)+DC-SIGN; (B) G27-EG_4-Man(75%)+DC-SIGN; (C) G27-EG_4-Man(50%)+DC-SIGN; (D) G27-EG_4-Man(25%)+DC-SIGN; (E) G27-EG_4-DiMan (100%)+DC-SIGN; (B) G27-EG_4-DiMan(75%)+DC-SIGN; (C) G27-EG_4-DiMan(50%)+DC-SIGN; (D) G27-EG_4-DiMan(25%)+ DC-SIGN. Each concentration was done in duplicate and their average fluorescence spectra was constructed.

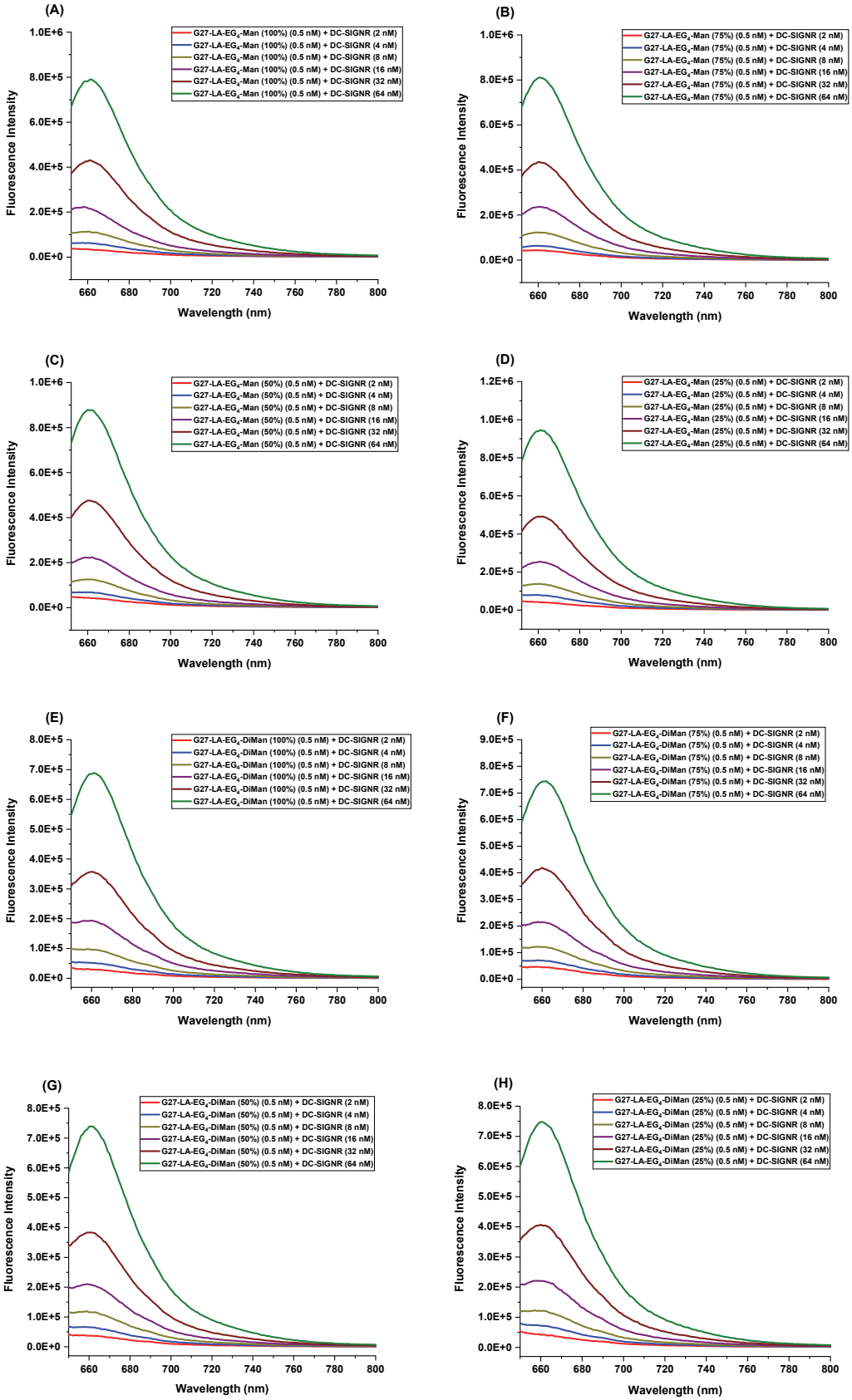

Figure A.4.4. The fluorescence spectra of (A) G27-EG_4-Man (100%)+DC-SIGNR; (B) G27-EG_4-Man(75%)+DC-SIGNR; (C) G27-EG_4-Man(50%)+DC-SIGNR; (D) G27-EG_4-Man(25%)+DC-SIGNR; (E) G27-EG_4-DiMan (100%)+DC-SIGNR; (B) G27-EG_4-DiMan(75%)+DC-SIGNR; (C) G27-EG_4-DiMan(50%)+DC-SIGNR; (D) G27-EG_4-DiMan(25%)+DC-SIGNR. Each concentration was done in duplicate and their average fluorescence spectra was constructed.

A.5. Fluorescence Spectra for GNP-OH + DC-SIGN/R and GNP-OH + DC-SIGN/R + Mannose

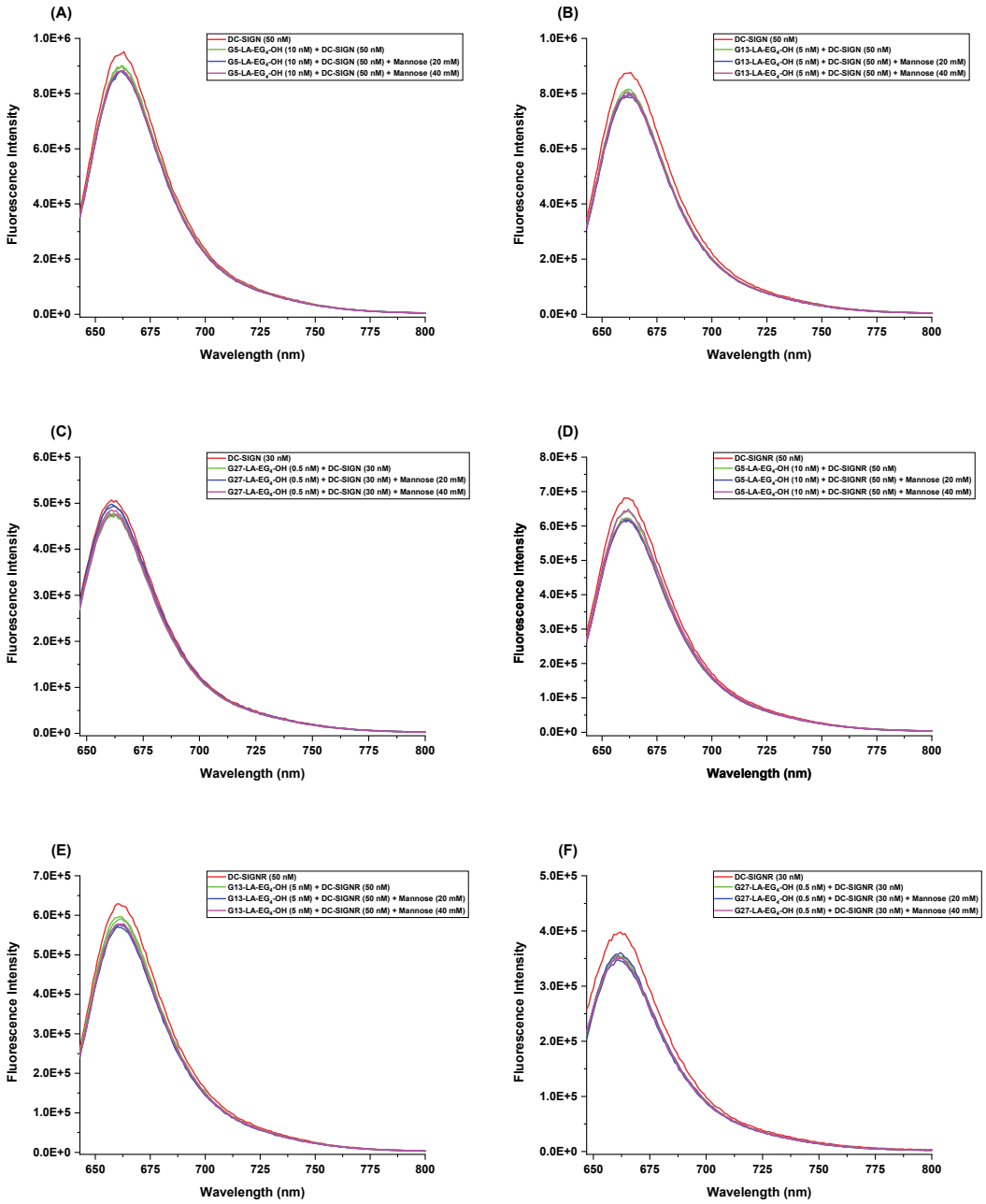

Figure A.5.1. The fluorescence spectra of (A) DC-SIGN (50 nM), G5-EG_4-OH+DC-SIGN, and G5-EG_4-OH+DC-SIGN+Mannose; (B) DC-SIGN (50 nM), G13-EG_4-OH+DC-SIGN, and G13-EG_4-OH+DC-SIGN+Mannose; (C) DC-SIGN (30 nM), G27-EG_4-OH+DC-SIGN, and G27-EG_4-OH+DC-SIGN+Mannose; (D) DC-SIGNR (50 nM), G5-EG_4-OH+DC-SIGNR, and G5-EG_4-OH+DC-SIGNR+Mannose; (E) DC-SIGNR (50 nM), G13-EG_4-OH+DC-SIGNR, and G13-EG_4-OH+DC-SIGNR+Mannose; (F) DC-SIGNR (30 nM), G27-EG_4-OH+DC-SIGNR, and G27-EG_4-OH+DC-SIGNR +Mannose. Each concentration was done in duplicate and their average fluorescence spectra was constructed.

A.6. Determination of PGR Ratio for DLS Studies

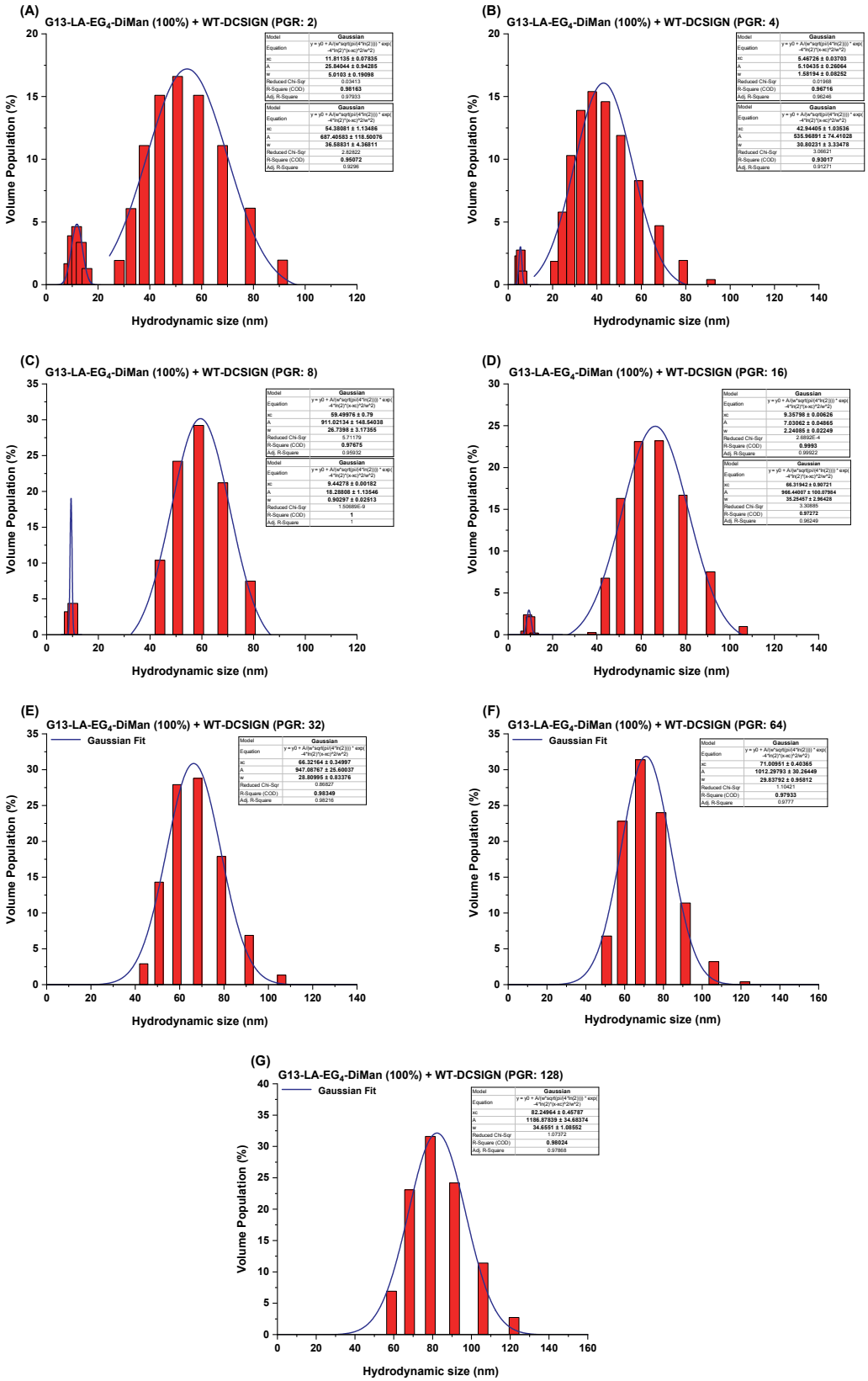

Figure A.6.1. Hydrodynamic size distribution histograms for DC-SIGN binding with G13-EG_4-DiMan at a PGR of 2 (A); 4 (B); 8 (C); 16 (D); 32 (E); 64 (F); 128 (G).

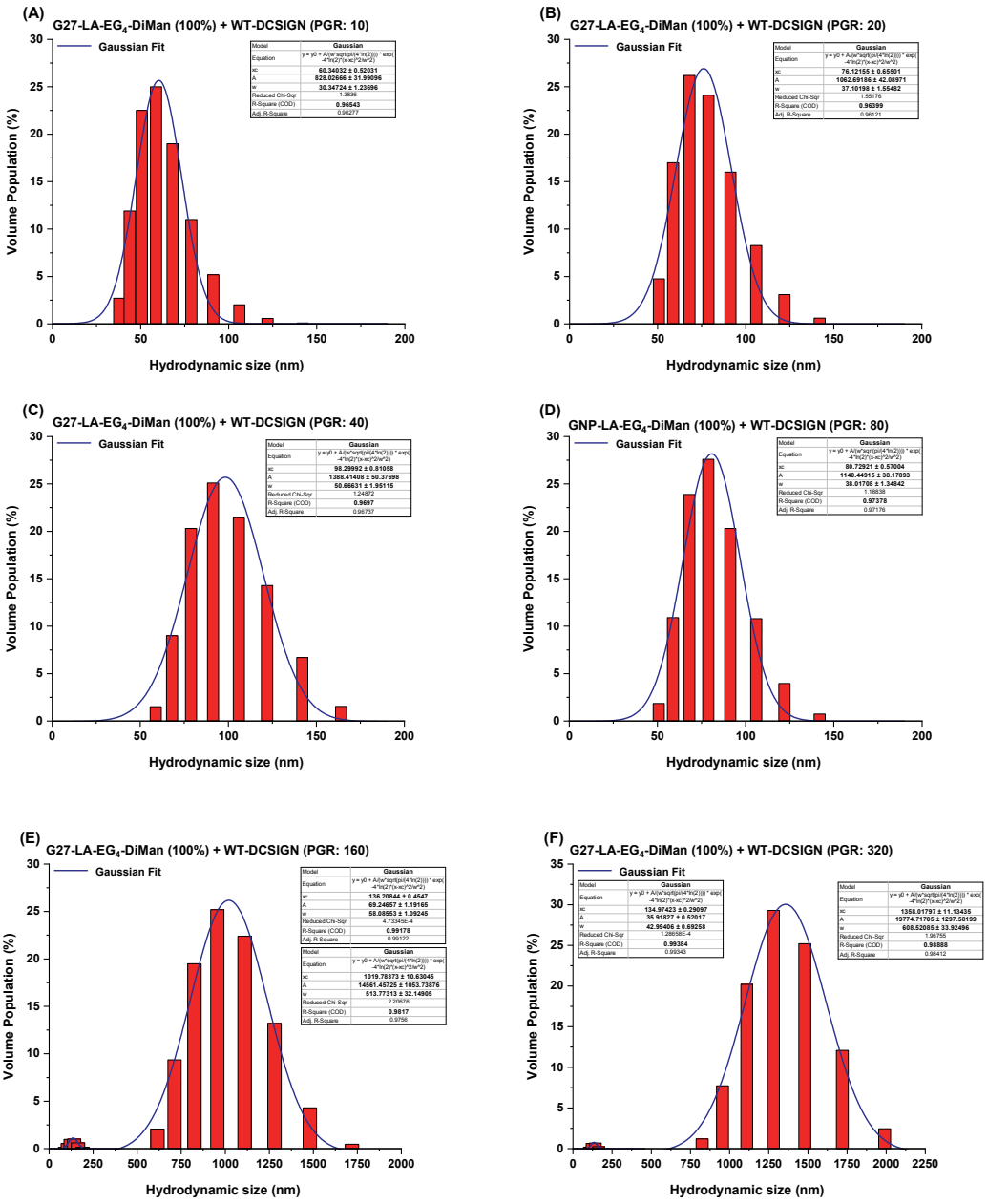

Figure A.6.2. Hydrodynamic size distribution histograms for DC-SIGN binding with G27-EG_4-DiMan at a PGR of 10 (A); 20 (B); 40 (C); 80 (D); 160 (E); and 320 (F).

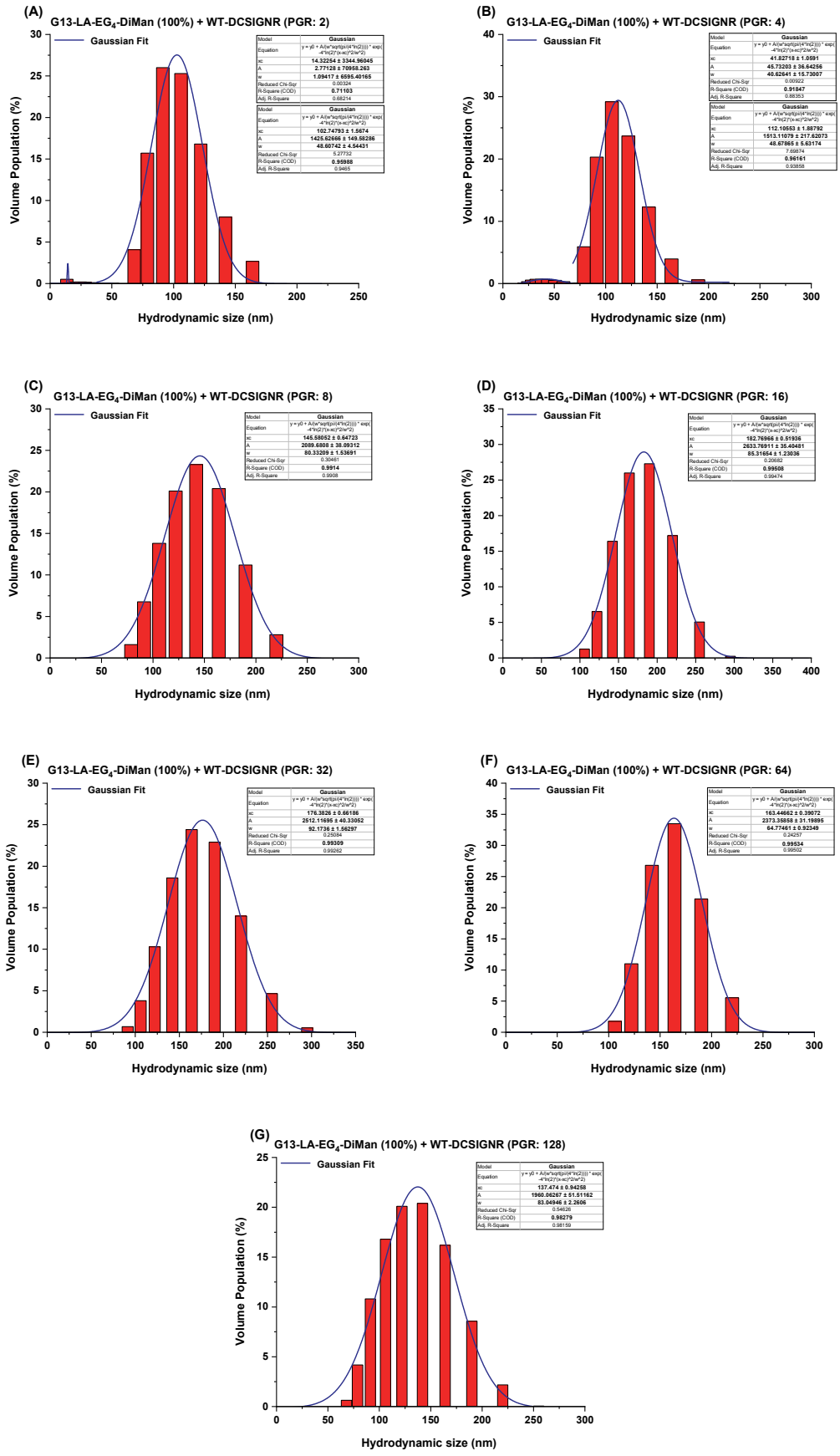

Figure A.6.3. Hydrodynamic size distribution histograms for DC-SIGNR binding with G27-EG_4-DiMan at a PGR of 2 (A); 4 (B); 8 (C); 16 (D); 32 (E); 64 (F) and 128 (G).

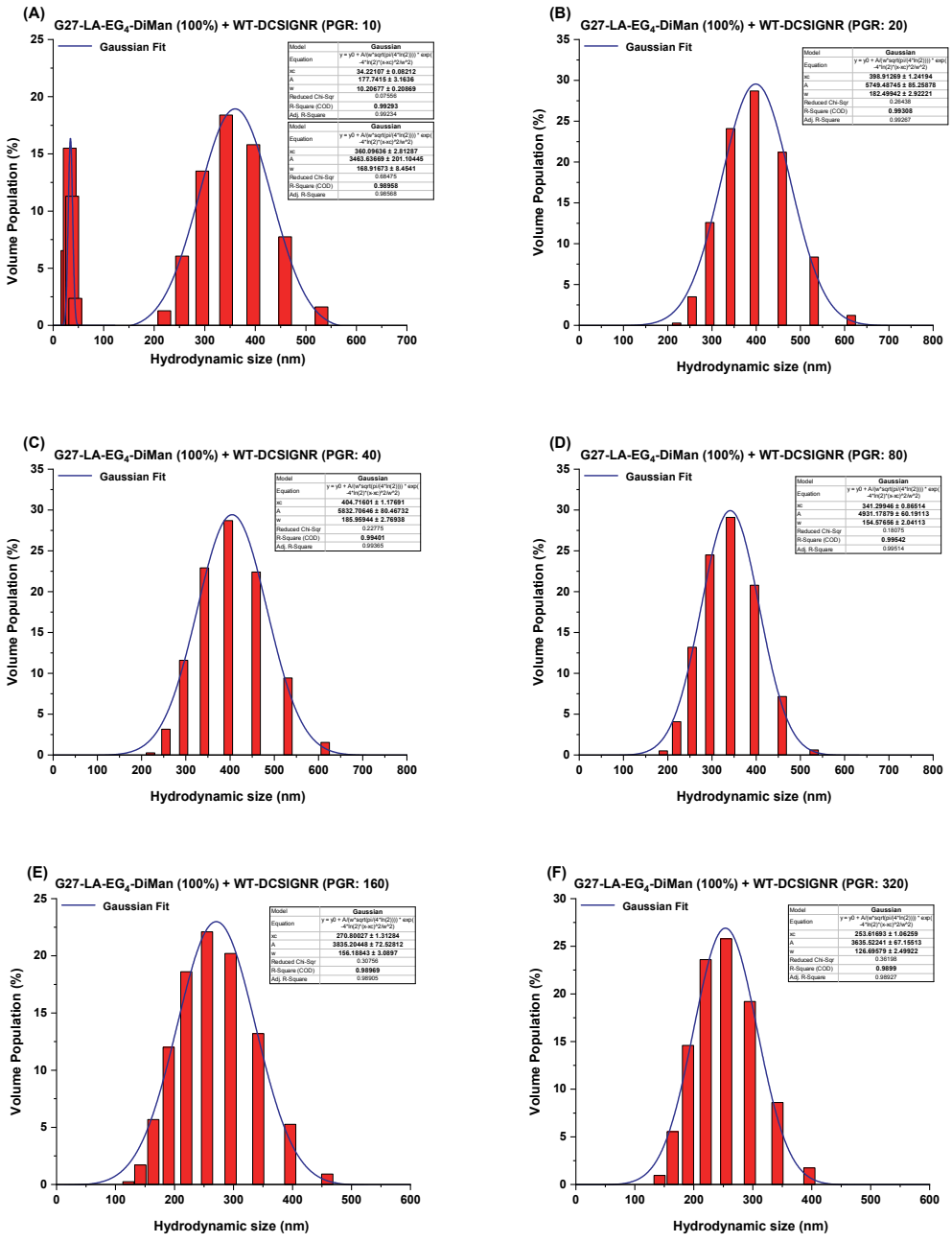

Figure A.6.4. Hydrodynamic size distribution histograms for DC-SIGNR binding with G27-EG_4-DiMan at a PGR of 10 (A); 20 (B); 40 (C); 80 (D); 160 (E); and 320 (F).

A.7. Time-dependent Hydrodynamic Size Histograms for GNP-glycans binding with DC-SIGN/R

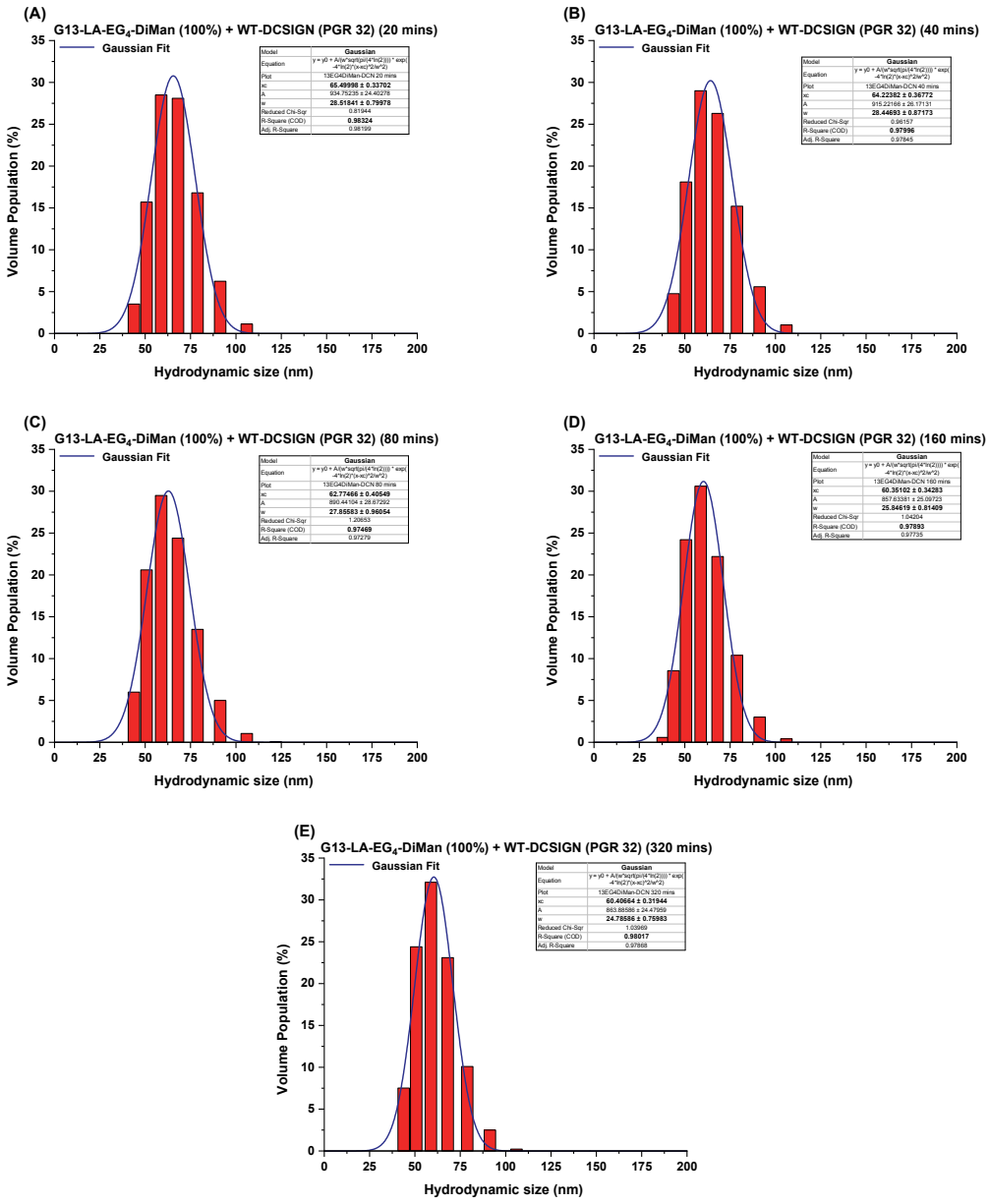

Figure A.7.1. Hydrodynamic size distribution histograms for G13-EG_4-DiMan binding with DC-SIGN at a PGR of 32 after mixed for 20 (A); 40 (B); 80 (C); 160 (D); and 320 mins (E).

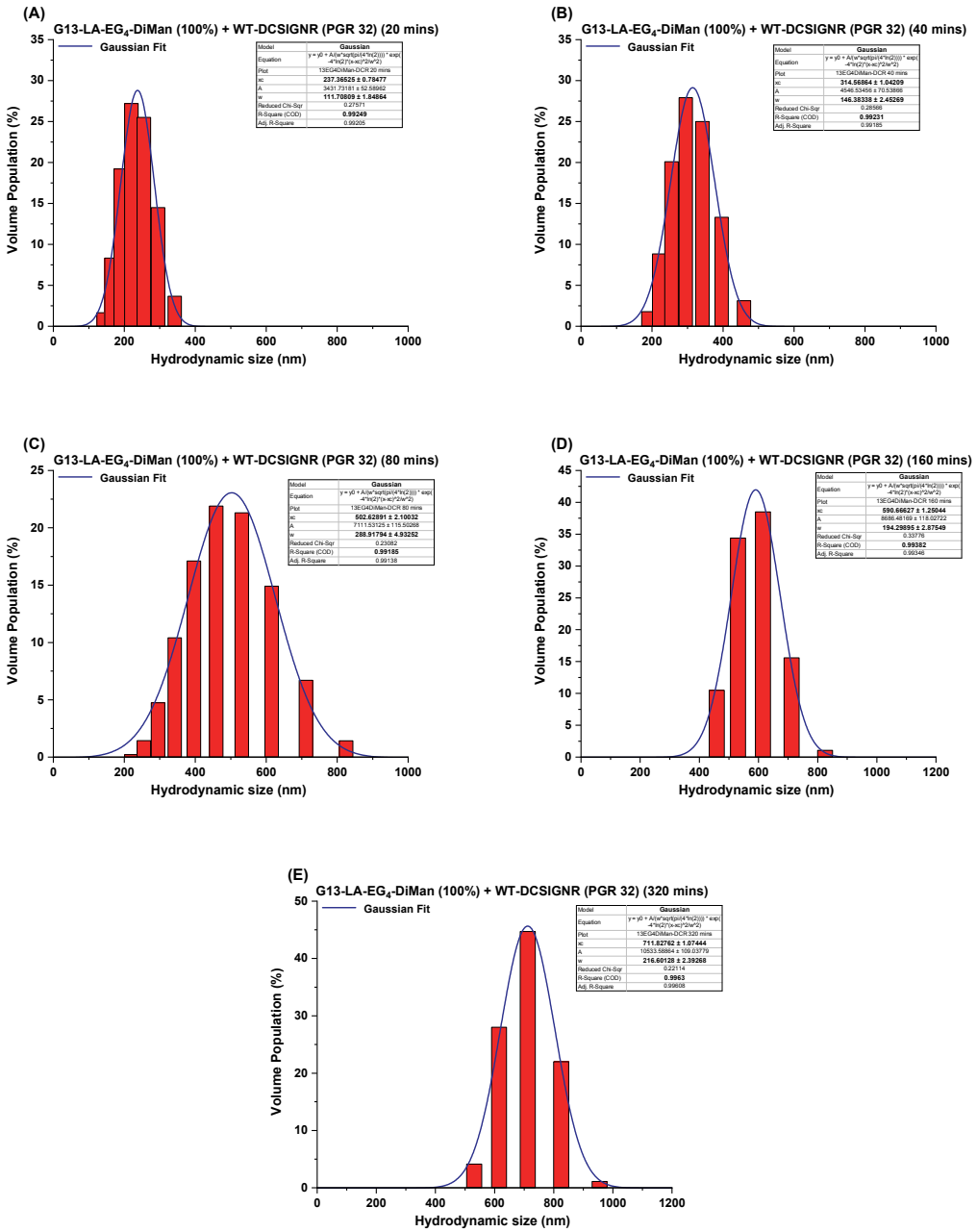

Figure A.7.2. Hydrodynamic size distribution histograms for G13-EG_4-DiMan binding with DC-SIGNR at a PGR of 32 after mixed for 20 (A); 40 (B); 80 (C); 160 (D); and 320 mins (E).

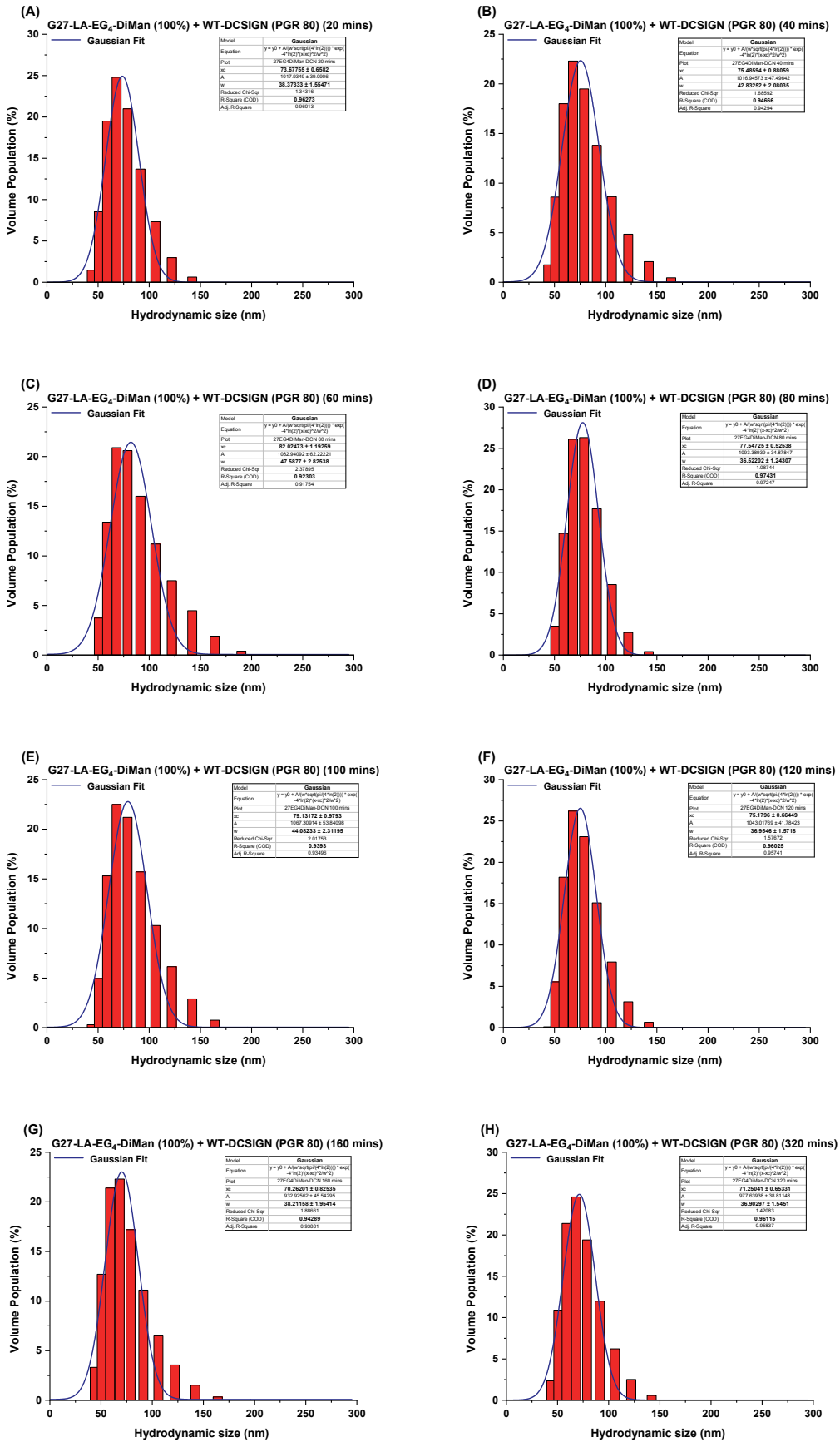

Figure A.7.3. Hydrodynamic size distribution histograms for G27-EG_4-DiMan binding with DC-SIGN at a PGR of 80 after mixed for 20 (A); 40 (B); 60 (C); 80 (D); 100 (E); 120 (F); 160 (G); and 320 mins (H).

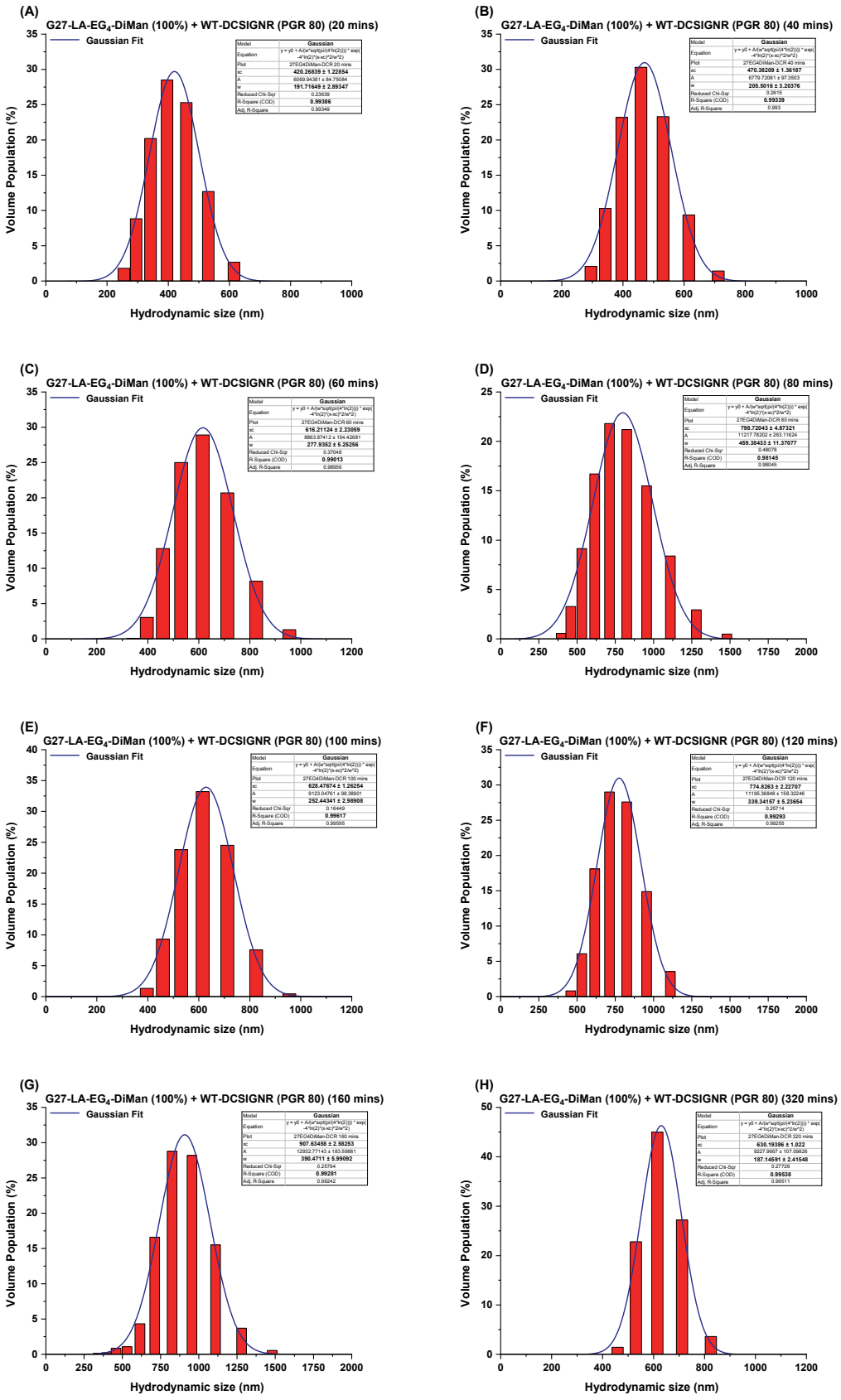

Figure A.7.4. Hydrodynamic size distribution histograms for G27-EG_4-DiMan binding with DC-SIGNR at a PGR of 80 after mixed for 20 (A); 40 (B); 60 (C); 80 (D); 100 (E); 120 (F); 160 (G); and 320 mins (H).

A.8. Fluorescence Spectra for DC-SIGN/R Binding Thermodynamics with GNPs.

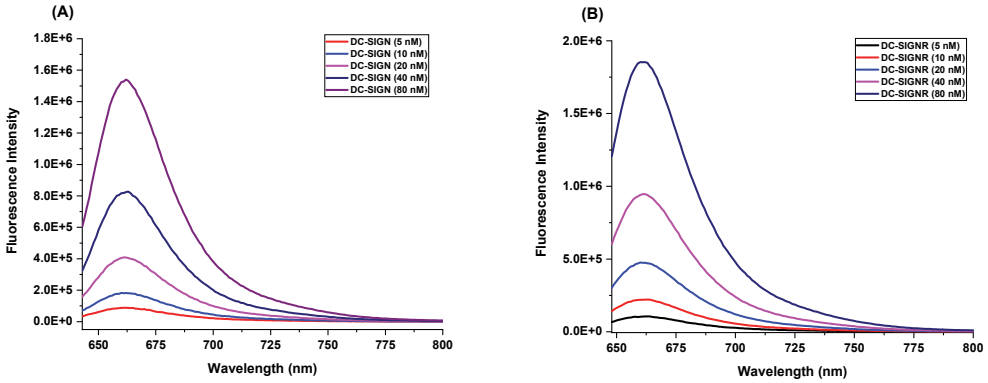

Figure A.8.1. The fluorescence spectra of (A) DC-SIGN; (B) DC-SIGNR

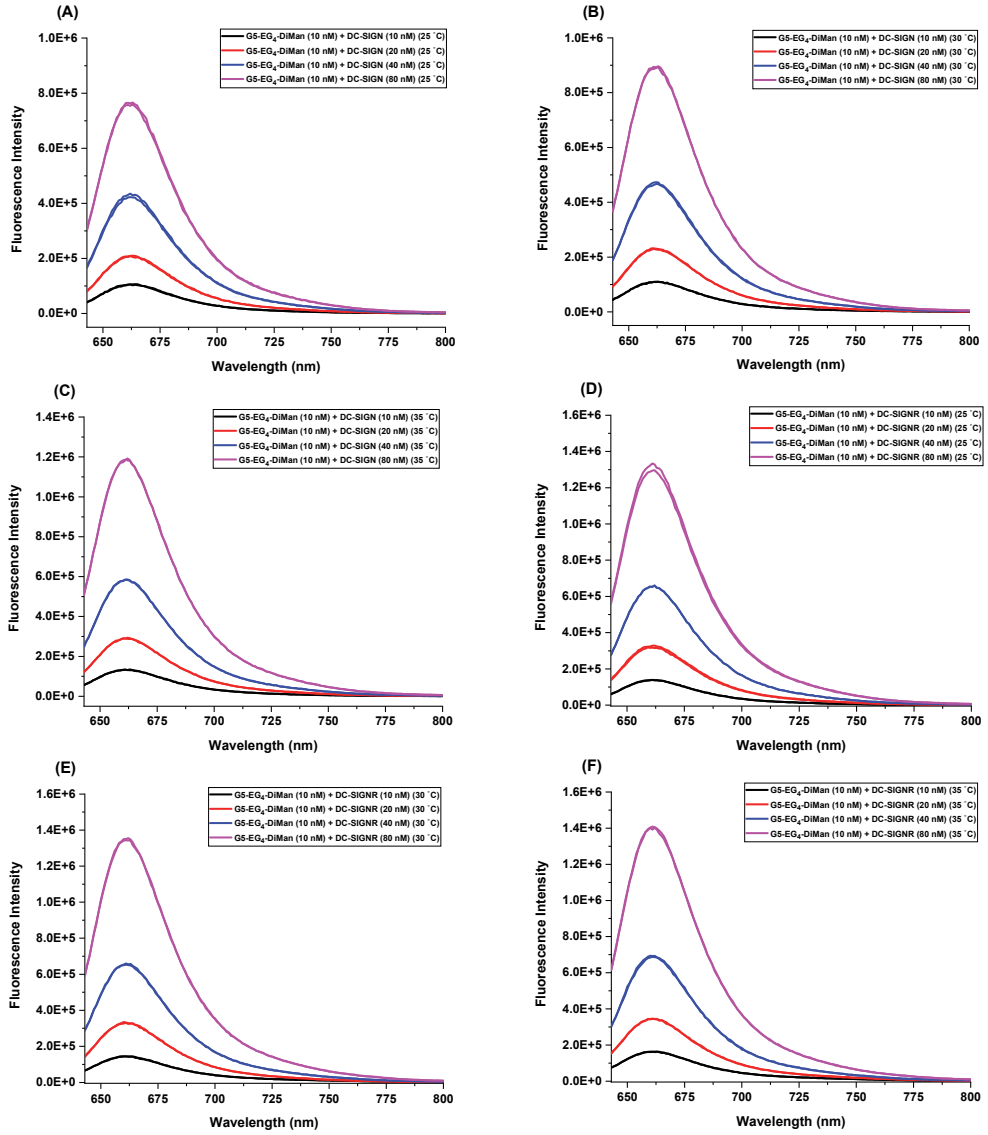

Figure A.8.2. The fluorescence spectra of G5-EG_4-DiMan+DC-SIGN at 25 ˚C (A); 30 ˚C (B); 35 ˚C (C) and G5-EG_4-DiMan+DC-SIGNR at 25 ˚C (D); 30 ˚C (E); 35 ˚C (F). Each concentration was done in duplicate.

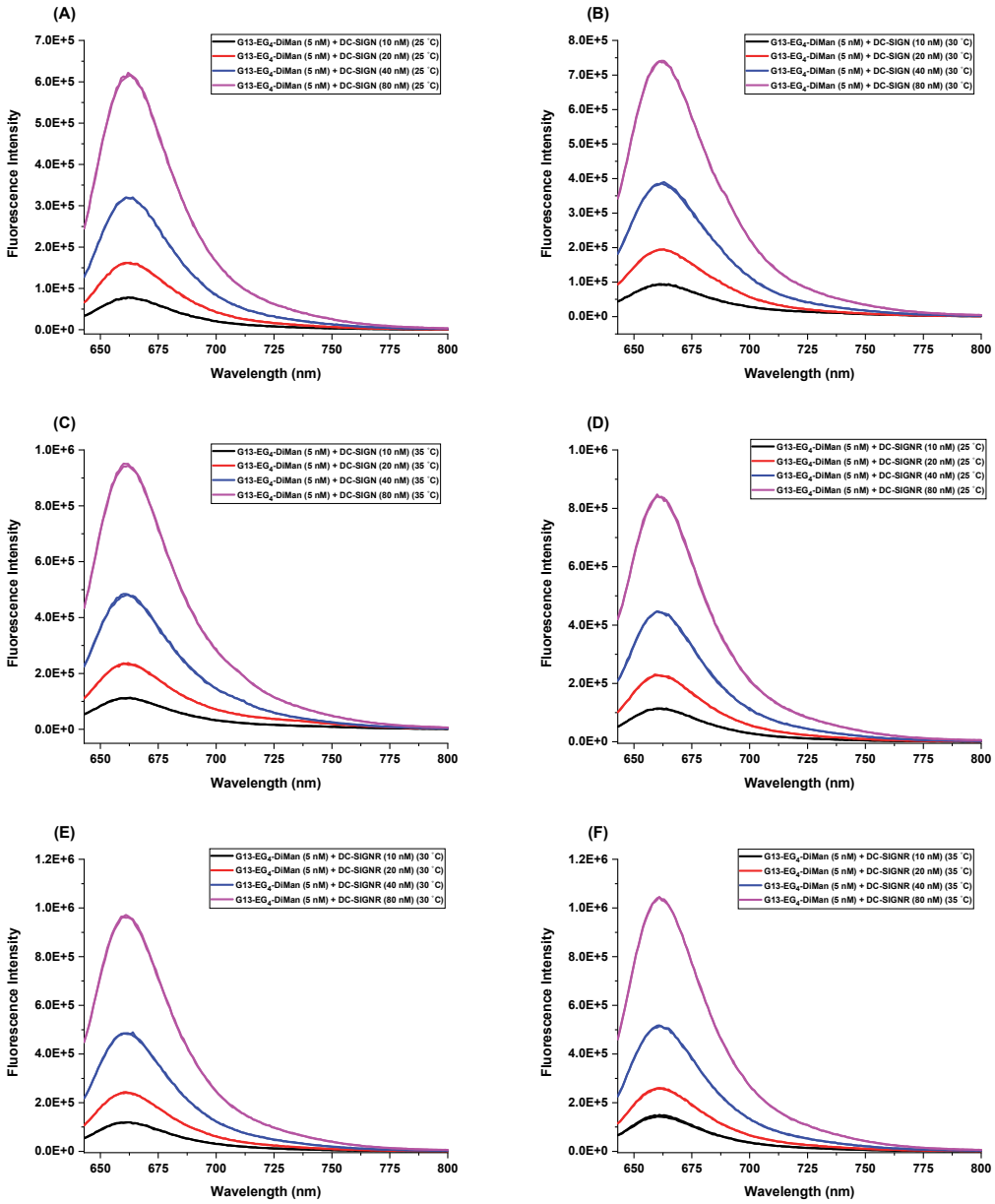

Figure A.8.3. The fluorescence spectra of G13-EG_4-DiMan+DC-SIGN at 25 ˚C (A); 30 ˚C (B); 35 ˚C (C) and G13-EG_4-DiMan+DC-SIGNR at 25 ˚C (D); 30 ˚C (E); 35 ˚C (F). Each concentration was done in duplicate and their average fluorescence spectra was constructed.

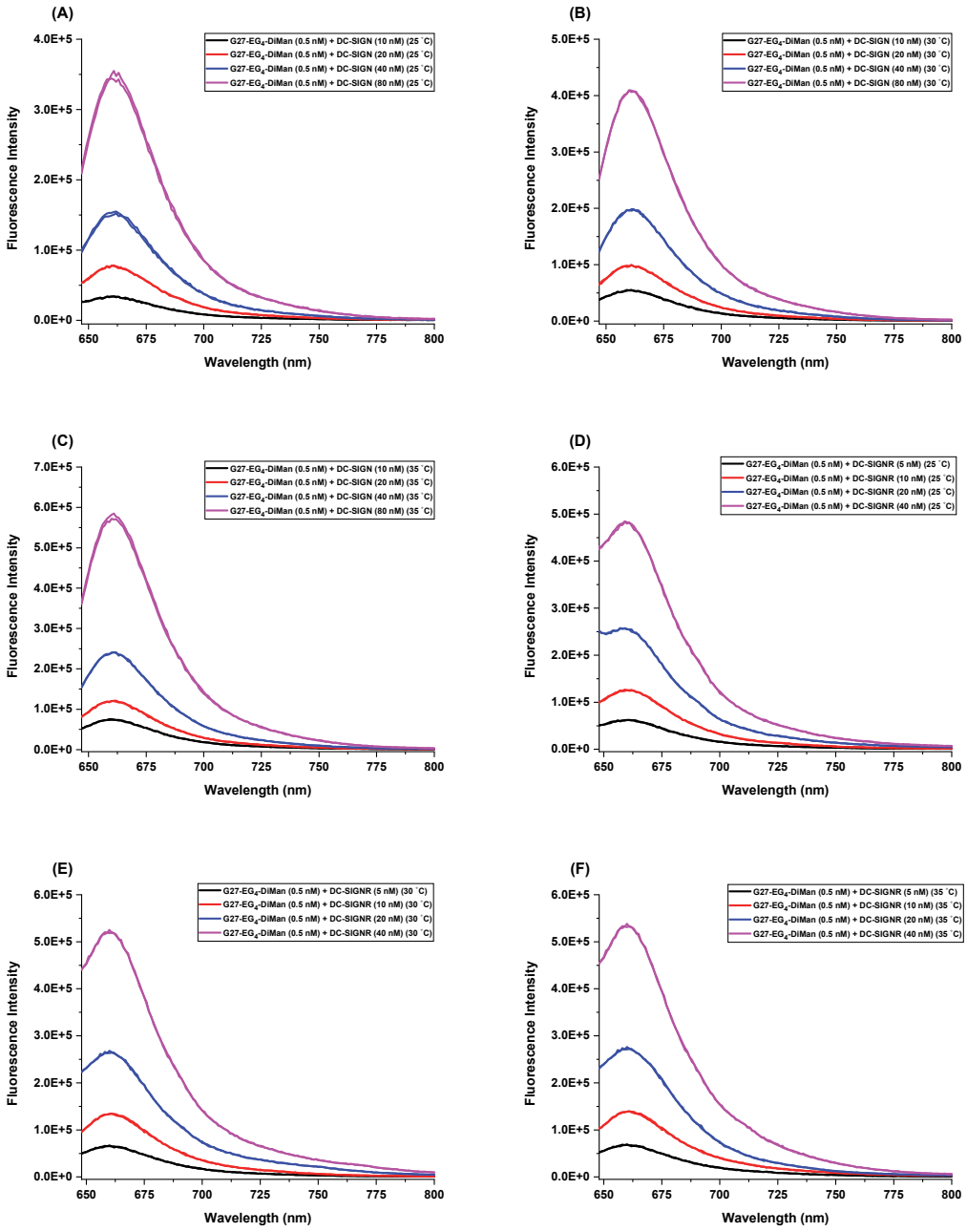

Figure A.8.4. The fluorescence spectra of G27-EG_4-DiMan+DC-SIGN at 25 ˚C (A); 30 ˚C (B); 35 ˚C (C) and G27-EG_4-DiMan+DC-SIGNR at 25 ˚C (D); 30 ˚C (E); 35 ˚C (F). Each concentration was done in duplicate and their average fluorescence spectra was constructed.

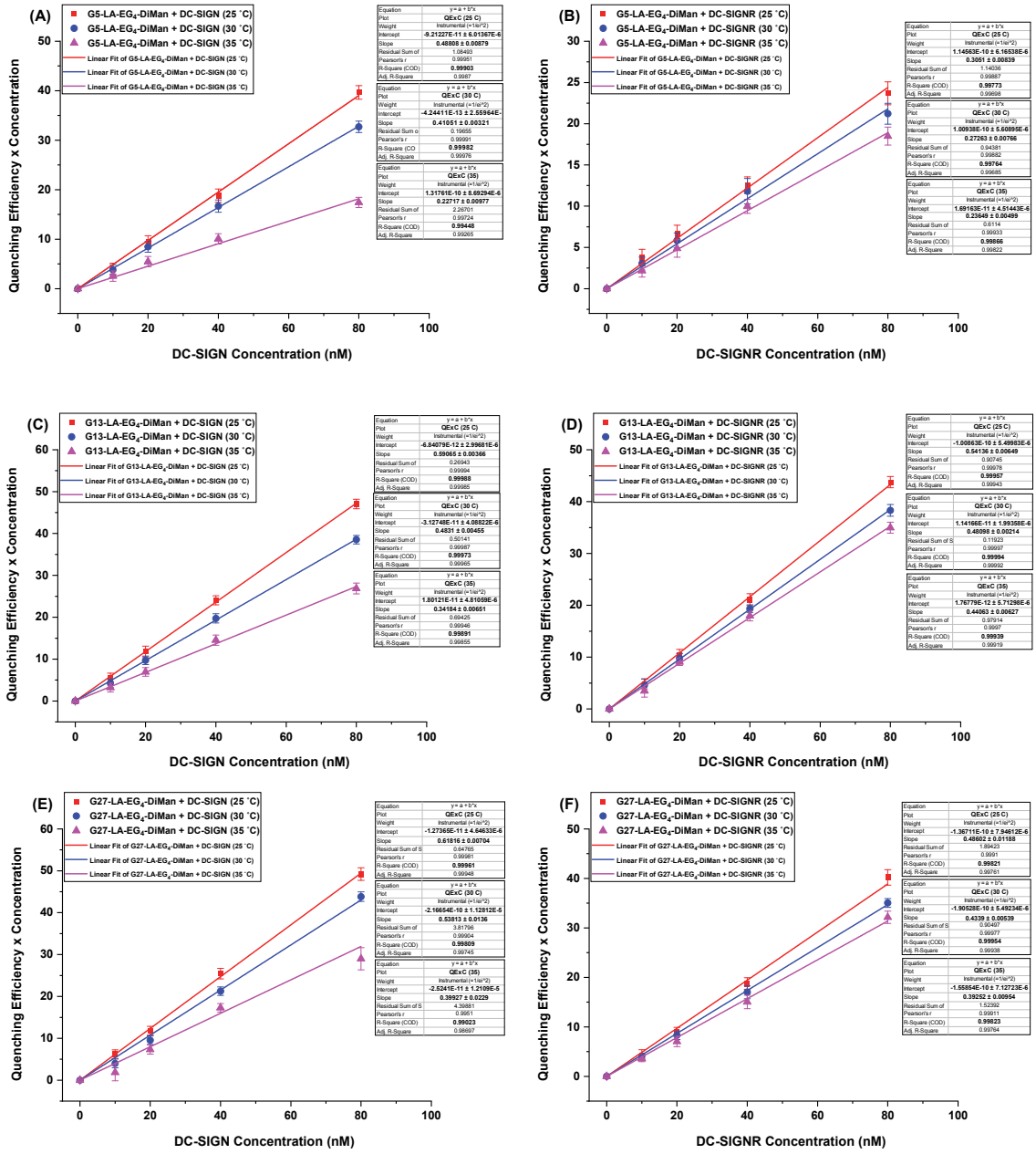

Figure A.8.5. The QE x protein concentration versus protein concentration plots of (A) G5-EG_4-DiMan+DC-SIGN; (B) G5-EG_4-DiMan+DC-SIGNR; (C) G13-EG_4-DiMan+DC-SIGN; (D) G13-EG_4-DiMan+DC-SIGNR; (E) G27-EG_4-DiMan+DC-SIGN; (F) G27-EG_4-DiMan+DC-SIGNR at three different temperatures.

A.9. Viral Inhibition Studies

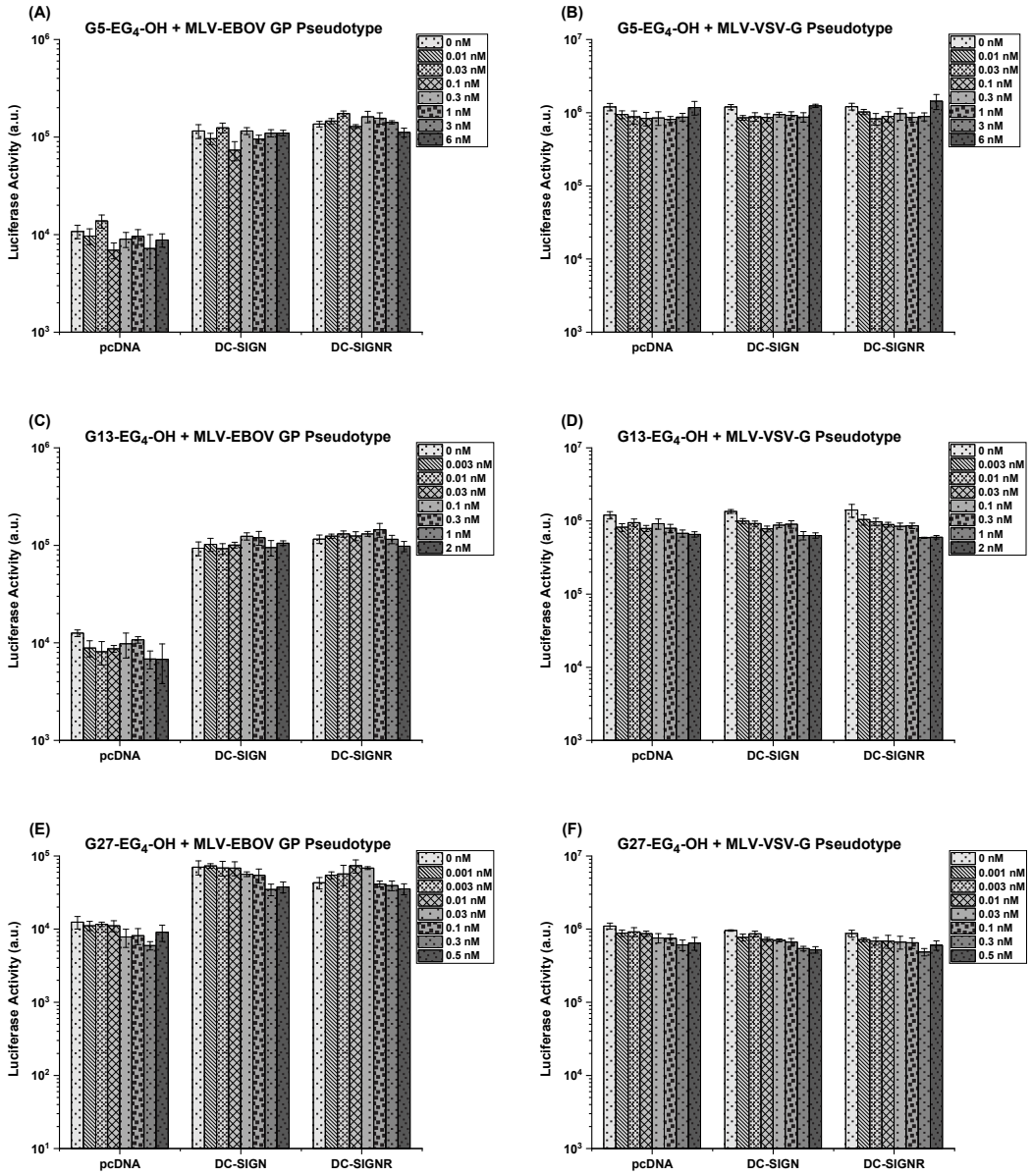

Figure A.9.1. The cellular luciferase activities of 293T cells pre-treated with varied concentrations of G5-EG_4-OH (A, B), G13-EG_4-OH (C, D), and G27-EG_4-OH (E, F) and then trans-infected MLV vector carrying the EBOV-GP (A, C, E) or the control VSV-G (B, D, F). The data are presented as mean±standard deviation three separate experiments.

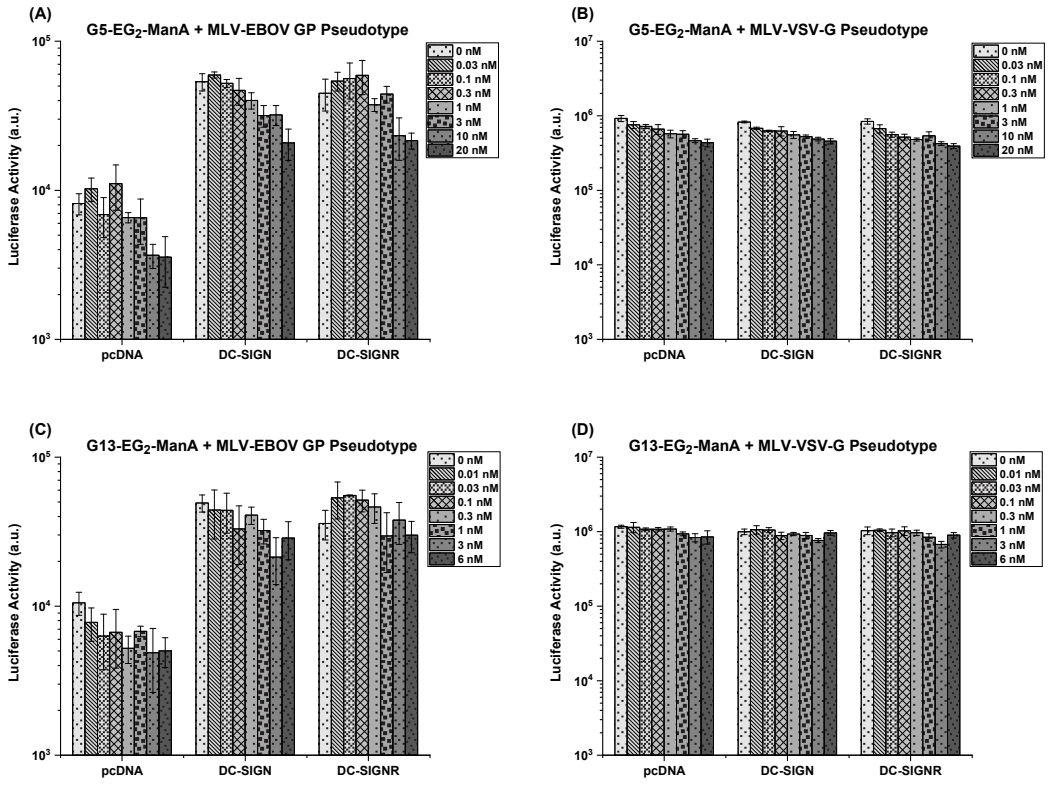

Figure A.9.2. The cellular luciferase activities of 293T cells pre-treated with varied concentrations of G5-EG_2-ManA (A, B), G13-EG_2-ManA (C, D), and then trans-infected MLV vector carrying the EBOV-GP (A, C) or the control VSV-G (B, D). The data are presented as mean±standard deviation three separate experiments.

A.10. pH-Switching Studies

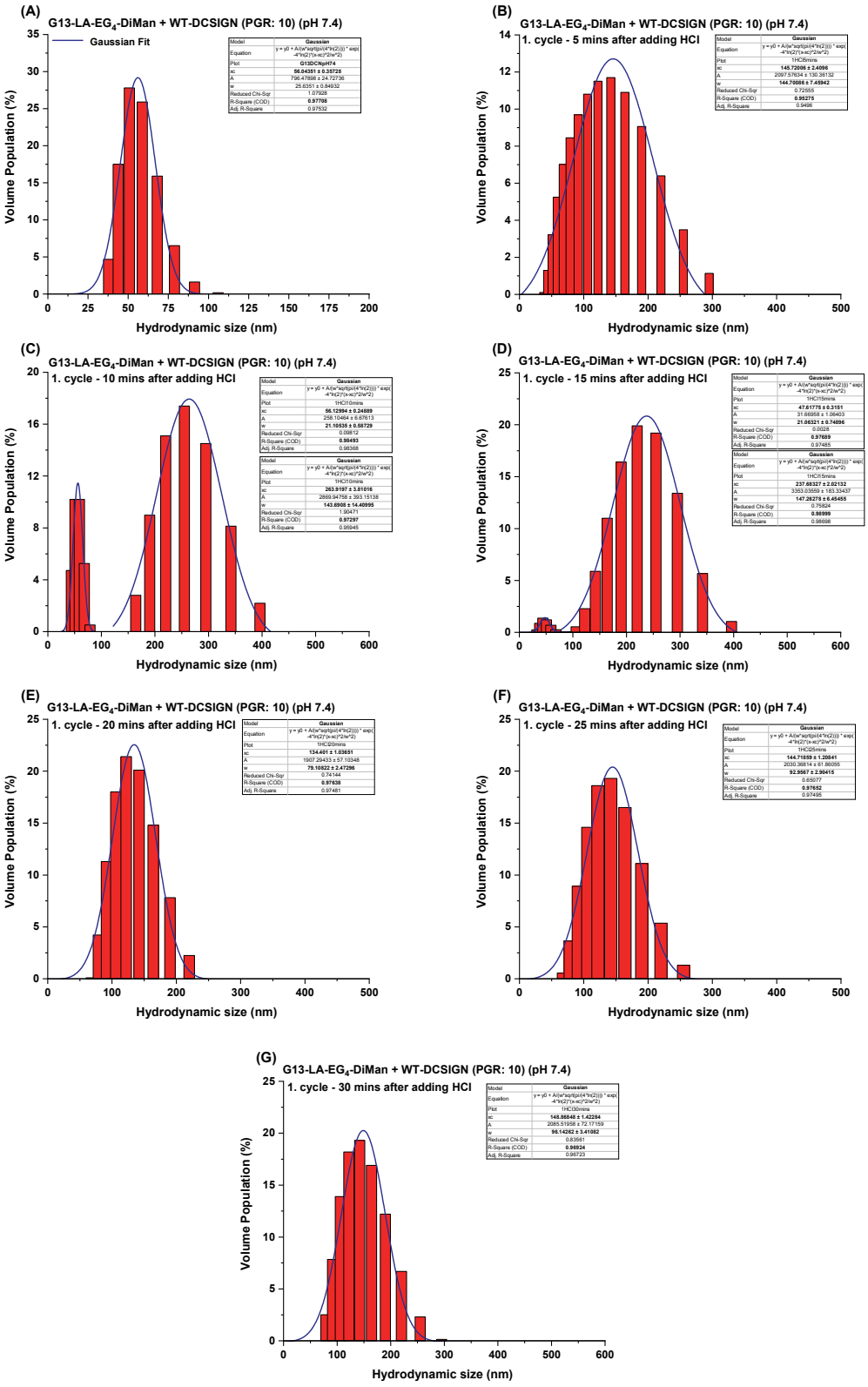

Figure A.10.1. D_h sizes of G13-EG_4-DiMan+DC-SIGN ((A) at pH 7.4) when pH is switched from 7.4 to 5.0 (cycle 1). (B) 5 mins, (C) 10 mins; (D) 15 mins; (E) 20 mins; (F) 25 mins; (G) 30 mins after adding HCl.

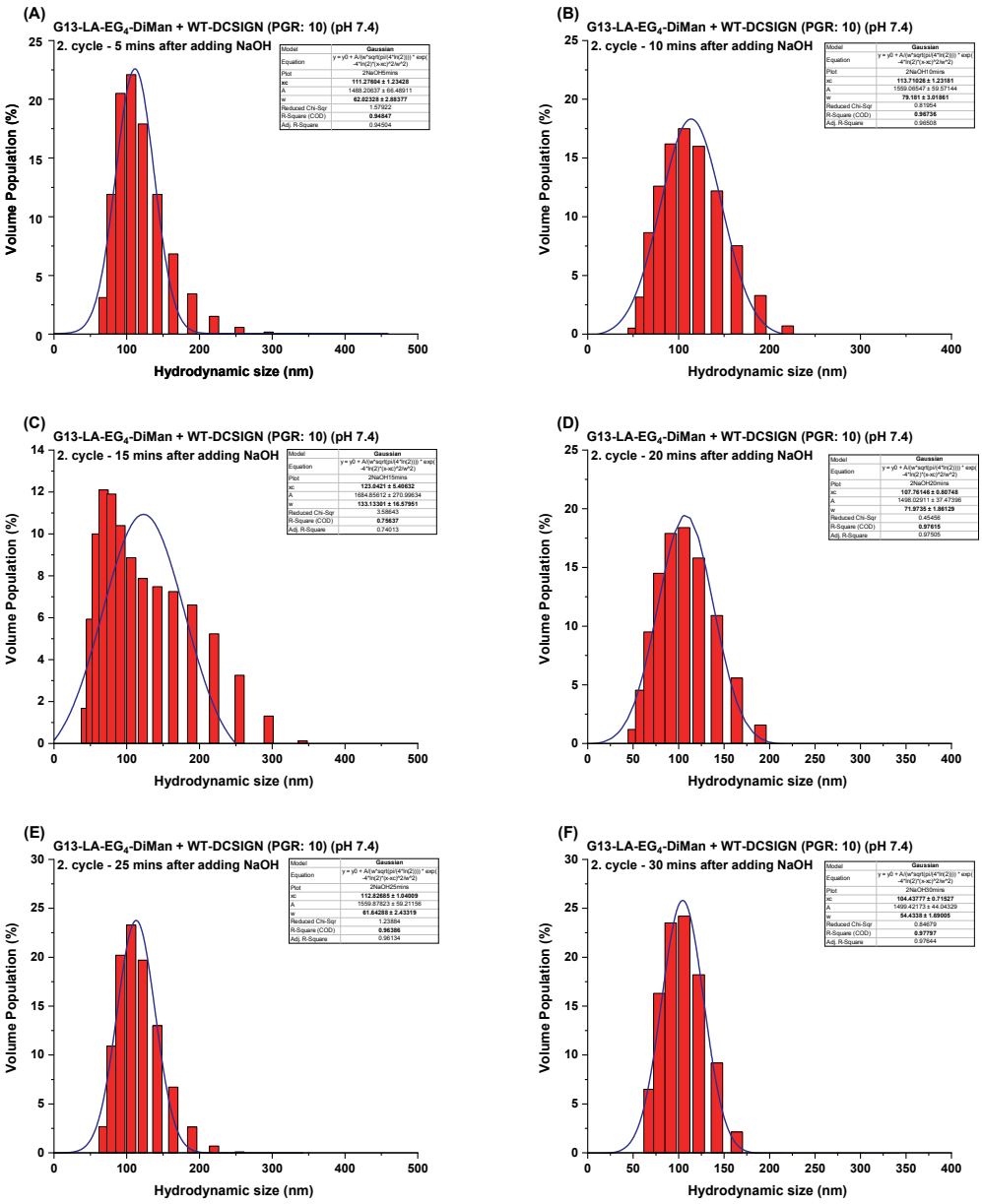

Figure A.10.2. D_h sizes of G13-EG_4-DiMan+DC-SIGN when pH is switched from 5.0 to 7.4 (cycle 2). (A) 5 mins, (B) 10 mins; (C) 15 mins; (D) 20 mins; (E) 25 mins; (F) 30 mins after adding NaOH.

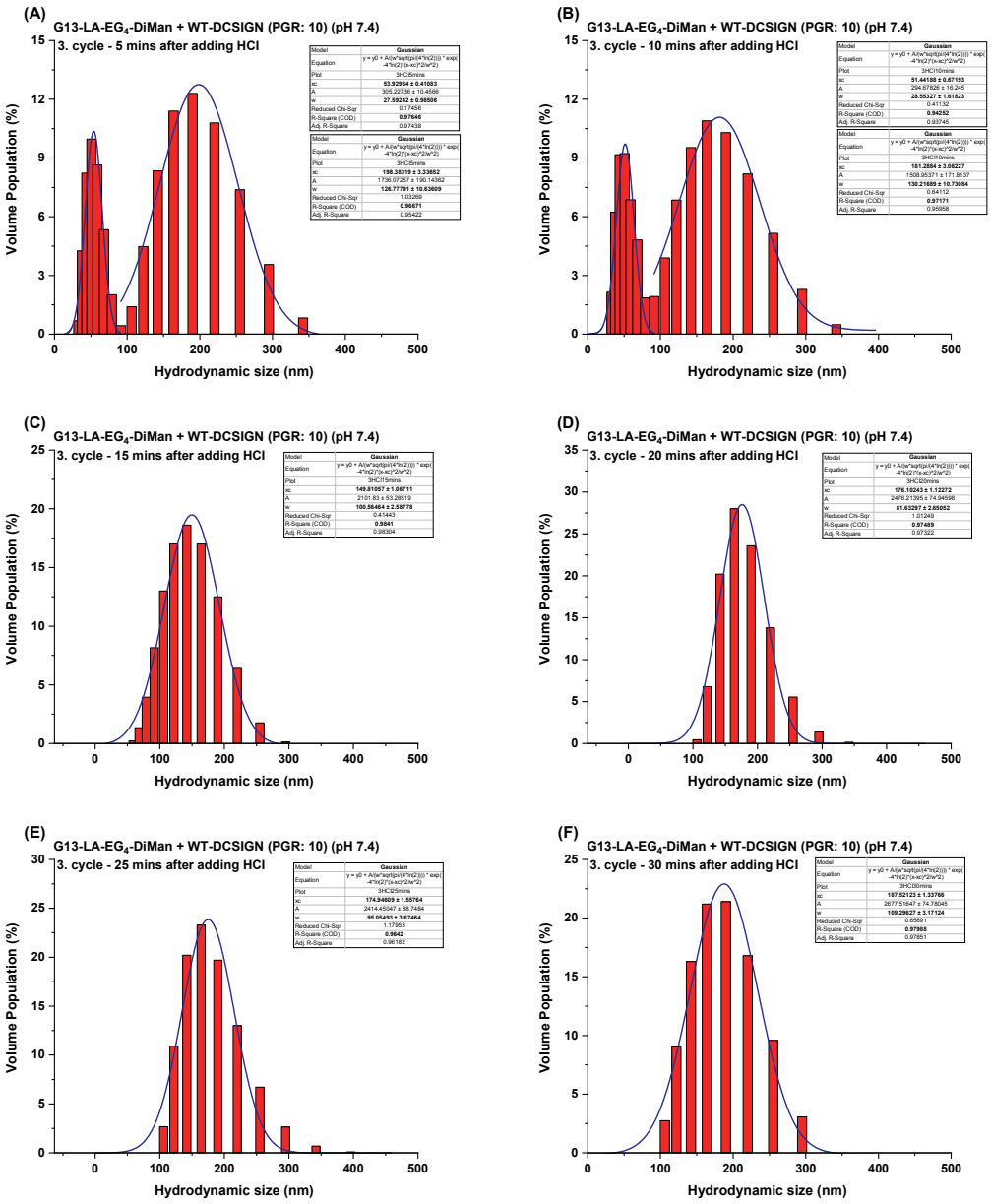

Figure A.10.3. D_h sizes of G13-EG$_4$-DiMan+DC-SIGN when pH is switched from 7.4 to 5.0 (cycle 3). (A) 5 mins, (B) 10 mins; (C) 15 mins; (D) 20 mins; (E) 25 mins; (F) 30 mins after adding HCl

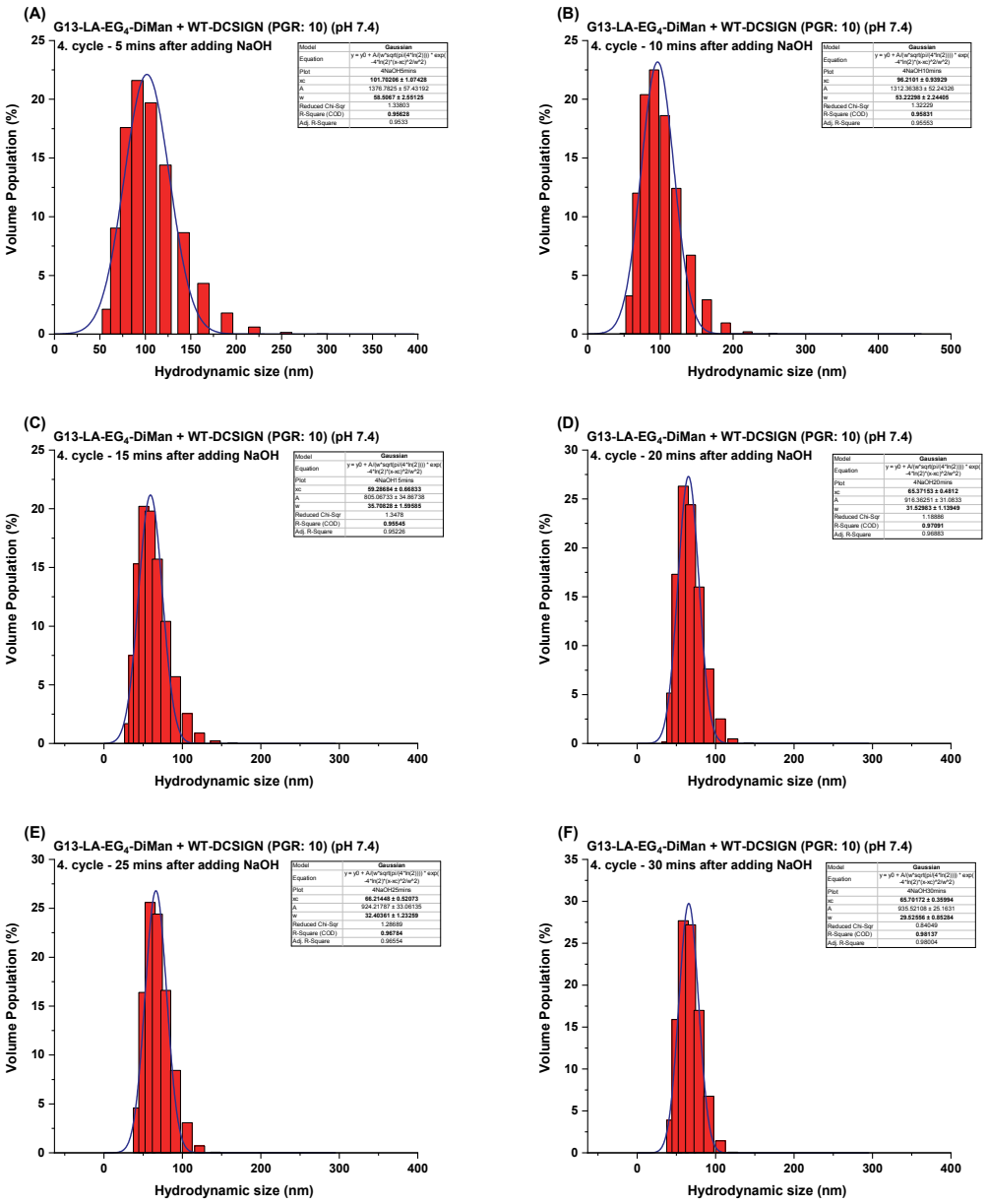

Figure A.10.4. D_h sizes of G13-EG_4-DiMan+DC-SIGN when pH is switched from 5.0 to 7.4 (cycle 4). (A) 5 mins, (B) 10 mins; (C) 15 mins; (D) 20 mins; (E) 25 mins; (F) 30 mins after adding NaOH.

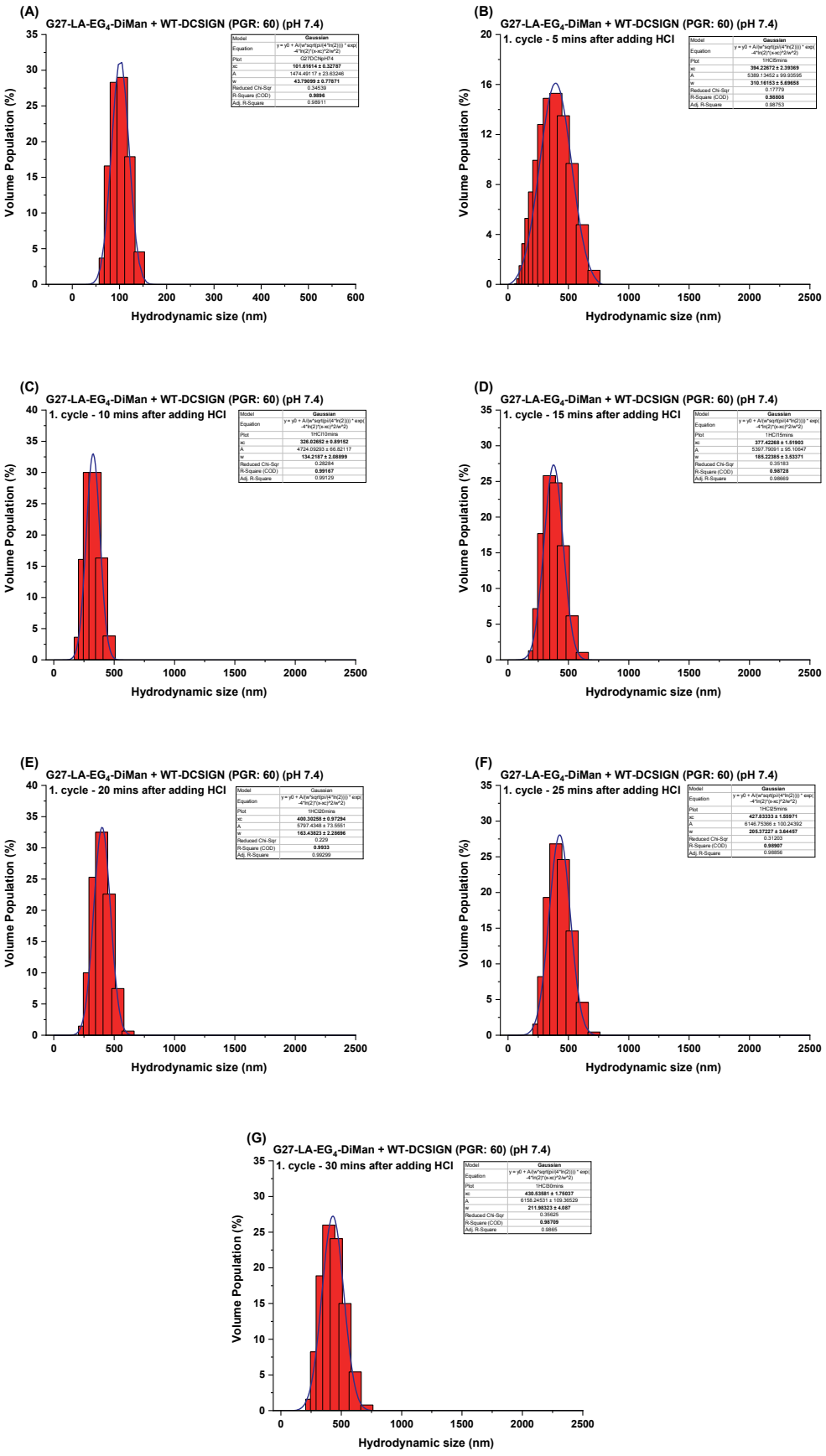

Figure A.10.5. D_h sizes of G27-EG_4-DiMan+DC-SIGN ((A) at pH 7.4) when pH is switched from 7.4 to 5.0 (cycle 1). (B) 5 mins, (C) 10 mins; (D) 15 mins; (E) 20 mins; (F) 25 mins; (G) 30 mins after adding HCl.

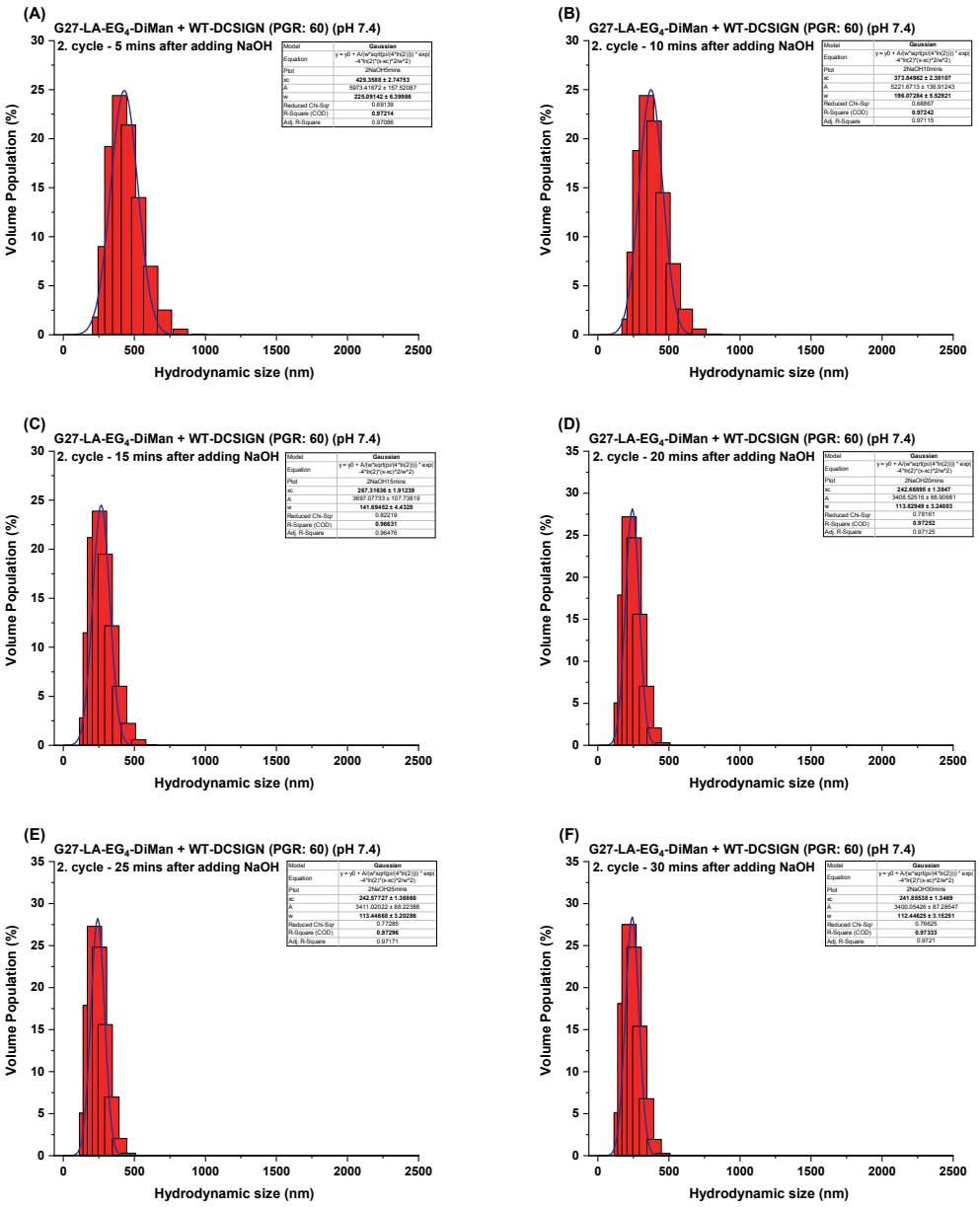

Figure A.10.6. D_h sizes of G27-EG_4-DiMan+DC-SIGN when pH is switched from 5.0 to 7.4 (cycle 2). (A) 5 mins, (B) 10 mins; (C) 15 mins; (D) 20 mins; (E) 25 mins; (F) 30 mins after adding NaOH.

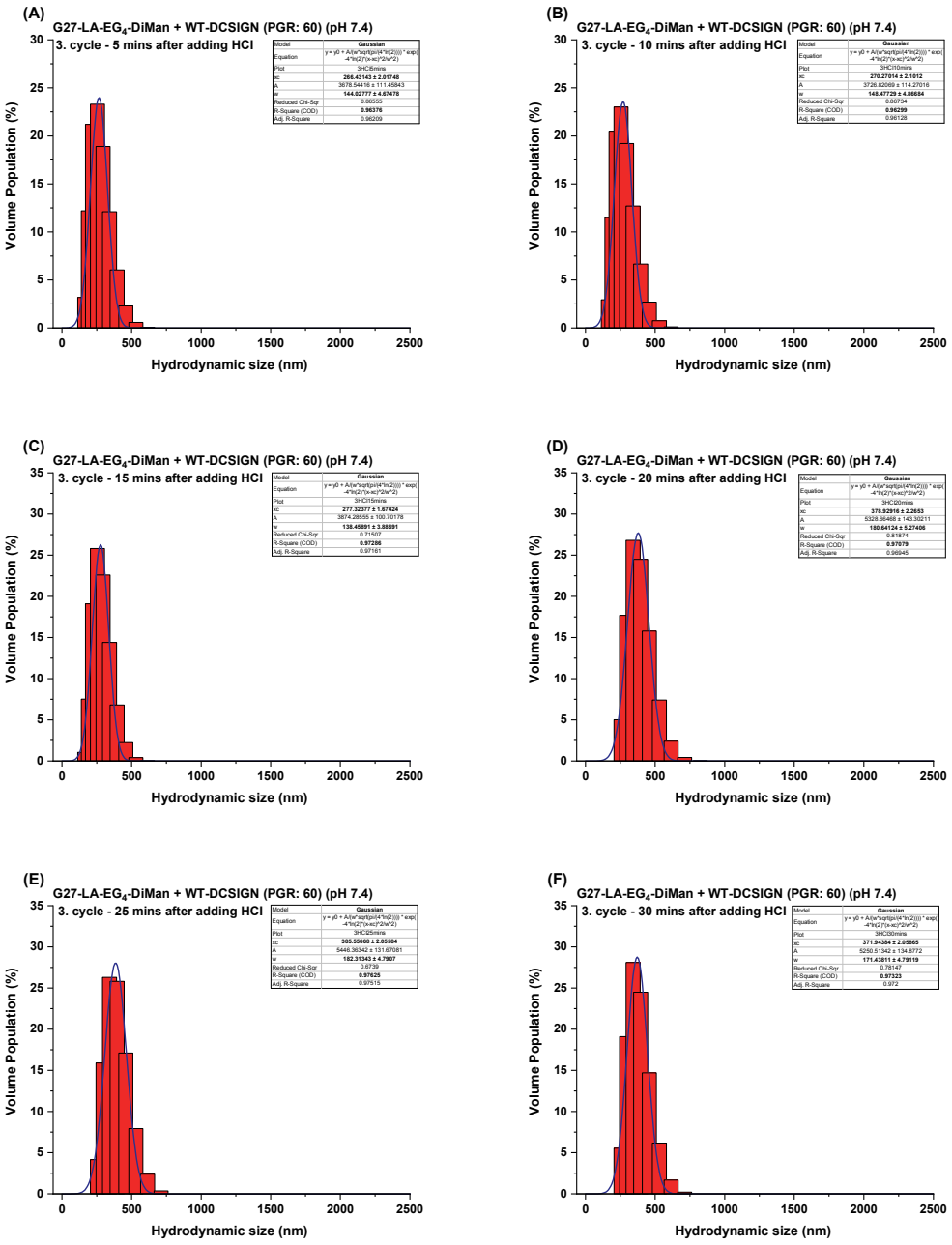

Figure A.10.7. D_h sizes of G27-EG$_4$-DiMan+DC-SIGN when pH is switched from 7.4 to 5.0 (cycle 3). (A) 5 mins, (B) 10 mins; (C) 15 mins; (D) 20 mins; (E) 25 mins; (F) 30 mins after adding HCl.

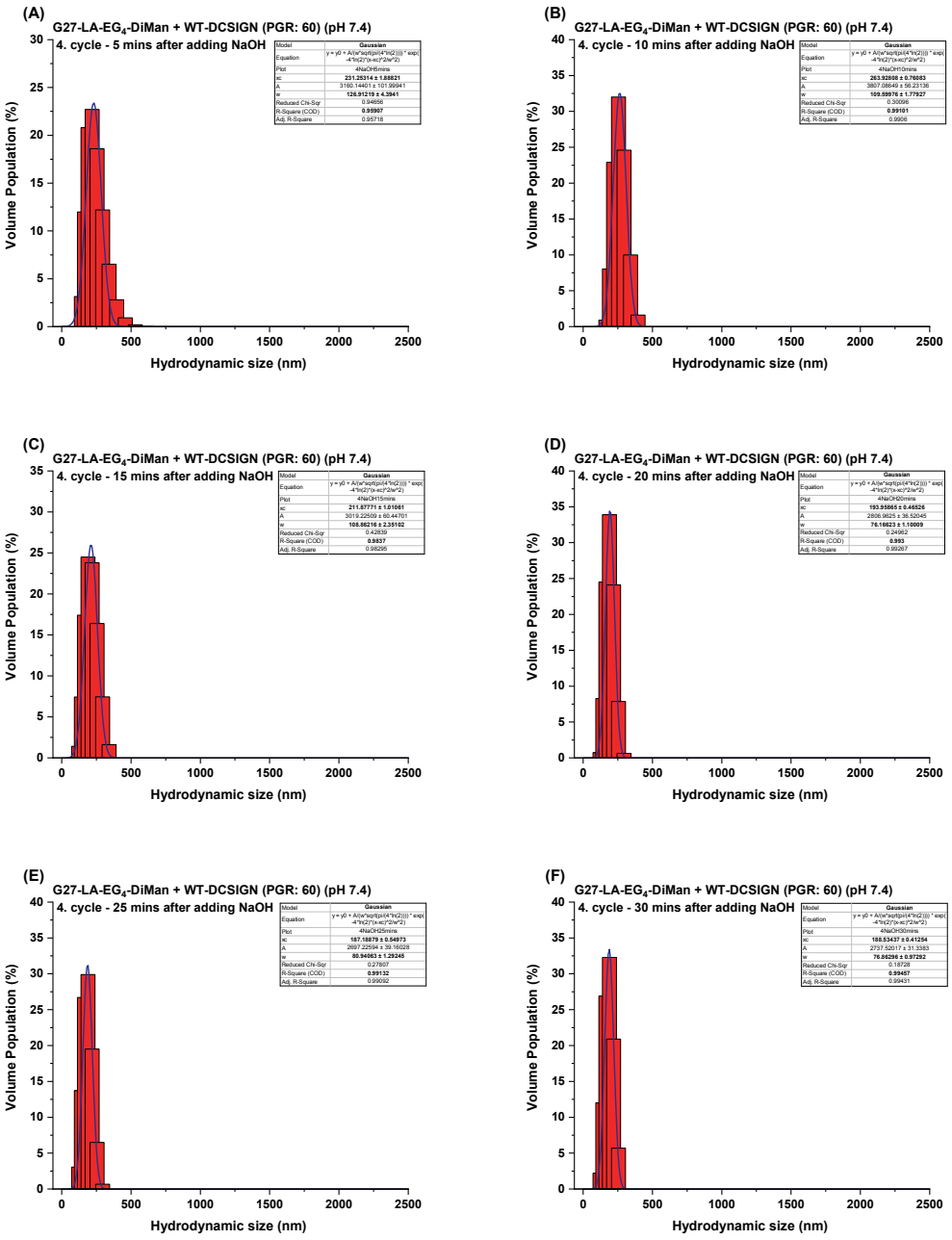

Figure A.10.8. D_h sizes of G27-EG$_4$-DiMan+DC-SIGN when pH is switched from 5.0 to 7.4 (cycle 4). (A) 5 mins, (B) 10 mins; (C) 15 mins; (D) 20 mins; (E) 25 mins; (F) 30 mins after adding NaOH.

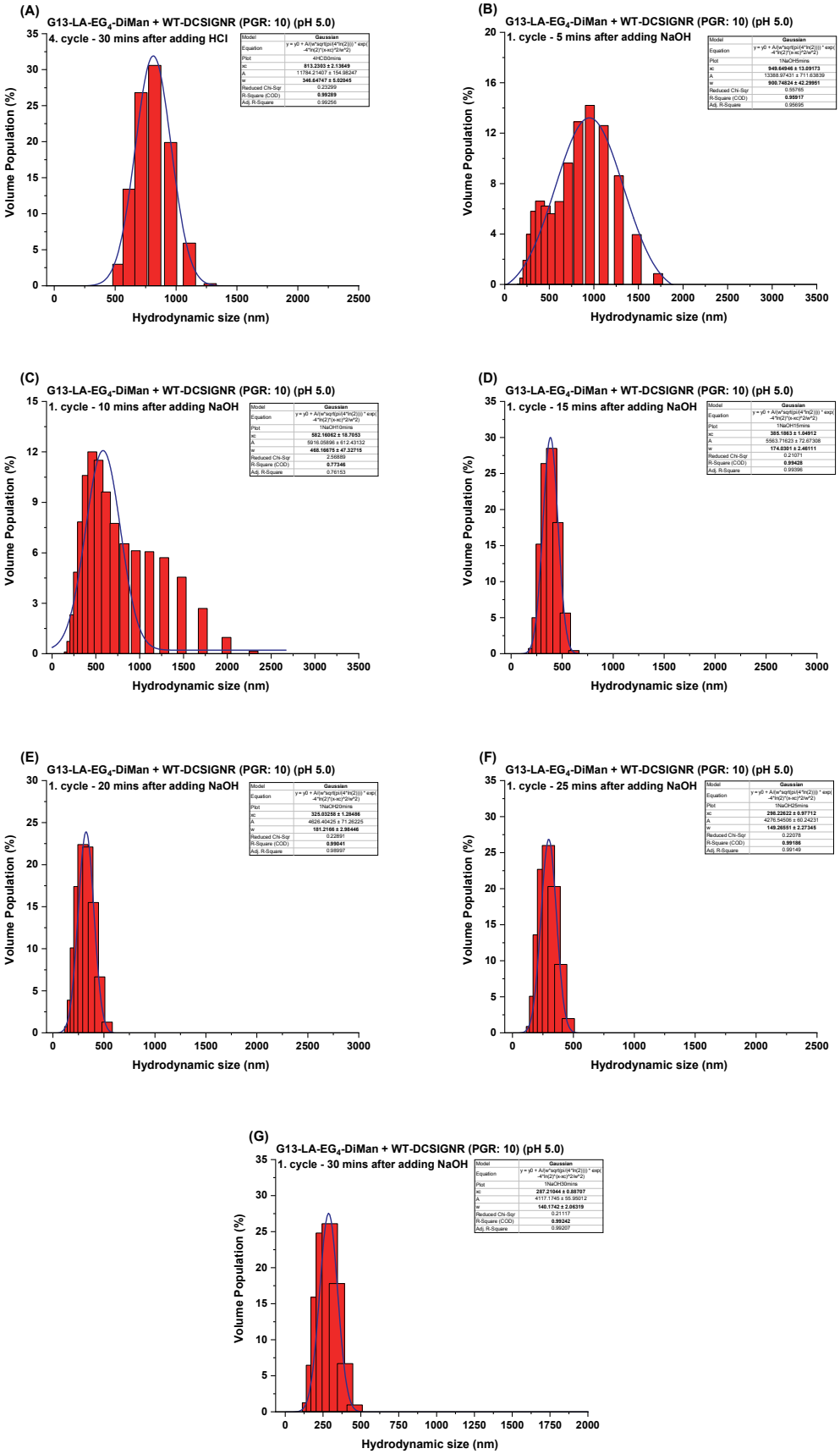

Figure A.10.9. D_h sizes of G13-EG_4-DiMan+DC-SIGNR ((A) at pH 5.0) when pH is switched from 5.0 to 7.4 (cycle 1). (B) 5 mins, (C) 10 mins; (D) 15 mins; (E) 20 mins; (F) 25 mins; (G) 30 mins after adding NaOH.

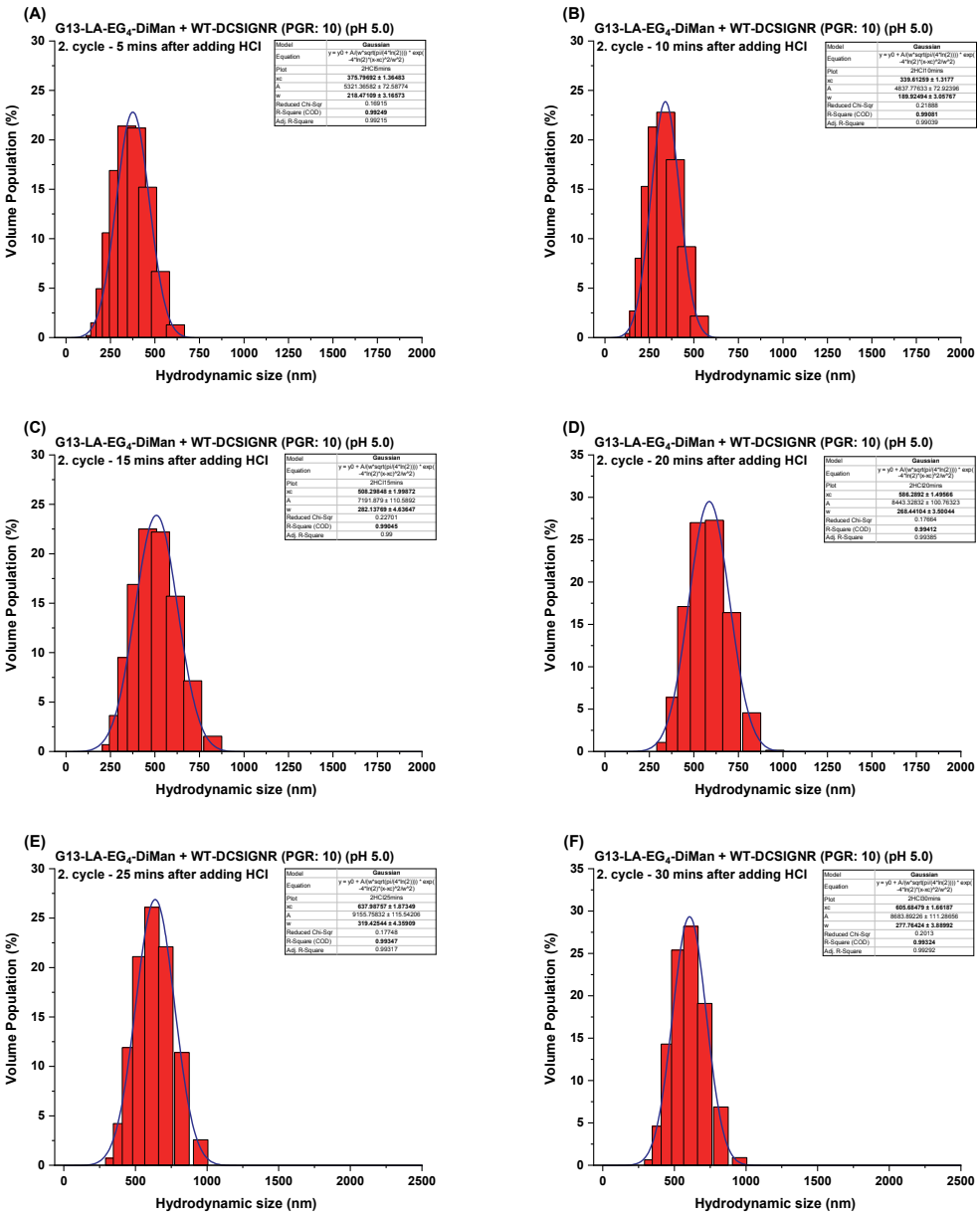

Figure A.10.10. D_h sizes of G13-EG$_4$-DiMan+DC-SIGNR when pH is switched from 7.4 to 5.0 (cycle 2). (A) 5 mins, (B) 10 mins; (C) 15 mins; (D) 20 mins; (E) 25 mins; (F) 30 mins after adding HCl.

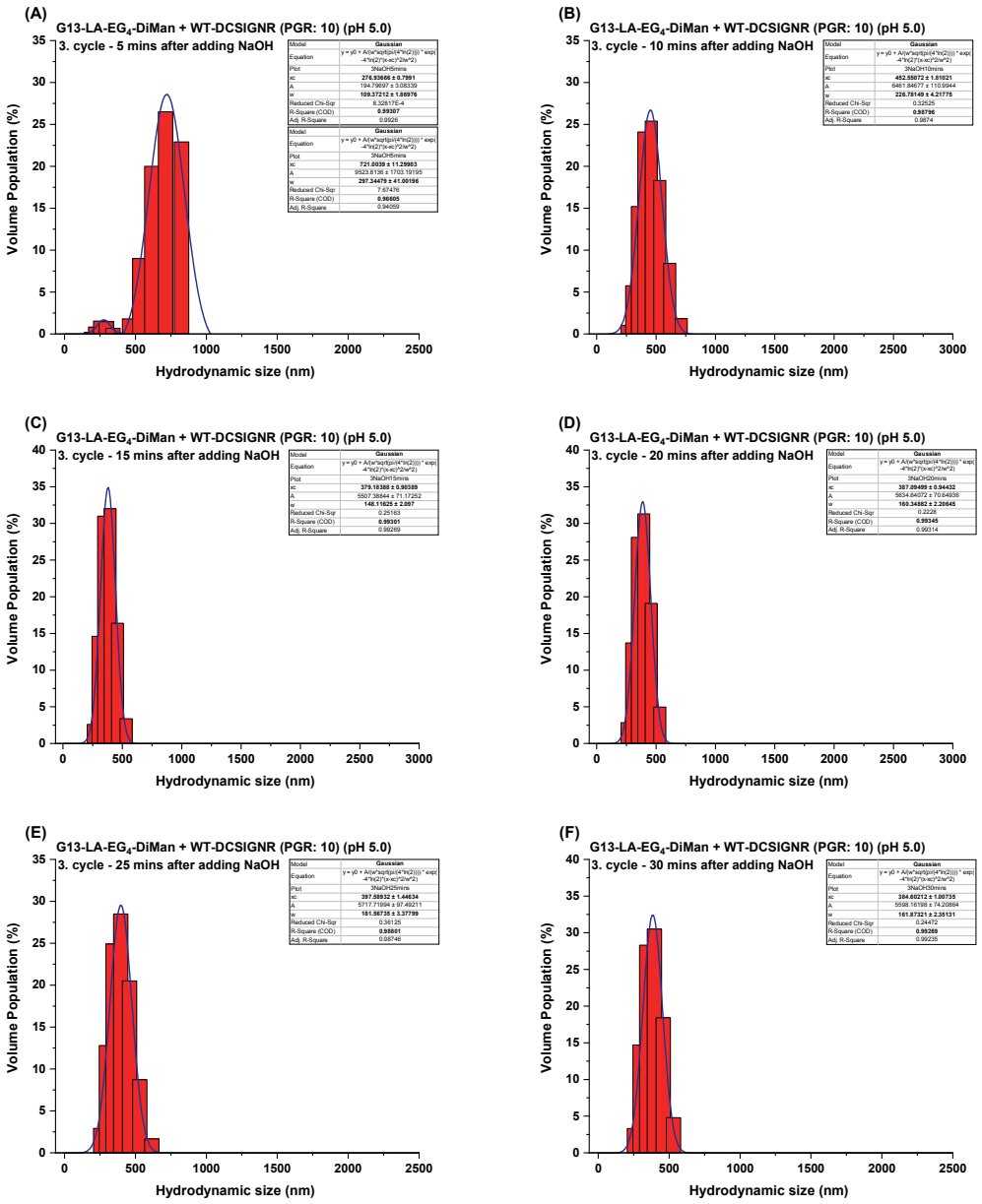

Figure A.10.11. D_h sizes of G13-EG_4-DiMan+DC-SIGNR when pH is switched from 5.0 to 7.4 (cycle 3). (A) 5 mins, (B) 10 mins; (C) 15 mins; (D) 20 mins; (E) 25 mins; (F) 30 mins after adding NaOH.

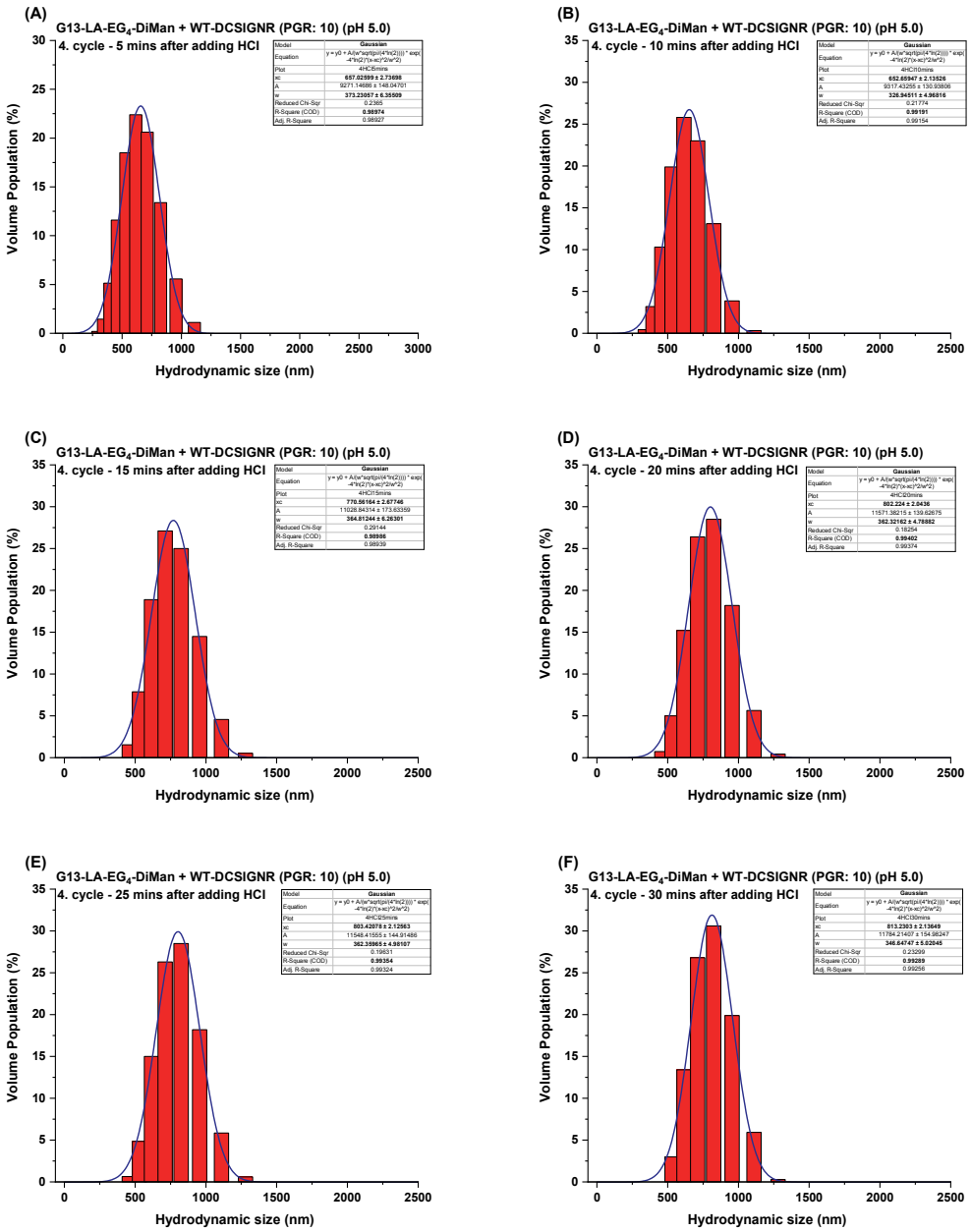

Figure A.10.12. D_h sizes of G13-EG_4-DiMan+DC-SIGNR when pH is switched from 7.4 to 5.0 (cycle 4). (A) 5 mins, (B) 10 mins; (C) 15 mins; (D) 20 mins; (E) 25 mins; (F) 30 mins after adding HCl.

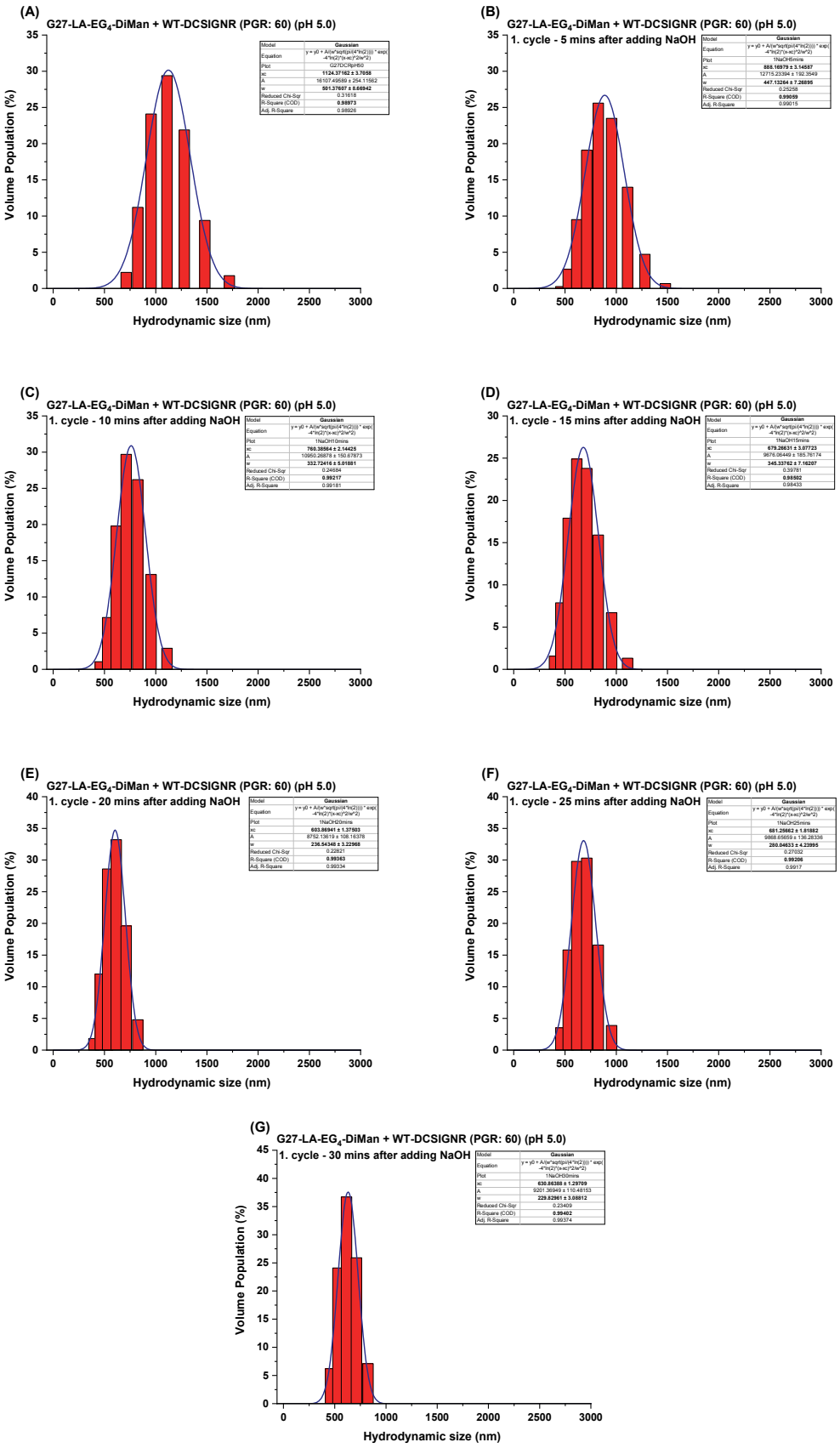

Figure A.10.13. D_h sizes of G27-EG$_4$-DiMan+DC-SIGNR ((A) at pH 5.0) when pH is switched from 5.0 to 7.4 (cycle 1). (B) 5 mins, (C) 10 mins; (D) 15 mins; (E) 20 mins; (F) 25 mins; (G) 30 mins after adding NaOH.

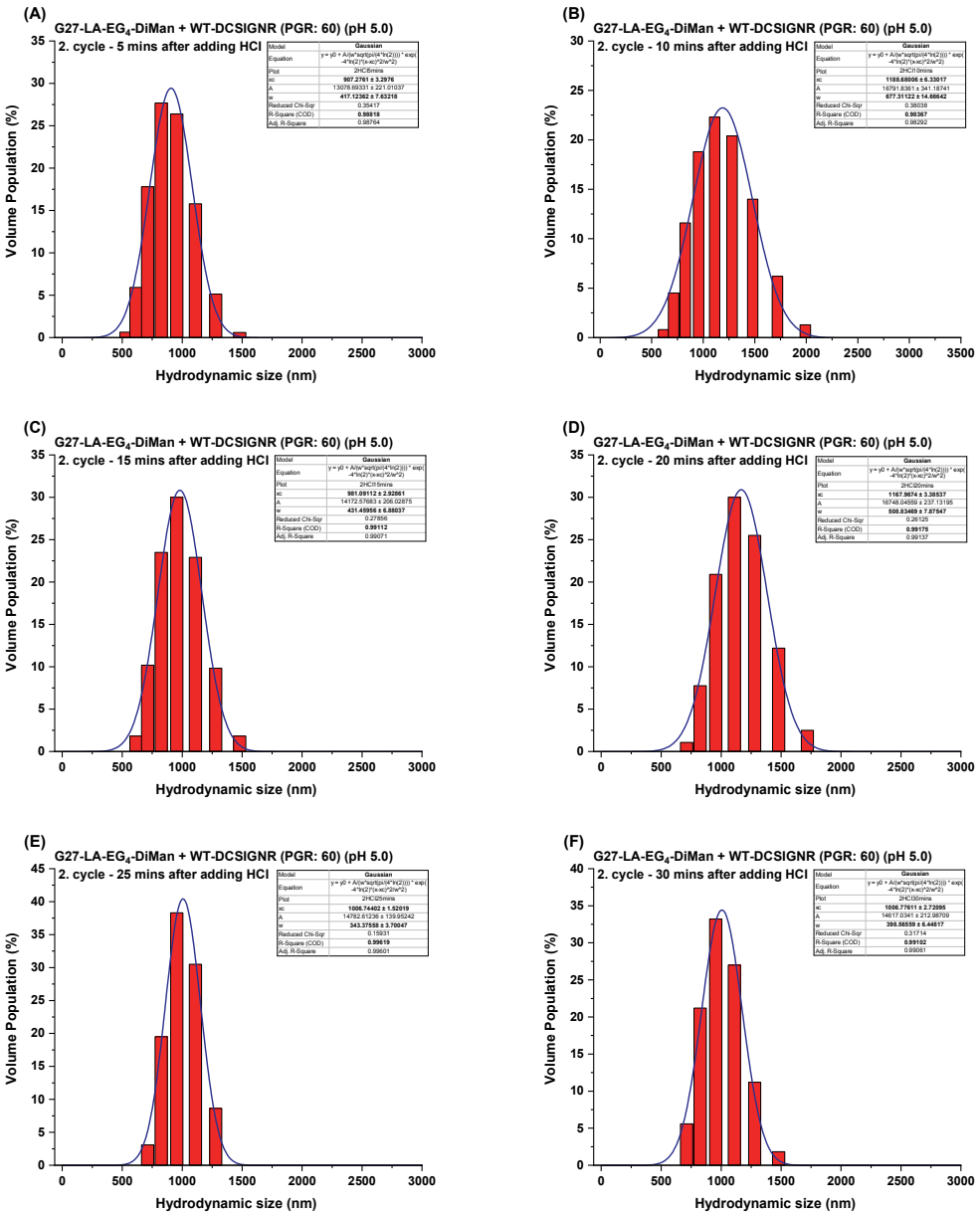

Figure A.10.14. D_h sizes of G27-EG_4-DiMan+DC-SIGNR when pH is switched from 7.4 to 5.0 (cycle 2). (A) 5 mins, (B) 10 mins; (C) 15 mins; (D) 20 mins; (E) 25 mins; (F) 30 mins after adding HCl.

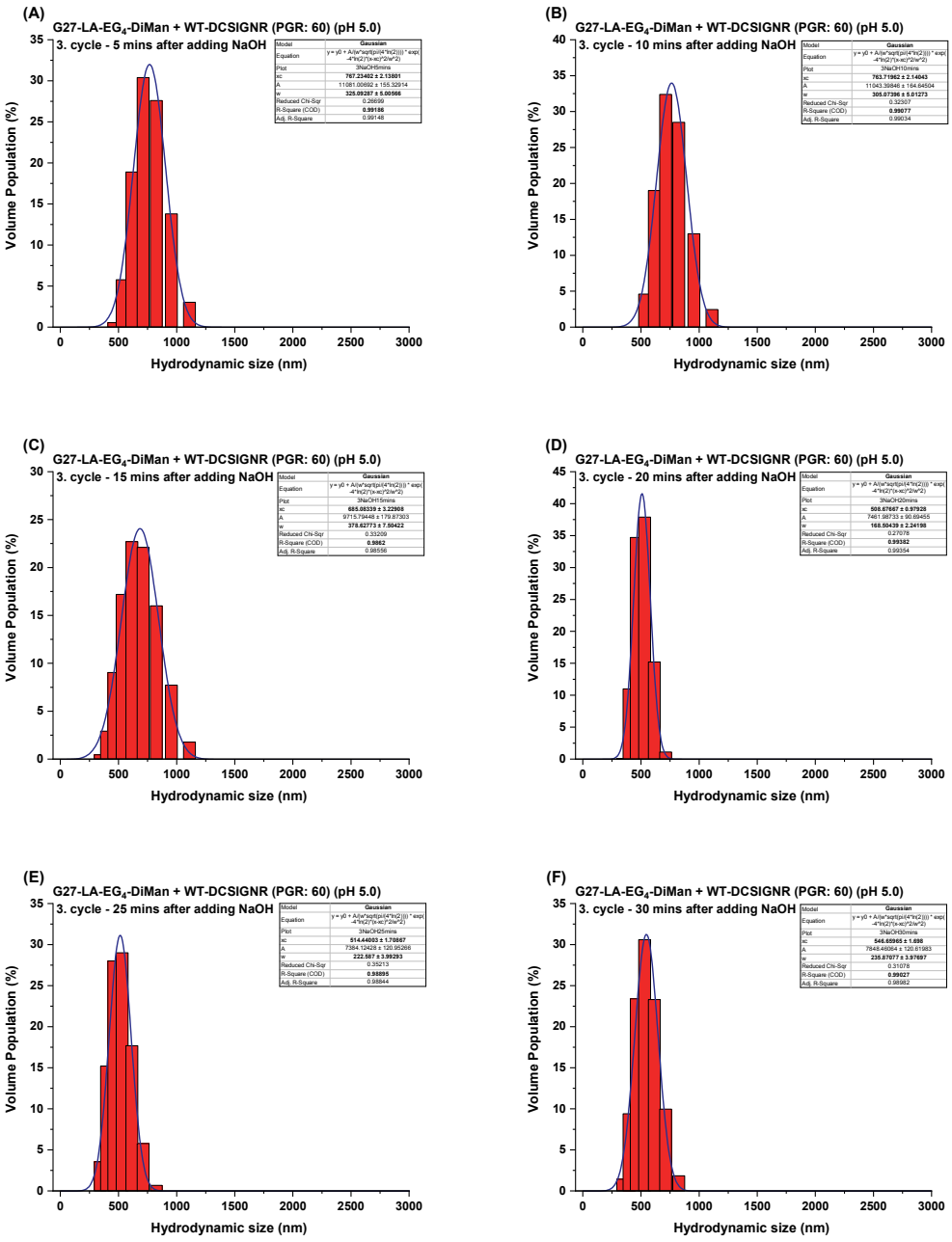

Figure A.10.15. D_h sizes of G27-EG$_4$-DiMan+DC-SIGNR when pH is switched from 5.0 to 7.4 (cycle 3). (A) 5 mins, (B) 10 mins; (C) 15 mins; (D) 20 mins; (E) 25 mins; (F) 30 mins after adding NaOH.

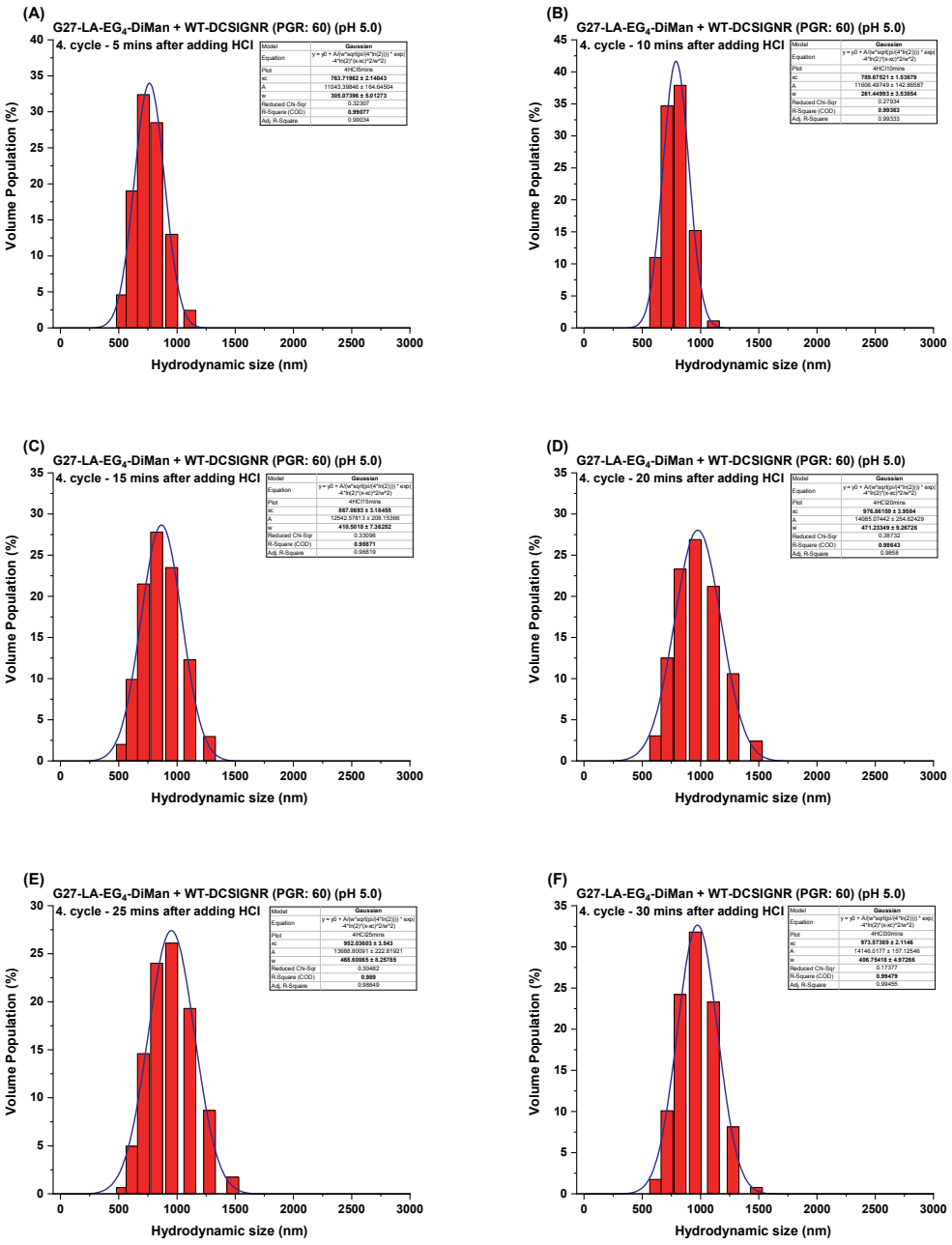

Figure A.10.16. D_h sizes of G27-EG$_4$-DiMan+DC-SIGNR when pH is switched from 7.4 to 5.0 (cycle 4). (A) 5 mins, (B) 10 mins; (C) 15 mins; (D) 20 mins; (E) 25 mins; (F) 30 mins after adding NaOH.